

# BULLETIN OF THE MINERAL RESEARCH AND EXPLORATION

2024

173

ISSN : 0026-4563  
E-ISSN : 2651-3048

## CONTENTS

### Research Articles

- Modelling and computation of gravitational attraction, gradient tensors, rotational and horizontal invariants of Asteroid Bennu (101955), Itokawa (25143) and Eros (433) via 2D Non-Uniform FFT .....1  
İlkin ÖZSÖZ
- Coal quality, mineralogy, petrography, and geochemistry of the high-strontium Bozburun lignite (Malatya, eastern Türkiye) .....19  
Rıza Görkem OSKAY and Ali İhsan KARAYİĞİT
- Vitrinite reflectances and mineralogy of coal clasts in the Late Carboniferous sequences in the two-deep research wells from the Kozlu coalfield (Zonguldak Basin, NW Türkiye).....55  
Ali İhsan KARAYİĞİT and Rıza Görkem OSKAY
- Magnetic inversion modeling of subsurface geologic structures for mineral deposits mapping in southeastern Nigeria.....85  
Ema M. ABRAHAM, Ayatu O. USMAN, Kelvin I. CHIMA, George-best AZUOKO and Iheanyi IKEAZOTA
- Paleocene-Eocene foraminifera from the Tuz Gölü Basin (Salt Lake Basin, Central Türkiye) and their paleoenvironmental interpretations .....107  
Muhittin GÖRMÜŞ, Mustafa YILDIZ, Alper BOZKURT and Aynur HAKYEMEZ
- Active tectonics of western Kosova: Insights from geomorphic and structural analyses..... 153  
Alper GÜRBÜZ, Astrit SHALA, Shemi MUSTAFA and Aytekin ERTEN
- Time-lapse ground penetrating radar (GPR) imaging of used engine oil contamination .....175  
Hafız MOHAMMED NAZİFİ, Ertan PEKŞEN, Ertuğrul GÜRBÜZ and Levent GÜLEN
- A simple and practical tool for indirect determination of the unconfined compressive strength of most common construction materials .....189  
Kamil KAYABALI, Turgay BEYAZ, İlknur KARAASLAN ÖZDEMİR and Deniz YILMAZ
- Evaluation of radioactive properties and microfaunal evidence in the Bosphorus and the Dardanelles straits and Golden Horn sediments...203  
İpek F. BARUT, Engin MERİÇ, Atike NAZİK, Mustafa ERYILMAZ, Feyza DİNÇER and Erol KAM
- Anthropogenic problems threatening major cities: Largest surface deformations observed in Hatay, Türkiye based on SBAS-InSAR .....235  
Şükrü Onur KARACA, Gültekin ERTEN, Semih ERGİNTAV and Shuhab D. KHAN
- Bulletin of the Mineral Research and Exploration Notes to the Authors .....253

**OWNER ON BEHALF OF MTA GENERAL DIRECTORATE  
GENERAL DIRECTOR**

Vedat YANIK

**EXECUTIVE PUBLICATION EDITORIAL BOARD**

Şule GÜRBOĞA (Chairman)

Ural ŞAVUR

Buğra ÇAVDAR

Recep GÜNEY

Neşe OYAL

Selim ÖZALP

Feyza ŞAHİN KILAVUZ

**EDITOR-IN-CHIEF**

Halim MUTLU (Ankara-Türkiye)

**EDITORIAL BOARD**

Orhan R. ABBASOV (Azerbaijan)

Sinan AKISKA (Ankara-Türkiye)

Oğuz ALTUN (Ankara-Türkiye)

Hasret Ozan AVCI (Ankara-Türkiye)

Ali Cemal BENİM (Germany)

Andrea BROGI (Italy)

Ayşe CEBE (Ankara-Türkiye)

Xi-Jie CHEN (Beijing-China)

Dornadula CHANDRASEKHARAM (India)

Buğra ÇAVDAR (Ankara-Türkiye)

Aydın ÇİÇEK (Ankara-Türkiye)

Okay ÇİMEN (Tunceli-Türkiye)

Sevda DEMİR (Ankara-Türkiye)

İsmail DEMİRCİ (Ankara-Türkiye)

Kıymet DENİZ (Ankara-Türkiye)

Fuat ERKÜL (Antalya-Türkiye)

Ranjith Pathegama GAMAGE (Monash-Australia)

Şule GÜRBOĞA (Ankara-Türkiye)

Recep GÜNEY (Ankara-Türkiye)

Alper GÜRBÜZ (Niğde-Türkiye)

Tuba ISIK (Ankara-Türkiye)

Olca İNANÇ (Ankara-Türkiye)

Doğan KALAFAT (İstanbul-Türkiye)

Ferhat KAYA (Finland)

Sándor KELE (Budapest-Hungary)

Cumhur Özcan KILIÇ (Ankara-Türkiye)

Onur Eser KÖK (Hatay-Türkiye)

Büşra Bihter KURT (Ankara-Türkiye)

Timothy KUSKY (China)

David LENTZ (New Brunswick-Canada)

Kotha MAHENDER (India)

Mustapha MEGHRAOUI (France)

Robert MORITZ (Geneve-Switzerland)

Soumyajit MUKHERJEE (India)

Roland OBERHAENSLI (Germany)

Neşe OYAL (Ankara-Türkiye)

Semiha ÖNCÜ (Ankara-Türkiye)

Selim ÖZALP (Ankara-Türkiye)

Ayşe ÖZDEMİR (Van-Türkiye)

Şafak Gökhan ÖZKAN (İstanbul-Türkiye)

Eren PAMUK (Ankara-Türkiye)

Spyridon PAVLIDES (Egypt)

Franco PIRAJNO (Australia)

Mavinakere Eshwaraiah RAGHUNANDAN (Malaysia)

Rossana SANFILIPPO (Italy)

Ökmen SÜMER (İzmir-Türkiye)

Deniz TİRİNGA (Ankara-Türkiye)

Orlando VASELLI (Italy)

Lu WANG (China)

Ergül YAŞAR (Ankara -Türkiye)

**ADVISORY BOARD**

Erdin BOZKURT (Ankara-Türkiye)

Osman ÇANDAN (İzmir-Türkiye)

Ahmet GÖKÇE (Sivas-Türkiye)

M. Cemal GÖNCÜOĞLU (Ankara-Türkiye)

Nilgün GÜLEÇ (Ankara-Türkiye)

Cahit HELVACI (İzmir-Türkiye)

Kamil KAYABALI (Ankara-Türkiye)

Nuretdin KAYMAKÇI (Ankara-Türkiye)

Aral İ. OKAY (İstanbul-Türkiye)

Cengiz OKUYUCU (Konya-Türkiye)

Osman PARLAK (Adana- Türkiye)

Okan TÜYSÜZ (İstanbul-Türkiye)

İbrahim UYSAL (Trabzon-Türkiye)

Taner ÜNLÜ (Ankara-Türkiye)

Yücel YILMAZ (İstanbul-Türkiye)

**MANAGING EDITOR**

Banu Ebru BİNAL (Head of the Department of Scientific Documentation and Presentation), e-posta: banu.binal@mta.gov.tr

**LOCATION OF MANAGEMENT**

Bilimsel Dokümantasyon ve Tanıtma Dairesi Başkanlığı

Maden Tetkik ve Arama Genel Müdürlüğü

Çukurambar Mahallesi

Dumlupınar Bulvarı No: 11 06530

Çankaya/ANKARA

e-mail: bilimsel\_daiesi@mta.gov.tr

Bull. Min. Res. Exp. is indexed and abstracted in TR Dizin, Emerging Source Citation Index (ESCI), Scopus, The ICI Journals Master List (Copernicus), Directory of Open Access Journals (DOAJ), Open Academic Journals Index (OAJI), Georef, MIAR, EBSCO and Zoological Record.

The Bulletin of the Mineral Research and Exploration is published in three issues in a year. Each volume is published in Turkish and English in pdf format on the website of Bulletin of the Mineral Research and Exploration and English issue published in print. The English volume of the "Bulletin of the Mineral Research and Exploration" can be obtained from "BDT Department" free of charge, either directly or ordered by adding postage fee from the correspondence address. Typesetting and printing operations are carried out and followed by the Publication Service of the Scientific Documentation and Publicity Department. e-mail: bilimsel\_daiesi@mta.gov.tr

The section of "notes to the authors", format, copyright and other information can be obtained from www.mta.gov.tr as PDF files.

**Printed Date:** 22.04.2024

**Printing House:** Kuban Matbaacılık - İvedik Organize Sanayi Matbaacılar Sitesi 1514. Sokak No: 20

Phone: 0312 395 2070 • Fax: 0312 395 3723 • www.kubanmatbaa.com

**Periodical**

**ISSN:** 0026-4563

**E-ISSN:** 2651-3048

© All rights reserved. This journal and the individual contributions including in the issue are under copyright by the General Directorate of Mineral Research and Exploration (MTA), and may not be reproduced, resold, and used without permission and addressing the bulletin.



# Bulletin of the Mineral Research and Exploration

<http://bulletin.mta.gov.tr>



## Modelling and computation of gravitational attraction, gradient tensors, rotational and horizontal invariants of Asteroid Bennu (101955), Itokawa (25143) and Eros (433) via 2D Non-Uniform FFT

İlkin ÖZSÖZ<sup>a\*</sup>

<sup>a</sup> General Directorate of Mineral Research and Exploration, Department of Marine Research, Ankara, Türkiye

Research Article

Keywords:

2D NU-FFT, Bennu (101955), Itokawa (25143), Eros (433), Gravity gradient tensors.

### ABSTRACT

*The internal structure and mass distribution of the terrestrial objects are yet unknown. The 2D gravity model with a constant density of the terrestrial objects can shed light on the surficial or textural heterogeneity due to topographic variations of the terrestrial objects. Three different asteroids, which are Bennu (101955), Itokawa (25143) and Eros (433) are modelled in this study. During the modelling phase, a different number of edges, elements, nodes, and faces are used to describe the 3D models of Bennu, Itokawa, and Eros. These 3D models are used in 2D Non-Uniform Fast Fourier Transform (NU-FFT) applications to obtain gravitational attraction with a constant density polyhedron model. Tensor gradients and tensor invariants of the modelled gravity anomaly are calculated. Three major outcomes are interpreted from tensor gradient and tensor invariants. Firstly, textural heterogeneity due to relatively low topography is detected in the central part of Bennu. Secondly, considerably different properties which can be related to surface variations between the two lobes of Itokawa are observed. Lastly, directional surficial heterogeneities were detected in Eros.*

Received Date: 28.04.2022

Accepted Date: 14.02.2023

## 1. Introduction

The forward solution of the gravity potential and its derivatives are considered to have a widespread application for different subjects. The gravity potential is described as a volume integral, and the volume integral is generally solved in the space domain by analytical methods. Alternatively, spectral-domain solutions can be used to solve volume integrals. If space domain and spectral domain solutions are compared, it is possible to say that space domain solutions are more accurate but cost more computation time. Therefore, spectral-domain solutions are the more appropriate

method for computing the gravity effect of the 2D/3D grids with small grid spacing.

Cooley and Tukey (1965) fundamentally described the FFT algorithm. In this study, FFT process was applied in three steps. Firstly, the Fourier transform of the given 2D/3D grid is computed. Then, the data is analytically or numerically solved in the spectral domain. Lastly, the spectrum is transformed back to the space domain by the inverse Fourier transform. Analytical solutions of the gravity effect in the spectral domain for the rectangular prism with constant and variable density are derived by many authors

Citation Info: Önsöz, İ. 2024. Modelling and computation of gravitational attraction, gradient tensors, rotational and horizontal invariants of Asteroid Bennu (101955), Itokawa (25143) and Eros (433) via 2D Non-Uniform FFT. Bulletin of the Mineral Research and Exploration 173, 1-18. <https://doi.org/10.19111/bulletinofmre.1251299>

\*Corresponding author: İlkin ÖZSÖZ, [ilkin.ozsoz@mta.gov.tr](mailto:ilkin.ozsoz@mta.gov.tr)

(Bhattacharyya, 1966; Chai and Hinze, 1988; Chenot and Debeglia, 1990; Lee and Biehler, 1991; Tontini et al., 2009; Wu and Chen, 2016). Furthermore, these analytical solutions of the gravity effect can be derived using polyhedron models with constant or variable density (Pedersen, 1978; Wu, 1983; Hansen and Wang, 1988).

The gravity vector and its gradient tensor can be expressed by differential relation in the spectral-domain (Wu, 2019). Wu and Chen (2016) mentioned the major limitations of the Fourier transform are quadrature error and truncation error within the computed forward anomaly. In order to eliminate major drawbacks of Fourier-domain methods, the non-uniform FFT (NU-FFT) technique was introduced by Wu and Tian (2014) and Wu (2021). This technique uses both the shift sampling method (Chai and Hinze, 1988) and Gauss quadrature rules. Many authors (Wu and Tian, 2014; Wu, 2016; Wu and Chen, 2016; Wu and Lin, 2017; Wu, 2019; Wu, 2021*a*) showed that the NU-FFT algorithm produces better results than the conventional FFT algorithm for arbitrary-shaped models. Furthermore, less quadrature error was observed in NU-FFT results than in conventional FFT. However, neither NUFFT nor traditional FFT methods can eliminate truncation errors, which are controlled by Nyquist frequency.

NU-FFT and gradient tensor applications in the spectral domain were applied to Bennu, Itokawa, and Eros asteroids. The noticeable properties of Bennu, Itokawa and Eros can be summarised as; (1) weathering, impact, and other processes have altered the surface of Bennu, as evidenced by mass displacement, cracks, and craters (Barnouin et al., 2019; DellaGiustina et al., 2019; Walsh et al., 2019), (2) Itokawa appears to be composed of a rubble-pile structure rather than a single integrated mass (Saito et al., 2006), (3) Eros has a cratered surface and is also encrusted in a layer of regolith and rocks (Veverka et al., 2001; Chapman et al., 2002; Robinson et al., 2002; Thomas et al., 2002; Richardson et al., 2004).

The aim of this paper is to digitize 3D models of Itokawa, Eros and Bennu asteroids and compute their gravity anomalies and gradient tensors by the 2D NU-FFT technique. The modelled gradient tensors are

used in the computation of rotational and horizontal invariants which can be used as edge detection techniques, surficial heterogeneity analysis due to abnormal elevation or topography for the asteroid models. The paper offers that digitising various file extensions (“*.off*”, “*.stl*”, “*.ply*” and “*.mesh*”) to obtain elements, faces and edges of the provided 3D model and compute its gravity anomaly and gradients for rotational and horizontal invariant techniques to detect major surficial heterogeneities of the celestial bodies. Briefly, the results of this study indicate that an anomalous forward modelled gravity anomaly due to relatively low topography is discovered in the middle region of Bennu, significant differences in surficial properties are seen between Itokawa’s two lobes and directional surficial heterogeneities were discovered in Eros. The gravity field of planetary bodies could identify information about interior mass distribution if direct gravity observations were available (Scheeres et al., 2020). However, forward modelled gravity fields with constant density can only clarify the surficial or textural heterogeneities of terrestrial bodies. Since the constant density forward modelling algorithm was used, the inner structure of the asteroid could not be interpreted. The lows and highs in gravity anomaly and its derivatives can be linked to topographical variations.

## 2. Physical Properties of Asteroid Bennu, Itokawa and Eros

### 2.1. Asteroid Bennu (101955)

The asteroid was discovered on 11 September 1999 by the Lincoln Near-Earth Asteroid Research program (Stokes et al., 2000). Bennu (101955) is a small near-Earth celestial body with a half kilometer diameter and an equatorial bulge (Figure 1). The structure of the asteroid Bennu is a rubble-pile, which is inferred from low-density measurements, and its surface is rocky (Barnouin et al., 2019; DellaGiustina et al., 2019; Lauretta et al., 2019; Scheeres et al., 2019; McMahon et al., 2020). Scheeres et al., (2019) suggested that the dynamical evolution of Bennu is quite complex owing to the non-spherical shape of its body.

The surface of Bennu is affected by weathering, impact, and other processes since mass movement, fractures, and craters are noted (Barnouin et al., 2019;

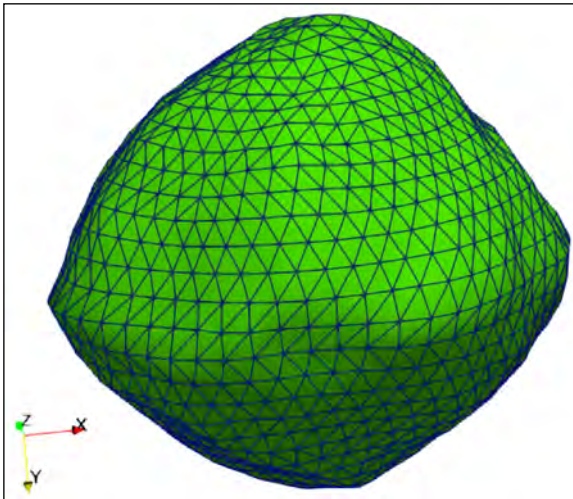


Figure 1- Shape of the asteroid Bennu with digitised edges.

DellaGiustina et al., 2019; Walsh et al., 2019). Signs of exfoliation events are observed in the boulders of Bennu due to the existence of disaggregated thin layers at the surface (Molaro et al., 2020a). According to Molaro et al., (2020b), physical features of an asteroid Bennu stems from the thermal fatigue process, which might be linked to thermal cycling (Holzhausen, 1989).

Asteroid Bennu was modelled (Molaro et al., 2015; Hazeli et al., 2018; El Mir et al., 2019) and laboratory studies (Thirumalai and Demou, 1970; Levi, 1973; Delbo et al., 2014) were conducted in terms of the thermal fatigue process by many researchers. The results of models and laboratory work suggested that chemical and biogenic weathering due to thermal fatigue triggered the exfoliation of rock boulders (Waragai, 1998; McFadden et al., 2005; Fletcher et al., 2006; Eppes et al., 2010; Eppes and Keanini, 2017; Lamp et al., 2017).

Chesley et al. (2014) investigated the bulk density of Bennu via orbital deviations and thermal missions. The estimated bulk density of asteroid Bennu is

$1260 \pm 70 \text{ kg/m}^3$ . Furthermore, they shed light on the rubble-pile internal structure of Bennu by presenting the macro-porosity range as  $40 \pm 10 \%$ . The mass of the terrestrial body is estimated as  $7.8 \pm 0.9 * 10^{10} \text{ kg}$  and  $GM = 5.2 \pm 0.6 \text{ m}^3/\text{s}^2$  (Chesley et al., 2014). The size and shape parameters of Bennu are provided in Table 1.

## 2.2. Asteroid Itokawa (25143)

The asteroid was discovered on 26 September 1998 by the Lincoln Near-Earth Asteroid Research program (Stokes et al., 2000). In November 2005, the Hayabusa spacecraft collected regolith samples on the asteroid's surface, and these samples returned to Earth in June 2010 (Yano et al., 2006; Tanbakouei et al., 2019). Nakamura et al. (2011) showed that vast rocks and stones are non-uniformly distributed on Itokawa's surface. Itokawa seems likely to have a rubble-pile structure instead of a single consolidated structure. A wide range of boulder sizes, ranging from meters to hundreds of meters, are analysed on the surface of Itokawa (Saito et al., 2006).

Fujiwara et al. (2006) resembled Itokawa's shape to a sea otter (Figure 2). The asteroid consisted of a smaller head part and a larger body part. The head part of Itokawa has more facets (Saito et al., 2006) rather than the body part and this physical characteristic has been taken into account during the modelling stage. The body and head parts have a rounded shape which indicates a long period of evolution (Fujiwara et al., 2006).

Whiteley et al. (2002) claimed that Itokawa might be either a loosely consolidated body or a young terrestrial body that has been exposed to collisional disruption. Large facets on Itokawa indicate that the asteroid has experienced large impacts in the past, but these impacts cannot be transmitted to the internal

Table 1- Bennu size and shape parameters (Lauretta et al., 2015)

Parameter	Value	Uncertainty ( $\pm$ )
Mean diameter (m)	492	20
Polar dimension (m)	508	52
Equatorial dimensions (m)	565 x 535	10
Volume ( $\text{km}^3$ )	0.0623	0.006
Surface Area ( $\text{km}^2$ )	0.786	0.04

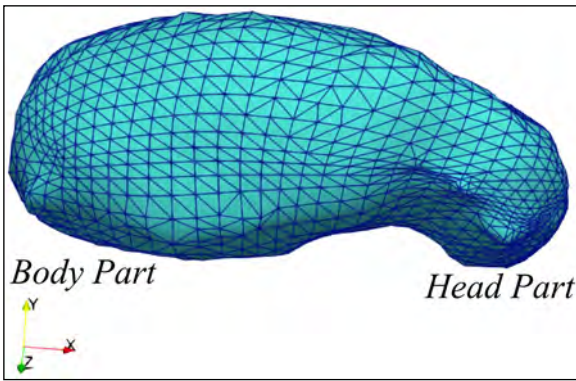


Figure 2- Shape of the asteroid Itokawa with digitised edges.

body due to the high porosity structure (Asphaug et al., 1998).

There are two scenarios for the origin of Itokawa. The first scenario suggests that the head part and body part were formed separately (Saito et al., 2006). Then, these two parts contacted at a relatively slow speed, and the original shape of the body and head parts was protected (Saito et al., 2006). The second scenario suggests that a large impact formed the neck part, which is located between the head and body parts (Fujiwara et al., 1993). Before the impact event, the asteroid was a single body (Fujiwara et al., 1993).

The physical properties of asteroid Itokawa were found by the Hayabusa spacecraft. These properties are provided in Table 2.

### 2.3. Asteroid Eros (433)

Asteroid Eros was discovered on 13 August 1989 by Gustav Witt (Yeomans, 1995) and it was observed before any definition between 30 November 1988 and 5 December 1988 with the Arecibo telescope (Ostro et al., 1992; Magri et al., 2001). Near-Earth Asteroid Rendezvous (NEAR) mission (Cheng et al., 1997) provided crucial information about Eros' pole orientation, spin rate, orbit, mineralogy, chemical

composition and internal structure (McCoy et al., 2000). The mission was started on 14 February 2000. The results of the mission indicated that Eros has a cratered surface and covered with a regolith layer and boulders (Veveřka et al., 2001; Chapman et al., 2002; Robinson et al., 2002; Thomas et al., 2002; Richardson et al., 2004).

Eros is an S-class asteroid (Figure 3) that is composed of pyroxene, olivine, plagioclase, and ordinary chondrites (McCoy et al., 2000). There are two theories about the formation of the asteroid Eros. The first theory claims that space weathering and differentiation processes result in hemispheric-scale heterogeneity (Murchie and Pieters, 1996; Veverka et al., 1999). The other theory states that the existence of ordinary chondrites presents unaltered composition from the solar system's formation process. The chemical structure of ordinary chondrites is almost identical to that of the Sun. Therefore, it might be said that Eros is an unaltered body after the accretion of the chondrites (Yeomans, 1995).

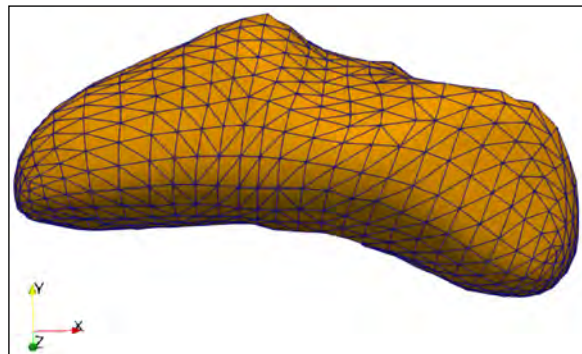


Figure 3- Shape of the asteroid Eros with digitised edges.

The Near mission provided the size and shape parameters of Asteroid Eros. These parameters of the Asteroid Eros are illustrated in Table 3.

Table 2- Itokawa size and shape parameters (Fujiwara et al., 2006).

Parameter	Value	Uncertainty ( $\pm$ )
Size (m)	535 x 294 x 209	1
Density (kg/cm <sup>3</sup> )	1000	130
Mass (kg)	3.51 x 10 <sup>10</sup>	0.105 x 10 <sup>10</sup>
Volume (m <sup>3</sup> )	1.84 x 10 <sup>7</sup>	0.092 x 10 <sup>7</sup>

Table 3- Eros size and shape parameters (Miller et al., 2002; Konopliv et al., 2002; Kanamaru et al., 2019).

Parameter	Value	Uncertainty ( $\pm$ )
Size (km)	13 x 13 x 33	–
Density (kg/cm <sup>3</sup> )	2670	30
Mass (kg)	6.6904 x 10 <sup>15</sup>	0.003 x 10 <sup>15</sup>
Volume (km <sup>3</sup> )	2503	25

### 3. Methods

#### 3.1. Digitizing and Re-Modelling of 3D Asteroid Models

3D models of the asteroids were downloaded from <https://solarsystem.nasa.gov/>. The models can be downloaded as either gITF or USDZ file. In this paper, gITF file (.glb) format is used for Bennu, Itokawa and Eros models.

The “gITF” file format can be visualised in ParaView which is open-source data analysis and visualisation software. Paraview’s Visualisation Toolkit comprises C++, Java and Python libraries to process the input model and visualise the processed model. For a large dataset, ParaView can use distributed memory to shorten the processing time. Furthermore, ParaView allows users to convert file formats from “.glb” to “.stl” (Ayachit et al., 2015). In this study, the “.stl” file format is required to digitise edges, elements (or mesh tetrahedral), faces, and nodes (or mesh points) of the given 3D model. Therefore, Paraview was used for the conversion of data formats to “.stl” and for visualising the converted 3D model (Table 4).

After conversion from “.glb” to “.stl”, data is ready for the digitising phase. Tetgen open-source C++ program can be used for digitising processes for arbitrary complex models. It can generate tetrahedral meshes to detect edges, elements, faces, and nodes of the given model. Various file extensions (.off, .stl, .ply and .mesh) are readable in Tetgen (Si, 2015). In this study, the “.stl” format, which was converted from “.glb” in Paraview, was used as an input file extension

in Tetgen. To extract, nodes (.node), elements (.ele), faces (.face) and edges (.edge), “tetgen -fe Name.stl” command was run in Windows Powershell or Git Bash. The outputs of Tetgen were used in Matlab code for re-modelling asteroids Bennu, Itokawa and Eros.

#### 3.2. 2D Non-Uniform FFT (NU-FFT)

The defects of standard FFT based forward solutions are the finite length and discretization effects (Wu and Tian, 2014). Wu and Tian (2014) described the finite length effect as a cut point of an infinite Fourier integral at the Nyquist frequency. Furthermore, the discretization effect stems from the finite integral’s maximum and minimum limits at the Nyquist frequency.

Finite length errors can be ignored for potential field studies due to the amplitude of the spectrum decaying exponentially with increasing wavenumber. However, the discretization effect cannot be neglected since the oscillations of the Fourier integral may be inadequately covered by the trapezoidal rule. In this case, a smaller interval for the trapezoidal rule is mandatory for the standard FFT method. In other words, grid expansion should be applied to avoid the discretization effect. The other option to minimize discretization error is using the 2D Gaussian quadrature rule. Additionally, the standard FFT forward results produce quite reliable results as long as the source lies in the centre of the window. However, if the position of the source does not lie in the centre of the window, the edge effects tend to occur. This problem can be solved by grid

Table 4- Number of digitised faces, edges, elements and nodes for each input model.

Model Name	Faces	Edges	Elements	Nodes
Bennu	9750	6895	4202	1348
Itokawa	10299	7135	4488	1325
Eros	5680	3993	2456	770

expansion in the standard FFT methods, whereas the 2D Gaussian quadrature rule can automatically solve the problem via the shift-sampling technique.

According to Barnett (1976), polyhedral bodies which include polygonal bodies, can be re-modelled by triangular surfaces. Then, the 2D Gaussian quadrature rule is applied to the modelled triangular surfaces with NU-FFT ( Lee and Greengard, 2005; Greengard and Lee, 2006; Keiner et al., 2009; Wu, 2016; Barnett et al., 2019; Barnett, 2021). A combination of the Gaussian quadrature rule and NU-FFT was introduced by Wu, (2021a).

In the cartesian coordinate system,  $r = (x, y, z)$  presents gravity field coordinates and  $\check{r} = (\check{x}, \check{y}, \check{z})$  are the coordinates of the source body. For the wavenumber domain,  $(k_x, k_y)$  corresponds to  $(x, y)$  spatial domain coordinates on a constant level ( $z = z_0$ ). The gravity potential  $U$  can be used to obtain gravity fields in different directions and tensor gravity components in the wavenumber domain (Wu, 2016).

$$\begin{bmatrix} g_x & g_y & g_z \\ T_{xx} & T_{yy} & T_{zz} \\ T_{xy} & T_{xz} & T_{yz} \end{bmatrix} = \mathcal{F}^{-1} \left[ \begin{bmatrix} ik_x & ik_y & |k| \\ -k_x^2 & -k_y^2 & |k|^2 \\ -k_x k_y & ik_x |k| & ik_y |k| \end{bmatrix} \times \mathcal{F}(U) \right]$$

where  $|k| = \sqrt{k_x^2 + k_y^2}$ ,  $g_x$ ,  $g_y$  and  $g_z$  denotes first derivative of gravity potential  $U$  and  $T_{xx}, T_{yy}, T_{zz}, T_{xy}, T_{xz}, T_{yz}$  are the second derivatives of  $U$ .

The computation of  $U$  is a somewhat complex procedure for polyhedral bodies with constant density. If a polyhedron has  $N_F$  faces, the unit normal of each face is described as  $n_i = (\alpha_i, \beta_i, \gamma_i)$ , where  $i = 1, \dots, N_F$ . Additionally,  $J_i$  denotes 2D Gaussian quadrature order applied to the  $i^{\text{th}}$  facet of the polyhedron, with  $j = 1, \dots, J_i$  the index for the corresponding Gaussian nodes and weights.

Gaussian nodes and weights are represented by  $\check{r}_{i,j}$  and  $w_{i,j}$ . The index  $l$  can be replaced by the index of Gaussian quadrature nodes and weights  $(i, j)$  (Wu, 2021a):

$$N_{MP} = \sum_{i=1}^{N_F} J_i$$

$$w_{l_{1 \leq l \leq N_{MP}}} = \{w_{1,1}, \dots, w_{1,J_1}, w_{2,1}, \dots, w_{2,J_2}, \dots, w_{N_F,1}, \dots, w_{N_F,J_{N_F}}\},$$

$$\check{r}_{l_{1 \leq l \leq N_{MP}}} = \{\check{r}_{1,1}, \dots, \check{r}_{1,J_1}, \check{r}_{2,1}, \dots, \check{r}_{2,J_2}, \dots, \check{r}_{N_F,1}, \dots, \check{r}_{N_F,J_{N_F}}\},$$

$$n_{l_{1 \leq l \leq N_{MP}}} = \{n_1, \dots, n_1, n_2, \dots, n_2, \dots, n_{N_F}, \dots, n_{N_F}\},$$

where  $n_1, \dots, n_1, n_2, \dots, n_2$  and  $n_{N_F}, \dots, n_{N_F}$  are repeated by  $J_1, J_2$  and  $J_{N_F}$  times, respectively. Hence vertical component of the gravitational vector  $[g_z(r)]$  can be written as (Wu, 2021a):

$$g_z(r) = -G\rho_0 \sum_{i=1}^{N_{MP}} w_i \gamma_i \frac{1}{|r-\check{r}_i|} \text{ if } \check{n}_i = (\alpha_i, \beta_i, \gamma_i)$$

where  $|r - \check{r}_i|$  is Euclidian distance between the gravity field point and the quadrature point,  $G = 6.67 \times 10^{-11} m^3 kg^{-1}s^{-2}$  and  $\rho_0 (kg/m^3)$  constant density of the polyhedral body. For 2D approximation, the gravitational effect is calculated on a constant plane  $z = z_0$ . Then 2D Fourier transform is applied to both sides of equation (6) (Parker, 1973; Wu, 2021a):

$$\mathcal{F}[g_z(r_0)] = -2\pi G\rho_0 e^{ik(z_0 - \check{z}_{ref})} \sum_{n=0}^{N_T} \frac{(-1)^n}{n!} |k|^{n-1} \Theta_n$$

$$\Theta_n = \mathcal{F}_{2D}^{NU} [w_i \gamma_i (\check{z}_i - \check{z}_{ref})^n]$$

$$\check{z}_{ref} = [\min(\check{z}_i) + \max(\check{z}_i)]/2$$

where  $N_T$  is Taylor series expansion order,  $\check{z}_{ref}$  denotes reference level (Wu and Lin, 2017),  $\mathcal{F}_{2D}^{NU}$  represents 2D NU-FFT application (Greengard and Lee, 2006; Wu, 2018) and  $\check{z}_i$  is depth coordinates. Finally, the Fourier transform of the gravitational potential  $\mathcal{F}(U)$  is obtained by (Wu, 2016):

$$\mathcal{F}(U) = \frac{1}{|k|} \mathcal{F}[g_z(r_0)]$$

Once  $\mathcal{F}(U)$  is computed, vector components of the gravity potential  $U$  is computed by equation (1). In this study, the combination of 2D NU-FFT type 1 and 2D Gaussian quadrature rule, which was proposed by Wu, (2021), is used to compute the gravitational attraction of the terrestrial bodies.

### 3.3. Invariant Methods

The gradient tensors can be estimated from the total magnetic field anomaly or gravity data. The important factor is the aerial coverage of the data during the tensor estimation process (Nelson, 1988a, b; Pedersen and Rasmussen, 1990).

It is known that the gravity field varies smoothly, and the decay of the field is described by the inverse square power. Additionally, invariants of the gravity field decay as inverse fourth to the ninth power. Therefore, the gradient tensors and computed invariants provide high-resolution near-surface information (Klokočník et al., 2014). The gravity gradient tensors can be described as second derivatives of the gravitational potential,  $U$  (see equation (1)). The outside of the source masses, tensor components satisfy Laplace's equation similar to the disturbing potential ( $U$ ) (Floberghagen et al., 2011).

Each gravity gradient tensor contains a different type of information about the variation of the gravity field. Specifically,  $T_{zz}$  component provides geological contact information (zero contours) while the horizontal components diagnose the shape of the source body (Murphy and Dickinson, 2009; Klokočník et al., 2014). Individually, inflection points in  $T_{xx}$  and  $T_{yy}$  represent the source edge, maximum (peak) and minimum (troughs) in  $T_{xz}$  and  $T_{yz}$  are indicators of the source edge, centre point of peaks and troughs in  $T_{xy}$  marks the centre of the mass. If there is an asymmetry in  $T_{xy}$ , it indicates a dipping body. Rotational and horizontal invariants are obtained by the combination of the gravity gradient tensors.

The reason for the computation of gradient tensors and their invariants is to monitor small-scale variations in potential field data. It should be noted that gradient tensors and invariants do not provide additional information that is not already contained in the potential field. However, they may provide different insights for the interpretation stage (Pedersen and Rasmussen, 1990).

Invariants can be grouped into 2 categories; rotational and horizontal invariants. Rotational invariants are described as (Pedersen and Rasmussen, 1990; Pawlowski, 2012; Klokočník et al., 2014):

$$I_1 = T_{xx}T_{yy} + T_{yy}T_{zz} + T_{xx}T_{zz} - T_{xy}^2 - T_{yz}^2 - T_{xz}^2$$

$$I_2 = T_{xx}(T_{yy}T_{zz} - T_{yz}^2) + T_{xy}(T_{yz}T_{xz} - T_{xy}T_{zz}) + T_{xz}(T_{xy}T_{yz} - T_{xz}T_{yy})$$

Characteristics of  $I_1$  is similar to analytic signal, but the output is always negative. Additionally,  $I_2$  is the measure of the 3D-ness of input.

Horizontal invariants, including total horizontal derivative (THDR) and magnitude of curvature (MC), aim to detect edges of contact. The horizontal invariants can be written as (Murphy, 2007; Murphy and Dickinson, 2009):

$$THDR = \sqrt{T_{xz}^2 + T_{yz}^2}$$

$$MC = \sqrt{(T_{yy} - T_{xx})^2 + 4T_{xy}^2}$$

Peaks in  $THDR$  output clarify the edges of the source, whereas local minima in  $MC$  output detect the edge of contact. Since both  $THDR$  and  $MC$  mark the edge of the input, cross-checking between the two methods provides a more reliable interpretation.

#### 4. Findings and Discussion

In this section, estimated gravity anomalies, tensor components, and invariants of the asteroids Bennu, Itokawa, and Eros are presented. Additionally, the surficial heterogeneities in terms of the forward modelled gravity anomaly with constant density of these terrestrial objects is discussed. Each result is computed by the MATLAB code, proposed by Wu, (2021b) and a colormap of the results is generated by ColorBrewer (Cynthia, 2002).

Polyhedral models are quite convenient for estimating the gravity fields of arbitrarily-shaped objects. However, polyhedral models require two assumptions; (1) the asteroid should have a polyhedral shape, (2) the density of the polyhedral shape is constant (Werner and Scheeres, 1996; Kanamaru and Sasaki, 2019).

Typically, asteroids less than 10 km in dimension tend to have rubble pile structures (Scheeres et al., 2015). It should be re-mentioned that Asteroid Bennu has a rubble-pile structure with different sizes of boulders. Hence, the size differences would disrupt the computed gravity anomaly (Scheeres et al., 2020). The gravity anomaly of Bennu is computed by a 2D NU-FFT application. The computation parameters are discussed in Section 2.1. Figure 4 indicates the 2D and 3D input models of the asteroid Bennu and the first derivatives of gravity potential ( $g_x, g_y, g_z$ ).

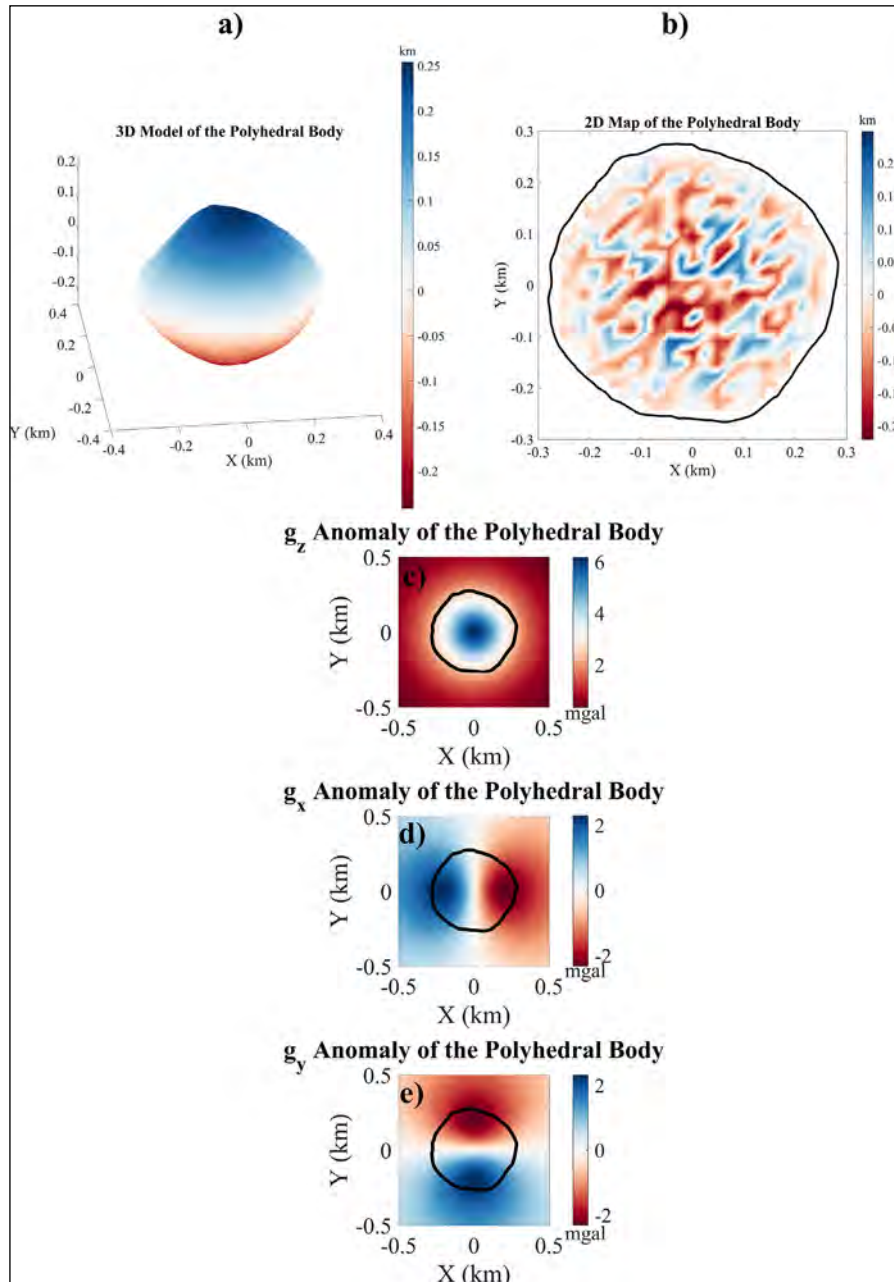


Figure 4- First derivative results for Asteroid Bennu (101955): a) 3D model of input, b) 2D model of input, c) vertical component of gravity potential  $U$ , d) X component of gravity potential  $U$ , e) Y component of gravity potential  $U$ . Solid black line delineates the boundaries of the Asteroid Bennu.

In Figure 4, the central part of the body is marked in  $g_x$  and  $g_y$  components along y and x directions, respectively. Furthermore, horizontal variations at  $z=z_0$  of gravity anomaly are delineated in  $g_z$  component. Although the first derivative of gravity potential  $U$  produces interpretable results, better evaluation can be done by tensor components and invariant of the gravity field (Figure 5).

In Figure 5, the minimum estimated gravity values at the equator and centre of asteroid Bennu are compatible with previous studies (Hirabayashi and Scheeres, 2014; Sánchez and Scheeres, 2014; Lauretta et al., 2019; Scheeres et al., 2019, 2020). In the equatorial region, the material is migrating to the region where compaction is less dominant. Additionally, an equatorial bulge occurs due to the

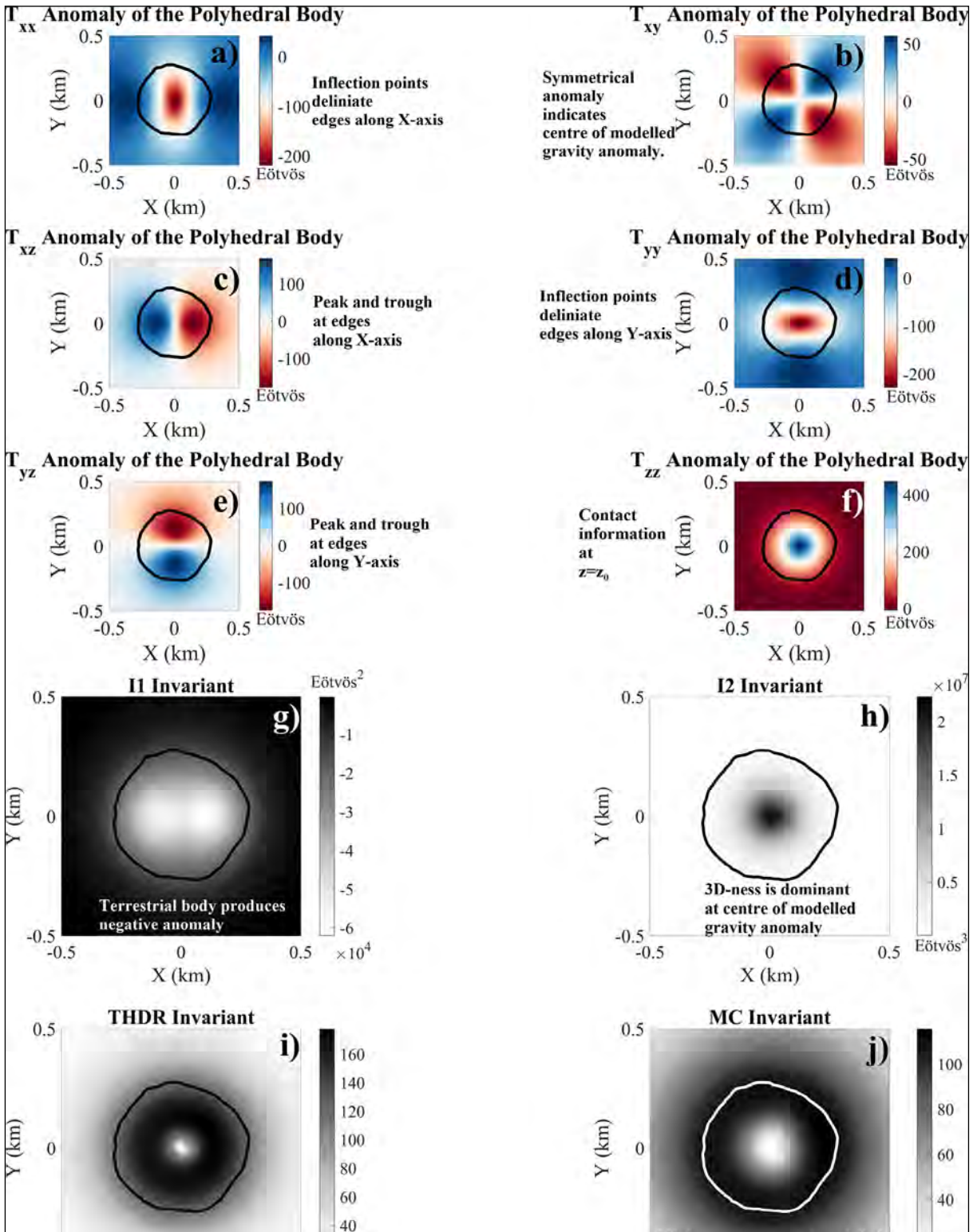


Figure 5- Second derivative results for Asteroid Bennu (101955): a)  $T_{xx}$ , b)  $T_{xy}$ , c)  $T_{xz}$ , d)  $T_{yy}$ , e)  $T_{yz}$ , f)  $T_{zz}$ , g)  $I_1$ , h)  $I_2$ , i) THDR and j) MC.

fast spin rate of the asteroid and material migration (Hirabayashi and Scheeres, 2014; Sánchez and Scheeres, 2014).

A low gravity anomaly in the equatorial bulge of the asteroid Bennu can be associated with relatively low topography. Since the heterogeneity of this zone is quite dominant, tensors and invariants delineate its horizontal variations at  $z=z_0$ . Especially in  $g_{xy}$  anomaly, symmetrical peaks and troughs indicate the centre of topographic undulations with constant density.  $I_1$  invariant provides less information about the lower topography zone, whereas  $I_2$ ,  $MC$  and  $THDR$  more susceptible to variations of surficial heterogeneity.

The shape of the asteroid Bennu is more uniform than that of Itokawa. NU-FFT becomes more prominent when computing gravitational attraction of non-uniform arbitrary shapes such as Itokawa and Eros. The gravity anomaly of Itokawa is calculated via the same method that was used for the asteroid Bennu. The computation parameters are discussed in Section 2.2. Figure 6 indicates the 2D and 3D input models of Asteroid Itokawa and the first derivatives of gravity potential ( $g_x, g_y, g_z$ ).

The internal structure and mass distribution of the asteroid Itokawa are yet unknown. It is known that the bulk porosity of Itokawa is approximately 40 % (Saito et al., 2006; Sánchez and Scheeres, 2014) and the mean density is roughly 1900 kg/m<sup>3</sup> (Abe et al., 2006; Fujiwara et al., 2006).

The computed gravitational attraction results shed light on the surficial heterogeneity of Itokawa. However, the high or low density regions cannot be obtained since constant density polyhedral models are used. It is possible to say that, we assume the head and body parts of Itokawa have the same density and variations in the computed gravity anomaly should be linked to surficial heterogeneity. Sorsa et al. (2020) proposed that both lobes of Itokawa have a uniform structure and surface composition. Furthermore, the differences between lobes might be linked to void space distribution or high density metallic fragments.

The first derivative of gravity potential indicates that the body and head parts have distinct gravity

anomalies. In Figure 6c and 6d, the body part produces a distinctly higher gravity anomaly, while the head part has a lower gravity anomaly. Although the head part has higher density values (Kanamaru and Sasaki, 2019; Sorsa et al., 2020), lower gravity anomalies are estimated in  $g_z$  and  $g_x$ . It is worth noting that using constant density models during the computation of gravity anomaly does not provide a reliable density distribution. Therefore, estimated gravity anomalies cannot be associated with the density distribution of the terrestrial body. The computed gravity anomaly with constant density contrast distribution is the direct output of the surficial or textural heterogeneity. To detect variations in forward modelled gravity anomaly with constant density contrast, tensor gradient and invariant applications tend to produce more interpretable output than first derivative anomalies (Figure 7).

In Figure 7, surficial heterogeneity analysis presents anomalous characteristics in the body part, and this is compatible with the previous findings (Kanamaru and Sasaki, 2019; Sorsa et al., 2020). Tensor gradients  $T_{xx}$  and  $T_{yy}$  delineate the edge of the structural heterogeneity zone along the x and y axes. Asymmetrical anomalies in  $T_{xy}$  indicate that the position of the surficial heterogeneity is either close to the body or head part. Horizontal variations at  $z=z_0$  can be tracked in  $T_{zz}$  anomaly. It is possible to say that horizontal variations forward modelled gravity anomalies with constant density contrast are observed near the body part.  $THDR$  and  $MC$  outputs present extremum points where anomalous topographical variations are detected. Negative anomalies towards the body part indicate a major source of gravity anomalies in  $I_1$  invariant. The 3D-ness of anomaly ( $I_2$  anomaly) has a positive correlation with topographic highs and lows. The lowest values of  $I_2$  distributed at the centre of the body whereas the highest value of  $I_2$  is observed towards the body part. On the whole, the edge detection results indicate that there are textural heterogeneities towards the body part of the Asteroid Itokawa. Direct measurements and observations from this region may provide prominent knowledge of the nature of Itokawa.

Unlike asteroid Itokawa, Eros (433) is nearly homogeneous. Furthermore, a uniform density

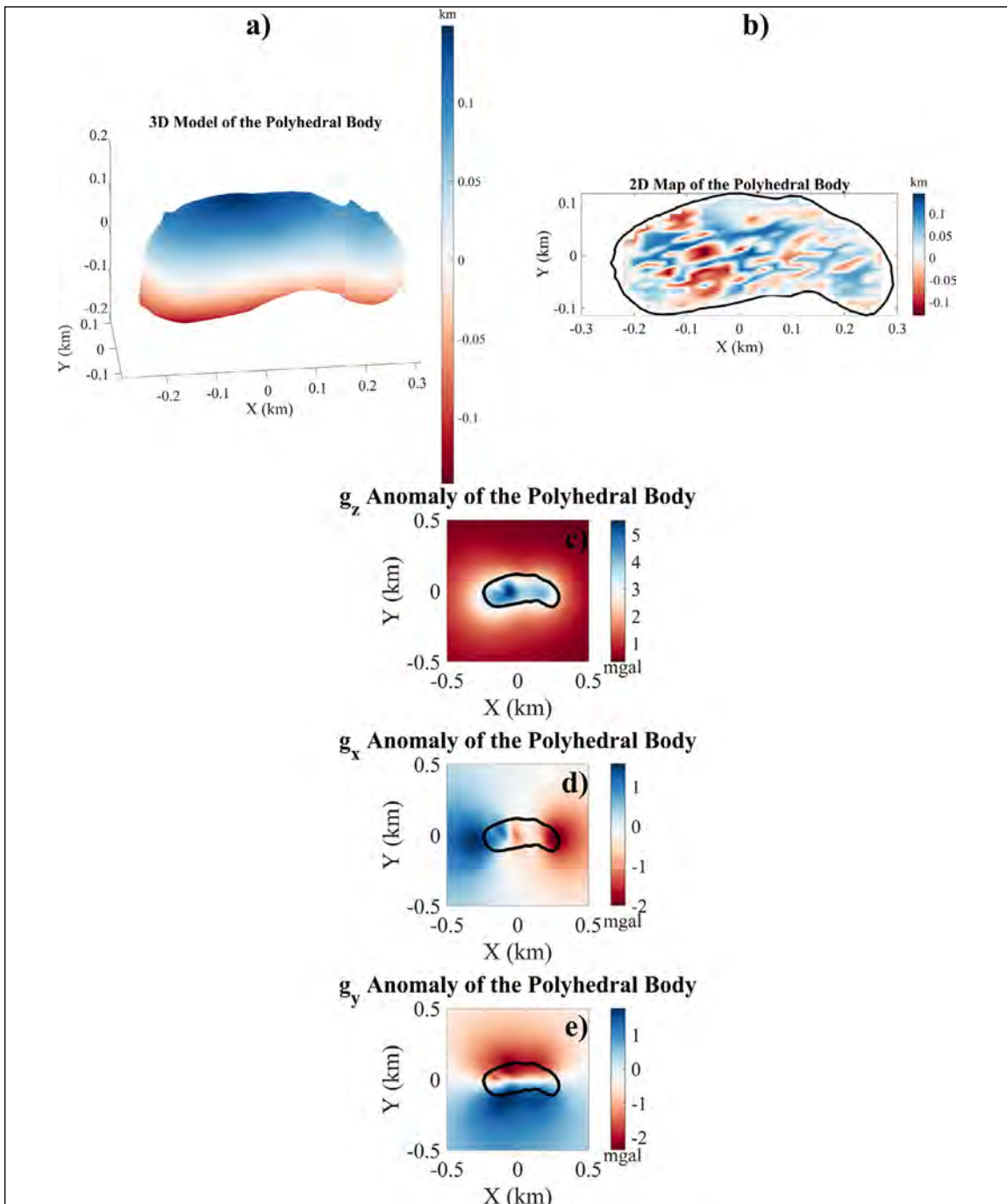


Figure 6- First derivative results for Asteroid Itokawa (25143): a) 3D model of input, b) 2D model of input, c) vertical component of gravity potential ( $U$ ), d) X component of gravity potential ( $U$ ), e) Y component of gravity potential ( $U$ ). Solid black line delineates boundaries of the Asteroid Itokawa.

distribution is observed in the asteroid Eros (Garnier et al., 2002). Trombka et al. (2000) studied the elemental composition of Eros via the NEAR (Cheng et al. 1997) X-ray spectrometer and their findings indicated anomalous characteristics of Himeros depression (saddle-shaped structure). In order to

interpret the surficial heterogeneities of Eros and Himeros depression, the first derivatives and 2D/3D model of Asteroid Eros are illustrated in Figure 8.

Figure 8 depicts a roughly homogeneous textural heterogeneity along the X and Y axes in  $g_y$  and  $g_z$ .

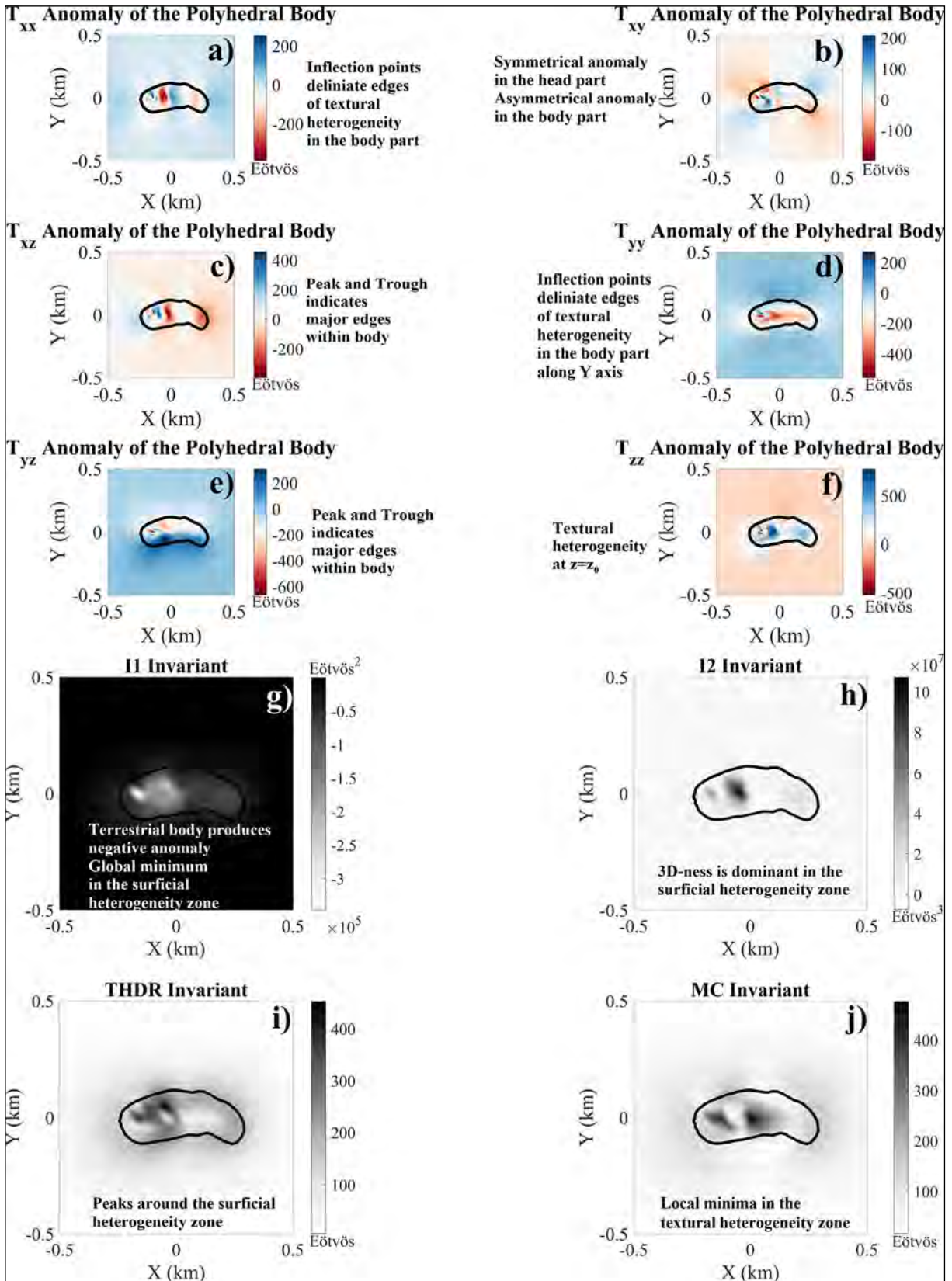


Figure 7- Second derivative results for Asteroid Itokawa (25143): a)  $T_{xx}$ , b)  $T_{xy}$ , c)  $T_{xz}$ , d)  $T_{yy}$ , e)  $T_{yz}$ , f)  $T_{zz}$ , g)  $I_1$ , h)  $I_2$ , i)  $THDR$  and j)  $MC$ .

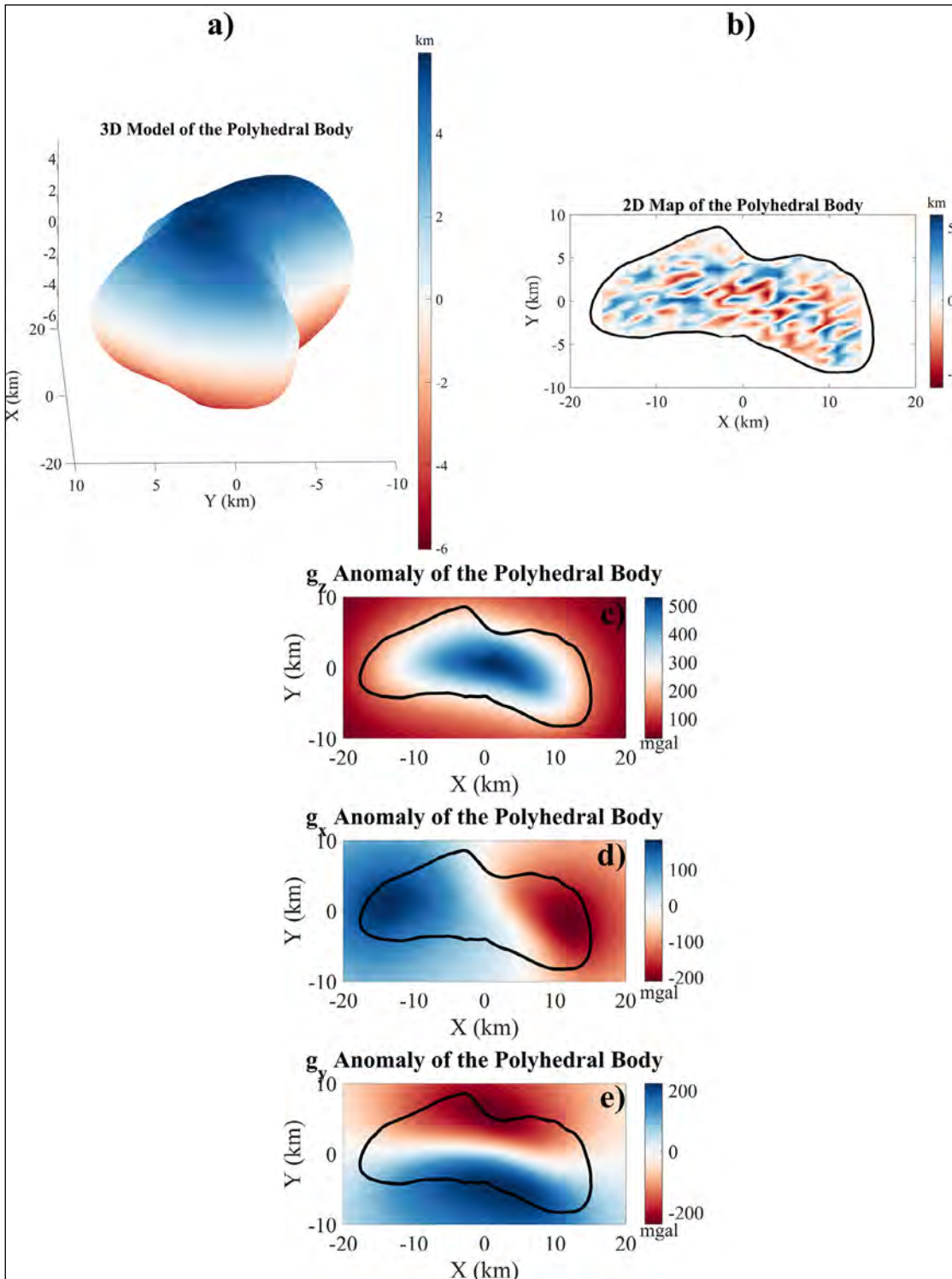


Figure 8- First derivative results for Asteroid Eros (433): a) 3D model of input, b) 2D model of input, c) vertical component of gravity potential  $U$ , d) X component of gravity potential  $U$ , e) Y component of gravity potential  $U$ . Solid black line delineates boundaries of the Asteroid Eros.

However,  $g_x$  is not symmetrical with respect to the centre of the body. This asymmetrical behaviour might be associated with heterogeneity along the

X-axis. To provide a better explanation for the surficial heterogeneity, tensors and invariants are computed (Figure 9).

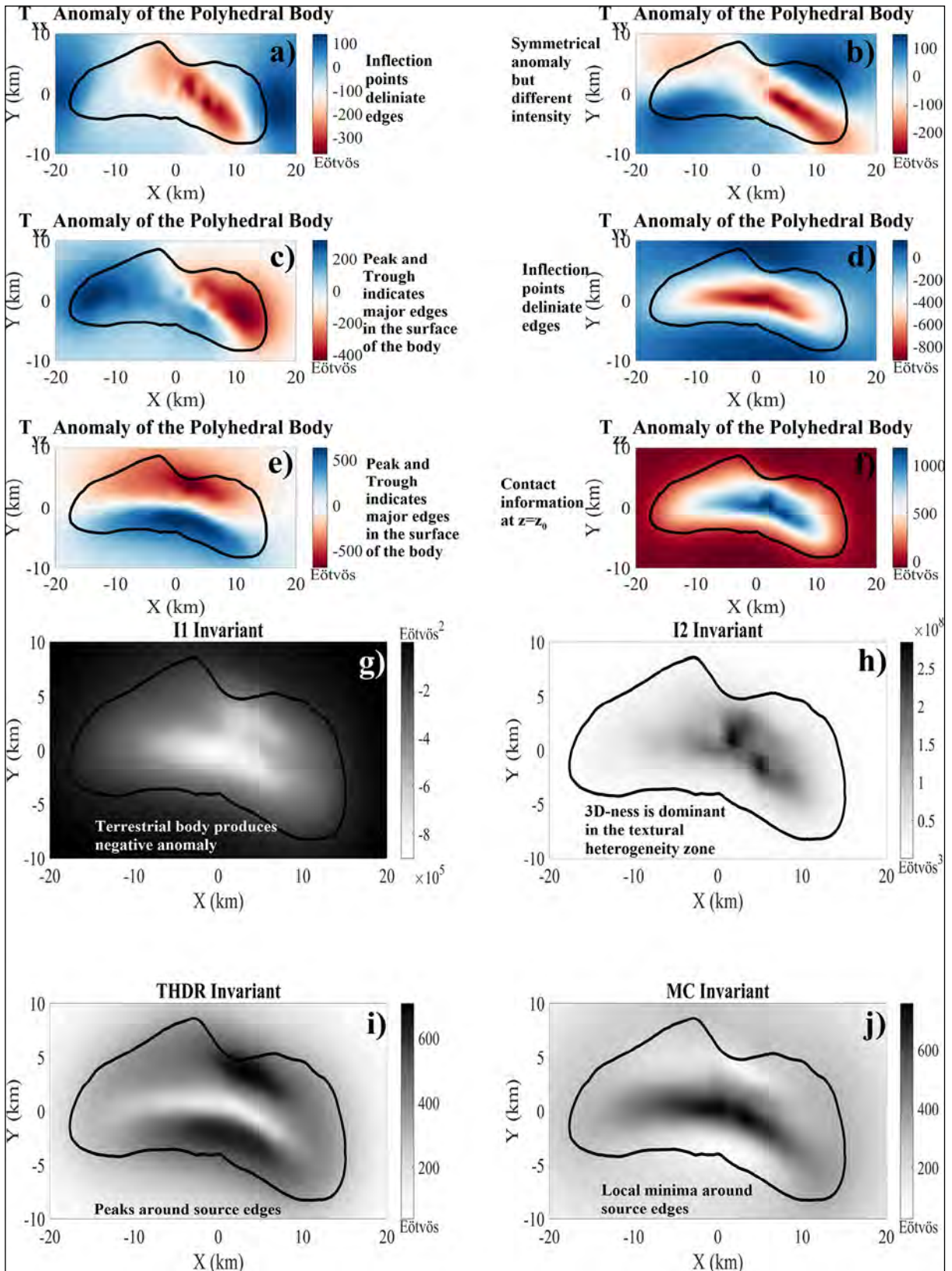


Figure 9- Second derivative results for Asteroid Eros (433): a)  $T_{xx}$ , b)  $T_{xy}$ , c)  $T_{xz}$ , d)  $T_{yy}$ , e)  $T_{yz}$ , f)  $T_{zz}$ , g)  $I_1$ , h)  $I_2$ , i)  $THDR$  and j)  $MC$ .

For Asteroid Eros, tensors and invariants have different characteristics. For example, findings in  $T_{yy}$  indicate uniform distribution along the Y direction while  $T_{xx}$  presents heterogeneous distribution along the X-axis. This heterogeneous distribution might be linked to the saddle-shaped Himeros depression. This anomaly is compatible with the results of Trombka et al. (2000) and Garmier et al. (2002). Furthermore,  $T_{xz}$  can be used to analyse the gravity effect of Himeros depression with a roughly -100 Eötvös value. It is worth mentioning again that, although the gravity anomaly of the Himeros depression is relatively higher (Garmier et al., 2002), our study presents a lower gravity value in that region. The reason for our density models are constant and the aim is to detect surficial heterogeneities. The maximum and minimum distributions in  $T_{xy}$  are symmetrical but their intensity indicates asymmetrical behaviour around the Himeros depression.

With the exception of  $I_2$ , the invariant methods exhibit structure-centred anomalies. However,  $I_2$  invariant detects surficial heterogeneities in the Himeros depression, since 3D characteristics of anomaly vary in that region.  $I_2$  invariant successfully determines the location of the heterogeneous zone. *THDR* and *MC* findings validated the nearly homogeneous structure of Eros (433) which was proposed by Garmier et al. (2002).

## 5. Conclusion

Information about terrestrial bodies is quite limited. Constant density forward modelling sheds light on the heterogeneities related to topographical variations. The computed gravity anomalies with constant density cannot classify high and low density regions, but they detect surficial diversity in these regions. The findings in this study were compared to previous studies for asteroids Bennu, Itokawa and Eros.

Specific characteristics of three asteroids are detected in this study. For Bennu (101955), textural heterogeneities are observed in the central part of the body. The gravity tensor and invariant of Itokawa (25143) reflect different surficial properties of the head and body parts. Finally, directional differences are detected for the asteroid Eros (433). Along the Y direction, surficial distribution in Eros

is nearly uniform, whereas surficial heterogeneities are interpreted along the X direction and Himeros depression.

## References

- Abe, S., Mukai, T., Hirata, N., Barnouin-Jha, O. S., Cheng, A. F., Demura, H., Gaskell, R. W., Hashimoto, T., Hiraoka, K., Honda, T., Kubota, T., Matsuoka, M., Mizuno, T., Nakamura, R., Scheeres, D. J., Yoshikawa, M. 2006. Mass and local topography measurements of Itokawa by Hayabusa. *Science* 312 (5778), 1344–1347.
- Asphaug, E., Ostro, S. J., Hudson, R. S., Scheeres, D. J., Benz, W. 1998. Disruption of kilometre-sized asteroids by energetic collisions. *Nature* 393(6684), 437–440.
- Ayachit, U., Bauer, A., Geveci, B. 2015. ParaView catalyst: Enabling in situ data analysis and visualization. Proceedings of ISAV 2015: 1st International Workshop on In Situ Infrastructures for Enabling Extreme-Scale Analysis and Visualization, Held in conjunction with SC 2015: The International Conference for High Performance Computing, Networking, Storage 25–29.
- Barnett, C. T. 1976. Theoretical modeling of the magnetic and gravitational fields of an arbitrarily shaped three-dimensional body. *Geophysics* 41(6), 1353–1364.
- Barnett, A. H. 2021. Aliasing error of the  $\exp(\beta_1 - z_2)$  kernel in the nonuniform fast Fourier transform. *Applied and Computational Harmonic Analysis* 51, 1–16.
- Barnett, A. H., Magland, J., Klinteberg, L. A. F. 2019. A parallel nonuniform fast fourier transform library based on an “Exponential of Semicircle” kernel. *Journal on Scientific Computing* 41(5), C479–C504.
- Barnouin, O. S., Daly, M. G., Palmer, E. E. 2019. Shape of (101955) Bennu indicative of a rubble pile with internal stiffness. *Nature Geoscience* 12 (4), 247–252.
- Bhattacharyya, B. K. 1966. Continuous spectrum of the total-magnetic-field anomaly due to a rectangular prismatic body. *Geophysics* 31 (1), 97–121.
- Chai, Y., Hinze, W. J. 1988. Gravity inversion of an interface above which the density contrast varies exponentially with depth. *Geophysics* 53 (6), 837–845.
- Chapman, C. R., Merline, W. J., Thomas, P. C., Joseph, J., Cheng, A. F., Izenberg, N. 2002. Impact history of Eros: Craters and boulders. *Icarus* 155 (1), 104–118.
- Cheng, A. F., Santo, A. G., Heeres, K. J., Landshof, J. A., Farquhar, R. W., Gold, R. E., Lee, S. C. 1997. Near-Earth Asteroid Rendezvous: Mission

- overview. *Journal of Geophysical Research: Planets* 102 (E10), 23695–23708.
- Chenot, D., Debeglia, N. 1990. Three-dimensional gravity or magnetic constrained depth inversion with lateral and vertical variation of contrast. *Geophysics* 55(3), 327–335.
- Chesley, S. R., Farnocchia, D., Nolan, M. C., Vokrouhlický, D., Chodas, P. W., Milani, A., Spoto, F., Rozitis, B., Benner, L. A. M., Bottke, W. F., Busch, M. W., Emery, J. P., Howell, E. S., Lauretta, D. S., Margot, J. L., Taylor, P. A. 2014. Orbit and bulk density of the OSIRIS-REx target Asteroid (101955) Bennu. *Icarus* 235, 5–22.
- Cooley, J. W., Tukey, J. W. 1965. An algorithm for the machine calculation of complex Fourier series. *Mathematics of Computation* 19 (90), 297.
- Cynthia, A. 2002. Brewer. Available at: <http://www.colorbrewer.org>.
- Delbo, M., Libourel, G., Wilkerson, J., Murdoch, N., Michel, P., Ramesh, K. T., Ganino, C., Verati, C., Marchi, S. 2014. Thermal fatigue as the origin of regolith on small asteroids. *Nature* 508 (7495), 233–236.
- DellaGiustina, D. N., Emery, J. P., Golish, D. R. 2019. Properties of rubble-pile asteroid (101955) Bennu from OSIRIS-REx imaging and thermal analysis. *Nature Astronomy* 3 (4), 341–351.
- El Mir, C., Ramesh, K. T., Delbo, M. 2019. The efficiency of thermal fatigue in regolith generation on small airless bodies. *Icarus* 333, 356–370.
- Eppes, M. C., Keanini, R. 2017. Mechanical weathering and rock erosion by climate-dependent subcritical cracking. *Reviews of Geophysics* 55 (2), 470–508.
- Eppes, M. C., McFadden, L. D., Wegmann, K. W., Scuderi, L. A. 2010. Cracks in desert pavement rocks: Further insights into mechanical weathering by directional insolation. *Geomorphology* 123 (1–2), 97–108.
- Fletcher, R. C., Buss, H. L., Brantley, S. L. 2006. A spheroidal weathering model coupling porewater chemistry to soil thicknesses during steady-state denudation. *Earth and Planetary Science Letters* 244 (1–2), 444–457.
- Floberghagen, R., Fehringer, M., Lamarre, D., Muzi, D., Frommknecht, B., Steiger, C., Piñeiro, J., da Costa Human Spaceflight, A. 2011. Mission design, operation and exploitation of the gravity field and steady-state ocean circulation explorer mission. *Journal of Geodesy* 85 (11), 749–758.
- Fujiwara, A., Kadono, T., Nakamura, A. 1993. Cratering experiments into curved surfaces and their implication for craters on small satellites. *Icarus* 105 (2), 345–350.
- Fujiwara, A., Kawaguchi, J., Yeomans, D. K. 2006. The rubble-pile asteroid Itokawa as observed by Hayabusa. *Science* 312 (5778), 1330–1334.
- Garmier, R., Barriot, J. P., Konopliv, A. S., Yeomans, D. K. 2002. Modeling of the Eros gravity field as an ellipsoidal harmonic expansion from the NEAR Doppler tracking data. *Geophysical Research Letters* 29 (8), 72–1.
- Greengard, L., Lee, J. Y. 2006. Accelerating the nonuniform fast Fourier transform. *Society for Industrial and Applied Mathematics* 46 (3), 443–454.
- Hansen, R. O., Wang, X. 1988. Simplified frequency-domain expressions for potential fields of arbitrary three-dimensional bodies. *Geophysics* 53 (3), 365–374.
- Hazeli, K., El Mir, C., Papanikolaou, S., Delbo, M., Ramesh, K. T. 2018. The origins of asteroidal rock disaggregation: Interplay of thermal fatigue and microstructure. *Icarus* 304, 172–182.
- Hirabayashi, M., Scheeres, D. J. 2014. Stress and failure analysis of rapidly rotating asteroid (29075) 1950 DA. *The Astrophysical Journal Letters* 798 (1), L8.
- Holzhausen, G. R. 1989. Origin of sheet structure, 1. Morphology and boundary conditions. *Engineering Geology* 27 (1–4), 225–278.
- Kanamaru, M., Sasaki, S. 2019. Estimation of interior density distribution for small bodies: The case of asteroid Itokawa. *Transactions of the Japan Society for Aeronautical and Space Sciences: Aerospace Technology Japan* 17 (3), 270–275.
- Kanamaru, M., Sasaki, S., Wiczeorek, M. 2019. Density distribution of asteroid 25143 Itokawa based on smooth terrain shape. *Planetary and Space Science* 174, 32–42.
- Keiner, J., Kunis, S., Potts, D. 2009. Using NFFT 3---A software library for various nonequispaced fast Fourier transforms. *Association for Computing Machinery Transactions on Mathematical Software (TOMS)* 36 (4).
- Klokočník, J., Kostelecký, J., Kalvoda, J., Eppelbaum, L. V., Bezděk, A. 2014. Gravity disturbances, Marussi tensor, invariants and other functions of the geopotential represented by EGM 2008. *Journal of Earth Science Research* 2 (3), 88–101.
- Konopliv, A. S., Miller, J. K., Owen, W. M., Yeomans, D. K., Giorgini, J. D., Garmier, R., Barriot, J. P. 2002. A global solution for the gravity field, rotation, landmarks, and ephemeris of Eros. *Icarus* 160 (2), 289–299.
- Lamp, J. L., Marchant, D. R., Mackay, S. L., Head, J. W. 2017. Thermal stress weathering and the spalling of Antarctic rocks. *Journal of Geophysical Research: Earth Surface* 122 (1), 3–24.
- Lauretta, D. S., Bartels, A. E., Barucci, M. A. 2015. The OSIRIS-REx target asteroid (101955) Bennu: Constraints on its physical, geological, and dynamical nature from astronomical observations. *Meteoritics and Planetary Science* 50, 834–849.

- Lauretta, D. S., DellaGiustina, D. N., Bennett, C. A. 2019. The unexpected surface of asteroid (101955) Benu. *Nature* 568 (7750), 55–60.
- Lee, T., Biehler, S. 1991. Inversion modeling of gravity with prismatic mass bodies. *Geophysics* 56 (9), 1365–1376.
- Lee, J. Y., Greengard, L. 2005. The type 3 nonuniform FFT and its applications. *Journal of Computational Physics* 206 (1), 1–5.
- Levi, F. A. 1973. Thermal fatigue: a possible source of structural modifications in meteorites. *Meteoritics* 8 (3), 209–221.
- Magri, C., Consolmagno, G. J., Ostrch, S. J., Benner, L. A. M., Beeney, B. R. 2001. Radar constraints on asteroid regolith properties using 433 Eros as ground truth. *Meteoritics and Planetary Science* 36 (12), 1697–1709.
- McCoy, T. J., Nittler, L. R., Burbine, T. H., Trombka, J. I., Clark, P. E., Murphy, M. E. 2000. Anatomy of a partially differentiated asteroid: A “NEAR”-sighted view of Acapulcoites and Lodranites. *Icarus* 148 (1), 29–36.
- McFadden, L. D., Eppes, M. C., Gillespie, A. R., Hallet, B. 2005. Physical weathering in arid landscapes due to diurnal variation in the direction of solar heating. *Geological Society of America Bulletin* 117 (1–2), 161–173.
- McMahon, J. W., Scheeres, D. J., Chesley, S. R., French, A., Brack, D., Farnocchia, D., Takahashi, Y., Rozitis, B., Tricarico, P., Mazarico, E., Bierhaus, B., Emery, J. P., Hergenrother, C. W., Lauretta, D. S. 2020. Dynamical evolution of simulated particles ejected from Asteroid Benu. *Journal of Geophysical Research: Planets* 125 (8), e2019JE006229.
- Miller, J. K., Konopliv, A. S., Antreasian, P. G., Bordi, J. J., Chesley, S., Helfrich, C. E., Owen, W. M., Wang, T. C., Williams, B. G., Yeomans, D. K., Scheeres, D. J. 2002. Determination of shape, gravity, and rotational state of asteroid 433 Eros. *Icarus* 155 (1), 3–17.
- Molaro, J. L., Byrne, S., Langer, S. A. 2015. Grain-scale thermoelastic stresses and spatiotemporal temperature gradients on airless bodies, implications for rock breakdown. *Journal of Geophysical Research: Planets* 120 (2), 255–277.
- Molaro, J. L., Walsh, K. J., Jawin, E. R. 2020a. In situ evidence of thermally induced rock breakdown widespread on Benu’s surface. *Nature Communications* 11 (1), 1–11.
- Molaro, J. L., Hergenrother, C. W., Chesley, S. R., Walsh, K. J., Hanna, R. D., Haberle, C. W., Schwartz, S. R., Ballouz, R. L., Bottke, W. F., Campins, H. J., Lauretta, D. S. 2020b. Thermal fatigue as a driving mechanism for activity on Asteroid Benu. *Journal of Geophysical Research: Planets* 125 (8), e2019JE006325.
- Murchie, S. L., Pieters, C. M. 1996. Spectral properties and rotational spectral heterogeneity of 433 Eros. *Journal of Geophysical Research: Planets* 101 (E1), 2201–2214.
- Murphy, C. A. 2007. Interpreting FTG Gravity Data using Horizontal Tensor Components. *Electromagnetic, Gravity and Magnetic International Workshop 2017*, cp-166-00004.
- Murphy, C., Dickinson, J. 2009. Exploring exploration play models with ftg gravity data. *European Association of Geoscientists and Engineers*, cp-241-00020.
- Nakamura, T., Noguchi, T., Tanaka, M. 2011. Itokawa Dust Particles: A direct link between s-type asteroids and ordinary chondrites. *Science* 333 (6046), 1113.
- Nelson, J. B. 1988a. Calculation of the magnetic gradient tensor from total field gradient measurements and its application to geophysical interpretation. *Geophysics* 53 (7), 957–966.
- Nelson, J. B. 1988b. Comparison of gradient analysis techniques for linear two-dimensional magnetic sources. *Geophysics* 53(8), 1088–1095.
- Ostro, S. J., Campbell, D. B., Simpson, R. A. 1992. Europa, Ganymede, and Callisto: New radar results from Arecibo and Goldstone. *Journal of Geophysical Research* 97 (E11), 18227.
- Parker, R. L. 1973. The rapid calculation of potential anomalies. *Geophysical Journal International* 31 (4), 447–455.
- Pawlowski, B. 2012. Gravity gradiometry in resource exploration. *The Leading Edge* 17 (1), 51.
- Pedersen, L. B. 1978. Wavenumber domain expressions for potential fields from arbitrary 2-, 2½-, and 3-dimensional bodies. *Geophysics* 43 (3), 626–630.
- Pedersen, L. B., Rasmussen, T. M. 1990. The gradient tensor of potential field anomalies: some implications on data collection and data processing of maps. *Geophysics* 55 (12), 1558–1566.
- Richardson, J. E., Melosh, H. J., Greenberg, R. 2004. Impact-induced seismic activity on asteroid 433 Eros: A surface modification process. *Science* 306 (5701), 1526–1529.
- Robinson, M. S., Thomas, P. C., Veverka, J. 2002. The geology of 433 Eros. *Meteoritics and Planetary Science* 37 (12), 1651–1684.
- Saito, J., Miyamoto, H., Nakamura, R. 2006. Detailed images of Asteroid 25143 Itokawa from Hayabusa. *Science* 312 (5778), 1341.
- Sánchez, P., Scheeres, D. J. 2014. The strength of regolith and rubble pile asteroids. *Meteoritics and Planetary Science* 49 (5), 788–811.

- Scheeres, D. J., Britt, D., Carry, B., Holsapple, K. A. 2015. Asteroid interiors and morphology. *Asteroids IV*, 745–766.
- Scheeres, D. J., McMahon, J. W., French, A. S. 2019. The dynamic geophysical environment of (101955) Benu based on OSIRIS-REx measurements. *Nature Astronomy* 3 (4), 352–361.
- Scheeres, D. J., French, A. S., Tricarico, P. 2020. Heterogeneous mass distribution of the rubble-pile asteroid (101955) Benu. *Science Advances* 6 (41).
- Si, H. 2015. TetGen, a delaunay-based quality tetrahedral mesh generator. *Association for Computing Machinery Transactions on Mathematical Software* 41(2).
- Sorsa, L. I., Takala, M., Bambach, P., Deller, J., Vilenius, E., Agarwal, J., Carroll, K. A., Karatekin, Ö., Pursiainen, S. 2020. Tomographic inversion of gravity gradient field for a synthetic Itokawa model. *Icarus* 336, 113425.
- Stokes, G. H., Evans, J. B., Vighh, H. E. M., Shelly, F. C., Pearce, E. C. 2000. Lincoln Near-Earth Asteroid Program (LINEAR). *Icarus* 148 (1), 21–28.
- Tanbakouei, S., Trigo-Rodriguez, J. M., Sort, J., Michel, P., Blum, J., Nakamura, T., Williams, I. 2019. Mechanical properties of particles from the surface of asteroid 25143 Itokawa. *Astronomy and Astrophysics* 629, A119.
- Thirumalai, K., Demou, S. G. 1970. Effect of reduced pressure on thermal-expansion behavior of rocks and its significance to thermal fragmentation. *Journal of Applied Physics* 41(13), 5147–5151.
- Thomas, P. C., Joseph, J., Carcich, B. 2002. Eros: Shape, topography, and slope processes. *Icarus* 155 (1), 18–37.
- Tontini, F. C., Cocchi, L., Carmisciano, C. 2009. Rapid 3-d forward model of potential fields with application to the palinuro seamount magnetic anomaly (Southern Tyrrhenian Sea, Italy). *Journal of Geophysical Research: Solid Earth* 114 (2), 2103.
- Trombka, J. I., Squyres, S. W., Bruckner, J. 2000. The Elemental Composition of Asteroid 433 Eros: Results of the NEAR-Shoemaker X-ray Spectrometer. *Science* 289 (5487), 2101–2105.
- Veverka, J., Thomas, P. C., Bell, J. F. 1999. Imaging of Asteroid 433 Eros during NEARs Flyby Reconnaissance. *Science* 285 (5427), 562–564.
- Veverka, J., Thomas, P. C., Robinson, M. 2001. Imaging of small-scale features on 433 Eros from NEAR: Evidence for a complex regolith. *Science* 292 (5516), 484–488.
- Walsh, K. J., Jawin, E. R., Ballouz, R. L. 2019. Craters, boulders and regolith of (101955) Benu indicative of an old and dynamic surface. *Nature Geoscience* 12 (4), 242–246.
- Waragai, T. 1998. Effects of rock surface temperature on exfoliation, rock varnish, and lichens on a boulder in the Hunza Valley. *Arctic and Alpine Research* 30 (2), 184–192.
- Werner, R. A., Scheeres, D. J. 1996. Exterior gravitation of a polyhedron derived and compared with harmonic and mascon gravitation representations of asteroid 4769 Castalia. *Celestial Mechanics and Dynamical Astronomy* 65 (3), 313–344.
- Whiteley, R. J., Tholen, D. J., Hergenrother, C. W. 2002. Lightcurve Analysis of four new monolithic fast-rotating asteroids. *Icarus* 157 (1), 139–154.
- Wu, X. 1983. The computation of the spectrum of potential field due to 3-D arbitrary bodies with physical parameters varying with depth. *Acta Geophysica Sinica* 26 (2), 177–187.
- Wu, L. 2016. Efficient modelling of gravity effects due to topographic masses using the Gauss-FFT method. *Geophysical Journal International* 205 (1), 160–178.
- Wu, L. 2018. Comparison of 3-D Fourier forward algorithms for gravity modelling of prismatic bodies with polynomial density distribution. *Geophysical Journal International* 215 (3), 1865–1886.
- Wu, L. 2019. Fourier-domain modeling of gravity effects caused by polyhedral bodies. *Journal of Geodesy* 93 (5), 635–653.
- Wu, L. 2021a. Modified Parker’s method for gravitational forward and inverse modeling using general polyhedral models. *Journal of Geophysical Research: Solid Earth* 126 (10).
- Wu, L. 2021b. Data and code for “Modified Parker’s method for gravitational forward and inverse modeling using general polyhedral models”.
- Wu, L., Tian, G. 2014. High-precision fourier forward modeling of potential fields. *Geophysics* 79 (5), G59–G68.
- Wu, L., Chen, L. 2016. Fourier forward modeling of vector and tensor gravity fields due to prismatic bodies with variable density contrast. *Geophysics* 81 (1), G13–G26.
- Wu, L., Lin, Q. 2017. Improved Parker’s method for topographic models using Chebyshev series and low rank approximation. *Geophysical Journal International* 209 (2), 1296–1325.
- Yano, H., Kubota, T., Miyamoto, H., Okada, T., Scheeres, D., Takagi, Y., Yoshida, K., Abe, M. 2006. Touchdown of the Hayabusa spacecraft at the muses sea on Itokawa. *Science* 312 (5778), 1350–1353.
- Yeomans, D. K. 1995. Asteroid 433 Eros: the target body of the NEAR mission. *Journal of the Astronautical Sciences* 43 (4), 417–426.



# Bulletin of the Mineral Research and Exploration

<http://bulletin.mta.gov.tr>



## Coal quality, mineralogy, petrography, and geochemistry of the high-strontium Bozburun lignite (Malatya, eastern Türkiye)

Rıza Görkem OSKAY<sup>a\*</sup> and Ali İhsan KARAYİĞİT<sup>b</sup>

<sup>a</sup> Hacettepe University, Başkent OSB Technical Sciences Vocational School, Ankara, Türkiye

<sup>b</sup> Hacettepe University, Faculty of Engineering, Department of Geological Engineering, Ankara, Türkiye

Research Article

### Keywords:

Malatya Basin, Miocene, Maceral, Celestine, Barite.

### ABSTRACT

The Bozburun coalfield hosts a late Miocene 1.1 m thick coal seam. This study aims to determine coal quality, mineralogy, petrography and geochemistry, and controlling factors of elemental enrichments. The coals are generally black and greyish black in colour, and the low part of the seam commonly includes fossil shell remains. The ash yield displays a decreasing trend towards the upper part of the seam; in turn, gross calorific and total C values increase upwards. The total S content being generally higher than 5% (on dry basis), displays an increasing trend towards the upper part. In the entire seam, huminite is the most common maceral group, while inertinite and liptinite display variable proportions. The identified minerals by XRD are mainly quartz, clay minerals, calcite, pyrite, and aragonite (in fossil shell remains-bearing samples), whereas feldspars and marcasite determined in a few samples. Furthermore, in the coal samples, celestine and barite were identified by SEM-EDX. This study indicates that precipitation of celestine and Sr-bearing barite grains during diagenetic stage and Sr-uptake by mollusc within the palaeomire caused Sr enrichment in the entire seam. Overall, the water influx and redox conditions controlled the mineralogical and the elemental compositions of the coal seam.

Received Date: 23.06.2022

Accepted Date: 01.11.2022

## 1. Introduction

The mineralogical and geochemical features of coal and coal combustion remains have been the subject of several studies because of the hazardous elements and critical elements contained (e.g., Dai et al., 2012a, 2020a, b, 2021; Dai and Finkelman, 2018; Hower et al., 2020, 2022). Besides, more recent studies show that these features of coal beds and partings in combination with coal petrography, palaeontological, and sedimentological data could provide significant information about the depositional conditions in the palaeomires (e.g., Finkelman et al., 2019; Dai et al., 2020a; Hood et al., 2020) for this purpose, indicative

elements, and element ratios have been used (e.g., Goodarzi and Swaine, 1994; Dai et al., 2015a, 2018, 2020a; Spiro et al., 2019). For example, distributions of As, U, and Mo contents, along with Th/U ratio, are used for the determination of palaeoredox conditions in palaeomires, while distributions of total S, B, and Mo contents and Sr/Ba ratio serves as palaeosalinity indicator in palaeomires (Goodarzi and Swaine, 1994; Spiro et al., 2019; Dai et al., 2020a; Goodarzi et al., 2020; Çelik et al., 2021). Nevertheless, these index elements and elemental ratios should be used with caution, since coal seams have heterogeneous elemental and mineralogical compositions and certain

Citation Info: Oskay, R. G., Karayığit, A. İ. 2024. Coal quality, mineralogy, petrography, and geochemistry of the high-strontium Bozburun lignite (Malatya, eastern Türkiye). Bulletin of the Mineral Research and Exploration 173, 19-54. <https://doi.org/10.19111/bulletinofmre.1198192>

\*Corresponding author: Rıza Görkem OSKAY, [rizagorkemoskay@hacettepe.edu.tr](mailto:rizagorkemoskay@hacettepe.edu.tr)

accessory minerals (e.g., barite, chromite, monazite) can increase the concentrations of certain indicator elements (Finkelman et al., 2019; Dai et al., 2020a, b; Karayiğit et al., 2020a, b).

The petrographical and geochemical features of Turkish low-rank coals, particularly of the early-middle Miocene coals in western and central Anatolia, are well documented as a result of their use as feed coals in power plants (Querol et al., 1997; Karayiğit et al., 2000, 2017a; Tuncalı et al., 2002; Palmer et al., 2004). However, the coalfields of eastern Anatolia, with the exception of Kangal and Afşin-Elbistan coalfields, have received less attention (Karayiğit and Gayer, 2000; Karayiğit et al., 2001, 2019; Sütçü and Karayiğit, 2015). The tectonic evolution of eastern Anatolia during late Cenozoic times resulted in the formation of several sedimentary basins (e.g., Afşin-Elbistan, Gölbaşı, Sivas-Kangal and Malatya), which host mineable late Miocene and Plio-Pleistocene coal seams (Tuncalı et al., 2002; Kaymakçı et al., 2006; Sütçü and Karayiğit, 2015; Karayiğit et al., 2016; Yılmaz, 2019; Seyitoğlu et al., 2022). Another result of the tectonic activity is the development of regional volcanic activity from the early Miocene to Pliocene (Figure 1a) (Kocaaslan and Ersoy, 2018; Di Giuseppe

et al., 2021). Hence, volcanic complexes (Yamadağ and Kepezdağ) and volcanic fields (Kangal and Sivas) were developed.

The Bozburun coalfield is located in the Malatya Basin (Figure 2) and hosts a 1.1 m thick economic coal seam. Previous studies have mostly focused on the sedimentological and palaeontological properties of the Cenozoic sedimentary rocks and the petrogenesis of Cenozoic volcanic rocks in the Malatya Basin (Ercan and Asutay, 1993; Türkmen et al., 2004, 2007, 2011; Ekici et al., 2007; Nazik et al., 2008; Koç-Taşgım, 2011). Although coal seam exploitation in the study area began in early 1990s (Önal, 1995), only one coal geology study from the western part of the Bozburun coalfield has been conducted to date. In there, the coal seam displays relatively small thickness, and coal beds-bearing outcrops are located in the northern part of the Malatya Basin (Yalçın-Erik and Ay, 2020). The results of the previous coal geology study show that the coal displays significantly high ash yield and total sulphur content, and the coal is of subbituminous rank. The biomarker data supports the previous palynological results from Önal (1995) and Türkmen et al. (2004), indicating that the peat-forming vegetation was a mix of herbaceous

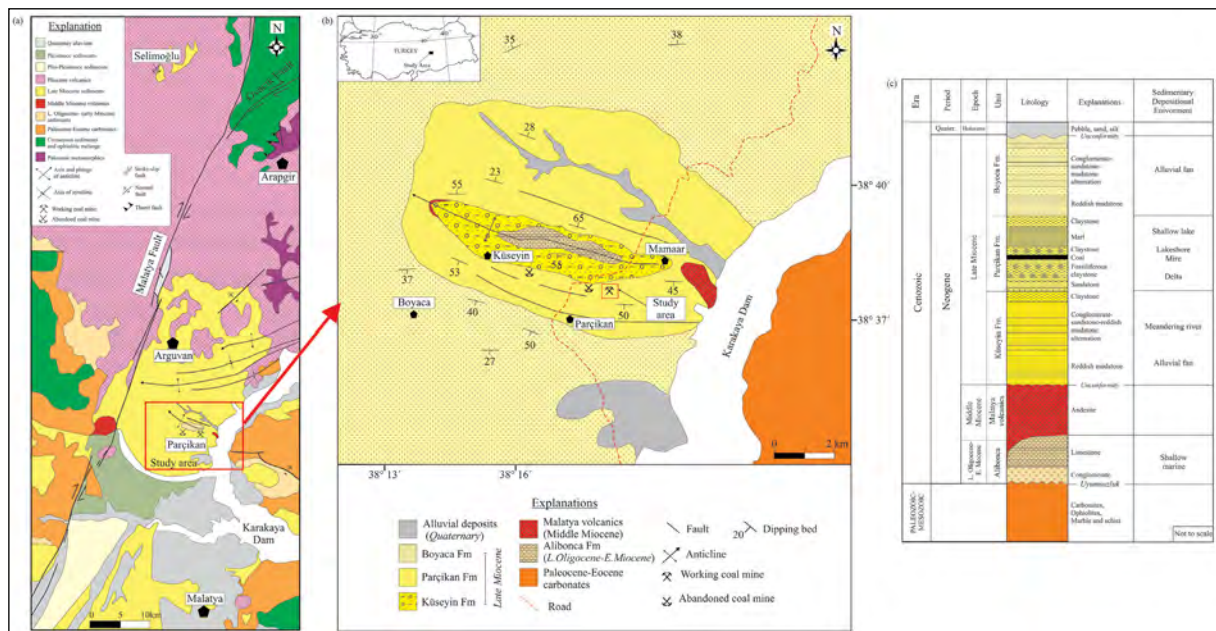


Figure 1- a) Regional geological map of the surrounding area of the Bozburun coalfield (modified from geological map of Türkiye, 1/500.000-scale), b) simplified geological map of the study area (modified from Türkmen et al., 2004; Sümengen, 2016), c) generalized stratigraphic column in the study area (modified from Türkmen et al., 2004).

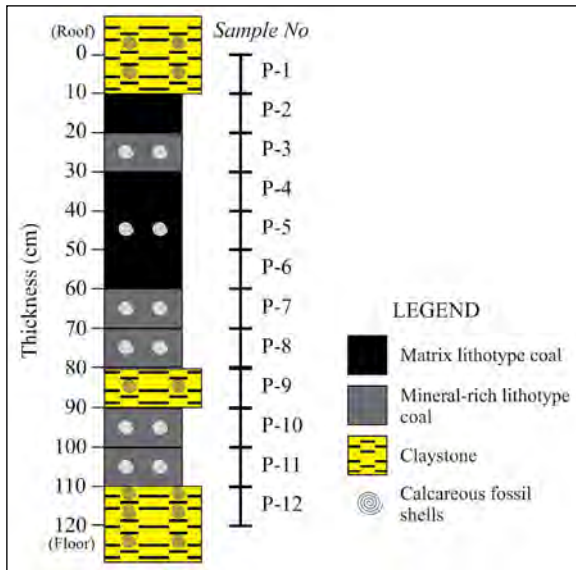


Figure 2- The sampled profile at the Bozburun coalfield.

and woody plants. Nevertheless, detailed elemental composition and paleoenvironmental reconstruction of the Bozburun coalfield are still lacking. Considering the volcanic activity in the Malatya Basin, the coal rank of the Bozburun coalfield might have differences from the northernmost of the Malatya Basin (Figure 1a). Therefore, this study focuses on determining the factors controlling the coal quality, the petrographical, mineralogical, and geochemical features of the late Miocene coal in the eastern part of the Bozburun coalfield and reconstructing the palaeoenvironment during the peat accumulation. The specific goal of the current study is to ascertain factors controlling coal rank variation in the Malatya Basin.

## 2. Geological Setting

The Bozburun coalfield is located in the southernmost of the NE–SW trending Malatya Basin, which is controlled by the Malatya Fault Zone (Figure 1a) (Kaymakçı et al., 2006; Sançar et al., 2019). The pre-Neogene basement consists of Permo-Triassic Keban metamorphics (marble and schist), middle Triassic-early Cretaceous Kuluncak ophiolite, late Cretaceous Elazığ magmatics (andesite, basalt, diorite, and gabbro), and Palaeocene to late Eocene marine carbonates with gypsum lenses and beds (Figure 1b-c) (Türkmen et al., 2007; Koç-Taşgın, 2011; Sümengen, 2016). The Malatya Basin begun developing during early Miocene due to regional extensional tectonic

regime (Kaymakçı et al., 2006). Thus, the Neogene basinal infillings started with late Oligocene (?)–early Miocene shallow marine deposits (Alibonca Formation), and this unit is conformably overlain by middle Miocene Malatya volcanics (andesite and basalt) of the Yamadağ volcanic complex (Ercan and Asutay, 1993; Önal, 1995; Türkmen et al., 2004, 2007; Koç-Taşgın, 2011; Sümengen, 2016; Kocaarslan and Ersoy, 2018; Di Giuseppe et al., 2021). Terrestrial conditions became dominant in the Malatya Basin during the late Miocene and these units inequitably overlay early-middle Miocene units (Figure 1c). The total thickness of late Miocene basinal infillings in the study area is around 1200 m and is divided into three formations (Türkmen et al., 2004, 2007; Nazik et al., 2008; Koç-Taşgın, 2011), from bottom to top, Küseyin Formation, Bozburun Formation, and Boyaca Formation (Figure 1c).

The Küseyin Formation is composed of alteration of conglomerate, sandstone, and reddish mudstone with freshwater mollusc-bearing limestone (Türkmen et al., 2004, 2007; Nazik et al., 2008; Koç-Taşgın, 2011). The sedimentological features of Küseyin Formation imply that the formation was deposited under alluvial fan and meandering river conditions where small freshwater ponds and lakes were developed (Türkmen et al., 2004, 2007; Koç-Taşgın, 2011). The ostracod fauna hosted in sediments suggest freshwater to oligohaline conditions (Nazik et al., 2008). The coal-bearing Bozburun Formation overlies conformably the Küseyin Formation and commences with current- or wave-ripple cross-laminated sandstone, plant remains-bearing greyish green claystone, a coal seam, fossiliferous marl and limestone, and reddish mudstone (Türkmen et al., 2004, 2007; Sümengen, 2016) (Figure 1b). Previous sedimentological and palaeontological studies show that the Bozburun Formation was deposited in shallow lakes associated with peatlands and deltaic areas (Önal, 1995; Türkmen et al., 2004, 2007; Nazik et al., 2008). Furthermore, the identified palynoflora from the Bozburun coal seam implies that palaeomires were developed under freshwater lakeshore and floodplain conditions, while the ostracod and gastropod fauna from the Bozburun Formation show that freshwater and brackish conditions were developed during the late Miocene.

The Boyaca Formation is widely exposed in the study area and consists of reddish mudstone, mudstone, and an alternation of planar parallel-stratified conglomerate, planar cross-stratified sandstone, and reddish mudstone (Figure 1b), related to alluvial fan conditions (Türkmen et al., 2007; Koç-Taşgın, 2011). During late Miocene to Pliocene, a compressional tectonic regime caused the deformation of Miocene formations in the Malatya Basin, which could be observed as hydroplastic deformation horizons within the late Miocene formations (Kaymakçı et al., 2006; Koç-Taşgın, 2011) (Figure 1b). Even though late Pliocene basalt lava flows are common in the northern part of the Malatya Basin (Ercan and Asutay, 1993; Ekici et al., 2007; Kocaaslan and Ersoy, 2018; Di Giuseppe et al., 2021) Late Pliocene basalt lavas or volcanic rocks are not exposed within the Bozburun coalfield. Finally, all Neogene units are overlain by unconformably unconsolidated Quaternary sediments (pebbles, sand, and silt) (Figure 1c).

### 3. Samples and Applied Methodology

In this study, a total of twelve samples (nine coal, one floor, one roof, and one parting) were obtained from the working coal face of an underground mine in the eastern part of Bozburun coalfield (Figure 2). The lithotype descriptions of the coal samples were performed following the International Committee for Coal and Organic (ICCP) nomenclature (ICCP, 1993). Standard proximate, ultimate and petrographic analyses, as well as calorific determination were conducted at Hacetepe University. Coal petrography analyses were performed using polished blocks prepared according to the ASTM D2797/D2797M (2019) and examined under a coal petrography microscope. The maceral nomenclature followed ICCP System 1994 (ICCP, 2001; Sýkorová et al., 2005; Pickel et al., 2017). For rank determination, the mean random huminite reflectance measurements (%Rr) were exclusively performed on uliminite B following ISO 7404-5 (2009) standard.

For X-ray powder diffraction (XRD) analysis of raw coal and non-coal samples, a Bruker D8 equipment at the General Directorate of Mineral Research and Exploration (MTA) (Ankara, Türkiye) was used. EVA<sup>+</sup> software (Bruker) was used for semi-

quantitative determination of the mineralogical composition of the samples. For a better detailed mineralogical composition and determining accessory phases selected six coal (P-4, -5, -6, -8, -10, -11) and two non-coal samples (P-1 and -9) examined using FEI Quanta 400 FEI-SEM-EDX at the MTA. For these examination polished blocs were coated with carbon. The powered raw coal and non-coal samples pellets with KBr mixture were examined using a Perkin Elmer Spectrum-II (Fourier transform-infrared spectrometry (FT-IR) instrument. The XRF, ICP-OES, and ICP-MS analyses of all samples were conducted at the MTA. The major oxide contents were determined from raw samples using XRF equipment. For determination of minor and trace elemental compositions using ICP-OES and MS analyses, all samples were firstly ashed at 550 °C, for complete the removing of organic fraction of samples, in a muffle furnace. The digested solutions were prepared from ashed samples using in perchloric acid, aqua regia, nitric acid and concentrated hydrochloric acid following Nadkarni (1980) methodology. Minor and trace elemental compositions were determined using ICP-OES and ICP-MS equipment. External and internal standards were used for checking the accuracy of the analyses.

### 4. Findings

#### 4.1. Coal Quality

The coal samples are generally black and greyish black in colour. In the low part of the seam, calcareous fossil remains-bearing bands were identified. In the upper part of the seam, the matrix lithotype dominates, i.e., black-coloured gelified humic mass without any mineral impurities and/or with mineral impurities thinner than 1 mm, were identified. In the low part the mineral-rich lithotype prevails, i.e., greyish in colour and containing fossil shell remains-bearing thicker than 1 mm (Table 1, Figure 2). The roof rock sample is fossiliferous claystone, while the parting and floor rock samples are fossiliferous carbonaceous claystone (Figure 2). Furthermore, parting and roof rock samples also contain disseminated carbonized fossil plant litter remains.

Table 1- The results of proximate and ultimate analyses of coal and coal samples, as well as of the calorific value determination of coal samples ((VM: volatile matter, GCV: gross calorific value; asr: as-received basis; d: dry basis; daf: dry, ash-free basis; \*oxygen content is calculated by subtraction [O = 100 – (C + H + S + N + ash)] on dry basis).

Sample No	Sampling Interval (cm)		Lithology for Non-coal samples/ Coal Lithotype	Moisture (wt.%, asr)	Ash yield	VM	GCV (MJ/kg, daf)	C	H	N	S	O*
					(wt.%, d)	(wt.%, d)						
P-1	0	10	Claystone	14.5	69.0	31.0	na	9.6	na	na	0.01	na
P-2	10	20	Matrix	25.6	30.6	40.9	28.4	49.9	5.4	1.2	6.8	6.1
P-3	20	30	Mineral-rich	24.4	48.3	35.0	26.2	36.5	4.3	0.8	6.3	3.8
P-4	30	40	Matrix	26.7	32.3	42.2	28.3	49.6	5.5	1.1	6.6	4.8
P-5	40	50	Matrix	22.3	32.0	43.4	28.5	50.5	5.4	1.1	6.4	4.5
P-6	50	60	Matrix	26.8	20.8	42.7	28.8	58.7	6.2	1.3	4.6	8.4
P-7	60	70	Mineral-rich	23.2	74.4	19.8	16.7	15.6	3.0	0.3	2.6	4.2
P-8	70	80	Mineral-rich	25.8	42.6	34.9	27.0	40.6	4.3	0.9	6.6	5.0
P-9	80	90	Carbonaceous claystone	17.1	62.0	38.0	na	12.8	na	na	0.1	na
P-10	90	100	Mineral-rich	19.6	60.6	39.4	8.6	17.4	1.5	0.1	0.3	20.1
P-11	100	110	Mineral-rich	19.4	62.7	37.3	6.7	15.6	1.4	0.1	0.4	19.8
P-12	110	120	Carbonaceous claystone	20.4	87.6	12.4	na	4.7	1.7	0.0	1.7	4.3

The ash yield displays a decreasing trend towards the upper part of the seam (Figure 3); in turn, the gross calorific value (GCV) and total C content are relatively high in this part. These trends are clearly related to the matrix lithotype in the upper part of the seam (Table 1). Furthermore, the total S content displays an increasing trend towards the upper part, where total S content is high (> 5%, on dry basis) (Table 1 and Figure 3). As expected, the volatile matter contents of fossil shell remain-bearing samples are deceptively higher than this in the other samples. This could be related

to the breakdown of the calcareous remains (Table 1). Similarly, relatively high volatile matter content is also generally reported from fossil shell-bearing Turkish Cenozoic coalfields such as Afşin-Elbistan, Soma, Kangal, Milas, and Karapınar coalfields (Karayığit et al., 2001, 2017a, 2019; Bückün et al., 2015; Oskay et al., 2016, 2019). The hydrogen content of the matrix samples is relatively higher (5.4-6.2%, on dry basis) than this of the mineral-rich ones (1.4-4.3%, on dry basis).

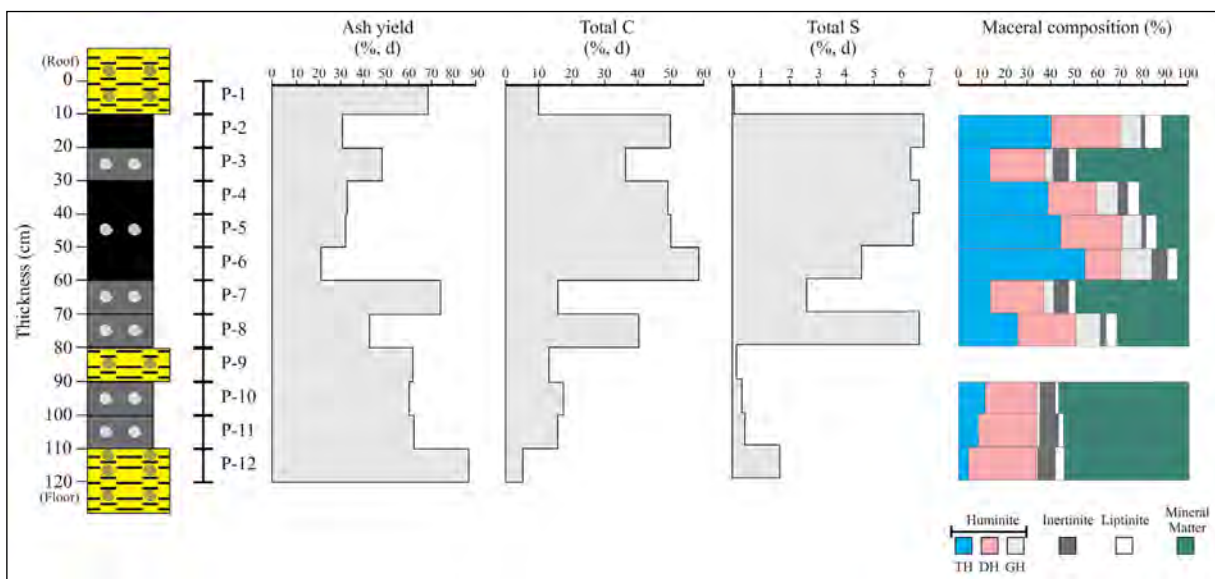


Figure 3- Vertical distribution of ash yield, total C and S, and maceral contents (on whole-basis) through the studied seam (for lithostratigraphic column, see Figure 2).

#### 4.2. Maceral Composition and Huminite Reflectance

Huminite is the most common maceral group (34.1-84.5%, on a whole basis) in the studied samples, while inertinite (1.3-8.3%, on a whole-basis) and liptinite (1.5-6.7%, on a whole-basis) display variable proportions in the entire seam (Table 2 and Figure 3).

Telohuminite is the prevalent huminite maceral subgroup in the matrix lithotype samples, whereas detrohuminite displays generally higher proportions in the mineral-rich matrix samples (Figure 4). Textinite prevails generally in the matrix lithotype (Figures 4a-b) with telohuminite being mainly represented by ulminite (Figures 4a-c and e, and 5a). Porigelinite, resinite and corpohuminite commonly fill cell lumens of textinite (Figures 5a-b). The ulminite B variety is generally well gelified; however, the ulminite A variety exhibits very weak brownish fluorescence (Figures 5a-b). Densinite has higher proportions in the matrix samples, whereas in the mineral-rich ones, attrinite is more common. Inertinite (e.g., inertodetrinite and fusinite) and liptinite macerals (e.g., sporinite and liptodetrinite) are generally embedded within densinite (Figures 4d and 5c-d). Furthermore, attrinite appears generally within clay mineral aggregates (Figures 5c and f). Corpohuminite is the prevalent gelohuminite maceral in the coal samples and, as mentioned above, is mostly observed as cell-lumens infilling, as well as phlobaphinite (Figure 4a). The latter one could also be

an indicator of woody peat-forming plants (Sýkorová et al., 2005). As noted above, porigelinite is identified within telohuminite macerals (Figure 4b), while levigelite is identified in the entire seam (Figure 4d).

The inertinite content is generally higher than 10% (on a mineral matter-free basis) in the low part of the seam, and fusinite, inertodetrinite, and semifusinite are identified in the entire seam. Inertodetrinite, fusinite, and semifusinite macerals are mostly observed within clay aggregates and densinite (Figures 4d and 5c-d), while individual fusinite and semifusinite macerals are also identified in the coal samples (Figure 5f). Funginite is less common in the coal samples and is mostly identified within ulminite (Figure 4c). Liptinite proportions show an increasing trend towards the upper part of the seam (Figure 3), which resulted in increased H contents. Cutinite, liptodetrinite and sporinite are identified in all the samples (Figures 4e-f). The presence of fluorinite-variety resinite could also imply the existence of *Myrica* within the palaeomire, which is also supported by the presence of *Myrica* pollen according to Türkmen et al. (2004). The identified minerals under white-incident light are mostly clay mineral aggregates and framboidal pyrite grains and agglomerates, and rarely syngenetic carbonate bands (Figures 4b-d, and 5c and f). Furthermore, calcareous fossil shell fragments and possible diatom remains and/or sponge spicules are also included (Figure 5e).

Table 2- Maceral composition (vol%) and mean random ulminite reflectance (%Rr) of the studied coal samples and floor sample (P-12) (TH: telohuminite, DH: detrohuminite, GH: gelohuminite, H: huminite, I: inertinite, L: liptinite, MM: mineral matter, Stdv: standard deviation).

Sample No	Petrographic Composition (vol%)							%Rr ± Stdv	Maceral Indices (dimensionless)						
	TH	DH	GH	H	I	L	MM vol%, on whole basis		A	B	C	TPI	GI	VI	GWI
	vol%, on mineral-free basis														
P-2	46.0	33.6	10.9	90.5	1.9	7.6	11.9		56.1	42.0	1.9	1.4	2.3	1.3	0.8
P-3	27.0	46.3	7.7	81.0	12.6	6.4	49.1		31.9	55.5	12.6	0.6	0.9	0.6	1.9
P-4	49.0	27.0	12.0	88.0	5.2	6.8	21.1	0.31±0.01	55.5	39.4	5.1	1.4	2.3	1.7	0.9
P-5	51.7	30.7	10.2	92.6	1.5	5.9	13.4		58.0	40.5	1.5	1.5	3.1	1.5	0.6
P-6	57.9	16.6	14.2	88.7	6.7	4.6	4.7	0.32±0.01	66.5	26.8	6.7	2.6	4.0	2.9	0.6
P-7	27.2	46.2	7.7	81.1	12.5	6.4	49.0		32.0	55.4	12.5	0.6	0.9	0.6	1.9
P-8	37.2	36.9	15.9	90.0	3.1	6.9	31.2	0.32±0.01	42.6	54.3	3.1	0.8	2.8	1.0	1.5
P-10	27.6	52.0	2.2	81.8	14.8	3.4	57.0	0.32±0.01	29.6	55.6	14.9	0.5	0.4	0.5	1.8
P-11	19.0	55.6	3.0	77.6	18.1	4.3	54.4		21.4	60.4	18.2	0.3	0.3	0.4	1.7
P-12	9.1	64.4	1.0	74.5	16.7	8.8	54.1		13.1	70.1	16.8	0.1	0.1	0.2	1.6

The mean random huminite reflectance (%Rr) values ranges between 0.31-0.32% (Table 2). These values are generally lower than the reported measured ones (0.38-0.51%) from the western part of the coalfield by Yalçın-Erik and Ay (2021).

### 4.3. Mineralogy

#### 4.3.1. Minerals in Coal Samples

The minerals identified by XRD in the bulk coal samples, are calcite, clay minerals (illite and smectite),

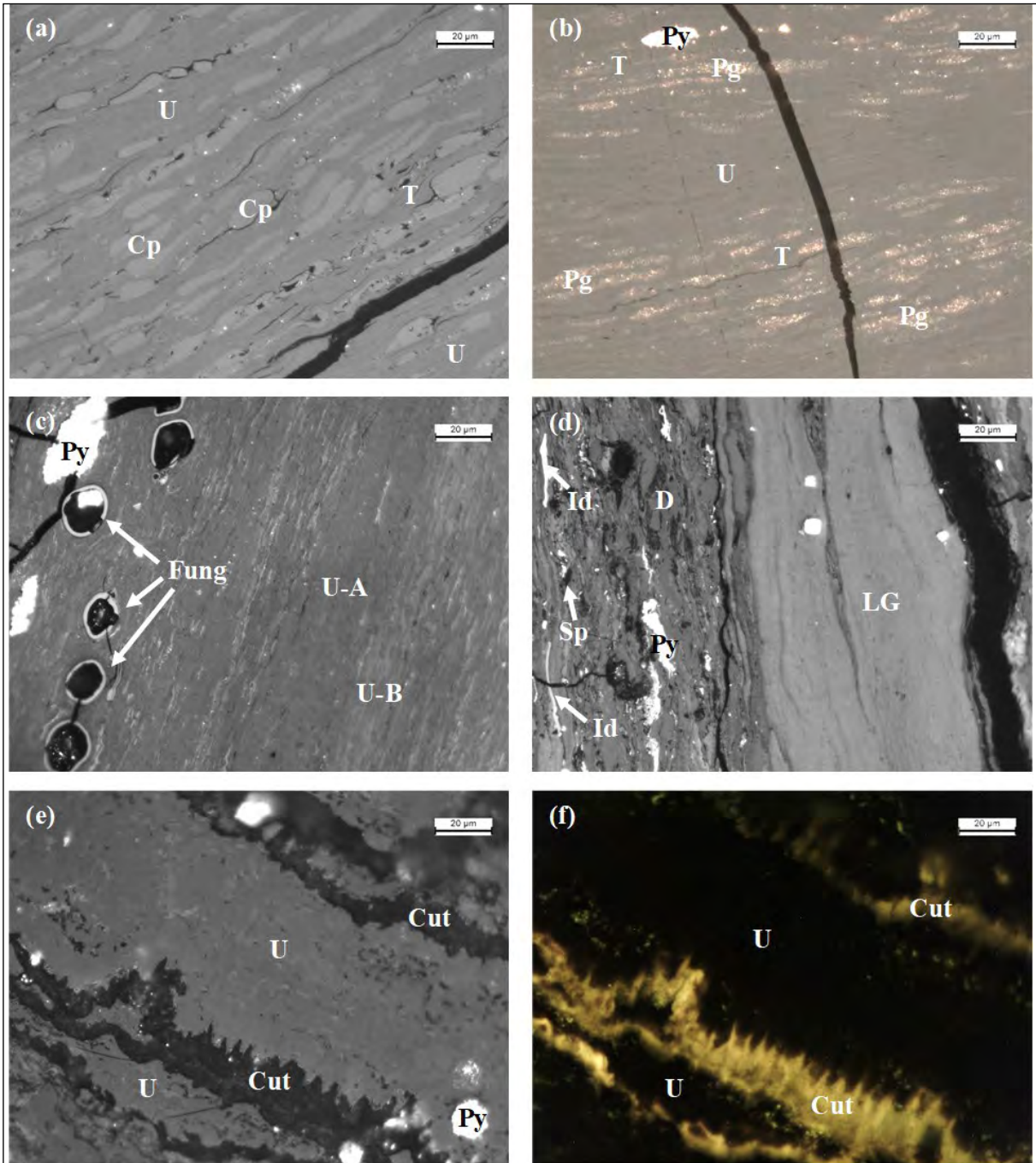


Figure 4- Selected photomicrographs of the Bozburun coal samples. All photomicrographs are taken under incident white light (a-e) or blue-light excitation (f), in oil immersion, 500× total magnification (Abbreviations: textinite (T), ulminite (U), ulminite-A (U-A), ulminite-B (U-B); densinite (D), corphuminite (Cp), porigelinite (Pg), levigelinite (LG), inertodetrinite (Id), funginite (Fung); sporinite (Sp); cutinite (Cut), and pyrite (Py)).

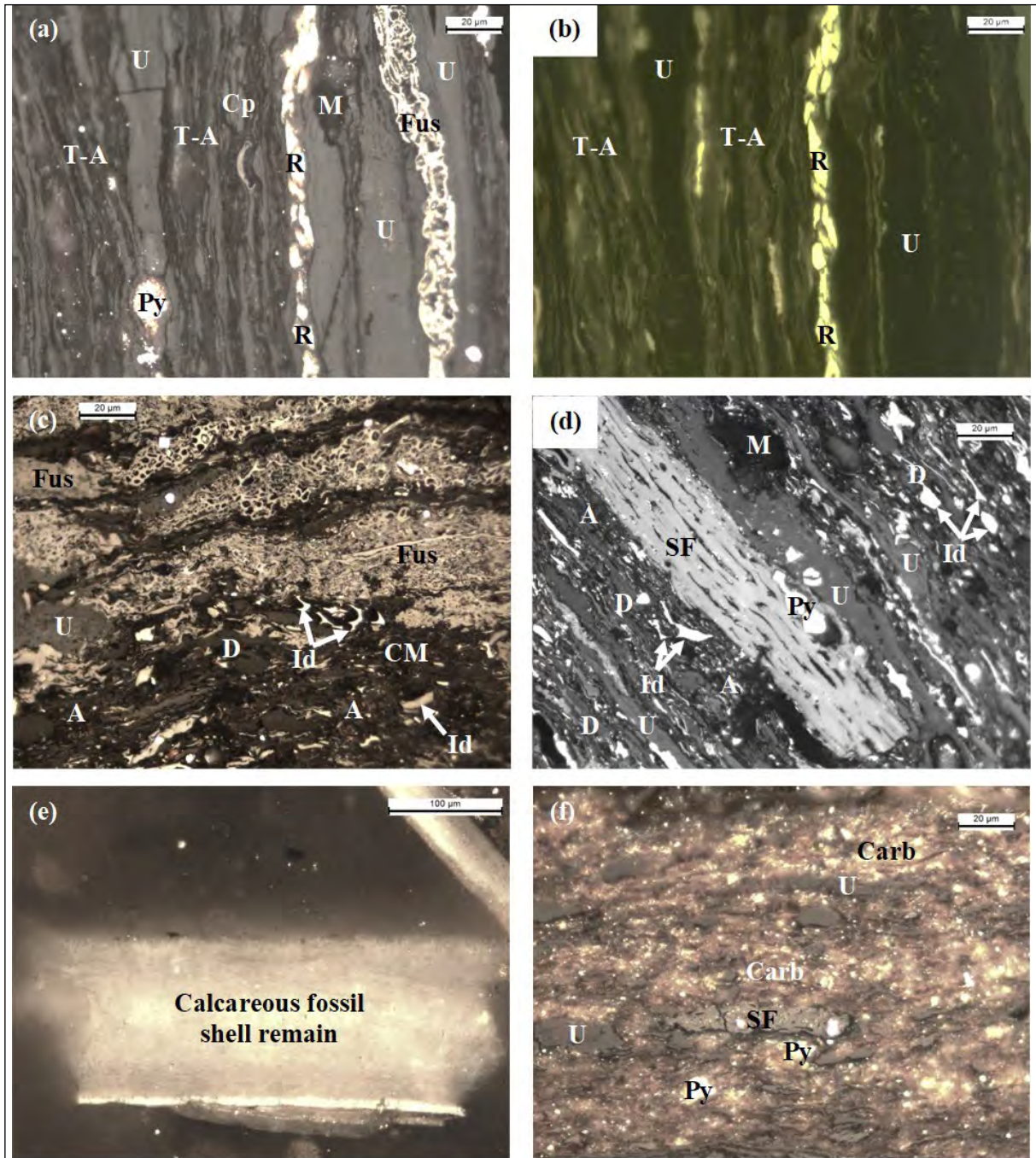


Figure 5- Selected photomicrographs of the Bozburun coal samples; a), c), d), e), f) all photomicrographs are taken under incident white light, b) blue-light excitation in oil immersion, 500× total magnification (Abbreviations: textinite-A (T-A), ulminite (U), attrinite (A), densinite (D), fusinite (Fus), semifusinite (SF), inertodetrinite (Id), resinite (R), pyrite (Py), clay mineral (CM), syngenetic carbonate (Carb), and mineral-matter (M)).

quartz, and pyrite (Table 3); a similar mineralogical composition is also obtained from the western part of the basin (Yalçın-Erik and Ay, 2021). Furthermore, in fossil shell-bearing samples, aragonite is also detected, and feldspars and marcasite are determined as minor phases (Table 3). Clay and carbonate minerals are

abundant to dominant phases, while quartz is generally a minor phase. The SEM-EDX data agrees with the XRD data, and chlorite (chamosite), Cl/F-apatite, celestine, dolomite, barite, sphalerite, titanite (sphen), and Ti-oxides, are identified as accessory phases (Table 3). In addition, pyritized calcareous fossil

Table 3- Semi-quantitative mineralogical composition of the Bozburun coal and non-coal samples based on XRD and SEM-EDX analyses (+++ = dominant phase (> 40%), ++ = abundant phase (10–20%), + = minor phase (< 10%) by XRD, a: accessory mineral detected by SEM-EDX).

Mineral	Sample											
	P-1	P-2	P-3	P-4	P-5	P-6	P-7	P-8	P-9	P-10	P-11	P-12
Quartz	+	+	+	+	+	+	+	+	+	+	+	+
Clay Minerals	+	+++	+++	+++	+++	+++	+++	+++	a	a	a	+++
Feldspar	a				+	a		a	a	a	a	+
Titanite	a					a						
Calcite	+++		+	++	++		+	+	+++	+++	+++	+
Aragonite			++		++						++	
Dolomite	a			a								
Pyrite	+	+++	++	++	++	+	+	+	+	a	+	+
Marcasite					a					+		
Sphalerite								a				
Celestine	a									a		
Barite	a											
Apatite						a			a	a		
Ti-oxides						a						

shell fragments and diatom/freshwater sponge spike remains, and fossil bone remains of Ca-phosphate composition were also identified using SEM-EDX.

#### 4.3.2. Minerals in Non-coal Samples

According to XRD data, the minerals in the non-coal samples are similar to these of the coal samples. Calcite, clay minerals (smectite, illite and chlorite), quartz, and pyrite are identified in all non-coal samples (Table 3). Furthermore, feldspars are also detected from the floor sample. As expected, calcite is generally the dominant phase in the roof and parting samples in calcareous fossil remains-bearing samples, whereas in the floor sample clay minerals are predominant (Table 3). Quartz and pyrite are minor phases in the non-coal samples.

#### 4.4. FT-IR Analysis

Selected FT-IR spectra are reported in Figure 6. The bands around wavenumbers 1030 and 530  $\text{cm}^{-1}$  could be originated from clay minerals (Georgakopoulos et al., 2003; Madejova, 2003). Furthermore, the intense bands at 3400  $\text{cm}^{-1}$  could also be attributed to clay minerals or more possibly with OH-stretching vibration (Madejova, 2003; Djowe et al., 2013; Jiang et al., 2021). The band around 470  $\text{cm}^{-1}$  could be attributed to quartz/silica grains (Çetinkaya and

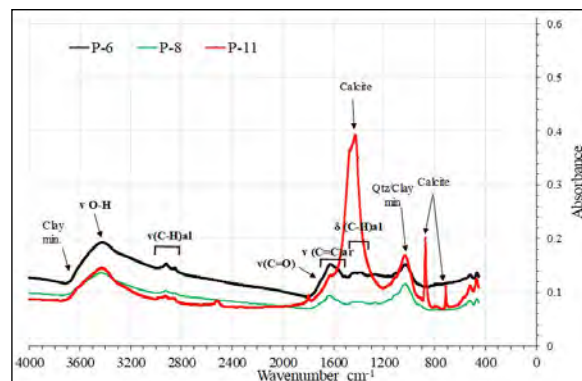


Figure 6- FT-IR spectra of selected Bozburun samples.

Yürüm, 2000; Georgakopoulos et al., 2003; Naik et al., 2021) however, the lack of intense bands at 1100  $\text{cm}^{-1}$  might not imply a lack of quartz/silica in the samples. This may be caused by the strong absorption of clay minerals and the overlap of quartz peak at 1100  $\text{cm}^{-1}$ . Strong and board peaks around 1425, 875, and 711  $\text{cm}^{-1}$ , particularly in the sample P-11, clearly result from calcite and/or fossil shell remains; similar peaks were also reported from fossil shell remains bands-bearing Turkish Neogene coals (e.g., Soma and Muğla Basins) (Çetinkaya and Yürüm, 2000; Baysal et al., 2016). The peaks at 2851  $\text{cm}^{-1}$  and 1385  $\text{cm}^{-1}$ , and 2920  $\text{cm}^{-1}$  could imply the existence of aliphatic  $\text{CH}_2$  and  $\text{CH}_3$  symmetric and aliphatic C-H asymmetric

stretching vibrations, respectively (Oikonomopoulos et al., 2013; Chen et al., 2015; Jiang et al., 2021; Naik et al., 2021). The oxygen-containing functional groups (e.g., C=O and C=C aromatic ring) in coal samples could be evident with the peaks between 1613-1630  $\text{cm}^{-1}$  (Georgakopoulos et al., 2003; Chen et al., 2015; Çelik et al., 2021).

#### 4.5. Geochemistry

The major oxide contents of studied samples are reported in Table 4. The  $\text{SiO}_2$  (8.4-46.8%, on whole coal basis) and  $\text{Al}_2\text{O}_3$  (3.1-11.6%, on whole coal basis) contents of the coal samples are generally higher than inorganic samples. The CaO contents of fossil shell-bearing coal samples (34.5-37.6%, on coal basis) in the low part of seam, floor and intercalation samples (33.3-36.8%, on whole rock basis) are significantly higher than coal samples in the upper part of seam (1.5-6.0%, on whole coal basis) (Table 4). The contents of  $\text{SiO}_2$ ,  $\text{TiO}_2$ ,  $\text{Al}_2\text{O}_3$ ,  $\text{Na}_2\text{O}$ , and  $\text{K}_2\text{O}$  display increasing trends towards the central part of the seam (Figure 7 and Table 4). As expected, the CaO content decreases towards the upper parts of the seam, and the  $\text{Fe}_2\text{O}_3$  and MnO contents do not show any significant changes throughout the seam (Figure 7). The average concentrations of trace elements in analysed coal samples using ICP-MS do not exceed 100 ppm on a whole coal basis, except B and Sr concentrations (Tables 4 and 5). The average B concentration of coal samples is 161 ppm (Tables 4 and 5), whereas the average concentration of Sr is 1021 ppm, and the Sr concentration of sample P-10 is 6814 ppm on a whole coal basis (Tables 4 and 5). Like the coal samples, the average Sr concentration of non-coal samples exceeds 1000 ppm on a whole rock basis (Tables 4 and 6). In addition, the average Ba concentration of non-coal samples is higher than 100 ppm on a whole rock basis (Tables 4 and 6). The concentrations of trace elements in the coal samples are mostly less than 5 ppm, while the average concentrations of rare earth elements and Y (REY) contents do not exceed 1 ppm on a whole coal basis, except Y and La (Table 5).

The concentration coefficient (CC) of coal and non-coal samples was calculated for determining elemental enrichments (Tables 5 and 6). This calculation is based on dividing average concentrations of elements into

Clarke values for low-rank coals and sedimentary rocks (Ketriss and Yudovich, 2009; Dai et al., 2015b). Nickel (CC = 10.4) is the only significantly enriched element in coal samples, and the other enriched elements are Sr (CC = 8.5), As (CC = 5.8), Mo (CC = 5.4), and U (CC = 5.1). Furthermore, slightly enriched elements in coal samples are Cr (4.4), V (4.4), P (3.8), Ti (2.5), B (2.9), Rb (2.3), and Zn (2.1), whereas Ba and most of REY are depleted (CC<0.5) (Table 5). The remaining elements display concentrations close to the Clarke values of low-rank coals. In non-coal samples, the majority of elements are depleted (Table 6); nevertheless, the slightly enriched elements in non-coal samples are Sr (CC = 4.0), As (CC = 2.7), and Ni (CC = 2.2). The elements P, Ti, Cr, Mn, Co, Ba, Pb, and U have average concentration close to Clarke values of the sedimentary rocks (Table 6). Furthermore, outlook coefficient ( $C_{\text{out}}$ ) of REY and  $\Sigma\text{REY}$  oxides values of coal and non-coal samples are within non-promising for REY recovery potential (Seredin and Dai, 2012). Of note, the ashing temperature might also cause the volatilization of As and B in coal samples; therefore, their CC might be higher than the measured concentrations.

## 5. Discussions

### 5.1. Coal Rank

The measured Rr values (0.31-0.32%) and the determined gross calorific values (6.7-28.8 MJ/kg, on dry, ash-free basis) of the coal samples imply that the Bozburun coal seam is of low rank C-B (lignite) according to ASTM D388-19a (2021), E.C.E-UN (1998) and ISO 11760 (2005) classifications. The coal samples are also classified as moderate to high ash yield coal and very low to moderate grade coal according to ISO 11760 (2005) and E.C.E-UN (1998) classification, respectively. Considering the ash yields of the mineral-rich lithotype samples from the low part of the seam, these samples could be classified as carbonaceous shale. Nevertheless, this identification could not be accurate since calcareous fossil shell remains-bearing bands are included in these samples.

In comparison with the reported measured Rr values (0.38-0.51%) from the western part of the Bozburun coalfield, and the northern part of the

Table 4- Elemental composition of coal and non-coal samples (all on whole rock-basis) in the Bozburun coalfield. All results in ppm, except otherwise cited (LOI: loss on ignition, bdl: below detection limit).

Element	Sample											
	P-1	P-2	P-3	P-4	P-5	P-6	P-7	P-8	P-9	P-10	P-11	P-12
LOI (%)	31.0	72.4	55.1	70.6	70.7	81.6	26.7	60.6	37.2	38.7	37.0	37.0
SiO <sub>2</sub> (%)	21.7	12.9	22.7	11.8	11.0	8.4	46.8	22.1	15.1	10.7	15.4	33.1
TiO <sub>2</sub> (%)	0.2	0.3	0.3	0.2	0.2	0.2	0.7	0.4	0.1	0.2	0.2	0.7
Al <sub>2</sub> O <sub>3</sub> (%)	5.9	4.0	6.3	3.3	3.1	2.2	11.6	5.6	4.3	3.1	4.7	10.9
Fe <sub>2</sub> O <sub>3</sub> (%)	3.4	5.5	6.3	5.6	5.5	3.3	5.8	6.3	2.4	6.1	4.6	6.7
MnO (%)	0.11	0.05	0.07	0.06	0.07	0.04	0.08	0.07	0.09	0.09	0.07	0.09
MgO (%)	2.6	2.2	2.8	2.1	2.2	1.7	3.6	2.4	2.7	2.1	2.0	4.3
CaO (%)	33.3	1.5	4.8	5.1	6.0	1.4	2.2	1.0	36.8	37.6	34.5	4.3
Na <sub>2</sub> O (%)	0.4	0.6	0.7	0.6	0.6	0.6	0.8	0.7	0.3	0.3	0.3	0.9
K <sub>2</sub> O (%)	1.2	0.4	0.7	0.4	0.4	0.4	1.5	0.8	0.8	0.7	1.0	1.8
P <sub>2</sub> O <sub>5</sub> (%)	0.12	0.12	0.22	0.22	0.25	0.18	0.07	0.06	0.13	0.28	0.15	0.13
Li	bdl	10	12	6.0	7.2	5.5	14	14	bdl	bdl	bdl	8.4
B	15	216	146	234	235	297	87	170	17	37	28	30
Sc	3.4	2.6	2.9	2.2	2.6	2.2	7.6	4.5	2.2	2.1	2.4	5.9
V	20	70	142	81	89	110	82	152	21	69	74	43
Cr	63	57	66	45	55	47	126	104	41	45	49	108
Co	4.1	8.9	8.0	3.7	3.5	3.6	14	12	3.1	5.4	5.5	15
Ni	43	103	153	55	64	40	142	147	31	70	68	166
Cu	7.5	8.3	14	11	9.8	10	13	11	8.0	13	12	15
Zn	21	37	24	22	26	23	94	59	17	26	33	84
Ga	bdl	4.2	4.9	4.0	4.0	2.7	7.6	6.0	bdl	4.2	bdl	6.8
As	23	22	66	75	115	12	19	35	10	33	18	29
Rb	15	12	20	15	15	11	66	26	18	16	22	68
Sr	1794	244	239	329	269	240	162	216	1218	6813	679	244
Y	3.6	2.2	3.5	2.2	2.3	5.4	8.5	5.5	3.0	2.7	3.6	5.3
Cd	bdl	bdl	bdl	bdl	1.7	0.9	bdl	bdl	bdl	bdl	bdl	bdl
Mo	bdl	14.7	8.9	16.1	16.1	19.5	4.8	13.6	bdl	6.6	7.4	bdl
Sb	bdl	bdl	6.6	bdl	bdl	bdl	bdl	bdl	bdl	bdl	bdl	bdl
Ba	478	32	33	33	26	16	56	35	126	181	97	47
La	4.6	3.1	5.3	3.1	3.6	4.7	16	6.6	3.2	3.0	4.5	13
Ce	8.5	6.5	11	5.6	6.3	7.9	30	12	5.6	5.4	7.8	24
Pr	1.1	0.7	1.3	0.7	0.8	1.0	4.0	1.6	0.7	0.7	1.0	3.2
Nd	3.5	2.4	4.2	2.2	2.6	3.5	13	5.0	2.4	2.4	3.4	10
Eu	0.3	0.1	0.2	0.1	0.1	0.2	0.7	0.3	0.2	0.2	0.2	0.4
Gd	0.7	0.4	0.8	0.4	0.5	0.8	2.3	1.1	0.6	0.5	0.7	1.9
Tb	0.14	0.08	0.13	0.09	0.09	0.15	0.4	0.2	0.06	0.06	0.12	0.3
Dy	0.6	0.4	0.7	0.3	0.4	0.7	1.8	1.0	0.4	0.4	0.6	1.3
Ho	0.14	0.08	0.13	0.09	0.09	0.16	0.3	0.2	0.06	0.06	0.12	0.3
Er	0.3	0.2	0.4	0.2	0.2	0.4	0.8	0.6	0.2	0.2	0.3	0.4
Tm	bdl	bdl	bdl	bdl	bdl	0.07	0.14	0.08	bdl	bdl	bdl	0.08
Yb	0.3	0.2	0.3	0.2	0.2	0.4	0.6	0.5	0.2	0.2	0.2	0.5
Lu	bdl	bdl	bdl	bdl	bdl	0.05	0.07	0.08	bdl	bdl	bdl	bdl
Hf	2.0	1.3	1.0	0.9	1.3	0.7	1.7	2.9	bdl	0.8	0.6	1.4
Pb	bdl	6.1	bdl	3.7	5.8	4.5	14.4	10.8	bdl	bdl	9.2	16.9
Th	1.6	1.9	2.8	1.3	1.6	1.3	6.9	3.3	1.1	1.0	1.4	5.7
U	0.7	10.9	15.5	16.7	19.6	20.4	9.5	19.2	2.0	9.8	10.0	4.4

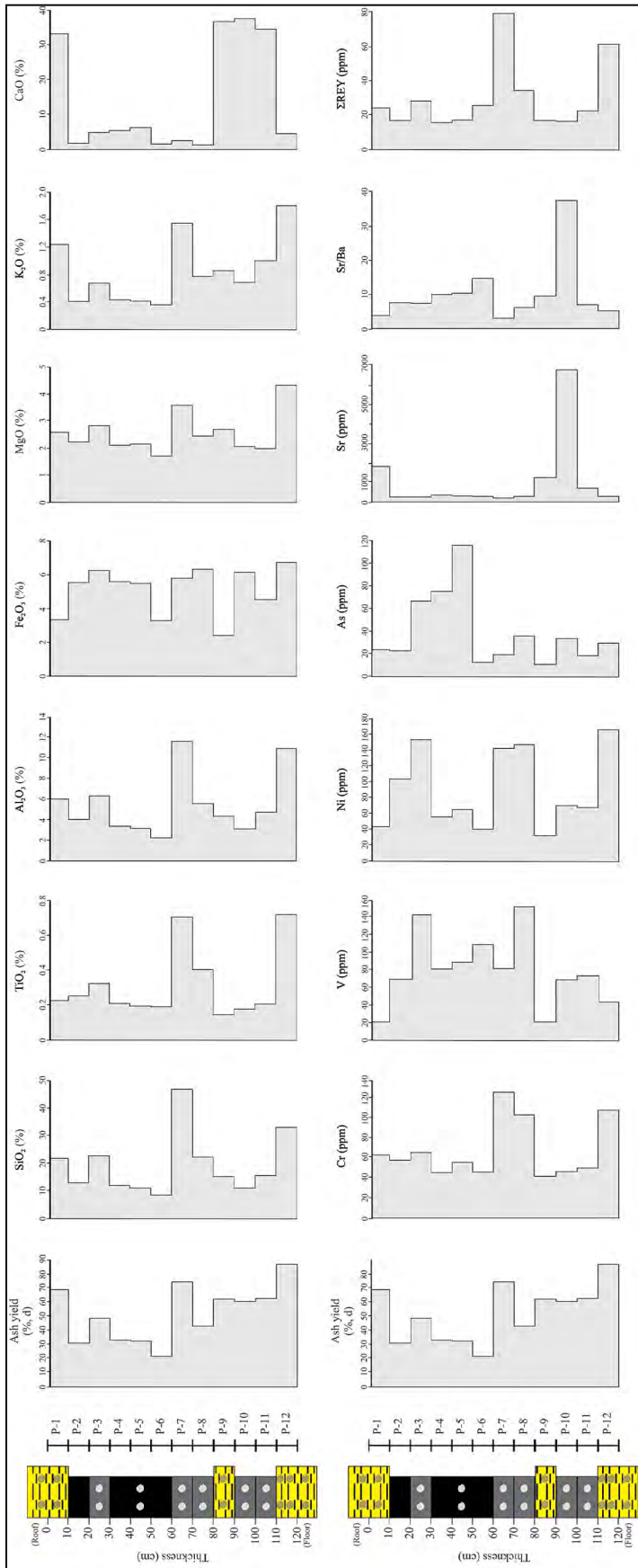


Table 5- Weighted average of the Ti, P, Mn, minor and trace elements (in ppm) for the Bozburun coal samples and their comparison with worldwide coals (a: from Swaine (1990); b: from Ketris and Yudovich (2009). Elements in bold are enriched.

Element	Most world coals <sup>a</sup>	Clarke values for low-rank coals	Bozburun coal samples	Concentration coefficient (CC)
Li	1-80	10	7.7	0.8
<b>B</b>	<b>5-400</b>	<b>56</b>	<b>161</b>	<b>2.9</b>
<b>P</b>	<b>10-3000</b>	<b>200</b>	<b>757</b>	<b>3.8</b>
Sc	1-10	4.1	3.2	0.8
<b>Ti</b>	<b>10-2000</b>	<b>720</b>	<b>1769</b>	<b>2.5</b>
<b>V</b>	<b>2-100</b>	<b>22</b>	<b>96</b>	<b>4.4</b>
<b>Cr</b>	<b>0.5-60</b>	<b>15</b>	<b>66</b>	<b>4.4</b>
<b>Mn</b>	<b>5-300</b>	<b>100</b>	<b>517</b>	<b>5.2</b>
Co	0.5-30	4.2	7.2	1.7
<b>Ni</b>	<b>0.5-50</b>	<b>9.0</b>	<b>94</b>	<b>10.4</b>
Cu	0.5-50	15	11	0.8
<b>Zn</b>	<b>5-300</b>	<b>18</b>	<b>38</b>	<b>2.1</b>
Ga	1-20	5.5	4.2	0.8
<b>As</b>	<b>0.5-80</b>	<b>7.6</b>	<b>44</b>	<b>5.8</b>
Rb	2-50	10	23	2.3
<b>Sr</b>	<b>15-500</b>	<b>120</b>	<b>1021</b>	<b>8.5</b>
Y	2-50	8.6	4.0	0.5
Cd	0.1-3	0.24	0.3	1.2
<b>Mo</b>	<b>0.1-10</b>	<b>2.2</b>	<b>12</b>	<b>5.4</b>
Sb	0.5-10	0.84	0.7	0.9
Ba	20-100	150	57	0.4
La	1-40	10	5.6	0.6
Ce	2-70	7.2	10	1.4
Pr	1-10	3.5	1.3	0.4
Nd	3-30	11	4.3	0.4
Eu	0.1-2	0.5	0.2	0.5
Gd	0.1-4	2.6	0.8	0.3
Tb	0.1-1	0.32	0.1	0.5
Dy	1-4	2.0	0.7	0.3
Ho	0.1-2	0.5	0.1	0.3
Er	1-3	0.85	0.4	0.4
Tm	0.5-3	0.31	0.0	0.2
Yb	0.3-3	1.0	0.3	0.3
Lu	0.03-1	0.19	0.02	0.1
Hf	0.4-5	1.2	1.2	1.0
Pb	2-80	6.6	6.1	0.9
Th	0.5-10	3.3	2.4	0.7
<b>U</b>	<b>0.5-10</b>	<b>2.9</b>	<b>15</b>	<b>5.0</b>

Table 6- Weighted average of the Ti, P, Mn, minor and trace elements (in ppm) for the Bozburun non-coal samples and their comparison with worldwide coals [a: from Ketris and Yudovich (2009)].

Element	Clarke values for sedimentary rocks <sup>a</sup>	Bozburun non-coal samples	Concentration coefficient (CC)
Li	33	2.8	0.1
B	72	20	0.3
P	670	567	0.8
Sc	9.6	3.8	0.4
Ti	3740	2180	0.6
V	91	28	0.3
Cr	58	71	1.2
Mn	830	755	0.9
Co	14	7.4	0.5
<b>Ni</b>	<b>37</b>	<b>80</b>	<b>2.2</b>
Cu	31	10	0.3
Zn	43	41	0.9
Ga	12	2.3	0.2
<b>As</b>	<b>7.6</b>	<b>20.7</b>	<b>2.7</b>
Rb	94	33.4	0.4
<b>Sr</b>	<b>270</b>	<b>1085</b>	<b>4.0</b>
Y	29	4.0	0.1
Ba	410	217	0.5
La	32	6.8	0.2
Ce	52	13	0.2
Pr	6.8	1.7	0.2
Nd	24	5.4	0.2
Eu	0.94	0.3	0.3
Gd	4	1.1	0.3
Tb	0.69	0.2	0.3
Dy	3.6	0.8	0.2
Ho	0.92	0.2	0.2
Er	1.7	0.3	0.2
Tm	0.78	0.03	0.0
Yb	2	0.3	0.2
Hf	3.9	1.1	0.3
Pb	12	5.6	0.5
Th	7.7	2.8	0.4
U	3.4	2.4	0.7

Malatya Basin (0.68-0.79%) (Karayiğit and Whateley, 1997; Yalçın-Erik and Ay, 2021), the studied samples generally display relatively low R<sub>r</sub> values (Table 3). Furthermore, the calculated R<sub>r</sub> values using Rock-Eval pyrolysis data obtained from the western part of the Bozburun coalfield and coal beds outcropping north of Arguvan town (Yalçın-Erik and Ay, 2021), strongly vary from 0.20-0.69%. This parameter is proposed for organic-rich rock and/or bituminous shale samples by Jarvie et al. (2001), and its application to humic coals, particularly on Cenozoic low-rank coals, could be very problematic due to the presence of certain compounds (Zdravkov et al., 2006; Hazra et al., 2019; Çelik et al., 2021). For instance, the oxygenated functional groups in ulminite macerals (e.g., ulminite A or resin-impregnated ulminite A) or the breakdown of carbonate minerals could elevate S<sub>3</sub> peak values; hence, the T<sub>max</sub> values are suppressed and calculated R<sub>r</sub> values could be reduced. Considering the presence of oxygen-containing functional groups in the FT-IR spectra and the carbonate minerals in the coal samples, the calculated R<sub>r</sub> values from Rock-Eval pyrolysis data should be used with caution as a rank parameter for the Bozburun coal. As mentioned above, the presence of H-rich compounds could also cause a reduction of the R<sub>r</sub> values. The reported palynological and biomarker datasets from the Bozburun coalfield imply the existence of H-rich peat-forming plants (e.g., Taxodaeaceae-Cupresseeae) within the palaeomire (Önal, 1995; Türkmen et al., 2007; Yalçın-Erik and Ay, 2021). Thus, significantly low R<sub>r</sub> values (e.g., 0.27) were calculated from coals according to Rock-Eval data. Nevertheless, the coal petrography data indicates that the potential influence of H-rich ulminite macerals on R<sub>r</sub> values may be very limited, because ulminite B is the dominant telohuminite and ulminite A in the studied samples displays very weak fluorescence only (Figure 5b).

Another possibility controlling R<sub>r</sub> differences within the Malatya Basin could be the tectonic deformation. Since the study area faced post-coalification regional tectonic deformation, the R<sub>r</sub> values might have been affected (Hower and Gayer, 2002). This also seems to be not possible due to the lack of any deformed macerals in the coal samples. In the northern part of Malatya Basin, Pliocene basalts

and andesitic domes of the Yamadağ volcanics are widely exposed and overlay late Miocene coal-bearing sequences (Karayiğit and Whateley, 1997; Ekici et al., 2007). The measured R<sub>r</sub> values of the coal seams in the Selimoğlu coalfield are around 0.70%, which indicates bituminous rank. Nevertheless, the elevated measured R<sub>r</sub> values are obviously controlled by heat flow due to post-coalification andesitic domes in the Selimoğlu coalfield (Karayiğit and Whateley, 1997). Considering the presence of Pliocene volcanic rocks and lavas north of Arguvan town, the reported slightly high calculated R<sub>r</sub> values of the coal beds outcropping in this area (Kuyudere and Akören locations in Figure 1a), could be related to increased heat flow in the northern part of Malatya Basin (Yalçın-Erik and Ay, 2021).

Since the Pliocene volcanic rocks are observed in the Bozburun coalfield, the relative differences on measured R<sub>r</sub> values among the coalfield may not be related to influence of heat flow, like in the northern part of the Malatya Basin. Nevertheless, alkaline conditions within the palaeomire could cause biogeochemical gelification of organic matter; in turn, high gelification degree of organic matter could result in an increase of the R<sub>r</sub> values (Dehmer, 1995). As can be seen in sections 5.2 and 5.4, gelification index (GI) values are different within the coalfield and carbonate minerals are more common in the western part of the Bozburun coalfield, the studied section and the western part of the Bozburun coalfield display relatively small R<sub>r</sub> differences due to biogeochemical gelification and alkaline conditions within the palaeomire. Overall, coal-rank variations were developed from the northern (Selimoğlu coalfield) to the southern part (Bozburun coalfield) of the Malatya Basin due to post-coalification volcanic activity; biogeochemical gelification within the palaeomires caused variations in R<sub>r</sub> values within the Bozburun coalfield.

## 5.2. Provenance of minerals

Quartz/silica is mostly identified as irregularly shaped individual grains during SEM-EDX examination (Figure 8a and d), which indicates a clastic origin. In some samples, partially pyritized siliceous skeletons of diatoms and/or sponge spicules are also detected (Figure 8e). Such remains suggest

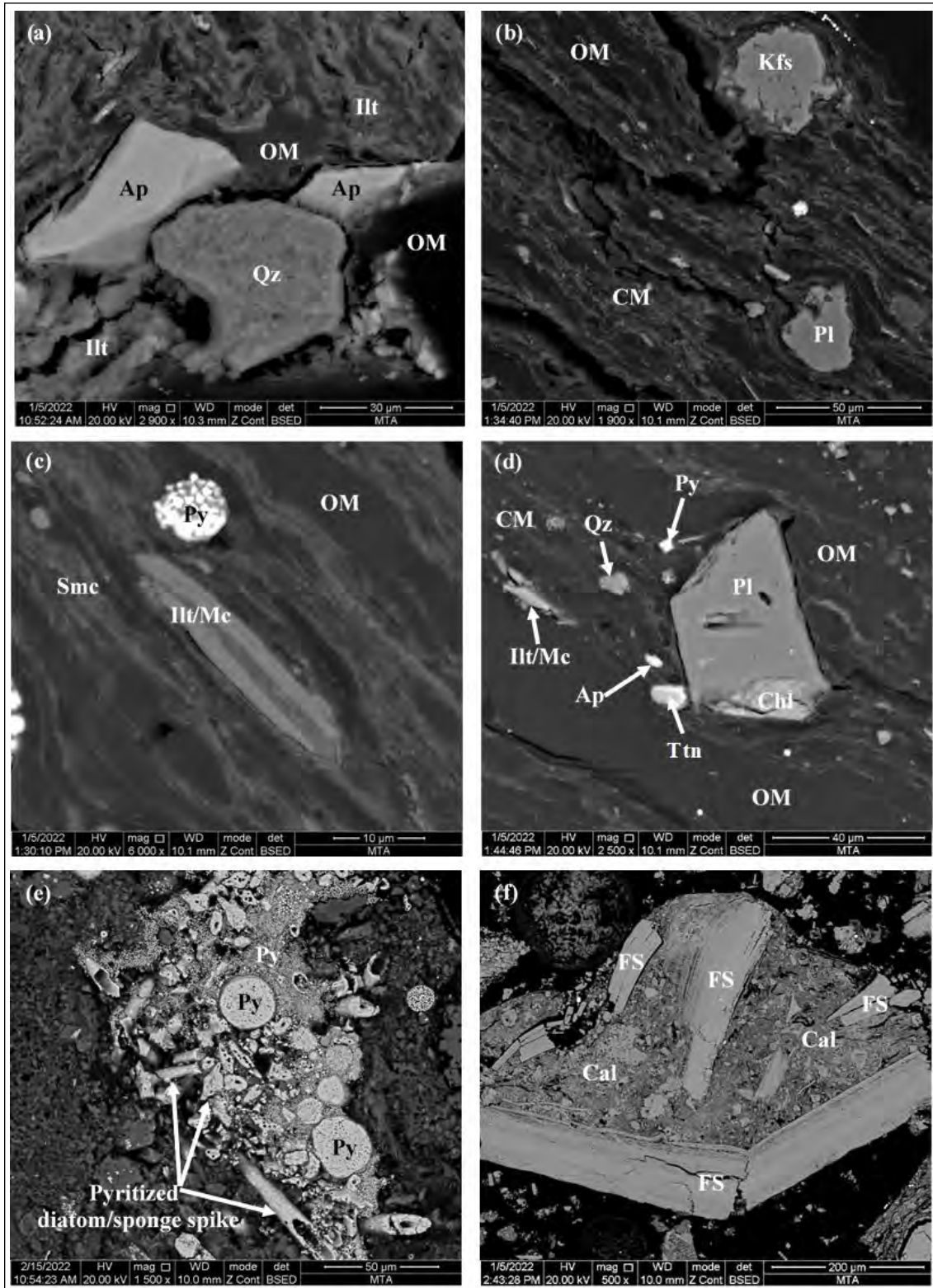


Figure 8- Selected SEM backscattered (BSE) images from the Bozburun samples: a) apatite (Ap), quartz (Qz) and organic matter (OM) associated with illite (Illt), b) K-feldspar (Kfs), plagioclase (Pl) and organic matter associated with clay minerals (CM), c) illite/mica (Illt/Mc) and organic matter associated with smectite (Smc) and framboidal pyrite (Py) grain, d) apatite (Ap), chlorite (Chl), quartz (Qz), plagioclase (Pl), titanite (Ttn), illite/mica (Illt/Mc) and organic matter (OM) associated with clay minerals (CM), e) pyritized possible diatom/sponge spike and framboidal pyrite (Py) aggregates, f) calcite (Cal) and fossil shell remains (FS).

that silica in coal samples is also biogenic in origin (Ward, 2002; Oskay et al., 2016; Çelik et al., 2021). Even though feldspar is a minor phase, K-feldspar and plagioclase grains are commonly observed during the SEM-EDX study. Like quartz, feldspar grains are identified as irregular shaped individual grains with sharp edges within clay mineral aggregates (Figure 8b and d). This implies short-distance transport of feldspar grains from the adjacent areas. The clastic sources for feldspars presumably are mainly the middle Miocene Malatya volcanics, and, in a lesser extent, the late Cretaceous Elazığ magmatics of the basements.

Clay minerals are identified as aggregates hosting also other mineral grains (e.g., Cl/F-apatite, quartz, feldspars, and titanite) and organic matter (Figures 8a-d). The clay aggregates mostly consist of smectite and subordinately illitic according to the SEM-EDX data. Illite components mostly derive as clastic input into the palaeomire (Siavalas et al., 2009), while smectite mostly originates from alteration of syngenetic or epiclastic volcanic input (Bohor and Triplehorn, 1993; Dai et al., 2017, 2020a; Karayiğit et al., 2020b). Since illitic aggregates are more common in the low part of the seam, illite aggregates in samples are syngenetic and clastic in origin. Furthermore, the individual illite/mica grains in the clay matrices could also be related to clastic input from the middle Miocene Malatya volcanic and/or magmatic rocks in the pre-Neogene basement (Figures 8c-d). The alterations of clastic input from the Malatya volcanics within the mires could result in syngenetic smectite formation under hydrogeologically closed system. During the SEM observations, lath-shaped Fe-rich chlorite (chamosite) grains are generally observed within the clay aggregates. Also, chlorite overgrowths are detected around feldspar grains (Figure 8d). These could indicate that chlorite is either derived from clastic inputs into palaeomires or alteration of feldspar grains within the paleomires and/or early diagenetic stages (Ward, 2002; Hower et al., 2015).

Carbonate minerals generally appear in form of carbonate bands and calcareous fossil shell remains, and rarely as individual calcite and dolomite grains (Figures 8f, 9a-b). These observations might imply

that the carbonates are clearly syngenetic originating from clastic input from the Permo-Triassic Keban metamorphics (e.g., marbles) or the pre-Neogene carbonates. Besides, calcareous fossil fragments, which are partially pyritized, are commonly observed in fossil shell remains-bearing samples (Figures 9a-b). Aragonite is generally detected as an abundant phase in the XRD patterns in a few fossil shell remains-bearing samples. However, aragonite was not detected in some calcareous fossil remains-bearing samples, whilst calcite is detected instead of aragonite (Table 3). This could be related to the conversion of aragonite to its polymorph calcite within the palaeomire or during a diagenetic stage (Querol et al., 1999; Ward, 2002). The predominance of carbonate minerals and the presence of partially pyritized calcareous fossil shell remains could indicate neutral to weak alkaline conditions (Kortenski, 1992; Karayiğit et al., 2017a;). However, the lack of carbonate minerals and the existence of framboidal pyrite grains and siliceous fossil remains (e.g., diatom) in the upper seam part point to low pH values of mire water or the Ca contents of influenced water into palaeomires was decreased (Kortenski, 1992; Dai et al., 2020a). Thus, syngenetic carbonate formation was limited due to increased acidity of palaeomire during late stages of peat accumulation in the Bozburun coalfield. Overall, syngenetic carbonate formation in the Bozburun palaeomire was controlled by the Ca-rich water influx along with clastic influx.

Pyrite is generally observed as individual framboidal aggregates within organic matter (e.g., ulminite), and framboidal and euhedral pyrite grains aggregate during coal petrography and SEM studies (Figures 4b, c, e, 5a, f, 8c, e, 9a). Additionally, cleat/fracture pyrite-infillings, and pyritized plant tissues, siliceous skeletons of diatoms and/or sponge spicules, and fossil shell remains, as mentioned above, are contained in coal samples (Figure 8e, f, 9c). These findings suggest that framboidal pyrite grains were precipitated within the palaeomire and/or early diagenetic stages as a result of sulphate-reducing bacteria and sulphate-rich water influx into palaeomires (Querol et al., 1989). The cleat/fracture pyrite-infillings are presumably controlled by precipitation of sulphate-rich porewaters during coalification. Another sulphide mineral identified by XRD is

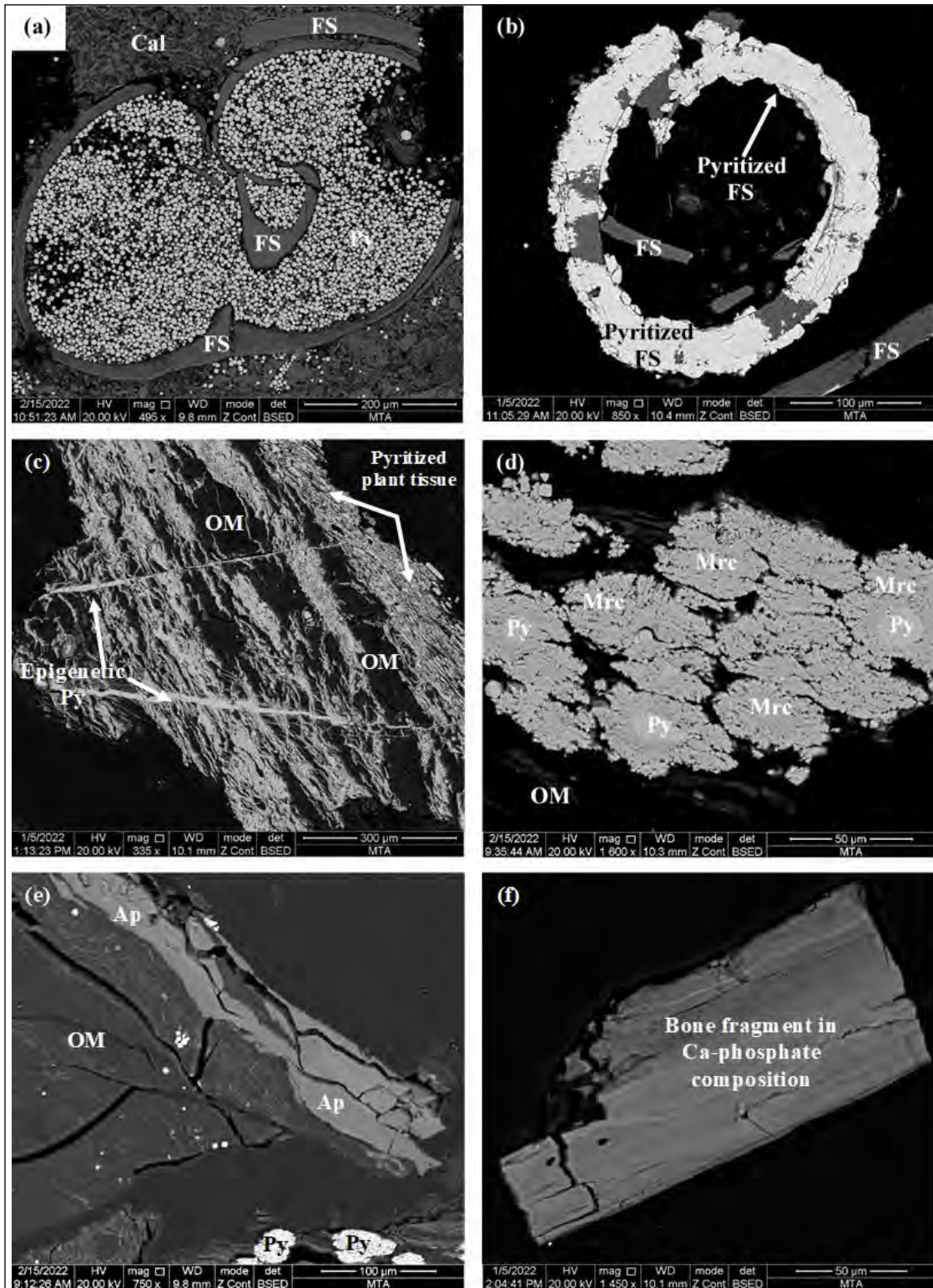


Figure 9- Selected SEM-BSE images from the Bozburun samples: a) calcite (Cal), fossil shell remains (FS) and euhedral pyrite grains, b) fossil shell remains (FS) and pyritized fossil shell remain, c) marcasite (Mrc) overgrowths around framboidal pyrite (Py) grains within organic matter (OM), d) epigenetic cleat/fracture pyrite infillings (Py) with organic matter and pyritized plant tissue, e) cleat/fracture apatite infillings (Ap) within organic matter (OM) and framboidal pyrite (Py) grains and f) fossil bone remain in Ca-phosphate composition.

marcasite (Table 3), and dendritic-like marcasite was identified as overgrowths around framboidal nucleated pyrite grains in a few samples by SEM-EDX (Figure 9d). Marcasite in coal is sometimes thought to be an indicator of marine influence in palaeomires and/or hydrothermal solution penetration (Querol et al., 1989; Rieder et al., 2007); however, both cases can be ruled out based on palaeontological data from the seam and the lack of cleat/fracture marcasite-infillings. Marcasite overgrowths around nuclei of framboidal pyrite grains; on the other hand, it forms replacing early diagenetic framboidal pyrite grains during the late diagenetic stages (Querol et al., 1989; Ruppert et al., 2005; Kolker, 2012). For such marcasite formation, pH should be lower than 5.0 (Ruppert et al., 2005); despite the fact that the co-existence of syngenetic pyrite grains and carbonate bands in these samples could indicate that marcasite formation was developed under weak acidic to neutral conditions. Other sulphide mineral that was identified by SEM-EDX in coal samples is sphalerite (Table 3), and its presence within clay mineral aggregates indicates a clastic origin. These micron-sized sphalerite grains are presumably derived from volcanic and/or magmatic rocks in the adjacent areas as clastic inputs into the palaeomire.

Apatite is the only identified phosphate mineral in the Bozburun coalfield by SEM-EDX, and apatite grains are identified within the clay mineral aggregates and/or syngenetic carbonate bands (Figures 8a, d, 9e, f, 10a), which indicate detrital origin for apatite. The presence of measurable Cl, F, and Sr (Figure 10a) in these grains could also imply that apatite grains have volcanogenic origin (Bohor and Triplehorn, 1993; Dai et al., 2020a). Beside individual apatite grains, cleat/fracture apatite-infillings (Figure 9e) and Ca-phosphate fossil bone remains (Figure 9f) are also observed during SEM-EDX analysis in a few samples. Cleat/fracture apatite-infillings are mostly derived from reactions between liberated P from decay of plant matter and dissolved CaO in porewater during coalification, while Ca-phosphate fossil bone remains are related to biogenic activities within the palaeomire (Ward, 2002). Hence, apatite has both syngenetic (clastic and biogenic) and epigenetic origin.

The identified sulphate minerals in the samples are barite ( $\text{BaSO}_4$ ) and celestine ( $\text{SrSO}_4$ ). Celestine grains are identified as euhedral individual grains within the syngenetic carbonate bands in coal samples and roof rock samples (Figure 10b-f). In addition, individual euhedral barite grains and barite-celestine ( $\text{Ba, SrSO}_4$ ) solid solution overgrowths associated with syngenetic carbonate bands and rarely feldspar grains are also observed in the roof sample (Figure 10e-f). Barite is a common sulphate mineral in coal, while celestine in coal is less common. Both sulphate minerals generally originate from the precipitation of sulphate-rich solutions during coalification and/or leached solutions overlying marine sediments, and syngenetic barite in coal seams is very rare (Finkelman et al., 2019; Dai et al., 2020a, 2021; Karayiğit et al., 2020a). The authigenic formation of celestine is generally related to evaporation of seawater or reactions between Sr-bearing hypersaline fluids with gypsum/anhydrite (Honar, 2004). However, the identified mollusc fauna from the Bozburun coalfield implies freshwater to oligohaline conditions during the late Miocene. Therefore, any influence of marine and/or hypersaline water influence on the palaeomire and/or onset of geochemical coalification could be ruled out for the study area. Celestine and Sr-bearing barite have been found within cavities of syngenetic framboidal pyrite grains in Turkish Neogene coals, as well as Sr-bearing barite overgrowths around feldspars (e.g., Kangal/Sivas and Keles and Orhaneli/Bursa) (Karayiğit et al., 2019, 2021; Çelik et al., 2021). In these coalfields, altered tuff layers are located in the coal seams, and liberated Sr and Ba from alteration of volcanogenic minerals (e.g., Sr-/Ba-bearing feldspars) and/or air-fall ash (tephra) within paleomires were reacted with sulphuric acid in the palaeomire. As a result of sulphate-reducing bacteria activity in the palaeomire, celestine and Sr-bearing barite were precipitated along with syngenetic framboidal pyrite grains. Furthermore, the geochemical data from the Yamadağ volcanic complex reported high Ba and especially high Sr contents of Miocene andesite and basalt (Kocaaslan and Ersoy, 2018; Di Giuseppe et al., 2021). In the roof rock samples, the presence of barite grains and overgrowth barite-celestine solid solution associated with feldspar grains could explain the source of Ba and Sr in the roof rock samples. The presence of Sr-

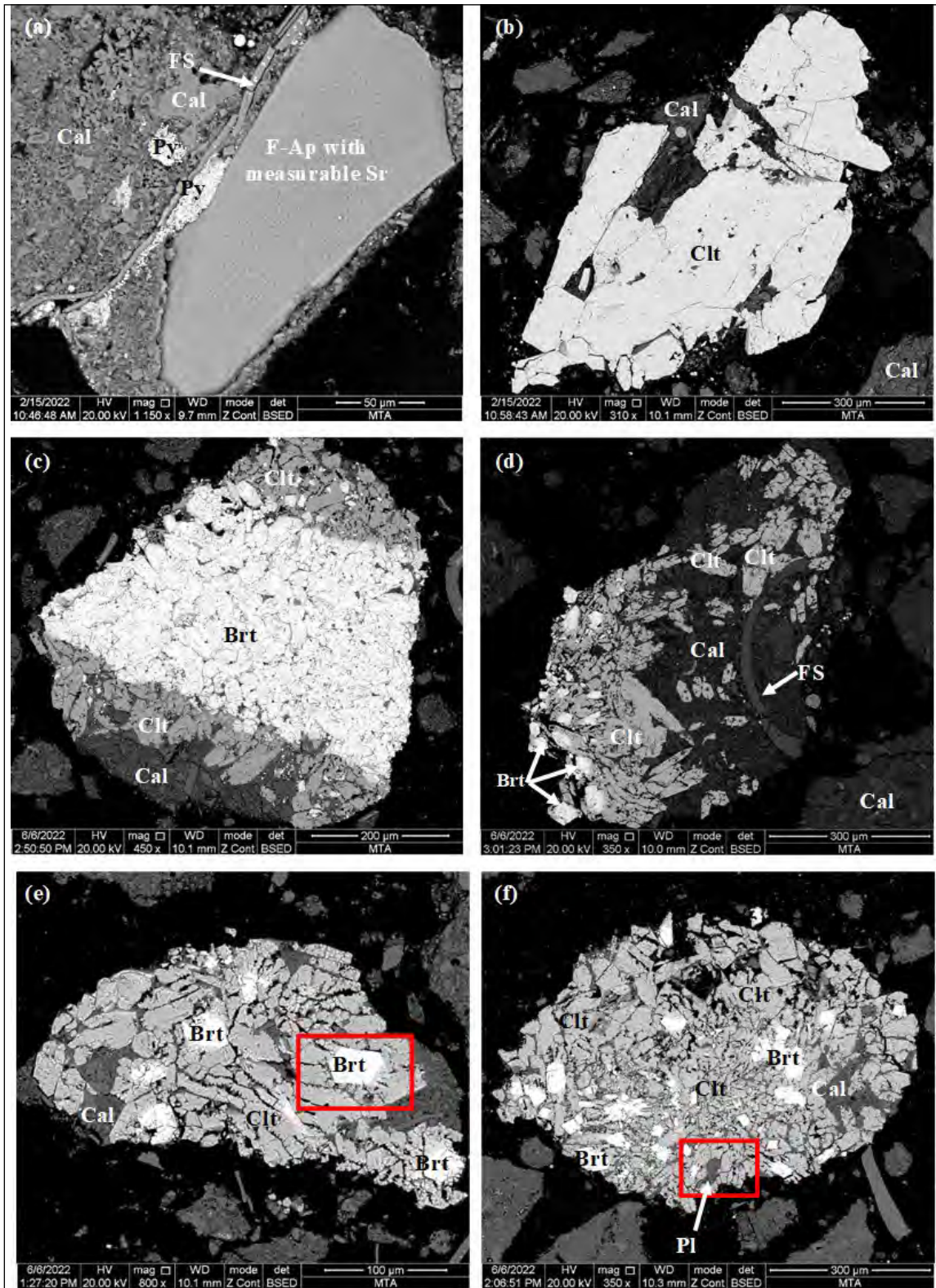


Figure 10- Selected SEM-BSE images from the Bozburun samples; a) fluorapatite (F-Ap) with measurable Sr and fossil shell (FS) remains within syngenetic carbonate bands (Cal) and framboidal pyrite (Py) grains, b) authigenic celestine (Clt) grains and syngenetic carbonates (Cal), c), f) celestine (Clt) and barite (Brt) within syngenetic carbonates and clastic plagioclase (Pl) grains and fossil shell (FS) remains. (Highlighted area in images e and d are reported in Figures 13 and 14, respectively).

bearing volcanogenic apatite grains could be another evidence of a clastic volcanogenic mineral source for Sr in the samples. Even though Ba and Sr could be derived from alteration of volcanogenic minerals in the Bozburun palaeomire, no altered tuff layer was identified in the coal seam and/or volcanic rocks were not observed from the overlying units in the coalfield. Therefore, the necessary Ba and Sr ions should have derived from another main source instead of clastic feldspar grains from middle Miocene volcanic rocks in the basin.

Economic gypsum and celestine deposits are found in late Cretaceous, Eocene, and early Miocene marine carbonates in the neighbouring Sivas Basin (Tekin et al., 2002). Similarly, Palaeogene-late Eocene marine carbonates in the basement rocks of the Malatya Basin contain gypsum layers and lenses like those in the Sivas Basin (Sümengen, 2016). Strontium is more soluble in aquatic environments than Ba (Hanor, 2004), and additional Sr could be introduced into the Bozburun palaeomire by dissolved sulphate-rich water from the gypsum-bearing Palaeogene-late Eocene marine carbonate. Therefore, alteration of clastic Ba-and Sr-rich feldspars from the middle Miocene Malatya volcanics and/or sulphate-rich water influx from the gypsum-bearing pre-Neogene units could be a source for Ba and Sr ions in the Bozburun palaeomire. Besides, Sr could display a high concentration in aragonitic mollusc shells, and this element could be essential for biogenic aragonite precipitation in the aquatic system (Hanor, 2004; Böning and Bard, 2009; Brisset et al., 2017) as well as Sr-bearing calcareous fossil shell remains were reported from some Turkish Neogene coalfields (Karayiğit et al., 2000). Hence, introduced Sr from alteration of clastic feldspar grains in the palaeomire and/or sulphate-rich water influx could be uptaken by molluscs. With this assumption, a measurable amount of Sr should be traced by SEM-EDX from calcareous fossil shell remains in the studied samples. During the SEM-EDX observation, Sr was rarely detected from these remains (Figure 11); nevertheless, Sr could also be released from aragonitic fossil shell remains during calcination in the depositional environment at an early diagenetic stage (Querol et al., 1999; Hanor, 2004; Marcano et al., 2015). Furthermore, Sr could not be incorporated

into calcite due to its bigger ionic radius than this of  $\text{Ca}^{2+}$  (Langston et al., 1998; Finch and Allison, 2008). Thus, liberated Sr ions from calcination of fossil remains also seem having reacted with dissolved sulphate ions in the mire water. Overall, authigenic barite and celestine, and barite-celestine solid solution formation took place during diagenetic stages.

### 5.3. Factors Controlling the Elemental Distribution

The statistical approach is commonly applied for determining mode of occurrence of elements in coal (Dai et al., 2021). Nevertheless, recent studies denoted that the statistical approach should be cooperated with SEM-EDX or other direct methods in order to eliminate misinterpretations (Dai et al., 2021; Xu et al., 2022; Eminağaoğlu et al., 2022). Therefore, both statistical and SEM-EDX analyses were here applied in order to accurately identify the controlling factors of elemental distribution. The major oxides, such as  $\text{SiO}_2$ ,  $\text{TiO}_2$ ,  $\text{MgO}$ , and  $\text{K}_2\text{O}$ , display positive correlations with ash yield and  $\text{Al}_2\text{O}_3$  content (Table 7); which indicates aluminosilicate mineral affinity. The SEM-EDX data also agrees with this observation, and the contents in  $\text{TiO}_2$ ,  $\text{MgO}$ ,  $\text{K}_2\text{O}$ , and  $\text{Na}_2\text{O}$  are determined from clay minerals. Besides clay minerals, feldspar grains in the samples are another source of  $\text{K}_2\text{O}$  and  $\text{Na}_2\text{O}$ . In addition,  $\text{Al}_2\text{O}_3$  contents of the samples show positive correlations with elements like Ga, Rb, Ni, and the REY (Table 7), which also imply an aluminosilicate affinity. Since aluminosilicate minerals in the samples are clastic in origin, clastic influx from volcanic and metamorphic rocks into the palaeomire could control their distributions and enrichment. This might also explain why  $\text{P}_2\text{O}_5$  concentrations are high in clastic apatite-bearing samples (Figures 8a and 10a, and Table 4). Additionally, measurable Mg is also determined from fossil shell fragments (Figure 11). Furthermore,  $\text{TiO}_2$  displays a moderate positive correlation with  $\text{Fe}_2\text{O}_3$ , which could be related to the accessory Ti-oxide and/or titanite in the samples (Figure 8d). The lack of correlation among  $\text{Fe}_2\text{O}_3$ , ash yield, total S,  $\text{Al}_2\text{O}_3$ , and  $\text{SiO}_2$  contents could imply an intermediate affinity for  $\text{Fe}_2\text{O}_3$ ; however, Fe is also detected in clay minerals, sulphides, and sulphates in the samples. Therefore, iron seems having an inorganic affinity in the samples.

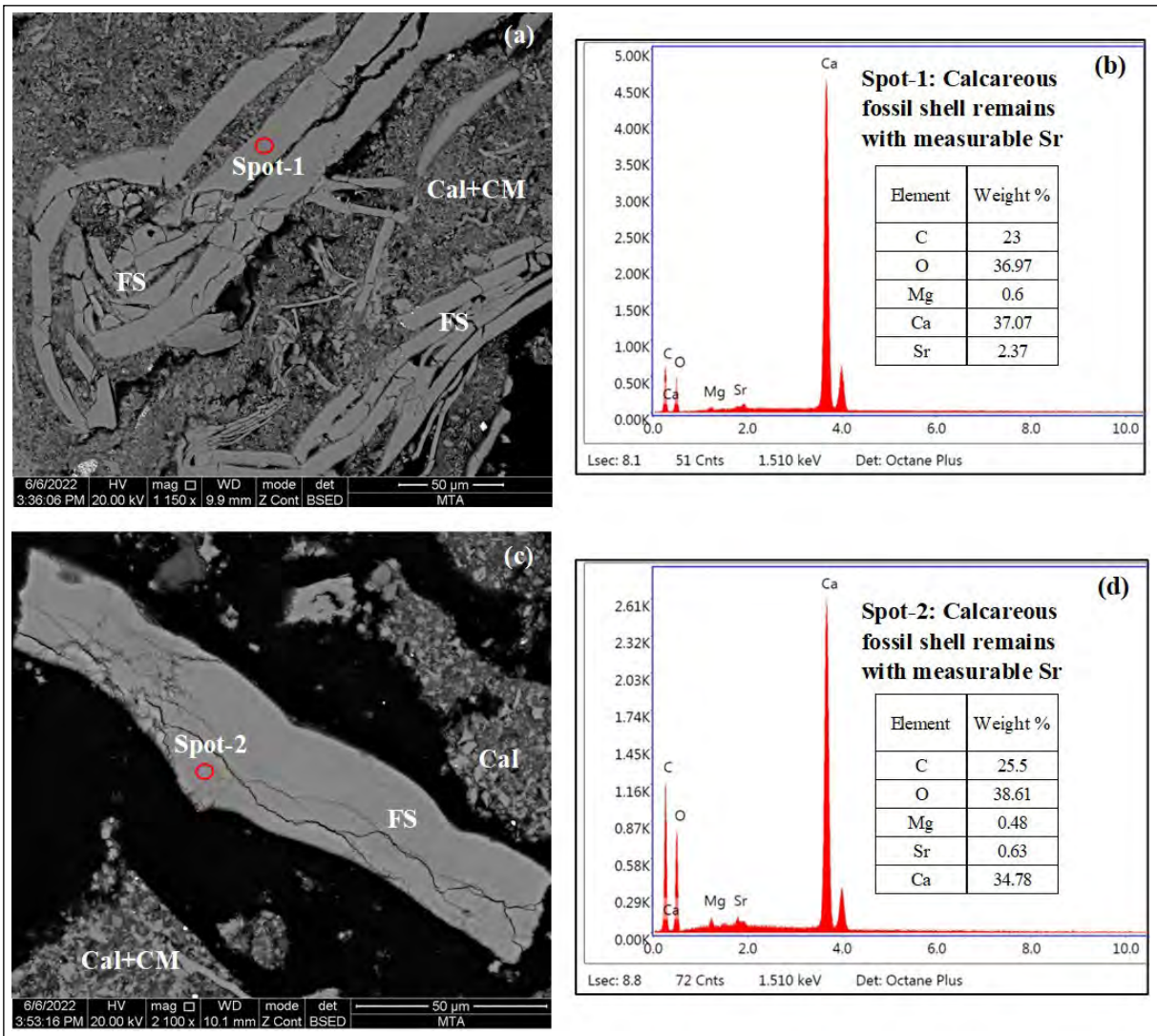


Figure 11- SEM-BSE images; a), c) SEM-EDX spectra of fossil shell (FS) in syngenetic carbonate (Cal), b) and d) SEM-EDX spectra of clay mineral (CM) matrix.

Table 7- Element affinities with ash yield (%), d) deduced from the calculation of Pearson's correlation coefficients.

Correlation with ash $0.70 \leq r < 1.0$
$Al_2O_3$ , MgO, $K_2O$ , Ga
Correlation with ash $0.40 \leq r < 0.70$
$SiO_2$ , $TiO_2$ , MnO, Sc, Cr, Rb, La, Ce, Eu, Gd, Tb
Correlation with ash $r \geq -0.40$
B, V, Mo, U, total S
Correlation with $Al_2O_3$ $0.70 \leq r < 1.0$
$SiO_2$ , $TiO_2$ , MgO, $K_2O$ , Sc, Cr, Co, Ni, Zn, Ga, Rb, Y, La, Ce, Pr, Nd, Eu, Gd, Tb, Dy, Ho, Er, Yb, Th
Correlation with $Al_2O_3$ $0.40 \leq r < 0.70$
$Na_2O$ , Li, Cu, Pb
Correlation with $Fe_2O_3$ $0.50 \leq r < 1.0$
Li, Ga, Co, Cu, Ni, Pb, Zn, total S
Correlation with CaO $0.50 \leq r < 1.0$
Ba, Sr
Correlation with total S $0.50 \leq r < 1.0$
B, Mo, V, As

The CaO displays a weak positive correlation with ash yields. The organic matter contains measurable by SEM-EDX amounts of Ca and S. This data implies an organic affinity for CaO. In Turkish Neogene coals, sulphate minerals, particularly gypsum/anhydrite, are reported as minor phases due to the evaporation of porewater during storage or reactions between liberated sulphuric acid from pyrite oxidation and CaO in porewater or organic matter (Karayığit et al., 2017a, 2021). In contrast, gypsum/anhydrite are lacking from XRD and are also not identified during SEM examination. Although additional high-resolution analysis should be needed, measurable Ca and S in the organic matter might be an indicator for sub-micron sized gypsum/anhydrite grains (Finkelman et al., 2019; Dai et al., 2020b). Therefore, Ca seems to have an inorganic rather than organic affinity. Supporting this assumption, the CaO concentrations are generally high in fossil shell fragments and syngenetic carbonate-bearing samples. Thus, the CaO in samples has a carbonate affinity. Furthermore, the CaO displays moderate positive correlations with Ba ( $r_{CaO} = 0.67$ ) and Sr ( $r_{CaO} = 0.65$ ). These correlations again imply the sulphate affinity for CaO, which is supported by measurable Ca from barite and celestine by SEM-EDX (Figures 12-14). Although CaO does not show any meaningful correlations with  $Al_2O_3$  and  $P_2O_5$ , CaO in the samples could also be partially affiliated with apatite, Ca-phosphate fossil bone remains, and feldspar grains in the samples. Hence, CaO is mainly derived from carbonate minerals, and to a lower degree with sulphates, apatite and feldspars.

The Sr-enrichment in coal is related to epigenetic sulphate (e.g., celestine and Sr-bearing barite and gypsum/anhydrite) minerals, carbonate minerals (e.g., strontianite); and/or clastic feldspar grains, biogenic aragonite, and syngenetic phosphate and zeolite minerals (Pollock et al., 2000; Dai et al., 2012b, 2021; Karayığit et al., 2020b; Spiro et al., 2019; Çelik et al., 2021; Du et al., 2021). In the studied samples, Sr, as mentioned above, only displays a positive moderate correlation with CaO. This correlation and the presence of measurable Sr in fossil shells could easily imply a carbonate affinity for Sr (Figure 11). However, this could be only applicable for some samples due to the presence of celestine and

Sr-bearing Cl/F-apatite grains in coal and roof rock samples (Figure 10a). In the roof rock sample, Sr is also measured from barite grains (Figures 13 and 14). Therefore, significantly high Sr concentrations in samples are mainly controlled by sulphate minerals. Furthermore, measurable Sr is not traced by SEM-EDX from organic matter, which indicates a clear inorganic affinity for Sr.

The B concentrations of the Bozburun coal samples are generally higher than 110 ppm (Table 4). Such concentrations could be evidence of paralic conditions (Goodarzi and Swaine, 1994; Goodarzi et al., 2020). The reported palynoflora and mollusc fauna from the Bozburun Formation suggest that freshwater conditions have been common (Türkmen et al., 2004; Nazik et al., 2008). The B-enrichment in coal was not always controlled by seawater and the presence of clay minerals or certain detritus accessory minerals (e.g., tourmaline). Boron uptake by peat-forming plants could cause B-enrichment (Boyd, 2002; Karayığit et al., 2020a, b, 2021; Dai et al., 2021). The Turkish Neogene coals have B concentrations higher than 110 ppm despite their formation under freshwater conditions (Karayığit et al., 2000; Tuncalı et al., 2002; Palmer et al., 2004). Boron has been derived from the wash-out from the volcanic rocks in the adjacent areas. Since middle Miocene volcanic rocks are close to the Bozburun coalfield, similar controlling parameters seem to have been developed for B enrichment. The strong negative correlation between B and ash yield ( $r_{ash} = -0.933$ ) could easily indicate an organic affinity for B and possible B uptake by plants in the mires. Boron, however, could easily be incorporated into clay minerals in the palaeomires, and the presence of clay minerals and illite/mica grains could also imply that B enrichment in the samples is also partially controlled by aluminosilicate minerals.

Chromium enrichment in Turkish Neogene coals is mostly related to clastic chromite grains derived from ophiolites in the basement (Karayığit et al., 2000, 2020a, 2021; Palmer et al., 2004; Çelik et al., 2021). Ophiolites, like in other Turkish Neogene coalfields, are found in the Bozburun coalfield's adjacent areas (Figure 1a), and chromitites reported from these ophiolites (Uysal et al., 2007). However,

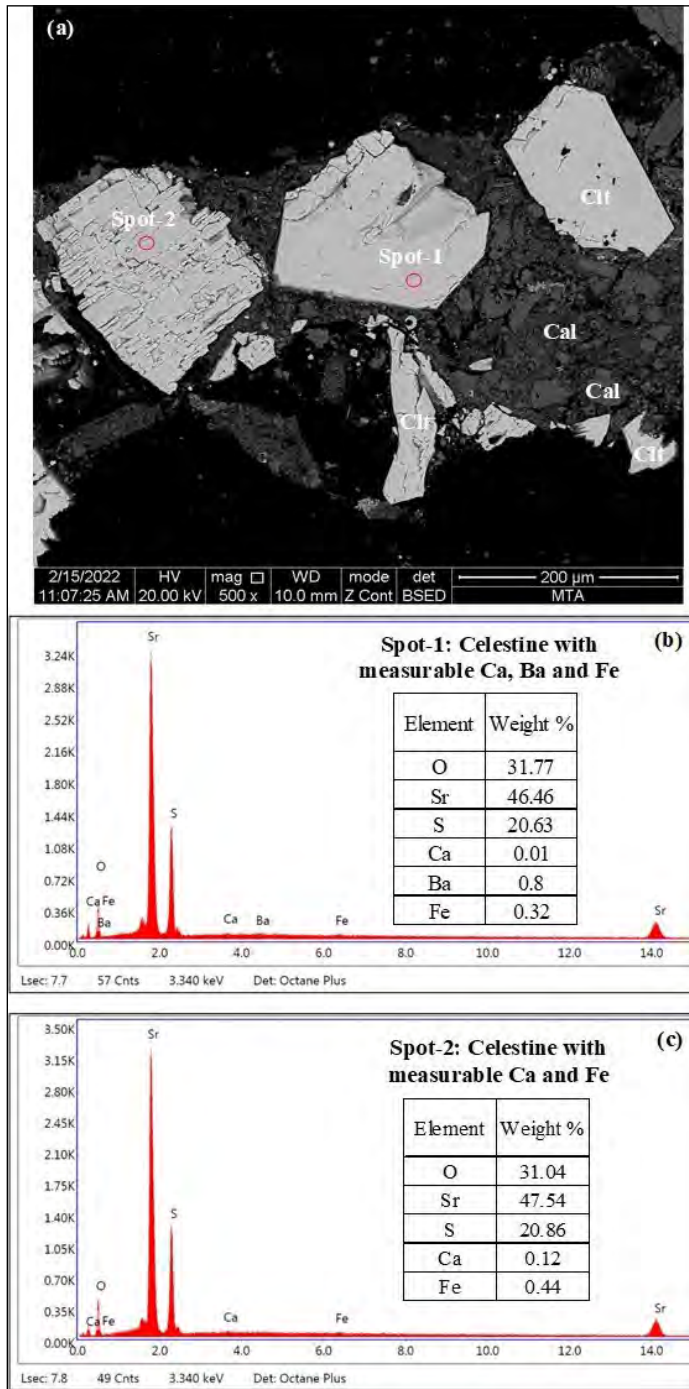


Figure 12-SEM-BSE images; a) SEM-EDX spectra, b), c) of authigenic celestine (Clt) grains within syngenetic carbonate (Cal) band.

chromite grains were not found in the samples during the SEM observations. Apart from clastic chromite grains, clastic input from ophiolitic rock within the palaeomire and their alteration by-products could control Cr enrichment of coal (Ruppert et al., 1996; Dai et al., 2021). In such cases, chlorite (chamosite)

may contain  $\text{Cr}^{3+}$  and/or  $\text{Fe}^{3+}$  which could be partially replaced by  $\text{Cr}^{3+}$ . Considering the presence of clastic chlorite (chamosite) in the samples and strong positive correlations among Cr,  $\text{Al}_2\text{O}_3$ ,  $\text{SiO}_2$  and MgO (Table 7), it is possible that Cr enrichment was controlled by clastic chlorite grains. Nickel is another element

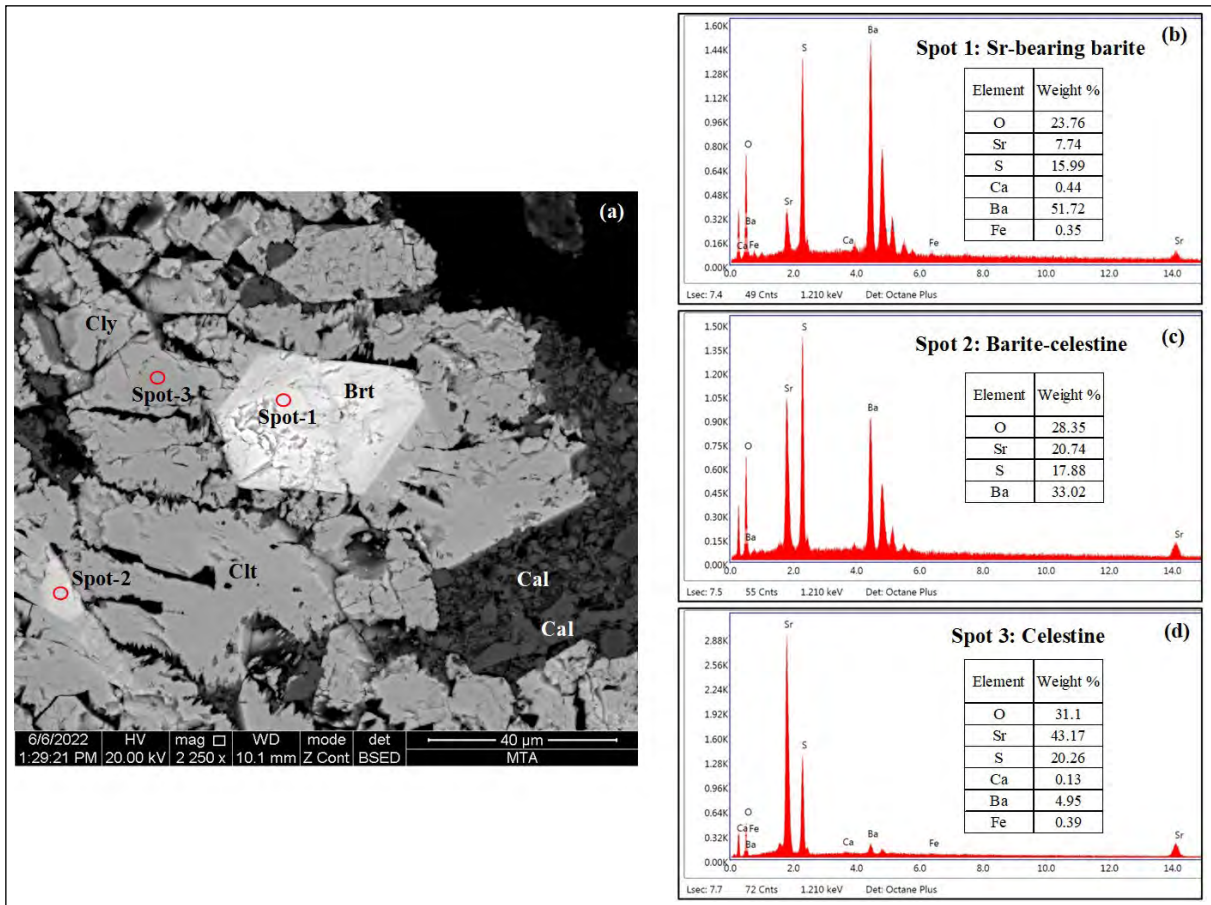


Figure 13- SEM-BSE images; a) SEM-EDX spectra, b), d) of barite (Brt) and celestine (Clt) within syngenetic carbonate (Cal) band.

which could be associated with clay minerals in coal or clastic input from the basement ophiolites (Ruppert et al., 1996). The positive moderate correlations among Ni,  $Al_2O_3$ , and  $SiO_2$  also suggest an aluminosilicate affinity for Ni (Table 7); however, the SEM-EDX indicates another affinity for Ni. During the SEM-EDX studies, measurable Ni and As contents were detected in matrices of framboidal pyrite aggregates and/or marcasite overgrowths around nuclei of framboidal pyrite (Figure 15). As the samples contain more Ni- and As-bearing marcasite overgrowths, Ni and As enrichments in the coal samples might be took place during the late diagenetic stages The MnO does not display any significant correlation with ash yield, total S, or any other elements, which implies an intermediate affinity for MnO. In contrast, Mn is detected from euhedral framboidal grains (Figure 16). Hence, MnO shows a sulphide affinity. While elements Cu, Zn, and Pb were not detected in the framboidal pyrite grains, these elements generally display concentrations in

framboidal pyrite grains below the detection limit of conventional SEM equipment (Hower et al., 2008; Kolker, 2012). The moderate positive correlation between  $Fe_2O_3$  and Zn can also be controlled by sphalerite grains in the samples (Figure 8b).

The elements V, Mo, and U also have negative correlations with ash yields (Table 7), which implies an organic affinity. Furthermore, V, Mo, and U elements show positive correlations with total S contents (Table 7), which are typical for Turkish Neogene coals. The enrichment of these elements in coal, on the other hand, could have been controlled by redox conditions (Arbuzov et al., 2011; Dai et al., 2021). These elements are generally enriched due to the development of anoxic conditions within the palaeomire and, in some cases, neutral to weak alkaline conditions. The latter one could be possible since fossil shell fragments and syngenetic carbonate bands are common in the samples. In the Turkish Neogene coals (e.g., Soma,

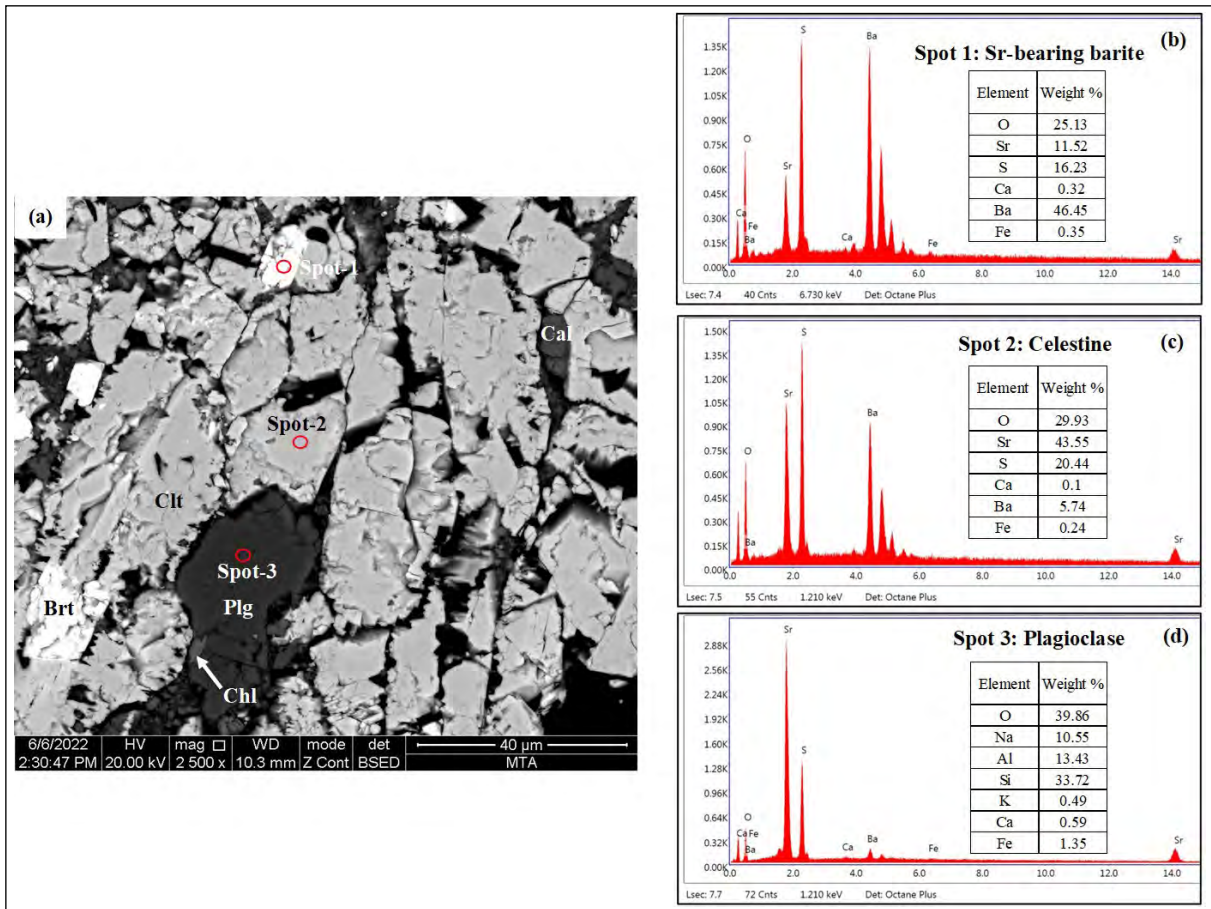


Figure 14- SEM-BSE images; a) and SEM-EDX spectra, b), d) of barite (Brt) and celestine (Clt) around clastic plagioclase (Plg) grain, and calcite (Cal) and chlorite (Chl).

Orhaneli, and Çayırhan coalfields), the alterations of synchronous volcanic input and/or clastic influx into the palaeomire could cause V, Mo, and U enrichment due to anoxic conditions (Querol et al., 1997; Palmer et al., 2004; Karayığit et al., 2017a, 2021b, 2022). Considering that the middle Miocene volcanic rocks are exposed in the eastern margins of the coalfield, the source of V, Mo, and U could have been related to clastic input. These elements could be taken by peat-forming plants, like B; thus, they are enriched in coal samples. This could also explain their positive correlation with B.

#### 5.4. Depositional Environment

The coal facies diagrams are the most common approach for assessing the depositional conditions during peat accumulation; nevertheless, these diagrams should be supported by sedimentological, palaeontological, mineralogical, and geochemical

(e.g., biomarker) data from coal seams due to the complex nature of the peatlands and uncertainties about the origin of some macerals (Crosdale, 1993; Moore and Shearer, 2003; Oikonomopoulos et al., 2015; Dai et al., 2020a; Guo et al., 2020; Liu et al., 2020; Hower and Eble, 2022). Therefore, in this study, the coal facies data is interpreted along with elemental and mineralogical compositions of the studied samples, and published sedimentological, palaeontological, and organic-geochemical data from the Bozburun coalfield (Türkmen et al., 2004; Nazik et al., 2008; Yalçın-Erik and Ay, 2021). The coal samples are generally plotted close to the mid-point between the A and B apexes on Mukhopadhyay's (1989) ternary diagram (Figure 17). The presence of both woody and herbaceous peat-forming plants in the palaeomires resulted in such distribution. In addition, some mineral-rich samples from the low part of the seam are plotted close to apex B, which suggests the predominance of herbaceous

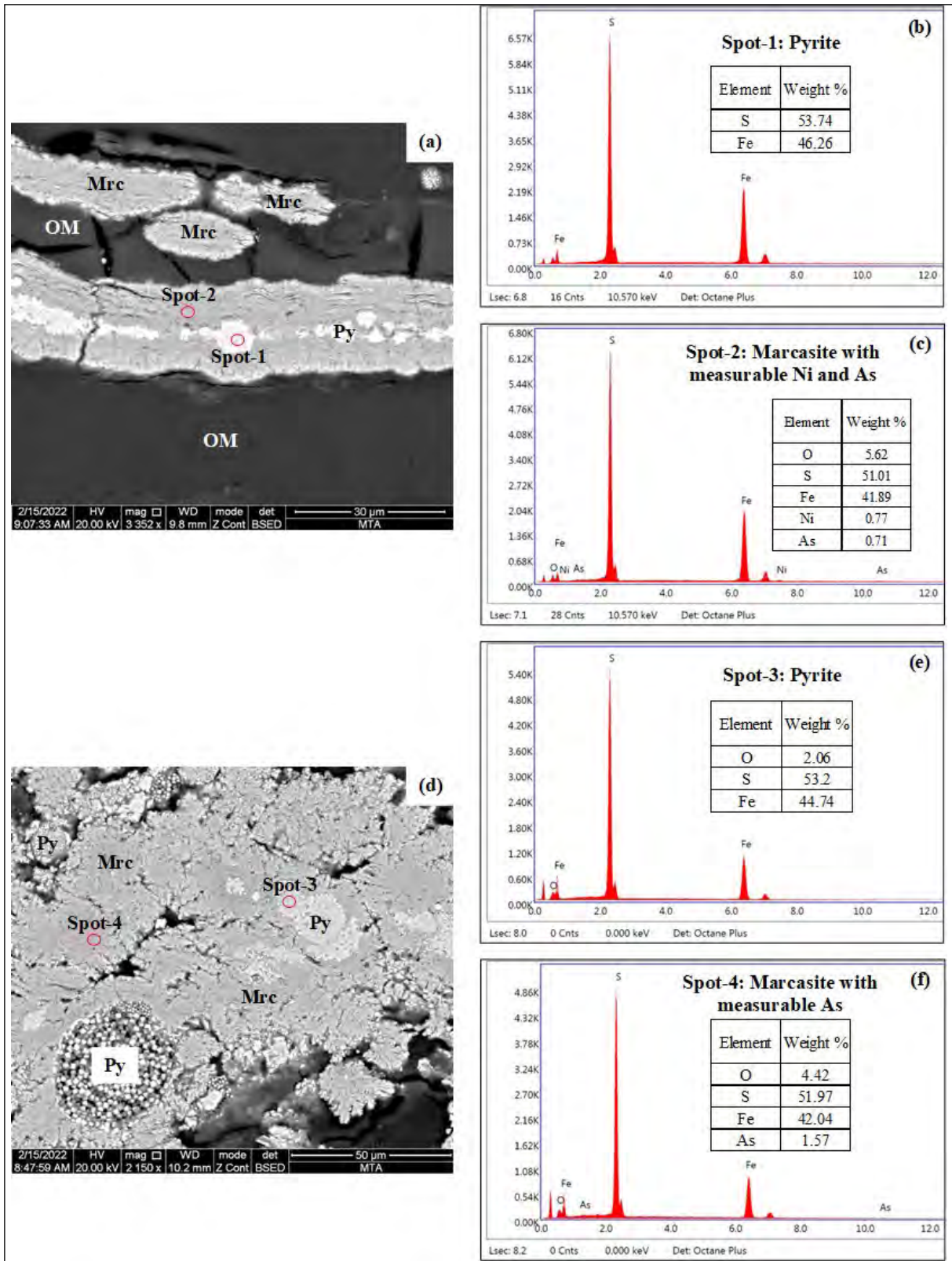


Figure 15- a, d) SEM-BSE images of pyrite (Py) and b), c), e) and f) SEM-EDX spectra (b, c, e and f) marcasite (Mrc).

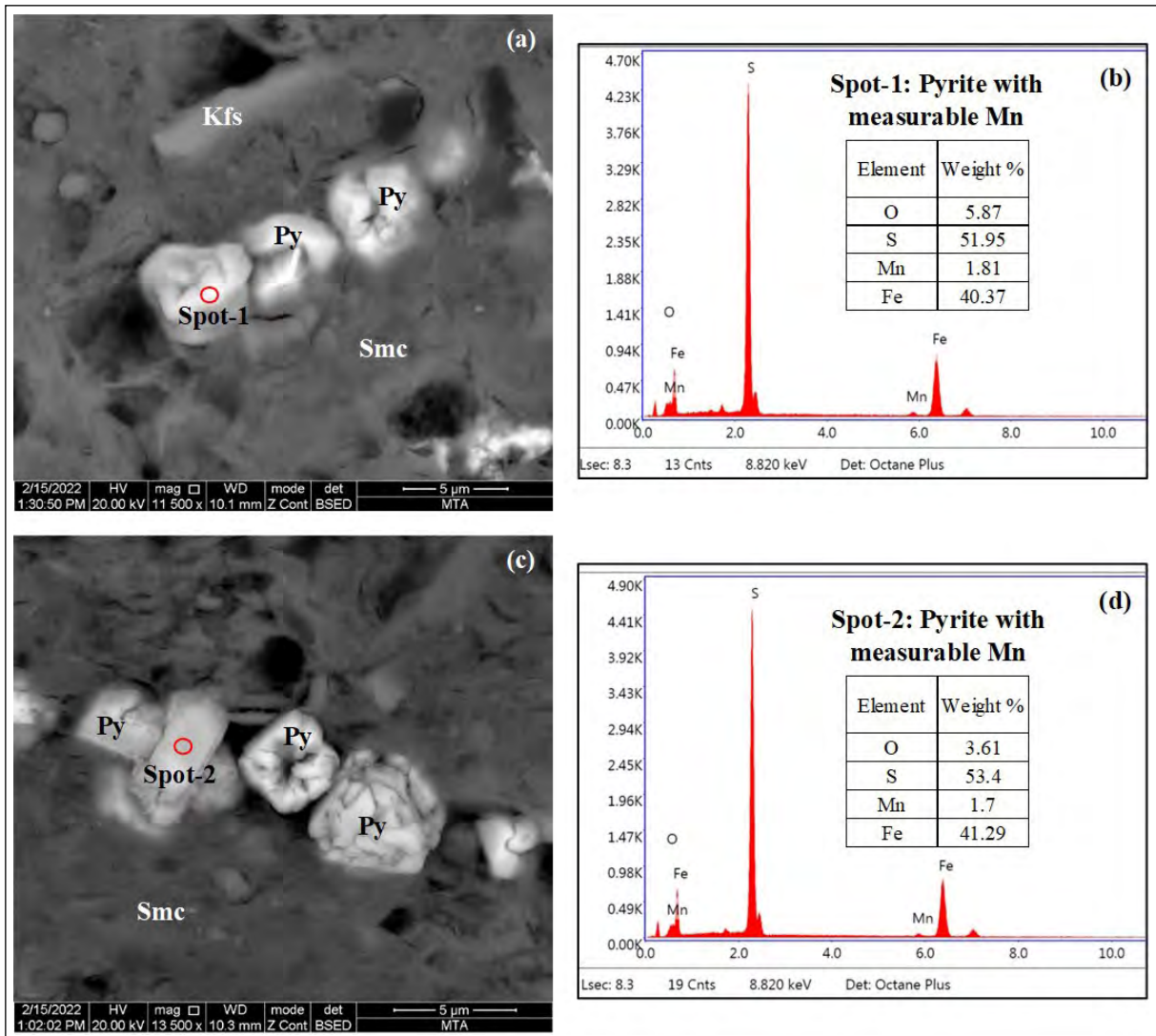


Figure 16- SEM-BSE images (a-c) and SEM-EDX spectra (b-d) of pyrite (Py) grains within smectite (Smc).

peat-forming plants and/or macrophyte in palaeomires. The relatively high total inertinite contents (> 10% on a mineral matter-free basis) of these samples could have been controlled by oxic conditions such as these caused by exposure of peat surface due to very low watertable and/or wildfires on palaeomire's surface or in the surrounding area (Figure 17). The presence of semifusinite and fusinite macerals in these coal samples are an indicator of wildfires within the palaeomire (O'Keefe et al., 2013; Hower et al., 2021). Char-rich lithotype should be observed in the studied coal seam a, if such thermal oxidation took place in the palaeomire (O'Keefe et al., 2013). In the studied profile, however, neither char-rich lithotypes nor char bands were observed. High inertinite contents do not

always relate to oxic conditions in the palaeomire, and the presence of allochthonous inertinite macerals could result in higher inertinite contents (O'Keefe et al., 2013; Oskay et al., 2019). In the coal samples, semifusinite, fusinite, and inertodetrinite macerals are mostly associated with clay mineral aggregates and/or detrohuminite macerals. Thus, the high inertinite content in the low part of the seam are due to inertinite transport by surface water/windblown or mechanical degradation and subsequent oxidation in the palaeomire.

The Gelification Index (GI) vs Tissue Preservation Index (TPI) and the Groundwater Index (GWI) vs Vegetation (VI) diagrams were used in order to

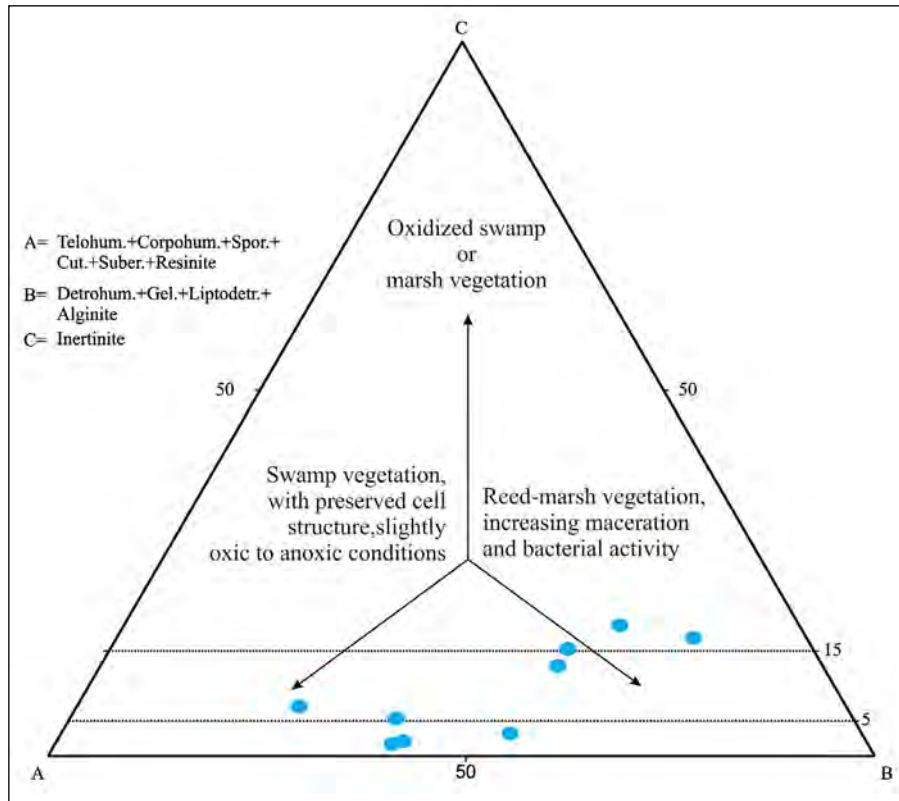


Figure 17- The Bozburun coal samples on Mukhopadhyay's ternary diagram (after Mukhopadhyay, 1989).

evaluate the preservation of organic matter and the vegetation type in the palaeomire (Figure 18). These diagrams were firstly proposed for late Palaeozoic coals of Canada and Australia by Calder et al. (1991) and Diessel (1992), respectively. Since the Cenozoic flora differs from the late Palaeozoic one, in this study the modifications proposed by Kalaitzidis et al. (2004) are applied. The TPI and VI values vary widely in the studied profile (Figure 18), which could imply variable preservation degree of organic matter and/or variations in the peat-forming vegetation. Additionally, the reported TPI (0.17-0.33) and VI (0.38-0.81) values from the western part of the Bozburun coalfield indicate vegetation variations in the palaeomire during the late Miocene (Yalçın-Erik and Ay, 2021). It is worth mentioning that the reported gelohuminite contents are very high in the western part of the Bozburun coalfield, which in turn, reduces TPI and VI values. Despite this, increasing trends of TPI and VI values towards the upper part of the studied profile were calculated (Figure 18 and Table 2). The TPI and VI values from the low part of the seam are generally lower than 1.0, which indicates the predominance

of herbaceous peat-forming plants during the initial stages of peat accumulation (Oskay et al., 2016; Guo et al., 2020). The presence of palynomorphs related to reed and macrophyte plants, as well as the short-chain *n*-alkanes in the Bozburun coalfield also support this assumption (Türkmen et al., 2004; Yalçın-Erik and Ay, 2021). Furthermore, freshwater gastropod remains and syngenetic carbonate bands in coal seam could also be another evidence for lakeshore (limnetic) conditions and/or Ca-rich water influx into the palaeomire (Siavalas et al., 2009; Karayığit et al., 2017a). Hence, the Ca concentration of the coal samples is significantly higher in this part of the seam (Figure 7 and Table 4), and alkaline conditions seem to be more common. Gelification of organic matter is supposed to be high due to bacterial activity forced by the increased alkalinity (Dehmer, 1995; Zdravkov et al., 2006; Stock et al., 2016); however, the GI values are generally lower than 1.0 in this part of the seam. Fluctuating water tables might also cause mechanical degradation of herbaceous plant matter and allochthonous inertinite macerals (Mach et al., 2013; O'Keefe et al., 2013). Thus, the attrinite and

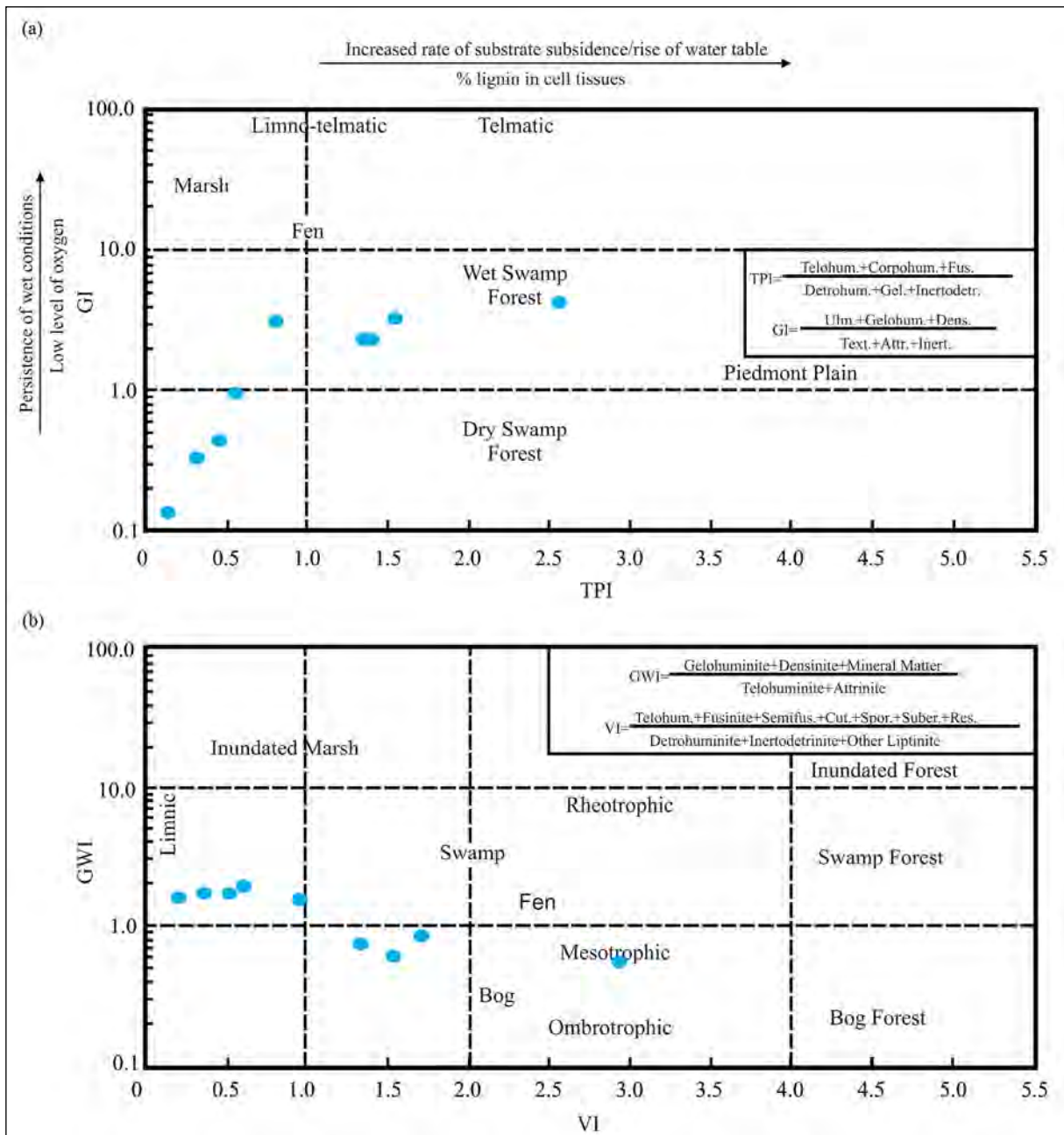


Figure 18- The distributions of the Bozburun coal samples on; a) GI vs. TPI plot of (after Diessel, 1992, modified from Kalaitzidis et al., 2004), b) VI vs. GWI plot of (after Calder et al., 1991, modified from Kalaitzidis et al., 2004).

inertodetrinite contents could be high; in turn, the GI values of the low part are low.

In contrast to the low profile part, the relatively higher TPI and VI values (Figure 18 and Table 2) in the central and upper parts of the seam imply an increased contribution of forested vegetation (Oikonomopoulos et al., 2015; Omodeo-Salé et al., 2017; Oskay et al., 2019; Karayığit et al., 2020a). Furthermore, the

reported existence of certain palynomorphs (e.g., *Inaperturopollenitis dubius*) and the long-chain *n*-alkanes point to coniferous peat-forming plants (Türkmen et al., 2004; Yalçın-Erik and Ay, 2021). This could also explain fluorescent ulminite A macerals in this part of seam, which is related to the presence of H-rich compounds in peat-forming plants and/or a coniferous peat-forming vegetation in the palaeomires

(Mastalerz et al., 2013; Karayığit et al., 2017*b*, 2020*b*; Oskay et al., 2019; Kus et al., 2020). Such vegetation is typical for wet-forest mires in flood and/or upper delta plains (Buillit et al., 2002). Supporting this assumption, previous sedimentological studies from the southern part of the Malatya Basin show that the Bozburun Formation was deposited under shallow lake and deltaic conditions. Furthermore, the watertable was generally stable and clastic influx could be low under such conditions; thus, anoxic conditions resulted in relatively good preservation of organic matter (Zdravkov et al., 2006; Mach et al., 2013; Kus et al., 2020). The anoxic conditions could be evident from the syngenetic framboidal pyrite grains and the decrease trend of ash yield upwards. The reported pristane/phytane (Pr/Rh) ratio from the Bozburun coalfield could also imply anoxic conditions (Yalçın-Erik and Ay, 2021). The GWI values of the coal samples from the upper part of the seam, however, are relatively low (Figure 18b), which is acceptable for telohuminitic-rich coals (Kalaitzidis et al., 2004; Oikonomopoulos et al., 2015; Karayığit et al., 2017*a*). The relatively high GI values and the syngenetic carbonate along with calcareous fossil remains could also imply that Ca-rich water influx and/or aquifer support into the palaeomire was continuous and gelification of organic matter is relatively high during the late stages of peat accumulation (Dehmer, 1995; Stock et al., 2016). Hence, the pH value of the mire water is alkaline, and concentrations of redox sensitive elements (e.g., Mo) are enriched in the upper part of the seam (Figure 7). The source of Ca-rich water could derive from the Palaeocene to late Eocene marine carbonates in the basement. As mentioned previously, these carbonates also contain gypsum layers; thus, the aquifer from these carbonates could also enrich the peat with sulphates. This supply could also cause the formation of authigenic sulphate minerals (e.g., celestine) since Sr is soluble in sulphate-rich waters (Honar, 2004). In general, the Sr/Ba ratios higher than 1 along with high total S content could be an indicator of marine influence during peat accumulation and/or penetrating solutions from the overlying marine sediments (Spiro et al., 2019; Medunić et al., 2020; Lui et al., 2021). Both cases seem to have been impossible for the Bozburun coalfield, since only terrestrial and lacustrine conditions were developed in the

Malatya Basin during the late Miocene. As mentioned previously, the alteration of clastic feldspar grains from the middle Miocene volcanic rocks could be also provided additional Sr<sup>2+</sup> ions. In turn, Sr/Ba ratios and total S contents of coal samples are elevated and could be high like paralic coals. Nevertheless, sulphate-rich water influx into the palaeomire may also cause weak brackish conditions, and this could explain the presence of freshwater to oligohaline mollusc fauna in the Bozburun coalfield and the presence of salinity indicator biomarkers (Nazik et al., 2008; Yalçın-Erik and Ay, 2021). Besides, the significantly high Ba and Sr contents could also indicate subsidence ratio during the late Miocene in the study area was optimal for the fixation of Ba and Sr in sulphate minerals in the palaeomires (Hower and Eble, 2022). Moreover, the variations on clastic-influx ratio, common peat-forming vegetation and mire water chemistry between western and eastern parts of the Bozburun coalfield seem to cause differences on coal quality parameters and mineralogy.

## 6. Results

Changes in peat-forming environment, redox conditions, clastic influx, and chemistry of water supply in the palaeomire have implications for coal quality, mineralogical, and elemental composition of the late Miocene coal seam in the eastern part of the Bozburun coalfield. The low part of the seam was accumulated under limnetic conditions, which were open to clastic influx and water table fluctuation, and Ca-rich water influx was high into the palaeomire. Hence, detrital detrital, allochthonous inertinite, and calcareous fossil shell remains were commonly identified, and ash yields and volatile matter contents are relatively higher in this part of the seam. Furthermore, Ca-rich water influx resulted in the formation of neutral to weak alkaline conditions, which allowed authigenic formation of syngenetic carbonate minerals. Thus, CaO concentrations of the coal samples are significantly high in this part of the seam. The increasing trends of telohuminitic proportions, TPI, and VI values towards the upper part of the seam could imply the formation of pure telmatic (wet-forest mire) conditions during the late stages of peat accumulation. Low clastic influx and stable water table conditions led to the establishment of anoxic conditions, in which authigenic framboidal

pyrite grains and marcasite overgrowth formed. Thus, chalcophile elements were enriched in the coal. Furthermore, continuous Ca-rich water influx into the palaeomire seems to control gelification of organic matter. The co-existence of syngenetic framboidal pyrite grains and carbonate minerals in the palaeomire of the upper part also implies weak acidic to neutral conditions; in turn, V, Mo and U are enriched in this part.

The high Sr/Ba ratios, the high total S contents and the presence of authigenic marcasite in the coal samples might be an indication of marine influence and/or penetration of porewater from overlying marine sediments. All these are clearly inapplicable in the Bozburun coalfield due to the freshwater mollusc remains, and the freshwater peat-forming plants according to previously published palaeontological and biomarker data. The formation of celestine and Ca- and Sr-bearing barite during diagenetic stages could be related to Sr-bearing sulphate-rich water influx into the palaeomire from gypsum-bearing Palaeogene and late Eocene carbonates and clastic feldspar grains from middle Miocene volcanic rocks. In addition, Sr uptake by mollusc fauna within the palaeomire could also cause elevated Sr-concentrations in fossil shell fragments-bearing coal and non-coal samples. Overall, the chemical composition of the water supplied the palaeomire and the redox conditions controlled the mineralogical and the elemental compositions in the eastern part of the Bozburun coalfield.

### Acknowledgements

This study is not supported by any external funds. Preliminary results of this study have been presented at the 74<sup>th</sup> Geological Congress of Turkey (Ankara/Türkiye). The authors would like to thank Bahadır Madencilik Co. for sampling permission; to Mr. Vakkas KARAOĞLU and Mr. Vedat Gök (Bahadır Madencilik Co.) for their assistance during the field work; Dr. Emine CİCİOĞLU -Sütçü, Mr. Yılmaz BULUT, Mr. Bülent BAŞARA, Mr. Arif TALAY, and Mr. Ufuk KİBAR (MTA) for their help at different stages of the analytical procedures; and Prof. Dr. James HOWER (University of Kentucky, Center for Applied Energy Research) for his comments and suggestions during the manuscript preparation.

### References

- American Society for Testing and Materials (ASTM) D2797/D2797M. 2019. Standard practice for preparing coal samples for microscopical analysis by reflected light. ASTM International, 5.
- American Society for Testing and Materials (ASTM) D388-19a. 2021. Standard classification of coals by rank. ASTM International, 8.
- Arbuzov, S. I., Volostnov, A. V., Rikhvanov, L. P., Mezhibor, A. M., Ilenok, S. S. 2011. Geochemistry of radioactive elements (U, Th) in coal and peat of northern Asia (Siberia, Russian Far East, Kazakhstan, and Mongolia). *International Journal of Coal Geology* 86, 318-328.
- Baysal, M., Yürüm, A., Yıldız, B., Yürüm, Y. 2016. Structure of some western Anatolia coals investigated by FTIR, Raman, <sup>13</sup>C solid state NMR spectroscopy and X-ray diffraction. *International Journal of Coal Geology* 163, 166-176.
- Bohor, B. F., Triplehorn, D. M. 1993. Tonsteins: Altered volcanic-ash layers in coal-bearing sequences. *Geological Society of America Special Papers* 285, 1-44.
- Boyd, R. J. 2002. The partitioning behaviour of boron from tourmaline during ashing of coal. *International Journal of Coal Geology* 53, 43-54.
- Böning, P., Bard, E. 2009. Millennial/centennial-scale thermocline ventilation changes in the Indian Ocean as reflected by aragonite preservation and geochemical variations in Arabian Sea sediments. *Geochimica et Cosmochimica Acta* 73, 6771-6788.
- Brisset, E., Djamali, M., Bard, E., Borschneck, D., Gandouin, E., Garcia, M., Stevens, L., Tachikawa, K. 2017. Late Holocene hydrology of Lake Maharlou, southwest Iran, inferred from high-resolution sedimentological and geochemical analyses. *Journal of Paleolimnology* 61, 111-128.
- Buillit, N., Lallier-Vergès, E., Pradier, B., Nicolas, G. 2002. Coal petrographic genetic units in deltaic-plain deposits of the Campanian Mesa Verde Group (New Mexico, USA). *International Journal of Coal Geology* 51, 93-110.
- Büçkün, Z., Inaner, H., Oskay, R. G., Christanis, K. 2015. Palaeoenvironmental reconstruction of Hüsamlar coal seam, SW Turkey. *Journal of Earth System Science* 124, 729-746.
- Calder, J. H., Gibling, M. R., Mukhopadhyay, P. K. 1991. Peat formation in a Westphalian B piedmont setting, Cumberland Basin, Nova Scotia: implications for the maceral-based interpretation of reotrophic and raised paleomires. *Bulletin de la Société Géologique de France* 162, 283-298.
- Chen, Y., Zou, C., Mastalerz, M., Hu, S., Gasaway, C., Tao, X. 2015. Applications of micro-Fourier transform

- infrared spectroscopy (FTIR) in the geological sciences-a review. *International Journal of Molecular Sciences* 16, 30223-30250.
- Crosdale, P. J. 1993. Coal maceral ratios as indicators of environment of deposition: do they work for ombrogenous mires? An example from the Miocene of New Zealand. *Organic Geochemistry* 20, 797-809.
- Çelik, Y., Karayığit, A. I., Oskay, R. G., Kayseri-Özer, M. S., Christanis, K., Hower, J. C., Querol, X. 2021. A multidisciplinary study and palaeoenvironmental interpretation of middle Miocene Keles lignite (Harmançık Basin, NW Turkey), with emphasis on syngenetic zeolite formation. *International Journal of Coal Geology* 237, 103691.
- Çetinkaya, S., Yürüm, Y. 2000. Oxidative pyrolysis of Turkish lignites in air up to 500°C. *Fuel Processing Technology* 67, 177-189.
- Dai, S., Finkelman, R.B. 2018. Coal as a promising source of critical elements: Progress and future prospects. *International Journal of Coal Geology* 186, 155-164.
- Dai, S., Ren, D., Chou, C-L., Finkelman, R. B., Seredin, V. V., Zhou, Y. 2012a. Geochemistry of trace elements in Chinese coals: A review of abundances, genetic types, impacts on human health, and industrial utilization. *International Journal of Coal Geology* 94, 3-21.
- Dai, S., Zou, J., Jiang, Y., Ward, C., Wang, X., Li, T., Xue, W., Liu, S., Tian, H., Sun, X., Zhou, D. 2012b. Mineralogical and geochemical compositions of the Pennsylvanian coal in the Adaohai Mine, Daqingshan Coalfield, Inner Mongolia, China: Modes of occurrence and origin of diasporite, gorceixite, and ammonian illite. *International Journal of Coal Geology* 94, 250-270.
- Dai, S., Liu, J., Ward, C. R., Hower, J. C., Xie, P., Jiang, Y., Hood, M. M., O'Keefe, J. M. K., Song, H. 2015a. Petrological, geochemical, and mineralogical compositions of the low-Ge coals from the Shengli Coalfield, China: A comparative study with Ge-rich coals and a formation model for coal-hosted Ge ore deposit. *Ore Geology Reviews* 71, 318-349.
- Dai, S., Seredin, V. V., Ward, C. R., Hower, J. C., Xing, Y., Zhang, W., Song, W., Wang, P. 2015b. Enrichment of U–Se–Mo–Re–V in coals preserved within marine carbonate successions: geochemical and mineralogical data from the Late Permian Guiding Coalfield, Guizhou, China. *Mineralium Deposita* 50, 159-186.
- Dai, S., Ward, C. R., Graham, I. T., French, D., Hower, J. C., Zhao, L., Wang, X. 2017. Altered volcanic ashes in coal and coal-bearing sequences: A review of their nature and significance. *Earth-Science Reviews* 175, 44-74.
- Dai, S., Ji, D., Ward, C. R., French, D., Hower, J. C., Yan, X., Wei, Q. 2018. Mississippian anthracites in Guangxi Province, southern China: Petrological, mineralogical, and rare earth element evidence for high-temperature solutions. *International Journal of Coal Geology* 197, 84-114.
- Dai, S., Bechtel, A., Eble, C. F., Flores, R. M., French, D., Graham, I. T., Hood, M. M., Hower, J. C., Korasidis, V. A., Moore, T. A., Püttmann, W., Wei, Q. 2020a. Recognition of peat depositional environments in coal: A review. *International Journal of Coal Geology* 219, 103383.
- Dai S., Hower, J. C., Finkelman, R. B., Graham, I. T., French, D., Ward, C. R., Eskenazy, G., Wei, Q., Zhao, L. 2020b. Organic associations of non-mineral elements in coal: A review. *International Journal of Coal Geology* 218, 103347.
- Dai S., Finkelman, R. B., French, D., Hower, J. C., Graham, I. T., Zhao, F. 2021. Modes of occurrence of elements in coal: A critical evaluation. *Earth-Science Reviews* 222, 103815.
- Dehmer, J. 1995. Petrological and organic geochemical investigation of recent peats with known environments of deposition. *International Journal of Coal Geology* 28, 111-138.
- Diessel, C. F. K. 1992. *Coal-Bearing Depositional Systems*. Springer, 721.
- Di Giuseppe, P., Agostini, S., Di Vincenzo, G., Manetti, P., Savaşçın, M. Y., Conticelli, S. 2021. From subduction to strike slip-related volcanism: insights from Sr, Nd, and Pb isotopes and geochronology of lavas from Sivas–Malatya region, Central Eastern Anatolia. *International Journal of Earth Sciences* 110, 849-874.
- Djowe, A. T., Laminsi, S., Njopwouo, D., Acayanka, E., Gaigneaux, E. M. 2013. Surface modification of smectite clay induced by non-thermal gliding arc plasma at atmospheric pressure. *Plasma Chemistry and Plasma Processing* 33, 707-723.
- Du, F., Ning, S., Qiao, J., Tan, F., Zhao, X., Zhang, W., Li, C., Luo, Z., He, X. 2021. Geochemical and Mineralogical Characteristics of the Li-Sr-Enriched Coal in the Wenjiaba Mine, Guizhou, SW China. *ACS Omega* 6, 8816-8828.
- Economic Commission for Europe-United Nations (E.C.E.-U.N.). 1998. *International classification of in-seam coals*. ECE, 41.
- Ekici, T., Alpaslan, M., Parlak, O., Temel, A. 2007. Geochemistry of the Pliocene basalts erupted along the Malatya-Ovacik fault zone (MOFZ), eastern Anatolia, Turkey: Implications for source characteristics and partial melting processes. *Geochemistry* 67, 201-212.
- Eminağaoğlu, M., Oskay, R. G., Karayığit, A. I. 2022. Evaluation of elemental affinities in coal using agglomerative hierarchical clustering algorithm:

- A case study in a thick and mineable coal seam (km<sup>2</sup>) from Soma Basin (W. Turkey). *International Journal of Coal Geology* 259, 104045.
- Ercan, T., Asutay, H. J. 1993. Petrology of Neogene–Quaternary volcanics in Malatya-Elazığ-Tunceli-Bingöl-Diyarbakır region. *Proceedings of A. Suat Erk Geology Symposium 2-5 September 1991, Ankara*, 291–302 (in Turkish with English abstract).
- Finch, A. A., Allison, N. 2008. Coordination of Sr and Mg in calcite and aragonite. *Mineralogical Magazine* 71, 539-552.
- Finkelman, R. B., Dai, S., French, D. 2019. The importance of minerals in coal as the hosts of chemical elements. *International Journal of Coal Geology* 212, 103251.
- Georgakopoulos, A., Iordanidis, A., Kapina, V. 2003. Study of low rank Greek coals using FTIR spectroscopy. *Energy Sources* 25, 995-1005.
- Goodarzi, F., Swaine, D. J. 1994. The influence of geological factors on the concentration of boron in Australian and Canadian coals. *Chemical Geology* 118, 301-318.
- Goodarzi, F., Gentzis, T., Hofmeister, H. 2020. Elemental composition of fluvial-lacustrine and lacustrine coal-bearing environments, British Columbia, Canada. *Energy and Fuels* 34, 16046-16058.
- Guo, Q., Littke, R., Sun, Y., Zieger, L. 2020. Depositional history of low-mature coals from the Puyang Basin, Yunnan Province, China. *International Journal of Coal Geology* 221, 103428.
- Hazra, B., Karacan, C. Ö., Tiwari, D. M., Singh, P. K., Singh, A. K. 2019. Insights from Rock-Eval analysis on the influence of sample weight on hydrocarbon generation from Lower Permian organic matter rich rocks, West Bokaro basin, India. *Marine and Petroleum Geology* 106, 160-170.
- Honar, J. S. 2004. A model for the origin of large carbonate- and evaporite-hosted celestine (SrSO<sub>4</sub>) deposits. *Sedimentary Research* 74, 168-175.
- Hood, M. M., Eble, C. F., Hower, J. C., Dai, S. 2020. Geochemistry, petrology, and palynology of the Princess No. 3 coal, Greenup County, Kentucky. *International Journal of Coal Science and Technology* 7, 633-651.
- Hower, J. C., Gayer, R. A. 2002. Mechanisms of coal metamorphism: case studies from Paleozoic coalfields. *International Journal of Coal Geology* 50, 215-245.
- Hower, J. C., Eble, C. F. 2022. Petrology, palynology, and geochemistry of the Pond Creek coal (Pennsylvanian, Duckmantian), Pike County, Kentucky: Overprints of penecontemporaneous tectonism and peat doming. *International Journal of Coal Geology* 258, 104027.
- Hower, J. C., Campbell, J. L. I., Teesdale, W. J., Nejedly, Z., Robertson, J. D. 2008. Scanning proton microprobe analysis of mercury and other trace elements in Fe-sulfides from a Kentucky coal. *International Journal of Coal Geology* 75, 88-92.
- Hower, J. C., Eble, C. F., O’Keefe, J. M. K., Dai, S., Wang, P., Xie, P., Liu, J., Ward, C. R., French, D. 2015. Petrology, palynology, and geochemistry of Gray Hawk coal (Early Pennsylvanian, Langsettian) in Eastern Kentucky, USA. *Minerals* 5, 592-622.
- Hower, J. C., Qian, D., Briot, N. J., Hood, M. M., Eble C. F. 2020. Mineralogy of a rare earth element-rich Manchester coal lithotype, Clay County, Kentucky. *International Journal of Coal Geology* 220, 103413.
- Hower, J. C., Eble, C. F., O’Keefe, J. M. K. 2021. Phyteral perspectives: Every maceral tells a story. *International Journal of Coal Geology* 247, 103849.
- Hower, J. C., Eble, C. F., Xie, P., Liu, J., Fu, B., Hood M. M. 2022. Aspects of rare earth element enrichment in Allegheny Plateau coals, Pennsylvania, USA. *Applied Geochemistry* 136, 105150.
- International Committee for Coal Petrology (ICCP). 1993. *International Handbook of Coal Petrography*, Centre National de la Recherche Scientifique, 146.
- International Committee for Coal Petrology (ICCP). 2001. *New inertinite classification (ICCP System 1994)*. *Fuel* 80, 459-471.
- International Standard Organisation (ISO) 11760. 2005. *Classification of coals*. International Organization for Standardization, 9.
- Jarvie, D. M., Claxton, B. L., Henk, F., Breyer, J. T. 2001. Oil and shale gas from the Barnett Shale, Fort Worth basin, Texas. *AAPG Annual Convention, Denver, Colorado, AAPG Search and Discovery Article*.
- Jiang, J., Zhang, S., Longhurst, P., Yang, W., Zheng, S. 2021. Molecular structure characterization of bituminous coal in Northern China via XRD, Raman and FTIR spectroscopy. *Spectrochimica Acta - Part A: Molecular and Biomolecular Spectroscopy* 255, 119724.
- Kalaitzidis, S., Bouzinos, A., Papazisimou, S., Christanis, K. 2004. A short-term establishment of forest fen habitat during Pliocene lignite formation in the Ptolemais Basin, NW Macedonia, Greece. *International Journal of Coal Geology* 57, 243-263.
- Karayığıt, A. İ., Whateley, M. K. G. 1997. The origin and properties of a coal seam associated with continental thin micritic limestones, Selimoglu-Divriği, Turkey. *Geological Society Special Publication* 125, 101-114.

- Karayığit, A. İ., Gayer, R. A. 2000. Trace elements in a Pliocene-Pleistocene lignite profile from the Afsin-Elbistan field, Eastern Turkey. *Energy Sources* 22, 13-21.
- Karayığit, A. İ., Gayer, R. A., Querol, X., Onacak, T. 2000. Contents of major and trace elements in feed coals from Turkish coal-fired power plants. *International Journal of Coal Geology* 44, 69-184.
- Karayığit, A. İ., Gayer, R. A., Ortac, F. E., Goldsmith, S. 2001. Trace elements in the Lower Pliocene fossiliferous Kangal lignites, Sivas, Turkey. *International Journal of Coal Geology* 47, 73-89.
- Karayığit, A. İ., Oskay, R. G., Tuncer, A., A. Gümüş, B., Şengüler, İ., Yaradılmış, H., Tunoğlu, C. 2016. A multidisciplinary study of the Gölbaşı-Harmanlı coal seam, SE Turkey. *International Journal of Coal Geology* 167, 31-47.
- Karayığit, A. İ., Littke, R., Querol, X., Tim, J., Oskay, R. G., Kimon, C. 2017a. The Miocene coal seams in the Soma Basin (W. Turkey): Insights from coal petrography, mineralogy and geochemistry. *International Journal of Coal Geology* 173, 110-128.
- Karayığit, A. İ., Bircan, C., Mastalerz, M., Oskay, R. G., Querol, X., Lieberman, N. R., Türkmen, İ. 2017b. Coal characteristics, elemental composition and modes of occurrence of some elements in the İsaalan coal (Balıkesir, NW Turkey). *International Journal of Coal Geology* 172, 43-59.
- Karayığit, A. İ., Mastalerz, M., Oskay, R. G., Gayer, R. A. 2018. Coal petrography, mineralogy, elemental compositions and palaeoenvironmental interpretation of late Carboniferous coal seams in three wells from the Kozlu coalfield (Zonguldak Basin, NW Turkey). *International Journal of Coal Geology* 187, 54-70.
- Karayığit, A. İ., Oskay, R. G., Gayer, R. A. 2019. Mineralogy and geochemistry of feed coals and combustion residues of the Kangal power plant (Sivas, Turkey). *Turkish Journal of Earth Sciences* 28, 436-456.
- Karayığit, A. İ., Atalay, M., Oskay, R. G., Córdoba, P., Querol, X., Bulut, Y. 2020a. Variations in elemental and mineralogical compositions of Late Oligocene, Early and Middle Miocene coal seams in the Kale-Tavas Molasse sub-basin, SW Turkey. *International Journal of Coal Geology* 218, 103366.
- Karayığit, A. İ., Bircan, C., Oskay, R. G., Türkmen, İ., Querol, X. 2020b. The geology, mineralogy, petrography, and geochemistry of the Miocene Dursunbey coal within fluvio-lacustrine deposits, Balıkesir (Western Turkey). *International Journal of Coal Geology* 228, 103548.
- Karayığit, A. İ., Yerin, Ü. O., Oskay, R. G., Bulut, Y., Córdoba, P. 2021. Enrichment and distribution of elements in the middle Miocene coal seams in the Orhanlı coalfield (NW Turkey). *International Journal of Coal Geology* 247, 103854.
- Kaymakçı, N., İnceöz, M., Ertepinar, P. 2006. 3D-architecture and neogene evolution of the Malatya basin: inferences for the kinematics of the Malatya and Ovacık Fault zones. *Turkish Journal of Earth Sciences* 15, 123-154.
- Ketris, M. P., Yudovich Ya. E. 2009. Estimations of Clarkes for carbonaceous biolithes: World averages for trace element contents in black shales and coals. *International Journal of Coal Geology* 78, 135-148.
- Kocaaslan, A., Ersoy, Y. E. 2018. Petrologic evolution of Miocene-Pliocene mafic volcanism in the Kangal and Gürün basins (Sivas-Malatya), central east Anatolia: Evidence for Miocene anorogenic magmas contaminated by continental crust. *Lithos* 310-311, 392-408.
- Koç-Taşgın, C. 2011. Seismically-generated hydroplastic deformation structures in the Late Miocene lacustrine deposits of the Malatya Basin, eastern Turkey. *Sedimentary Geology* 235, 264-276.
- Kolker, A. 2012. Minor element distribution in iron disulfides in coal: A geochemical review. *International Journal of Coal Geology* 94, 32-43.
- Kortenski, J. 1992. Carbonate minerals in Bulgarian coals with different degrees of coalification. *International Journal of Coal Geology* 20, 225-242.
- Kus, J., Dolezych, M., Schneider, W., Hofmann, T., Visině-Rajczi, E. 2020. Coal petrological and xylotomical characterization of Miocene lignites and in-situ fossil tree stumps and trunks from Lusatia region, Germany: palaeoenvironment and taphonomy assessment. *International Journal of Coal Geology* 217, 103283.
- Langston, W. J., Bebianno, M. J., Burt, G. R. 1998. Metal handling strategies in molluscs. Langston, W. J. and Bebianno, M. J. (Ed.). *Metal metabolism in aquatic environments*. Chapman and Hall. London, 219-283.
- Liu, J., Dai, S., Hower, J. C., Moore, T. A., Moroeng, O., Nechaev, V. P., Petrenko, T. I., French, D., Graham, I. T., Song, X. 2020. Stable isotopes of organic carbon, palynology, and petrography of a thick low-rank Miocene coal within the Mile Basin, Yunnan Province, China: implications for palaeoclimate and sedimentary conditions. *Organic Geochemistry* 149, 104103.
- Mach, K., Sýkorová, I., Konzalová, M., Opluštil, S. 2013. Effect of relative lake-level changes in mire-lake system on the petrographic and floristic compositions of a coal seam, in the Most Basin (Miocene), Czech Republic. *International Journal of Coal Geology* 105, 120-136.
- Madejova, J. 2003. FTIR techniques in clay mineral studies. *Vibrational Spectroscopy* 31, 1-10.

- Marcano, M. C., Frank, T. D., Mukasa, S. B., Lohmann, K. C., Taviani, M. 2015. Diagenetic incorporation of Sr into aragonitic bivalve shells: implications for chronostratigraphic and palaeoenvironmental interpretations. *Depositional Record* 1, 38-52
- Mastalerz, M., Hower, J. C., Taulbee, D. N. 2013. Variations in chemistry of macerals as reflected by micro-scale analysis of a Spanish coal. *Geologica Acta* 11, 483-493.
- Medunić, G., Grigore, M., Dai, S., Berti, D., Hochella, M. F., Mastalerz, M., Valentim, B., Guedes, A., Hower, J. C. 2020. Characterization of superhigh-organic-sulfur Raša coal, Istria, Croatia, and its environmental implication. *International Journal of Coal Geology* 217, 103344.
- Moore, T. A., Shearer, J. C. 2003. Peat/coal type and depositional environment – are they related? *International Journal of Coal Geology* 56, 233-252.
- Mukhopadhyay, P. 1989. Organic petrography and organic geochemistry of tertiary coals from Texas in relation to depositional environment and hydrocarbon generation. Report of Investigations, Bureau of Economic Geology, 118.
- Nadkarni, R. A. 1980. Multitechnique multielemental analysis of coal and fly ash. *Analytical Chemistry* 52, 929-935.
- Naik, A. S., Behera, B., Shukla, U. K., Sahu, H. B., Singh, P. K., Mohanty, D., Sahoo, K., Chatterjee, D. 2021. Mineralogical Studies of Mahanadi Basin coals based on FTIR, XRD and Microscopy: A Geological Perspective. *Journal of the Geological Society of India* 97, 1019-1027.
- Nazik, A., Türkmen, I., Koç, C., Aksoy, E., Avşar, N., Yayık, H. 2008. Fresh and brackish water ostracods of Upper Miocene deposits, Arguvan/Malatya (Eastern Anatolia). *Turkish Journal of Earth Sciences* 17, 481-495.
- Oikonomopoulos I. K., Perraki, M., Tougiannidis, N., Perraki T., Frey M. J., Antoniadis, P., Ricken, W. 2013. A comparative study on structural differences of xylite and matrix lignite lithotypes by means of FT-IR, XRD, SEM and TGA analyses: An example from the Neogene Greek lignite deposits. *International Journal of Coal Geology* 115, 1-12.
- Oikonomopoulos, I. K., Kaouras, G., Tougiannidis, N., Ricken, W., Gurk, M., Antoniadis, P. 2015. The depositional conditions and the palaeoenvironment of the Achlada xylite-dominated lignite in western Makedonia, Greece. *Palaeogeography, Palaeoclimatology, Palaeoecology* 440, 777-792.
- O'Keefe, J. M. K., Bechtel, A., Christanis, K., Dai, S., DiMichele, W. A., Eble, C. F., Esterle, J. S., Mastalerz, M., Raymond, A. L., Valentim, B. V., Wagner, N. J., Ward, C. R. 2013. On the fundamental difference between coal rank and coal type. *International Journal of Coal Geology* 118, 58-87.
- Omodeo-Salé, S., Deschamps, R., Michel, P., Chauveau, B., Suárez-Ruiz, I. 2017. The coal-bearing strata of the lower cretaceous Mannville Group (Western Canadian sedimentary basin, South Central Alberta), part 2: factors controlling the composition of organic matter accumulations. *International Journal of Coal Geology* 179, 219-241.
- Oskay, R. G., Christanis, K., Inaner, H., Salman, M., Taka, M. 2016. Palaeoenvironmental reconstruction of the eastern part of the Karapınar-Ayrancı coal deposit (Central Turkey). *International Journal of Coal Geology* 163, 100-111.
- Oskay, R. G., Bechtel, A., Karayiğit, A. İ. 2019. Mineralogy, petrography and organic geochemistry of Miocene coal seams in the Kınık coalfield (Soma Basin-Western Turkey): Insights into depositional environment and palaeovegetation. *International Journal of Coal Geology* 210, 103205.
- Önal, M. 1995. Stratigraphy, coal potential and neotectonics of Malatya graben. Süleyman Demirel Üniversitesi, Mühendislik Mimarlık Fakültesi Jeoloji Seksiyonu 8, 159-175 (in Turkish with English abstract).
- Palmer, C. A., Tuncali, E., Dennen, K. O., Coburn, T. C., Finkelman, R. B. 2004. Characterization of Turkish coals: a nationwide perspective. *International Journal of Coal Geology* 60, 85-115.
- Pickel, W., Kus, J., Flores, D., Kalaitzidis, S., Christanis, K., Cardott, B. J., Misz-Kennan, M., Rodrigues, S., Hentschel, A., Hamor-Vido, M., Crosdale, P., Wagner, N., ICCP. 2017. Classification of liptinite-ICCP System 1994. *International Journal of Coal Geology* 169, 40-61.
- Pollock, S. M., Goodarzi, F., Riediger, C. L. 2000. Mineralogical and elemental variation of coal from Alberta, Canada: an example from the No. 2 seam, Genesee Mine. *International Journal of Coal Geology* 43, 259-286.
- Querol, X., Chinenon S., Lopez-Soler A. 1989. Iron sulfide precipitation sequence in Albian coals from the Maestrazgo Basin, southeastern Iberian Range, northeastern Spain. *International Journal of Coal Geology* 11, 171-189.
- Querol, X., Whateley, M. K. G., Fernández-Turiel, J. L., Tuncali, E. 1997. Geological controls on the mineralogy and geochemistry of the Beypazari lignite, central Anatolia, Turkey. *International Journal of Coal Geology* 33, 255-271.
- Querol, X., Alastuey, A., Plana, F., Lopez-Soler, A., Tuncali, E., Toprak, S., Ocakoğlu, F., Köker, A. 1999. Coal geology and coal quality of the Miocene Mugla basin, southwestern Anatolia, Turkey. *International Journal of Coal Geology* 41, 311-332.
- Rieder, M., Crelling, J. C., Šustai, O., Drábek M., Weiss, Z., Klementová, M. 2007. Arsenic in iron disulfides in a brown coal from the North Bohemian Basin,

- Czech Republic. *International Journal of Coal Geology* 71, 115-121.
- Ruppert, L., Finkelman, R., Boti, E., Milosavljevic, M., Tewalt, S., Simon, N., Dulong, F. 1996. Origin and significance of high nickel and chromium concentrations in pliocene lignite of the Kosovo Basin, Serbia. *International Journal of Coal Geology* 29, 235-258.
- Ruppert, L. F., Hower, J. C., Eble, C. F. 2005. Arsenic-bearing pyrite and marcasite in the Fire Clay coal bed, Middle Pennsylvanian Breathitt Formation, eastern Kentucky. *International Journal of Coal Geology* 63, 27-35.
- Sançar, T., Zabcı, C., Karabacak, V., Yazıcı, M., Akyüz, H. S. 2019. Geometry and Paleoseismology of the Malatya Fault (Malatya-Ovacık Fault Zone), Eastern Turkey: Implications for intraplate deformation of the Anatolian Scholle. *Journal of Seismology* 23, 319-340.
- Seredin, V. V., Dai, S. 2012. Coal deposits as potential alternative sources for lanthanides and yttrium. *International Journal of Coal Geology* 94, 67-93.
- Seyitoğlu, G., Aktuğ, B., Esat, K., Kaypak, B. 2022. Neotectonics of Turkey (Türkiye) and surrounding regions: a new perspective with block modelling. *Geologica Acta* 20(4), 1-21.
- Siavalas, G., Linou, M., Chatziapostolou, A., Kalaitzidis, S., Papaefthymiou, H., Christanis, K. 2009. Palaeoenvironment of seam I in the Marathousa lignite mine, Megalopolis basin (southern Greece). *International Journal of Coal Geology* 78, 233-248.
- Sümengen, M. 2016. Malatya-K40 sheet. 1:100.000 scaled Series of Geological Maps of Turkey. General Directorate of Mineral Research and Exploration Publication, 29.
- Spiro, B. F., Liu, J., Dai, S., Zeng, R., Large, D., French, D. 2019. Marine derived  $^{87}\text{Sr}/^{86}\text{Sr}$  in coal, a new key to geochronology and palaeoenvironment: elucidation of the India-Eurasia and China-Indochina collisions in Yunnan, China. *International Journal of Coal Geology* 215, 103304.
- Stock, A. T., Littke, R., Lücke, A., Zieger, L., Thielemann, T. 2016. Miocene depositional environment and climate in western Europe: The lignite deposits of the Lower Rhine Basin, Germany. *International Journal of Coal Geology* 157, 2-18.
- Sütçü, E. C., Karayığıt, A. İ. 2015. Mineral matter, major and trace element content of the Afşin-Elbistan coals, Kahramanmaraş, Turkey. *International Journal of Coal Geology* 144-145, 111-129.
- Swaine, D. J. 1990. Trace Elements in Coal. Butterworth, 278.
- Sýkorová, I., Pickel, W., Christanis, K., Wolf, M., Taylor, G. H., Flores, D. 2005. Classification of huminite - ICCP System 1994. *International Journal of Coal Geology* 62, 85-106.
- Tekin, E., Varol, B., Ayan, Z., Satır, M. 2002. Epigenetic origin of celestite deposits in the Tertiary Sivas Basin: new mineralogical and geochemical evidence. *Neues Jahrbuch für Mineralogie - Monatshefte* 7, 289-318.
- Tuncaltı, E., Çiftçi, B., Yavuz, N., Toprak, S., Köker, A., Gencer, Z., Ayçık, H., Pahin, N. 2002. Chemical and technological properties of Turkish Tertiary coals. General Directorate of Mineral Research and Exploration Publication, 401.
- Türkmen, İ., Aksoy, E., Koç, C. 2007. Alluvial and lacustrine facies in an extensional basin: Miocene of the Malatya Basin, eastern Turkey. *Journal of Asian Earth Sciences* 30, 181-198.
- Türkmen, İ., Koç, C., Aksoy, E., Avşar, N., Dinçer, F. 2004. Stratigraphy and depositional environments of Neogene units in the area of Arguvan-Bozburun (Malatya, E. Turkey). *Geosound/Yerbilimleri* 44-45, 57-73 (in Turkish with English abstract).
- Türkmen, İ., Taşgin, C. K., Avşar, N., Aksoy, E. 2011. Sedimentological characteristics of Alibonca Formation (Upper Oligocene-Lower Miocene) near Arapgir-Yoncalı area (Malatya). *Yerbilimleri/Earth Sciences* 32, 235-254 (in Turkish with English abstract).
- Uysal, I., Zaccarini, F., Garuti, G., Meisel, T., Tarkian, M., Bernhardt, H. J., Sadıklar, M. B. 2007. Ophiolitic chromitites from the Kahramanmaraş area, southeastern Turkey: Their platinum-group elements (PGE) geochemistry, mineralogy and Os-isotope signature. *Ofoliti* 32, 151-161.
- Ward, C. F. 2002. Analysis and significance of mineral matter in coal seams. *International Journal of Coal Geology* 50, 135-168.
- Xu, N., Xu, C., Finkelman, R. B., Engle, M. A., Li, Q., Peng, M., He, L., Huang, B., Yang, Y. 2022. Coal elemental (compositional) data analysis with hierarchical clustering algorithms. *International Journal of Coal Geology* 249, 103892.
- Yalçın-Erik, N., Ay, F. 2021. Use of petrological and organic geochemical data in determining hydrocarbon generation potential of coals: miocene coals of Malatya Basin (Eastern Anatolia-Turkey). *International Journal of Coal Science and Technology* 8, 510-533.
- Yılmaz, Y. 2019. Southeast Anatolian Orogenic Belt revisited (geology and evolution). *Canadian Journal of Earth Sciences* 56, 1163-1180.
- Zdravkov, A., Kostova, I., Sachsenhofer, R. F., Korstanski, J. 2006. Reconstruction of paleoenvironment during coal deposition in the Neogene Karlovo graben, Bulgaria. *International Journal of Coal Geology* 67, 79-94.



# Bulletin of the Mineral Research and Exploration

<http://bulletin.mta.gov.tr>



## Vitrinite reflectances and mineralogy of coal clasts in the Late Carboniferous sequences in the two-deep research wells from the Kozlu coalfield (Zonguldak Basin, NW Türkiye)

Ali İhsan KARAYİĞİT<sup>a\*</sup> and Rıza Görkem OSKAY<sup>b</sup>

<sup>a</sup> Hacettepe University, Faculty of Engineering, Department of Geological Engineering, Ankara, Türkiye

<sup>b</sup> Hacettepe University, Başkent OSB Technical Sciences Vocational School, Ankara, Türkiye

Research Article

### Keywords:

Zonguldak Basin, Late Carboniferous, Coal Petrography, Coal Clast, Erosion of Coal Seams.

### ABSTRACT

Fifty-four coal clast samples in the siliciclastic rocks (e.g., sandstone and conglomerate) were collected from cores of two-deep research wells (K20H and K20K) drilled at the Kozlu coalfield in Zonguldak Basin, and for the first time, they were evaluated using mineralogy by XRD and SEM-EDX and random vitrinite reflectance (%Rr) measurements in order to find out their origin and timing. Petrographic observations on polish surfaces show that the coal clasts are either entirely xylitic/vitrinitic particles or coals including a broader range of macerals. The detected minerals in the samples are mostly derived from the parental coal seams and, to a lesser extent, precipitated from penetrated pore-water in the cleats/fractures of clasts. The %Rr values of coal clasts in Carboniferous sediments are generally relatively higher than those measured in the coal seams due to weak oxidation during transportation. Furthermore, similar mineralogical and maceral compositions between coal clasts and coal seams imply that these clasts were mainly eroded during the peatification and/or early coalification of parental seams and display similar coalification patterns. The close %Rr value of a coal clast sample in the Early Aptian Zonguldak Formation and Carboniferous coal seams could suggest that this coal clast sample is presumably derived from the coal seams eroded during Early Aptian.

Received Date: 16.07.2022

Accepted Date: 23.11.2022

## 1. Introduction

Peat beds and coal-bearing sequences could be eroded due to several reasons (e.g., flooding events and mass movements during peat formation or fluvial and marine influence after coalification) (Petersen et al., 1998; Geršlová et al., 2016; Izart et al., 2016; Martínek et al., 2017; Bicca et al., 2020). As a result, coal clasts and/or coal-placers could be observed within the synchronous siliciclastic sediments and marine carbonates of coal seams and in modern marine sediments (Littke et al., 1989; Hower et al., 2001; Pešek and Sýkorová, 2006; Dill et al., 2017,

2021; Zhang et al., 2019; Yang et al., 2020). Coal clasts are commonly found in Carboniferous coal-bearing sequences and range in size from a millimeter to tens of centimeters. Fragments of pebble-sized coal particles and/or in some cases coalified woody material (xylite) within clastic sediments (e.g., sandstone, conglomerate) were reported from several late Palaeozoic coal basins in Europe since the early 20<sup>th</sup> century (Pešek and Sýkorová, 2006). However, there are a limited number of detailed studies conducted on coal clasts mainly focused within Late Carboniferous coal basins in central Europe and South

Citation Info: Karayığit, A. İ., Oskay, R. G. 2024. Vitrinite reflectances and mineralogy of coal clasts in the Late Carboniferous sequences in the two-deep research wells from the Kozlu coalfield (Zonguldak Basin, NW Türkiye). Bulletin of the Mineral Research and Exploration 173, 55-83. <https://doi.org/10.19111/bulletinofmre.1209127>

\*Corresponding author: Ali İhsan KARAYİĞİT, [aik@hacettepe.edu.tr](mailto:aik@hacettepe.edu.tr)

Wales (Littke et al., 1989; Paszkowski et al. 1995; Gayer et al., 1996; Kožušníková et al., 1999; Daněk et al., 2002; Misz-Kennan et al., 2019; Suchý et al., 2019; Yang et al., 2020). These studies show that the maceral and mineralogical composition, random vitrinite reflectance (%Rr) values, palynological properties, and size and shapes could provide data about the timing of erosion of Late Carboniferous seams, the origin and possible transportation distance (e.g., a short distance) of coal clasts, and, in some cases, maturation and coal bed methane potential of late Palaeozoic coal-bearing sequences. For instance, the relatively lower %Rr values of coal clasts than the closest late Palaeozoic coal seams within the basin could imply that coal clasts are derived from coal seams in the proximity of coal-bearing sequence due to erosion of these coal seams before coalification. Furthermore, their palynoflora composition could also provide their origin, and more importantly, whether the coal clast-bearing sediments were deposited after a hiatus.

The Zonguldak Basin is located in the NW Türkiye (Figure 1a) and hosts major economic bituminous coal resources in Türkiye within the late Palaeozoic sequences (Figure 1b and 1c) (Karayığit et al., 1998; 2018a). Previous studies of the coal seams of Carboniferous age in the Zonguldak Basin show that the late Paleozoic coal seams display similar palynoflora and coal petrographical features to late Palaeozoic coal basins in the east and central Europe (Akgün and Akyol, 1992; Karayığit, 1992; Karayığit et al., 1998, 2018a, b; Cleal and Van Waveren, 2012; Cleal et al., 2017, 2018; Opluštil et al., 2018). Furthermore, the sedimentological data from the Carboniferous coal seams show that the roof rocks of Carboniferous coal seams are mainly made up of conglomerates and sandstones, which mostly overlie coal seams with erosional bases, and possible erosion of Early Carboniferous (Serpukhovian-Bashkirian) sequences during the Late Carboniferous (Duckmantian-Asturian) was also assumed (Zijlstra, 1952; Kerey, 1985; Opluštil et al., 2018). In addition, the 1-D thermal history modelling from coal seams in the Zonguldak Basin implies possible erosion events during the Carboniferous, Permian, and afterward (Yalçın et al., 2002; Karayığit et al., 2018a). Hence, it is acceptable to observe coal clasts within Carboniferous

and Cretaceous sequences in the Zonguldak Basin, but no data was published regarding the coal clasts from coal mines in the Zonguldak Basin. However, during the late 1990s, several deep research wells were drilled by Turkish Hard Coal Enterprise (TTK) in the Kozlu coalfield in order to find out the evolution, geological features, and coalbed methane potential of coal seams within the Carboniferous formations (Alacağzı, Kozlu, and Karadon, Formations) (Figures 1c and 1d), and several studies have been done from these exploration wells (e.g., Gürdal and Yalçın, 2000, 2001, Yürüm et al., 2001a, b; Yalçın et al., 2002; Gürdal et al., 2004; Karayığit et al., 2018a). During the drilling, several coal clast-bearing sediments were cored from Carboniferous formations (Oktay, 1995); however, only very limited palynological data from coal clasts from the Karadon Formation were conducted for age determination (Akgün et al., 1997) and no petrographical investigation and/or their origins have been reported to date. This study aims to present the first detailed vitrinite reflectance and mineralogical data of Late Palaeozoic, as well as Early Aptian coal clast within İnciğez clastics in the Zonguldak Basin. The special target of the study is to find out the origin and timing of these coal clasts in order to estimate whether the erosion took place during peat accumulation or coal formation.

## 2. Geological Settings

The pre-Carboniferous basement rocks in the basin are mainly the Silurian Hamzafakı Formation (metasediments and shales with diabase and andesite dykes and sills) and the Devonian Göktepe (metasediments with diabase and andesite dykes) and Yılanlı (marine limestone and dolomite) formations (Figure 1b). The Carboniferous coal-bearing sequences are divided into three formations, namely, Alacağzı, Kozlu, and Karadon (Figure 1b). The Alacağzı Formation is composed of alterations of sandstone, claystone, siltstone, and coal seams (Figure 1b), which were deposited under deltaic conditions during Serpukhovian-Bashkirian (Namurian) (Ağralı, 1963; Akyol, 1972, Kerey, 1985; Akgün and Akyol, 1992; Yalçın et al., 2002; Cleal et al., 2017). The Kozlu Formation conformably overlays the Alacağzı Formation and consists of conglomerate, sandstone, siltstone, claystone, and coal seams alternations (Figure

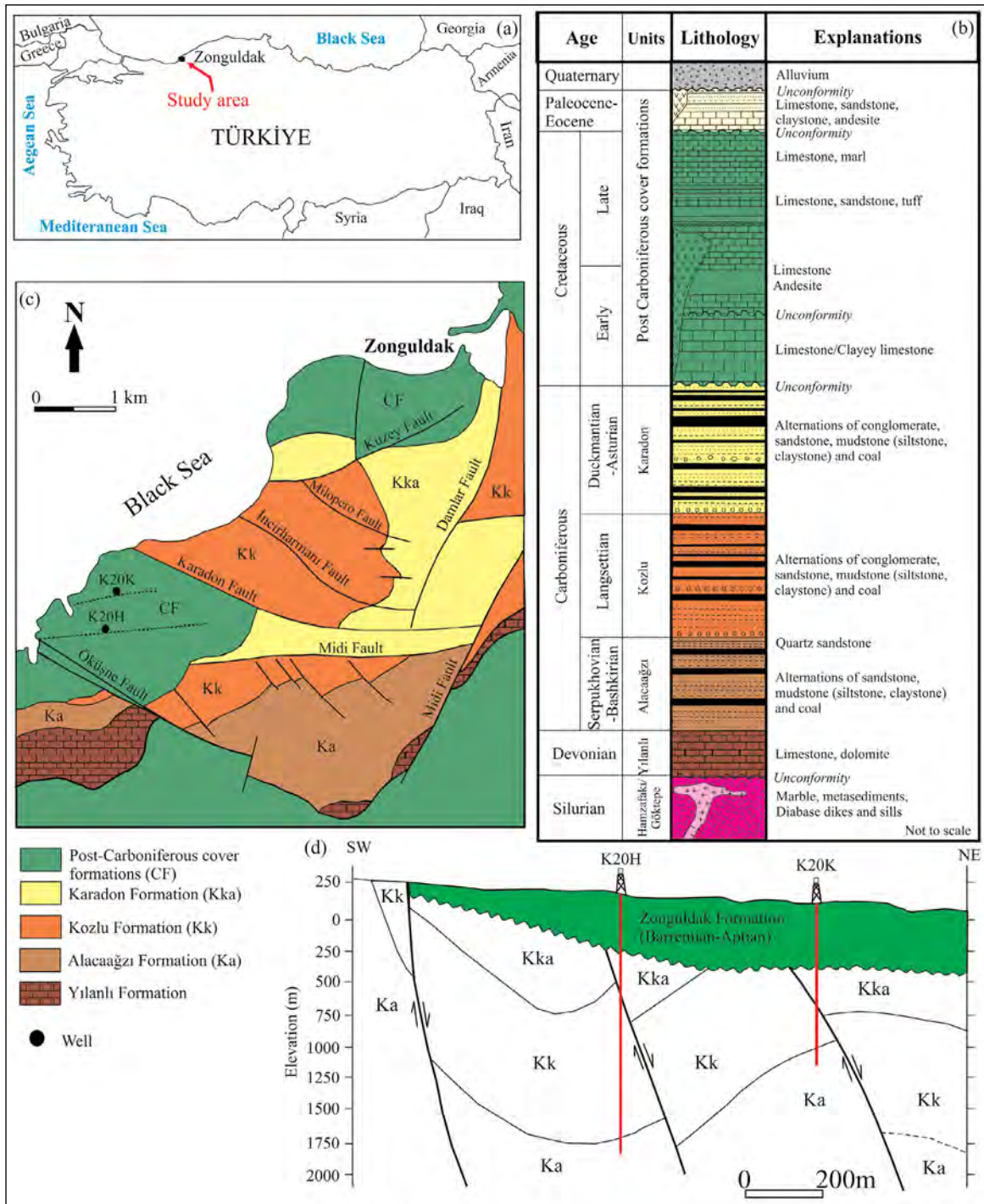


Figure 1- a) Location map of Zonguldak Basin, b) generalized stratigraphic column of surrounding area of the Kozlu coalfield, c) regional geological map of Zonguldak Basin, and d) simplified cross-section between studied wells (modified from Ksk et al., 1997; Yalm et al., 2002; Karayiit et al., 2018a).

1b). Previous sedimentological and palaeontological studies from the formation suggest that the formation was interpreted to have been deposited under mainly fluvial conditions (deltaic and meandering rivers) and lacustrine conditions during the Langsettian

(Westphalian A) (Aralı, 1970; Akyol, 1972; Kerey, 1985; Akgn and Akyol, 1992; Oktay, 1995; Yalm et al., 2002; Cleal and Van Waveren, 2012; Oplutil et al., 2018). The Kozlu Formation is conformably overlain by the Karadon Formation (Figure 1b) and

consists of alternations of conglomerate, sandstone, siltstone, claystone, and coal seams, as in the Kozlu Formation. This formation was deposited under fluvial conditions (deltaic and meandering river) and lacustrine conditions during the Duckmantian-Asturian (Westphalian B to D) (Ağralı, 1970; Kerey, 1985; Akgün and Akyol, 1992; Oktay, 1995; Yalçın et al., 2002; Cleal and Van Waveren, 2012; Opluštil et al., 2018).

Post-Carboniferous formations in the basin are mostly comprised of the Early Cretaceous Zonguldak Formation (Figure 1c and 1d) (Kerey, 1985; Karayığit et al., 1998; Yalçın et al., 2002; Tüysüz et al., 2016). Even though the existence of coal clasts and coaly material were reported from the Zonguldak Formation (Mann et al., 1995; Yalçın et al., 2002), no coal seams were reported from this formation to date. The Zonguldak Formation is divided into four members, from bottom to top, lower Barremian Öküşne clastics member, Barremian Öküşne member, Early Aptian İnciğez clastics member, and Aptian Kapuz member (Küskü et al., 1997; Yalçın et al., 2002). The lower Barremian Öküşne clastics member composed of alternations of conglomerate, and sandstone-mudstone alternations, whereas Early Aptian İnciğez clastics members are alternations of conglomerate, sandstone, siltstone, claystone, and limestone. The Barremian Öküşne member is mainly made up of dolomitic limestone, and the Aptian Kapuz member is composed of sandy limestone and limestone. The orogenic movements from Hercynian to Alpine resulted in the development of several regional reverse faults and folds in the Zonguldak Basin (Figure 1c and 1d) (Okay et al., 1994; Yalçın et al., 2002; Okay and Nikishin, 2015). Thus, Carboniferous and Cretaceous sediments in the basin are deformed. Furthermore, post-Carboniferous dykes also intruded Carboniferous and Cretaceous formations in the basin (Karayığit, 1992; Karayığit et al., 1998; Yalçın et al., 2002).

### 3. Material and Applied Methodology

A total of fifty-four coal clast samples were obtained from different depths of the K20K and K20H research wells drilled at the Kozlu coalfield (Table 1). In this study, five coal clast samples (two from the K20K and three from the K20H) were examined from the Alacaağzı Formation; thirty-six coal clast samples

(six from the K20K and thirty from the K20H) from the Kozlu Formation; twelve coal clast samples (four from the K20K and eight from the K20H) from the Karadon Formation; and only one coal clast sample from the limestone of the Early Aptian İnciğez clastics (Zonguldak Formation) was cored in the K20K well. The depths of identified formations in the K20H wells from bottom to top; 1891.00-2002.20-m Alacaağzı Formation, 715.30-1891.00-m Kozlu Formation, 424.70-715.3-m Karadon Formation, and 0-424.70-m Zonguldak Formation (287.00-424.70 Öküşne clastics and 0-287.00-m Öküşne limestone), while in the K20K well, 1119.90-1251.65-m Alacaağzı Formation, 793.05-1119.90-m Kozlu Formation, 468.70-793.05-m Karadon Formation, and 0-468.70 Zonguldak Formation (264.55-468.70-m Öküşne limestone, 203.00-264.55-m İnciğez clastics, and 0-203-m Kapuz limestone) (Figure 1d).

The fundamental petrographic observations of samples were conducted from polished coal blocks, which were prepared according to ASTM D2797/D2797M (2011) standard, under a reflected light microscope (Leica DM4000M coupled with J&M equipment and software) at Hacettepe University. The maceral identification was done according to the ICCP 1994 classification as modified by ICCP (1998 and 2001), and Pickel et al. (2017). The random vitrinite reflectance measurements (%Rr) were conducted mainly from collotelinite following the ISO 7404-5 (2009) standard using an oil-immersion 50X objective. The mineralogical compositions of suitable twenty-eight studied coal clast samples in both wells (one sample from the Zonguldak Formation, five samples from the Karadon Formation, eighteen samples from the Kozlu Formation, and four samples from the Alacaağzı Formation) were determined using an X-ray powder diffraction (XRD) with a Cu anode tube at Hacettepe University. In order to examine mineralogical compositions in detail, selected eight polished samples (K20K-O2, and -08, K20H-O1, -05, -07, -015, -039, and -041) were coated with carbon and examined under Scanning Electron Microscope (SEM) equipped with Energy Dispersive X-Ray Analysis (EDX) in the General Directorate of Mineral Research and Exploration (MTA) and Hacettepe University.

Table 1- The list of coal clasts samples from K20K and K20H research wells and their depths and lithology of embedded sediment.

Well	Formation	Age	Sample No	Sampling depth (m)	Lithology of embedded sediment
K20K	Zonguldak (İnciğez clastics)	Early Aptian	K20K-O1	250.65	Pyritized limestone
	Karadon	Langsettian (Westphalian A)	K20K-O2	700.50	Conglomerate
			K20K-O3	710.50	Conglomerate
			K20K-O4	770.55	Conglomerate
			K20K-O5	789.15	Conglomerate
	Kozlu	Duckmantian-Asturian (Westphalian B-D)	K20K-O6	1030.10	Sandstone
			K20K-O7	1033.70	Conglomerate
			K20K-O8	1037.55	Conglomerate
			K20K-O9	1042.45	Conglomerate
			K20K-O10	1055.85	Conglomerate
			K20K-O11	1099.50	Sandstone
	Alacağzı	Serpukhovian-Bashkirian (Namurian)	K20K-O12	1125.80	Conglomerate
			K20K-O13	1230.95	Conglomerate
K20H	Karadon	Langsettian (Westphalian A)	K20H-O1	431.70	Sandstone
			K20H-O2	451.00	Sandstone
			K20H-O3	455.40	Conglomerate
			K20H-O4	458.80	Conglomerate
			K20H-O5	527.30	Sandstone
			K20H-O6	541.00	Sandstone
			K20H-O7	636.20	Sandstone
			K20H-O8	686.30	Sandstone
	Kozlu	Duckmantian-Asturian (Westphalian B-D)	K20H-O9	754.80	Conglomerate
			K20H-O10	760.20	Conglomerate
			K20H-O11	813.40	Conglomerate
			K20H-O12	829.25	Conglomerate
			K20H-O13	1002.80	Conglomerate
			K20H-O14	1010.70	Conglomerate
			K20H-O15	1025.65	Conglomerate
			K20H-O16	1045.70	Sandstone
			K20H-O17	1061.30	Sandstone
			K20H-O18	1081.60	Sandstone
			K20H-O19	1101.80	Conglomerate
			K20H-O20	1118.30	Conglomerate
			K20H-O21	1136.20	Conglomerate
			K20H-O22	1141.40	Conglomerate
			K20H-O23	1146.80	Conglomerate
			K20H-O24	1162.20	Sandstone
			K20H-O25	1207.20	Claystone
			K20H-O26	1219.35	Sandstone
			K20H-O27	1244.60	Conglomerate
			K20H-O28	1281.30	Sandstone
			K20H-O29	1296.80	Conglomerate
			K20H-O30	1358.50	Sandstone
			K20H-O31	1447.00	Sandstone
			K20H-O32	1474.20	Conglomerate
			K20H-O33	1484.05	Conglomerate
			K20H-O34	1542.60	Conglomerate
			K20H-O35	1624.50	Conglomerate
			K20H-O36	1803.80	Conglomerate
			K20H-O37	1834.20	Sandstone
			K20H-O38	1850.00	Conglomerate
	Alacağzı	Serpukhovian-Bashkirian (Namurian)	K20H-O39	1900.00	Sandstone
			K20H-O40	1972.30	Sandstone
			K20H-O41	1981.00	Pebbly sandstone

## 4. Findings

### 4.1. Macroscopic Description

The studied coal clast samples are variable in centimeter size (from 1 to 5 cm), and generally have surface areas around 1 cm<sup>3</sup> (Figure 2). The samples are mostly vitrinitic/xylic and mostly dull bright sub-angular to angular and rarely rounded fragments and do not display any certain orientations (Figure 2). Furthermore, cleat/fracture carbonates were macroscopically observed in a few samples from the Late Carboniferous samples, and these cleat/fracture infillings are not observed in the coal clast-bearing embedded sediments. In contrast, cleat/fracture pyrite infillings are observed from the sample and embedded coal clast sample in the İnciğez clastics of the Zonguldak Formation. The investigated coal clast samples from the Late Carboniferous formations are mainly obtained from sandstone and conglomerate layers overlying coal seams, while one sample is obtained from a limestone bed within İnciğez clastics of the Zonguldak Formation.

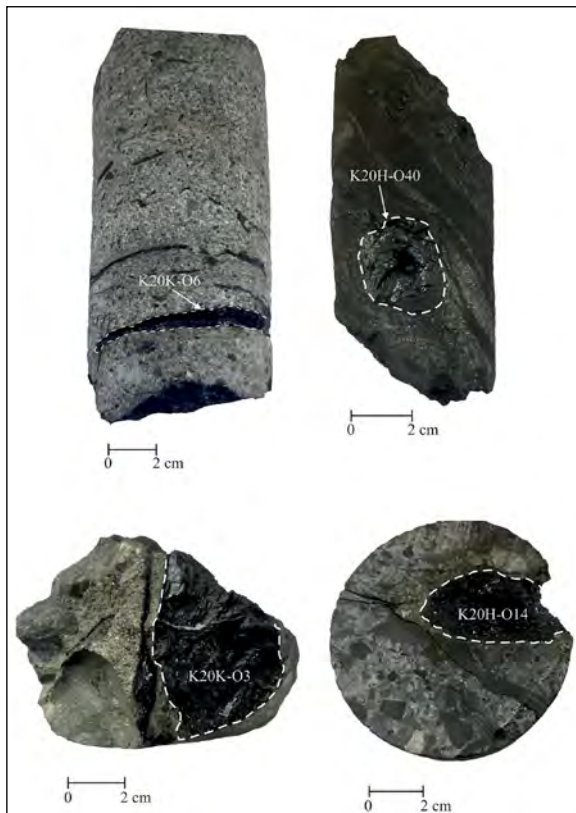


Figure 2- Selected photographs of the studied coal clast samples.

### 4.2. Coal petrography and Vitrinite Reflectance of Coal Clasts

The coal petrography examinations show that the majority of samples are composed only of vitrinite macerals, with liptinite and inertinite macerals rarely observed (Figures 3-7). Therefore, no detailed maceral counts were done from the studied clast samples. Collotelinite is the most common vitrinite maceral in all investigated samples (Figures 3b-f, 4a, 4b, 5a, 5b, 6a, 6b, and 7a, 7b), while telinite is more common in the xylic/vitrinitic clast samples (Figures 3a-c and 5a). Collodetrinite and vitrodetrinite are other vitrinite macerals identified from the samples (Figures 3b, 4c and f, 5d, 6c, 6d, and 7a), while corpogelinite is identified in the clast sample from the Zonguldak Formation (Figure 3a). More importantly, deformed and/or brecciated vitrinite grains (Figures 3e, 4e, 5c, 5d, and 6a) and vitrinite with micro-cracks and -fissures (Figures 3e, 3f, 4b, and 5e) were observed in all studied formations. The existence of such grains could indicate that the peat slides during peat formation and/or mainly tectonic deformations during post-coalification (Tailis, 1985; Xie et al., 2019; Hower et al., 2021). The latter possibility seems to be more common since the Carboniferous coal seams in the Zonguldak coalfield were deformed due to orogenic events (Yalçın et al., 2002; Okay and Nikishin, 2015; Karayığit et al., 2018a). In addition, oxidized vitrinite grains with dark oxidation rims (Figures 7c and 7d) are observed in coal clasts from the Alacağzı Formation samples, and vitrinite grains in clast samples from conglomerates of the Kozlu and Alacağzı formations might also display possible brittle deformation around the clastic mineral matter (Figures 4f, 5f, and 6f).

Inertinite and liptinite macerals are embedded within collodetrinite (Figures 4a-d, 5b, 5c, and 6c, 6d), as reported in the coal seams in both wells (Karayığit et al., 2018a). Fusinite, semifusinite, macrinite, and inertodetrinite are the generally observed inertinite group macerals, while micrinite bands within collodetrinite are also identified in some samples (Figures 4a-c, 5b, 5d, and 6c, 6d). Similar to the Kozlu and Karadon formations in the studied wells and Amasra coalfield (Karayığit et al., 2018a, b), sporinite is commonly identified in the studied samples (Figure 4a, 4c, and 4d), and cutinite is also rarely identified. In the Karadon Formation, liptinite

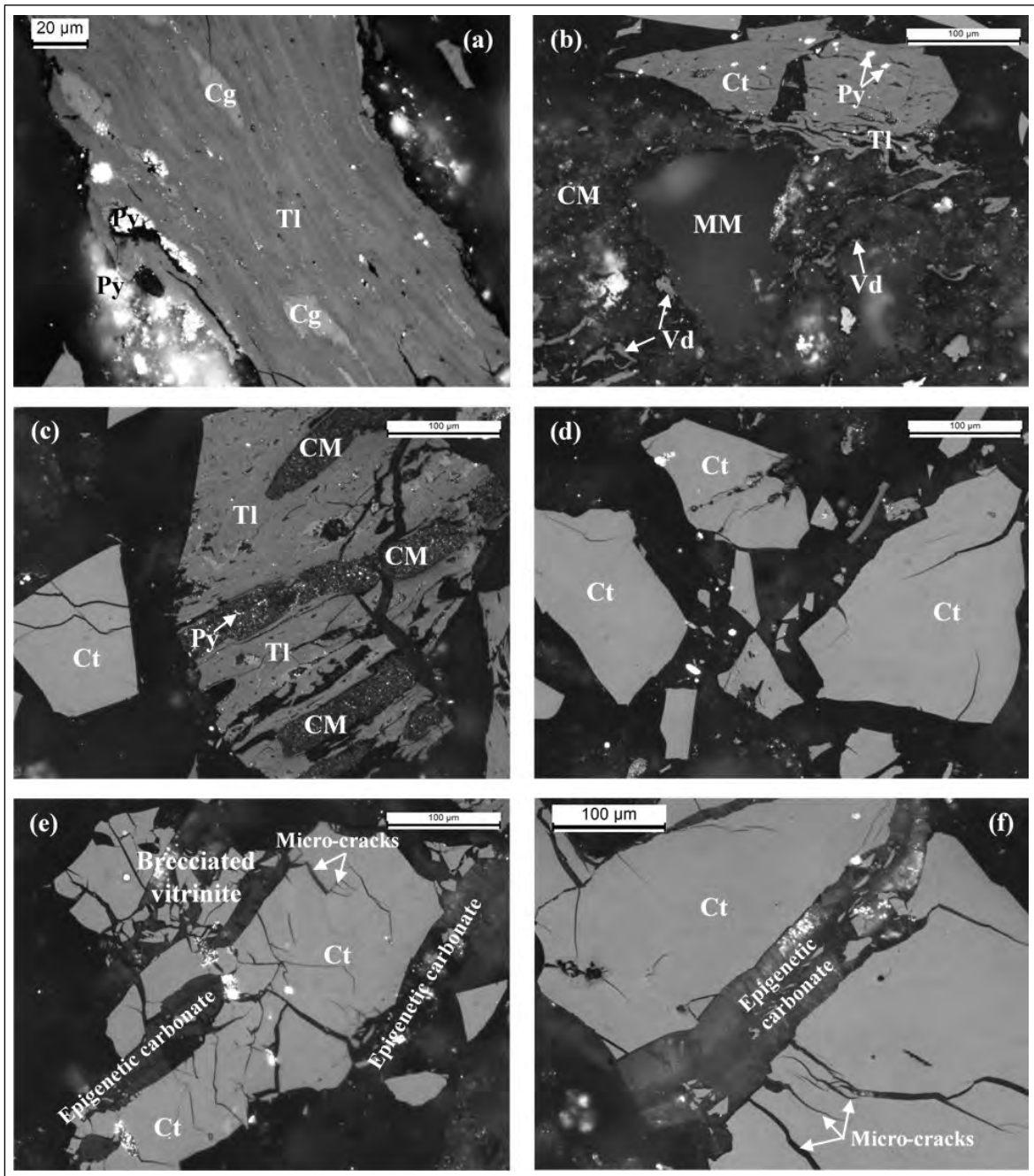


Figure 3- Selected microphotographs of clast sample (K20K-O1) from the Zonguldak Formation; a) tellinite (TI) and cell-lumen infilling corpopellinite (Cp), and framboidal pyrite (Py) grain; b) tellinite (TI), framboidal pyrite (Py) grains within collotelinitite (Ct), and vitrodetrinite (Vd) and mineral matter (MM) within clay mineral (CM) matrix, c) collotelinitite (Ct), and tellinite (TI) and cell-lumen infilling clay mineral (CM) and pyrite (Py), d) collotelinitite (Ct), e) and f) epigenetic carbonate cleat/fracture infilling between micro-cracks-bearing collotelinitite (Ct) and brecciated vitrinite grains. All photomicrographs are taken under incident white light and oil immersion,  $500\times$  total magnification. The %Rr value of the sample is  $1.01\pm 0.02$ .

macerals, particularly sporinite, in some samples display a very weak fluorescent colour under blue-light excitation (Figures 4c, 4d), while in the Kozlu Formation sporinite shows a pale grey colour under incident light (Figure 5c). The cleat/fracture carbonate

mineral-infillings are commonly identified in between the brecciated vitrinite grains (Figures 3e, 3f, 4e, and 7c), which was also commonly reported from coal seams in the studied wells by Karayığit et al. (2018a). In addition, cleat/fracture pyrite-infillings

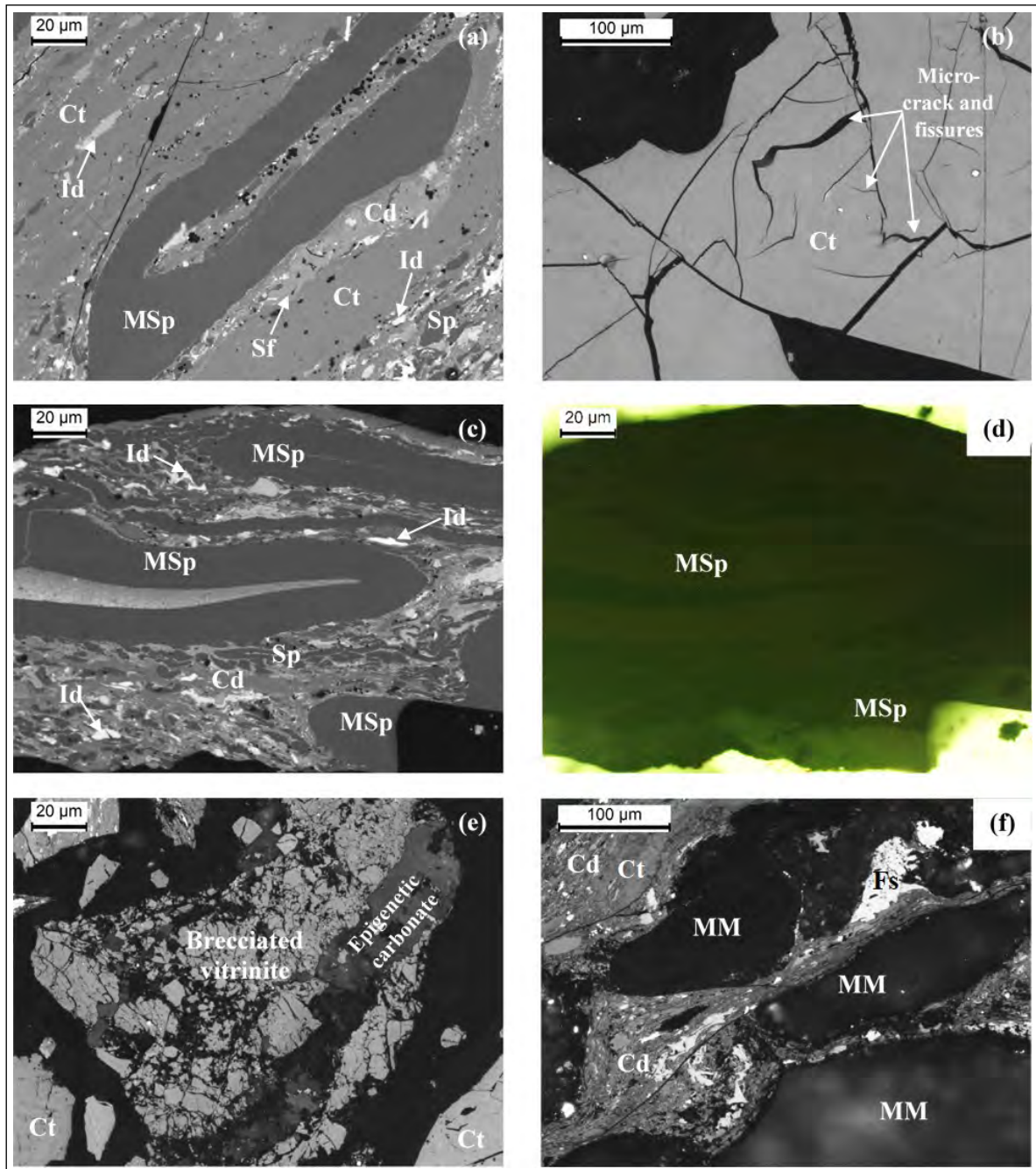


Figure 4- Selected microphotographs of clast samples from the Karadon Formation; a) intertodetrinite (Id), semifusinite (Sf), mega-sporinite (MSp) and sporinite (Sp) embedded within collodetrinite (Cd) and collotelinite (Ct), b) micro-cracks and -fissures within collotelinite (Ct), c) and d) intertodetrinite (Id), mega-sporinite (MSp) and sporinite (Sp) embedded within collodetrinite (Cd), e) epigenetic carbonate mineral-infillings between brecciated vitrinite and collotelinite (Ct), f) collodetrinite (Cd) mineral-matter (MM) and fusinite (Fs) within display plastic deformation. All photomicrographs are taken under incident white light (a, b, c, e and f) and blue-light excitation (c), oil immersion, 500 × total magnification. Images a, c, and d from K20H-O3 (% $R_t$ =0.94±0.02), b from K20H-O1 (% $R_t$ =0.98±0.02), e and f from K20H-O7 (% $R_t$ =0.99±0.02).

and pyritized macerals were also detected in some samples. Other identified minerals using white incident light under a coal petrography microscope are framboidal pyrite grains (Figures 3a and 7a), and

rarely clay mineral aggregates (Figure 3b, 3c, and 7a) and syngenetic carbonate minerals (Figures 7a, 7b). In the Alacağzı Formation, a few flake graphite grains were identified (Figures 7e, 7f). Considering

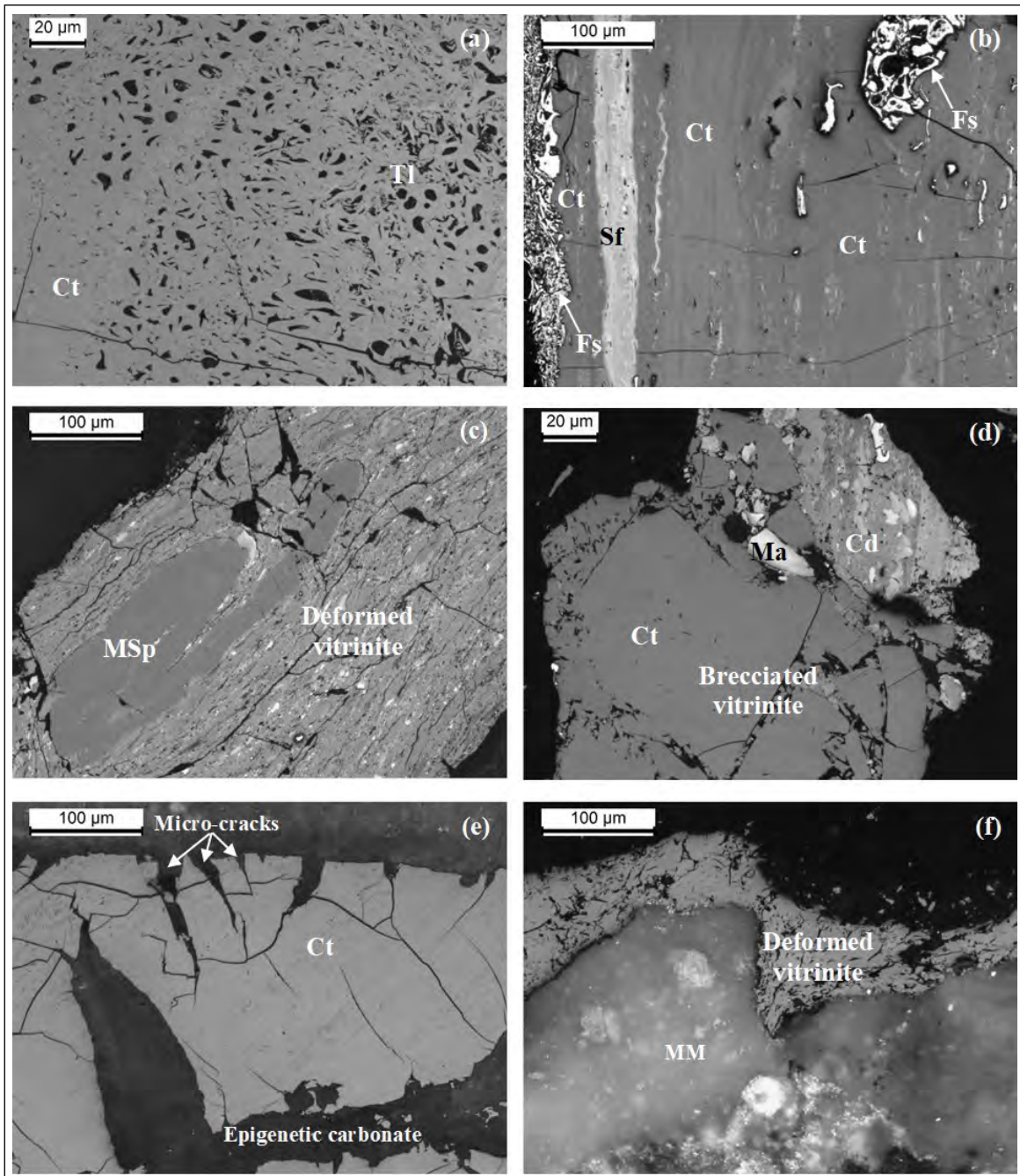


Figure 5- Selected microphotographs of clast samples from the Kozlu Formation; a) tellinite (Tl) and collotelinites (Ct), b) collotelinites (Ct), fusinite (Fs) and semifusinite (Sf), c) deformed vitrinite and mega-sporinite (MSP) grain; d) collodetrinite (Cd), macrinite (Ma), collotelinites (Ct), and brecciated vitrinite grains, e) micro-cracks-bearing collotelinites (Ct) and epigenetic carbonate cleat/fracture infilling, f) deformed vitrinite around mineral matter (MM). All photomicrographs are taken under incident white light and oil immersion,  $500\times$  total magnification. Images a and b from K20K-O7 ( $\%R_r=1.26\pm 0.02$ ), c from K20H-O10 ( $\%R_r=1.06\pm 0.03$ ), d from K20H-O33 ( $\%R_r=1.32\pm 0.03$ ), e from K20K-O8 ( $\%R_r=1.28\pm 0.03$ ), f from K20H-O22 ( $\%R_r=1.23\pm 0.03$ ).

the lack of thermal impact and natural coke formation in the studied wells, the graphite grains were derived as clastic inputs into parental coal seams from presumably Silurian Hamzafakı Formation and/or

Devonian Göktepe Formation, where metasediments were intruded with magmatic dykes (Küskü et al., 1997; Karayiğit et al., 2018a).

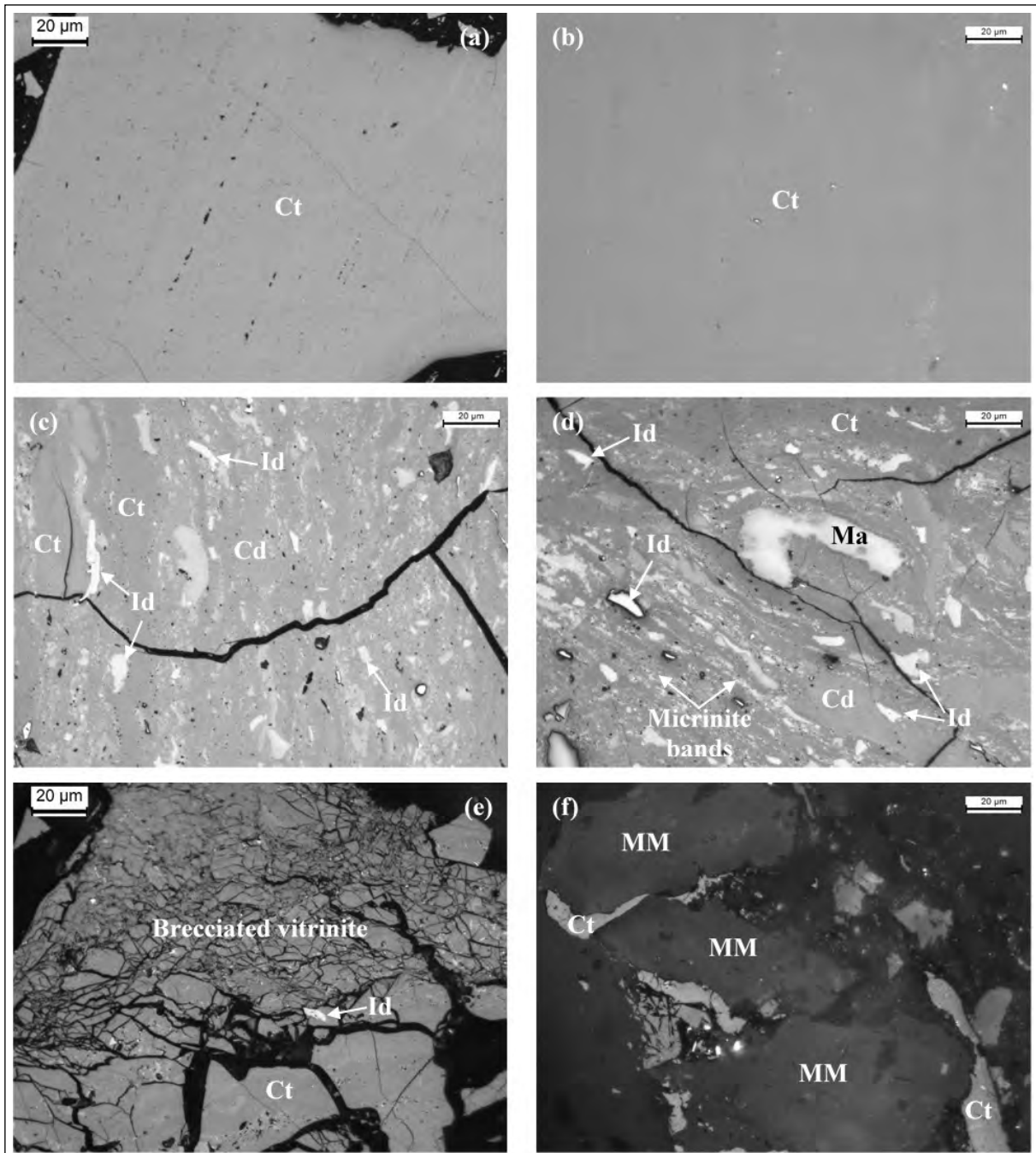


Figure 6- Selected microphotographs of clast samples from the Alacaagzi Formation; a), b) collotelinite (Ct), c), d) collodetrinite (Cd), and inverteidetrinite (Id), macrinite (Ma) and micrinite bands embedded within collodetrinite (Cd), e) deformed collotelinite (Ct) around mineral-matter (MM), f) collotelinite (Ct), inverteidetrinite (Id) and brecciated vitrinite grains. All photomicrographs are taken under incident white light and oil immersion,  $500\times$  total magnification. Images a and c from K20H-O41 ( $\%R_r=1.73\pm 0.03$ ), b from K20K-O12 ( $\%R_r=1.29\pm 0.02$ ), d and e from K20K-O13 ( $\%R_r=1.29\pm 0.03$ ), f from K20H-O40 ( $\%R_r=1.72\pm 0.03$ ).

The  $\%R_r$  values of coal clast samples from the Alacaagzi Formation show significant differences between K20H ( $1.70\%-1.72\%\pm 0.03$ ) and K20K ( $1.29\%\pm 0.02$ ) wells (Table 2). The samples of the Kozlu Formation in the K20H well have  $\%R_r$  values

of  $1.08-1.31\pm 0.02$ , while the  $\%R_r$  values of samples obtained from this formation in the K20K well display a wide range and vary from  $1.04\pm 0.02$  to  $1.52\pm 0.03$  (Table 2). The Karadon Formation samples cored in the K20K well have  $\%R_r$  values ranging from

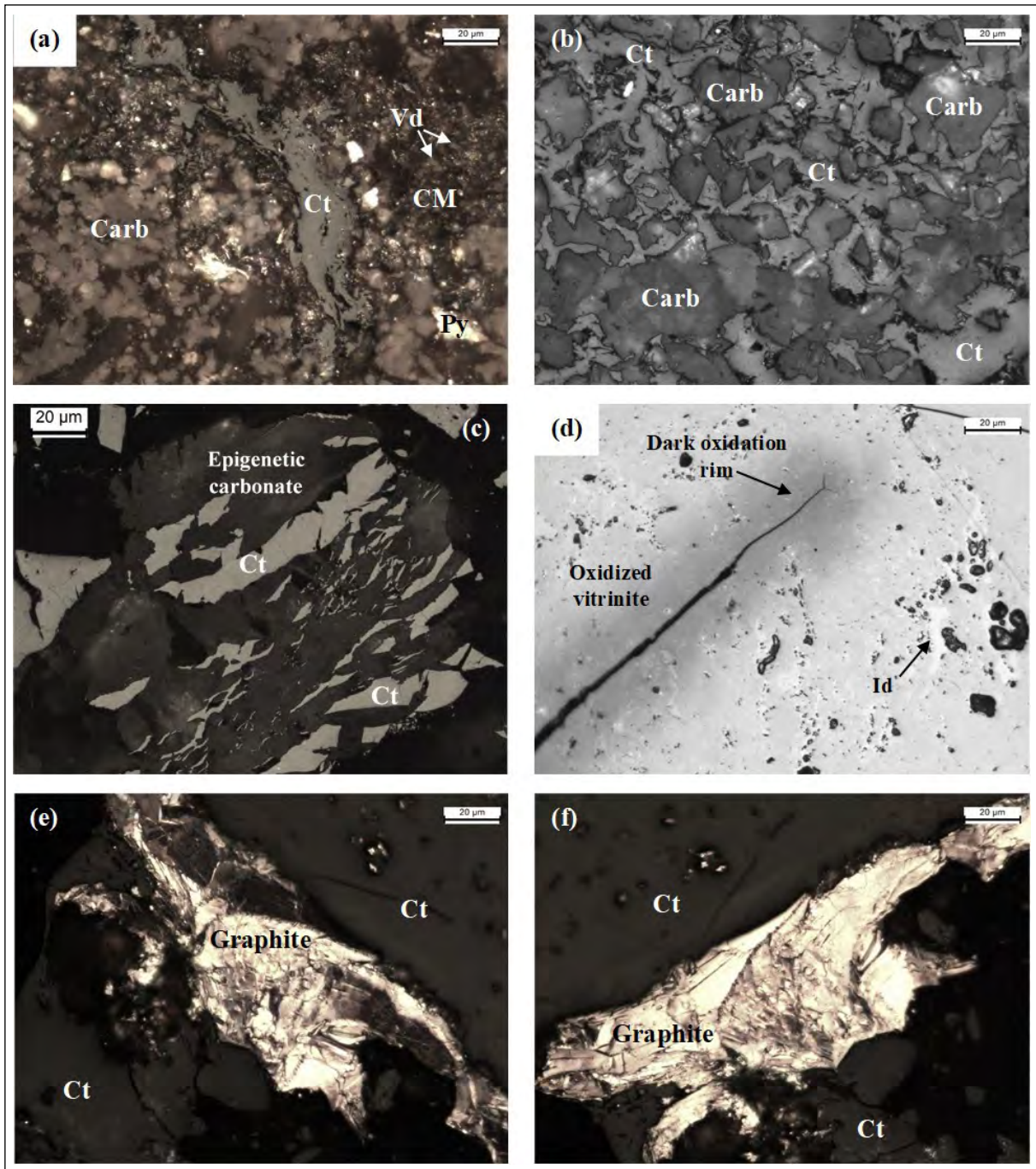


Figure 7- Selected microphotographs of clast samples from the Alacağzı Formation; a) collotelinite (Ct) and vitrodetrinite (Vd) within clay mineral (CM) matrix, syngenetic carbonate (Carb) grains, and pyrite (Py), b) collotelinite (Ct) and carbonate (Carb) grains; c) oxidized vitrinite with dark oxidation rim and inertodetrinite (Id), d) epigenetic carbonate cleat/fracture infillings between brecciated collotelinite (Ct) grains, and e), f) clastic graphite grain, possibly derived from pre-Carboniferous basement, and collotelinite (Ct). All photomicrographs are taken under incident white light (a-d) and partially crossed polarizers (e-f), oil immersion,  $500\times$  total magnification. Images from a, b, d-f from K20K-O13 ( $\%R_t=1.29\pm 0.03$ ), c from K20H-O40 ( $\%R_t=1.72\pm 0.03$ ).

1.02-1.05 $\pm$ 0.03, whereas the  $\%R_t$  values of samples of this formation from the K20H well are almost within the range of standard derivation of ones from the K20H well and vary from 0.94 $\pm$ 0.02 to

1.06 $\pm$ 0.02 (Table 2). Finally, the  $\%R_t$  value of a coal clast sample (K20K-O1) from the Early Aptian İnciğez clastics is 1.01 $\pm$ 0.02 (Table 2).

Table 2- The random reflectance (%Rr) of collotelinite and standard deviation (Stdv) of coal clasts samples from K20K and K20H research wells.

Well	Formation	Age	Sample No	%Rr $\pm$ Stdv
K20K	Zonguldak	Early Aptian	K20K-O1	1.01 $\pm$ 0.02
	Karadon	Langsettian (Westphalian A)	K20K-O2	1.05 $\pm$ 0.02
			K20K-O3	1.05 $\pm$ 0.02
			K20K-O4	1.05 $\pm$ 0.02
			K20K-O5	1.02 $\pm$ 0.02
			K20K-O6	1.08 $\pm$ 0.02
	Kozlu	Duckmantian-Asturian (Westphalian B-D)	K20K-O7	1.26 $\pm$ 0.02
			K20K-O8	1.28 $\pm$ 0.03
			K20K-O9	1.31 $\pm$ 0.03
			K20K-O10	1.18 $\pm$ 0.03
			K20K-O11	1.19 $\pm$ 0.02
	Alacağzı	Serpukhovian-Bashkirian (Namurian)	K20K-O12	1.29 $\pm$ 0.02
			K20K-O13	1.29 $\pm$ 0.03
K20H	Karadon	Langsettian (Westphalian A)	K20H-O1	1.04 $\pm$ 0.03
			K20H-O2	0.98 $\pm$ 0.02
			K20H-O3	0.94 $\pm$ 0.02
			K20H-O4	0.99 $\pm$ 0.03
			K20H-O5	1.00 $\pm$ 0.03
			K20H-O6	1.00 $\pm$ 0.02
			K20H-O7	0.99 $\pm$ 0.02
			K20H-O8	1.06 $\pm$ 0.02
	Kozlu	Duckmantian-Asturian (Westphalian B-D)	K20H-O9	1.04 $\pm$ 0.02
			K20H-O10	1.06 $\pm$ 0.03
			K20H-O11	1.06 $\pm$ 0.02
			K20H-O12	1.10 $\pm$ 0.02
			K20H-O13	1.16 $\pm$ 0.03
			K20H-O14	1.18 $\pm$ 0.02
			K20H-O15	1.15 $\pm$ 0.02
			K20H-O16	1.19 $\pm$ 0.02
			K20H-O17	1.15 $\pm$ 0.02
			K20H-O18	1.28 $\pm$ 0.02
			K20H-O19	1.28 $\pm$ 0.03
			K20H-O20	1.19 $\pm$ 0.03
			K20H-O21	1.22 $\pm$ 0.02
			K20H-O22	1.23 $\pm$ 0.03
			K20H-O23	1.24 $\pm$ 0.03
			K20H-O24	1.31 $\pm$ 0.02
			K20H-O25	1.30 $\pm$ 0.02
			K20H-O26	1.20 $\pm$ 0.02
			K20H-O27	1.26 $\pm$ 0.03
			K20H-O28	1.25 $\pm$ 0.03
			K20H-O29	1.27 $\pm$ 0.03
			K20H-O30	1.31 $\pm$ 0.02
			K20H-O31	1.42 $\pm$ 0.02
			K20H-O32	1.32 $\pm$ 0.03
			K20H-O33	1.32 $\pm$ 0.03
			K20H-O34	1.41 $\pm$ 0.02
			K20H-O35	1.49 $\pm$ 0.03
			K20H-O36	1.54 $\pm$ 0.02
			K20H-O37	1.54 $\pm$ 0.02
			K20H-O38	1.52 $\pm$ 0.03
	Alacağzı	Serpukhovian-Bashkirian (Namurian)	K20H-O39	1.70 $\pm$ 0.03
			K20H-O40	1.72 $\pm$ 0.03
			K20H-O41	1.73 $\pm$ 0.03

### 4.3. Mineralogy of Coal Clasts

The XRD results show that analysed coal clast samples from all studied formations display similar mineralogical compositions (Table 3). Quartz is detected as a generally abundant to dominant phase, while clay minerals (kaolinite and illite/mica) and feldspar are minor phases in the samples (Table 3). As expected, calcite is a dominant phase in the cleat/fracture carbonate-infillings-bearing samples, and dolomite and ankerite are detected as minor phases in these samples (Table 3). Siderite is found in one sample (K20K-O13) from the Alacağzı Formation (Table 3). Pyrite is an abundant phase in the samples from the Zonguldak Formation, while it is found as a minor phase in some samples from the Karadon and Kozlu formations (Table 3). Besides XRD analysis, anglesite, apatite, barite, chalcocopyrite, chlorite (chamosite), galena, monazite, sphalerite, titanite/sphene, Ti-oxides, and zircon are detected as accessory minerals according to the SEM-EDX data (Table 3).

## 5. Discussion

### 5.1. Origins of Minerals

The petrographical and SEM examinations indicate that minerals in the coal clast samples are derived from the parental Carboniferous coal seams and the precipitation of solutions cleats/fractures of coal clasts after the diagenesis of embedded sediments and early coalification of parental coal seams. Quartz, like in Carboniferous coal seams in the studied wells, is generally identified as individual grains within clay mineral matrices during SEM examination (Figures 8a, 8d, 8e, 8f, 9a and 10b). These grains are clearly derived as clastic inputs into palaeomires of parental coal seams. Clay mineral matrices associated with individual quartz, feldspars, apatite, monazite, titanite/sphene, and zircon grains and organic matter (macerals) were observed, and the SEM-EDX data showed that the matrices have mostly kaolinite and illitic compositions (Figures 8a-f and 10a-b). Similar associations within kaolinite matrices were also reported from the coal seams in the studied wells and other coalfields in the Zonguldak Basin (Karayığit et al., 2018a, b), and also from tonstein layers in the Zonguldak Basin (Burger et al., 2000), which were formed from alteration of synchronous and/or

epiclastic volcanic inputs within palaeomires during the Carboniferous. Hence, the identified kaolinite matrices and associated minerals from the investigated coal clast samples are derived from parental coal seams. Illitic matrices are presumably derived as clastic influx into palaeomires of the parental coal seams; nevertheless, these matrices might also be originated from the transformation of clastic smectite and/or interstratified illite/smectite matrices into illite during the diagenesis of embedded sediments. Besides, cleat/fracture kaolinite-infillings were also observed in some samples (Figures 9a-e). Since cleat/fracture kaolinite-infillings were observed as monomineral infilling or accompany with sulphide minerals (pyrite and galena), these infillings seem to be formed from the precipitation of Al and Si-rich hydrothermal solutions during either the early coalification stage of the parental seams, as like coal seams in both wells (Karayığit et al., 2018a), or more possible during the diagenesis of embedded sediments.

Carbonate minerals are mainly identified as individual grains (Figures 8a and 10a) and nodules (Figures 8c and 10b) within clay mineral matrices, and more commonly cleat/fracture infillings (Figures 9f and 10c-f), particularly from deformed and brecciated vitrinite grains-bearing samples.

These infillings are mostly calcite with detectable Mg and pure dolomite (Figures 10c-f), and, to a lesser extent, Fe-rich dolomite with measurable Mn (Figures 10e and 10f) and ankerite (Figures 9f and 10c). Such carbonate mineral-infillings are commonly reported in Permo-Carboniferous coals and mostly originate from the precipitation of Ca-rich hydrothermal solutions (Dawson et al., 2012; Permana et al., 2013; Xie et al., 2019; Valentim et al., 2020).

In accordance with this, Karayığit et al. (2018a) also assumed that these carbonate infillings are related to the precipitation of Ca-rich solutions derived by penetration of hydrothermal solutions or leached solutions from overlying Early Cretaceous limestones *via* fault zones into coal seams in the studied wells. Considering the presence of carbonate infillings between deformed and brecciated vitrinite grains in the studied samples, Ca-rich solutions could either have penetrated after the tectonic deformation of parental

Table 3- Minerals identified in the analyzed coal clast samples based on XRD and SEM-EDX analyses (+++ = dominant phase, ++ = abundant phase, + = minor phase by XRD, a: by SEM-EDX; Abbreviations: CM: clay minerals, Feld: feldspars, Ank/Dol: ankerite/dolomite, Mnz/Ap: monazite/apatite).

Well	Formation	Sample No	Quartz	CM	Feld	Titanite	Calcite	Ank/Dol	Siderite	Pyrite	Chalcocopyrite	Galena	Sphalerite	Ti-oxides	Mnz/Ap	Barite	Anglesite	Zircon		
K20K	Zonguldak	K20K-O1	+++	+			+	+		++										
		K20K-O2	++	a			+	a			+									
	Karadon	K20K-O3	++	+				+	++											
		K20K-O4	+++	+				+++	+											
		K20K-O5	+	+																
	Kozlu	K20K-O7	+						++											
		K20K-O8	a					a	a						a					
		K20K-O9	++					+	+											
	Alacaagzi	K20K-O10	+	+				+												
		K20K-O11	+++	++	+															
		K20K-O12	++	+					+											
		K20K-O13	+++	+	+			+		+										
	K20H	Karadon	K20H-O1	a	a			a	a		a		a						a	
K20H-O4			+	+++			+	+		+										
K20H-O5			a	a							a		a							
Kozlu		K20H-O7	a	a	a			a	a		a					a				
		K20H-O10	+++	++																
		K20H-O12	+	+				+++												
		K20H-O15	+++	+				++	+		+						a			a
		K20H-O19	+++	++	+															
		K20H-O20	++	+	+			+												
		K20H-O21	+	+																
		K20H-O22	+++	+++	+			+												
		K20H-O25	++	+				+												
		K20H-O26	+	++																
Alacaagzi	K20H-O27	+	++				+++	+++		+										
	K20H-O28	+	+																	
	K20H-O30	++	+				+	+												
	K20H-O32	+++	++																	
Alacaagzi	K20H-O33	+++	++	+			+++													
	K20H-O34	+	+	+																
	K20H-O39	+	a					+		a						a			a	
	K20H-O40	++	+	+				++												
		K20H-O41	a	a	a	a	a	a	a	a	a	a	a	a	a	a	a	a	a	

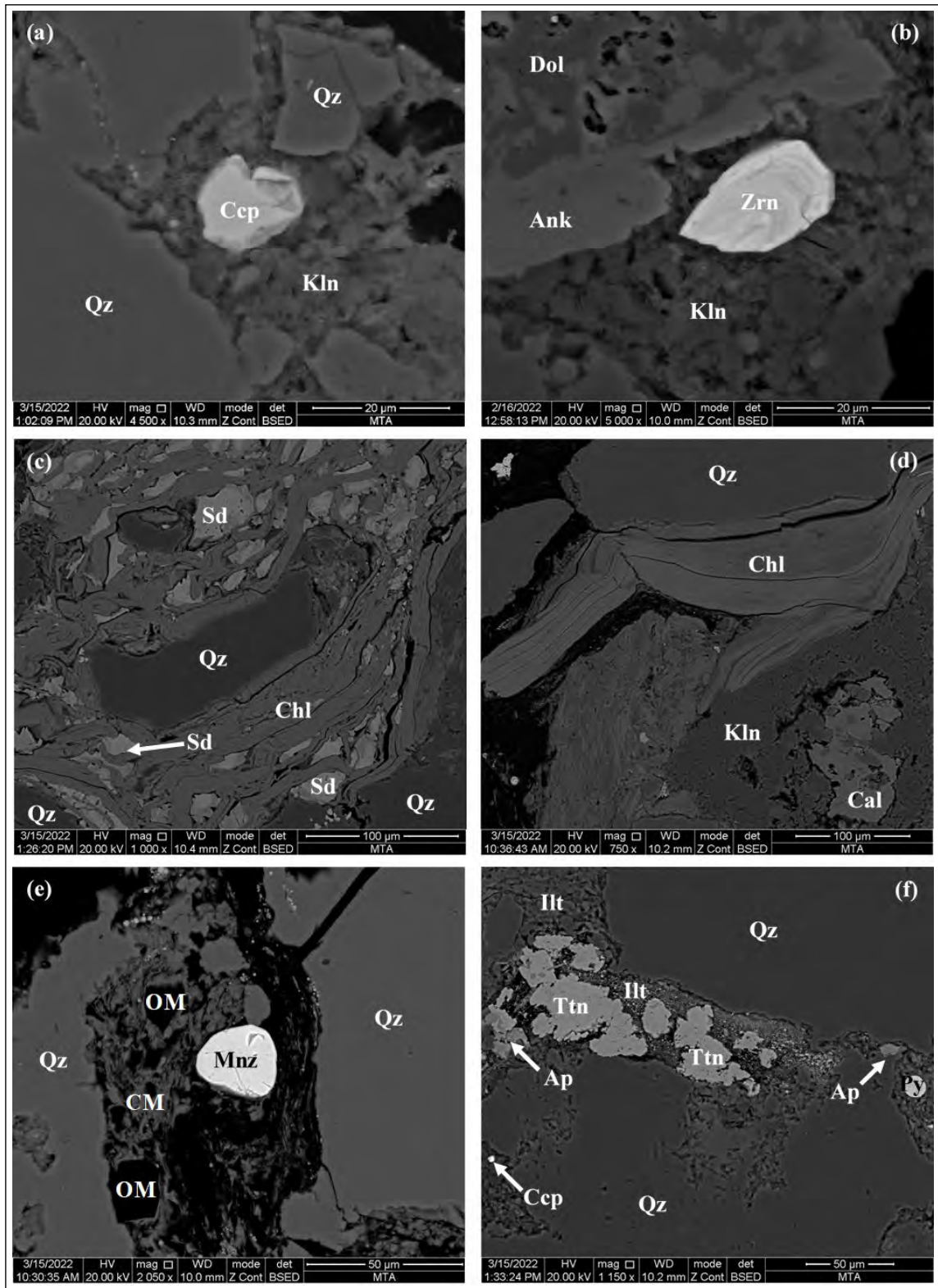


Figure 8- Selected SEM backscattered electrons (SEM-BSE) images; a), b) and d) ankerite (Ank), calcite (Cal), chlorite (Chl), chalcopyrite (Ccp), dolomite (Dol), quartz (Qz) and zircon (Zr) grains within kaolinitic (Kln) matrix, c) chlorite (Chl) associated with siderite (Sd) nodules and quartz (Qz) grains, e) monazite (Mnz) and quartz (Qz) grains and organic matter (OM) associated with clay mineral (CM), f) apatite (Ap), chalcopyrite (Ccp), quartz (Qz) and titanite (Ttn) grains within illitic (Illt) matrix. Images a from K20H-O15, b and f from K20H-O41, d and e from K20H-O7.

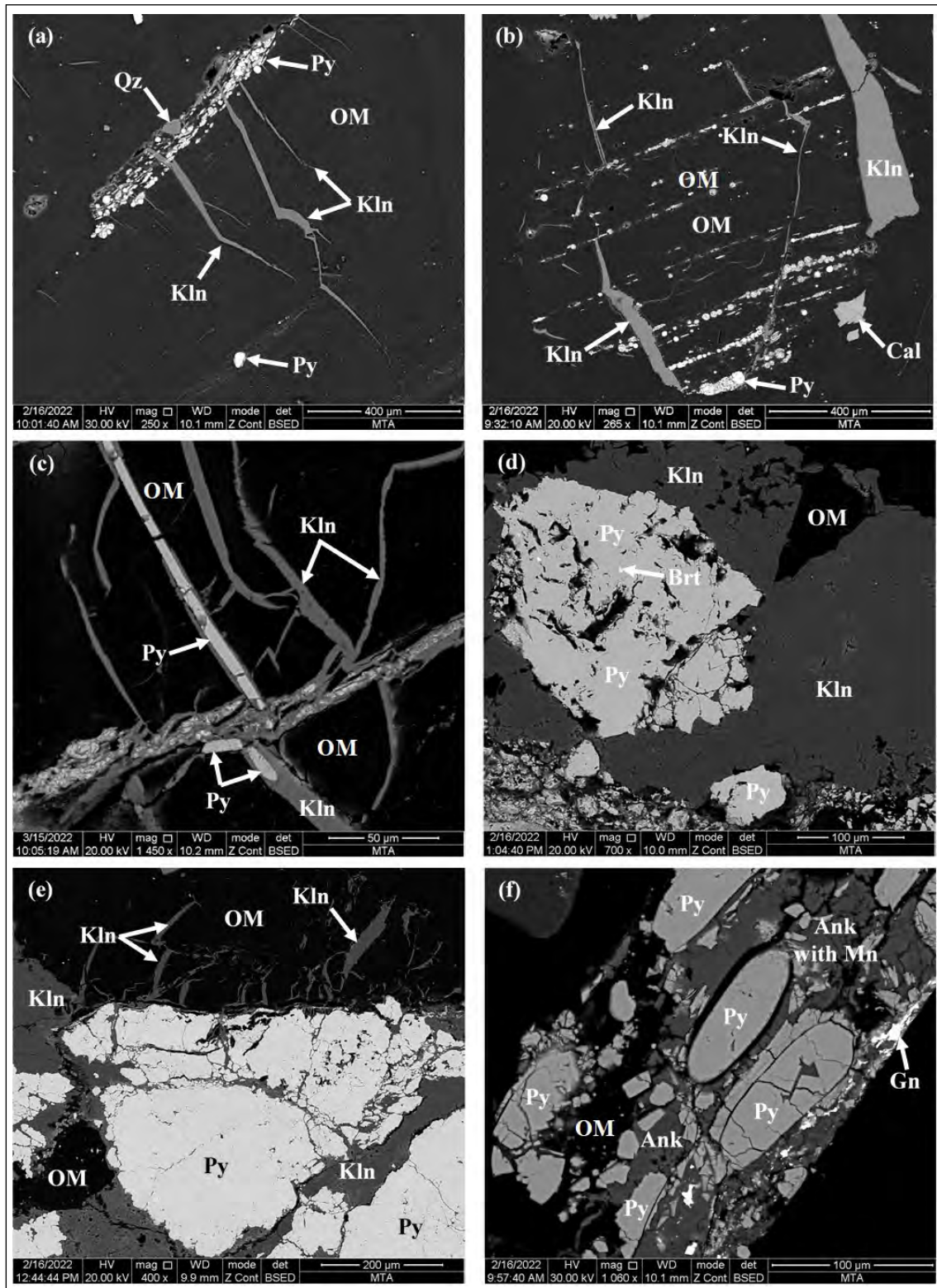


Figure 9- Selected SEM-BSE images; a), b) cleat/fracture kaolinite (Kln)-infillings within organic matter (OM), syngenetic framboidal pyrite (Py) grains and calcite (Cal) grains, c) cleat/fracture kaolinite (Kln) and pyrite (Py)-infillings within organic matter (OM), d) and f) cleat/fracture barite (Brt), pyrite (Py) and kaolinite (Kln)-infillings within organic matter (OM), e) cleat/fracture galena (Gn), pyrite (Py) and ankerite (Ank) with measurable Mn-infillings within organic matter (OM). Images a, b, e from K20H-O1, c from K20H-O7, d and f from K20H-O15.

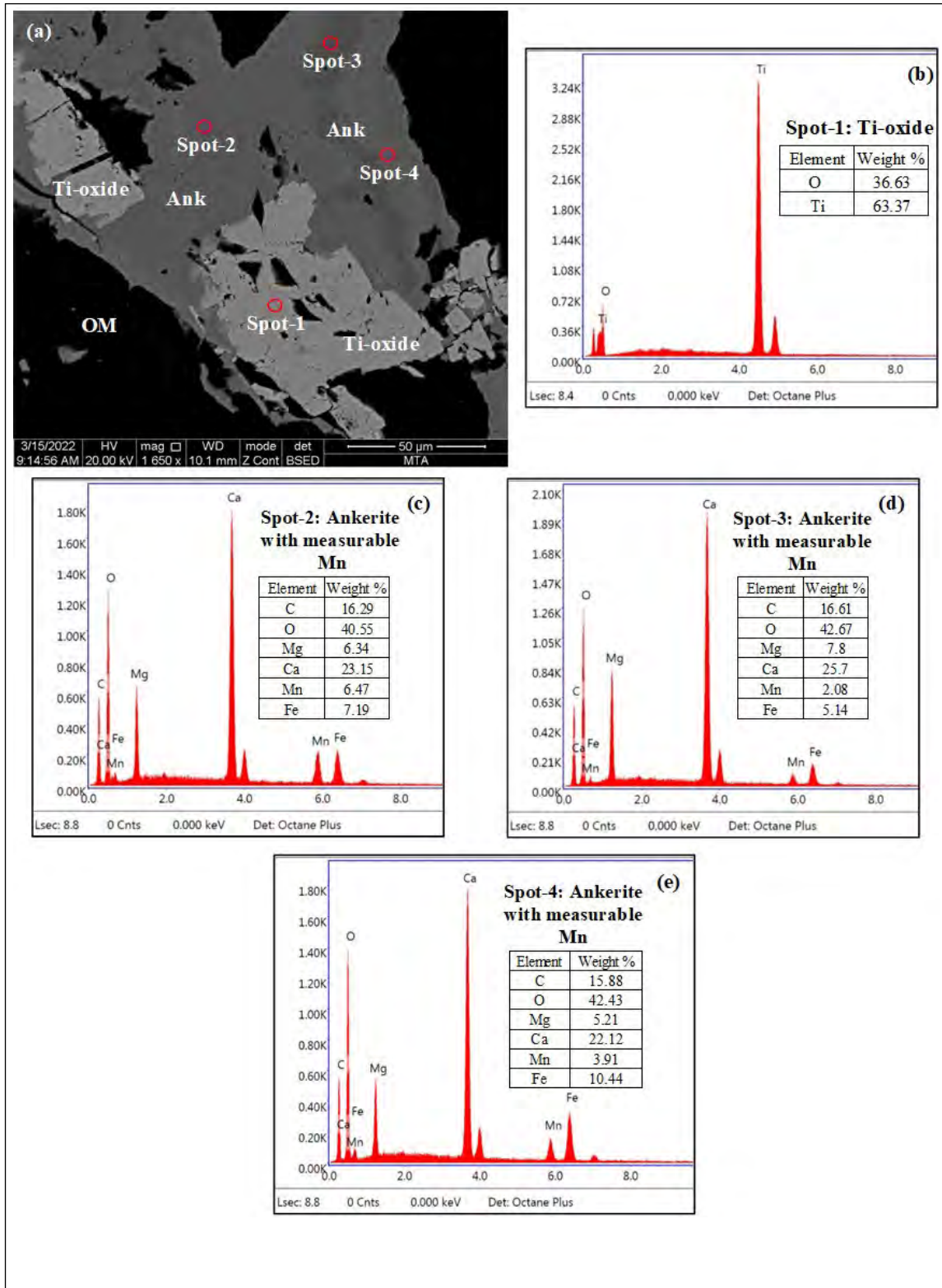


Figure 10- Selected SEM-BSE images; a) ankerite (Ank), dolomite (Dol) and zircon grains within illitic (Ilt) matrix, and cleat/fracture kaolinite (Kln)-infilling within organic matter (OM), b) siderite (Sd) nodule, plagioclase (Pl) and quartz (Qz) within illitic (Ilt) matrix, c), d) cleat/fracture ankerite (Ank), calcite (Cal) and quartz/silica (Qz)-infillings within organic matter (OM), e) and f) cleat/fracture calcite (Cal), dolomite (Dol) and Ti-oxide-infillings within organic matter (OM). Images a and c from K20H-O15, b from K20H-O41, d from K20H-O7, e and f from K20K-O8.

coal seams or embedded sediments. Nevertheless, the presence of carbonate-infillings in clast samples might also have originated from the precipitation of Ca-rich intra-formation solutions during the diagenesis of embedded limestone in case of the Zonguldak Formation or penetration of carbonate cement of conglomerate for Carboniferous clast samples. Nevertheless, the latter case was probably not common due to the lack of carbonate mineralization around Carboniferous coal clasts. Siderite nodules were detected rarely in a few samples within organic matter or clay matrices (Figure 8c and 10b), which implies these nodules originated from the parental coal seams and formed within palaeomires (Karayığit et al., 2017, 2018a, b; Dai et al., 2020). The formation of epigenetic Ti-oxide (anatase/rutile)-infillings in coals is mostly controlled by the precipitation of hydrothermal solutions (Zhao et al., 2018; Rodrigues et al., 2020; Liu et al., 2021). In the samples from the Kozlu Formation, cleat/fracture Ti-oxide infillings are associated with carbonate mineral-infillings (Figures 10f and 11). Such infillings were also developed from the precipitation of hydrothermal solutions.

Framboidal pyrite grains within organic matter are clearly related to parental coal seams (Figures 3a, 7a, 9a, 9b, and 12a). These framboidal pyrite grains formed authigenically within the palaeomires or early diagenesis of parental coal seams. The cleat/fracture pyrite-infillings were also commonly reported from the coal seams in the basin (Karayığit et al., 1998, 2018a, b), which were formed after the precipitation of Fe- and sulfate-rich from penetrated hydrothermal solutions during coalification. Similar cleat/fracture pyrite-infillings are also identified from the Carboniferous coal clasts (Figures 9c-f), which were also derived from the precipitation of penetrated hydrothermal solutions, as like the kaolinite and carbonate minerals. Even though the determination of the timing of penetration of such solutions could not be estimated accurately, these pyrite-infillings were presumably formed mainly during the diagenesis of embedded coal seams and, to a lesser extent, during the early coalification of parental coal seams. Considering the presence of macroscopically identified cleat/fracture pyrite-infillings in the Early Aptian coal clast sample, pyritized macerals and

cleat/fracture pyrite-infillings in this sample seem to have developed within the depositional environment during the Early Aptian and/or post-Aptian. Besides the cleat/fracture pyrite-infillings and framboidal pyrite grains, galena and chalcopyrite are other identified sulphide minerals in the samples. Galena is only identified as cleat/fracture infillings, and such infillings are generally accompanied by carbonate minerals (Figures 9f and 12) and kaolinite (Figure 13). Chalcopyrite is only observed as individual grains within clay mineral matrices (Figure 8a and f), which imply a clastic origin for such grains. Barite (Figure 9d) and anglesite (Figure 14) are also only detected as cleat/fracture infillings. Barite seems to have been formed either during the early coalification of parental coal seams and/or diagenesis of embedded sediments. The anglesite overgrowths around galena-infillings, which grew after galena formation, formed due to the alteration of galena-infillings by pore-waters or hydrothermal solutions after galena formation.

Although mono-mineralic cleat/fracture infillings (e.g., Figures 9a, 9b and 10c) are commonly observed in the samples, multi-mineralic (e.g., carbonate-sulphide minerals or kaolinite-sulphide minerals) infillings are also detected (e.g, Figures 9c-f, 10d-f, 11a, and 13), like coal seams in the studied wells. Such multi-mineralic mineral infillings also formed from the precipitation of hydrothermal solutions in coal (Hower et al., 2001; Dawson et al., 2012; Permana et al., 2013; Karayığit et al., 2018a; Liu et al., 2021); thus, these infillings might be derived from the mainly precipitation during mainly within parental coal seams and/or diagenesis of embedded sediments, particularly for coal clast sample from the Zonguldak Formation.

## 5.2. Ranks and Origins of Coal Clasts

The rank and grade determination of coal seams are based on a combination of several parameters (e.g., %Rr, gross calorific values, and ash yields); however, the size of investigated coal clast grains did not permit all desired proximate, ultimate, and calorific analyses for rank and grade determination. Therefore, the rank determination of the investigated samples is only based on %Rr values. The %Rr values of coal clasts of the Alacaagzi Formation, as mentioned previously, display differences (Table 2 and Figure 15);

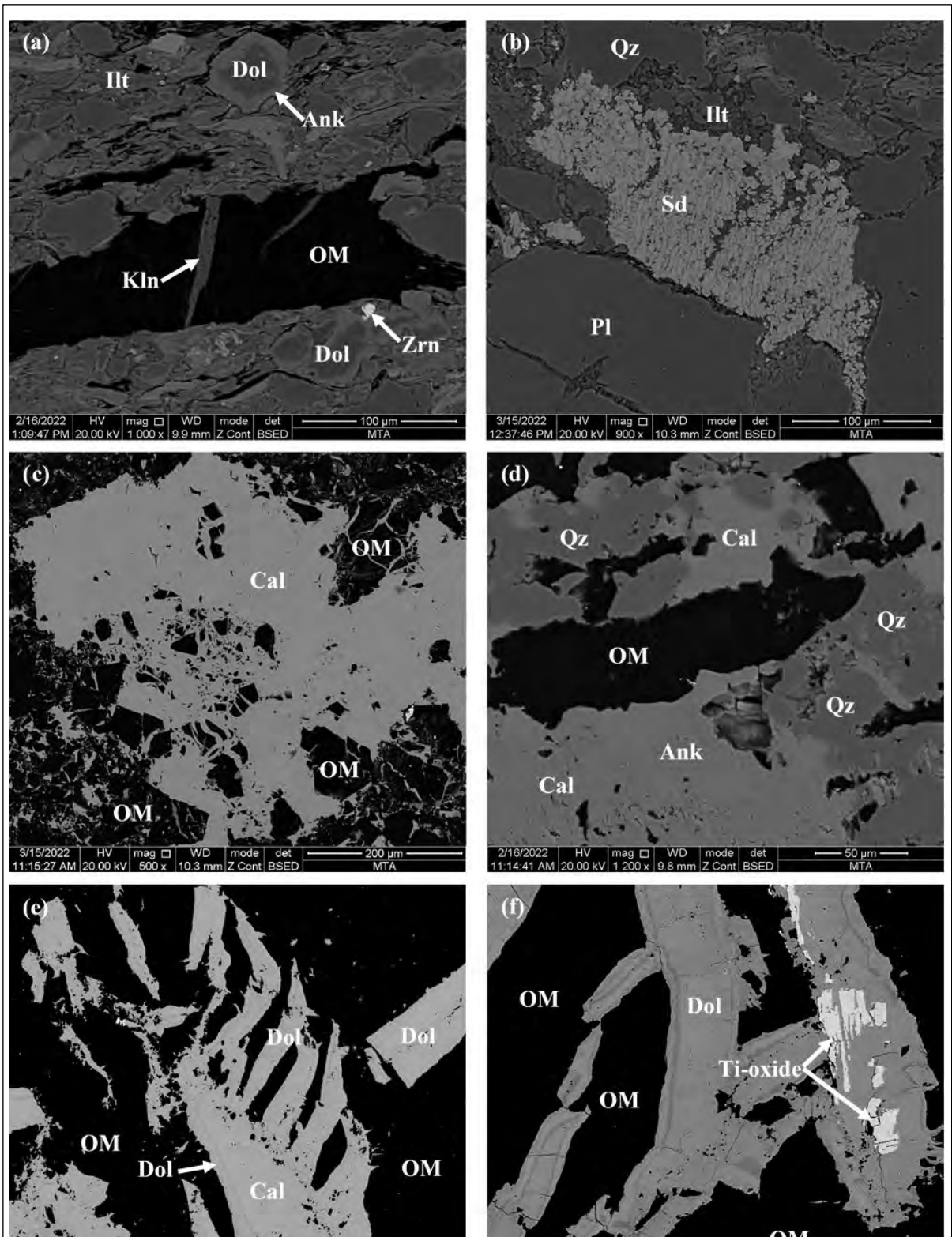


Figure 11- a) SEM-BSE image of cleat/fracture ankerite (Ank) and Ti-oxide-infillings within organic matter (OM), b) SEM-EDX spectra of Ti-oxide at spot-1 and c), d) ankerite with measurable Mn at spot-2. Image from K20K-O8.

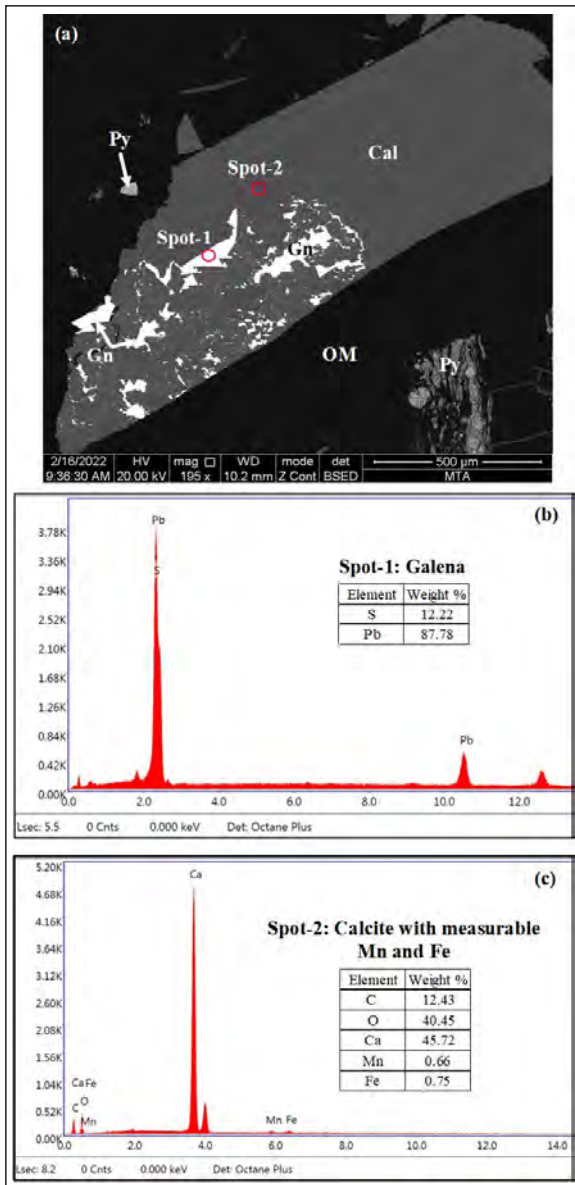


Figure 12- a) SEM-BSE image of cleat/fracture calcite (Cal) and galena (Gn)-infillings within organic matter (OM) and pyrite (Py), b) SEM-EDX spectra of galena at spot-1 and c) calcite with measurable Mn and Fe in image a. Image from K20H-O1.

thus, the samples of this formation have relative rank differences. Furthermore, the %Rr values of coal clasts could be very useful for determining the origin of coal clasts since coal clasts generally do not display diagenesis differences with parental coal seams (Gayer et al., 1996; Kožušniková et al., 1999; Daněk et al., 2002; Pešek and Sýkorová, 2006; Misz-Kennan et al., 2019). Of note, in some cases, coal clasts could display a lower rank than the parental coal seams.

The samples from the K20H well are of bituminous A (medium rank A) according to ISO 11760 (2005) coal-rank classification, while samples obtained from the K20K well are of bituminous B (medium rank B). This difference is not surprising since the Alacağzı Formation in the K20H well was cored to deeper depths than the K20K (Figures 1d and 15a), and %Rr values of coal seams in the Alacağzı Formation in the K20H well are relatively higher than coal seams in the K20K well (Karayığit et al., 2018a). Furthermore, the %Rr values of the Alacağzı coal clasts samples in the K20K are relatively higher than the coal seams in this well (Table 1 and Figure 15b), but the %Rr values are still within the range of standard deviation and close to the %R<sub>max</sub> values of coal seams in the Alacağzı Formation (Table 4). This difference could be controlled by the oxidation of clast samples during the transportation since micro-crack and -fissures-bearing vitrinite grains and oxidized vitrinite grains were observed in these samples. All these could imply that the erosion of paternal coal seams seems to take place during the peat stage and/or early stages of coalification and transportation of coal clasts sample took place in a short distance, while oxidation of coal clasts was limited.

In contrast with the K20K well (1.29%±0.02), the %Rr values of coal clast (1.70-1.73%±0.03) from the Alacağzı Formation in the K20H are slightly higher than coal seams (1.48-1.52%) of the Alacağzı Formation cored in this well (Table 4 and Figure 15a). This difference might be related to oxidation clast during transportation; however, this explanation could be applicable to sample K20H-O39, which was obtained from sandstone between two coal seams, and the remaining Alacağzı clast samples were obtained from conglomerate and sandstone layers beneath the coal seams in this well. This could easily suggest that the burial depth might increase their %Rr values, but the theoretically calculated %Rr values (1.48-1.52 %Rr) using the depth of these clasts (1900-1981 m beneath the surface) are close to the overlying coal seams (Figure 15a). Hence, burial depth impact might be limited on the coalification of these clast samples. These samples are also characterized by the presence of deformed and brecciated vitrinite grains (Figures 6e, 6f, and 7e). Previous palynological and palaeobotanical data from the coal-bearing formations

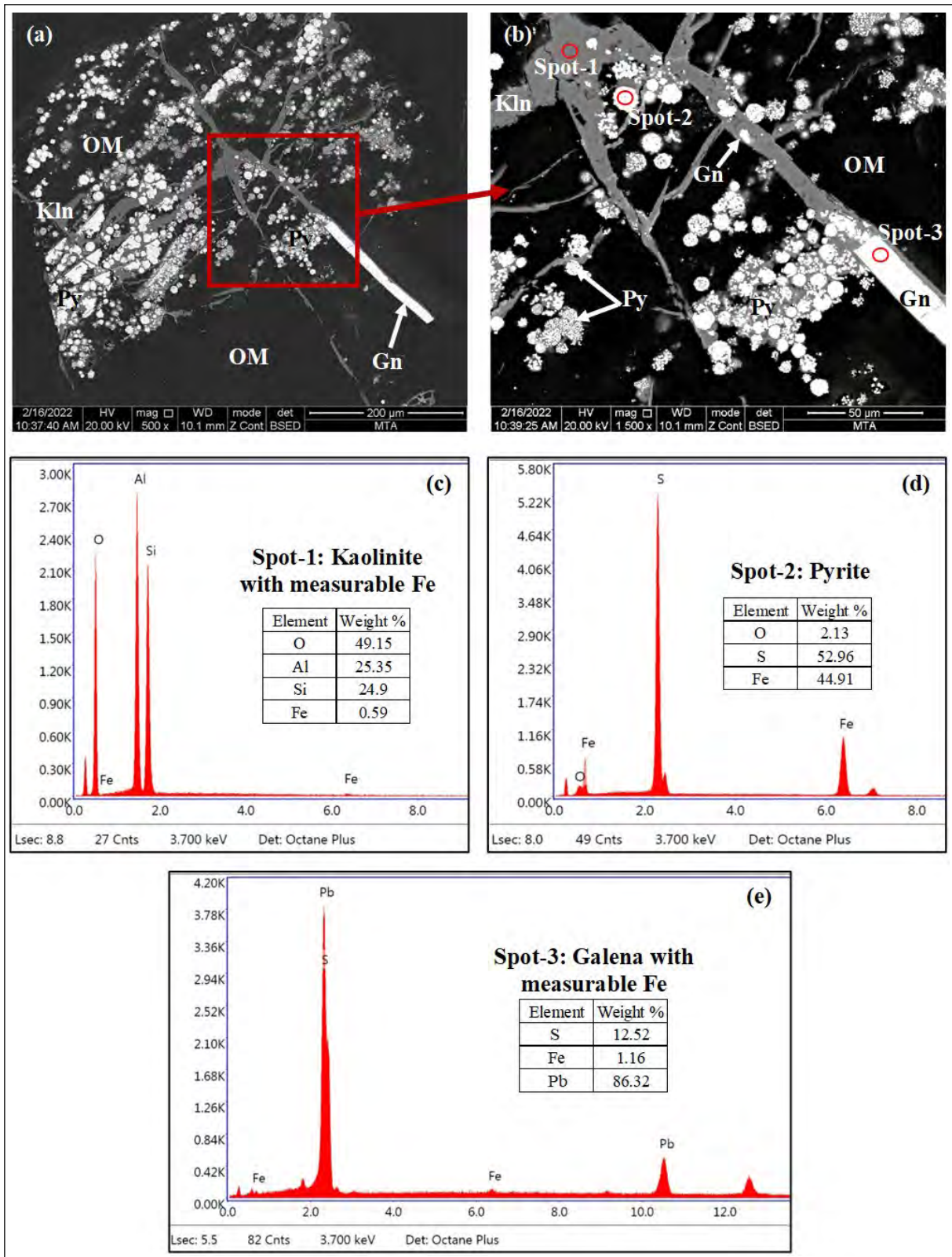


Figure 13- a, b) SEM-BSE image of cleat/fracture kaolinite (Kln) and galena (Gln)-infillings within organic matter (OM) and syngenetic framboidal pyrite (Py) grains within organic matter (OM), b) framboidal pyrite grain at spot-2, c) SEM-EDX spectra of kaolinite with measurable Fe at spot-1, and d) galena with measurable Fe at spot-2 image b. Image from K20H-O1.

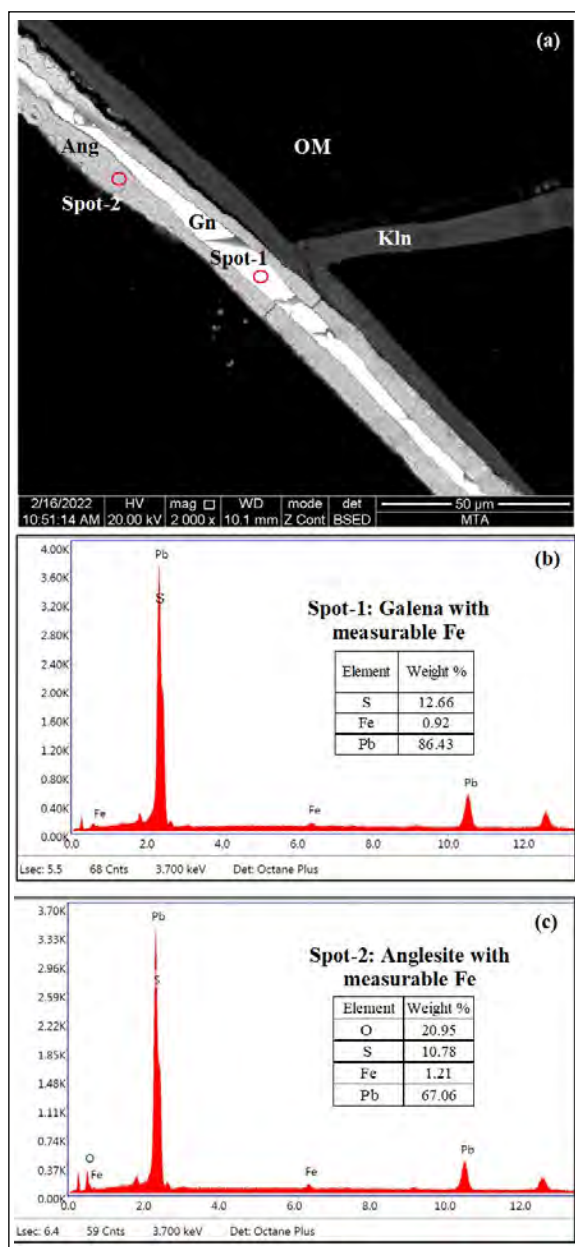


Figure 14- SEM-BSE image of cleat/fracture kaolinite (Kln), galena (Gn) and anglesite (Ang)-infillings within organic matter (OM); a) SEM-EDX spectra of galena with measurable Fe at spot-1 and b) anglesite with measurable Fe in image a. Image from K20H-O1.

in the Zonguldak Formation suggest a humid to seasonal dry climate conditions during Carboniferous (Akgün and Akyol, 1992; Opluštil et al., 2018). Under such conditions, the stability of the peat surface could be affected due to rewetting of the peat surface; in turn, peat-mires could slide, and these grains could be formed during the sliding of peat mires (Tallis, 1985; Daniels et al., 2008; Hower et al., 2021). The

seasonal dry climate conditions could also explain the existence of oxidized vitrinite grains in the coal clast samples from the Alacağzı Formation. Nevertheless, the post-coalification tectonic deformation, on the other hand, could cause the formation of brecciated vitrinite grains and following the emplacement of the epigenetic mineralization, could cause elevation of the %Rr values of coal seams (Hower and Davis, 1981; Hower et al., 2001; Hower and Gayer, 2002).

This could also cause the formation of micro-cracks on vitrinite grains. Similar assumptions were also made for the Carboniferous coal seams in the studied wells and the mono- or multi-mineralic cleat/fracture infillings formed due to the penetration of hydrothermal solutions during coalification (Karayiğit et al., 2018a). Since brecciated vitrinite grains and carbonate mineral-infillings (e.g., pure calcite and Fe-rich dolomite/ankerite, and ankerite) are commonly observed in the Alacağzı coal clast samples of the K20H well, the %Rr values of these coal clasts seem to be increased by tectonic deformation and following the precipitation of Ca-rich hydrothermal solutions. Furthermore, the calculated  $T_{peak}$  temperatures values of coal seams in the Alacağzı Formation from the K20H well using Barker and Pawlewicz's (1994) formula ( $T_{peak} = (\ln V R r \% + 1.19) / 0.00782$ ) range from 202 to 204 °C (Karayiğit et al., 2018a); while coal clast samples from this formation in the K20H are around 220°C, which could indicate possible hydrothermal solution penetration into embedded sediments, as like coal seams. All these imply that the erosion of paternal coal seams again took place during the late stages of peat formation and/or early coalification, and coal clasts beneath the coal seams of the Alacağzı coal seams in the K20H well display a similar coalification pattern with coal seams in this well and penetration of hydrothermal solutions is slightly increased coalification of these clasts. In any case, the Alacağzı coal clasts samples from the K20H well display a relatively higher coalification degree than the other studied coal clasts and coal seams in the studied wells. Although the palynological data from the coal clasts within the Alacağzı was not reported by Akgün et al. (1997), the observed maceral composition of coal clasts in this formation is similar to the coal seams cored in the Alacağzı Formation. This observation

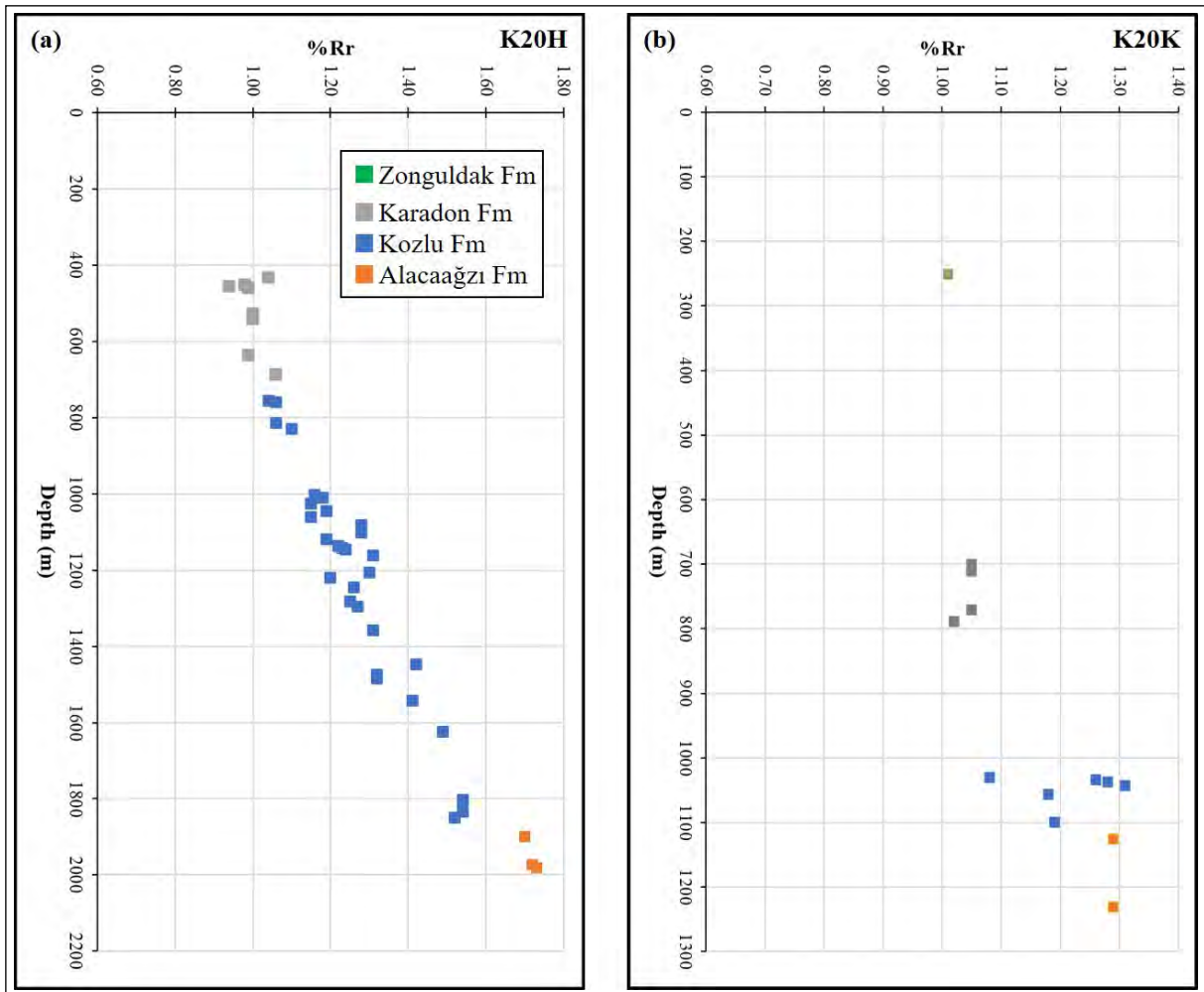


Figure 15- a) The vertical distributions of the measured  $%R_r$  from coal clasts and coal samples and calculated  $%R_r$  with depth in the K20H well and b) K20K well ( $%R_r$  data of coal samples are from Karayığit et al., 2018a).

along with the close  $%R_r$  values of coal clasts ( $1.70-1.73\% \pm 0.03$ ) and  $%R_{r_{max}}$  values ( $1.63-1.65\% \pm 0.05$ ) of coal seams in this formation imply that the coal clast samples in the Alacaağzı Formation could be originated from coal seams from this formation.

The  $%R_r$  values ( $1.08-1.31\%$  for K20H and  $1.04-1.52\%$  for K20K) of coal clast samples from the Kozlu Formation in both wells again display differences to each other (Table 2 and Figure 15), and the  $%R_r$  values of K20H samples are increased towards the

Table 4- The range of random reflectance ( $%R_r$ ) values of coal clast samples and coal seams in the studied wells, and ranges of measured  $R_{max}$  values of coal seams in the studied wells (a: from Karayığit et al., 2018a) (Abbreviations: Stdv: standard deviation).

Wells	Formation	$%R_r \pm \text{Stdv}$ of coal clast	$%R_r \pm \text{Stdv}$ of coal seam <sup>a</sup>	$%R_{max} \pm \text{Stdv}$ of coal seam <sup>a</sup>
K20K	Zonguldak	$1.01 \pm 0.02$	-	-
	Karadon	$1.02-1.05 \pm 0.02$	$0.78-1.01 \pm 0.04$	$0.82-1.10 \pm 0.03$
	Kozlu	$1.08-1.31 \pm 0.03$	$0.99-1.08 \pm 0.05$	$1.04-1.13 \pm 0.03$
	Alacaağzı	$1.29 \pm 0.03$	$1.18-1.28 \pm 0.07$	$1.22-1.35 \pm 0.03$
K20H	Karadon	$0.94-1.06 \pm 0.02$	$0.87 \pm 0.04$	$0.92 \pm 0.04$
	Kozlu	$1.04-1.52 \pm 0.03$	$0.97-1.46 \pm 0.06$	$1.00-1.57 \pm 0.07$
	Alacaağzı	$1.70-1.73 \pm 0.03$	$1.48-1.52 \pm 0.11$	$1.63-1.65 \pm 0.05$

lower parts of the formation (Figure 15). In turn, the rank of clast samples of the Kozlu Formation in this well varies from bituminous B (medium-rank B) rank to bituminous A (medium-rank A) rank according to ISO 11750 (2005). The %Rr values of coal clasts of the Kozlu Formation in the K20K well imply a bituminous B (medium-rank B) rank. The %Rr values of the coal clast samples from this formation in both wells are relatively lower than the %Rr values of the coal seams of the formation (Table 4 and Figure 15b). Considering the presence of brecciated vitrinite and carbonate mineral-infillings, as in the Alacağzı Formation, the relatively high %Rr values could be related to tectonic deformation and/or the influence of hydrothermal solutions. Nevertheless, the %Rr values of coal clast samples are generally within the ranges of the standard deviation of %Rr values ( $0.99-1.08\% \pm 0.05$  for K20K and  $0.97-1.46\% \pm 0.06$  for K20H) of coal seams in the Kozlu Formation, and the %R<sub>max</sub> values of these seams are close to the samples (Table 4). Additionally, the calculated T<sub>peak</sub> values from the coal clast are between 157 and 207°C, which is almost within the range of T<sub>peak</sub> values (148-201°C) of coal seams in Kozlu Formation in both wells (Karayığit et al., 2018a). Therefore, the impact of tectonic deformation and/or hydrothermal solutions was limited to coal clasts, and the coal clasts in this formation again seem to be transported a short distance from the parental coal seams after late peat stage and/or early coalification of these seams. The existence of micro-cracks and -fissures-bearing vitrinite grains and weathered liptinite macerals (Figure 5) in the samples of the Kozlu Formation could explain relatively higher %Rr values than the coal seams in this formation. Such oxidised macerals in coal seams and coal clasts could generally develop due to surface exposure of coal-bearing sequences and/or oxidation of coal clasts during transportation (Gayer et al., 1996; Daněk et al., 2002; Pešek and Sýkorová, 2006; Kus et al., 2017). The palynological data for the coal clast samples from the Kozlu Formation, like the coal clast samples from the Alacağzı Formation, was not reported from the studied wells by Akgün et al. (1997); however, the observed maceral composition and close %Rr values of coal clasts and coal seams and the %R<sub>max</sub> values ( $1.04-1.13\%$  for K20K and  $1.00-1.57\%$  for K20H) of coal seams in this formation could imply that coal

clasts presumably originated from coal seams in the Kozlu Formation.

The rank of coal clasts from the Karadon Formation in both wells is bituminous B (medium-rank B) according to ISO classification. The %Rr values ( $1.02-1.05\% \pm 0.02$ ) of coal clasts samples in the K20K well are within the ranges of the %Rr values ( $0.78-1.01\% \pm 0.04$ ) of coal seams in this formation (Tables 2 and 4), and the %R<sub>max</sub> values ( $0.82-1.10\%$ ) of this seam are similar to the %Rr values of coal clasts (Table 4 and Figure 15). Although one coal seam was cored in the K20H well, %Rr values ( $0.94-1.06\% \pm 0.02$ ) of coal clasts are relatively higher than the %Rr values of this seam, and the %R<sub>max</sub> value ( $0.92\% \pm 0.04$ ) of this seam is close to %Rr values (Table 4). This difference again could be related to oxidation during transportation since micro-cracks and -fissures-bearing vitrinite grains are also observed in these samples. Furthermore, again calculated T<sub>peak</sub> values (144-160°C) of coal clasts in this formation are close to the ranges of values of coal seams (120-153°C). Hence, coal clasts in the Karadon Formation, like other Carboniferous coal clasts, seem to have originated from the erosion of palaeomire during peat accumulation. The reported palynological data from the coal clasts from the 708.20-m in the K20K well and the coal clasts samples are approximately obtained equivalent depths with samples K20H/O4 and -O5 of by Akgün et al. (1997) support this assumption that these coal clasts were presumably originated from the Karadon Formation coal seams. Considering the Carboniferous formations (Alacağzı, Kozlu, and Karadon) in the studied wells were deposited under fluvial conditions and the roof rocks of coal seams in these formations are generally coal clasts-bearing sandstone and/or conglomerate layers, the examined Carboniferous samples clearly originated from Carboniferous coal seams, and these seams seem to have been eroded by mainly following fluvial conditions after the peat-formation and, to a lesser extent, sliding in peat-mires during the Carboniferous. The generated 1-D model using %Rr values from the studied wells by Karayığit et al. (2018a) also suggests erosional events during the Carboniferous. These also indicate that the Carboniferous coal clasts and parental coal seams generally experienced similar coalification

patterns, and oxidation during transportation seems to cause relatively higher %Rr values of Carboniferous coal clast samples, which also resulted in relatively high calculated  $T_{\text{peak}}$  values of coal clasts.

The measured %Rr value ( $1.01\% \pm 0.02$ ) of the coal clast sample from the Early Aptian İnciğez clastics suggests a bituminous coal rank for this clast according to ISO 11760 (2005) classification. Of note, Mann et al. (1995) and Yalçın (1995) reported that the %Rr values of Early Cretaceous sediments in the K20H research well in the Kozlu coalfield is between 0.61-0.68%. These values are lower than the investigated coal clast sample from the Zonguldak Formation in the K20K well, and %Rr value of this sample is quite similar to clast samples and coal seams from the Carboniferous formations (Table 4 and Figure 15b). Furthermore, the calculated  $T_{\text{peak}}$  value of this sample is  $153^{\circ}\text{C}$ , while using the reported %Rr values of Early Aptian İnciğez clastics are between  $89\text{-}130^{\circ}\text{C}$ . This difference could suggest that Early Aptian İnciğez clastics in the K20K were either affected by Cretaceous dykes in the basin or that this coal clast originated from the Carboniferous coal seams. The former case seems to be not possible due to the lack of thermally affected coal seams in both wells; nevertheless, this sample is mainly composed of telinite and collotelinite, and cleat/fracture carbonate mineral-infillings between the brecciated vitrinite grains were observed. These brecciated grains also contain micro-cracks and –fissures in this sample (Figures 3e-f). The existence of such brecciated vitrinite grains in the sample could suggest that these fragments either deformed during the coalification of parental coal seams or coal clast embedding sediments also experienced the same tectonic deformation as the encasing coal seams (Kožušniková et al., 1999; Hower et al., 2001; Xie et al., 2019). Furthermore, similar brecciated coal clasts within carbonate minerals-infillings were also reported within the Carboniferous marine carbonates in the western Kentucky coalfields (Valentim et al., 2013; 2020; Hower et al., 2020). Even though the coal metamorphism in the mentioned coalfield is quite more complex than the Kozlu coalfield, the %Rr values of brecciated clasts in the western Kentucky coalfields are high and are of anthracite-rank in comparison with Late Carboniferous seams

due to high-temperature thermal-fluid metamorphism. For such metamorphism, the investigated coal clast sample from the Early Aptian İnciğez clastics should contain relict liptinite macerals and natural coke structures; however, none of these were observed in the studied Early Aptian coal clast sample. Additionally, cleat/fracture carbonate-infillings in the sample are more simply related to the precipitation of Ca-rich intra-formation solutions during diagenesis rather than the precipitation of hydrothermal solutions since the Zonguldak Formation is mainly composed of marine carbonates. Hence, this sample is more likely to be derived from the Carboniferous coal seams in the Kozlu coalfield, which was presumably eroded after the coalification of coal seams in Karadon or Kozlu formations and/or due to uplift during the Early Cretaceous, instead of hydrothermal alteration of Early Aptian coal clasts and/or xylite fragment.

## 6. Results

The petrographical and SEM investigations of coal clast samples from the Carboniferous and Early Aptian formations in the K20H and K20K wells imply that the majority of identified minerals in the coal clasts mainly originated from the parental coal seams, while cleat/fracture and cell lumen mineral infillings were mainly formed during mainly early coalification of parental coal seams and diagenesis of embedded sediments. Nevertheless, the relatively high %Rr values of the investigated Carboniferous coal samples in comparison with the cored coal seams in both wells are generally related to the oxidation of coal clasts during transportation since surface oxidation derived micro-cracks and –fissures are commonly observed in these samples. Furthermore, this oxidation process seems to be more severe for the coal clast samples from the Kozlu Formation, where weathered sporinite macerals are commonly identified. Despite the presence of deformed and brecciated vitrinite grains and cleat/fracture carbonate-infillings within these grains, close %Rr values of coal clasts and %Rmax values of coal seams and  $T_{\text{peak}}$  values imply that the influence of post-coalification tectonic movements and penetrated hydrothermal solutions on the coalification of these clasts is limited, and clasts and their parental coal seams exhibit similar coalification patterns. Therefore,

Carboniferous coal clasts seem to have originated from the coal seams in the studied formations. Furthermore, their existence within conglomerate and sandstone layers overlying coal seams also suggest that these clasts were presumably eroded during peat formation or early coalification stages of parental coal seams by fluvial systems; nevertheless, sliding in peat mire during Carboniferous might also cause coal clast formation. The brecciated vitrinite grains could also suggest that the tectonic deformation took place during post-vitrinization event, or at least a post-lignite stage event. In contrast, coal clast samples in the Early Cretaceous Zonguldak Formation display relatively higher %Rr values than reported %Rr values of this formation, and close %Rr values with Carboniferous formations imply that this coal clast was presumably derived from eroded Late Carboniferous coal seams in the Zonguldak Basin after coalification and/or due to uplift during the Cretaceous. The cleat/fracture carbonate mineral-infillings between brecciated vitrinite grains in this sample might have developed from the precipitation of Ca-rich solutions during the diagenesis of this formation or more possibly formed during the coalification of the parental coal seam due to the presence of similar multi-mineralic cleat/fracture infillings in the coal seams in the studied wells. Overall, all the studied coal clast samples originated from the Carboniferous coal seams in the Kozlu coalfield, and display generally similar features to Carboniferous coal clasts from central Europe and South Wales.

### Acknowledgements

A part of this study is supported by the Turkish Scientific and Technological Research Council of Turkey (TÜBİTAK) under the project YDABCAG-70. The authors would like to thank Prof. Dr. J. HOWER (University of Kentucky) his suggestions during the manuscript preparations.

### References

- Ağralı, B. 1963. Etude des microspores du Namurien a Tarlaağzı (Amasra, Turquie). *Annales de la Société Géologique du Nord* t83, 145-159 (in French).
- Ağralı, B. 1970. Étude des Microspores du bassin Carbonifère d'Amasra. *Bulletin of the Mineral Research and Exploration* 75, 28-68 (in French with Turkish abstract).
- Akgün, F., Akyol, E. 1992. Palynology and paleoecology of the coals in the Amasra-Bartın Carboniferous Basin *Turkish Journal of Earth Sciences* 1, 49-56 (in Turkish with English abstract).
- Akgün, F., Uzun, N., Akyol, E. 1997. Palynology. Yalçın, M. N. (Ed.). A multidisciplinary approach on Kozlu K20/H and K20/K wells. TÜBİTAK YDABÇAG-70 Project Report, Ankara (in Turkish) (unpublished).
- Akyol, E. 1972. Etudes palynologiques des veines du Namurien et du Westphalien A, recoupees par les ailes sud et est d'une galerie de cote -50a Asma, Üzülmöz-Zonguldak. *Bulletin of the Mineral Research and Exploration* 83, 50-104 (in French with Turkish abstract).
- American Society for Testing and Materials (ASTM) D2797/D2797M. 2011. Standard practice for preparing coal samples for microscopical analysis by reflected light. ASTM International, 5.
- Barker, C. E., Pawlewicz, M. J. 1994. Calculation of vitrinite reflectance from thermal histories and peak temperatures. A comparison of methods. Mukhopadhyay, P. K., Dow W. G. (Ed.). *Vitrinite Reflectance as a Maturity Parameter: Applications and Limitations*, ACS Symposium Series 570, Chicago, 216-229.
- Barker, C. E., Pawlewicz, M. J. 1994. Calculation of vitrinite reflectance from thermal histories and peak temperatures. A comparison of methods. Mukhopadhyay, P. K., Dow, W. G. (Eds.). *Vitrinite Reflectance as a Maturity Parameter: Applications and Limitations*. ACS Symposium Series volume 570. ACS Publication, Washington, 216-229.
- Bicca, M. M., Kalkreuth, W., da Silva, T. F., de Oliveira, C. H. E., Genezini, F. A. 2020. Thermal and depositional history of Early-Permian Rio Bonito Formation of southern Paraná Basin-Brazil. *International Journal of Coal Geology* 228, 103554.
- Burger, K., Bandelow, F. K., Bieg, G. 2000. Pyroclastic kaolin coal-tonsteins of the Upper Carboniferous of Zonguldak and Amasra, Turkey. *International Journal of Coal Geology* 45, 39-53.
- Cleal, C. J., Van Waveren, I. M. 2012. A reappraisal of the Carboniferous macrofloras of the Zonguldak-Amasra. Coal Basin, north-western Turkey. *Geologia Croatica* 65, 283-297.
- Cleal, C. J., Stolle, E., Van Waveren, I. M., King, S., Didari, V. 2017. Carboniferous plant fossils from northern Turkey in the Jongmans Collection, Naturalis, Leiden. *Paleontological Journal* 51, 770-777.
- Cleal, C. J., Stolle, E., Van Waveren, I. M., King, S., Didari, V. 2018. Macrofloral biostratigraphy

- of the upper Bashkirian Kozlu Formation, Zonguldak coalfield, north Turkey. *Nurgaloev, D., Barclay, M., Nikolaeva, S., Silantiev, V., Zharinova, V., Vasilyeva O. (Ed.). Advances in Devonian, Carboniferous and Permian Research: Stratigraphy, Environments, Climate and Resources. Filodiritto, Bologna, 82-90.*
- Dai, S., Bechtel, A., Eble, C. F., Flores, R. M., French, D., Graham, I. T., Hood, M. M., Hower, J. C., Korasidis, V. A., Moore, T. A., Püttmann, W., Wei, Q. 2020a. Recognition of peat depositional environments in coal: A review. *International Journal of Coal Geology* 219, 103383.
- Daněk, V., Pešek, J., Valterová, P. 2002. Coal clasts in the Bolsovian (Westphalian C) sequence of the Kladno-Rakovník continental basin (Czech Republic): implication of the timing of maturation. *Polish Geological Institute Special Paper* 7, 63-78.
- Daniels, S. M., Agnew, C. T., Allott, T. E. H., Evans, M. G. 2008. Water table variability and runoff generation in an eroded peatland, South Pennines, UK. *Journal of Hydrology* 361, 214-226.
- Dawson, G. K. W., Golding, S. D., Esterle, J. S., Massarotto, P. 2012. Occurrence of minerals within fractures and matrix of selected Bowen and Ruhr Basin coals. *International Journal of Coal Geology* 94, 150-166.
- Dill, H. G., Kus, J., Kaufhold, S., Rammlmair, D., Techmer, A. 2017. Oligo-Miocene coal in a microtidal environment reworked under Quaternary periglacial conditions (Western Falkland Islands/Isla Gran Malvina) coal formation and natural sand processing. *International Journal of Coal Geology* 174, 8-22.
- Dill, H. G., Kus, J., Andrei, B., Sorin-Ionut, B., Stephan, K., Borrego, A. G. 2021. Organic debris and allochthonous coal in Quaternary landforms within a periglacial setting (Longyearbyen Mining District, Norway) - A multi-disciplinary study (coal geology-geomorphology-sedimentology). *International Journal of Coal Geology* 233, 103625.
- Gayer, R. A., Pešek, J., Sýkorová, I., Valterová, P. 1996. Coal clasts in the upper Westphalian sequence of the South Wales coal basin: Implications for the timing of maturation and fracture permeability. *Geological Society Special Publication* 109, 103-120.
- Geršlová, E., Goldbach, M., Geršl, M., Skupien, P. 2016. Heat flow evolution, subsidence and erosion in Upper Silesian Coal Basin, Czech Republic. *International Journal of Coal Geology* 154-155, 30-42.
- Gürdal, G., Yalçın, M. N. 2000. Gas adsorption capacity of Carboniferous coals in the Zonguldak Basin (NW Turkey) and its controlling factors. *Fuel* 79, 1913-1924.
- Gürdal, G., Yalçın, M. N. 2001. Pore volume and surface area of the carboniferous coal from the Zonguldak Basin (NW Turkey) and their variations with rank and maceral composition. *International Journal of Coal Geology* 48, 133-144.
- Gürdal, G., Mann, U., Yalçın, M. N. 2004. Comparison of adsorption related properties of Zonguldak Basin coals (NW Turkey) obtained at two different adsorption temperatures of carbon dioxide. *Energy Source* 26, 1301-1312.
- Hower, J. C., Davis, A. 1981. Vitrinite reflectance anisotropy as a tectonic fabric element. *Geology* 9, 165-168.
- Hower, J. C., Gayer, R. A. 2002. Mechanisms of coal metamorphism: case studies from Paleozoic coalfields. *International Journal of Coal Geology* 50, 215-245.
- Hower, J. C., Williams, D. A., Eble, C. F., Sakulpitakphon, T., Moecher, D. P. 2001. Brecciated and mineralized coals in Union County, Western Kentucky coal field. *International Journal of Coal Geology* 47, 223-234.
- Hower, J. C., O'Keefe, J. M. K., Valentim, B., Guedes, A. 2021. Contrasts in maceral textures in progressive metamorphism versus near-surface hydrothermal metamorphism. *International Journal of Coal Geology* 246, 103840.
- International Committee for Coal Petrology (ICCP). 1998. The new vitrinite classification (ICCP System 1994). *Fuel* 77, 349-358.
- International Committee for Coal Petrology (ICCP). 2001. New inertinite classification (ICCP System 1994). *Fuel* 80, 459-471.
- International Organisation for Standardization (ISO) 11760. 2005. Classification of coals. International Organization for Standardization, 9.
- International Organization for Standardization (ISO) 7404-5. 2009. Methods for the Petrographic Analysis of Coal—Part 5: Method of determining microscopically the reflectance of vitrinite. International Organization for Standardization, 4.
- Izart, A., Barbarand, J., Michels, R., Privalov, V.A. 2016. Modelling of the thermal history of the Carboniferous Lorraine Coal Basin: Consequences for coal bed methane. *International Journal of Coal Geology* 168, 253-274.
- Karayığit, A. I. 1992. Linear relations among vitrinite reflections of coals in Zonguldak and Amasra basins. *Turkish Journal of Earth Sciences* 1, 43-48 (in Turkish with English abstract).
- Karayığit, A. I., Gayer, R. A., Demirel, I. H. 1998. Coal rank and petrography of Upper Carboniferous seams

- in the Amasra Coalfield Turkey. *International Journal of Coal Geology* 36, 277-294.
- Karayiğit, A. I., Littke, R., Querol, X., Jones, T., Oskay, R. G., Christanis, K. 2017. The Miocene coal seams in the Soma Basin (W. Turkey): Insights from coal petrography, mineralogy and geochemistry. *International Journal of Coal Geology* 173, 110-128.
- Karayiğit, A. I., Mastalerz, M., Oskay, R. G., Gayer, R. A. 2018a. Coal petrography, mineralogy, elemental compositions and palaeoenvironmental interpretation of Late Carboniferous coal seams in three wells from the Kozlu coalfield (Zonguldak Basin, NW Turkey). *International Journal of Coal Geology* 187, 54-70.
- Karayiğit, A. I., Mastalerz, M., Oskay, R. G., Buzkan, İ. 2018b. Bituminous coal seams from underground mines in the Zonguldak Basin (NW Turkey): Insights from mineralogy, coal petrography, rock-eval pyrolysis, and meso- and microporosity. *International Journal of Coal Geology* 199, 91-112.
- Karayiğit, A. I., Oskay, R. G., Bulut, Y., Mastalerz, M. 2020. Meso- and microporosity characteristics of Miocene lignite and subbituminous coals in the Kınık coalfield (Soma Basin, W. Turkey). *International Journal of Coal Geology* 232, 103624.
- Kerey, I. E. 1985. Facies and Tectonic Setting of the Upper Carboniferous Rocks of NW Turkey. Robertson, A. H. F., Dixon J. E. (Ed.). *The Geological Evolution of the Eastern Mediterranean*. Geological Society of London Special Publication 17, Geological Society of London, 123-128.
- Küskü, O., Canca, N., Hoşgörmez, H., İnan, S., Yalçın, M. N. 1997. Geology. In: Yalçın, M. N. (Ed.). *A multidisciplinary approach on Kozlu-K20/H and K20/K research wells. TÜBİTAK YDABÇAG-70 Project Report, Ankara* (in Turkish) (unpublished).
- Kožušniková, A., Martinec, P., Pešek, J., Valterová, P. 1999. Coal clasts in the Carboniferous sediments of the Upper Silesian basin. *Bulletin of Geosciences* 74, 109-114.
- Kus, J., Misz-Kennan, M., International Committee for Coal and Organic Petrology. 2017. Coal weathering and laboratory (artificial) coal oxidation. *International Journal of Coal Geology* 171, 12-36.
- Liu, J., Dai, S., Song, H., Nechaev, V. P., French, D., Spiro, B. F., Graham, I. T., Hower, J. C., Shao, L., Zhao, J. 2021. Geological factors controlling variations in the mineralogical and elemental compositions of Late Permian coals from the Zhijin-Nayong Coalfield, western Guizhou, China. *International Journal of Coal Geology* 247, 103855.
- Littke, R., Horsfield, B., Leythausen, D. 1989. Hydrocarbon distribution in coals and in dispersed organic matter of different maceral compositions and maturities. *Geologische Rundschau* 78, 391-410.
- Mann, U., Hertle, M., Horsfield, B., Radke, M., Schenk, H. J., Yalçın, M. N. 1995. Petrographical, organic-geochemical and petrophysical characterization of Upper Carboniferous coals from well K20/H, Zonguldak Basin. Yalçın, M. N., Gürdal, G. (Ed.). *Zonguldak Basin Research Wells-1. Special Publication of TÜBİTAK Marmara Research Centre, Kocaeli*, 133-166.
- Martínek, K., Pešek, J., Opluštil, S. 2017. Significant hiatuses in the terrestrial Late Variscan Central and Western Bohemian basins (Late Pennsylvanian-Early Cisuralian) and their possible tectonic and climatic links. *Geologica Carpathica* 68, 269-281.
- Misz-Kennan, M., Fabiańska, M., Ciesielczuk, J., Filipiak, P., Jura, D. 2019. Organic geochemistry and petrography of coal clasts deposited in Pennsylvanian sandstones (upper Silesian coal basin, Poland). 29<sup>th</sup> International Meeting on Organic Geochemistry (IMOG), 1-6 September 2019, Gothenburg, 1-2.
- Oktay, F. A. 1995. Sedimentological and petrographical properties of Carboniferous sequence drilled by K20/G well. Yalçın, M. N., Gürdal, G. (Ed.). *Zonguldak Basin Research Wells-I. TÜBİTAK-MAM Special Publications, Kocaeli*, 73-98 (in Turkish with English abstract).
- Okay, A. I., Nikishin, A. M. 2015. Tectonic evolution of the southern margin of Laurasia in the Black Sea region. *International Geology Reviews* 57, 1051-1076.
- Okay, A. I., Şengör, A. M. C., Görür, N. 1994. Kinematic history of the opening of the Black Sea and its effect on the surrounding regions. *Geology* 22, 267-270.
- Opluštil, S., Lojka, R., Pšenička, J., Yılmaz, Ç., Yılmaz, M. 2018. Sedimentology and stratigraphy of the Amasra coalfield (Pennsylvanian), NW Turkey – new insight from a 1 km thick section. *International Journal of Coal Geology* 195, 317-346.
- Paszkowski, M., Jachowicz, M., Michalik, M., Teller, L., Uchman, A., Urbanek, Z. 1995. Composition, age and provenance of gravel-sized clasts from the Upper Carboniferous of the Upper Silesia Coal Basin (Poland). *Studia Geologica Polonica* 108, 45-127.
- Petersen, H. I., Bojesen-Koefoed, J. A., Nytoft, H. P., Surlyk, F., Therkelsen, J., Vosgerau, H. 1998. Relative sea-level changes recorded by paralic liptinite-enriched coal facies cycles, Middle Jurassic Muslingebjerg Formation, Hochstetter Forland,

- Northeast Greenland. *International Journal of Coal Geology* 36, 1-30.
- Pešek, J., Sýkorová, I. 2006. A review of the timing of coalification in the light of coal seam erosion, elastic dykes and coal clasts. *International Journal of Coal Geology* 66, 13-34.
- Permana, A. K., Ward, C.R., Li, Z., Gurba, L. W. 2013. Distribution and origin of minerals in high-rank coals of the South Walker Creek area, Bowen Basin, Australia. *International Journal of Coal Geology* 116–117, 185-207.
- Pickel, W., Kus, J., Flores, D., Kalaitzidis, S., Christanis, K., Cardott, B. J., Misz-Kennan, M., Rodrigues, S., Hentschel, A., Hamor-Vido, M., Crosdale, P., Wagner, N., ICCP. 2017. Classification of liptinite-ICCP System 1994. *International Journal of Coal Geology* 169, 40-61.
- Rodrigues, S., Esterle, J., Ward, V., Glasser, L., Maquissene, T., Etchart, E. 2020. Flow structures and mineralisation in thermally altered coal from the Moatize Basin, Mozambique. *International Journal of Coal Geology* 228, 103551.
- Suchý, V., Filip, J., Sýkorová, I., Pešek, J., Kořínková, D. 2019. Palaeo-thermal and coalification history of Permo-Carboniferous sedimentary basins of central and Western Bohemia, Czech Republic: first insights from apatite fission track analysis and vitrinite reflectance modelling. *Bulletin of Geosciences* 94, 201-219.
- Tallis, J. H. 1985. Mass movement and erosion of a southern Pennine blanket peat. *Journal of Ecology* 73, 283-315.
- Tüysüz, O., Melinte-Dobrinescu, M. C., Yılmaz, İ. Ö., Kirici, S., Švabenická, L., Skupien, P. 2016. The Kapanboğazi formation: A key unit for understanding Late Cretaceous evolution of the Pontides, N Turkey. *Palaeogeography, Palaeoclimatology, Palaeoecology* 441, 565-581.
- Xie, P., Hower, J. C., Liu, X. 2019. Petrographic characteristics of the brecciated coals from Panxian county, Guizhou, southwestern China. *Fuel* 243, 1-9.
- Valentim, B., Hower, J. C., O'Keefe, J. M. K., Rodrigues, S., Riberio, J., Guedes, A. 2013. Notes on the origin of altered macerals in the Ragged Edge of the Pennsylvanian (Asturian) Herrin coalbed, Western Kentucky. *International Journal of Coal Geology* 115, 24-40.
- Valentim, B., Couto, H., French, D., Golding, S. D., Guimarães, F., Guedes, A., O'Keefe, J. M. K., Raymond, A. L., Santos, C., Valian, A., Ward, C. R., Hower, J. C. 2020. Could hot fluids be the cause of natural pyrolysis at the ragged edge of Herrin coal, Millport 7 ½' quadrangle, Hopkins County, Kentucky. *International Journal of Coal Geology* 231, 103603.
- Yalçın, M. N. 1995. Contribution of the Kozlu-K20/G well to the computer-aided modelling studies in the Zonguldak Basin. Yalçın, M. N., Gürdal, G. (Ed.). *Zonguldak Basin Research Wells-I. TÜBİTAK-MAM Special Publications*, Kocaeli, 173-196 (in Turkish with English abstract).
- Yalçın, M. N., Inan, S., Gürdal, G., Mann, U., Schaefer, R. G. 2002. Carboniferous coals of the Zonguldak Basin (northwest Turkey): Implications for coalbed methane potential. *AAPG Bulletin* 86, 1305-1328.
- Yang, G., Huang, W., Zhong, J., Sun, N. 2020. Occurrence, classification and formation mechanisms of the organic-rich clasts in the upper Paleozoic coal-bearing tight sandstone, northeastern margin of the Ordos Basin, China. *Energies* 13, 2694.
- Yürüm, Y., Dilara, B., Yalçın, M. N. 2001a. Change of the structure of coals from the Kozlu K20 G borehole of Zonguldak Basin with burial depth 1. *Chemical structure. Energy Source* 23, 511-520.
- Yürüm, Y., Dilara, B., Yalçın, M. N. 2001b. Change of the structure of coals from the KozluK20 G borehole of Zonguldak Basin with burial depth 2. *Macromolecular structure. Energy Source* 23, 521-527.
- Zhang, T., Wang, R., Polyak, L., Xiao, W. 2019. Enhanced deposition of coal fragments at the Chukchi margin, western Arctic Ocean: Implications for deglacial drainage history from the Laurentide Ice Sheet. *Quaternary Science Reviews* 218, 281-292.
- Zhao, L., Ward, C. R., French, D., Graham, I. T., Dai, S., Yang, C., Xie, P., Zhang, S. 2018. Origin of a kaolinite-NH<sub>4</sub>-illite-pyrophyllite-chlorite assemblage in a marine-influenced anthracite and associated strata from the Jincheng Coalfield, Qinshui Basin, Northern China. *International Journal of Coal Geology* 185, 61-78.
- Zijlstra, G. 1952. Erosion of the Namurian during the Westphalian b-c in the Zonguldak coal field (Turkey). *Bulletin of Mineral Research and Exploration* 42-43, 121-122.



# Bulletin of the Mineral Research and Exploration

<http://bulletin.mta.gov.tr>



## Magnetic inversion modeling of subsurface geologic structures for mineral deposits mapping in southeastern Nigeria

Ema M. ABRAHAM<sup>a\*</sup>, Ayatu O. USMAN<sup>a</sup>, Kelvin I. CHIMA<sup>a</sup>, George-best AZUOKO<sup>a</sup> and Iheanyi IKEAZOTA<sup>a</sup>

<sup>a</sup>Alex Ekwueme Federal University, Department of Geology/Geophysics, Ndufu-Alike Ikwo, P.M.B. 1010 Abakaliki, Ebonyi State, Nigeria

Research Article

### Keywords:

Magnetic modeling,  
Aeromagnetic data,  
Particle Swarm  
Optimization (PSO),  
Minerals, Depths.

### ABSTRACT

Magnetic inversion techniques have been implemented to infer the extension and geometry of magnetic structures and also evaluate its influence on mineralization within Abakaliki and its environs, southeastern Nigeria. The modeling approach considers the techniques of three-dimensional (3D) magnetic data inversion, Euler deconvolution, analytic signal inversion, Enhanced Local Wavenumber (ELW) Technique and Particle Swarm Optimization (PSO) to estimate source parameters and compare results. Model solutions were interpreted to represent possible geologic units with varying trends, housing mineralization within the study region. Results from inversion computation over some active mine locations show subsurface bodies with magnetic susceptibilities  $>0.00188$  SI. Model results also show structural sources with almost 5.5 km depth extension, stretching 18 km in the EW direction at Ngbo – Ekerigwe location. This could imply significant mineral deposits at the location. Inversion of both magnetic anomaly and analytical signal enabled derivation of the actual subsurface structures in the region, with most of the structures appearing as dykes with depths ranging from 0.2 – 1.8 km at most of the mining sites. Location and depths of some of the modeled intrusions have been corroborated with the active on-site mines. The delineation of mineralization structures by this study would guide systematic exploration in the region.

Received Date: 31.08.2022

Accepted Date: 30.03.2023

## 1. Introduction

Quantitative explanation of a potential field data includes assessment of depth, horizontal location, sources geometry as well as differences in the physical attributes (Essa and Abo-Ezz, 2021; Essa et al., 2021; Ganguli et al., 2021; Eshaghzadeh et al., 2020; Abraham and Alile, 2019; Essa et al., 2018; Aboud et al., 2018; Srivastava and Agarwal, 2010; Abdelrahman et al., 2003; Büyüksaraç et al., 1998, 2005). Modeling anomalies from a local magnetic field, and in particular, three - dimensional (3D) voxel-based modeling, is a contemporary and

important tool in exploration targeting (MacLeod and Ellis, 2013). Inversion for a physical property involves the subdivision of the causative sources into a collection of rectangular cells, whose density or magnetization contrasts are to be appraised to explain the true distribution of the geological sources (Yao, 2007). 3D magnetic inversion allows total use of information in magnetic anomalies, estimating a 3D discrete physical property distribution that can describe the discerned geophysical field data (Li and Sun, 2016; Mahmoodi et al., 2016). In oil exploration, credible appraisals of depth to magnetic basement are

Citation Info: Abraham, E. M., Usman A. O., Chima K. I., Azuoko G., Ikeazota I. 2024. Magnetic inversion modeling of subsurface geologic structures for mineral deposits mapping in southeastern Nigeria. Bulletin of the Mineral Research and Exploration 173, 85-105. <https://doi.org/10.19111/bulletinofmre.1267876>

\*Corresponding author: Ema M. ABRAHAM, [ema.abraham@funai.edu.ng](mailto:ema.abraham@funai.edu.ng)

needed for improved comprehending of the crucial first-order basin examination parameters (Srivastava and Agarwal, 2010; Li, 2003). Magnetic inversion technique can resolve magnetic bodies possibly associated with zones having abundance of magnetite and other magnetic minerals, rendering structural knowledge regarding these magnetic bodies and in numerous occasions, about the structural system of the mineralization (Couto et al., 2017). 3D inversions have assisted interpretations just as magnetic data aids the characterization of ore bodies (Leão-Santos et al., 2015; Büyüksaraç et al., 1998). On a regional scale, a cross-plot of density and susceptibility has been used (Melo et al., 2015; Kowalczyk et al., 2010) to define the classes of different lithologies and identify rock types. This approach can thus offer useful exploration information in areas with a paucity of geological information. Melo et al. (2015) used a comparable approach to demonstrate copper mineralization guided by the trend in the cross-plot of susceptibility and conductivity.

Various geophysical studies have been conducted around Abakaliki and environs. These include using Vertical Electrical Sounding (VES) technique to determine aquifer parameters, estimation of depth to magnetic source in a location closer to Abakaliki (Ugwu and Alasi, 2016), assessment of Curie Point Depth (CPD) (Abraham et al., 2018), hydrocarbon and mineral exploration prospect determination (Ezema et al., 2014) using aeromagnetic data and investigating the sequence of deposition of sedimentary strata in the region using seismic refraction and VES techniques (Agha and Arua, 2014). However, no three-dimensional (3D) inversion of magnetic data has been undertaken within the region towards the delineation of geological structures housing mineralization in the region. Inversion of magnetic survey data can offer restrictions on subsurface susceptibility allotments (Büyüksaraç et al., 2005; Lelievre, 2003). Abakaliki region is a mineralized province and has been documented to house great mineral potentials that include Lead, Zinc, Sodium Chloride, Silver, and Limestone (Abraham et al., 2018; Ugwu and Alasi, 2016; Ezema et al., 2014). This has been substantiated by mining activities (mostly local/small scale) ongoing in the region. Given the economic relevance

of these minerals and the need to quantify the deposits for productive, extensive, and sustainable mining, the Nigerian government authorized an airborne magnetic and radiometric survey in the region betwixt 2005 and 2009. A close relationship exists between the proportion of magnetic minerals and magnetic susceptibility in rocks. Iron oxides; pyrrhotite, cobalt, nickel, and metallic iron are noteworthy. As these minerals, to the greatest extent, go with economic mineral deposits, we could analyze magnetic survey data to gain information on potential drilling targets (Lelievre, 2003). The creation of 2D and 3D models of geophysical inversion and mineral potential modeling has added to the large precompetitive data available to explorers (Büyüksaraç et al., 2005, 1998). The area of coverage by this study locates within geographic latitudes  $6^{\circ}00'$  and  $6^{\circ}30' N$  and geographic longitudes  $8^{\circ}00'$  and  $8^{\circ}30' E$  within the sedimentary terrain of southeastern Nigeria (Figure 1).

Our study seeks to carry out 2D and 3D magnetic inversion modeling, identify sources location, and perform depth analysis to geologic units bearing possible minerals in Abakaliki and environ. A credible depth appraisal to the top of causative source enhances budgeting as well as scheming of drill holes and other exploitation projects (Srivastava and Agarwal, 2010). We anticipate that the effect of this study will emphasize mineralized geologic units and structural positions and augments mining certainty in the region.

### 1.1. Geological Setting

Following a series of tectonic activities and recurrent sedimentation in the Cretaceous time, the Nigeria-Benue trough was formed. The split of the continents resulted in an abrupt rift (aulacogen) that has been stuffed with transgressive and regressive sedimentary lay downs (Ugwu and Alasi, 2016).

The lower Benue trough is supported below by a thick sedimentary succession set down in the Cretaceous era. Four geological formations which include the Nkporo Shale (Campanian), the Awgu Shale (Coniacian), the Asu River Group (Albian) and the Eze-Aku Shale (Turonian), constitutes the sediments that happened in the Abakaliki Anticlinorium (Figure 2). The sedimentary sequence was influenced by

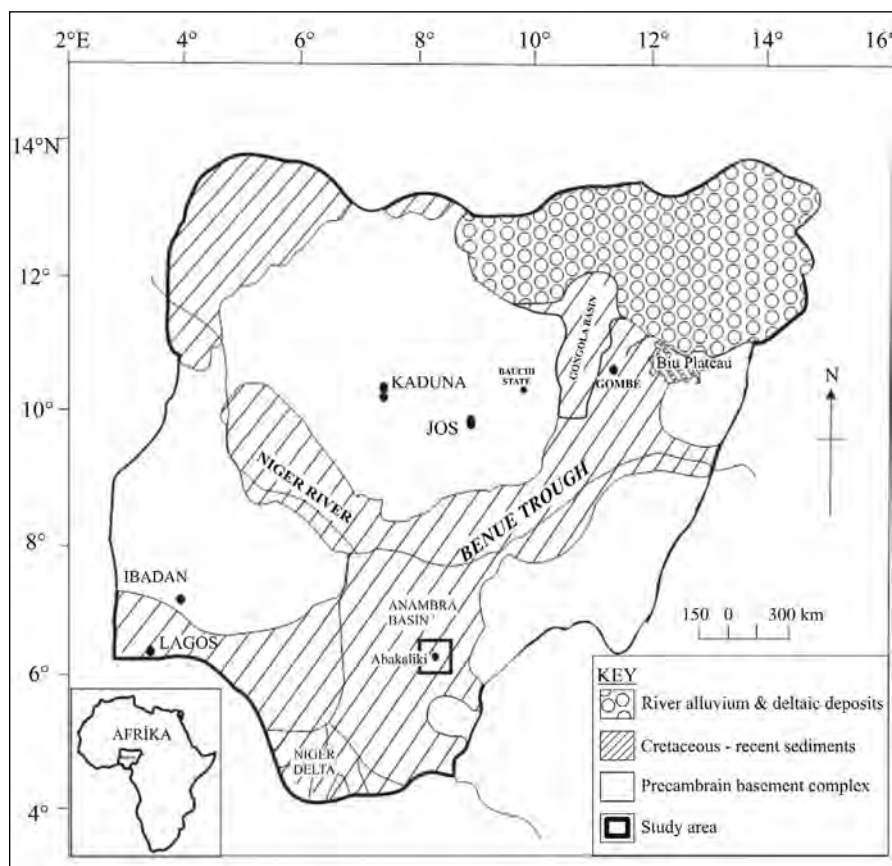


Figure 1- Map of Nigeria showing the general geology, location and coverage area of this study (modified from Abraham et al., 2018).

large-scale tectonic events that occur in two stages leading to folding of the sediments. Cenomanian and Santonian deformations affected the area with a large tectonic imprint (Nwachukwu, 1972; Olade, 1975; Ezema et al., 2014).

A general NE-SW trending fold characterized the Santonian deformation. The folding influenced the development of the Abakaliki Anticlinorium, a compressive structure marked with asymmetry and reversed faults. Benkhelil (1988) described the orogenic cycle of the anticlinorium to include sedimentation, magmatism, metamorphism, and compressive tectonism. Numerous intrusive bodies within the shale are due to magmatism that affected the Eze-Aku and Asu River Group (Figure 2). Majority of these intrusive has been concealed by the shale formation (general superficial geology) of the region as observed in the geology. This study offers supplemental information on the intrusive bodies including estimates of their respective depths.

Intermediate intrusive appear on the surface and could be seen in parts of the study area like the Abakaliki town. This intrusive appears as sills (Ezema et al., 2014; Ofoegbu, 1985; Eze and Mamah, 1985). The Abakaliki shale (Asu River Group) is of Albian age, dark gray, blocky and non-micaceous in most locations. The Asu River Group is predominantly shale and localized incidences of sandstone, siltstone, and limestone intercalations. Eze-Aku formation comprises of a succession of calcareous sandstones.

Figure 3 shows the lithostratigraphic section (Obarezi and Nwosu, 2013) of the two main geologic units recognized in the study area. The lithostratigraphic section was erected from acquired and logged geologic core data. The interpreted data shows the trend and structure that controls mineralization, mineralogy, and the sequence of deformation. Figure 4 displays images of the current open cast mining of lead-zinc (Pb-Zn) minerals by the locals within the study region. Current mining operations at these regions are largely done by

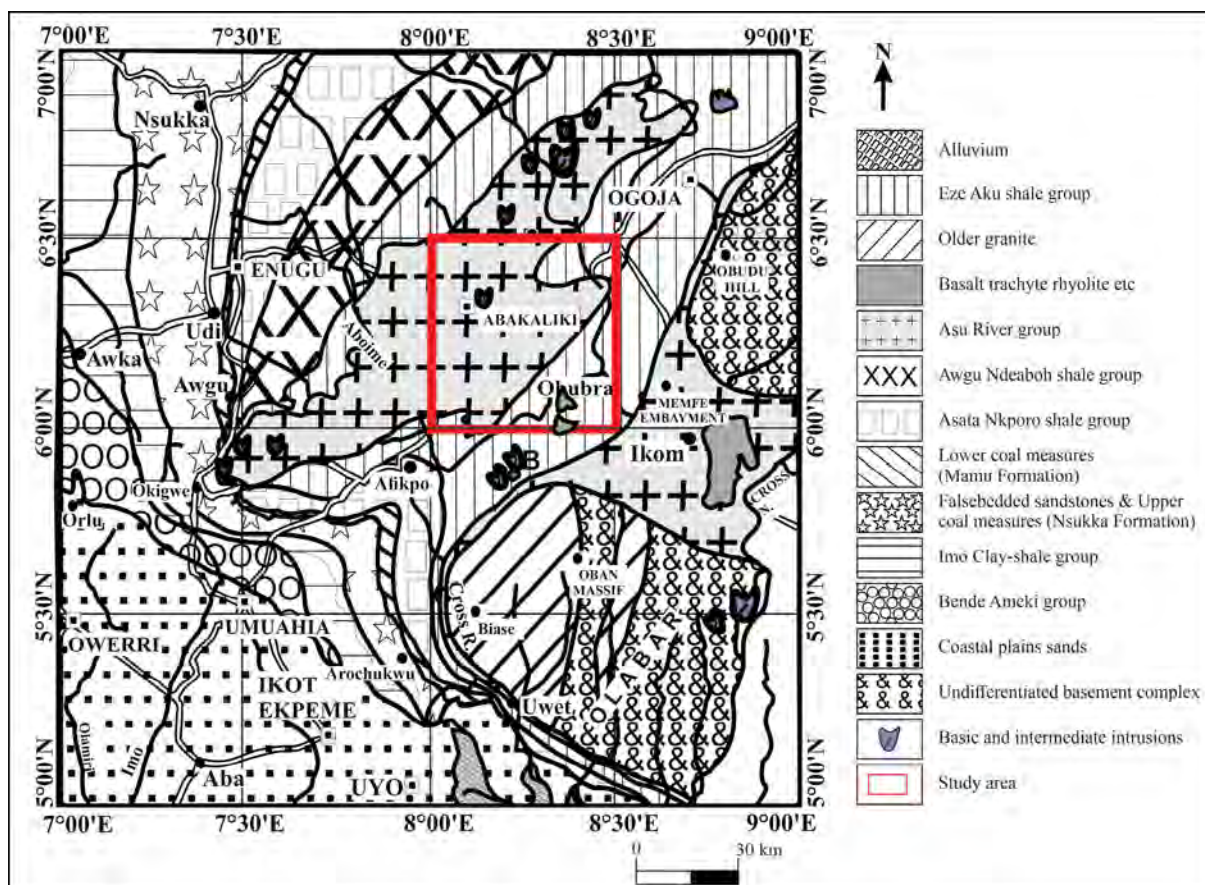


Figure 2- Detail geological map of southeastern Nigeria depicting the study area. The inserted red square represents the study area coverage in Figure 1 (modified from Abraham et al., 2018).

locals with crude tools and haphazard exploitation. Most of the mining is not mechanized as crude tools and poor excavation methods are employed by the locals to exploit these minerals. The water accumulations in some of the mines are mine water and rain accumulations.

## 2. Methods

Our study area is covered by a high-resolution digital aeromagnetic map sheet number 303 – Abakaliki, (Figure 5) spanning an area of approximately 3025 km<sup>2</sup>. The airborne data was acquired for the Nigerian Geological Survey Agency (NGSA) in 2005 and 2009. The entire data include approximately 2 km line of magnetic as well as radiometric surveys carried out at 500 m line spacing using 80 m terrain clearance. The regional field and diurnal magnetic effects were removed from the data. We applied the Reduction to Equator (RTE) correction (Leu, 1981; Jain, 1988; Abraham et al., 2018; Ganguli et al., 2021) assuming

a magnetic declination of  $-2.15^\circ$  and an inclination of  $-13.91^\circ$  for the study area utilizing the fast Fourier transform operator. Strong variations in magnetic intensities, suggesting different magnetic properties, could be discerned from the map.

Positive anomalies with higher values (90 – 94 nT) are observed at Onyen, Obubra, Ngbo, Abba Omega, and part of Enyigba localities. The positive anomalies at Obubra and Oyen regions may be due to intrusions of basalt, trachyte, Rhyolite and other intrusions within the region. This region locates within the Eze Aku Shale Group, largely notable for higher magnetic anomaly values (70 – 110 nT) (Figure 6). We note lower magnetic values around FUNAI, Ezzagu, and Egudenago localities between 19 nT and 40 nT. Within the Enyigba – FUNAI region, the notable lower magnetic anomaly unit observed, falls within the Asu River Group (Figure 6) and may be due to an intrusion within the Asu River shale formation. This

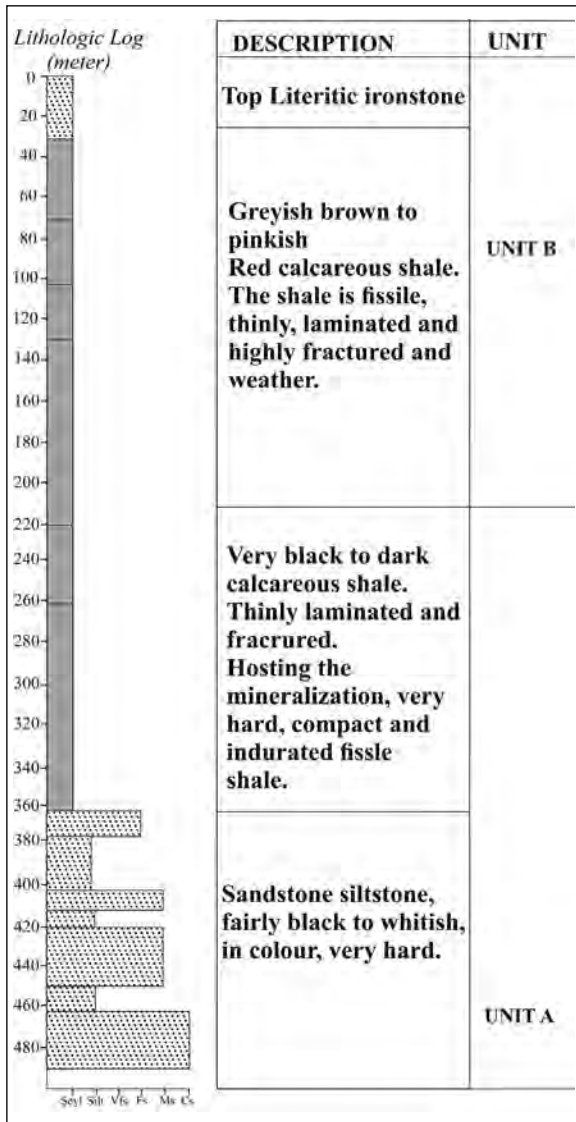


Figure 3- Lithostratigraphic section of the geologic units in the study area (modified from Obarezi and Nwosu, 2013)

may be true given the current exploitation of some mineral deposits from the region. A conspicuous E-W trending lower magnetic anomaly streak observed at northern region may be due to a lower magnetic susceptibility sill-like deposition located deeply in this region. The variation of magnetic strength (Total Field values) across the study area indicates the difference in susceptibility of the geological bodies, including mineralization and structures.

### 2.1. Magnetic Inversion

We present a brief theoretical insight into our adopted method for the 3D inversion. Pilkington



(a) Ameri Mine (8.067°E, 6.300°N)



(b) Enyigba Mine (8.106°E, 6.174°N)



(c) Ameka Mine (8.100°E, 6.150°N) (d) Mbaraeke Mine (8.270°E, 6.490°N)

Figure 4- Images of some of the mines location in which current mining of lead-zinc minerals is ongoing by the locals (as could be seen in the pictures).

(2009) used the Cauchy norm (Sacchi and Ulrych, 1995) to solve the 3D magnetic inverse problem for sparse models, i.e. those models in which the number of nonzero values that fit the data is minimized. The derived inversion is therefore regarded as geologically unconstrained, in comparison with constrained inversions in which hard geologic constraints like

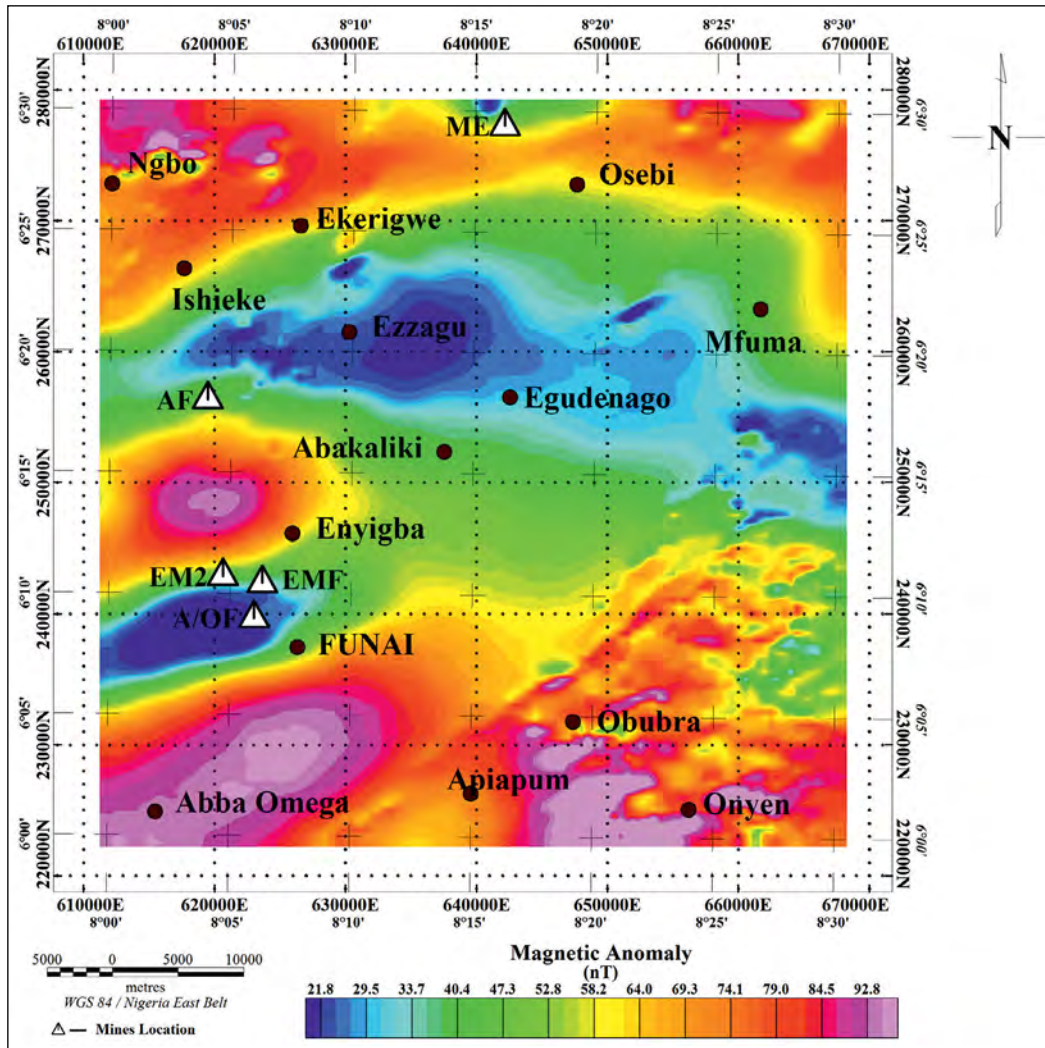


Figure 5- Aeromagnetic Anomaly map covering the region of study. Current and active mines (white triangles) are located on the map which includes the Ameri Mine Field (AF), Enyigba Mine Field (EMF), Ameka/Ohankwu Field (A/O), Mkpuma-Ekwaokuko Field (ME) and Enyigba Mine Field 2 (EM2).

for example drill hole intersections are included (Pilkington, 2009).

For our computations, we assumed that all sources are magnetized by induction, having a susceptibility range starting from 0.0001 SI, an inclination of  $-13^\circ$ , and declination  $-2^\circ$ . We inverted the entire dataset to produce a 3D voxel susceptibility model using Pilkington and Bardossy (2015) implementation in the GEOSOFT program.

### 2.2. 3D Euler Deconvolution

Among the goals for performing the 3D Euler, the process includes outputting a map that exposes the depths of the geologic sources perceived in a 2D

grid and their corresponding locations (Eshaghzadeh et al., 2020; Whitehead and Musselman, 2005). The standard 3D Euler technique is founded on Euler’s homogeneity equation – an equation relating the magnetic or gravity field along with its gradient constituents to source position, with structural index, SI (the degree of homogeneity N) (Thompson, 1982). An exponential factor analogous to the ratio by which the potential field falls off with distance when a source with a given geometry is taken into account. For our computations, we adopted the standard 3D design of Euler’s equation (Reid et al., 1990) as implemented by GEOSOFT Oasis Montaj software as:

$$x \frac{\partial T}{\partial x} + y \frac{\partial T}{\partial y} + z \frac{\partial T}{\partial z} + \eta T = x_0 \frac{\partial T}{\partial x} + y_0 \frac{\partial T}{\partial y} + z_0 \frac{\partial T}{\partial z} + \eta b \quad (1)$$

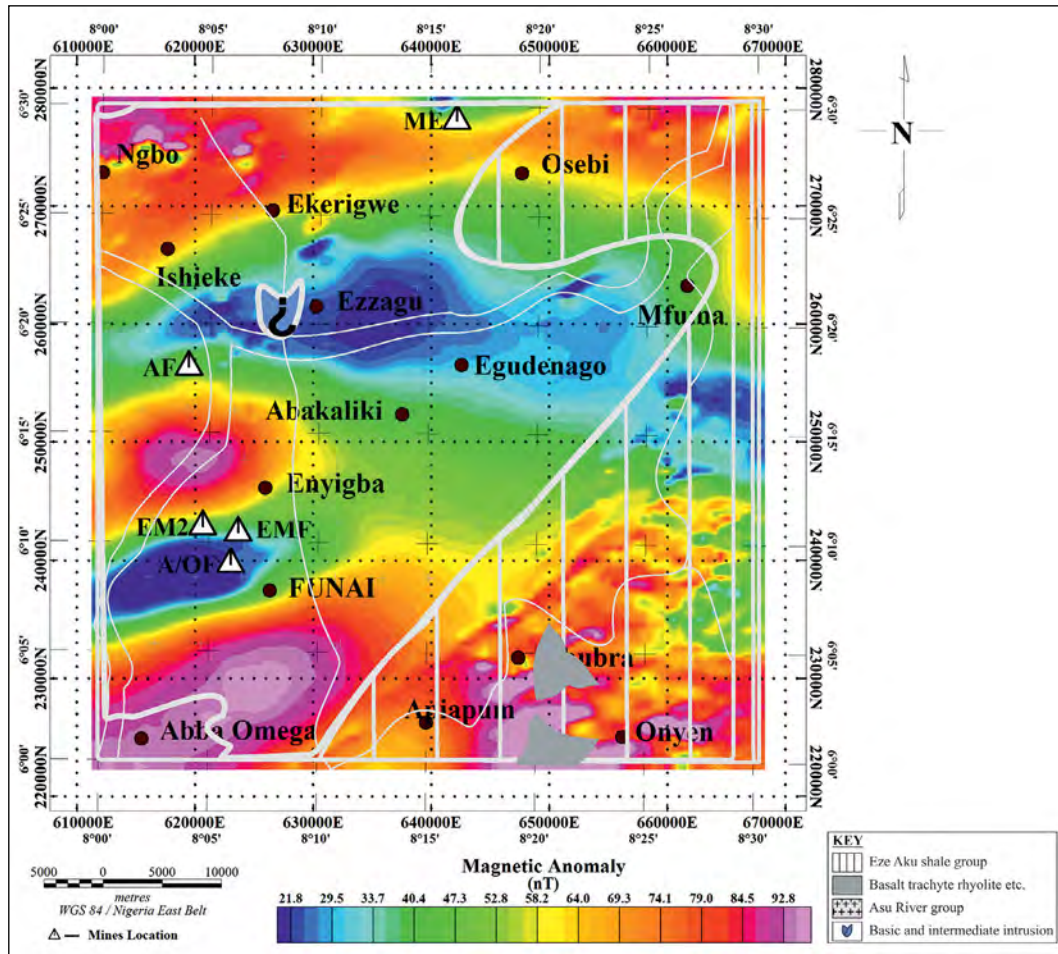


Figure 6- Aeromagnetic anomaly map with superimposed geology map of the study area.

where  $x$ ,  $y$  and  $z$  represents coordinates of a measuring point,  $x_o$ ,  $y_o$  and  $z_o$  represents coordinates of the source position of which the total field is discerned at  $x$ ,  $y$  and  $z$ ,  $b$  represent a base level,  $\eta$  represent the structural index (SI) and  $T$ , Total magnetic field. The source body type of interest determines the value of SI (Whitehead and Musselman, 2005). As an example (Kumar et al., 2020; Ganguli et al., 2019; Abraham and Alile, 2019; Thompson, 1982; Reid et al., 1990) proposes  $\eta = 0$  for a contact,  $\eta = 1$  (vertical dyke or the edge of a sill),  $\eta = 2$  (centre of a horizontal or vertical cylinder), and  $\eta = 3$  (centre of a magnetic orb or dipole). Euler's equation for magnetic data possesses a significant advantage because it is indifferent to magnetic inclination, declination, and remanence which constitute a constant, in the anomaly function of any given model. As we are interested in locating source contact/faults with depths, to model geological units influencing mineralization in Abakaliki and

environs, we adopted an SI of 0 (Reid and Thurston, 2014) and a window size  $\geq 10$  at 15% depth tolerance, for our computations.

### 2.3. Enhanced Local Wavenumber (ELW) Technique

Following the concept of local phase 2-D analytic signal of any constituents of the Earth's magnetic field assessments, an equation (autonomous of the causative source geometries) was obtained by Thurston and Smith (Thurston and Smith, 1997) utilizing second-order vertical and horizontal derivatives of magnetic anomalies. This includes the contact, thin sheet, pole and dipole, involving unknown parameters of location and depth only. Having known the horizontal position as well as depth parameters, the source geometry was further determined (Srivastava and Agarwal, 2010). For this study, we utilized a FORTRAN code developed by Agarwal and Srivastava (2008) to analyze field anomalies.

### 2.4. 3D Analytic Signal

Horizontal displacement regarding sources has always complicated the elucidation of observed magnetic anomalies. The non-vertical direction of the induced magnetization and geomagnetic field, results in displacement or skewness. To verify if the magnetic anomalies in the area were brought about by intrusions, we calculated the analytic signal response of the geomagnetic field. The 3D Analytic Signal amplitude is shown as (Roest et al., 1992; Riedel, 2008):

$$A(x, y) = \sqrt{\left(\frac{\partial T}{\partial x}\right)^2 + \left(\frac{\partial T}{\partial y}\right)^2 + \left(\frac{\partial T}{\partial z}\right)^2} \quad (2)$$

where  $T$  represents the observed field at  $x$  and  $y$ .

Despite this function not being a measurable parameter, it is highly fascinating in the context of interpretation, as it retains its independence in terms of the direction of magnetization, as well as the direction of the inducing field. This implies that all bodies with the same geometry have the same analytic signal. Maxima are displayed over magnetization contrasts and are independent of the ambient magnetic field including sources magnetization directions. These maxima thus outline the magnetic sources from their locations. The analytic signal is useful in identifying the edges of the magnetic source bodies, where remanence and/or low magnetic latitude (as in this study) makes interpretation difficult (Whitehead and Musselman, 2005).

### 2.5. Particle Swarm Optimization (PSO) and 2D Analytic Signal

To model the subsurface structure from the analytical signal and magnetic anomalies, we adopted the particle swarm optimization (PSO) technique. PSO results appear to be stable to a greater degree than other optimization techniques (Essa and Elhussien, 2020; Essa and Munsch, 2019; Srivastava and Agarwal, 2010). PSO (Srivastava et al., 2020; Srivardhan et al., 2016; Kennedy and Eberhart, 1995) is a global optimization method and is one of the accepted naturally influenced metaheuristic algorithms founded on the conduct of bird flocks as well as fish schools looking for food (Pallero et al., 2015). The purpose

of a geophysical inverse problem is to discover a best reasonable model explaining a collection of observed data like an  $M$ -dimensional optimization problem (Srivastava and Agarwal, 2010). Following Srivastava and Agarwal (2010), we take into account the mapping,  $g$  betwixt the ‘model space vector’,  $\mathbf{m}$  together with the ‘data space vector’,  $\mathbf{d}$  as

$$\mathbf{d} = g(\mathbf{m}), \quad (3)$$

Also, take into account that the model  $m_{true}$  produces the observed data,  $d_{obs}$ :

$$d_{obs} = g(m_{true}) \quad (4)$$

The objective function is defined as

$$E(\mathbf{m}) = [d_{obs} - g(\mathbf{m})]^T [d_{obs} - g(\mathbf{m})], \quad (5)$$

The superscript T represents the matrix transpose. When the appraised model  $\mathbf{m}$  comes near to the true model,  $m_{true}$ , the objective function  $E(\mathbf{m})$  tends to minimum.

For the PSO, a swarm of particles is chosen by chance from the  $M$ -dimensional model space vector in order that the position of each particle matches to a could be model. A particle  $i$  possesses the next attributes at the  $k$ th iteration (flight): (1) current location,  $m_i^k$  (2) the best location accomplished so far  $m_i^n$  and (3) velocity,  $V_i^k$ . A velocity adaptation of the particle is resolved together by the previous best position filled by the particle as well as the best position of the swarm for each of the iterations. Computation of a new position on account of the particle is performed utilizing the new velocity. The part of the velocity adaptation resolved by the individual’s previous best position is known as the ‘cognition’, and the part impacted by the best in the population is known as the ‘social’ part. The swarm, from the other point of view, possess but one characteristic, particularly, the best locations  $m_i^g$ , obtained up to the  $k$ th iteration. The cognitive and social knowledge determines the direction of each particle in the swarm. In mathematical form, this is described as (Srivastava and Agarwal, 2010):

$$m_i^{k+1} = m_i^k + a[V_i^k + b \text{ran}(\cdot)(m_i^n - m_i^k) + c \text{ran}(\cdot)(m_i^g - m_i^k)] \quad (6)$$

Parameters  $b$  and  $c$  stands for the learning rates controlling the cognition as well as the social knowledge, correspondingly. The parameter  $a$

represents the constriction factor established by (Clerc, 1999) and is nearly connected to the inertia factor while  $\text{ran}(\cdot)$  represents a random number generator (Press et al., 1994) picked in a uniform manner in the open interval (0, 1).

The amplitude of the Analytic Signal over a 2D source (AS) is a symmetrical function with peak almost agreeing with the upper corners of the causative source (Mehanee et al., 2021; Nabighian, 1972). Some researchers (Salem et al., 2005; Srivastava and Agarwal, 2010) demonstrated that AS of distinctive source geometries is capable of being approximated by a generalized equation following the form:

$$|A(x)| = \frac{K}{[(x - x_0)^2 + z_0^2]^q} \quad (7)$$

The amplitude factor,  $K$ , is connected to the physical characteristics of the source. The horizontal location and depth of the source is represented as  $x_0$  and  $z_0$ , correspondingly, and the shape factor is represented as  $q$ . Equation (7) attains a maximum at  $x = x_0$ . PSO was used to invert AS to resolve horizontal location and depth, amplitude factor ( $K$ ) and shape factor ( $q$ ) for every corner of the adopted model. These parameters are determined by designating search spaces for constant  $K$ , shape factor  $q$ , as well as the horizontal location and depth (in connection with data spacing). The amplitude of analytic signal AS of a 2D magnetic source model as approached by an  $m$ -sided polygon

is the sum of the  $m$  symmetric bell-shaped functions (equation 7) nearly centered atop corners of a polygon (Srivastava and Agarwal, 2010; Huang and Guan, 1998).

For the PSO implementation, we performed 10 independent runs utilizing 100 particles to achieve the optimum model parameters. Values 1, 2, and 2 were allocated for the inertia factor ( $a$ ) as well as the cognitive and social scaling factors ( $b$  and  $c$ ), correspondingly (Thompson, 1982). The variation in shape factor from 0.2 – 1.5 was considered to incorporate various types of source geometries. Results obtained from PSO were compared with those from ELW technique (Agarwal and Srivastava, 2008).

We computed a synthetic magnetic field data using a MATLAB program (Stocco et al., 2009). The code of the inversion routine is established on a weighted-damped least-squares algorithm, following a standard of balancing the weight of the data inaccuracies as well as the compactness of the solution.

### 3. Results

The best 3D susceptibility model was achieved at the 230<sup>th</sup> iteration on the magnetic anomalies with a root-mean-square (rms) error of 1.129485 nT and results displayed in Figure 7. Figure 8 displays the model result after clipping susceptibilities lower than 0.00113 SI. Figure 9 displays model result with superimposed magnetic data respectively.

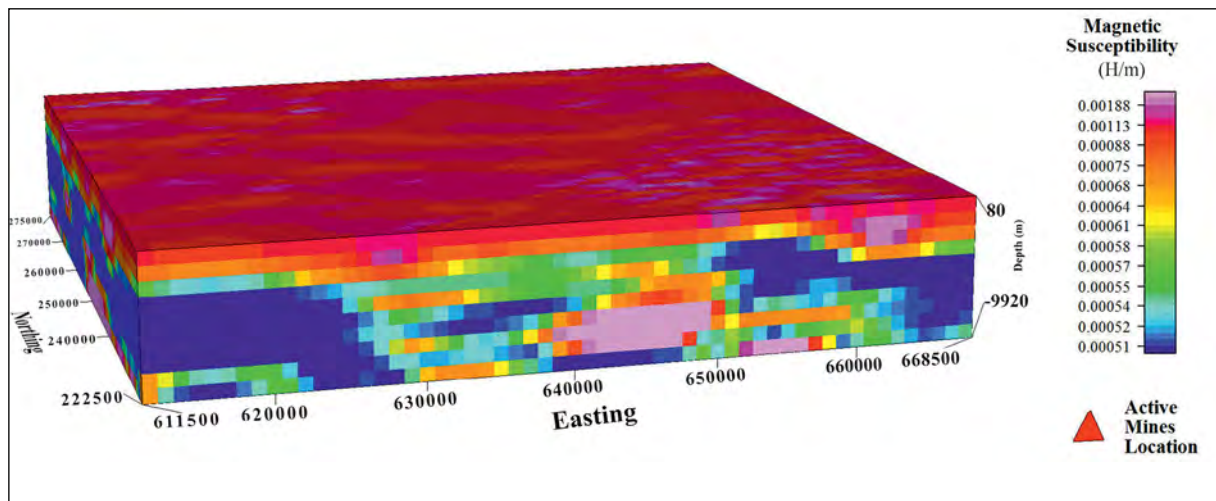


Figure 7- 3D model results from the inversion of magnetic data. The conspicuous contrast between the intruding structures and the host environment could be seen in the model with susceptibilities  $\geq 0.00113$  SI.

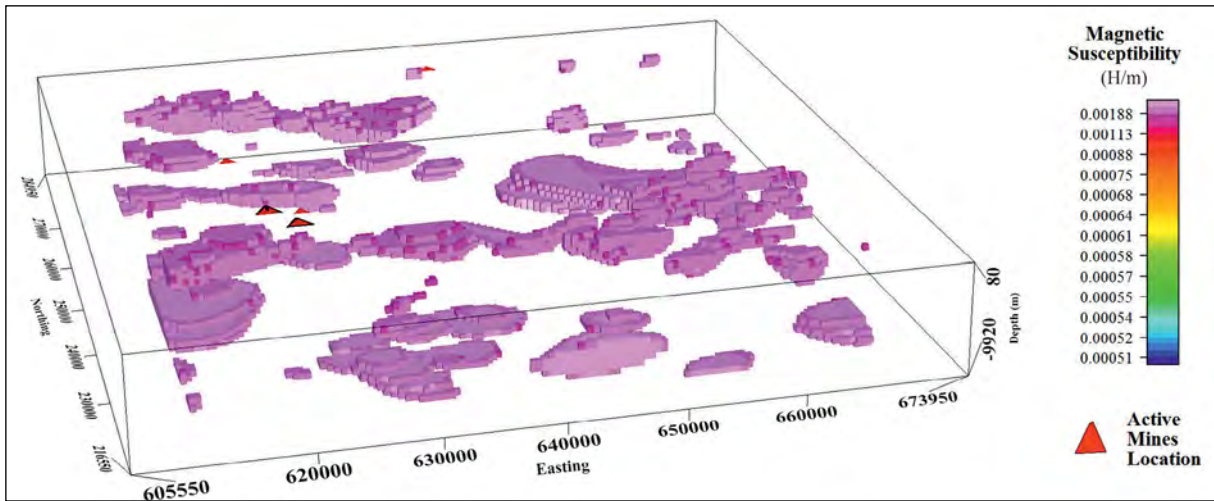


Figure 8- Model results after clipping susceptibilities lower than 0.00113 SI (Figure 7). A depth slice at -100 m was taken and the inversion model was constrained using information from Figure 2 (Geology) and 3 (Lithostratigraphic section) of Enyigba, in addition to Dobrin and Savit (1988).

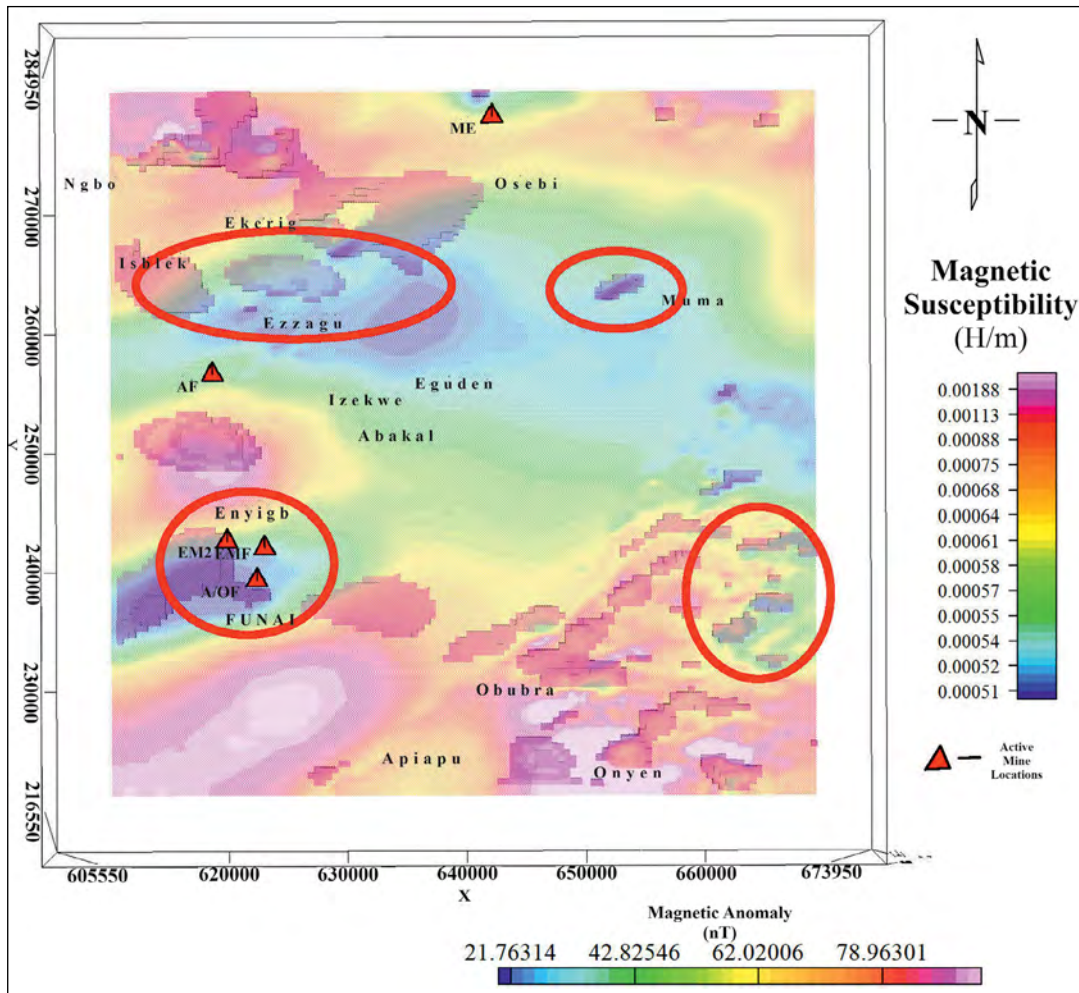


Figure 9- Plan view of the magnetic field anomaly (watermarked at 59% transparency) superimposed on the outlines of the model bodies. We noticed that some largely lower magnetic anomalies locate over high susceptibility units in the model (circled).

Results from 3D Euler deconvolution is presented in Figure 10. The presented result is a map showing Euler depth solutions superimposed on combined 3D susceptibility solutions (Plan view) map and magnetic anomaly data (with 59% transparency effect to enable see-through to some of the susceptibility solutions in the background).

The effect of the structural trends of possible subsurface geologic contacts mapped with the Euler deconvolution could be seen on the distribution of the model solutions from the inversion results (Figure 10). Parallel geologic structures trending NE–SW directions (inserted white lines), which may

be faults structures ‘sandwich’ the mines clusters at Enyigba – FUNAI enclave and appears to control the existence of the mineral deposits in the region. A similar structural network is also noticed at the Ameri Mine Field (AF), above the Enyigba town. These are observed on individual examination of the Plan View display of model solutions. Figure 11 shows a map of the Analytic Signal computation. The profiles on the map possesses various parameters as summarized in Table 1.

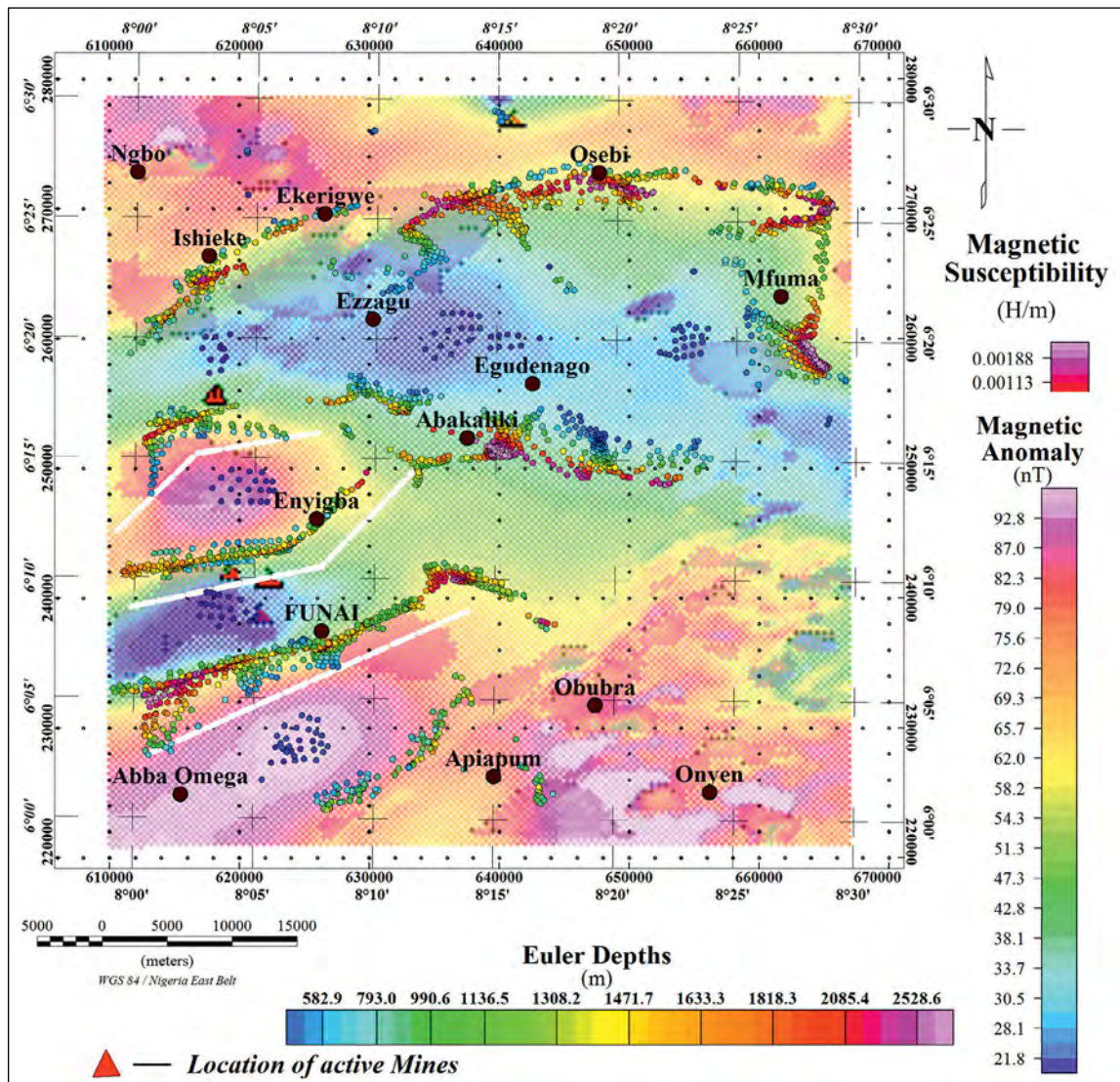


Figure 10- 3D Euler depths solutions overlain on the magnetic anomaly data (at 59% transparency) and 3D susceptibility model solutions.

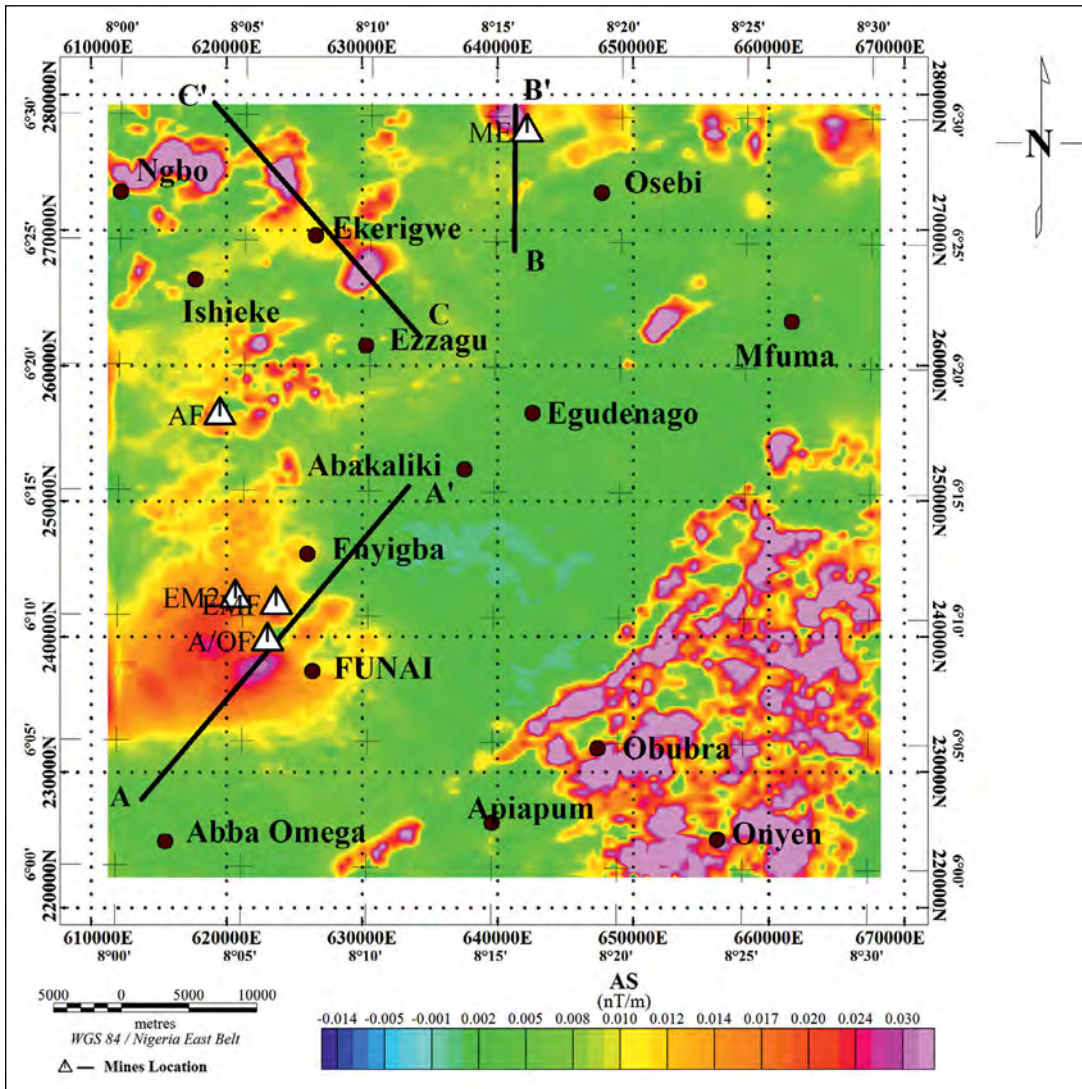


Figure 11- Analytic signal results of the study area. Various maxima observed on the map captures sources with strong magnetization contrast and provide information on their respective locations. Profiles AA', BB' and CC' are taken on suspected anomalies especially at current mining sites. These were inverted and analyze to derive the actual subsurface structures at these sites

Table 1- Profile parameters to include longitude, latitude, length and azimuth.

	Longitude (°)	Latitude (°)	Length (km)	Azimuth (°)
<b>Profile AA'</b>	8.02	6.04	104.60	49.81
	8.19	6.26		
<b>Profile BB'</b>	8.26	6.41	103.38	90.00
	8.26	6.51		
<b>Profile CC'</b>	8.20	6.35	23.24	138.81
	8.06	6.51		

The synthetic dyke model (Figure 12) was assigned a susceptibility of 0.005981 SI. The number of data points (101), profile length (100m), thickness (2m), depth to top of anomaly (4m) and depth to bottom (8m). 5% and 10% random noise was added to the

synthetic dataset and 2D analytic signal was computed from the noise corrupted synthetic anomalies using a frequency domain filtering undertaking as depicted by Agarwal and Srivastava (2008).

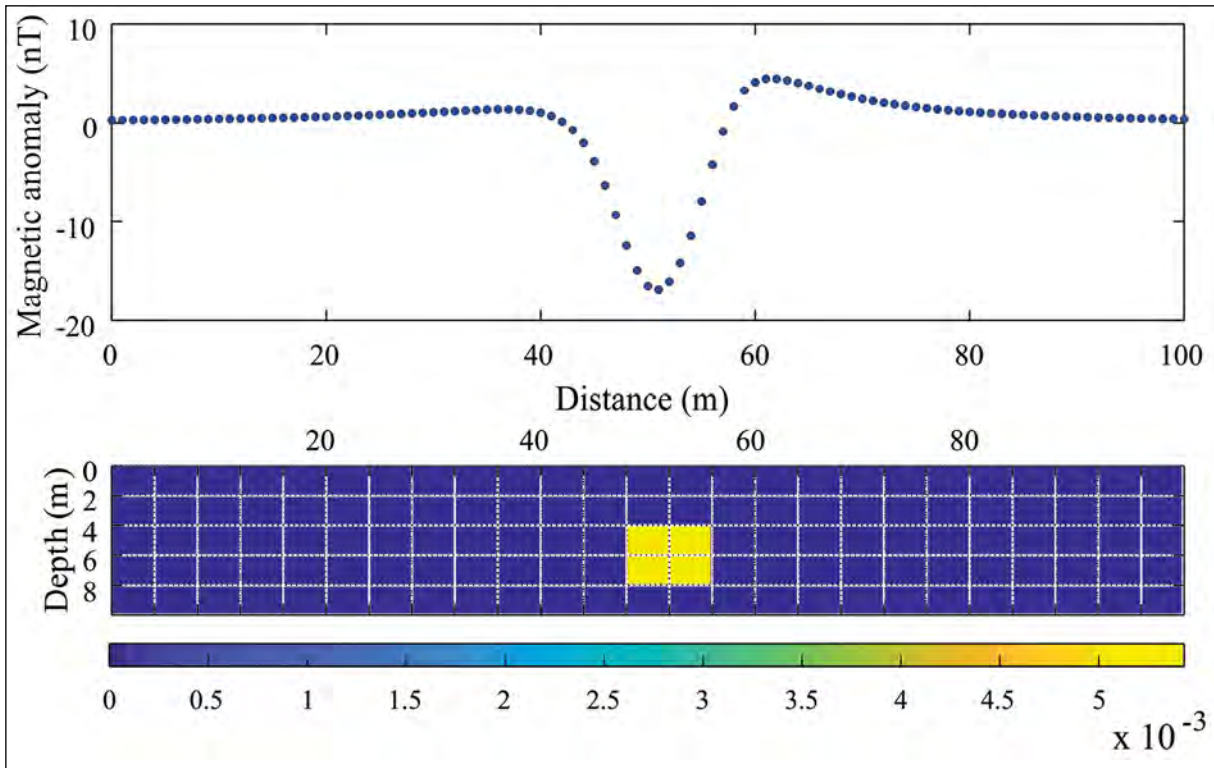


Figure 12- Synthetic anomaly with a dyke-like structure of 0.005982 magnetic susceptibility. Field intensity 33,000nT, inclination  $-10^\circ$ .

The PSO program was tested with parameters from the synthetic data before application to the anomaly profiles taken from our study region. Figure 13 shows a plot of the initial computation (at 0% noise data) and Table 2 displays model parameters reckoned from PSO for the single dyke structure with various noise percentages and the r.m.s. error. The computed amplitude of analytic (AS) of the synthetic magnetic

data is also shown on Figure 13. Model parameters were also computed with random noise addition of 5% and 10% successively.

We present the search spaces and computed/interpreted model parameters from PSO for profiles *AA'*, *BB'* and *CC'* on Tables 3, 4, and 5. Table 6 shows a comparison of interpreted model parameters from

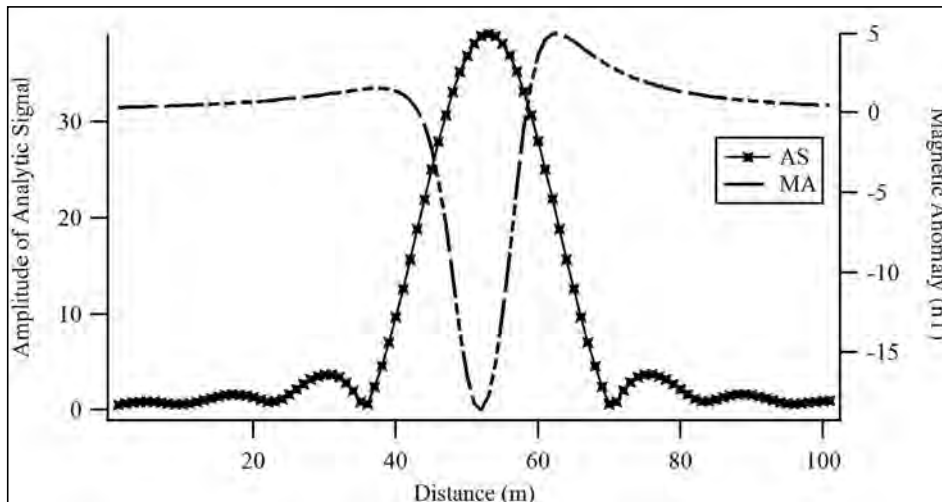


Figure 13- Synthetic Magnetic Anomaly data (0% noise) and its computed analytic signal.

Table 2- Model Parameters calculated from PSO for a single dyke with various noise percentages and their r.m.s. error.  $x_0$  and  $z_0$  are the coordinates of the source location in the unit of data spacing.

	True model	Model space		Computed model parameters with random noise percentage		
		Minimum	Maximum	0%	5%	10%
Amplitude	470	10	5000	490	515	520
$x_0$	55	10	100	56	56	58
$z_0$	4	1	12	4.5	4.5	4.8
$q$	1	0.2	1.5	1.0	1.0	0.9
rms Error				0.03	0.24	1.05

Data spacing = 1m

Table 3- Search space for profile  $AA'$  taken across a mine site within the region of study with computed PSO parameters.  $x_0$  and  $z_0$  are the coordinates of the source location in the unit of data spacing.

	Model space		Computed parameters from PSO
	Minimum	Maximum	
Amplitude	10	3000	355
$x_0$	1	20	12.5
$z_0$	0.1	10	1.8
$q$	0.2	1.5	0.9
r.m.s. error			0.1012

Data spacing = 0.5 km

Table 4- Search space for profile  $BB'$  taken across a mine site within the region of study with computed PSO parameters.  $x_0$  and  $z_0$  are the coordinate of the source location in the unit of data spacing.

	Model space		Computed parameters from PSO
	Minimum	Maximum	
Amplitude	10	5000	420
$x_0$	7	20	9
$z_0$	0.1	10	0.2
$q$	0.2	1.5	0.8
r.m.s. error			0.0682

Data spacing = 0.5 km

Table 5- Search space for profile  $CC'$  taken across two notable sources and the computed PSO parameters.  $x_0$  and  $z_0$  are the coordinates of the source location in the unit of data spacing.

	Bell 1		Computed parameters	Bell 2		Computed parameters
	Model space			Model space		
	Minimum	Maximum		Minimum	Maximum	
Amplitude	10	5000	590	10	5000	1120
$x_0$	2	10	6	10	30	16.1
$z_0$	0.1	10	0.4	0.1	10	0.29
$q$	0.2	1.5	0.9	0.2	1.5	0.88
r.m.s. error			0.1663			0.1882

Data spacing = 0.5 km

ELW and PSO computations for the respective profiles under consideration.

A plot of magnetic anomalies (MA), amplitude of analytic signal (AS) from measured magnetic anomalies and amplitude of analytic signal calculated by utilizing interpreted model parameters from profiles  $AA'$ ,  $BB'$  and  $CC'$  is shown in Figures 14, 15 and 16.

#### 4. Discussion

Tests on synthetic and field data (Pilkington, 2009) have shown that a more focused solution is produced from sparse inversion compared with a standard model – space, least-squares inversion. Our modeling results depicted in Figures 7 and 8 were realized from the modeling data of Figure 5. Figure 7 shows unit features embedded in the region. Various subsurface intrusions could be observed which contrasted with

Table 6- Interpreted model parameters from ELW and PSO modeling for profiles taken from the study region.

	Amplitude	Location (km)	Depth (km)	Structural Index
<b>Profile AA'</b>				
ELW	-	13.22	1.77	0.3
PSO	355	12.5	1.8	0.8
<b>Profile BB'</b>				
ELW	-	8.11	0.12	-0.35
PSO	420	9	0.2	0.8
<b>Profile CC' (S1)</b>				
ELW	-	5.28	0.38	0.85
PSO	590	6	0.4	0.9
<b>Profile CC' (S2)</b>				
ELW	-	15.34	0.27	1.02
PSO	1120	16.1	0.29	0.88

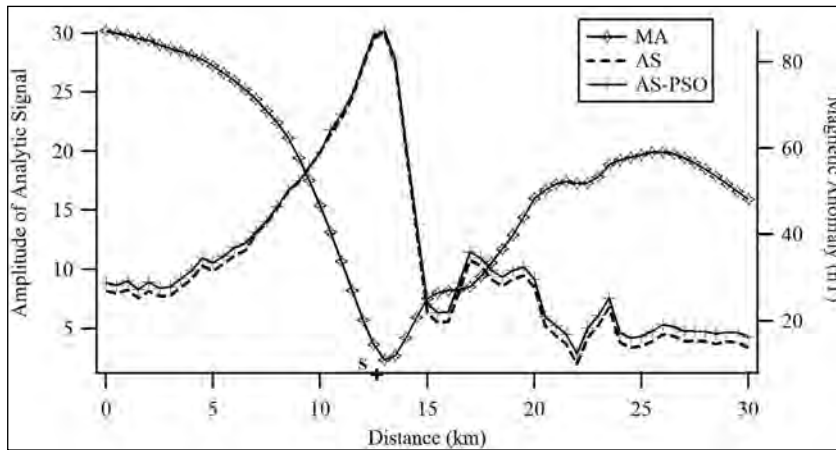


Figure 14- Magnetic anomaly (MA) over a source in profile AA' across the Enyigba mine site. AS, amplitude of 2D analytic signal from measured anomaly, AS-PSO, amplitude of analytic signal calculated by utilizing interpreted model parameters from PSO. The '+' sign indicate the horizontal position of the source.

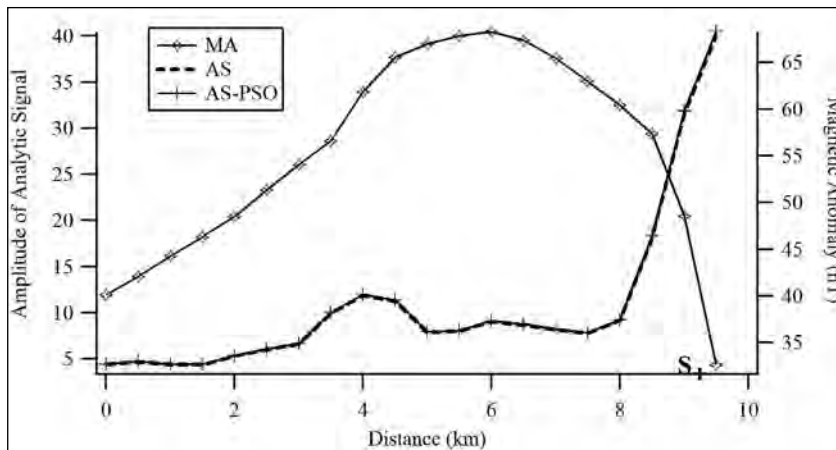


Figure 15- Magnetic anomaly (MA) over a source in profile BB' at Mkpuma-Ekwaokuko mine site. AS, amplitude of 2D analytic signal from measured anomaly, AS-PSO, amplitude of analytic signal calculated by utilizing interpreted model parameters from PSO. The '+' sign indicate the horizontal position of the source.

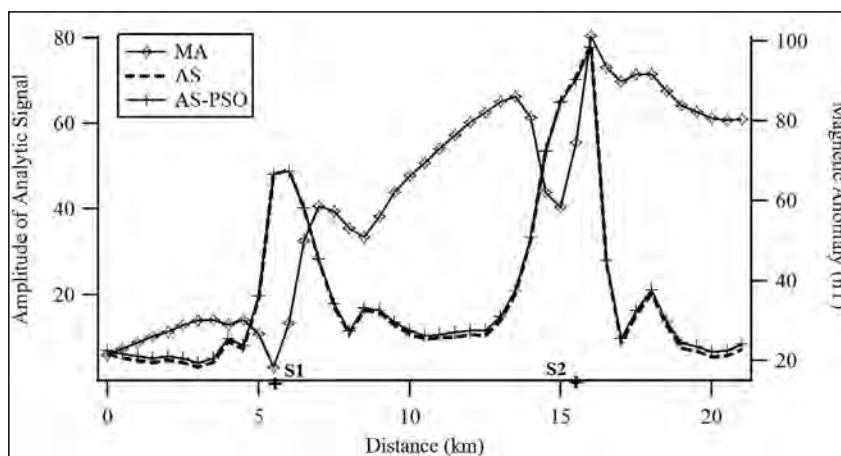


Figure 16- Magnetic anomaly (MA) over sources in profile *CC'*. AS, amplitude of 2D analytic signal from measured anomaly, AS-PSO, amplitude of analytic signal calculated by utilizing interpreted model parameters from PSO. The '+' sign indicates the horizontal position of the sources.

the background susceptibilities. We pegged the model susceptibility at 0.0005 *SI* due to the predominant background geology of the region (shale and sandstone with susceptibilities of 0.00065 and 0.0004 *SI*) (Dobrin and Savit, 1988; NGA, 2004) (Figure 7). We then clipped susceptibilities less than 0.00113 *SI* to bring out the contrasting bodies in the model.

Figure 8 displays various subsurface geologic features domiciled in the region. We interpret these features as geological units controlling mineralization in the region. To enable comparison and confirmation using the various locations of active mining activities in the region, we took a plan views of the modeled result (Figures 9 and 10). The model results capture most of the active mining locations in the region. The Enyigba mines location (Figure 9) indicates units with magnetic susceptibilities  $>0,00188$  *SI* Some of the lower magnetic anomalies locates over high susceptibility units (as indicated within the drawn circles). The geometry of the resolved units (Figures 9) implies the union of magnetic anomaly with a metamorphic rock enveloped by the predominant shale formation in the region. The mining of rocks with lead-zinc (Pb-Zn) mineralization at Enyigba, ilmenite, and pyroclastic rocks at Abakaliki confirms this deduction. We also spotted an intrusion around Abba Omega that we identified as representing units bearing copper (Cu) or barite minerals (GSNA, 2004). Intrusions observed at Obubra are directly associated with traced volcanic

rocks mapped as basalts, trachytes, and rhyolites (Figure 2) and that of the surrounding areas of Obubra (Eja and Ogurude localities) has an imposing record of lead (Pb) ore deposits. The inversion result at Ngbo – Ekerigwe area shows a significant magnetic body connected with intense remnant magnetization. The dimensions of the magnetic mass are almost 3.5 km in-depth extension and 18 km stretch in the northern E – W direction (Ngbo – Ekerigwe). This magnetic body has great prospectivity importance because of its structural and positional emplacement and could contribute to the metallogenic as well as structural comprehension of mineralization in the Asu River formation. Further integration with other geophysical data from the area could provide more information regarding the association of these magnetic bodies and yet to be discovered minerals in the region. Our modeling study has shown even more possible geological units hosting economically viable mineral resources yet recorded within the study region, showing subsurface extensions and their possible boundaries.

The Euler deconvolution map (Figure 10) shows derived source positions represented as circles and depth information proportional to their respective colour representations. We achieved good clustering of the solutions and they show definite magnetic trends aligning in the E–W, NW–SE, and NE–SW directions within the study region. The dominant linear features

trending NE – SW (FUNAI, Enyigba, Ishieke and Apiapum regions) and E – W (Abakaliki and Osebi regions) directions show many clustering and could be interpreted as faults within the study region. The NE – SW trend corresponds to the orientation of the trend produced by the Santonian deformation which affected the Lower Benue Trough (Ezema et al., 2014). Epigenetic fractures striking E-W, NW-SE, and N-S generally host mineralization (lead-zinc-baryte) in an area (Ford, 1981; Omada and Ike, 1996; Oha and Onuoha, 2013). We observed similar trends of anomalies over Abakaliki–Ugep regions as Anyanwu and Mamah outo (2013) from their analysis of Landsat Thematic Mapper and airborne magnetic data. Magnetic edges – notable faults have been marked with good precision using a series of depth-labeled Euler trends (Pallero et al., 2015). The alignment of clusters from the 3D Euler solutions along the edges of contrasting magnetic intensities is also noted (Figure 10), with the structural contacts from Euler deconvolution aligning around the major solutions of the 3D model at the north-central region of the study area.

The analytic signal was evaluated to assess how well our modeling study matches the geological units in the region. We note that the model result agrees to some degree with obvious features realized from the analytic signal results (Figure 11). The AS assesses the amplitude of the gradient of magnetization; the closer we are to the magnetic sources, the higher the amplitude of that gradient. We observed that while the analytic signal computation was able to resolve the location of the present mines, the sparseness model could not resolve most of these anomalies. Nevertheless, the 3D model performed excellently in identifying deeper bodies (depths > 5000 m) with significant susceptibility contrast. Isolated and secluded maxima of the analytic signal results visible at the N-W, N-E and S-W regions of the study area were interpreted as stemming from subsurface intrusions at the respective locations. We observed matches of prominent anomaly features on the analytic signal map and the model solutions mainly with features located around the Ngbo, Ekerigwe, Mfuma, Obubra, and Onyen localities. The spread-out maximas notable at the S-E region could be due partly to some subsurface intrusions at the region, and also

to the shallow crustal deposition of gravels, basalt and trachytes within the Eze Aku Shale formation of that region (Ovat, 2015). Obande et al. (2014) adopted a similar interpretation approach in their study area with similar magnetization properties. We recall that Figure 2 showed the basaltic and rhyolitic intrusions at Obubra which may also influence the magnetic anomaly record for the region.

Analysis of the AS by PSO technique (Tables 3, 4 and 5) indicates that the structural index of the anomaly source identified from processing Profile AA' data (Figures 11 and 14) suggests the presence of an intruded dyke structure within the region. The index value from ELW computation (0.3) may also hint on a closed interaction of contact sources with the dyke structure at this location. This contact source interaction is clearly seen on the overlain magnetic anomaly data with the Euler and 3D model solutions (Figure 10). NE – SW trending geologic contact sources are mapped around the Enyigba – FUNAI region, sandwiching the Enyigba mine fields and also following the mapped out isolated region by the analytic signal results as seen in Figure 10. The present Pb-Zn mineral mining operations in the area is noted to extend vertically downwards in the open cast mining pits at this location and may confirm our dyke structure interpretation of the anomaly from this location. The extension of these anomalies within and around the Enyigba mine field (Figure 10) may also suggest capturing the edges of a sill structure around the region. Profile BB' was considered given the presence of the Mkpuma-Ekwaokuko mine field (ME) (Figures 5 and 11) and a notable maximum from the analytic signal at that location. This site is currently being exploited for Pb-Zn minerals by the locals. Examinations of the magnetic anomalies indicate similar magnetic features with the Enyigba mine field location. However, the limited data at the time of this study restricted the extent of our profile, therefore we located our profile from the center of the examined anomaly outwards (Figure 11). Table 4 shows model search space and computed parameters from PSO for profile BB'. A r.m.s. error of 0.0682 was also achieved from the computations. PSO computed a depth of 0.2 km at horizontal distance of 9.0 km for the location. Figure 15 shows a plot of the magnetic

anomaly over the source in profile *BB'*. Computations using the ELW technique presented a depth of 0.12 km at a horizontal distance of 8.11 km. The structural indices from the ELW and PSO techniques (Table 6) reveals an interaction of contact sources with the dyke structure within the subsurface at that location. The AS computed from Profile *CC'* data exhibits two peaks of significantly different amplitudes (Figures 11 and 16). In the absence of drill hole information at this location, the AS computation has clearly revealed the presence of the two distinct sources along this profile. Our inversion of the AS involved fitting two bells corresponding to the two peaks observed. Table 5 presents the model parameter search spaces and the realized computed parameters from PSO for both bells (Profile *CC'*). The r.m.s. error is also shown. The peaks analyzed in these results may indicate causative sources located at S1 and S2 to be vertical dyke structures separated by approximately 3 km. The structural indices from the ELW and PSO computations (Table 6) confirm that the causative sources are vertical dyke structures intruded at the location.

## 5. Conclusion

We have performed a 3D magnetic inversion modeling of geologic units representing mineralization structures in Abakaliki and environs. The 3D inversion results aligned with the analytic signal solution calculated from the same anomaly data. This region in the southeastern zone of Nigeria is known to host vast mineral deposits of economic significance. Good clustering of the Euler deconvolution solutions were obtained for the region and revealed definite magnetic trends aligning in the E–W, NW–SE, and NE–SW directions. The dominant linear features trending NE – SW around the Enyigba mine fields have been noted to play an active role in the mineralization of the region. The contact sources interact with the dyke structure identified in the region using analytic signal technique and a global optimization technique (PSO). In general, PSO results are comparable to those achieved by the ELW technique and indicate stability of solutions and reliability of results. Several other subsurface geologic units which possibly represent mineralization structures in the region have been recognized. Inversion of both magnetic anomaly

and analytical signal has enabled derivation of the actual subsurface structures in the region with most of the structures appearing as dykes with depths ranging from 0.2 – 1.8 km at most of the mining sites in the region. Structural indices computed for the region have also indicated interaction of contact sources (faults and fractures) with identified dyke structures. This study has confirmed most of the sites currently being excavated for these minerals and also show potential sites whose locations were hitherto unknown which could also be considered for further exploration. Results have contributed to the knowledge base of geologic units representative of the mineralization structures in southeastern Nigeria. Quantitative analysis provided by this study would enable informed geotechnical engineering decisions especially at potential mining sites.

## Acknowledgments

We are grateful to the anonymous reviewers, including the editor, whose comments contributed to improve this manuscript. We also acknowledge Dr. Ben Earl Barrowes of Engineer Research and Development Center – U.S. Army for his advice on the programs. Dr. Harish Garg of Thapar Institute of Engineering and Technology, Patiala, School of Mathematics, is also recognized for his advice on the PSO program. This research did not receive any specific grant from funding agencies in the public, commercial, or not-for-profit sectors. We would like to declare that total compliance with ethical standards was observed in the preparation of this manuscript and the submitted manuscript poses no conflict of interest between the authors and any other party.

## References

- Abdelrahman, E. M., El-Araby, H. M., El-Araby, T. M., Essa, K. S. 2003. A least-squares minimization approach to depth determination from magnetic data: *Pure and Applied Geophysics* 160, 1259–1271.
- About, E., Wameyo, P., Alqahtani, F., Moufti, M. R. 2018. Imaging subsurface northern Rahat Volcanic Field, Madinah city, Saudi Arabia, using Magnetotelluric study. *Journal of Applied Geophysics* 159, 564 – 572.
- Abraham, E. M., Alile, O. M. 2019. Modelling Subsurface Geologic Structures at Ikogosi Geothermal Field,

- Southwestern Nigeria, using Gravity, Magnetics, and Seismic Interferometry Techniques. *Journal of Geophysics and Engineering* 16, 729–741.
- Abraham, E. M., Itumoh, O., Chukwu, C., Rock, O. 2018. Geothermal Energy Reconnaissance of Southeastern Nigeria from Analysis of Aeromagnetic and Gravity-Data. *Pure and Applied Geophysics*, 176, 22 – 36.
- Agarwal, B. N. P., Srivastava, S. 2008. FORTRAN codes to implement enhanced-local-wave-number technique to determine location, depth and shape of the causative source using magnetic anomaly. *Computer Geosciences* 34, 1843–1849.
- Agha, S. O., Arua, A. I. 2014. Integrated-geophysical investigation of sequence of deposition of sedimentary strata in Abakaliki, Nigeria. *European Journal of Physical and Agricultural Sciences* 2(1) 1-5.
- Anyanwu, G., Mamah, L. 2013. Structural Interpretation of Abakaliki-Ugep using Airborne magnetic and Landsat Thematic Mapper (TM) data. *Journal of Natural Science Research* 3(13) 20-31
- Benkhelil, J. 1988. Structure Et Evolution Geodynamique De basis Intercontinental De Ca Benoue (Nigeria). *Bulletin des Centres de Recherches Exploration – Production ELF Aquitaine* 1207, 29.
- Büyüksaraç, A., Reiprich, S., Ates, A. 1998. Three-dimensional magnetic model of amphibolite complex in Taskesti area, Mudurnu valley, North-West Turkey. *Journal Of The Balkan Geophysical Society* 1 (3) 44-52.
- Büyüksaraç, A., Jordanova, D., Ates, A., Karloukovski, V. 2005. Interpretation of the Gravity and Magnetic Anomalies of the Cappadocia Region, Central Turkey. *Pure Applied Geophysics* 162, 2197–2213.
- Clerc, M. 1999. The swarm and the queen: towards a deterministic and adaptive, particle swarm optimization. *The Proceedings of International Conference on Evolutionary Computing, Washington* 1951–1957.
- Couto, M. A., Aisengart, T., Barbosa, D., Ferreira, R. C. R., Baltazar, O. F., Marinho, M., Cavalcanti, A. D., Araujo, J. C. S. 2017. Magnetization-Vector Inversion, Application in quadrilatero Ferrifero region, MG, Brazil. 15<sup>th</sup> International Congress of the Brazil Geophysical Society, Rio de Janeiro, Brazil.
- Dobrin, M. B., Savit, C. H. 1988. Introduction to geophysical prospecting. McGraw-Hill Book Co. 867.
- Eshaghzadeh, A., Seyedi Sahebari, S., Dehghanpour, A. 2020. 3D inverse modeling of the gravity field due to a chromite deposit using the Marquardt's algorithm and forced neural network. *Bulletin of the Mineral Research and Exploration* 161, 33-47.
- Essa, K. S., Munsch, M. 2019. Gravity data interpretation using the particle swarm optimization method with application to mineral exploration. *Journal of Earth System Science* 128, 123.
- Essa, K. S., Elhussein, M. 2020. Interpretation of magnetic data through particle swarm optimization: Mineral exploration cases studies. *Natural Resources Research* 29, 521–537.
- Essa, K. S., Abo-Ezz, E. R. 2021. Potential field data interpretation to detect the parameters of buried geometries by applying a nonlinear least-squares approach. *Acta Geodaetica et Geophysica* 56, 387 – 406.
- Essa, K. S., Nady, A. G., Mostafa, M. S., Elhussein, M. 2018. Implementation of potential field data to depict the structural lineaments of the Sinai Peninsula, Egypt. *Journal of African Earth Sciences* 147, 43–53.
- Essa, K. S., Mehanee, S., Elhussein, M. 2021. Magnetic Data Profiles Interpretation for Mineralized Buried Structures Identification Applying the Variance Analysis Method. *Pure and Applied Geophysics* 178, 973–993.
- Eze, L. C., Mamah, L. I. 1985. Electromagnetic, and Ground Magnetic survey, over zones of Lead-Zinc Mineralization in Wanakom (Cross River State). *Journal of Earth sciences* 7, 749.
- Ezema, P. O., Doris, E. I., Ugwu, G. Z., Abdullahi, U. A. 2014. Hydrocarbon and mineral exploration in Abakaliki, southeastern-Nigeria. *The International Journal of Engineering and Science* 3(1), 24-30.
- Ford, S. O. 1981. The Economic Mineral Resources of the Benue-Trough. *Earth Evolution Sciences* 2, 154-163.
- Ganguli, S. S., Singh, S., Das, N., Maurya, D., Pal, S. K., Rama Rao, J. V. 2019. Gravity and magnetic survey in south western part of Cuddapah Basin, India and its implication for shallow crustal architecture and mineralization. *Journal of Geological Society of India* 93(4) 419-430.
- Ganguli, S. S., Pal, S. K., Kumar, S. K. P. 2021. Insights into the crustal architecture from the analysis of gravity and magnetic data across Salem-Attur Shear Zone (SASZ), Southern Granulite Terrane (SGT), India: an evidence of accretional tectonics. *Episodes* 44(4) 419 – 422.
- GSNA, 2004. Mineral resources map of Nigeria. Geological-Survey of Nigeria Agency(GSNA).
- Huang, L., Guan, Z. 1998. Discussion on Magnetic-interpretation using the 3-D analytic signal,

- by Walter R. Roest, Jacob Verhoef, and Mark Pilkington *Geophysics* 63, 667–670.
- Jain, S. 1988. Total magnetic field reduction—The Pole or Equator? A model study. *Canadian Journal of Exploration Geophysics* 24 (2) 185–192
- Kennedy, J., Eberhart, R. 1995. Particle-swarm optimization. *The Proceedings of IEEE Conference on Neural Networks*, Piscataway, NJ 1942–1948.
- Kowalczyk, P., Oldenburg, D., Phillips, N., Nguyen, T. H., Thomson, V. 2010. Acquisition and analysis of the 2007–2009 geosciences BC-airborne data. *The Australian, SEG-PESA Airborne, Gravity Workshop*.
- Kumar, S., Pal, S. K., Guha, A., Sahoo, S. D., Mukherjee, A. 2020. New insights on Kimberlite emplacement around the Bundelkhand Craton using integrated satellite-based remote sensing, gravity, and magnetic data. *Geocarto International* 37 (4) 999 – 1021.
- Leão-Santos, M., Li, Y., Moraes, R. 2015. Application of 3D-magnetic amplitude inversion, to iron oxide-copper-gold deposits, at low magnetic latitudes: A case-study from Carajas Mineral Province, Brazil. *Geophysics* 80(2) B13 – B22.
- Lelievre, P. G. 2003. Forward modeling and inversion of geophysical magnetic data. A master's thesis submitted to The University of British Columbia.
- Leu, L. K. 1981. Use of reduction-to-the-equator process for magnetic data interpretation. *Geophysics* 47, 445.
- Li, X. 2003. On the use of different methods for estimating magnetic depth. *Leading Edge* 22, 1090–1099.
- Li, Y., Sun, J. 2016. Geology-differentiation with uncertainty estimation using inverted-magnetization directions. *SEG International Exposition and 86th Annual Meeting* 2159
- MacLeod, I. N., Ellis, R. G. 2013. Magnetic vector inversion a simple approach to the challenge of varying direction of rock magnetization. *ASEG-PESA 2013. 23rd International Geophysical Conference and Exhibition, 11-14 August 2013-Melbourne, Australia*.
- Mahmoodi, O., Smith, R. S., Spicer, B. 2016. Using constrained, inversion of gravity and magnetic-field to produce a 3D litho-prediction model. *SEG Inter. Exposition and 86th Annual Meeting* 2170 – 2174.
- Mehanee, S., Essa, K. S., Diab, Z. E. 2021. Magnetic data interpretation using a new R-parameter imaging method with application to mineral exploration: *Natural Resources Research* 30, 77–95.
- Melo, A. T., Sun, J., Li, Y. 2015. Geophysical-inversions applied to geological differentiation, and deposit characterization: A case study at an IOCG deposit in Carajás-Mineral-Province, Brazil. *85th Annual International Meeting, SEG, Expanded Abstracts 2012–2016*.
- Nabighian, M. N. 1972. The analytic signal of two-dimensional magnetic bodies with polygonal cross-section: its properties and use for automated anomaly interpretation. *Geophysics* 37, 507–517
- NGA, 2004. *GM-SYS Gravity/Magnetic Modeling Software*. Northwest Geophysical Associates, Inc., USA.
- Nwachukwu, S. O. 1972. The Tectonic Evolution of the Southern Portion of the Benue Trough, Nigeria. *Geological Magazine* 109, 411-419.
- Obande, G. E., Lawal, K. M., Ahmed, L. A. 2014. Spectral analysis of aeromagnetic data for geothermal investigation of Wikki Warm Spring, north-east Nigeria. *Geothermics* 50, 85–90.
- Obarezi, J. E., Nwosu, J. I. 2013. Structural Controls, of Pb-Zn Mineralization, of Enyigba District, Abakaliki, Southeastern Nigeria. *Journal of Geology and Mining Research* 5 (11) 250-261.
- Ofoegbu, C. O. 1985. A review of the Geology of the Benue Trough, Nigeria, *Journal of African Earth Science* 3, 283.
- Oha, I. A., Onuoha, K. M. 2013. Contrasting Styles of Pb-Zn-Ba Mineralization in the Lower Benue Trough, Southern Nigeria. A paper presented at the 49th Annual International Conference and Exhibitions of the Nigerian Mining and Geosciences Society (NMGS), Ibadan, March 2013.
- Olade, M. A. 1975. Evolution of Nigeria's Benue-Trough (Aulacogen): A tectonic model. *Geological Magazine* 112, 575–581.
- Omada, J. I., Ike, E. C. 1996. On the Economic Appraisal and Genesis of the Barite Mineralization and Saline Springs in the Middle-Benue-Trough, Nigeria. *Journal of Mineralogy, Petrology and Economic Geology* 91,109-115
- Ovat, O. O. 2015. Obubra yesterday, today, and tomorrow: An assessment of the economic development of a local government area in Cross River State, Nigeria. *Journal of Economic and Sustainable Developments* 6 (20) 78 – 86.
- Pallero, J. L. G., Fernandez-Martinez, J. L., Bonvalot, S., Fudym, O. 2015. Gravity inversion and uncertainty assessment of basement relief via Particle Swarm Optimization. *Journal of Applied Geophysics* 116,180–191.
- Pilkington, M. 2009. 3D magnetic data-space inversion with sparseness constraints. *Geophysics* 74 (1) PL7-L15.

- Pilkington, M., Bardossy, Z. 2015. DSIM3D: software to perform unconstrained-3D-inversion of magnetic data. Geological Survey of Canada.
- Press, W. H., Teukolsky, S. A., Vetterling, W. T., Flannery, B. P. 1994. Numerical Recipes in FORTRAN. Cambridge University Press, New Delhi.
- Reid, A. B., Thurston, J. B. 2014. The structural index in gravity and magnetic interpretation: Errors, uses, and abuses. *Geophysics* 79, J61-J66.
- Reid, A. B., Allsop, J. M., Grauser, H., Millet, A. J., Somerton, I. N. 1990. Magnetic interpretation in 3D using Euler-Deconvolution. *Geophysics* 55, 80-91
- Riedel, S. 2008. Airborne-Based geophysical investigation in Dronning Maud land Antarctica. Dissertation, Christian Albrechts Universitat Zu Kiel, Kiel.
- Roest, W. R., Verhoef, J., Pilkington, M. 1992. Magnetic interpretation using the 3D analytic signal. *Geophysics* 57 (1) 116-125.
- Sacchi, M. D., Ulrych, T. J. 1995. High-resolution velocity gathers and offset space reconstruction: *Geophysics* 60, 1169–1177.
- Salem, A., Ravat, D., Smith, R. S., Ushijima, K. 2005. Interpretation of magnetic data using an enhanced local wave number (ELW) method. *Geophysics* 70, L7–L12.
- Srivardhan, V., Pal, S. K., Vaish, J., Kumar, S., Bharti, A. K., Priyam, P. 2016. Particle swarm optimization inversion of self-potential data for depth estimation of coal reserves over East Basuria colliery, Jharia coal field, India. *Environmental Earth Sciences* 75(8) 1-12.
- Srivastava, S., Agarwal, B. N. P. 2010. Inversion of the amplitude of the two-dimensional analytic signal of the magnetic anomaly by the particle swarm optimization technique. *Geophysical Journal International* 182, 652-662.
- Srivastava, S., Pal, S. K., Rajwardhan, K. 2020. A time-lapse study using Self-Potential and Electrical Resistivity Tomography methods for mapping of old mine working across railway-tracks in a part of Raniganj Coalfield, India. *Environmental Earth Sciences* 79, 332.
- Stocco, S., Godio, A., Sambuelli, L. 2009. Modelling and compact inversion of magnetic data: A Matlab code. *Computers and Geosciences* 35, 2111–2118
- Thompson, D. T. 1982. Eulph: A new technique, for making computer-assisted, depth- estimates, from magnetic data, *Geophysics* 47, 31-37
- Thurston, J. B., Smith, R. S. 1997. Automatic conversion of magnetic data to depth, dip, and susceptibility contrast using the SPITM method. *Geophysics* 62, 807–813.
- Ugwu, G. Z., Alasi, T. K. 2016. Aeromagnetic Survey for Determining Depth, to Magnetic Source of Abakaliki and Ugep Areas, of the Lower Benue Trough, Nigeria. *Engineering and Technology Journal* 1(1) 18 – 31.
- Whitehead, N., Musselman, C. 2005. Montaj Gravity/Magnetic interpretation: Processing, analysis, and visualization system, for 3-D inversion of potential field data, for Oasis montaj v6.1. Geosoft Inc. ON, Canada.
- Yao, C. 2007. Iterative 3-D gravity and magnetic inversion for physical properties. SEG/San Antonio 2007 Annual meeting 805 – 810.





# Bulletin of the Mineral Research and Exploration

<http://bulletin.mta.gov.tr>



## Paleocene-Eocene foraminifera from the Tuz Gölü Basin (Salt Lake Basin, Central Türkiye) and their paleoenvironmental interpretations

Muhittin GÖRMÜŞ<sup>a\*</sup>, Mustafa YILDIZ<sup>b</sup>, Alper BOZKURT<sup>c</sup> and Aynur HAKYEMEZ<sup>c</sup>

<sup>a</sup> Ankara University, Engineering Faculty, Geological Engineering Department, Ankara, Türkiye

<sup>b</sup> Aksaray University, Engineering Faculty, Geological Engineering Department, Aksaray, Türkiye

<sup>c</sup> General Directorate of Mineral Research and Exploration (MTA), Department of Geological Research, Ankara, Türkiye

Research Article

Keywords:

Paleocene, Eocene,  
Foraminifera, Central  
Türkiye.

### ABSTRACT

Paleocene-Eocene aged sediments from the east of Tuz Gölü Basin (Central Türkiye) provide significant data for foraminifera contents and their paleoenvironmental clues. They are important in revealing the stratigraphy of the region and the Paleocene-Eocene geological history of Türkiye. The sediments, composed mainly of carbonates, are known as Karapınaryaylası Formation. In this formation, benthic foraminifera representing SBZ2 to SBZ12 biozones corresponding to the Selandian-Late Cuisian time interval were identified in ten measured stratigraphical sections. The zonal interval from the E7 Zone (late Ypresian) to the E10 Zone (Lutetian) is characterized by the marker species of planktonic foraminifera defined in the clayey limestones from the uppermost part. The studied formation is divided into four main facies and eleven sub-microfacies types. The clayey limestone levels of the Karapınaryaylası Formation, which generally starts with a transgressive sequence, contain abundant planktonic foraminifera, while the lithologies of grainstone, packstone and wackestone are rich in benthic foraminifera. Benthic foraminifer assemblages indicate different paleoenvironments from lagoon to back-bank, bank and fore-bank. The obtained foraminiferal data show the Selandian-Lutetian age range and various paleoenvironments from the lagoon to the open sea.

Received Date: 06.09.2022

Accepted Date: 30.03.2023

## 1. Introduction

Kırşehir Block is located to the east of the graben basin known as the Tuz Gölü Graben (the Salt Lake) in the Central Anatolia Region and bounded by the Tuz Gölü Fault in the east of Tuz Gölü (Koçyiğit, 2000) (Figure 1). Two different study areas are near to the Tuzgölü Fault Zone in the southwest of the Kırşehir Block. The first area is approximately 20 square kilometres, including Elmakayası and Delikönü Hill, approximately 9 kilometres west of Aksaray, to the east of Tuz Gölü in the Kırşehir Block. The second is

about 12 square kilometres around Musular Hill, 16 kilometres far from the Aksaray city to the southeast (Figures 2-3).

Paleogene sediments in the area contain abundant amounts of different larger and smaller foraminifera. As it is known, Paleocene (66-56 Ma) and Eocene (56-33.9 Ma) Periods are the periods that play an important role in the explanation of the Cenozoic geological history with their benthic foraminifera contents. The Paleocene and Eocene Periods comprise benthic foraminiferal biozones and contents (i.e. Serra-Kiel et. al., 1998; Consorti and Schlagintweit, 2022).

Citation Info: Görmüş M., Yıldız M., Bozkurt A., Hakyemez A. 2024. Paleocene-Eocene foraminifera from the Tuz Gölü Basin (Salt Lake Basin, Central Türkiye) and their paleoenvironmental interpretations. Bulletin of the Mineral Research and Exploration 173, 107-151. <https://doi.org/10.19111/bulletinofmre.1268147>

\*Corresponding author: Muhittin GÖRMÜŞ, [mhtngrms@gmail.com](mailto:mhtngrms@gmail.com)

Although some studies particularly for the tectonics, sedimentology and hydrogeology of the Kırşehir Block and the Tuz Gölü Basin were presented in the symposiums held on (e.g. Derman and Tekin, 2000), detailed age data and paleoenvironments of Paleocene and Eocene sediments based on foraminiferal content are not well documented.

Only one research around Asmayaylası was carried out on the findings of planktonic foraminifera and particularly nannofossils from the Asmaboğazı and Karapınaryaylası formations by Yıldız (2000). She recorded the ages of the formations based on the following microorganisms: *Chiasmolithus danicus*, *Elpsolithus macellus*, *Fasciculithus tympaniformis*, *Heliolithus kleinpellii*–nannofossils and *Morozovella uncinata*, *M. angulata*, *Planorotalites pusilla*–

foraminifera in the Asmaboğazı Formation, Danian to Selandian in age; *Fasciculithus tympaniformis*–nannofossil, *Morozovella trinidadensis*, *Planorotalites compressa*, *Globigerina* sp., *Kathina selveri*, *Smoutina crysi*, *Miscellenea* sp., *Textularia* sp., Miliolidae and other microfossils in the Karapınaryaylası Formation, Selandian-Thanetian in age.

This study provides new detailed important data for the Karapınaryaylası Formation on both benthic and planktonic foraminifera, the Paleogene stratigraphy and geological history of the studied region. For this reason, biostratigraphic and environmental interpretations and approaches to geological history based on both larger and smaller benthic and planktonic foraminifera contents in the investigated areas were aimed in this study.

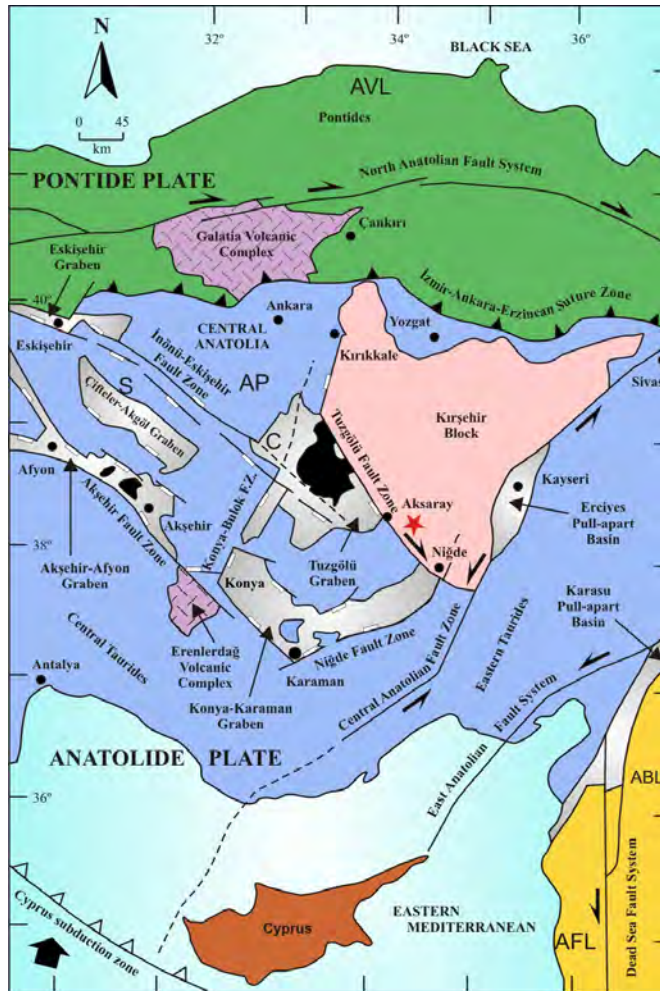


Figure 1- Location of the study area (red star) within the Kırşehir Block (re-drawn from Koçyiğit, 2000), A.P. Anatolian Plate, ABL. Arabian Plate, AFL. African Plate, AVL: Eurasia Plate, C. Cihanbeyli, S. Sivrihisar.

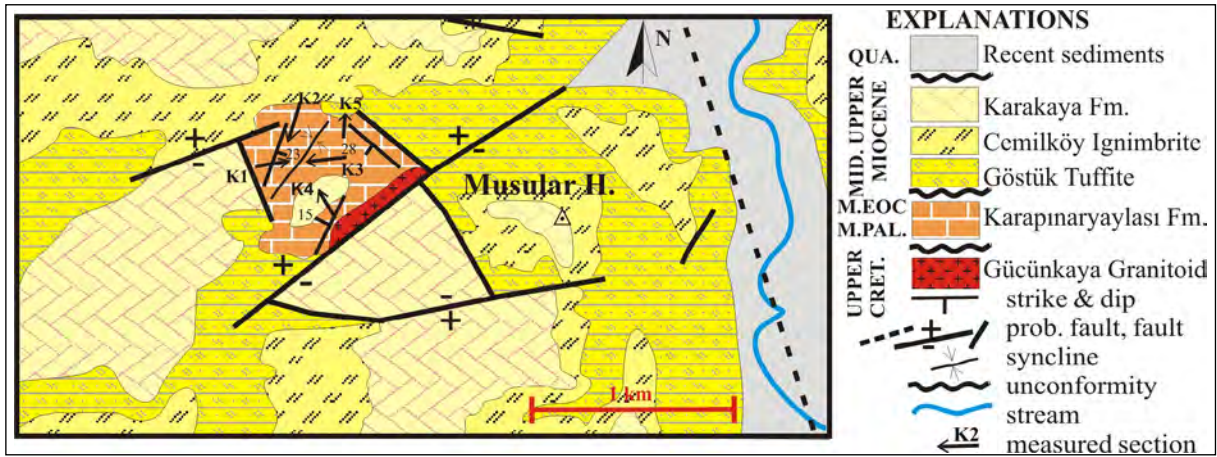


Figure 2- Geological map of the Musular Hill and its surrounding area, and measured section locations, CRET. Cretaceous, M.PAL. Middle Paleocene, M.Eoc. Middle Eocene, MID. Middle, QUA. Quaternary, Fm. Formation.

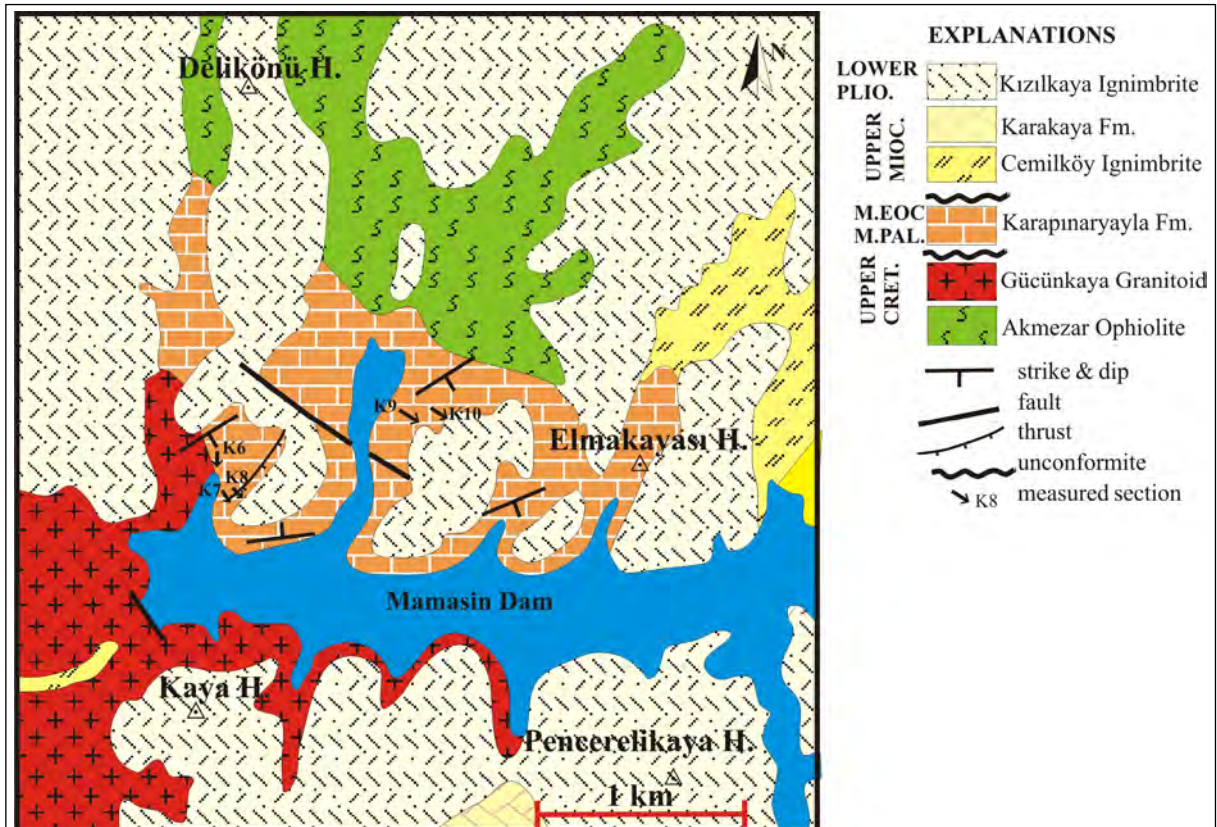


Figure 3- Geological map of the Elmakayası and Delikönü Hills and their surrounding area, and measured section locations. H. Hill, CRET. Cretaceous, M.PAL. Middle Paleocene, M.EOC. Middle Eocene, MIOC. Miocene, PLIO. Pliocene, Fm. Formation, Blue shows the water column of the Mamasin Dam.

## 2. Material and Method

Palaeocene-Eocene deposits were investigated by field studies carried out in the study areas. A total of ten stratigraphical sections were measured, five in the vicinity of Musular Hill and five in the vicinity of Elmakayası-

Delikönü area. Measured section thicknesses are between 20 and 55 meters (m). Laboratory studies were carried out at the Ankara University and MTA General Directory. Petrographic thin sections were taken from the collected hard rock samples. These samples were examined under the research microscope, and their

foraminifera contents were determined. Planktonic foraminifera were defined from thin sections because the washing processes carried out on hard limestones did not yield any better results. Postuma (1971) and Premoli Silva et al. (2003) are mainly followed for taxonomic analyses of planktonic foraminifera.

### 3. Stratigraphy

The geological maps and stratigraphical sequences in the studied areas are shown in Figures 2-3. The stratigraphical sequence can be summarised from bottom to top as follows: The Akmezar Ophiolite appears as basement rocks (Yıldız and Kalkan, 2018). These basement rocks are cut by the Gücünkaya Granitoid (Güllü and Yıldız, 2012). The Karapınaryaylası Formation overlies unconformably the basement rocks. It is composed of siliciclastic and carbonate sedimentary rocks, the Paleocene-Eocene in age. The relationship between the Paleogene deposits and its overlying middle-upper Miocene units namely as Göstük Tuffites, the Cemilköy Ignimbrite and Karakaya Formation is unconformable. The Pliocene-aged Kızılkaya Ignimbrite and Recent sediments observed towards the top are the youngest geological units (Figures 2 and 3). The subject of this study is only Paleocene-Eocene Karapınaryaylası Formation deposits. For this reason, the stratigraphic sequence has been considered as basement rocks, Paleocene-Eocene sediments and cover rocks.

#### 3.1. Basement Units

Ophiolites known as the Akmezar ophiolite (Yıldız and Kalkan, 2018) are located in the basement and crop out between Elmakayası and Delikönü hills. The Gücünkaya Granitoid outcrops in the northwest of Kale Tepe, west of Mamasin Dam. In the literature, the ages of these units are given as Late Cretaceous (Dirik and Erol, 2000; Güllü and Yıldız, 2012). Upper Cretaceous Asmaboğazı Formation has been aged as Paleocene by Yıldız (2000). Although this unit is not seen in the studied areas, it is known as the unit under the Paleocene-Eocene sediments (Yıldız, 2000).

#### 3.2. Paleocene-Eocene Sediments

Karapınaryaylası Formation was named for the first time by Dellaloğlu and Aksu (1984) from

Karapınaryaylası Village. The same name was also used by Oktay and Dellaloğlu (1987), Dellaloğlu (1991) and Yıldız (2000). The formation was reported with different age ranges and different names in different parts of the Central Anatolia Region. For example, Paleocene-aged sections are called Kırkkavak formation in the Haymana-Polatlı basin, and Eocene sediments are named Eskipolatlı formation (Görür and Derman, 1978; Derman, 1980). The unit crops out in a limited area in the northwest of Musular Hill in the Musular area and in the northern part of the Mamasin Dam in the Elmakayası-Delikönü area (Figures 2 and 3). The sequence starts with coarse to medium-grained siliciclastic sediments at the bottom. The thickness of the clastic layers at the base varies between 10-25 m. Medium, thick-bedded, red-coloured coarse and medium-grained clastics also contain mudstone intercalations. Towards the upper part of the formation, limestones are observed on the conglomerates and sandstones. The thickness of the limestones seen at the top of the Karapınaryaylası Formation is between 20 and 55 m. The upper limestones present lateral transitions or facies changes with red clayey limestones. Sandy and silty limestones are also observed at intermediate levels. It is stated that the Karapınaryaylası Formation overlies the Asmaboğazı Formation in the north of Aksaray (Yıldız, 2000). However, different rock unconformities are seen in the investigation areas. The unit's initiation with red-coloured clastics and the fact that the clastics contain pebbles of the underlying units indicates the presence of a distinct unconformity or with a differentiated rock as a nonconformity. Miocene-aged volcanoclastic units overlie the unit unconformably. Angular differences and age differences are clear. The formation has been aged as Selandian around Asmayaylası by Yıldız (2000).

In this study, the following benthic and planktonic foraminifera were identified, benthic foraminifera: *Alveolina* (*Alveolina*) cf. *acari* Bozkurt and Görmüş, *A. (A.)* aff. *avsari* Sirel and Acar, *A. (A.) barattoloi* Sirel and Acar, *A. (A.) corbarica* Hottinger, *A. (A.)* cf. *dolioliformis* Schwager, *A. (A.)* cf. *erki* Acar, *A. (A.)* cf. *laxa* Hottinger, *A. (A.) levantina* Hottinger, *A. (A.) violae* Checchia-Rispoli, *Ankaraella minima* Sirel, *Asterigerina rotula* (Kaufmann), *Gypsina*

*marianensis* Hanzawa, *Haymanella* cf. *elongata* Sirel, *H.* cf. *paleocenica* Sirel, *Idalina sinjarica* Grimsdale, *I.* cf. *causae* Sirel, *I.* cf. *grelaudae* Gallardo-Garcia and Serra-Kiel, *I.* cf. *pignatti* Gallardo-Garcia and Serra-Kiel, *Kayseriella decastroi* Sirel, *Lockhartia* cf. *conditi* (Nuttall), *L. haimeii* Davies, *Mississippiina binkhorsti* Reuss, *Orbitolites* cf. *complanatus* Lamarck, *Parahaymanella bozkurti* Acar, *Rotalia trochidiformis* (Lamarck), *Sphaerogypsina globula* (Reuss), *Triloculina tricarinata* (d'Orbigny), *T. angulata* Karrer, *Alveolina (Alveolina)* sp., *Amphistegina* sp., *Assilina* sp., *Asterigerina* sp., *Cribrobulimina* sp., *Discocyclina* sp., *Elazigina* sp., *Gyroidinella* sp., *Haymanella?* sp., *Heterostegina?* sp., *Lockhartia* sp., *Nummulites* sp., *Orbitolites* sp., *Opertorbitolites* sp., *Parahaymanella* sp., *Peneroplis* sp., *Quinqueloculina* sp., *Rotalia* sp., *Soriella?* sp., *Spiriloculina* sp., *Thalmanita* sp. According to the identified benthic foraminifer fossil findings, the age is Selandian-late Cuisian. Planktonic foraminifera contents are as follows: *Acarinina bullbrooki* (Bolli), *A. boudreauxi* Fleisher, *A. praetopilensis* (Blow) and *A. pseudosubspheerica* Pearson and Berggren; *Guembeltrioides nuttalli* (Hamilton), *Globigerinatheka kugleri* (Bolli, Loeblich and Tappan), *G. index* (Finlay) and *G. mexicana* (Cushman), towards to upper part *Guembeltrioides nuttalli* (Hamilton), *Morozovelloides bandyi* (Fleisher), *Pearsonites broedermanni* (Cushman and Bermudez), *Acarinina boudreauxi* Fleisher, *Acarinina pseudosubspheerica* Pearson and Berggren and *Turborotalia pomeroli* (Toumarkine and Bolli) were found. Based on the planktonic foraminiferal data, the age of the upper part of the formation is from Cuisian to Lutetian. Evaluation of all foraminiferal data shows that the age of the formation is from Selandian to Lutetian. Levels with small miliolids and alveolins indicate the back-reef paleoenvironment while rich nummulites show near the nummulit bank or fore bank deposits. Clayey carbonate deposits with rich planktonic foraminifera are from an open marine paleoenvironment.

### 3.3. Cover Rocks

Generally, horizontal volcanoclastic rocks are observed on the Paleocene-Eocene deposits. From bottom to top, these are the Middle-Upper

Miocene Göstük Tuffites, the Cemilköy Ignimbrite, the Karakaya Formation, the Pliocene Kızılkaya Ignimbrite and the Recent deposits (Figures 2-4).

## 4. Foraminiferal Contents and Biostratigraphy

Musular Hill and Elmakayası Hill and their surroundings are remarkable with their rich foraminifera contents (Figure 4). The figures 5-16 show foraminiferal distributions of ten measured sections and their correlations. The figures 17-18 indicate range distribution of some important benthic foraminifera and the zonal markers of the shallow benthic zones. Plate I to IX illustrates the foraminiferal content. The list of foraminiferal contents of the Karapınaryaylası Formation was presented above within the stratigraphy section. Considering the stratigraphical distributions of foraminifera, SBZ2 to SBZ12 biozones defined by Serra-Kiel et. al. (1998, 2020) were determined. In addition, planktonic foraminifers representing the E7-E10 planktonic biozones were also defined from thin sections. The biozone explanations are summarized as follows:

### 4.1. SBZ 2 (Selandian)

SBZ 2 was identified in K6 measured section (Figure 11). This biozone is characterized by the assemblage consisting of *Ankaraella minima*, *Kayseriella decastroi* and *Parahaymanella bozkurti* in the study area (Plate III, Figures 5-8, 17, 21). Although Sirel (1998) first reported *Kayseriella decastroi* from Danian, this species has been reported in Danian to Selandian beds by some later researchers (e.g., Ogorelec et al., 2001; Sirel, 2018). Finally, Serra-Kiel et al. (2020) defined this species as an index form of SBZ2 biozone. In addition, Acar (2019) indicated that the species *Ankaraella minima* and *Parahaymanella bozkurti* known from the Selandian are also significant species of SBZ2 biozone. Other associated miliolid fauna such as *Idalina causae*, *I. sinjarica* ranges to Thanetian and Ypresian (Serra-Kiel et al., 1998; Özgen-Erdem, 2008; Özgen-Erdem et al., 2016; Sirel, 2018; Bozkurt and Görmüş, 2021).

### 4.2. SBZ 3-4 (Thanetian)

These biozones were identified in K6 measured section (Figure 11). *Idalina causae*, *I. sinjarica* were

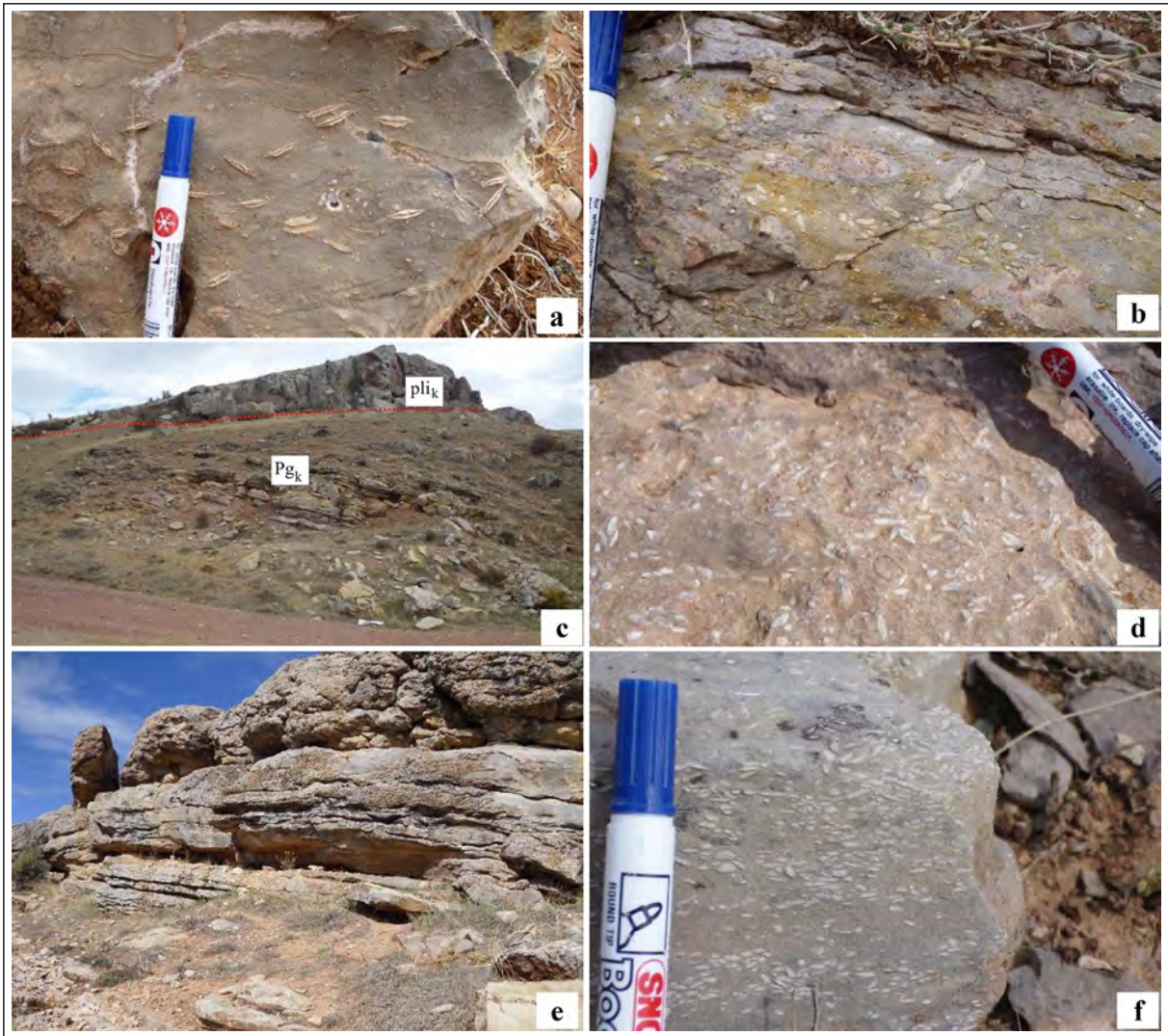


Figure 4- Field views of the Karapınaryaylası Formation, a) Nummulitid forms, b) Alveolinid forms, c) Delikönü Hill, K6 measured section (Pgk. Karapınaryaylası Fm., plik. Kızılkaya ignimbirite), d) Alveolinid forms, Elmakayası, K9 measured section, e) Carbonates (Musular, K5 measured section ), f) Alveolinid forms (K5 measured section).

seen in this zone of sediments (Plate II, Figures 22-23). Associated fauna is mainly smaller miliolids in wackestone lithology. The first appearances of *Lockhartia conditi* and *L. haimei* are reported as SBZ 3 and SBZ 4 by Serra-Kiel et al. (1998) and Hottinger (2014). However, these forms in our study were observed in the younger levels at the measured section 1 (Figure 5).

#### 4.3. SBZ 5-8 (Early - Middle Ilerdian)

SBZ 5-8 interval were identified in the K1, K3, K5 and K10 measured-sections (Figures 5, 7, 9, 15). These biozones were generally determined by species of the genus *Alveolina*. In the literature, it is known

that *A. (A.) acari*, *A. (A.) avsari*, *A. (A.) corbarica*, *A. (A.) dolioliformis*, *A. (A.) erki*, *A. (A.) laxa* range from SBZ 5 to SBZ 9 biozones (Serra-Kiel et al., 1998; Sirel and Acar, 2008; Özgen-Erdem, 2008; Bozkurt and Görmüş, 2021). Determination of the SBZ 5-7 in the K1 section (Figure 5) mainly relies on the occurrences of the species of *Lockhartia* (Figure 5; Plate VII, Figures 10-11). The time interval that *Lockhartia conditi* and *L. haimei* are found together corresponds to SBZs 4-7 (Figure 17). Other accompanying taxa in this section limit the age to be younger than SBZ 4 (Figure 5). In the K3 section (Figure 7), the *Alveolina* species, which were identified as *Alveolina* sp., resemble the Ilerdian forms. No species of the

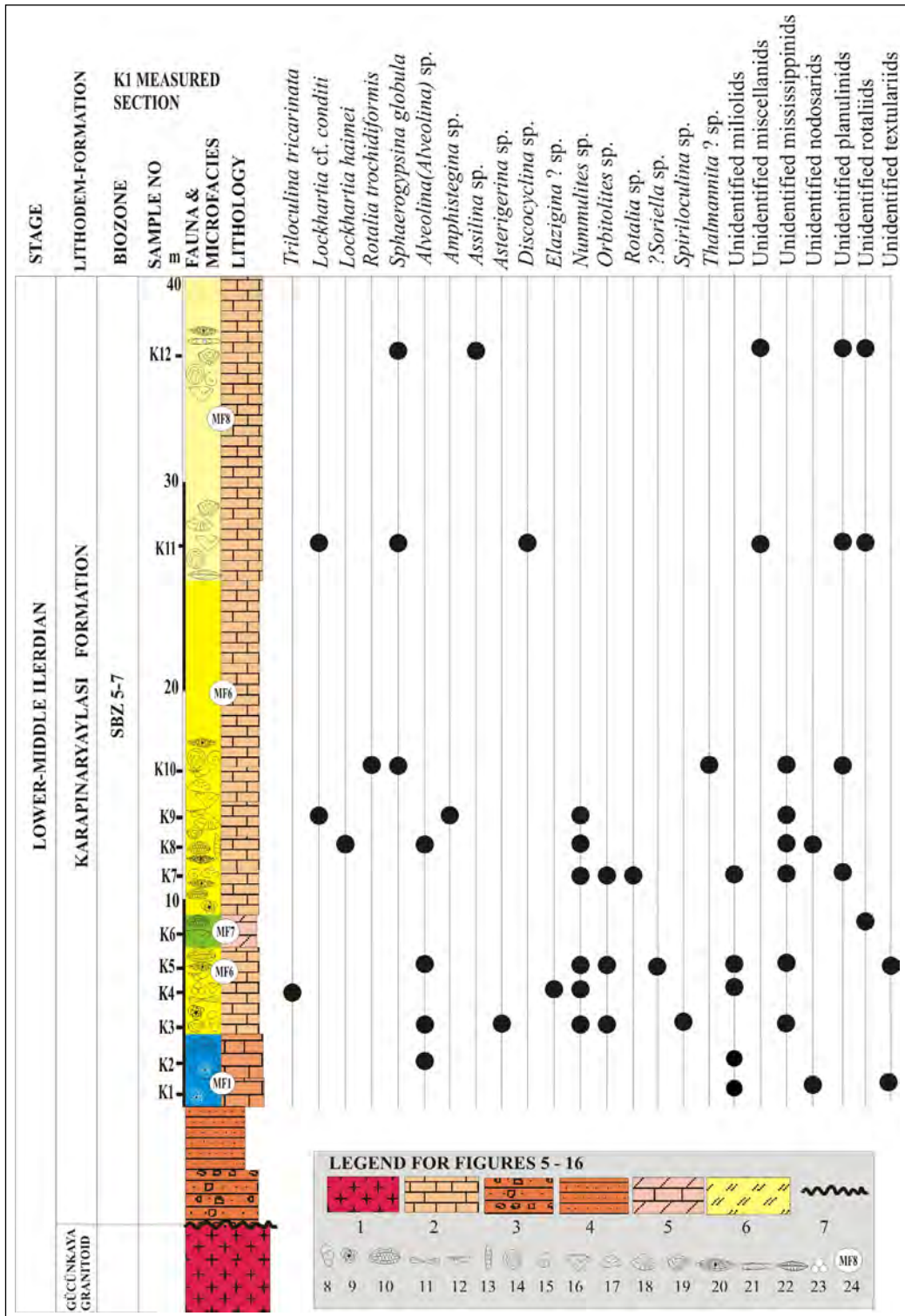


Figure 5- Measured Section 1 (K1) around the Musular Hill. 1. Granitoid, 2. Limestone, 3. Conglomerates, 4. Sandstones, 5. Limestone, dolomitic limestone, 6. Volcanoclastics, 7. Unconformity, 8. Textulariids, 9. Miliolids, 10. *Alveolina* sp., 11. *Orbitolites* sp.-*Operorbitolites* sp., 12. Mississippinids, 13. Nodosariids, 14. *Sphaerogypsina* sp., 15. *?Gyroidinella* sp., 16. Rotaliids, 17. *Rotalia* sp., 18. *Loekhartia* sp., 19. Miscellenid-rotaliids, 20. *Nummulites* sp., 21. *Assilina* sp., 22. *Discocyclina* sp., 23. Planktonic foraminifera, 24. Microfacies type.

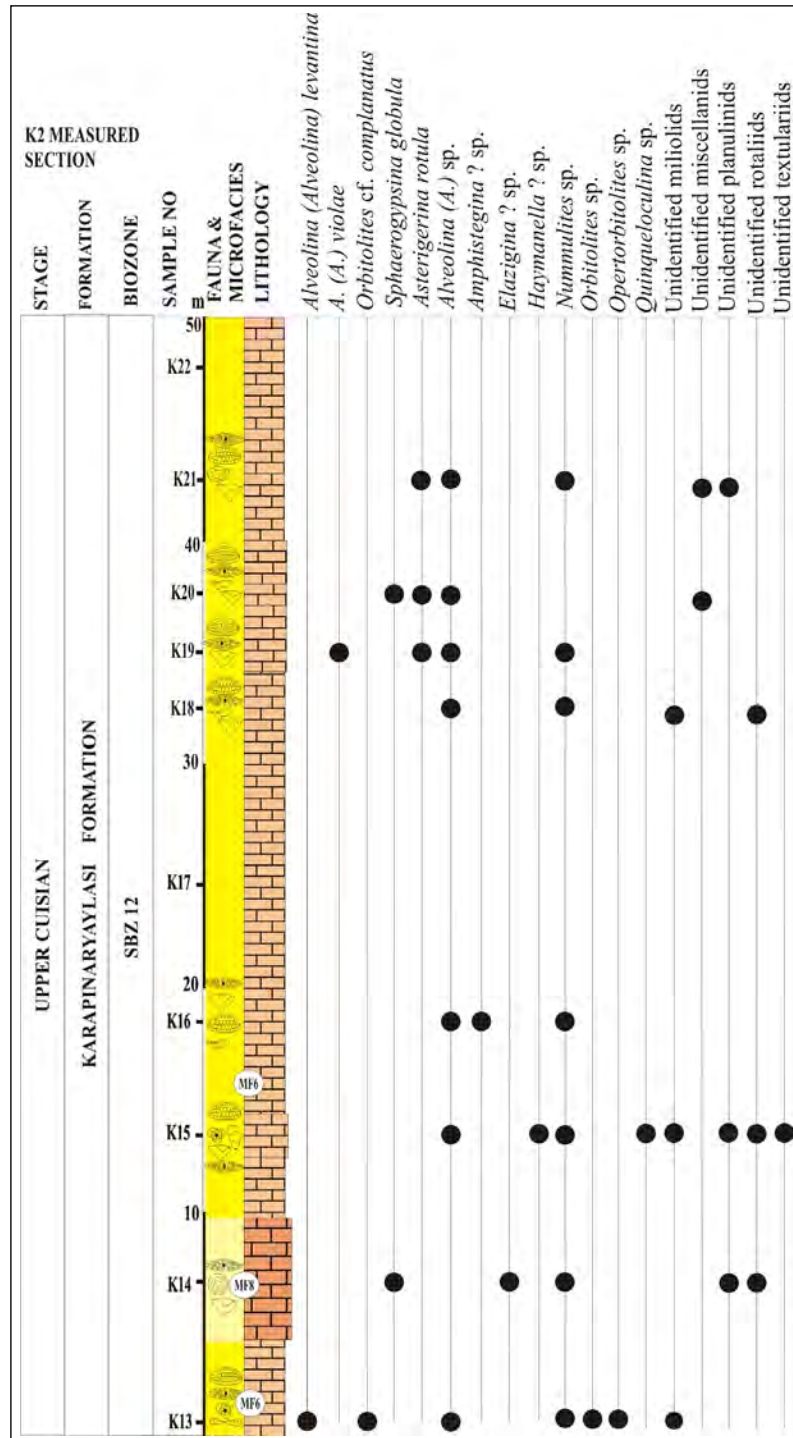


Figure 6- Measured Section 2 (K2) around the Musular Hill, see Figure 5 for legend.

subgenus *Alveolina* (*Alveolina*) is known from SBZ 3. Other larger benthic foraminifera determined in this section (e.g. *I. sinjarica*) offer that the age of this section should be older than late Ilerdian. In the K4 section (Figure 8), *Alveolina* species such as *A. (A.) cf. acari* (Plate IV, Figure 9) and *A. (A.) cf. laxa* (Plate

V, Figure 4) mark the SBZ 7 in the upper levels of the section. *A. (A.) corbarica* (Plate IV, Figures 3-4) and *A. (A.) cf. dolioliformis* (Plate IV, Figure 1) are the markers determining SBZ 7-8 biozones in K5 and K10 sections (Figures 9 and 15). Particular levels of some other sections examined in this study (such as

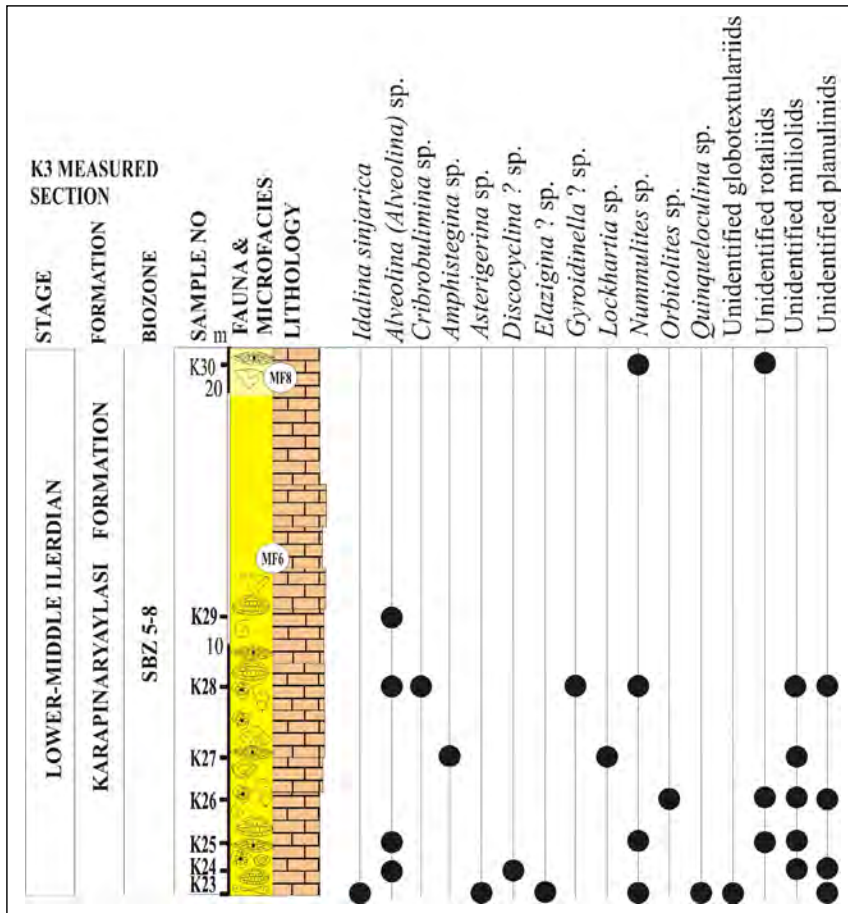


Figure 7- Measured Section 3 (K3) around the Musular Hill, see Figure 5 for legend.

upper parts of K6 and lower parts of K7 sections) indicate Ilerdian age with their benthic foraminiferal assemblages, yet not provide biozones (Figures 11 and 12).

#### 4.4. SBZ 10-12 (Cuisian)

SBZ 10-11 interval was mainly determined based on the occurrences of *Alveolina (Alveolina) barattoloi* (Figure 12; Plate IV, Figure 8). Sirel and Acar (2008) described *A. (A.) barattoloi* from SBZ 10 and the lower part of SBZ 11. In the K7 section of the study area, this species is also associated by *A. (A.)* aff. *avsari* (Figure 12; Plate V, Figure 11). In the K2 section (Figure 6), *A. (A.) levantina* (Plate IV, Figure 11) and *A. (A.) violae* (Plate IV, Figure 13) were the index taxa that define SBZ 12 (Figure 6). Serra-Kiel et al. (1998) report the biostratigraphical range of *A. (A.) levantina* from the upper part of SBZ11 to the end of SBZ12. Some researchers also suggest a wide range for this

species extending from SBZ11 to the lower part of SBZ 15 (Hottinger 1974; Drobne 1977; Serra-Kiel et al., 2016). In addition, Serra-Kiel et al. (1998) give the species *A. (A.) violae* as an index form of SBZ12.

#### 4.5. Zones E7-E10 (late Ypresian-Lutetian)

The lower part of the K8 section between samples K75-K78 contains rare and less diverse planktonic foraminifera (Figure 13). *Acarinina bullbrookii*, *A. boudreauxi*, *A. praetopilensis* and *A. pseudosubphaerica* in the assemblage (Plate IX, Figures 14-15, 19-21, 25-27, 31, 39-41, 42-43, 45-46) are the marker species of the E7 Zone (Berggren et al., 2006). The presence of *Guembeltrioides nuttalli* in K79 and *Globigerinatheka kugleri*, *G. index*, *G. mexicana* in K81 (Plate IX, Figures 6, 10) indicates the E8 and E9 zones, respectively (Berggren and Pearson, 2005; Premoli Silva et al., 2006; Wade et al., 2011). Samples K81-K83 in the upper part of the



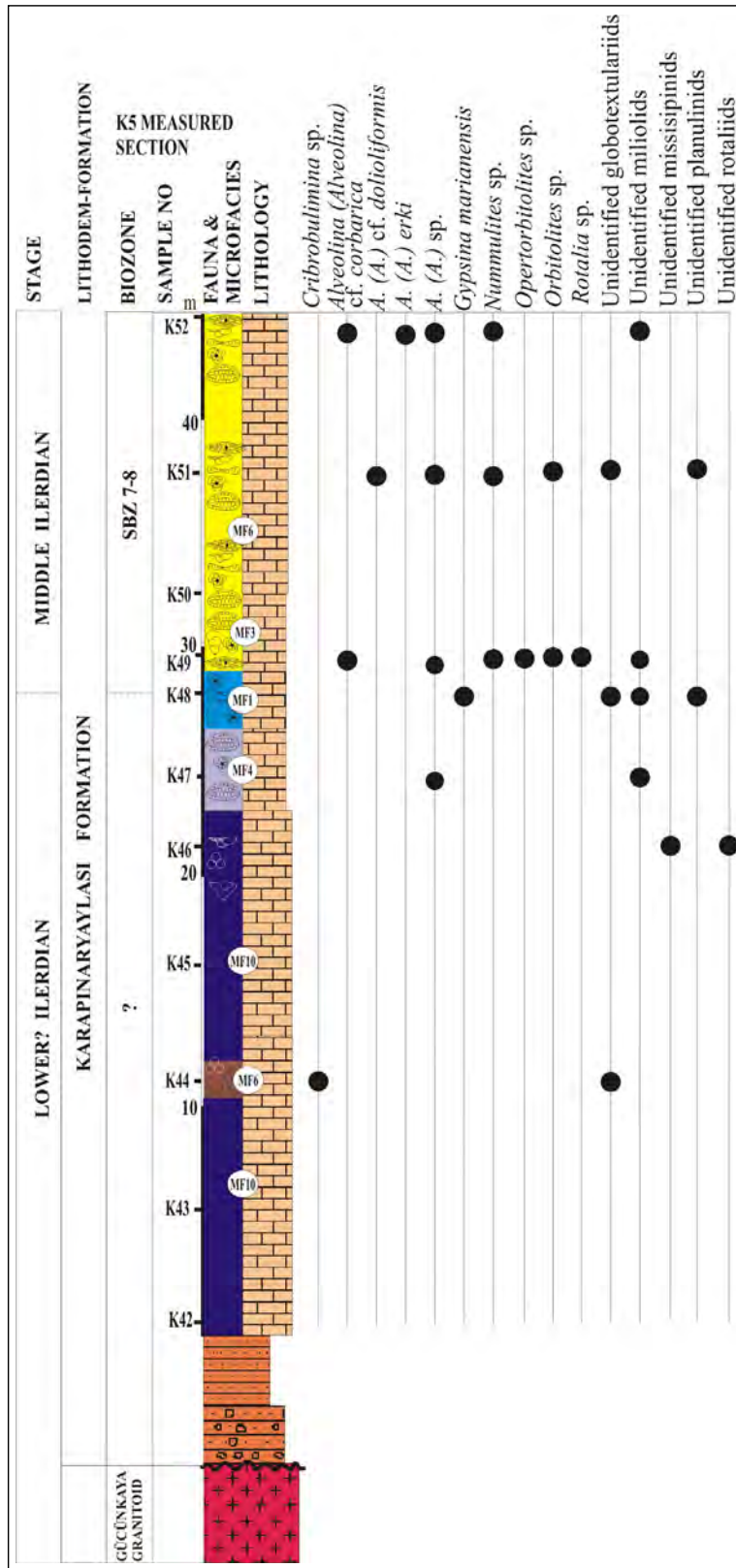


Figure 9- Measured Section 5(K5) around the Musular Hill, see Figure 5 for legend.

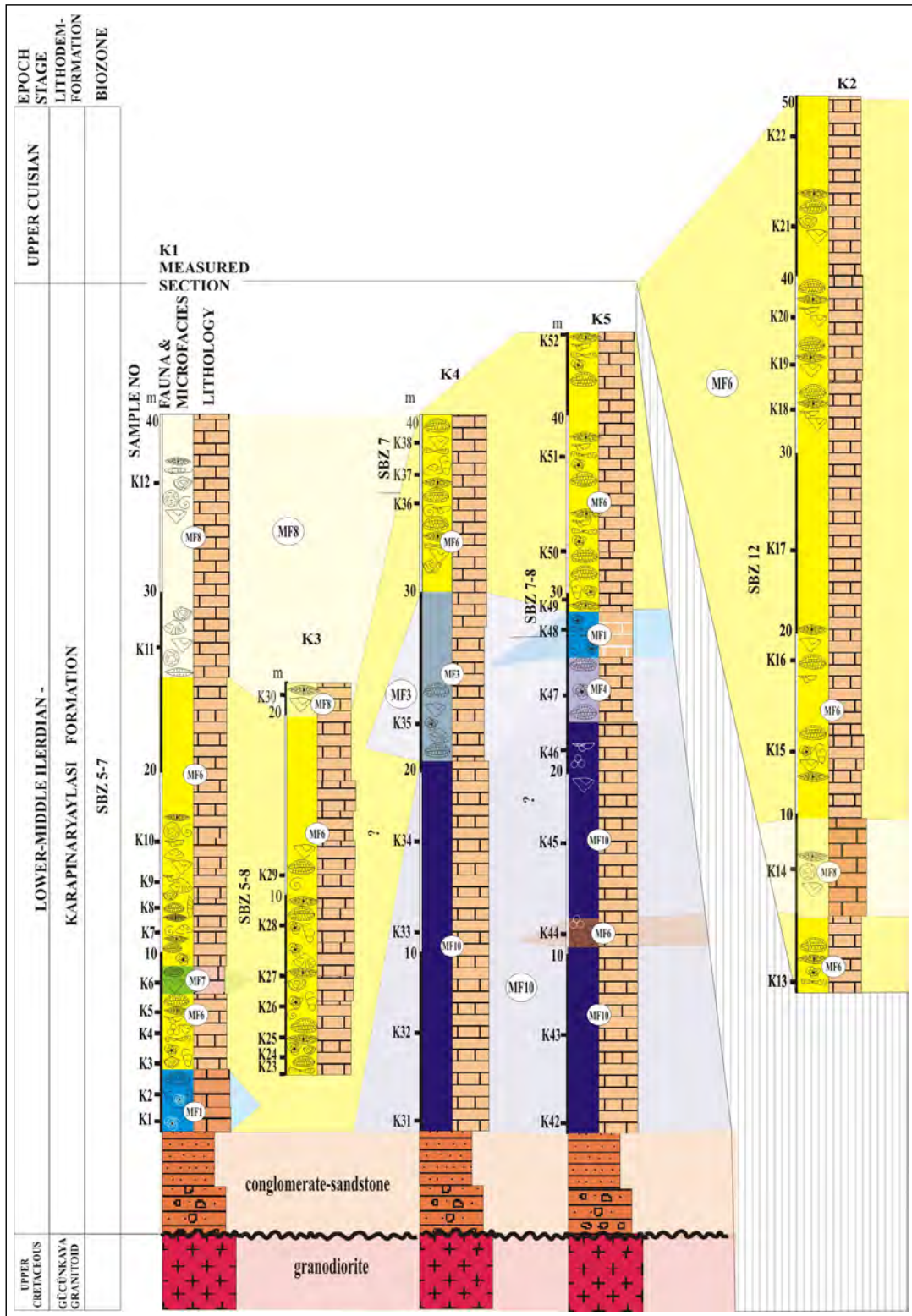


Figure 10- Correlation of measured sections around the Musular Hill, see Figure 5 for legend.

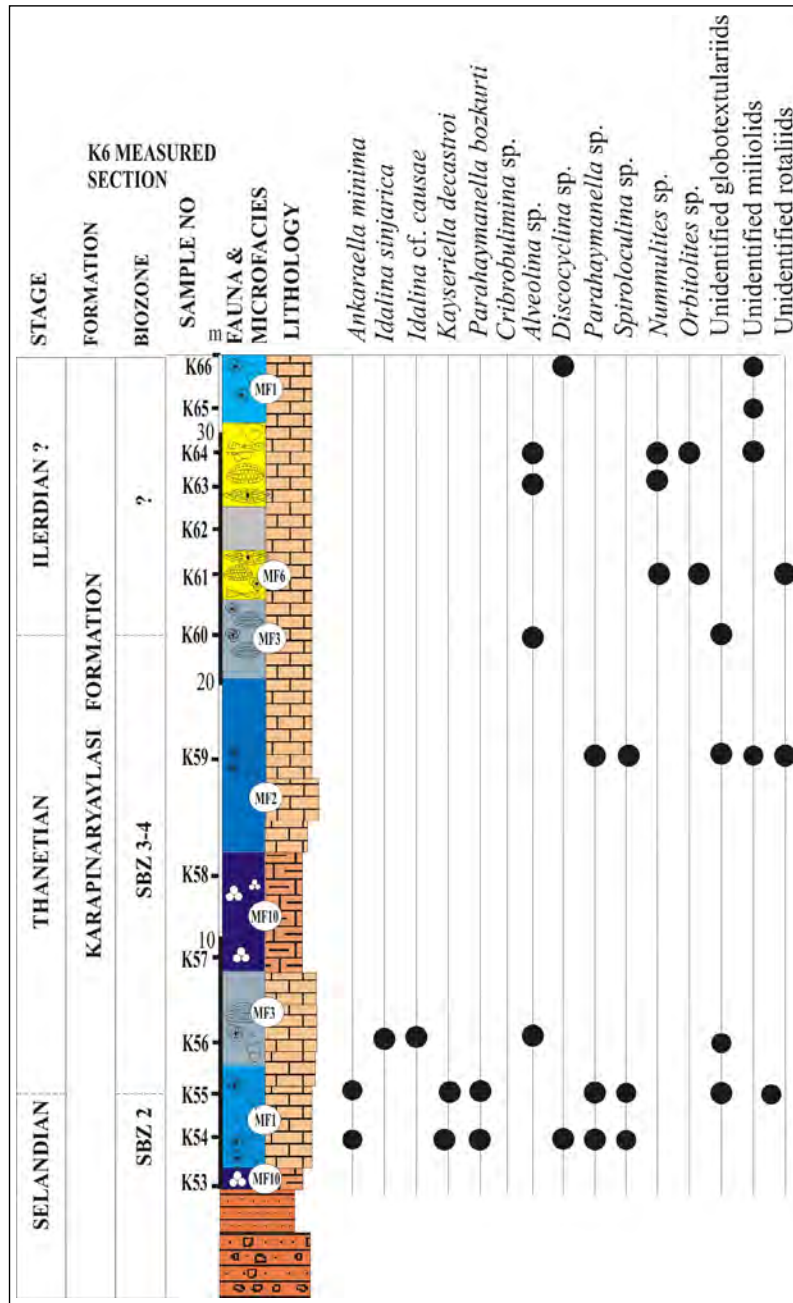


Figure 11- Measured Section 6 (K6) around Elmakayasi, see Figure 5 for legend.

section are represented by more abundant and diverse planktonic foraminiferal assemblages, including *Guembeltrioides nuttalli*, *Morozovelloides bandyi*, *Pearsonites broedermanni*, *Acarinina boudreauxi*, *Acarinina pseudosubspaeica* and *Turborotalia pomeroli* (Plate IX, Figures 7-8, 17, 34-36, 39, 41-42, 45-46, 48) and can be correlated with E9-E10 zones (Pearson et. al., 2006).

Benthic foraminiferal assemblage obtained in the section 9 cannot provide biozonation (Figure 14). However, the assemblage containing species such as *Idalina cf. grelaudae* (Plate II, Figure 5) and *Rotalia trochidiformis* suggests an interval of Ypresian-Lutetian.

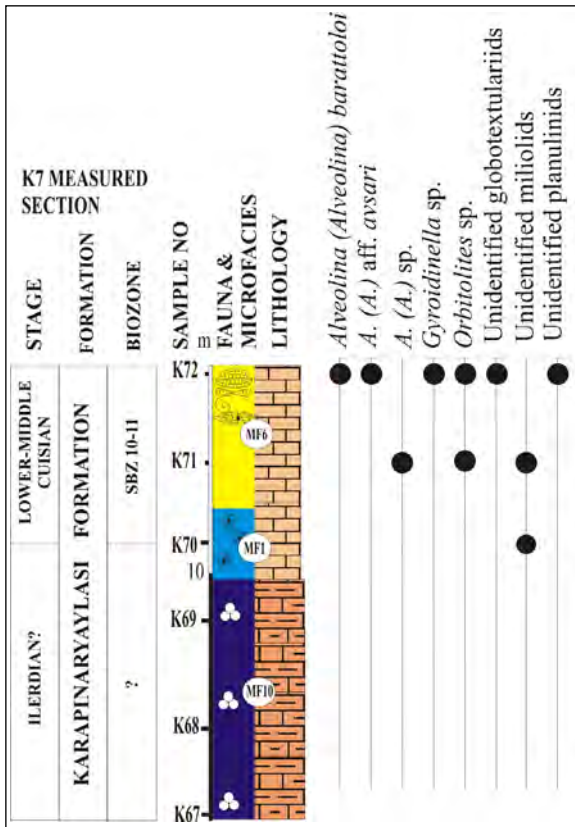


Figure 12- Measured Section 7 (K7) around Elmakayası, see Figure 5 for legend.

## 5. Microfacies and Paleoenvironmental Interpretations

The studied succession, which starts with siliciclastic rocks over the Gücünkaya Granitoid in the measured sections K1, K4 and K5, continues upwards with carbonate rocks in the Musular area (Figure 10). In sections K2 and K3, only carbonate rocks were measured. In the measured sections around the Elmakayası, the Gücünkaya Granitoid are only seen at the base of the K9 section (Figure 16). In the measured sections of K6, K9 and K10, the Karapınaryaylası Formation begins with siliciclastic rocks and continues with carbonates. In the measured sections of K9 and K10, Kızılkaya Ignimbrites unconformably cover the Karapınaryaylası Formation. The microfacies that can be identified in the Karapınaryaylası Formation deposits have lateral and vertical relationships with each other in both studied areas. The carbonate succession of the formation is divided into 4 main microfacies according to the dominant fossil contents and lithological features. These are miliolid-dominated

wackestone-packstone-grainstone (MMF1), miliolid-rotaliid-dominated wackestone-packstone (MMF2), and rotaliid-dominated wackestone-packstone (MMF3) and planktonic foraminifera dominated wackestone facies (MMF4) (Figure 19).

It is observed that these differentiated microfacies begin with lagoonal facies on the clastic deposits around Musular Tepe and pass upwards to shallow carbonate platform deposits dominated by rotaliid forms. In the vicinity of Elmakayası, it is observed that lagoonal and shallow facies have lateral and vertical facies that change each other. In this second area, the facies accompanied by planktic foraminiferous predominance indicate open marine paleoenvironment. The facies thicknesses are variable, and it has been revealed that facies containing miliolids and facies containing rotaliids are the most observed facies. In facies definitions, Dunham's (1962) nomenclature was used together with the dominant or important fossil groups and the lithological features. The general features and interpretations of identified main facies and subfacies can be summarized as follows:

### 5.1. Microfacies 1: Miliolid-dominated wackestone-packstone-grainstone facies (MMF1)

In these determined lithofacies, miliolids are the predominant fossil group within the various carbonate matrix. This facies is divided into five sub-facies within itself, and the explanations about the sub-facies are as follows:

#### 5.1.1. Smaller miliolid-dominated packstone-grainstone sub-facies (MF1)

Benthic foraminifers with a porcellaneous test, usually smaller than 2 mm, are common in a sparitic cement (Plate X, Figure 1-2, 13-14). It is usually grain-supported.

*Interpretation:* Miliolid dominance indicates the presence of a lagoonal environment (Hallock and Glenn, 1986; Armstrong and Brasier, 2005).

#### 5.1.2. Miliolid-textulariid dominated packstone sub-facies (MF2)

These facies, in which usually textulariid and small miliolid forms are observed together, are not very



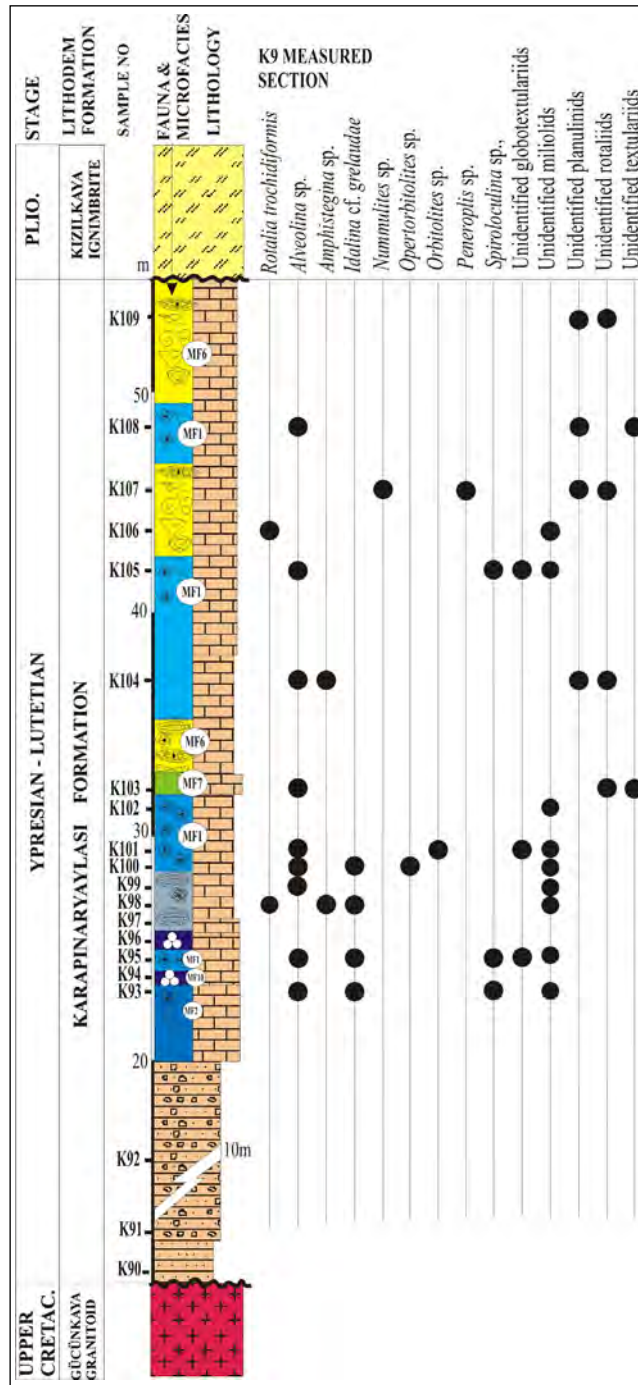


Figure 14- Measured Section 9 (K9) around Elmakayası, see Figure 5 for legend.

5.1.5. *Wackestone-packstone sub-facies containing less textulariid sub-facies (MF5)*

Facies which are not much common, are observed at mud-containing levels (Plate X, Figure 6). A small percentage of textulariid forms are seen between 2-5%.

*Interpretation:* Agglutinant-walled foraminifers refer to environments ranging from shallow to offshore environments (Armstrong and Brasier, 2005). These facies deposits have lateral relations with other miliolid-bearing facies. For this reason, it is thought that it was deposited in a shallow marine environment.

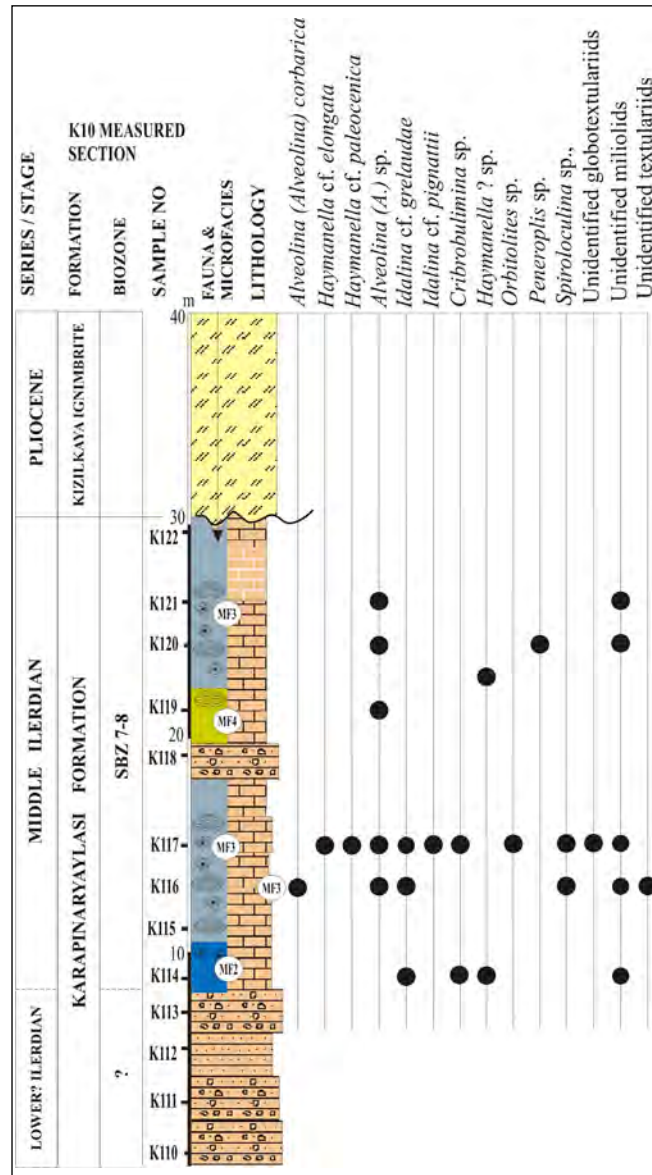


Figure 15- Measured Section 10 (K10) around Elmakayasi, see Figure 5 for legend.

5.2. Microfacies 2: Miliolid-rotaliid, dominated wackestone-packstone facies (MMF2)

In these determined lithofacies, miliolid and rotaliid forms are almost equal proportions. This facies only includes one sub-facies identified as MF6.

5.2.1. Alveolinid and nummulitid-dominated wackestone-packstone sub-facies (MF6)

In these determined lithofacies, miliolid and rotaliids are almost equal proportions (Plate X, Figure 7). Alveolinid and nummulitid forms are observed

together. Forms up to a few cm in size are in micritic cement.

*Interpretation:* The co-occurrence of nummulitids and alveolinids was interpreted as open-shelf lagoons (Amirshahkarami and Zebarjadi, 2018). Geel (2000) emphasized that this fossil association can be seen at depths of 50-80 m. It is seen that these facies, in which alveolinid and nummulitids are observed together, are close to the nummulite sets.



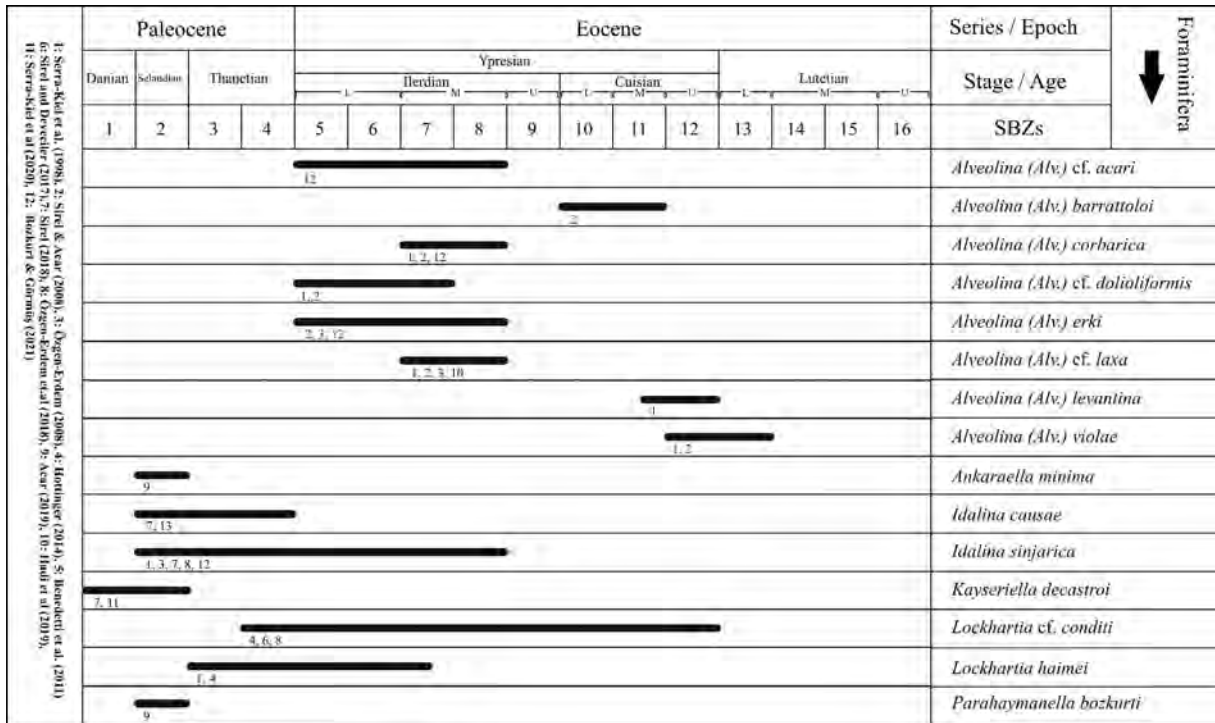


Figure 17- Range distribution of some important benthic foraminiferal species used in this study (Numbers located under the black lines indicate related literature in the box at the left, in which that age was assigned).

System	Series	Stage	Numerical Age (Ma)	Shallow Benthic Zones (SBZ)	Benthic Foraminiferal Species			
					Serra-Kiel et al (1998)	This study		
Paleogene	Eocene	Ypresian	47.8	SBZ 12	<i>Alveolina (Alveolina) violae</i> , <i>A.(A.) rakoveci</i> , <i>A.(A.) azzaroli</i> , <i>A.(A.) cuspidata</i> , <i>Nummulites manfredi</i> , <i>N. angularis</i> , <i>N. campestris</i> , <i>N. quasilaevigatus</i> , <i>N. caupennensis</i> , <i>Assilina maior</i> , <i>Ass. civillieri</i>	<i>Alveolina (Alveolina) barratoloi</i> , <i>A.(A.) levantina</i> , <i>A.(A.) violae</i>		
				SBZ 11	<i>Alveolina (Alveolina) dainelli</i> , <i>A.(A.) aff. canavarii</i> , <i>A.(A.) histrica histrica</i> , <i>A.(A.) decastroi</i> , <i>A.(A.) eremae</i> , <i>Nummulites praelaevigatus</i> , <i>N. hardigalensis contabricsus</i> , <i>N. kapellasi</i> , <i>N. escheri</i> , <i>N. nitidus</i> , <i>N. archiaci</i> , <i>Assilina laxispina</i> , <i>Discocyclina fortisi simferopolensis</i>			
				SBZ 10	<i>Alveolina (Alveolina) schwageri</i> , <i>A.(A.) indicatrix</i> , <i>A.(A.) canavarii</i> , <i>A.(A.) costinensis costinensis</i> , <i>A.(A.) haymanensis</i> , <i>A.(A.) minuta</i> , <i>Nummulites planulatus</i> , <i>N. aquitanicus</i> , <i>N. rotularius</i> , <i>N. hardigalensis hardigalensis</i> , <i>N. subramondi thalmani</i> , <i>N. pavloveci</i> , <i>N. subdistans</i> , <i>Assilina plana</i> , <i>Ass. placentula</i> , <i>Ass. aspensis</i> , <i>Ass. karreeri</i> , <i>Ass. escheri</i> , <i>Discocyclina archiaci archiaci</i>			
				Ypresian	52.5	SBZ 9	<i>Alveolina (Alveolina) trampina</i> , <i>A.(A.) ciltrea</i> , <i>A.(A.) polatiensis</i> , <i>Nummulites involutus</i> , <i>Assilina adriensis</i> , <i>Ass. pomeroli</i>	<i>Alveolina (Alveolina) aff. ucari</i> , <i>A.(A.) cf. avsari</i> , <i>A.(A.) cf. corbarica</i> , <i>A.(A.) cf. dolioformis</i> , <i>A.(A.) cf. erki</i> , <i>A.(A.) cf. laxa</i>
						SBZ 8	<i>Alveolina (Alveolina) corbarica</i> , <i>A.(A.) recundita</i> , <i>A.(A.) brassica</i> , <i>Nummulites exilis</i> , <i>N. ataticus</i> , <i>N. globulus namus</i> , <i>N. globulus latior</i> , <i>Assilina leymertei</i> , <i>Ass. canalifera</i>	
						SBZ 7	<i>Alveolina (Alveolina) moussoulenensis</i> , <i>A.(A.) subpyrenatica</i> , <i>A.(A.) laxa</i> , <i>A.(A.) dedolita</i> , <i>Nummulites robustiformis</i> , <i>N. carcasonensis</i> , <i>N. praecursor</i> , <i>N. oblatius</i> , <i>Assilina iranensis</i> , <i>Orbitolites schopeni nenuminae</i>	
	SBZ 6	<i>Alveolina (Alveolina) ellipsoidalis</i> , <i>A.(A.) daniensis</i> , <i>A.(A.) pasticillata</i> , <i>A.(A.) solida</i> , <i>Nummulites minervensis</i>						
	SBZ 5	<i>Orbitolites gracilis</i> , <i>Daviesina tenuis</i> , <i>Alveolina (Alveolina) vredenburgi</i> , <i>A.(A.) avellana avellana</i> , <i>A.(A.) aramea aramea</i> , <i>A.(A.) varians</i> , <i>Nummulites gamardensis</i> , <i>Assilina dandotica</i> , <i>Ass. prisca</i>						
	Paleocene	Thanetian	56.0			SBZ 4	<i>Alveolina (Glomulveolina) levis</i> , <i>Hottingeria lukasi</i> , <i>Miscellanea meandrina</i> , <i>Daviesina garumensis</i> , <i>Dicyokathina simplex</i> , <i>Nummulites catari</i> , <i>Assilina azilensis</i> , <i>Ass. yvettae</i>	
				SBZ 3	<i>Alveolina (Glomulveolina) primueva</i> , <i>Periloculina slovenica</i> , <i>Coskimon rujkae</i> , <i>Fallotella ulavensis</i> , <i>Cribrbulimina carnolica</i> , <i>Vania anatolica</i> , <i>Miscellanea yvettae</i> , <i>Ranikothalia bermudezi</i> , <i>Discocyclina seunest</i> , <i>Nummulites heberti</i>			
				SBZ 2	<i>Miscellanea globularis</i> , <i>Ornatononion minutus</i> , <i>Paralockhartia eos</i> , <i>Lockhartia akbari</i>			
			Selandian	59.2	SBZ 2		<i>Kayseriella decastroi</i> , <i>Ankaraella minima</i> , <i>Parahaymanella bozkurti</i>	
			61.6					

Figure 18- A table illustrating both the zonal markers of some shallow benthic zones (SBZs) and the taxa used in this study to define biozones.

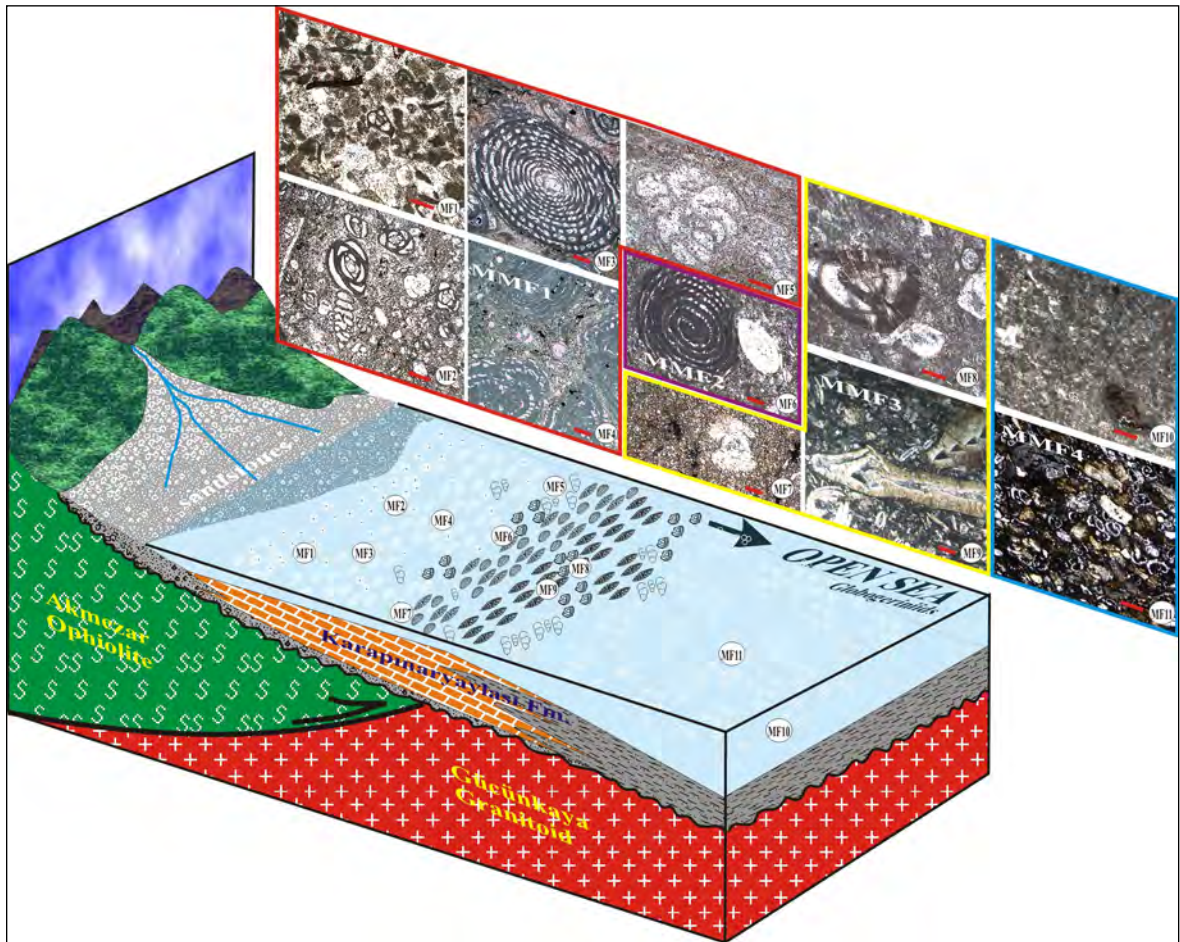


Figure 19- A schematic block diagram of the facies identified from the Karapınarayaylası Formation, MMF1. Miliolid-dominated wackestone-packstone-grainstone facies, MMF2. Miliolid-rotaliid, dominated wackestone-packstone facies, MMF3. Rotaliid-dominated wackestone-packstone facies, MMF4. Planktonic foraminifera-dominated wackestone, MF1. Smaller miliolid-dominated packstone-grainstone sub-facies, sample no 1; MF2. Miliolid-textulariid dominated packstone sub-facies, sample no 93; MF3. Alveolinid and other smaller miliolid-dominated packstone sub-facies, sample no 117; MF4. Alveolinid dominated packstone sub-facies, sample no 47; MF5. Wackestone-packstone sub-facies containing less textulariid, sample no 44; MF6. Alveolinid and nummulitid-dominated wackestone-packstone sub-facies, sample no 50; MF7. Less rotaliid bearing silty mudstone sub-facies, sample no 6; MF8. Rotaliid dominated wackestone-packstone sub-facies, sample no 11; MF9. Packstone containing *Nummulites*, *Assilina* and *Discocyclus*, sample no 73; MF10. Less planktonic foraminiferous mudstone sub-facies, sample no 56; MF11. Wackestone sub-facies with rich planktonic foraminifera, sample no 81, depth is unscaled, scale shows 200  $\mu$ . textulariids, smaller miliolids, alveolinids, rotaliids, nummulitids, planktonic foraminifera.

### 5.3.2. Rotaliid-dominated wackestone-packstone sub-facies (MF8)

Wackestones and packstones are dominated by rotaliid forms, and a few mm-sized rotaliids are dominant (Plate X, Figure 9).

*Interpretation:* Medium-sized rotaliids are common, and are thought to be near the nummulit bank, fore-bank or back-bank. Hallock and Glenn (1986) also mention the presence of medium-sized rotaliids shows open platform deposits.

### 5.3.3. Packstone containing *Nummulites*, *Assilina* and *Discocyclus* sub-facies (MF9)

The main microfauna of these facies are *Nummulites*, *Assilina* and *Discocyclus*. *Nummulites* and *Assilina* are more common (Plate X, Figure 10).

*Interpretation:* These levels, which include larger-sized *Nummulites*, *Assilina*, and *Discocyclus*, are associated with “nummulit sets”.

#### 5.4. Microfacies 4: Planktonic foraminifera-dominated wackestone (MMF4)

Planktic foraminifers are common in the lithofacies. This facies is divided into two sub-facies within itself.

##### 5.4.1. Less planktonic foraminiferous mudstone sub-facies (MF10)

Planktonic foraminifers are observed in the mudstones at a rate of 1-5% (Plate X, Figure 11).

*Interpretation:* Micritic carbonates are thought to be offshore sediments.

##### 5.4.2. Wackestone sub-facies with rich planktonic foraminifera (MF11)

In these biomicrite facies, in which globigerinid forms are rich (Plate X, Figure 12).

*Interpretation:* The dominance of planktonic foraminifera indicates an open marine environment (Armstrong and Brasier, 2005).

## 6. Conclusions

Paleocene-Eocene aged sediments in the east of Tuz Gölü Basin (Salt Lake, Central Anatolia) are known as the Karapınaryaylası Formation. The formation rests on the basement rocks unconformably. The formation represented by limestones and clayey limestones is rich in both benthic and planktonic foraminifera. In benthic foraminiferal biozonation, which is generally based on *Alveolina* species, it has been determined that the assemblages represent biozones between SBZ 2-12. In addition, it was determined that some levels in pelagic facies that do not contain benthic foraminifera correspond to E8-E10 biozones according to their planktonic foraminifer contents. For this reason, the age range of the formation is Selandian-Lutetian according to the determined species. Four main microfacies and eleven sub-microfacies have been identified. These are small miliolid dominated packstone-grainstone (MF1), miliolid-textulariid dominated packstone (MF2), alveolinid and small miliolid dominated packstone (MF3), alveolinid dominated packstone (MF4), less textulariid-containing wackestone-packstone (MF5),

alveolinid and nummulitid dominated wackestone-packstone (MF6), silty mudstone with less rotaliid (MF7), rotaliid dominated wackestone-packstone (MF8), *Nummulites*, *Assilina*, *Discocyclusina* packstone (MF9), mudstone with less planktonic foraminifera (MF10), and mudstone with rich planktonic foraminifera (MF11). Benthic and planktonic foraminifera descriptions and data obtained from microfacies studies indicate the Selandian-Lutetian age range and environments that developed from the lagoon to the open sea.

## References

- Acar, Ş. 2019. Selandian benthic foraminiferal assemblages of the southwestern Burdur (South of Lake Yarıklı, Western Turkey) and some taxonomic revisions. *Bulletin of the Mineral Research and Exploration* 158, 49-119.
- Amirshahkarami, M., Zebarjadi, E. 2018. Late Paleocene to Early Eocene larger benthic foraminifera biozones and microfacies in Estahbanate area, Southwest of Iran with Thetyan biozones correlation. *Carbonates and Evaporites* 33, 869–884.
- Armstrong, H. A., Brasier, M. D. 2005. *Microfossils*. Second Edition, Blackwell Publishing 305.
- Benedetti, A., Di Carlo, M., Pignatti, J. 2011. New Late Ypresian (Cuisian) Rotallids (Foraminiferida) from central and southern Italy and their biostratigraphic potential. *Turkish Journal of Earth Sciences* 20, 701-719.
- Berggren, W. A., Pearson, P. N. 2005. A revised tropical to subtropical Paleogene planktonic foraminiferal zonation. *Journal of Foraminiferal Research* 35, 279–298.
- Berggren, W. A., Pearson, P. N., Huber, B. T., Wade, B. S., 2006. Taxonomy, biostratigraphy, and phylogeny of Eocene Acarinina. In: Pearson P.N., Olsson R.K., Huber B.T., Hemleben C., Berggren W. A., (Eds.) *Atlas of Eocene planktonic foraminifera*. Cushman Foundation for Foraminiferal Research, Special Publication 41, 257-326.
- Bozkurt, A., Görmüş, M., 2021. Systematics, biostratigraphy and paleoenvironmental investigation of early Ypresian *Alveolina* assemblages in the northern part of Isparta Angle (Keçiborlu, Isparta, SW Turkey). *Bulletin of the Mineral Research and Exploration* 164, 183-229.
- Consorti, L., Schlagintweit F. 2022. Taxonomy and paleoecology of the Maastrichtian-Paleogene benthic foraminifer *Valvulineria orali* (Inan, 2003) comb. nov. *Journal of Mediterranean Earth Sciences* 14, 1-9.

- Dellaloğlu, A. A. 1991. Ankara-Temelli-Haymana-Kulu-Kırıkkale arasındaki alanine jeolojisi ve petrol olanakları. Türkiye Petrolleri Anonim Ortaklığı Rapor no: 3006, 186 (yayımlanmamış).
- Dellaloğlu, A. A., Aksu, R. 1984. Kulu, Şereflikoçhisar, Aksaray dolayının jeolojisi ve petrol olanakları. Türkiye Petrolleri Anonim Ortaklığı Rapor no: 2020. (yayımlanmamış).
- Derman, A. S. 1980. Tuzgölü doğu ve kuzeyinin jeolojisi. Türkiye Petrolleri Anonim Ortaklığı Rapor no: 1512, 41. (yayımlanmamış).
- Derman, A. S., Tekin, T. 2000. Haymana-Tuzgölü-Ulukışla Basenleri Uygulamalı Çalışma (Workshop), Aksaray Mühendislik Fakültesi, Sedimantoloji Çalışma Grubu, 9-11 Ekim 2000. Türkiye Petrol Jeologları Derneği 5, 217.
- Dirik, K., Erol, O. 2000. Tuzgölü ve civarının tektonomorfolojik evrimi, Orta Anadolu-Türkiye. Haymana-Tuzgölü-Ulukışla Basenleri Uygulamalı Çalışmayı 09-11 Ekim 2000, Bildiriler Kitabı, 23-46.
- Dunham, R. J. 1962. Classification of carbonate rocks according to depositional texture. In: Ham, W.E. (ed.): Classification of carbonate rocks. A symposium. American Association of Petroleum Geologists 1, 108-171.
- Drobne, K. 1977. Alvéolines paléogènes de la Slovénie et de l'Istrie. Mémoires Suisses de Paléontologie 99, 9-174.
- Geel T. 2000. Recognition of stratigraphic sequence in carbonate platform and slope: empirical models based on microfacies analysis of Paleogene deposits in southeastern Spain. Palaeogeography, Palaeoclimatology, Palaeoecology 155, 211-238.
- Görür, N., Derman, A. S. 1978. Tuzgölü-Haymana-Havzası'nın stratigrafik ve tektonik analizi: Türkiye Petrolleri Anonim Ortaklığı Rapor no: 1514, 60. (yayımlanmamış).
- Güllü, B., Yıldız, M. 2012. Gücünkaya (Aksaray) Granitoidinin Jeokimyasal-Petrolojik İncelenmesi, Orta Anadolu / Türkiye, V. Jeokimya Sempozyumu, Pamukkale Üniversitesi Bildiri Kitabı, S, 192-193.
- Hadi, M., Vahidina, M., Abbasi, N. 2019. Ilerdian-Cuisian alveolinids from the western Alborz and eastern Iran zones: systematic and biostratigraphic implications. Journal of Foraminiferal Research 49, 141-162.
- Hallock, P., Glenn, E. C. 1986. Larger Foraminifera: A Tool for Paleoenvironmental Analysis of Cenozoic Carbonate Depositional Facies. Palaios 1 (1), 55-64.
- Hottinger, L. 1974. Alveolinids, Cretaceous-Tertiary Larger Foraminifera. Esso Production Research-European Laboratories, Text and Plate 70.
- Hottinger, L. 2014. Paleogene Larger Rotaliid Foraminifera from the Western and Central Neotethys. Edited by Davide Bassi, Springer International Publishing Switzerland 196.
- Koçyiğit, A. 2000. Orta Anadolu'nun genel neotektonik özellikleri ve deprenselliği. Haymana-Tuzgölü-Ulukışla Basenleri Uygulamalı Çalışmayı, 09-11 Ekim, 2000, Bildiriler Kitabı, 1-26.
- Ogorelec, B., Drobne, K., Jurkovsek, T., Toman, M., 2001. Paleocene beds of the Liburnian Formation in Cebulovica (Slovenia, NW Adriatic Dinaric platform). Ljubljana, Geologija 44 (1), 15-65.
- Oktay, F. Y., Dellaloğlu, A. A., 1987. Tuz Gölü Havzası (Orta Anadolu) stratigrafisi üzerine yeni görüşler. 7. Petrol Kongresi, Bildiriler Kitabı, 312-321.
- Özgen-Erdem, N. 2008. Biostratigraphy of Thanetian-Ileridian benthic foraminifera in the Akçataş – Cebeci (NW Tosya- SE Kastamonu) region. Bulletin of the Mineral Research and Exploration 137, 49-59.
- Özgen-Erdem, N., Canbolat, M. Y., Sinanoğlu, D. 2016. Shallow Marine Benthic Foraminifera Assemblage of the Early Eocene Succession in the Northern Araç (Kastamonu) and Paleocological Interpretation. Geological Bulletin of Turkey 59 (3) 259-273.
- Pearson P. N., Olsson R. K., Huber B. T., Hemleben C., Berggren W. A. (Eds.) 2006. Atlas of Eocene planktonic foraminifera. Cushman Foundation for Foraminiferal Research, Special Publication 41, Fredericksburg, USA.
- Postuma, J. A. 1971. Manual of Planktonic Foraminifera. Elsevier Publishing Company, Amsterdam, 420p.
- Premoli, S. I., Rettori R., Verga D. 2003. Practical Manual of Paleocene and Eocene Planktonic Foraminifera (International School on Planktonic Foraminifera, 2nd Course). University of Perugia, Italy, 152p.
- Premoli, S. I., Wade, B. S., Pearson, P.N. 2006. Taxonomy, biostratigraphy, and phylogeny of *Globigerinatheka* and *Orbulinoides*. In: Pearson P.N., Olsson R.K., Huber B.T., Hemleben C., Berggren W. A., (Eds.) Atlas of Eocene planktonic foraminifera. Cushman Foundation for Foraminiferal Research, Special Publication, 41, 169-212.
- Serra-Kiel, J., Hottinger, L., Caus, E., Drobne, K., Ferrandez, C., Jauhri, A. K., Less, G., Pavlovec, R., Pignatti, J., Samso, J. M., Schaub, H., Sirel, E., Strougo, A., Tambareau, Y., Tosquella, J., Zakrevskaya, E. 1998. Larger foraminiferal biostratigraphy of the

- Tethyan Paleocene and Eocene. Bulletin Société Géologique France 169 (2), 281–299.
- Serra-Kiel, J., Gallardo-Garcia, A., Razin, Ph., Robinet, J., Roger, J., Grelaud, C., Leroy, S., Robin, C. 2016. Middle Eocene-Early Miocene larger foraminifera from Dhofar (Oman) and Socotra Island (Yemen). Arabian Journal of Geosciences 9, 344.
- Serra-Kiel, J., Vicedo, V., Baceta, J. I., Bernaola, G., Robador, A. 2020. Paleocene Larger Foraminifera from the Pyrenean Basin with a recalibration of the Paleocene Shallow Benthic Zones. Geologica Acta 18.8, 1-69, I-III.
- Sirel, E. 1998. Foraminiferal description and biostratigraphy of the Paleocene-Lower Eocene shallow-water limestone and discussion on the Cretaceous-Tertiary boundary in Turkey. Mineral Research and Exploration (MTA), General Directorate, Ankara, Monography Series 2, 1-117.
- Sirel, E. 2018. Revision of the Paleocene and partly early Eocene larger benthic foraminifera of Turkey. Ankara Üniversitesi Yayınları No:559, 200, 60.
- Sirel, E., Acar, Ş. 2008. Description and Biostratigraphy of the Thanetian-Bartonian Glomalveolinids and Alveolinids of Turkey. TMMOB Jeoloji Mühendisleri Odası Yayınları 103 (Chamber of Geological Engineers of Turkey, Publication 103), Scientific Synthesis of the Lifelong Achievement 2, 108, 108.
- Sirel, E., Deveciler, A. 2017. A new late Ypresian species of *Asterigerina* and the first records of *Ornatorotalia* and *Granorotalia* from the Thanetian and Upper Ypresian of Turkey. Rivista Italiana di Paleontologia e Stratigrafia 123 (1), 65-78.
- Wade, B. S., Pearson, P. N., Berggren, W. A., Pälike, H. 2011. Review and revision of Cenozoic tropical planktonic foraminiferal biostratigraphy and calibration to the geomagnetic polarity and astronomical time scale. Earth-Science Review 104, 111–142.
- Yıldız, A. 2000. Tuzgözü Havzası Doğusu (Altınkaya-Asmayaylası Yöresi) Asmaboğazı ve Karapınaryaylası formasyonlarının biyostratigrafisi. Haymana-Tuzgözü-Ulukışla Basenleri Uygulamalı Çalışmayı, 09-11 Ekim, 2000, Bildiriler Kitabı, 185-203.
- Yıldız, M., Kalkan, M. 2018. Petrographic and Geochemical Features of the Akmezar Ophiolite, Central Anatolia, Aksaray/Turkey, 9th International Symposium on Mediterranean Geology, Antalya / Turkey, Abstracts and Proceeding Book, 288.



## **PLATES**

**Plate I**

**1-3, 7:** Miliolid forms, longitudinal sections; **1.**Sample no.13, K2 Section, SBZ12; **2-3.**Sample no 59, K6 Section, SBZ3-4.

**4:** *Haymanella* cf. *elongata*, longitudinal section, Sample no. 117, K10 Section, SBZ7-8.

**5-6:** Textulariids?, Sample no 93, K9 Section, SBZ?

**7:** *Parahaymanella* sp., Sample no 59, K6 Section, SBZ3-4.

**8:** *Haymanella* cf. *paleocenica*, longitudinal section, Sample no. 117, K10 Section, SBZ7-8

**9-15:** *Cribrobulimina* sp; **9, 11, 13** Sample no. 117, K10 Section, SBZ7-8; **10.**Sample no 44, K5 Section, SBZ?; **12.**Sample no 114, K10 Section, SBZ7-8; **13.**Sample no. 54, K6 Section, SBZ3-4; **15.**Sample no 28, K3 Section, SBZ5-8.

**16-21:** Planspiral coiled textulariids, **16-17.**Sample no 93, K9 Section, SBZ?; **18.**Sample no 95, K9 Section, SBZ?; **19.**Sample no 59, K6 Section, SBZ3-4; **20.**Sample no 44, K5 Section, SBZ?; **21.**Sample no 56, K6 Section, SBZ3-4.

**22-24:** Biserial coiled textulariids, **22.**Sample no 59, K6 Section, SBZ3-4; **23.**Sample no 116, K10 Section, SBZ?; **24.**Sample no 54, K6 Section, SBZ3-4.

**25-26:** *Vulvulina* sp. **25.**Sample no 47, K5 Section, SBZ?; **26.**Sample no 23, K3 Section, SBZ5-8.

**27:** *Textularia* sp. Sample no 107, K9 Section, SBZ?.

**28-30:** Unidentified textulariids, **28.**Sample no 117, K10 Section, SBZ7-8, **29.**Sample no 105, K9 Section, SBZ?; **30.**Sample no 15, K2 Section, SBZ12.

**31-32:** Unidentified textulariids, **31.** Sample no 47, K5 Section, SBZ?; **32.** Sample no 114, K10 Section, SBZ7- 8.

**33-34:** Uniserial coiled textulariids, **33.** Sample no 56, K6 Section, SBZ3-4; **34.** Sample no 117, K10 Section, SBZ7-8.

**35-40:** *Bigenerina* sp. **35.** Sample no 114, K10 Section, SBZ7-8; **36-37.**Sample no 93, K9 Section, SBZ?; **38.** Sample no 47, K5 Section, SBZ?; **39.**Sample no 99, K9 Section, SBZ?; **40.**Sample no 100, K9 Section, SBZ?

**41:** Unidentified textulariids, Sample no 114, K10 Section, SBZ7-8

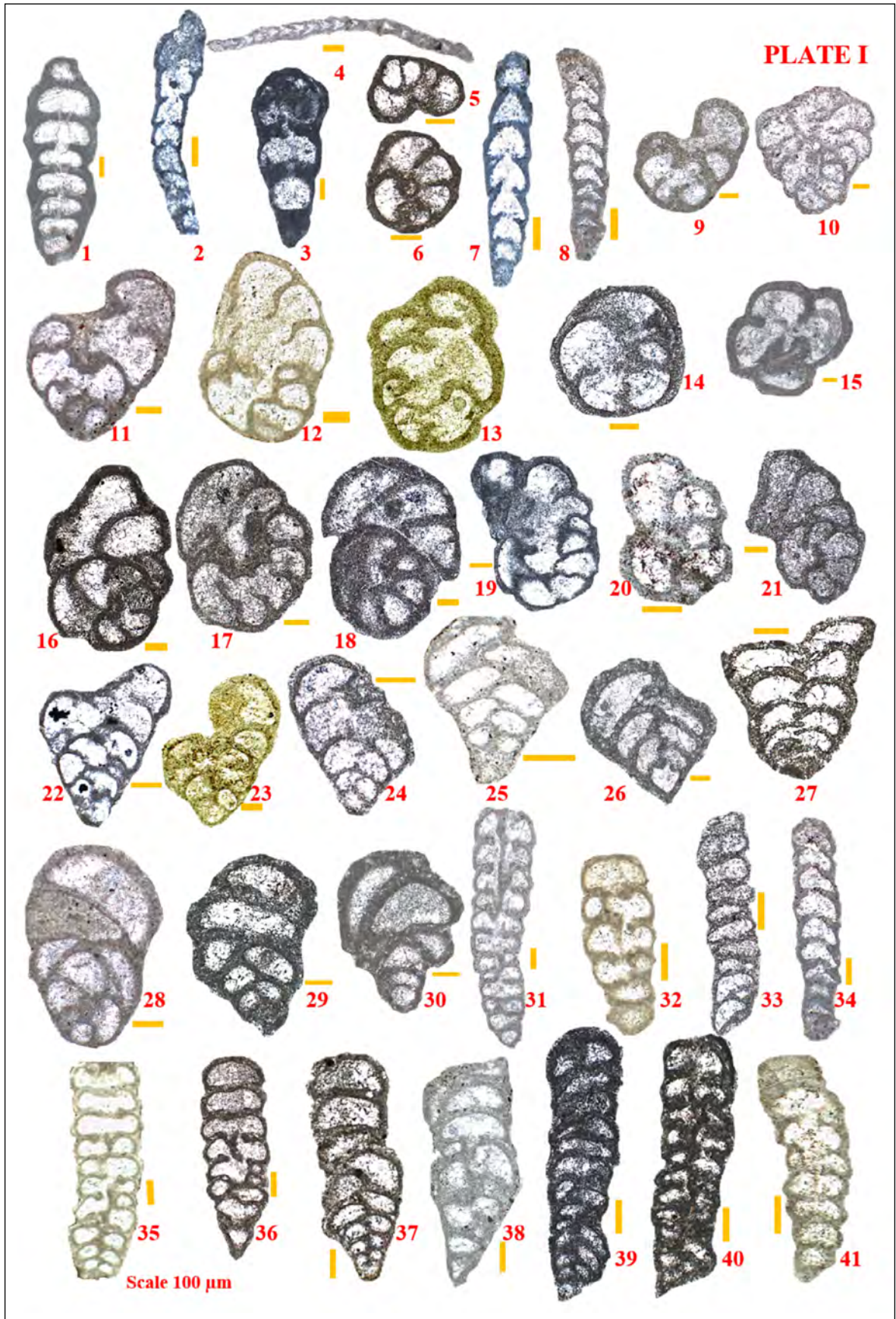


**Plate II**

**1-2:** *Peneroplis* sp., equatorial sections, **1.** Sample no 107, K9 Section, SBZ?; **2.** Sample no 1, K1 Section, SBZ5-7.

**3-4:** Unidentified miliolid, centered section perpendicular to the coiling axis, **3.** Sample no 15, K2 Section, SBZ12; **4.** Sample no 23, K3 Section, SBZ5-8.

**5:** *Idalina* cf. *grelaudae*, centered section perpendicular to the coiling axis, Sample no 95, K9 Section, SBZ?

**6-10:** Unidentified miliolids, centered section perpendicular to the coiling axis, **6.** Sample no 35, K4 Section, ?SBZ5-8; **7.** Sample no 94, K9 Section, SBZ?; **8.** Sample no 64, K6 Section, SBZ3-4.; **9.** Sample no 35; K4 Section, SBZ?; **10.** Sample no 93, K9 Section, ?SBZ10-11.

**11-14:** *Idalina* cf. *gralaudae*, centered section perpendicular to the coiling axis, **11-12, 14.** Sample no 117, K10, Section, SBZ7-8; **13.** Sample no 116, K10 Section, SBZ7-8

**15:** Unidentified miliolid, centered section perpendicular to the coiling axis, Sample no 1, K1 Section, SBZ5-7.

**16:** *Triloculina tricarinata*, Sample no 4, K1 Section, SBZ5-7.

**17-18:** *Triloculina angulata*, **17.** Sample no 15, K2 Section, SBZ12; **18.** Sample no 27, K3 Section, SBZ5-8 657

**19:** *Idalina* cf. *pignattii*?, Sample no 117, K10 Section, SBZ7-8.

**20-21:** Unidentified miliolids, centered section perpendicular to the coiling axis, **20-21.** Sample no 93, K9 Section, SBZ9.

**22:** *Idalina sinjarica*, Sample no 56, K6 Section, SBZ3-4.

**23:** *Idalina* cf. *causae*, Sample no 56, K6 Section, SBZ3-4. 662

**24-29:** Unidentified miliolids, **24.** longitudinal section, Sample no 4, K1 Section, SBZ5-7; **25.** uncentered section perpendicular to the coiling axis, Sample no 117, K10 Section, SBZ7-8; **26.** Unidentified miliolid, centered section perpendicular to the coiling axis, Sample no 35, K4 Section, SBZ?; **27.** Sample no 24, K3 Section, SBZ5-8; **28.** Sample no 2, K1 Section, SBZ5-7; **29.** Sample no 105, K9 Section, SBZ?. 666

**30:** *Idalina sinjarica*?, longitudinal section, Sample no 23, K3 Section, SBZ5-8. 667

**31-33:** Unidentified miliolids, **31.** Sample no 26, K3 Section, SBZ5-8; **32.** longitudinal section, Sample no 54, 668 K6 Section, SBZ3-4; **33.** Sample no: 54, K6 Section, SBZ3-4. 669

**34:** *Parahaymanella* sp., oblique equatorial section, Sample no 54, K6 Section, SBZ3-4. 670

**35-40:** Unidentified miliolids, **35.** Sample no 54, K6 Section, SBZ3-4; **36.** Sample no 66, K6 Section, SBZ3-4; 671 **37-38.** Sample no 55, K6 Section, SBZ3-4; **39-40.** Sample no 93, K9 Section, SBZ?



**Plate III**

**1-4:** *Unidentified miliolids*, **1-2.**Sample no 93, K9 Section, SBZ?; **3-4.**Sample no 95, K9 Section, SBZ?

**5-6:** *Ankaraella minima*, subvertical section, Sample no 55, K6 Section, SBZ3-4.

**7-8:** *Kayseriella decastroii*, subvertical section, Sample no 55, K6 Section, SBZ3-4.

**9:** *Spiroloculina* sp., subvertical section, Sample no 94, K9 Section, SBZ?

**10:** Unidentified miliolid, Sample no 2, K1 Section, SBZ5-7

**11-13:** *Spiroloculina* sp., subvertical section, **11.**Sample no 2, K1 Section, SBZ5-7; **12.**Sample no 116, K10 Section, SBZ7-8; **13.**Sample no 117, K10 Section, SBZ7-8.

**14-15:** Unidentified miliolids, **14.**Sample no 101, K9 Section, SBZ?; **15.**Sample no 116, K10 Section, SBZ7-8.

**16:** *Parahaymanella* sp., subequatorial section, Sample no 59, K6 Section, SBZ3-4.

**17:** *Parahaymanella bozkurti*, subequatorial section, Sample no 55, K6 Section, SBZ3-4.

**18:** Unidentified miliolid, Sample no 105, K9 Section, SBZ?.

**19-20:** *Parahaymanella?* sp., subequatorial section (?), **19-20.** Sample no 55, K6 Section, SBZ3-4.

**21:** *Parahaymanella bozkurti*, subequatorial section, Sample no 55, K6 Section, SBZ3-4.

**22:** *Parahaymanella* sp., subequatorial section, Sample no 55, K6 Section, SBZ3-4.

**23-26:** Unidentified miliolids (?), **23.** Sample no 102; **24-25.**Sample no 56, K6 Section, SBZ3-4; **26.** Sample no 47, K5 Section, SBZ?.

**27:** *Parahaymanella* sp., subequatorial section, Sample no 55, K6 Section, SBZ3-4.

**PLATE III**



**Plate IV**

**1:** *Alveolina* cf. *dolioliformis*, axial section, Sample no 51, K5 Section, SBZ7-8.

**2:** *Alveolina* cf. *corbarica*, uncentered axial section, Sample no 49, K5 Section, SBZ7-8.

**3-4:** *Alveolina corbarica*, axial sections, 3. Sample no 52, K5 Section, SBZ7-8; 4. Sample no 116, K10 Section, SBZ7-8

**5:** *Alveolina* cf. *levantina*, oblique axial section, Sample no 13, K2 Section, SBZ12.

**6-7:** *Alveolina* sp., **6.** oblique axial section, Sample no 51, K5 Section, SBZ7-8; **7.** tangential section, Sample no 116, K10 Section, SBZ7-8.

**8:** *Alveolina barattoloi*, slightly oblique axial section, Sample no 72, K7 Section, SBZ10-11.

**9:** *Alveolina* cf. *acari*, Sample no 37, K4 Section, SBZ7

**10:** *Alveolina* sp., tangential section, Sample no 52, K5 Section, SBZ7-8.

**11:** *Alveolina levantina*, axial section, Sample no 13, K12 Section, SBZ12.

**12:** *Alveolina erki*, axial section, Sample no 52, K5 Section, SBZ7-8.

**13:** *Alveolina violae*, Sample no 19, K2 Section, SBZ12.

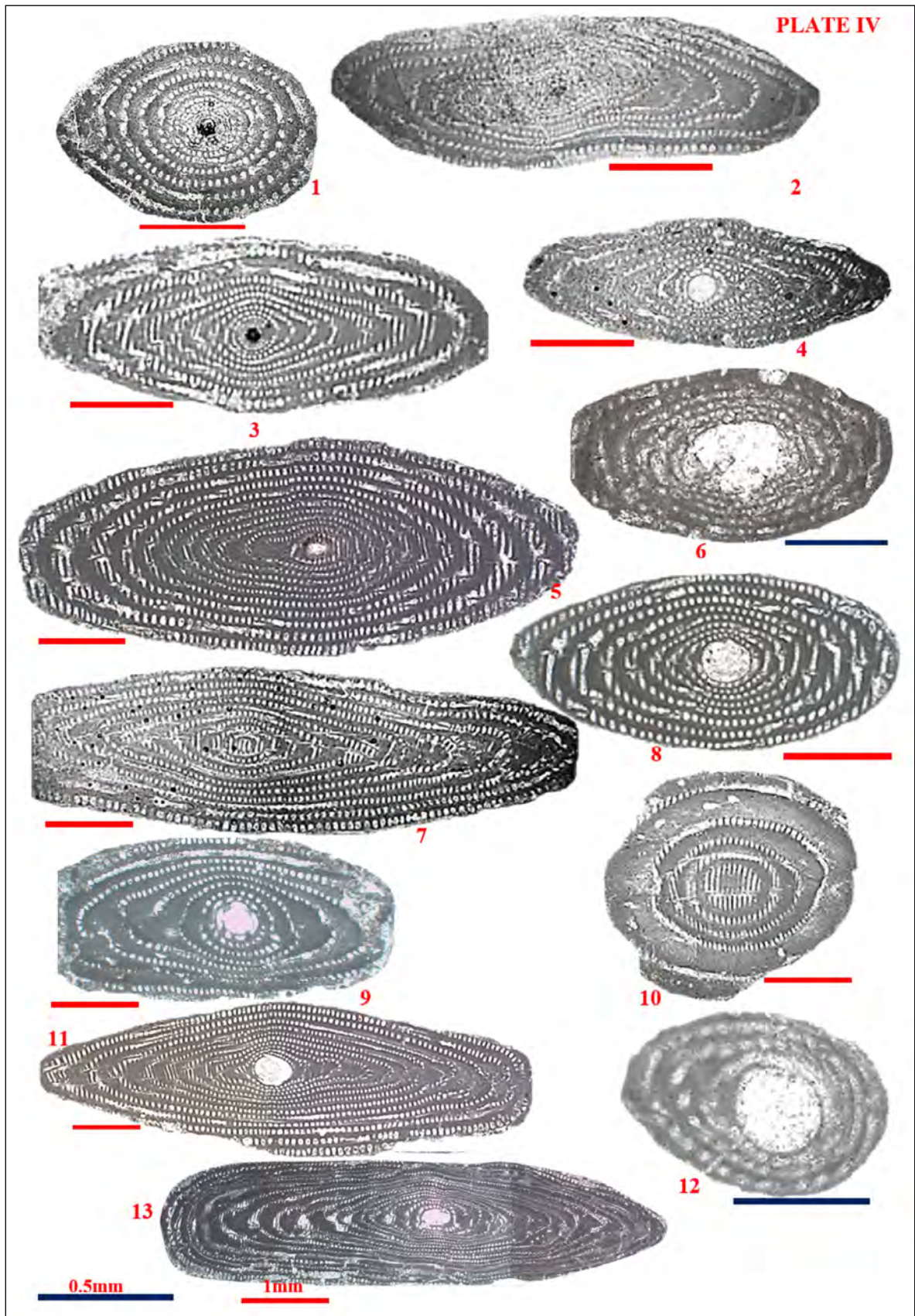


**Plate V**

**1-2:** *Alveolina* sp., oblique axial sections, Sample no 13, K2 Section, SBZ12.

**3:** *Alveolina* sp., oblique equatorial section; Sample no 56, K6 Section, SBZ3-4.

**4:** *Alveolina* cf. *laxa*, axial section with a broken juvenile stage, Sample no 37, K4 Section, SBZ7.

**5-10:** *Alveolina* sp., **5, 7.** oblique equatorial sections, Sample no 117, K10 Section, SBZ7-8; **6.** subequatorial section, Sample no 49, K5 Section, SBZ7-8; **8.** subequatorial section, Sample no 117, K10 Section, SBZ7-8;

**9.** oblique axial section, Sample no 56, K6 Section, SBZ3-4; **10.** subaxial section, Sample no 64, K6 Section, SBZ3-4.

**11:** *Alveolina* aff. *avsari*, slightly oblique axial section, Sample no 72, K7 Section, SBZ10-11.

**12-17:** *Alveolina* sp. **12.** oblique equatorial section, Sample no 105, K9 Section, SBZ?; **13.** nearly equatorial section, Sample no 35, K4 Section, SBZ?; **14-15.** axial sections, Sample no 98, K9 Section, SBZ?, **16.** equatorial section, Sample no 100, K9 Section, SBZ?, **17.** oblique section, Sample no 104, K9 Section, SBZ?.

**18-20:** Alveoliniids?, **18.** Sample no 98, K9 Section, SBZ?; **19.** Sample no 100, K9 Section, SBZ?; **20.** Sample no 102, K9 Section, SBZ?

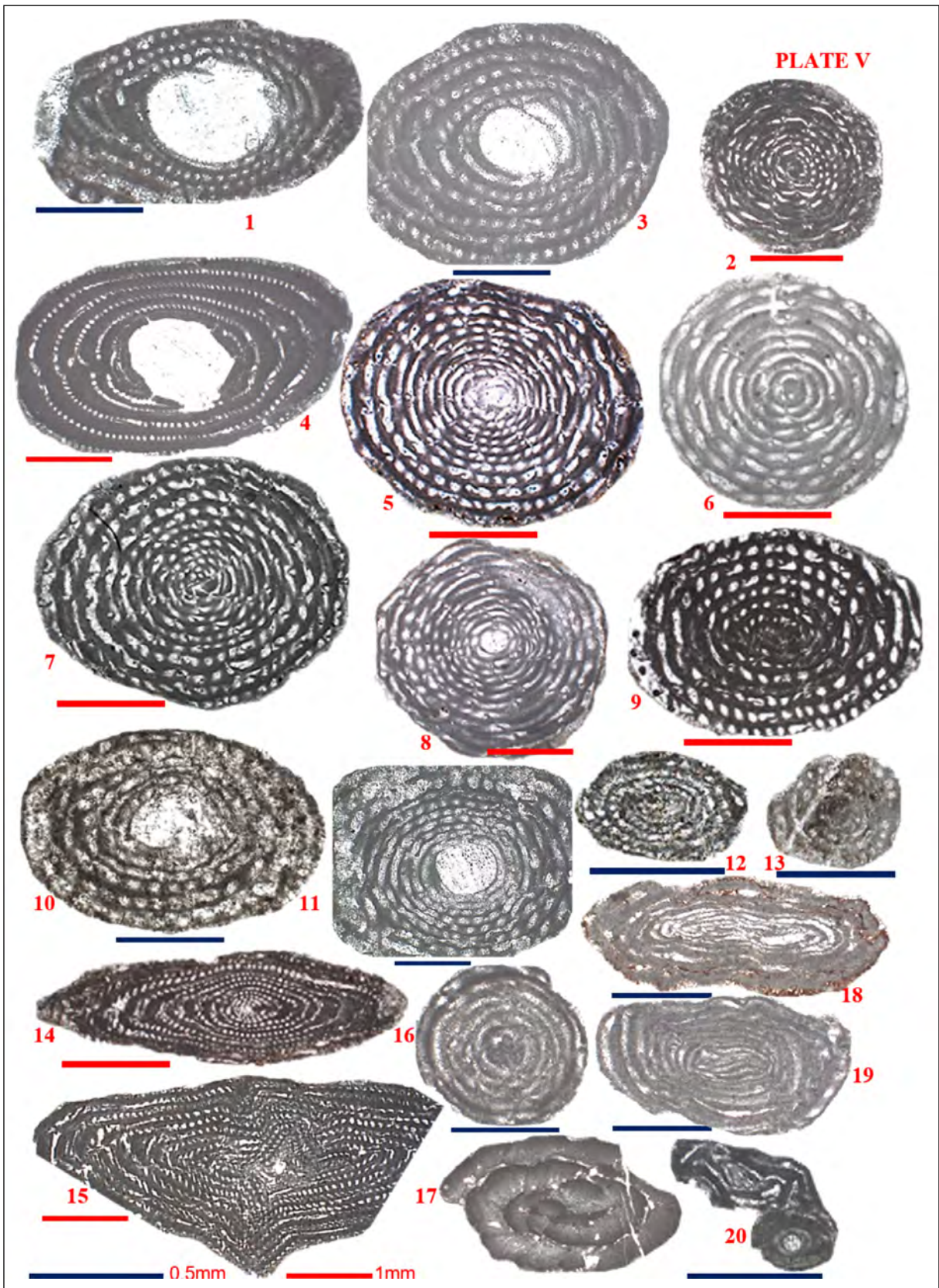


**Plate VI**

**1-5.** *Valvulineria orali*, equatorial sections or nearly equatorial sections, **1.** Sample no 3, K1 Section, SBZ5-7; **2.** Sample no 7, K1 Section, SBZ5-7; **3.** Sample no 12, K1 Section, SBZ5-7; **4.** Sample no 105, K9 Section, SBZ?; **5.** Sample no 109, K9 Section, SBZ?

**6:** *Gyroidinella* sp. Sample no 28, K3 Section, SBZ5-8

**7-10, 12-16:** ?*Valvulineria* sp. axial or oblique sections, **7.** Sample no 7, K1 Section, SBZ5-7; **8-9.** Sample no 11, K1 Section, SBZ5-7; **10.** Sample no 10, K1 Section, SBZ5-7; **12, 14, 15.** Sample no 109; K9 Section, SBZ?; **13.** Sample no 50, K2 Section, SBZ12; **16.** Sample no 3, K1 Section, SBZ5-7.

**11:** Rotaliid form, Sample no. 10, K1 Section, SBZ5-7.

**17-22:** Unidentified mississippinids, subaxial sections, **17.** Sample no 3, K1 Section, SBZ5-7; **18, 21.** Sample no 109, K9 Section, SBZ?; **19.** Sample no 107, K9 Section, SBZ?; **20.** Sample no 48, K5 Section, SBZ7-8, **22.** Sample no 109, K9 section.

**23:** *Orbitolites* sp. subaxial section, Sample no 13, K2 Section, SBZ12.

**24-25:** *Opertorbitolites* sp., oblique axial section of a broken specimen, **24.** Sample no 100, K9 Section, SBZ?;

**25.** Sample no 117, K10 Section, SBZ7-8.

**26-28:** *Orbitolites* sp., subaxial section, **26-27.** Sample no 13, K2 Section, SBZ12; **28.** Sample no. 101, K9 Section, SBZ?

**PLATE VI**

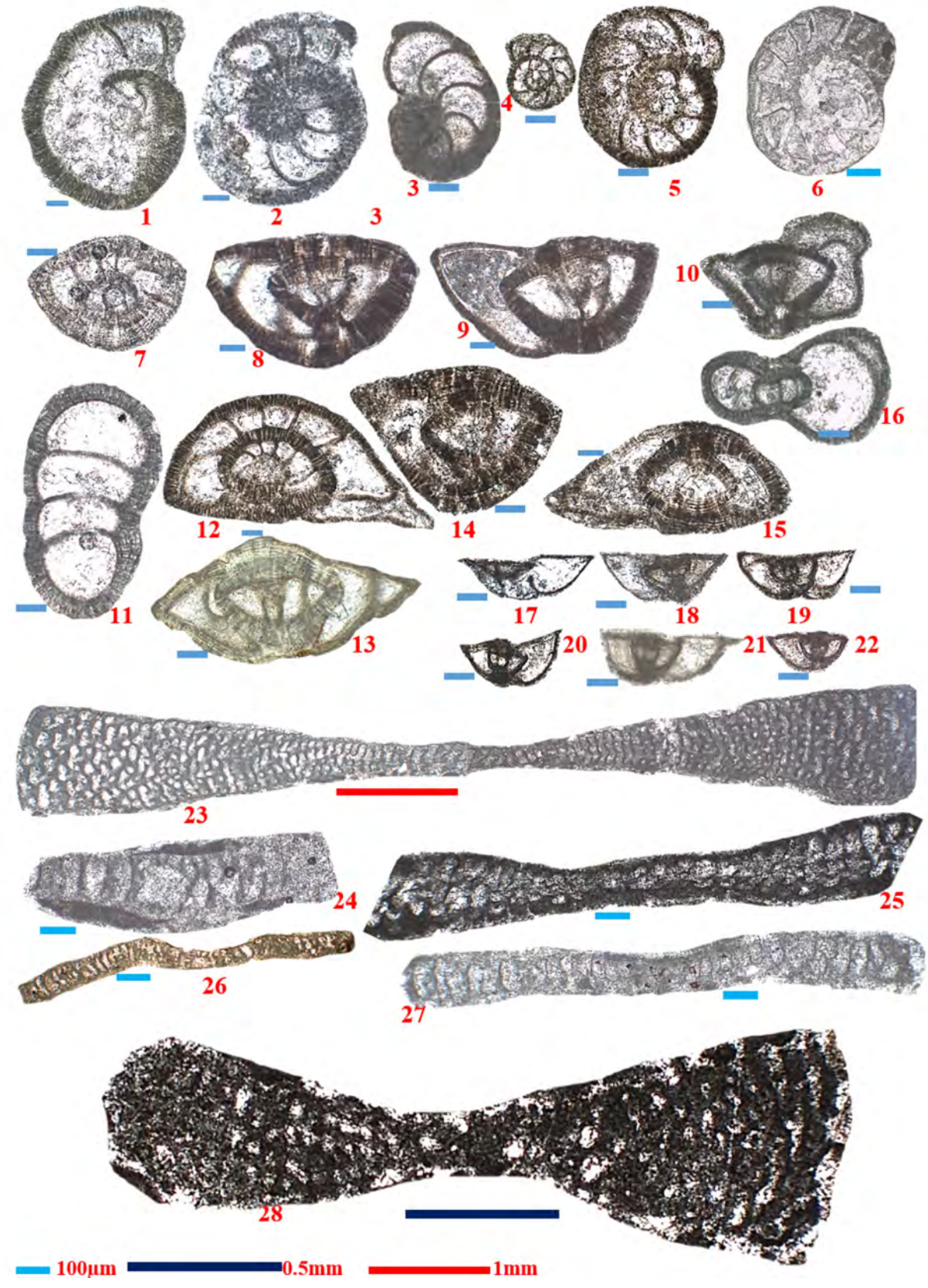


**Plate VII**

- 1:** Rotaliid, subaxial section, Sample no 3, K1 Section, SBZ5-7.
- 2-3:** *Pseudokathina selveri*, axial sections, **2.** Sample no 10, K1 Section, SBZ5-7; **3.** Sample no 107; K10 Section, SBZ7-8
- 4:** Rotaliid, Sample no 64, K6 Section, SBZ3-4.
- 5:** *Nummulites* sp., axial section, Sample no 16, K2 Section, SBZ12
- 6, 8:** *Rotalia trochidiformis*, subvertical sections, **6, 8.** Sample no 10, K1 Section, SBZ5-7.
- 7:** *Rotalia* sp., subvertical section, Sample no 8, K1 Section, SBZ5-7.
- 9:** *Thalmannita?* sp., axial section, Sample no 10, K1 Section, SBZ5-7.
- 10:** *Lockhartia haimei*, vertical section Sample no 8, K1 Section, SBZ5-7.
- 11:** *Lockhartia* cf. *conditi*, subvertical section, Sample no 11, K1 Section, SBZ5-7.
- 12:** *Lockhartia* sp., subvertical section, Sample no 98, K9 Section, SBZ?
- 13-17:** Unidentified rotaliids, subvertical sections, **13.** Sample no 73, K8 Section, E7-E10; **14.** Sample no 12, K1 Section, SBZ5-7; **15.** Sample no 104, K9 Section, SBZ?; **16.** Sample no 4, K1 Section, SBZ5-7; **17.** Sample no 8, K1 Section, SBZ5-7.
- 18:** Unidentified miscellanid, oblique section, Sample no 1, K1 Section, SBZ5-7
- 19:** Unidentified rotaliid, Sample no 11, K1 Section, SBZ5-7.
- 20:** *Soriella?* sp., vertical section, Sample no 5, K1 Section, SBZ5-7
- 21:** *Elazigina?* sp., Sample no 23, K3 Section, SBZ5-8
- 22-25:** Unidentified rotaliids, vertical section, **22.** Sample no 3, K1 Section, SBZ5-7; **23.** Sample no 7, K1 Section, SBZ5-7; **24.** Sample no 6, K1 Section, SBZ5-7; **25.** Sample no 10, K1 Section, SBZ5-7.
- 26:** *Gyroidinella* sp., equatorial section, Sample no 72, K7 Section, SBZ10-11.
- 27-29:** ?Unidentified rotaliids, **27.** Sample no 48, K5 Section, SBZ7-8; **28.** Sample no 10, K1 Section, SBZ5-7; **29.** Sample no 12, K1 Section, SBZ5-7.
- 30-31:** Nodosariids, vertical sections, **30-31.** Sample no 8, K1 Section, SBZ5-7.

**PLATE VII**



**Plate VIII**

**1-6:** *Discocyclina* sp., axial or subaxial sections, **1, 3.** Sample no 74, K8 Section, SBZ?; **2, 4, 6.** Sample no 73, K8 Section, SBZ?; **5.** Sample no 11, K1 Section, SBZ5-7.

**7-9:** *Nummulites* sp., axial sections, **7.** Sample no 52, K5 Section, SBZ7-8; **8.** Sample no 4, K1 Section, SBZ5-7;

**9.** Sample no 64, K6 Section, SBZ3-4.

**10:** *Asterigerina* ? sp., equatorial section, Sample no 52, K5 Section, SBZ7-8.

**11-13, 15:** *Nummulites* sp., axial sections, **11-12.** Sample no 13, K2 Section, SBZ12; **13.** Sample no 15, K2 Section, SBZ12; **15.** Sample no 74, K8 Section, SBZ?

**14:** *Heterostegina* ?, subaxial section, Sample no 74, K8 Section, SBZ?

**16:** Nummulitidae gen. indet., Sample no 73, K8 Section, SBZ?

**17:** *Ranikothalia* sp., subaxial sections, Sample no 73, K8 Section, SBZ?

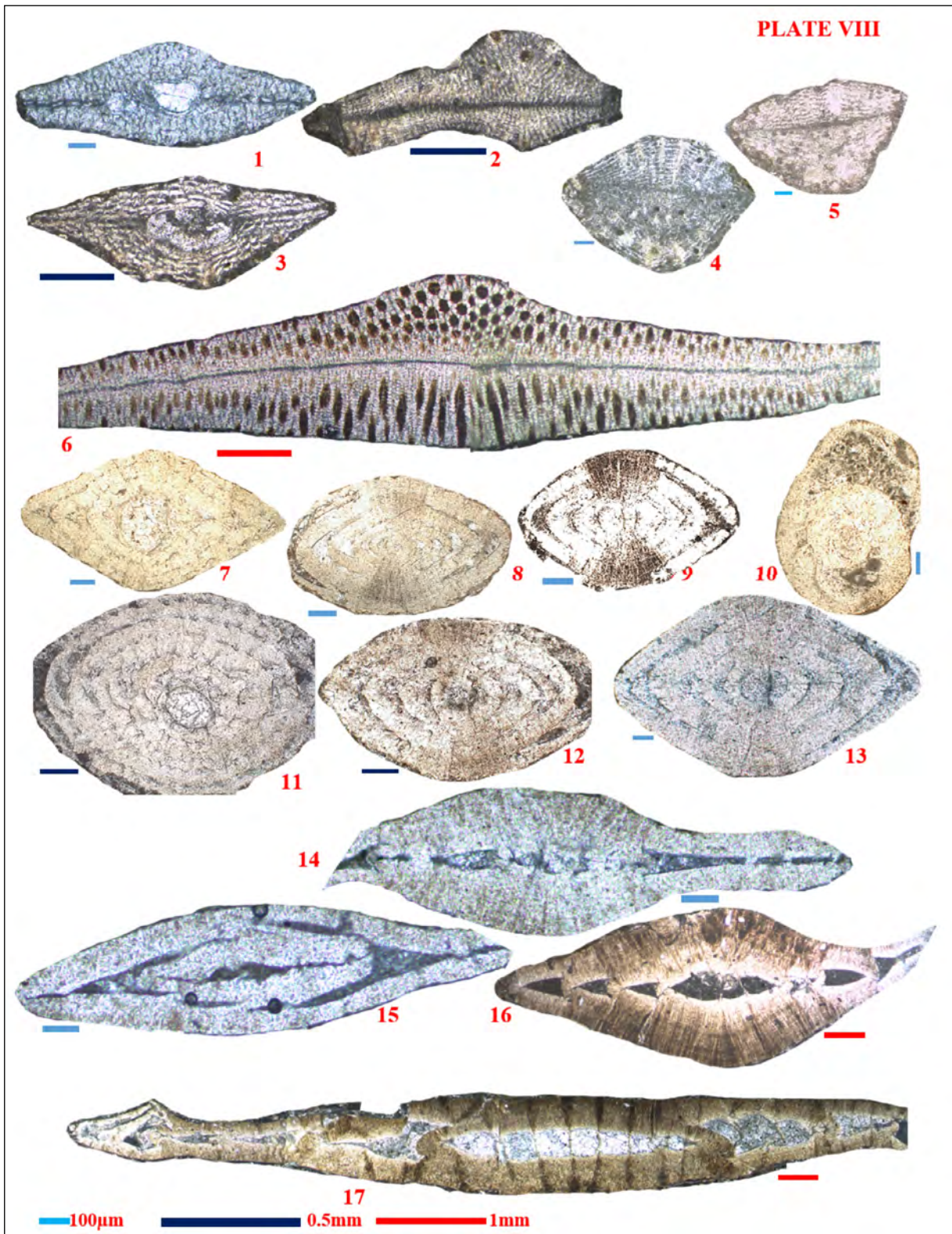


**Plate IX**

- 1, 3, 5:** *Globigerinatheka* sp., **1.** Sample no K83; K8 Section, E7-E10; **3, 5.** Sample no K81, K8 Section, E7-E10.
- 2, 10:** *Globigerinatheka index*, **2.** Sample no K82, K8 Section, E7-E10; **10.** Sample no K81, K8 Section, E7-E10.
- 4, 6:** *Globigerinatheka mexicana*, **4.** Sample no K83, K8 Section, E7-E10; **6.** Sample no K81, K8 Section, E7-E10.
- 7, 8:** *Guembelitrioides nuttalli*, Sample no K81, K8 Section, E7-E10.
- 9:** *Globigerinatheka kugleri*, Sample no K83, K8 Section, E7-E10.
- 11:** *Subbotina crociapertura*, Sample no K82, K8 Section, E7-E10.
- 12, 13:** *Pseudohastigerina micra*, Sample no K81, K8 Section, E7-E10.
- 14-15:** *Acarinina bullbrooki*, **14.** Sample no K83, K8 Section, E7-E10; **15.** Sample no K82, K8 Section, E7-E10.
- 16:** *Globigerinatheka subconglobata*, K82, K8 Section, E7-E10.
- 17:** *Turborotalia pomeroli*, K82, K8 Section, E7-E10.
- 18:** *Subbotina eocaena*, Sample no K82, K8 Section, E7-E10.
- 19-21:** *Acarinina bullbrooki*, **19.** Sample no K75, K8 Section, E7-E10; **20.** Sample no K83, K8 Section, E7-E10; **21.** Sample no K80, K8 Section, E7-E10.
- 22:** *Acarinina primitiva*, Sample no K78, K8 Section, E7-E10.
- 23:** *Turborotalia frontosa*, Sample no K82, K8 Section, E7-E10.
- 24:** *Turborotalia possagnoensis*, Sample no K83, K8 Section, E7-E10.
- 25-27:** *Acarinina praetopilensis*, **25.** Sample no K81, K8 Section, E7-E10; **26.** Sample no K77, K8 Section, E7-E10; **27.** Sample no K80, K8 Section, E7-E10.
- 28, 29:** *Globanomina australiformis*, Sample no K81, K8 Section, E7-E10.
- 30:** *Morozovelloides crassatus*, Sample no K83, K8 Section, E7-E10.
- 31:** *Acarinina praetopilensis*, Sample no K79, K8 Section, E7-E10.
- 32-33:** *Acarinina puntocarinata*, **32.** Sample no K82; **33.** Sample no K83;
- 34-36:** *Morozovelloides bandyi*, Sample no K82, K8 Section, E7-E10.
- 37:** *Acarinina* sp., Sample no K81, K8 Section, E7-E10.
- 38:** *Subbotina linaperta*, Sample no K77, K8 Section, E7-E10.
- 39-41:** *Acarinina boudreauxi*, **39.** Sample no K81, K8 Section, E7-E10; **40.** Sample no K76, K8 Section, E7-E10; **41.** Sample no K82, K8 Section, E7-E10.
- 42-43:** *Acarinina pseudosphaerica*, **42.** Sample no K81, K8 Section, E7-E10; **43.** Sample no K80, K8 Section, E7-E10.
- 44:** *Parasubbotina* sp., Sample no K81, K8 Section, E7-E10.
- 45-46:** *Acarinina pseudosphaerica*, **45.** Sample no K81, K8 Section, E7-E10; **46.** Sample no K82, K8 Section, E7-E10, K8 Section, E7-E10.
- 47-48:** *Pearsonites broedermanni*, **47.** Sample no K75, K8 Section, E7-E10; **48.** Sample no K83, K8 Section, E7-E10.
- 49-50:** *Planorotalites capdevilensis*, Sample no K81, K8 Section, E7-E10.

**PLATE IX**

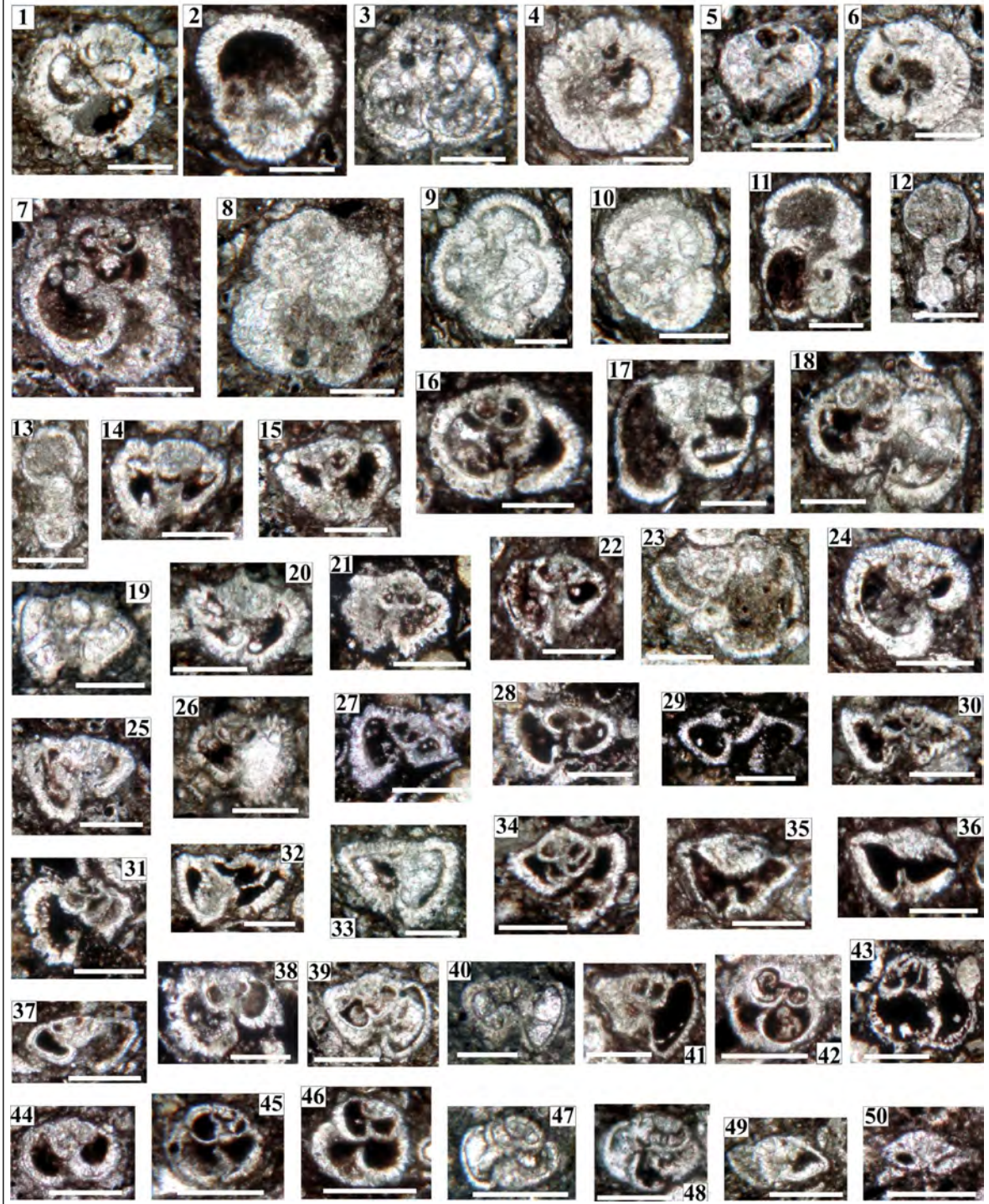
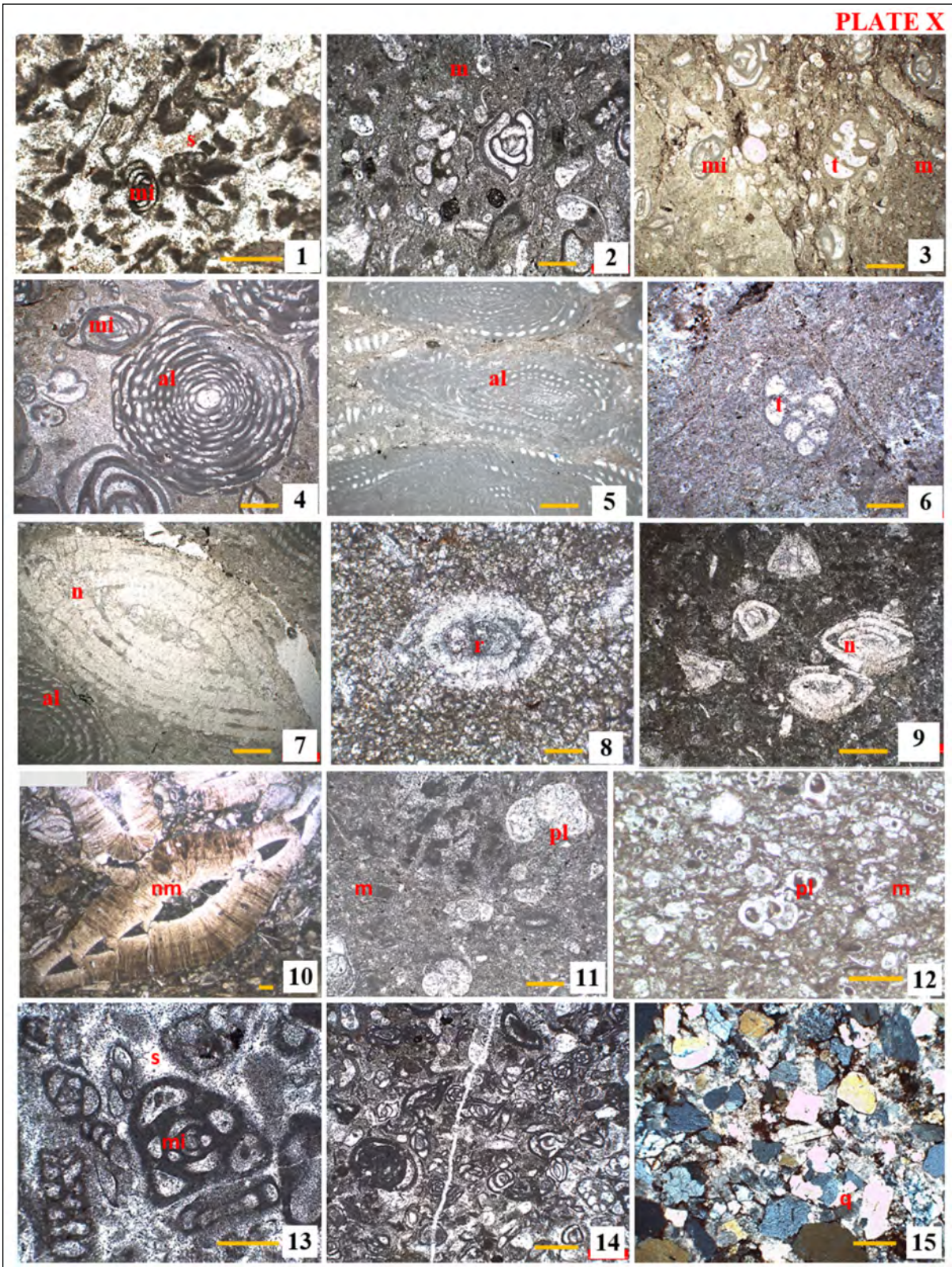


**Plate X**

Thin section views of described microfacies, mi. smaller miliolid, al. alveolinid, t. textulariid, n. nummulitids, r. rotaliid, pl. planktonic foraminifera, s. sparite, m. micrite, i. intraclast, q. quartz.

- 1-2:** MF1. Smaller miliolid-dominated packstone-grainstone sub-facies, sample no.1 and 54.
- 3:** MF2. Miliolid-textulariid dominated packstone sub-facies, sample no. 114
- 4:** MF3. Alveolinid and other smaller miliolid-dominated packstone sub-facies, sample no. 117
- 5:** MF4. Alveolinid-dominated packstone sub-facies, sample no. 47
- 6:** MF5. Wackestone-packstone sub-facies containing less textulariid, sample no. 44
- 7:** MF6. Alveolinid and nummulitid-dominated wackestone-packstone sub-facies, sample no. 49
- 8:** MF7. Less rotaliid bearing silty mudstone sub-facies, sample no. 6
- 9:** MF8. Rotaliid-dominated wackestone-packstone sub-facies, sample no.14
- 10:** MF9. Packstone containing nummulitid form, sample no. 73
- 11:** MF10. Less planktonic foraminiferous mudstone sub-facies, sample no. 56
- 12:** MF11. Wackestone sub-facies with rich planktonic foraminifera, sample no. 81
- 13-14:** MF1, sample no. 95
- 15:** Grain supported sandstones, Sample no 110.

**PLATE X**







# Bulletin of the Mineral Research and Exploration

<http://bulletin.mta.gov.tr>



## Active tectonics of western Kosovo: Insights from geomorphic and structural analyses

Alper GÜRBÜZ<sup>a</sup>, Astrit SHALA<sup>b\*</sup>, Shemsi MUSTAFA<sup>c</sup> and Aytekin ERTEN<sup>d</sup>

<sup>a</sup> Niğde Ömer Halisdemir University, Engineering Faculty, Department of Geological Engineering, 51240, Niğde, Türkiye

<sup>b</sup> University Isa Boletini Mitrovicë, Faculty of Geosciences, Department of Geology, Str.Ukshin Kovacica, 40000, Mitrovicë, Republic of Kosovo

<sup>c</sup> Ministry of Economy, Seismological Network of Kosovo, Geological Survey of Kosovo, 10000, Prishtinë, Republic of Kosovo

<sup>d</sup> Niğde Ömer Halisdemir University, Science Institute, Department of Geological Engineering, 51240, Niğde, Türkiye

Research Article

Keywords:

Neotectonics, Extensional Tectonics, Shkodër-Pejë Fault Zone, Balkans, Southeast Europe.

### ABSTRACT

Kosovo is located in a key position in the central-west part of the Balkans, providing an opportunity to understand the far-field effects of distributed intracontinental deformation caused by the Aegean extension in the south and Adriatic compression in the west. It is also situated along the NE-SW trending Shkodër-Pejë transverse zone, where the Dinarides and Albanides-Hellenides orogenic belts are juxtaposed. While the instrumental seismicity of Kosovo indicates the activity of this fault zone and many others, the active faults in the country were not discussed in detail in the current literature. In this study, we analyzed both the geomorphic and structural features of major mountain front faults in western Kosovo (i.e., Pejë, Istog, Krojmir, and Prizren faults) to reveal the relative assessment of their activities and kinematic characters. Geomorphic and morphometric analyses of all four different mountain fronts studied indicated high activity and tectonic uplift rates of over 0.5 mm/a. On the other hand, according to the collected kinematic data from the observed fault planes, the studied faults are mainly of normal character, representing a dominance of NW-SE-directed extension in western Kosovo, which is most probably caused by the rollback of the subducting slab in the Hellenic trench.

Received Date: 28.09.2022

Accepted Date: 10.10.2022

### 1. Introduction

Subduction of the African Plate beneath the Anatolian Plate along the Hellenic trench causes a widespread extension that is not limited to the Aegean Sea and affects a large region reaching the central Balkans in the north (Figure 1; e.g., Burchfiel et al., 2006, 2008; Kotzev et al., 2006; Métois et al., 2015). As clearly known, the southern Aegean Sea represents the most rapidly extending region in the world with a rate of 3.5 cm/a (e.g., Taymaz et al., 1990; Reilinger et al., 1997, 2006; McClusky et al., 2000; Le Pichon and Kreemer, 2010). On the other hand, the approximately

800 km long region between the Hellenic trench and the central Balkan Peninsula represents one of the largest intracontinental extensional domains in the world (D'Agostino et al., 2020). In addition to the major role of this extension, the western part of the Balkan Peninsula is also under the effect of compression, which is related to the slow collision between the Adriatic and the Eurasian plates along the Dinarides-Albanides-Hellenides (e.g., Baker et al., 1997; Louvari et al., 2001; Faccenna et al., 2003; Hollenstein et al., 2008; Jouanne et al., 2012; Métois et al., 2015; D'Agostino et al., 2020, 2022). Kosovo

Citation Info: Gürbüz, A., Shala, A., Mustafa, S., Erten, A. 2024. Active tectonics of western Kosovo: insights from geomorphic and structural analyses. Bulletin of the Mineral Research and Exploration 173, 153-173. <https://doi.org/10.19111/bulletinofmre.1186708>

\*Corresponding author: Astrit SHALA, [astrit-shala@hotmail.com](mailto:astrit-shala@hotmail.com)

is situated in a key position in the central-west part of the Balkan Peninsula representing the northern part under the influence of the Aegean extensional domain (Figure 1), and provides an opportunity to understand the far-field effects of distributed intracontinental deformation.

The above-mentioned recent framework of the Balkans is based mostly on the geodetic measurements and seismicity recorded in the last decades. However, the geological evolution of the region includes more on geodynamic context effective on today's activity. Kosovo is located where the Dinarides and Albanides-Hellenides orogenic belts are juxtaposed along the

NE-SW trending Shkodër-Pejë transverse zone (e.g., Aliaj, 1988; Papa et al., 1991; Muço, 1998; Handy et al., 2019). This structure is known since Aubouin et al., 1970 (i.e., *Tranversale de Scutari-Pec*) as one of the most important structural elements in the Balkan Peninsula since the Mesozoic. Geological data indicate a right-lateral offset of ophiolitic units along the Shkodër-Pejë transverse zone (Handy et al., 2019). In addition, palaeomagnetic studies demonstrate that this zone represents a separation line in the clockwise rotation of the Albanides-Hellenides at least since the early Neogene with respect to the Dinarides (Figure 1; e.g., Kissel and Laj, 1988; Kissel et al., 1995; Speranza et al., 1995; van Hinsbergen et al., 2005; Bradley et

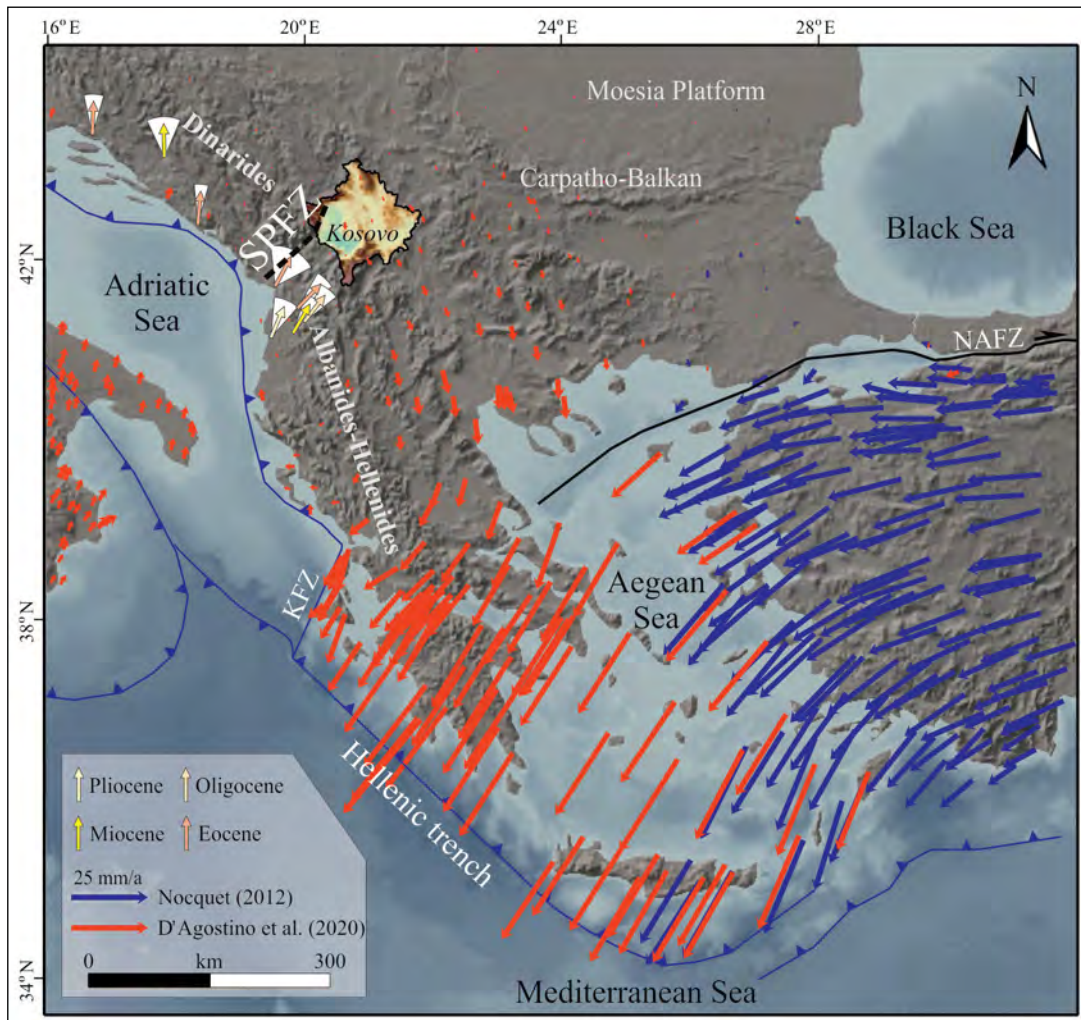


Figure 1- Location map of Kosovo within the active tectonic framework of the Balkan and the Aegean regions showing GPS velocity field with respect to Eurasia (modified from D'Agostino et al., 2020), and the palaeomagnetic declinations for different aged rocks around the Shkodër-Pejë fault zone (SPFZ) relative to African plate (compiled from Kissel et al., 1995 and Speranza et al., 1995 after D'Agostino et al., 2020). NAFZ – North Anatolian fault zone, KFZ - Kephallonia fault zone. For elevation scale of Kosovo please see Figure 3a.

al., 2013). Today, geomorphology, kinematic data, and seismic activity in the region represent that this structure is overprinted by a normal fault zone called the Shkodër-Pejë fault zone (e.g., Muço, 1998; Handy et al., 2015, 2019; Schmitz et al., 2020).

Kosovo includes the eastern part of the Shkodër-Pejë fault zone in its western part (Figure 1). Although the seismicity of the country in the instrumental period indicates the activity of this fault zone and many others (Figure 2a), the active faults in the region were not discussed well in the current literature. In our study, we analysed the geomorphic features of the western part of Kosovo to reveal the relative assessment of major mountain front faults, which are referred to according to the important settlements along the mountain fronts (i.e., Pejë, Istog, Krojmir, and Prizren faults). Because of their bordering position on some major cities of the country, such an approach is also very important in the first step to understanding their seismic risk potential for those cities (i.e., Prizren, Pejë).

## 2. Geographic and Geological Settings

Kosovo is situated on the central-west Balkan Peninsula at an average altitude of 800 m (Figure 1). Geographically, it is generally addressed within two

regions; the eastern part represents a plateau known as the Kosovo Basin, and the western part includes the lowest point (296 m asl), which is bordered by higher mountains with the highest point of the country (2647 m asl), known as Dukagjini Basin (Figure 3a). Eastern Kosovo includes three major drainage basins that flow towards different directions; the Ibër and Morava rivers flow north- and north-eastward into the Danube River towards the Black Sea, and the Lepenci River flows into the Vardar River towards the Aegean Sea in the south (Figure 3b). Almost all of western Kosovo is drained by the Drini i Bardhë River flowing into the Adriatic Sea to the west. While the climate is predominantly continental with cold winters and warm summers, the eastern and western regions represent some differences because of topographic characteristics. Eastern Kosovo represents a more continental climate with a precipitation ratio of 600 mm/a, whereas western Kosovo is influenced by the air masses crossing the Adriatic Sea resulting in higher precipitation ratios (e.g., Elezaj and Kodra, 2007).

Geologically, Kosovo is positioned where the Dinarides, Albanides-Hellenides, and Carpatho-Balkan units juxtaposed (e.g., Elezaj, 2009) (Figure 1). Thus, there are various sedimentary, magmatic,

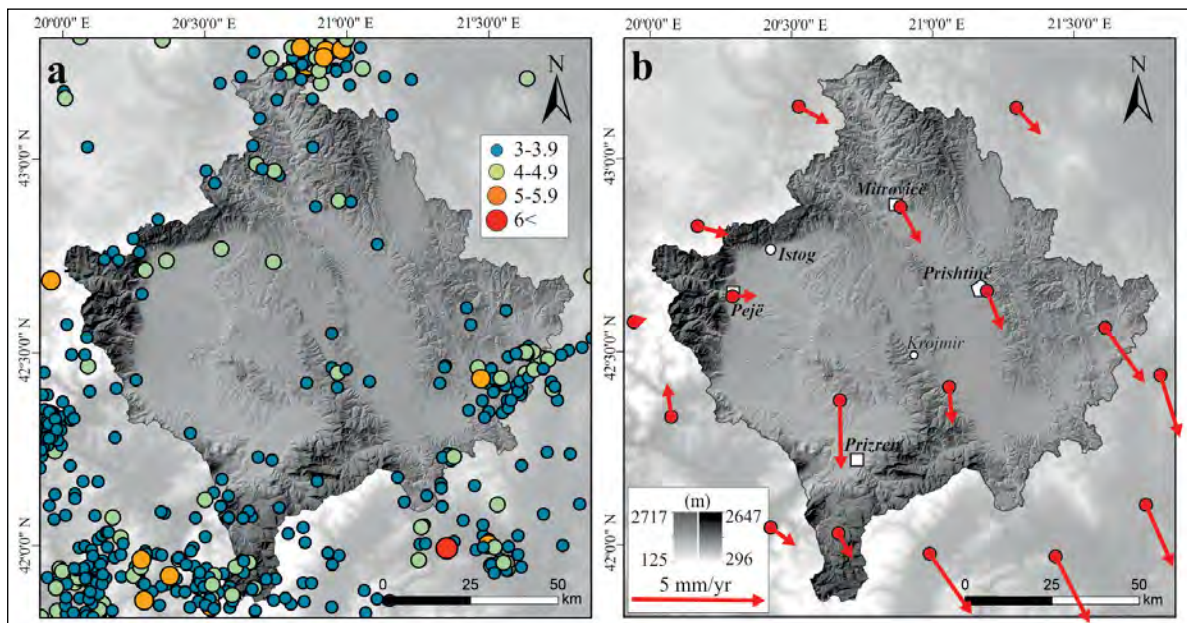


Figure 2- a) Seismicity of Kosovo between 1900-2020 from the USGS earthquake catalogue and b) GPS velocity field with respect to Eurasia from D'Agostino et al. (2020). Darker colour shade is for Kosovo from the topography digitized from 1:25.000 scaled maps in our study, and lighter shade is for the surrounding topography from SRTM.

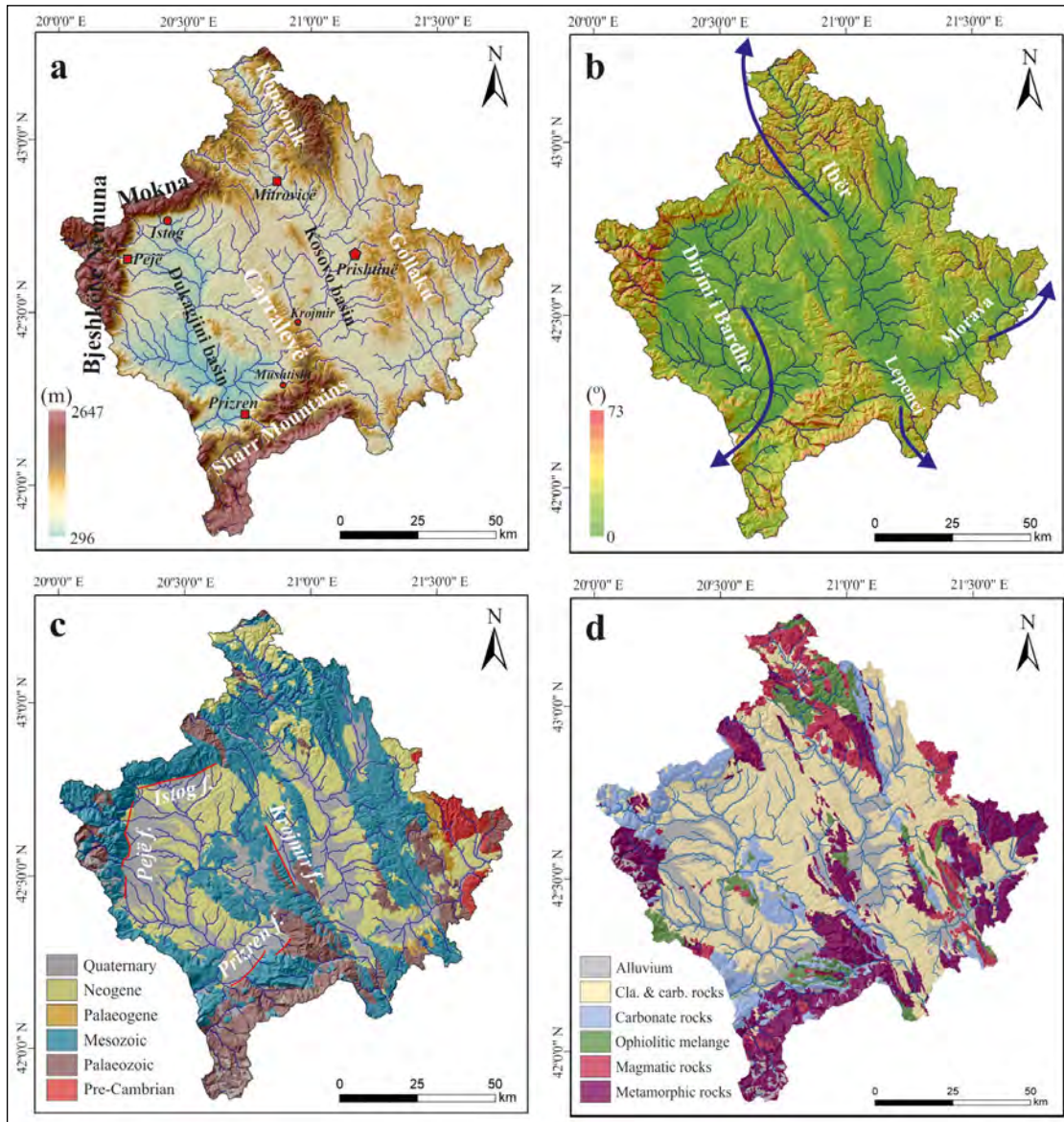


Figure 3- a) Physiographic image of Kosovo as digitized from 1:25.000 scaled topographic maps showing major ranges and basins, b) slope map of Kosovo and major drainage systems with their flowing directions, c) geological age map of Kosovo and the studied mountain front faults in our study (red lines; f – fault), d) lithology map of Kosovo. Both the age and lithology maps (c and d) are derived from KPMM (2006) which is based on Osnovna Geološko Karta SFRJ 1:100,000 – Geološki Institut, Beograd (1970-1984).

and metamorphic formations ranging from Pre-Cambrian to Quaternary complicated with folded and faulted architectures (Figures 3c and 3d). The oldest geologic units are mostly exposed to the mountainous regions surrounding the Kosovo and Dukagjini basins. While the Pre-Cambrian metamorphic rocks outcrop in the easternmost part of Kosovo, the Palaeozoic metamorphic and magmatic rocks are distributed whole of the country, but majorly exposed in the south, at the Sharr Mountains. On the other hand,

the Mesozoic units are represented by a variety of lithology including ophiolitic melange, metamorphic, magmatic, and sedimentary rocks (mostly carbonates), and distributed widely in the country. The Neogene units consist of sedimentary and volcanic rocks that are particularly important in the geological evolution of Kosovo, because of their spatial distributions covering most of the Kosovo and Dukagjini basins, which are majorly delimited by the neotectonic structures (e.g., Elezaj, 2009, 2012). The Quaternary units are also

very important because of their positions controlled by recent drainage patterns and mainly by mountain front faults, which are the focus point of our study.

### 3. Methods

#### 3.1. Geomorphic Analyses

In this study, we constructed a digital elevation model (DEM) of Kosovo with 10 m resolution by digitizing 1:25000 scale topographic maps. To quantify the geomorphic responses to active tectonics we used indices including mountain front sinuosity ( $S_{mf}$ ), basin shape ratio ( $B_s$ ), asymmetry factor ( $A_f$ ), valley floor width-to-height ( $V_f$ ), hypsometric curve and integral ( $HI$ ), and normalized steepness index ( $k_{sn}$ ). To select the ideal mountain fronts and related uplifted areas for analyses, we derived Red Relief Image Map of Kosovo providing detailed terrain surface information from our 10 m resolution DEM. After selecting four mountain fronts that correspond to neotectonic structures referred to as Pejë, Istog, Krojmir, and Prizren faults, we analysed 40 drainage basins on the mountains and ridges related to the mentioned mountain fronts and calculated the relative tectonic activity classes of each mountain front fault geomorphometrically. Lastly, we visited these locations to make field observations for interpreting our morphometric results reliable.

##### 3.1.1. Red Relief Image Map

Red relief image map (RRIM) build by the derivation of negative openness, positive openness, and slope images obtained from the DEM, and is very useful in active tectonics (e.g., Yao et al., 2019). While negative openness represents concavity of the terrain surface by highlighting depressions, positive openness represents convexity by highlighting ridges and crests (e.g., Yokoyama et al., 2002; Ulusoy et al., 2020). Chiba et al. (2008) suggested a parameter based on

$$I = (O_p - O_n)/2 \quad (1)$$

where  $O_p$  is positive and  $O_n$  is negative openness that eliminates incident light direction dependency and expresses both concavity and convexity. RRIM is based on this parameter shown in a greyscale overlain by a red colour-scale slope image (Chiba et al., 2008; Figure 4).

##### 3.1.2. Mountain Front Sinuosity

The mountain front sinuosity index ( $S_{mf}$ ), which reflects the balance between tectonic activity and erosion affecting a mountain front, is defined as

$$S_{mf} = L_{mf}/L_s \quad (2)$$

where  $L_{mf}$  is the length of the mountain-piedmont junction and  $L_s$  is the straight-line length of the mountain front (Bull and McFadden, 1977). While values close to 1.0 reflect less sinuous, relatively straight mountain fronts related to high tectonic activity, higher values represent high sinuosity related to the dominance of erosional processes over tectonic activity and reflect relative quiescent (e.g. Keller, 1986; Silva et al., 2003). In this study, we calculated  $S_{mf}$  index for 4 mountain fronts.

##### 3.1.3. Basin Shape Ratio

The drainage basin shape index ( $B_s$ ) of streams crossing mountain fronts reflects base-level changes arising from relative tectonic uplift and is defined by an elongation ratio expressed as

$$B_s = B_l/B_w \quad (3)$$

where  $B_l$  is the length and  $B_w$  is the width of the basin (Ramirez-Herrera, 1998). High values are associated with elongated basins indicating relatively high tectonic activity and rapidly uplifted mountain fronts, whereas low values represent more circular basins related to low tectonic activity (e.g. Ramirez-Herrera, 1998; El Hamdouni et al., 2008). This index was calculated for the 40 drainage basins of streams on the studied ranges in the western half of Kosovo in order to identify the elongated basins revealing rapid uplift.

##### 3.1.4. Asymmetry Factor

The drainage basin asymmetry factor ( $A_f$ ), which evaluates the tilting of the drainage basin related to tectonic activity, is calculated through

$$A_f = (A_r/A_t) 100 \quad (4)$$

where  $A_r$  is the area of the basin to the right of the trunk stream while facing downstream, and  $A_t$  is the total area of the drainage basin (Hare and Gardner, 1985). If the value is close to 50, the basin evaluated has less

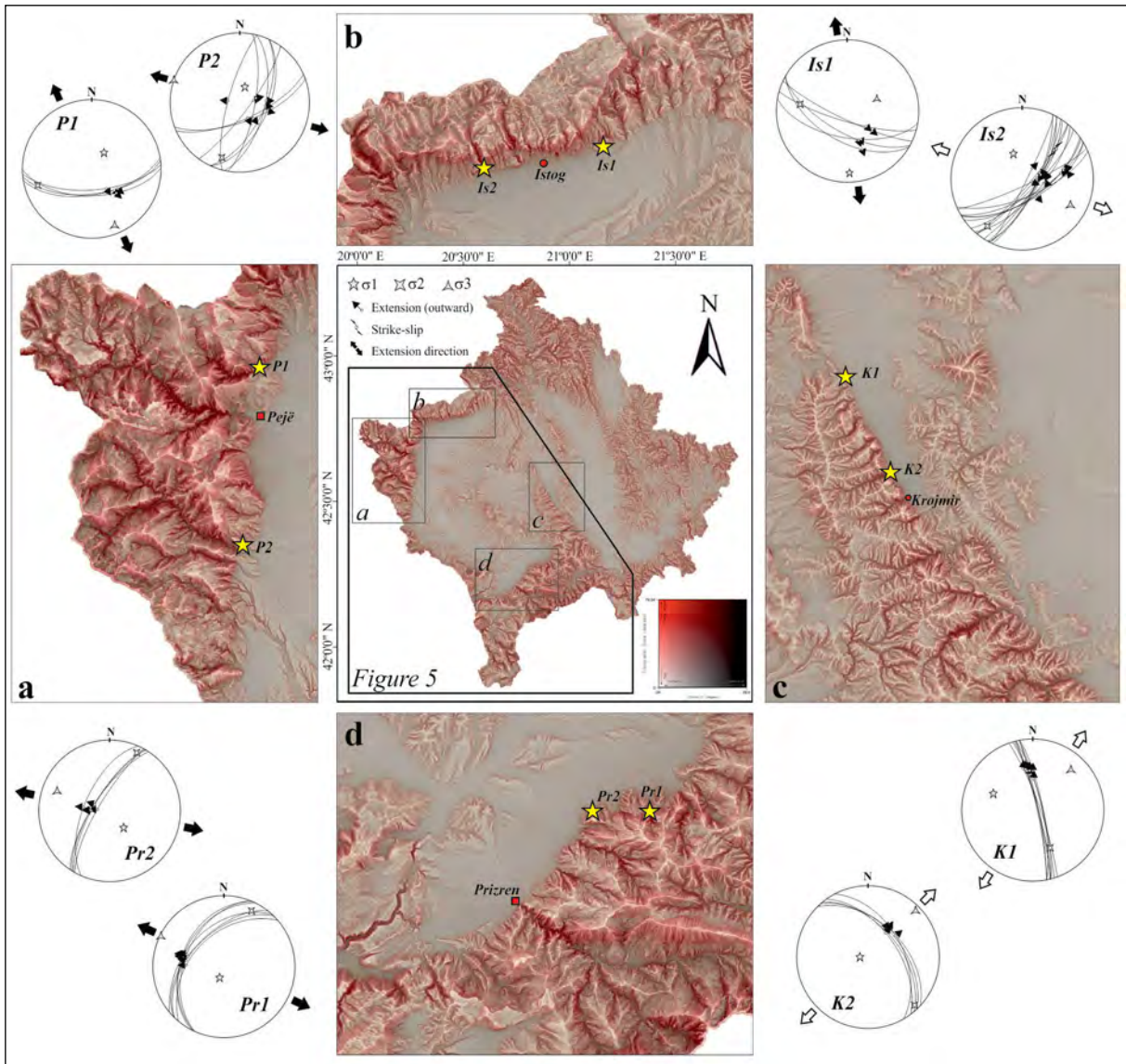


Figure 4- The Red Relief Image Map (RRIM) of Kosovo represents the geomorphic traces of studied mountain front faults and cyclographical traces, stress orientations and striations collected from the faults (Lower hemisphere equal area projection). Yellow stars with P – Pejë, Is – Istog, K – Krojmir and Pr – Prizren indicate measured fault plane locations.

or no tilting and is stable, whereas values far below or far above 50 represent the drainage basin is under the effect of tectonic tilting and/or differential erosion of lithology and is unstable (e.g. Keller and Pinter, 2002; El Hamdouni et al., 2008). In our study, the asymmetry factor is calculated for 40 drainage basins on four ridges to consider any tilting process related to active tectonic deformation and/or lithological control.

### 3.1.5. Valley Floor Width-to-Height Ratio

The valley floor width-to-height ratio ( $V_f$ ) of streams differentiates the wide floored valleys and

narrow floored valleys relative to their wall heights and is computed by

$$V_f = 2V_{fw} / [(E_{ld} - E_{sc}) + (E_{rd} - E_{sc})] \quad (5)$$

where  $V_{fw}$  is the width of the valley floor,  $E_{ld}$  and  $E_{rd}$  are the elevations of the left and right sides of the valley, and  $E_{sc}$  is the elevation of the valley floor (Bull and McFadden, 1977). While  $V_f$  values lower than 1.0 represent V-shaped valleys associated with high incision rates, values higher than 1.0 indicate U-shaped valleys related to high lateral erosion (Bull and McFadden, 1977; Silva et al., 2003). The incision

is generally related to uplift, thus the index represents tectonic activity (El Hamdouni et al., 2008). Because of  $V_f$  values can considerably change related to their positions along the valley (Ramirez-Herrera, 1998), to make meaningful comparisons among different valleys values are often calculated at a given distance from the stream mouth (Silva et al., 2003; Cheng et al., 2018). In our study, positions of the  $V_f$  cross-sections have been chosen with a distance of 1 km from each of the 40 stream mouths.

### 3.1.6. Hypsometry

Hypsometry is an important approach for active tectonics (e.g. Keller and Pinter, 2002) and is highly sensitive to continued topographic evolution (e.g. Harlin, 1978; Mayer, 1990). The hypsometric curves are constructed by plotting the proportion of total basin elevation versus the proportion of total basin area, thus expressing the volume of a basin that has not been eroded (e.g. El Hamdouni et al., 2008). The hypsometric integral ( $HI$ ) index describes the distribution of elevation of a given area of a landscape, particularly for drainage basins, (Strahler, 1952) and is calculated as

$$HI = (H_{mean} - H_{min}) / (H_{max} - H_{min}) \quad (6)$$

where  $H_{mean}$  is the mean,  $H_{max}$  is the maximum, and  $H_{min}$  is the minimum elevations (e.g. Pike and Wilson, 1971; Mayer, 1990; Keller and Pinter, 2002). While high values generally indicate low eroded material and a young landscape probably produced by active tectonics, low values majorly represent high erosion rates and less tectonic uplift (e.g. El Hamdouni et al., 2008). In our study, we computed the hypsometric curves and integrals for 40 drainage basins to discuss the roles of constructive tectonic and destructive erosive forces.

### 3.1.7. Normalized Channel Steepness Index

The normalized channel steepness index ( $k_{sn}$ ) is a convenient approach for active ranges to Figure out a relative assessment of tectonic uplift rates (e.g., Wobus et al., 2006; Dibiase et al., 2010; Kirby and Whipple, 2012). Because the channel steepness index is sensitive to changes in uplift rates, lithology and climate at steady-state, while the concavity of most stream channels on mountains has uniform concavity

independent from the uplift rates (Snyder et al., 2000; Whipple, 2004; Kirby and Whipple, 2012). Normalization of this index is useful to compare streams and catchments of different drainage areas through their profile morphology (Sukhishvili et al., 2021). Streams on both bedrock and alluvial rivers have typically concave profiles that can be described by an empirical power law relationship:

$$k_{sn} = SA^\theta \quad (7)$$

Where  $S$  is the slope,  $A$  is the drainage area and  $\theta$  is the channel concavity index (Flint, 1974; Sukhishvili et al., 2021). Practically, values between 0.4 and 0.5 work well for most mountain streams as a reference concavity ( $\theta_{ref}$ ) (Kirby and Whipple, 2012); thus, we used 0.45 for  $\theta_{ref}$  in this study as generally accepted (e.g., Kirby and Whipple, 2012; Han et al., 2017; Kothiyari et al., 2020). We mapped  $k_{sn}$  values of the fluvial systems in western Kosovo based on construction through the kernel density values, which indicate how well features are clustered Figure 11 (e.g., Sun and Mann, 2021).

## 3.2. Structural Analyses

In the field, a total of 58 fault slip data were collected and analysed, which are considered as the younger movements for the studied mountain front faults (12 data from 2 locations on the Pejë, 21 data from 2 locations on the Istog, 13 data from 2 locations on the Krojmir and 12 data from 2 locations on the Prizren mountain fronts). We used WinTensor 5.9.2 (Delvaux and Sperner, 2003) for stress analyses.

## 4. Results

### 4.1. Pejë Fault

NNE-SSW-directed Pejë fault bounds the Dukagjini Basin from the west with a length of ~35 km. The fault defines the front of Bjeshkët e Nemuna mountains with a sharp slope break (Figures 3b, 3c, and 4), which consists of Palaeozoic and Mesozoic metamorphic and Mesozoic carbonate rocks (Figures 3c and 3d), and represents an  $S_{mf}$  value of 1.26 (Table 1). Ten drainage basins that analyzed related to the Pejë fault have  $V_f$  values in the range of 0.03 and 0.29, values of  $B_s$  ranging from 1.55 to 5.29,  $A_f$  values between 29.66 and 76.33, and  $HI$  values

ranging from 0.41 to 0.58 (Figure 5; Table 1). The hypsometric curves represent a majorly mature to a bit young stage, approximately from south to north (Figure 11). The  $k_{sn}$  analyses of the streams on the Bjeshkët e Nemuna Mountains represent high values, particularly in the northern part where the lithology is mainly represented by carbonate sedimentary rocks (Figure 6). The geomorphology of this mountain front actually supports these morphometric results with clear geomorphic proofs of activity such as trapezoidal to triangular facets and well-developed piedmont and alluvial fan deposits (Figure 7). According to

the kinematic data collected from the field in two locations, the eastward dipping normal fault indicates WNW-ESE-directed extension (Figures 4 and 7; Table 2). While we could not observe a direct contact of the fault plane with Quaternary deposits, the strikes of the fault planes are compatible with the ~ N-S orientation of the fault (Figure 4).

#### 4.2. Istog Fault

The E-W trending and southward dipping Istog fault bounds the Mokna Mountains from the south along a ~25 km long front that corresponds to the

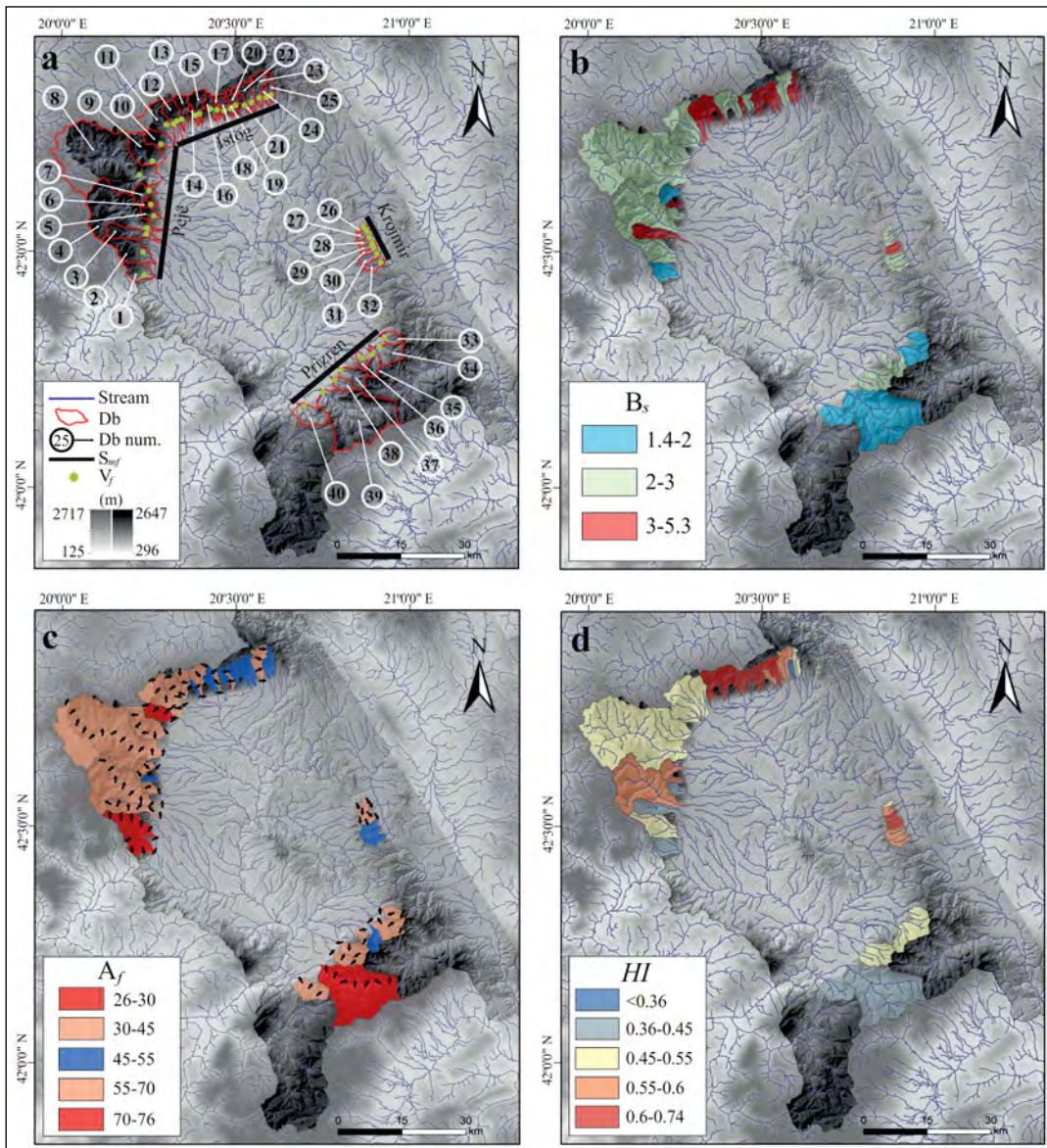


Figure 5- a) Index map for the locations of calculated  $S_{mf}$ ,  $V_f$  and other indices for the drainage basins (Db – drainage basin), b)  $B_s$ , c)  $A_f$ , and d)  $HI$  values calculated for these drainage basins along the studied parts of the mountain front faults.

Table 1- Results of the morphometric indices used for the studied four mountain front faults in western Kosovo.

Mountain front fault	$S_{mf}$	Drainage basin no.	$V_f$	$B_s$	$A_f$	$HI$
Pejë	1.26	1	0.05	1.61	29.66	0.41
		2	0.29	2.21	75.35	0.47
		3	0.12	5.29	68.09	0.45
		4	0.06	2.57	68.78	0.56
		5	0.1	2.14	55.62	0.42
		6	0.1	3.73	47.58	0.55
		7	0.06	1.55	38.38	0.58
		8	0.03	2.3	55.89	0.54
		9	0.03	2.27	41.38	0.55
		10	0.05	2.14	76.33	0.54
Istog	1.06	11	0.1	2.29	65.53	0.53
		12	0.14	3.87	57.86	0.51
		13	0.15	4.1	37.51	0.66
		14	0.13	5.31	52.72	0.63
		15	0.08	2.93	58.73	0.72
		16	0.08	2.95	53.06	0.65
		17	0.17	4.79	41.22	0.65
		18	0.39	2.97	53.14	0.73
		19	0.1	4.84	40.26	0.66
		20	0.05	4.27	46.23	0.74
		21	0.15	4.83	48.25	0.55
		22	0.25	3.08	47.19	0.6
		23	0.09	2.86	62.93	0.56
		24	0.15	4.13	46.83	0.36
		25	0.31	4.96	47.52	0.46
Krojmir	1.11	26	0.22	2.72	34.4	0.5
		27	0.16	2.14	36.47	0.58
		28	0.17	2.64	40.53	0.6
		29	0.09	3.2	42.92	0.61
		30	0.16	4.16	49.15	0.61
		31	0.13	2.64	47.62	0.59
		32	0.08	2.09	46.63	0.59
Prizren	1.28	33	0.17	1.9	63.06	0.47
		34	0.18	1.58	33.77	0.52
		35	0.16	2.24	49.52	0.51
		36	0.15	2.03	30.1	0.44
		37	0.12	2.19	56.76	0.52
		38	0.12	2.23	40.13	0.47
		39	0.14	1.4	26.03	0.42
		40	0.29	1.55	40.12	0.45

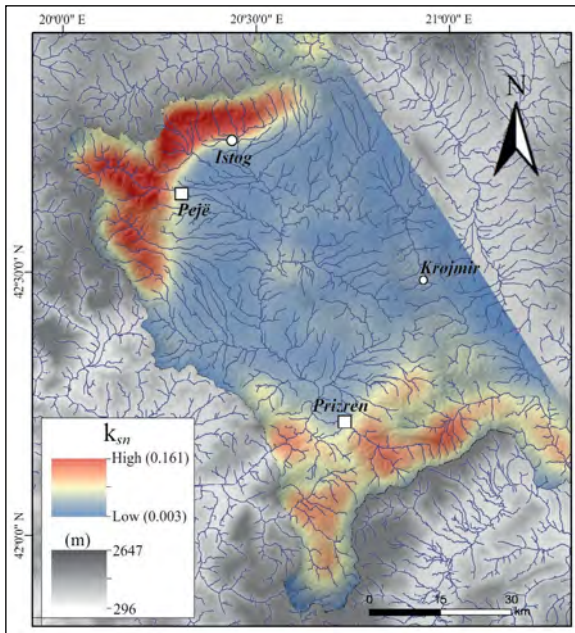


Figure 6- The  $k_{sn}$  map of western Kosovo constructed through the kernel density values.

northern margin of the Dukagjini Basin (Figures 3b, 3c, and 4). Except for a little area of metamorphic and magmatic rocks to the easternmost part of the mountain, the main lithology cut by the Istog fault is Mesozoic carbonate rocks (Figures 3c and 3d). The mountain front has a  $S_{mf}$  value of 1.06, which is the lowest  $S_{mf}$  value among the studied four mountain fronts (Table 1). Among the studied mountain front faults, the Istog fault was studied through the highest number of drainage basins. Fifteen drainage basins have the  $V_f$  values in the range of 0.05 and 0.39, values of  $B_s$  ranging from 2.29 to 5.31,  $A_f$  values

between 37.51 and 65.53, and hypsometric integral values ranging from 0.36 to 0.74 (Figure 5; Table 1). Almost whole of the drainage basins on the Mokna Mountains represents the youthful stage according to hypsometric curves (Figure 11). According to the  $k_{sn}$  analyses, while the values decrease towards the east along the mountains, this region represents the highest  $k_{sn}$  values in western Kosovo (Figure 6). In addition to these, morphometric proofs of high activity level, geomorphic observations of a steep scarp with trapezoidal and triangular facets, deeply incised valleys, and aligned water springs along the Istog fault also indicate the rapid uplift/high activity (Figure 8). In the field, we measured fault slip data at two locations on the eastern and western parts of the Istog fault (Table 2). Our data represent normal faulting developed as a result of NW-SE-directed extension in the region (Figure 4). Particularly to the western part of the fault, the brecciated fault plane with contact in Quaternary deposits including normal drag fold represents the fault character and its activity in the Quaternary period (Figure 8).

#### 4.3. Krojmir Fault

NW-SE trending and eastward dipping Krojmir fault delimits the Carralevë Mountains from the east with a steep slope, which is located in central Kosovo, that separates the Dukagjini basin from the Kosovo basin (Figures 3b, 3c and 4). Among the heights delimited by the studied faults, the Carralevë Mountains represent the lowest topography with a maximum height of 1177 m. The main lithology

Table 2- Fault slip data measured along the studied mountain fronts in western Kosovo ( $\sigma_1$ ,  $\sigma_2$  and  $\sigma_3$ : Trend and plunge of principal stress axes; R: Stress ratio).

Mountain front fault	Location	Coordinate		$\sigma_1$	$\sigma_2$	$\sigma_3$	R	N	Age/Lithology
		North	East						
Pejë	P1	42° 42' 19"	20° 17' 28"	037/67	253/19	159/13	0.49	4	Mesozoic / limestone
	P2	42° 33' 22"	20° 16' 15"	018/72	198/18	288/00	0.38	8	Mesozoic / metaclastics
Istog	Is1	42° 47' 41"	20° 31' 49"	068/53	278/33	178/14	0.5	5	Mesozoic / metacarbonates
	Is2	42° 46' 42"	20° 24' 15"	341/59	217/18	118/23	0.53	16	Mesozoic / limestone and volcanosedimentary
Krojmir	K1	42° 34' 8"	20° 52' 16"	293/40	155/42	043/23	0.5	8	Mesozoic / serpentinite
	K2	42° 30' 5"	20° 54' 58"	267/80	136/06	046/07	0.49	5	Mesozoic / serpentinite
Prizren	Pr1	42° 16' 34"	20° 51' 58"	201/76	026/14	296/01	0.57	7	Mesozoic/ limestone
	Pr2	42° 16' 41"	20° 48' 49"	144/69	030/09	297/18	0.5	5	Mesozoic / peridotite



Figure 7- Field photos from the Pejë mountain front fault; a) slope break on the topography to the south of Pejë. b) triangular facets to the southwest of Deçan, c), d) and e) fault plane and kinematic indicators observed in P1 (please see Figure 4 for the location). In (e) the right-lateral slip represents older movement and it is overprinted by normal slip with left-lateral component representing the younger movement on the fault plane.

includes Palaeozoic metamorphic rocks and Mesozoic volcanoclastic rocks, serpentinites, carbonate, and clastic sedimentary rocks (Figures 3c and 3d) The Krojmir fault extends more than 30 km; however, actually, the slope break delimiting the studied part of the mountainous topography corresponds to a length of ~15 km. The mountain front created by the Krojmir fault has a  $S_{mf}$  value of 1.11, which is the

second lowest value after the Istog fault (Table 1). Only seven drainage basins corresponding to the southern half of the studied mountain front were analysed morphometrically. The  $V_f$  values range from 0.08 and 0.22,  $B_s$  values are between 2.09 and 4.16,  $A_f$  values range between 34.40 and 49.15, and  $HI$  values range from 0.5 to 0.61 (Figure 5; Table 1). Hypsometric curves of the drainage basins on the



Figure 8- Field photos from the Istog mountain front fault; a) slope break on the topography, b) faulted topography and deeply incised valley representing rapid tectonic uplift, c) Istog water spring is one of the most important water sources of Kosovo, which is positioned on the Istog fault, d) fault plane observed in Is2 (please see Figure 4 for the location). Please note the normal drag fold (hanging-wall syncline) in Quaternary deposits associated with friction during the uplift of the footwall.

Carralevë Mountains dominantly represent a young stage (Figure 11). However, the streams on this part of the mountains have the lowest  $k_{sn}$  values among the studied ranges, because of the low strength of clastic rocks. On the other hand, geomorphological field observations along the fault support the general geomorphometric results indicating its activity with well-developed triangular facets along a straight line (Figure 9). Among all the mountain front faults studied in this study, with respect to its clear imprint on the topography, finding a reliable young fault plane is hard along the Krojmir fault because of highly deformed older lithological units. However, on the northern and southern parts of the fault, the kinematic data collected from two locations on serpentinites indicate both oblique-slip and normal faulting with NE-SW directed extension (Figures 4 and 9; Table 2).

#### 4.4. Prizren Fault

NE-SW trending and NW-wards dipping Prizren fault bounds the Dukagjini Basin from the south

with a ~30 km length (Figures 3b, 3c, and 4). This line also coincides with the northern front of the Sharr Mountains, which is one of the major ranges in the region with a maximum height of 2651 m (Figures 3a and 4). The Sharr Mountains consist of a variety of lithology among the other studied mountains including Palaeozoic metamorphic rocks and Mesozoic magmatic, metamorphic, ophiolitic melange, and carbonate rocks (Figures 3c and 3d).  $S_{mf}$  value for the Sharr Mountains along the Prizren fault is 1.28, which is the lowest among the studied faults (Table 1). Geomorphometric indices applied for eight drainage basins on the range represent  $V_f$  values ranging from 0.12 to 0.29,  $B_s$  values between 1.4 and 2.24,  $A_f$  values ranging from 26.3 to 63.06, and hypsometric integral values between 0.42 and 0.52 (Figure 5; Table 1). Hypsometric curves of the drainage basins flowing towards the Dukagjini Basin on the Sharr Mountains majorly represent the mature stage (Figure 11). The streams represent the second lowest  $k_{sn}$  values among the studied ranges. Triangular



Figure 9- Field photos from the Krojmir mountain front fault; a) slope break on the topography, b), c) triangular facets. Fault planes in d) K1 and e) K2 locations to the north and south of the mountain front fault, respectively. Please see Figure 4 for the locations.

facets and alluvial fans are aligned along the Prizren fault (Figure 10). In the field, we observed a normal fault plane coincides with the topographic trace of the Prizren fault towards east (Figures 10c and 10d). Kinematic data on the fault plane represent NW-SE-directed extension (Pr1; Figure 4, Table 2).

## 5. Discussion

### 5.1. Assessment of Relative Activity and Implications on the Seismicity of Western Kosovo

Tectonic activity classification based on the correlation of  $S_{mf}$  and  $V_f$  indices is helpful to evaluate

the relative activity of mountain front faults (e.g., Bull and McFadden, 1977; Rockwell et al., 1985; Silva et al., 2003). According to our results, all of the studied faults are within Class 1 representing high activity, which also indicates uplift rates of  $>0.5$  mm/a (Figure 12). These results are also coherent with the results of individual other indices, such as with  $B_s$  and  $HI$  (Table 1; Figure 5d), pointing out the higher activities of the Istog and Krojmir faults. These are followed by the activity levels of Pejë and Prizren faults, respectively. According to the  $A_f$  values, the Istog and Krojmir faults represent the more neutral character, while the drainage basins along the Pejë and Prizren mountain



Figure 10- Field photos from the Prizren mountain front fault; a) triangular facets, b) slope break on the topography. c, d) Observed normal fault plane in Pr1. Please see Figure 4 for the location.

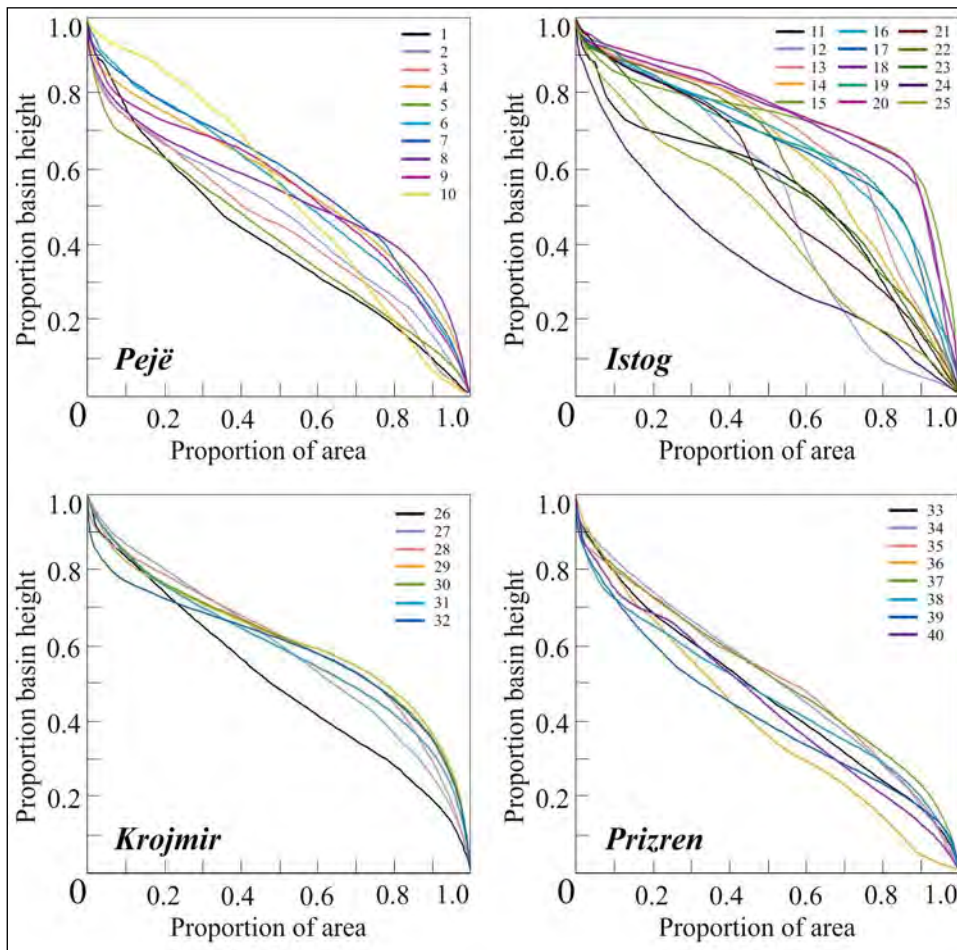


Figure 11- Hypsometric curves of the drainage basins on the studied mountain front faults.

front faults have prominent asymmetries, most probably because of weaker lithological features on the last two mountain fronts consisting of ophiolitic melange and metamorphic rocks. On the other hand, the  $k_{sn}$  values represent the higher activity along the Pejë and Istog normal faults clearly than the Prizren and Krojmir faults. D'Agostini et al. (2022) suggested that the Istog fault has no significant evidence of recent activity, and the Pejë fault is more active than the Istog based on their observations. However, according to our aforementioned geomorphometric results, the Istog fault represents higher activity. Among the studied mountain front faults, while all of them have direct contact majorly with the Quaternary deposits (Figure 3c) showing their probable activities in this period, observed normal drag fold within the colluvial deposits on the Istog fault represents the effect of normal faulting on the Quaternary units (Figure 8d). Evaluating their geomorphic, morphometric and

structural features together, the studied Pejë, Istog, Krojmir, and Prizren normal faults are active faults that can create earthquakes with magnitudes 6.4 to 6.8, according to the empirical relationship of Wells and Coppersmith (1994), if they ruptured along their mountain front total lengths.

Today, Kosovo exhibits moderate seismicity (Sulstarova and Aliaj, 2001; Elezaj, 2002; Muço et al., 2012). However, there are important historical records in the country (Mustafa et al., 2020). Among them, there are two historical earthquakes corresponding to the studied faults in our study with magnitudes 6.6 (1456 earthquake) at Prizren and 6.0 (1662 earthquake) at Pejë (Orana et al., 1985; Muço et al., 2012; Mustafa, 2016). On the other hand, whereas some important earthquakes recorded in the instrumental period with a magnitude over 5 within the boundaries of the country (24/4/2002 earthquake at Gjilan, SE of Kosovo),

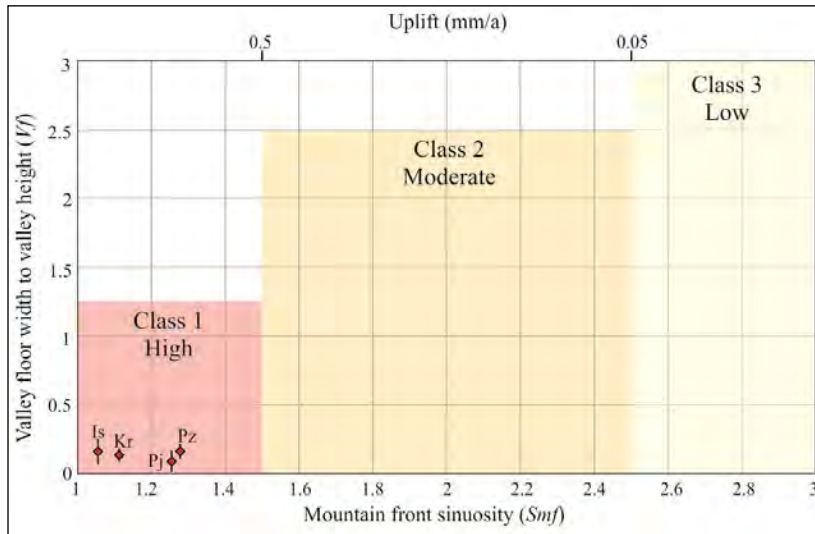


Figure 12- Inferred activity classes of the studied mountain front faults in western Kosovo based on the plot of  $S_{mf}$  vs  $V_f$  after Bull and McFadden (1977), and inferred uplift rates ( $U$ ) after Rockwell et al. (1985).

among the studied faults, the Istog and Krojmir faults have records reaching over the magnitude 4.5 (Figure 2a). Both the historical and instrumental seismicity recorded in western Kosovo also support our aforementioned results and implications, which can be summarized as a high activity class for all the studied mountain front faults.

## 5.2. Implications on the Regional Tectonics

At the Dinarides-Hellenides belt transition, Neogene tectonics, and associated fault systems are regulated by mechanisms induced by the Hellenic slab roll-back (Figure 1a) (e.g., Handy et al., 2019). As aforementioned, the Shkodër-Pejë transverse zone was originally a transform fault as evidenced by the 100 km displacement of the ophiolitic melanges to the north and south of the fault; however, today, it represents normal fault character as evidenced by the kinematic data collected majorly in northern Albania and southern Montenegro, enabling the rotation movement of the Albanides-Hellenides with respect to Dinarides (e.g., Handy et al., 2015, 2019; Biermans et al., 2019). According to our field observations, fault slip data on the planes of the Pejë fault, which corresponds to the eastern extension of the Shkodër-Pejë fault zone (e.g., Handy et al., 2015, 2019), supported the normal faulting in the region (e.g., D'Agostino et al., 2022). On the other hand, while our geomorphic

analyses along the four mountain fronts in western Kosovo represented high activity, the  $k_{sm}$  values clearly shone out the higher activity of Pejë and Istog faults and supporting their probable continuity as part of an important fault zone (i.e., Shkodër-Pejë fault zone), as suggested by some authors (e.g., Schmid et al., 2020). The Prizren fault also shows normal fault character as evidenced by the kinematic data. The Krojmir fault exhibits fault slip data indicating oblique and normal character. In such a scene, while the Pejë, Istog and Prizren faults represent NW-SE-directed extension in the region, the Krojmir fault has kinematic indicators supporting NE-SW-oriented extension.

Such an extensional tectonic regime has been known for the south Balkans since the Palaeogene, however, the recent phase of extension in the region started just after a short post-Palaeogene shortening, in the early Neogene (e.g., Burchfiel et al., 2000, 2006, 2008; Dumurdzanov et al., 2005). Since that time, the Albanides-Hellenides has rotated clockwise with respect to Dinarides and Africa (Figure 1; Kissel et al., 1995; Speranze et al., 1995; van Hinsbergen et al., 2005; Handy et al., 2019; D'Agostino et al., 2020) because of pulling along the Hellenic trench and tearing of the underlying Adriatic plate (e.g., Handy et al., 2019). On the other hand, there is a contraction to the west between the Adriatic and Eurasian plates,

which is associated with great earthquakes responsible for many casualties and economic losses (e.g., 1979 Montenegro earthquake -  $M_w=7.1$ , and 2019 Albania earthquake -  $M_w=6.4$ ; Benetatos and Kiratzi, 2006; Papadopoulos et al., 2020). However, this NE-SW trending contraction is replaced by an extension in the hinterland due to rollback (e.g., D'Agostino et al., 2008, 2020; Nocquet, 2012; Biermanns et al., 2022). Because of the effects of extension caused by the rollback of subducting slabs in the Aegean and Adriatic seas, and the clockwise rotation of the Albanides-Hellenides to the south of Shkodër-Pejë fault zone (e.g., Jouanne et al., 2012; Faccenna et al., 2014; Handy et al., 2015; Biermanns et al., 2022), western Kosovo has mountain fronts controlled by majorly normal faults representing a dominance NW-SE-directed extension in this part of Balkans, coherent with the GPS data (Figures 1 and 2b).

## 6. Conclusions

The topographic features of the country represent faulted mountain fronts with clear geomorphic indicators of activity, particularly in western Kosovo delimiting the Dukagjini Basin. In this study, to understand the active tectonics of western Kosovo and make implications on its seismicity, we obtained results from different geomorphometric analyses, geomorphological observations, and structural measurements.

According to the results of geomorphometric analyses of the studied four different mountain fronts, the Pejë, Istog, Krojmir, and Prizren faults are all classified in Class I as high activity and indicating tectonic uplift rates of over 0.5 mm/a according to the calculated  $S_{mf}$  and  $V_f$  values. Among them, the ENE-WSW trending Istog fault clearly separated from the others with its higher  $B_s$  and  $HI$  values indicating its higher activity. The NNW-SSE-directed Krojmir, the NNE-SSW trending Pejë, and the NE-SW-oriented Prizren faults follow it, respectively. However, all the studied faults are highly active and can create earthquakes with magnitudes between 6.4 and 6.8, if they will be ruptured all along the related mountain fronts. On the other hand, according to  $k_{sn}$  values,

the Pejë and Istog faults are clearly the highest and indicate a probable structural continuity. As known for a long time, the orogens of Dinarides to the north and Albanides-Hellenides to the south are separated by a fault zone known as the Shkodër-Pejë fault zone reaching northern Kosovo. According to the geomorphometric analyses, the Istog fault can be interpreted as the eastern continuity of the Shkodër-Pejë fault zone together with the Pejë fault and represent its importance for the seismicity of western Kosovo. In the field, we observed many indicators of high activity/rapid uplift along the studied mountain front faults imprinted geomorphologically, such as trapezoidal to triangular facets, steep scarps, deeply incised valleys, and well-developed alluvial fan deposits. On the other hand, according to the collected kinematic data from the fault planes observed on each of the studied faults, the NNE-SSW trending Pejë, the ENE-WSW-directed Istog, and the NE-SW-oriented Prizren faults are normal faults, and represent NW-SE-directed extension. The NW-SE trending Krojmir fault represents an oblique and normal character with NE-SW-oriented extension.

Relative activity and general structural pattern of the studied faults indicate the dominant role of the eastern part of the Shkodër-Pejë fault zone in western Kosovo (i.e., Pejë and Istog faults) and the major role of NW-SE-directed active extension. This extension is most probably caused by the effect of the rollback of the subducting slab in the Hellenic trench and the related clockwise rotation of the Albanides-Hellenides to the south of the Shkodër-Pejë fault zone. However, for a well-understanding of the active tectonics and seismicity of whole the country, eastern Kosovo should also be studied, where the structural pattern seems a little bit different and the major part of the population and industry of the country is hosted.

## Acknowledgements

The authors are grateful to two reviewers for their constructive criticisms and to Dr. Ercan SANGU for suggestions on the kinematic analysis. The stress analysis results were obtained using Win-Tensor, a software developed by Dr. Damien DELVAUX, Royal Museum for Central Africa, Tervuren, Belgium.

## References

- Aliaj, Sh. 1988. Neotectonics and seismicity of Albania. Ph.D. Thesis, 265, Archive of Seismological Institute, Albanian.
- Aubouin, J., Blanchet, R., Cadet, J. P., Celet, P., Charvet, J., Chorowicz, J., Cousin, M., Rampnoux, J. P. 1970. Essai sur la géologie des Dinarides. Bulletin de la Société géologique de France 7(6), 1060-1095.
- Baker, C., Hatzfeld, D.L., Lyon-Caen, H., Papadimitriou, E., Rigo, A. 1997. Earthquake mechanisms of the Adriatic Sea and Western Greece: Implications for the oceanic subduction-continental collision transition. *Geophysical Journal International* 131(3), 556-594.
- Benetatos, C., Kiratzi, A. 2006. Finite-fault slip models for the 15 April 1979 (Mw 7.1) Montenegro earthquake and its strongest aftershock of 24 May 1979 (Mw 6.2). *Tectonophysics* 421 (1–2), 129–143.
- Biermanns, P., Schmitz, B., Ustaszewski, K., Reicherter, K. 2019. Tectonic geomorphology and Quaternary landscape development in the Albania – Montenegro border region: an inventory. *Geomorphology* 326, 116–131.
- Biermanns, P., Schmitz, B., Mechernich, S., Weismüller, C., Onuzi, K., Ustaszewski, K., Reicherter, K. 2022. Aegean-style extensional deformation in the contractional southern Dinarides: incipient normal fault scarps in Montenegro. *Solid Earth* 13(6), 957-974.
- Bradley, K. E., Vassilakis, E., Hosa, A., Weiss, B. P. 2013. Segmentation of the Hel-lenides recorded by Pliocene initiation of clockwise block rotation in Central Greece. *Earth Planet Science Letters* 362, 6–19.
- Bull, W. B., McFadden, L. D. 1977. Tectonic geomorphology north and south of the Garlock Fault, California. Doehering, D. O. (Ed.). *Geomorphology of Arid Regions*. Binghamton, State University of New York, Proceedings of the 8th Annual Geomorphology Symposium Proceedings, 115-138.
- Burchfiel, C. B., Nakov, R., Tzankov, T., Royden, L. H. 2000. Cenozoic extension in Bulgaria and northern Greece: the northern part of the Aegean extensional regime. *Geological Society of London, Special Publications* 173(1), 325-352.
- Burchfiel, B. C., King, R. W., Todosov, A., Kotzev, V., Durmurdzanov, N., Serafimovski, T., Nurce, B. 2006. GPS results for Macedonia and its importance for the tectonics of the Southern Balkan extensional regime. *Tectonophysics* 413(3-4), 239-248.
- Burchfiel, B. C., King, R. W., Nakov, R., Tzankov, T., Durmurdzanov, N., Todosov, A., Nurce, B. 2008. Patterns of Cenozoic Extensional Tectonism in the South Balkan Extensional System. In *Earthquake Monitoring and Seismic Hazard Mitigation in Balkan Countries*, Springer, Dordrecht.
- Cheng, Y., He, C., Rao, G., Yan, B., Lin, A., Hu, J., Yangli, L., Yao, Q. 2018. Geomorphological and structural characterization of the southern Weihe Graben, central China: Implications for fault segmentation. *Tectonophysics* 722, 11-24.
- Chiba, T., Kaneta, S. I., Suzuki, Y. 2008. Red relief image map: new visualization method for three dimensional data. *The International Archives of the Photogrammetry, Remote Sensing and Spatial Information Sciences* 37(B2), 1071-1076.
- D'Agostino, N., Avallone, A., Cheloni, D., D'Anastasio, E., Mantenuto, S., Selvaggi, G. 2008. Active tectonics of the Adriatic region from GPS and earthquake slip vectors. *Journal of Geophysical Research* 113(B12), B0940.
- D'Agostino, N., Métois, M., Koci, R., Duni, L., Kuka, N., Ganas, A., Georgiev, I., Jouanne, F., Kaludjerovic, N., Kandić, R. 2020. Active crustal deformation and rotations in the southwestern Balkans from continuous GPS measurements. *Earth and Planetary Science Letters* 539, 116246.
- D'Agostino, N., Copley, A., Jackson, J., Koçi, R., Hajrullai, A., Duni, L., Kuka, N. 2022. Active tectonics and fault evolution in the Western Balkans. *Geophysical Journal International* 231(3), 2102-2126.
- Delvaux, D., Sperner, B. 2003. Stress tensor inversion from fault kinematic indicators and focal mechanism data: the TENSOR program. Nieuwland, D. (Ed.). *New Insights into Structural Interpretation and Modelling*. Geological Society of London, Special Publications 212, 75-100.
- Dibiase, R. A., Whipple, K. X., Heimsath, A. M., Ouimet, W. B. 2010. Landscape form and millennial erosion rates in the San Gabriel Mountains, CA. *Earth and Planetary Science Letters* 289(1-2), 134-144.
- Dumurdzanov, N., Serafimovski, T., Burchfiel, B. C. 2005. Cenozoic tectonics of Macedonia and its relation to the South Balkan extensional regime. *Geosphere* 1(1), 1-22.
- Elezaj, Z. 2002. Seismotectonic characteristics of Kosovo as basis for its seismic zonation. Ph.D. Thesis, Prishtina, Kosovo (in Albanian).
- Elezaj, Z. 2009. Seismotectonic settings of Kosovo. *Journal of International Environmental Application and Science* 4(2), 167-176.

- Elezaj, Z. 2012. Late and young tectonics (Neotectonics) and seismicity of Kosovo. *Journal of International Environmental Application and Science* 7(4), 744-749.
- Elezaj, Z., Kodra, A. 2007. Gjeologjia e Kosovës. Univ. i Prishtinës, Fak. i Xehetarisë dhe Metalurgjisë Mitrovicë 293.
- El Hamdouni, R., Irigaray, C., Fernández, T., Chacón, J., Keller, E. A. 2008. Assessment of relative active tectonics, southwest border of the Sierra Nevada (southern Spain). *Geomorphology* 96(1-2), 150-173.
- Faccenna, C., Jolivet, L., Piromallo, C., Morelli, A. 2003. Subduction and the depth of convection in the Mediterranean mantle. *Journal of Geophysical Research: Solid Earth* 108(B2), 2099.
- Facenna, C., Becker, T.W., Auer, L., Billi, A., Boschi, L., Brun, J.P., Capitanio, F.A., Funicello, F., Horvath, F., Jolivet, L., Piromallo, C., Royden, L., Rossetti, F., Serpelloni, E. 2014. Mantle dynamics in the Mediterranean. *Review of Geophysics* 52(3), 283-332.
- Flint, J. J. 1974. Stream gradient as a function of order, magnitude, and discharge. *Water Resources Research*, 10(5), 969-973.
- Han, Z., Li, X., Wang, N., Chen, G., Wang, X., Lu, H. 2017. Application of river longitudinal profile morphometrics to reveal the uplift of Lushan Mountain. *Acta Geologica Sinica* 91(5), 1644-1652.
- Handy, M. R., Ustaszewski, K., Kissling, E. 2015. Reconstructing the Alps-Carpathians-Dinarides as a key to understanding switches in subduction polarity, slab gaps and surface motion. *International Journal of Earth Sciences* 104(1), 1-26.
- Handy, M. R., Giese, J., Schmid, S. M., Pleuger, J., Spakman, W., Onuzi, K., Ustaszewski, K. 2019. Coupled crust-mantle response to slab tearing, bending, and rollback along the Dinaride-Hellenide orogen. *Tectonics* 38(8), 2803-2828.
- Hare, P. W., Gardner, T. W. 1985. Geomorphic indicators of vertical neotectonism along converging plate margins, Nicoya Peninsula, Costa Rica. *Tectonic Geomorphology* 4, 75-104.
- Harlin, J. M. 1978. Statistical moments of the hypsometric curve and its density function. *Journal of the International Association for Mathematical Geology* 10(1), 59-72.
- Hollenstein, C., Müller, M.D., Geiger, A., Kahle, H. G. 2008. Crustal motion and deformation in Greece from a decade of GPS measurements, 1993-2003. *Tectonophysics* 449(1-4), 17-40.
- Jouanne, F., Mugnier, J. L., Koçi. R., Bushati., S., Matev, K., Kuka, N., Shinko, I., Koçiaj, S., Duni, L. 2012. GPS constrains on current tectonics of Albania. *Tectonophysics* 554-557, 50-62.
- Keller, E. A. 1986. Investigation of active tectonics: use of surficial Earth processes, In Wallace (Ed.). *Active Tectonics, Studies in Geophysics*, National Academy Press, Washington, DC, 136-147.
- Keller, E. A., Pinter N. 2002. *Active Tectonics: Earthquakes, Uplift and Landscapes*. Prentice Hall, New Jersey.
- Kirby, E., Whipple, K. X. 2012. Expression of active tectonics in erosional landscapes. *Journal of Structural Geology* 44, 54-75.
- Kissel, C., Laj, C. 1988. The tertiary geodynamical evolution of the Aegean arc: a paleomagnetic reconstruction. *Tectonophysics* 146, 183-201.
- Kissel, C., Speranza, F., Milicevic, V. 1995. Paleomagnetism of external southern and central Dinarides and northern Albanides: implications for the Cenozoic activity of the Scutari-Pec transverse zone. *Journal of Geophysical Research, Solid Earth* (1978-2012)100 (100), 14999-15007.
- Kothyari, G. C., Kotlia, B. S., Talukdar, R., Pant, C .C., Joshi, M. 2020. Evidences of neotectonic activity along Goriganga river, higher central Kumaun Himalaya, India. *Geological Journal* 55(9), 6123-6146.
- Kotzev, K., Nakov, R., Georgiev, T., Burchfiel, B., King, R. 2006. Crustal motion and strain accumulation in western Bulgaria. *Tectonophysics* 413, 127-145.
- KPMM. 2006. Geological map of Kosovo 1:200,000 scale. Komisioni i Pavarur për Miniera dhe Minerale, Prishtinë, Kosovo, 1 sheet.
- Le Pichon, X., Kreemer, C. 2010. The Miocene-to-present kinematic evolution of the Eastern Mediterranean and Middle East and its implications for dynamics. *Annual Review of Earth and Planetary Sciences* 38, 323-351.
- Louvari, E., Kiratzi, A., Papazachos, B., Hatzidimitriou, P. 2001. Fault-plane solutions determined by waveform modeling confirm tectonic collision in the Eastern Adriatic. *Pure Applied Geophysics* 158, 1613-1637.
- Mayer, L. 1990. *Introduction to Quantitative Geomorphology*. Prentice Hall, Englewood, Cliffs, NJ.
- McClusky, S., Balassanian, S., Barka, A., Demir, C., Ergintav, S., Georgiev, I., Gurkan, O., Hamburger, M., Hurst, K., Kahle, H., Kastens, K., Kekelidze, G., King, R., Kotzev, V., Lenk, O., Mahmoud, S., Mishin, A., Nadariya, M., Ouzounis, A., Paradissis, D., Peter, Y., Prilepin, M., Reilinger, R., Sanli, I., Seeger, H., Tealeb, A., Toksöz,

- M.N., Veis, G. 2000. Global positioning system constraints on plate kinematics and dynamics in the eastern Mediterranean and Caucasus. *Journal of Geophysical Research and Solid Earth* 105, 5695–5719.
- Métois, M., D’Agostino, N., Avallone, A., Chamot-Rooke, N., Rabaute, A., Duni, L., Kuka, N., Koci, R., Georgiev, I. 2015. Insights on continental collisional processes from GPS data: dynamics of the peri-Adriatic belts. *Journal of Geophysical Research and Solid Earth* 120, 8701–8719.
- Muço, B. 1998. Catalogue of ML 3.0 earthquakes in Albania from 1976 to 1995 and distribution of 25 seismic energy released. *Tectonophysics* 292, 311–319.
- Muço, B., Alexiev, G., Aliaj, S., Elezi, Z., Grecu, B., Mandrescu, N., Milutinovic, Z., Radulian, M., Rangelov, B., Shkupi, D. 2012. Geohazards assessment and mapping of some Balkan countries. *Natural Hazards* 64(2), 943-981.
- Mustafa, S. 2016. Characteristic of the tectonic, seismicity, active faults and earth crust model, as basis for generation of synthetic accelerograms. PhD Thesis, “Ss. Cyril and Methodius” University in Skopje, Institute of Earthquake Engineering and Engineering Seismology – Skopje Republic of Macedonia, 193 p.
- Mustafa, S., Krelani, V., Beqiri, L., Sinani, B. 2020. Seismic activity and essential seismological characteristics of the Kosovo territory. UBT International Conference 242.
- Nocquet, J. M. 2012. Present-day kinematics of the Mediterranean: a comprehensive overview of GPS results. *Tectonophysics* 579, 220–242.
- Orana, Xh., Arsovski, M., Mihailov, V. 1985. The seismotectonic features of Kosovo. IZIIS, Skopje (in Macedonian).
- Papa, A., Hyseni, A., Leci, V., Prenci J. 1991. Pasqyrini istilit tektonik të Albanideve të Jashtne në molasën er. rltèsirès pranadrietike. Bu.l. Sbken. Gjeol. 1, 197-206.
- Papadopoulos, G. A., Agalos, A., Carydis, P., Lekkas, E., Mavroulis, S., Triantafyllou, I. 2020. The 26 November 2019 Mw 6.4 Albania Destructive Earthquake. *Seismological Society of America* 91(6), 3129-3138.
- Pike, R. J., Wilson, S. E. 1971. Elevation–relief ratio, hypsometric integral, and geomorphic area-altitude analysis. *Geological Society of America Bulletin* 82, 1079–1084.
- Ramírez-Herrera, M. T. 1998. Geomorphic assessment of active tectonics in the Acambay Graben, Mexican volcanic belt. *Earth Surface Processes and Landforms* 23(4), 317-332.
- Reilinger, R. E., McClusky, S. C., Oral, M. B., King, R. W., Toksöz, M. N. 1997. Global positioning system measurements of present-day crustal movements in the Arabia–Africa–Eurasia plate collision zone. *Journal of Geophysical Research* 102, 9983–9999.
- Reilinger, R., McClusky, S., Vernant, P., Lawrence, S., Ergintav, S., Cakmak, R., Özener, H., Kadirov, F., Guliev, İ., Stepanyan, R., Nadariya, Hahubia, G., Mahmoud, S. K. Sakr, ArRajehi, A., Paradissis, D., A. Al-Aydrus, A., Prilepin, M., Guseva, T., Evren, E., Dmitrotsa, A., Filikov, S. V., Gomez, F., Al-Ghazzi, R., Karam, G. 2006. GPS constraints on continental deformation in the Africa–Arabia–Eurasia continental collision zone and implications for the dynamics of plate interactions. *Journal of Geophysical Research* 111, B05411.
- Rockwell, T. K., Keller, E. A., Johnson, D. L. 1985. Tectonic geomorphology of alluvial fans and mountain fronts near Ventura, California. In: Morisawa, M. (Ed.). *Tectonic Geomorphology. Proceedings of the 15th Annual Geomorphology Symposium.* Allen and Unwin Publishers, Boston, MA, 183–207.
- Schmid, S. M., Fügenschuh, B., Kounov, A., Mačenco, L., Nievergelt, P., Oberhänsli, R., ... van Hinsbergen, D. J. 2020. Tectonic units of the Alpine collision zone between Eastern Alps and western Turkey. *Gondwana Research* 78, 308-374.
- Schmitz, B., Biermanns, P., Hinsch, R., Đaković, M., Onuzi, K., Reicherter, K., Ustaszewski, K. 2020. Ongoing shortening in the Dinarides fold-and-thrust belt: A new structural model of the 1979 (Mw 7.1) Montenegro earthquake epicentral region. *Journal of Structural Geology* 141, 104192.
- Silva, P. G., Goy, J. L., Zazo, C., Bardaji, T. 2003. Fault-generated mountain fronts in southeast Spain: geomorphologic assessment of tectonic and seismic activity. *Geomorphology* 50(1-3), 203-225.
- Snyder, N. P., Whipple, K. X., Tucker, G. E., Merritts, D. J. 2000. Landscape response to tectonic forcing: DEM analysis of stream profiles in the Mendocino triple junction region, northern California. *Geological Society of America Bulletin* 112(8), 1250 – 1263.
- Speranza, F., Islami, I., Kissel, C., Hyseni, A. 1995. Paleomagnetic evidence for Ceno-zoic clockwise rotation of the external Albanides. *Earth Planet of Science Letters* 129, 121–134.
- Strahler, A. N. 1952. Hypsometric (area-altitude) analysis of erosional topography. *The Geological Society of America Bulletin* 63(11), 1117-1142.

- Sulstarova, E., Aliaj Sh. 2001. Seismic hazard assessment in Albania. In: Muço, B., Fuga, P. (Ed.). *Albanian Journal of Natural and Technical Sciences X*, 89–101.
- Sukhishvili, L., Forte, A. M., Merebashvili, G., Leonard, J., Whipple, K. X., Javakhishvili, Z., Heimsath, A., Godoladze, T. 2021. Active deformation and Plio-Pleistocene fluvial reorganization of the western Kura fold–thrust belt, Georgia: implications for the evolution of the Greater Caucasus Mountains. *Geological Magazine* 158(4), 583-597.
- Sun, L., Mann, P. 2021. Along-Strike Rapid Structural and Geomorphic Transition From Transpression to Strike-Slip to Transtension Related to Active Microplate Rotation, Papua New Guinea. *Frontiers in Earth Scienc*, 9, 652352.
- Taymaz, T., Jackson, J., Westaway, R. 1990. Earthquake mechanisms in the Hellenic Trench near Crete. *Geophysical Journal of International* 102, 695–731.
- Ulusoy, İ., Diker, C., Şen, E., Aydın, E., Akkaş, E., Gümüş, E., ... Erkut, V., 2020. Surface expressions of morphostructural features at Hasandağ stratovolcano on DEM datasets. *Mediterranean Geoscience Reviews*, 1-17.
- Wells, D. L., Coppersmith, K. J. 1994. New empirical relationships among magnitude, rupture length, rupture width, rupture area, and surface displacement. *Bulletin of the Seismological Society of America* 84(4), 974-1002.
- Whipple, K. X. 2004. Bedrock rivers and the geomorphology of active orogens. *Annual Revision Earth Planet of Science*, 32, 151-185.
- Wobus, C., Whipple, K. X., Kirby, E., Snyder, N., Johnson, J., Spyropolou, K., Crosby, B., Sheehan, D. 2006. Tectonics from topography: Procedures, promise, and pitfalls. In: Willett, S. D., Hovius, N., Brandon, M. T., Fisher, D. M.(Ed.). *Tectonics, Climate, and Landscape Evolution*, 55–74. Geological Society of America.
- van Hinsbergen, D., Langereis, C., Meulenkamp, J. 2005. Revision of the timing magnitude and distribution of Neogene rotations in the western Aegean region. *Tectonophysics* 396, 1–34.
- Yao, W., Liu-Zeng, J., Oskin, M. E., Wang, W., Li, Z., Prush, V., ... Klinger, Y. 2019. Reevaluation of the late Pleistocene slip rate of the Haiyuan fault near Songshan, Gansu Province, China. *Journal of Geophysical Research: Solid Earth* 124(5), 5217-5240.
- Yokoyama, R., Shirasawa, M., Pike, R. J. 2002. Visualizing topography by openness: a new application of image processing to digital elevation models. *Photogrammetric Engineering and Remote Sensing* 68(3), 257-266.





# Bulletin of the Mineral Research and Exploration

<http://bulletin.mta.gov.tr>



## Time-lapse ground penetrating radar (GPR) imaging of used engine oil contamination

Hafız MOHAMMED NAZİFİ<sup>a\*</sup>, Ertan PEKŞEN<sup>b</sup>, Ertuğrul GÜRBÜZ<sup>a</sup> and Levent GÜLEN<sup>a</sup>

<sup>a</sup> Sakarya University, Department of Geophysical Engineering, Sakarya University, Sakarya, Türkiye

<sup>b</sup> Kocaeli University, Department of Geophysical Engineering, Kocaeli, Türkiye

Research Article

Keywords:

Ground Penetrating Radar (GPR), Used Engine Oil (UEO), Contamination, Light Non-Aqueous Phase Liquid (LNAPL), Environmental Geophysics.

### ABSTRACT

Time-Lapse Ground Penetrating Radar (GPR) was employed to study used engine oil (UEO) contamination of sandy environment in laboratory setting. GPR is a near-surface geophysical method that uses electromagnetic field to provide image of the dielectric properties of earth materials to detect structures and changes in material properties within the subsurface. This research aimed to detect, monitor and map the migration of UEO contaminant in sand. The results of this study revealed that the migration of the UEO contamination in homogeneously laid sand is non-uniform. UEO plumes were identified as high amplitude signals with enhanced reflectivity. There was a progressive decrease in GPR signal amplitudes (reflection reduction) within the contaminated area of the tank with time. This decrease of GPR signal amplitudes was interpreted as caused by the evaporation of some portion of the UEO in the vadose zone as a result of temperature increase in time and also due to the occurrence of UEO biodegradation. The time-lapse GPR proved to be an effective technique for detecting, monitoring, and mapping UEO migration within sand tank in laboratory setting.

Received Date: 29.10.2022

Accepted Date: 12.04.2023

## 1. Introduction

The modern world suffers from environment problems such as soil and groundwater contamination as a result of anthropogenic activities. Improper disposal of UEO cause serious environmental issue. The UEO is used as an auxiliary fuel in industrial steam boilers, domestic oil burners, utility steam boilers, waste disposal incinerators and rotary cement kilns (ATSDR, 1997). It is also used as a component in asphalt. UEO is re-refined to make lubricating oil. Maceiras et al. (2017) stated that 45 million tons (estimated) of UEO are generated each year in the world and about only 18 million tons of this oil collected and disposed properly. El-Fadel and Khoury (2001), estimated that in 1995 less than 45% of UEO were being collected world-wide and about 55%

of UEO were either misused or discarded into the environment by the end user.

The health risks and their effects on livestock caused by UEO contaminations of soil and water bodies include convulsions, muscle twitching, neurological disorders, blindness, hyperirritability and depression. It also includes development of liver or kidney disease, possible damage to the bone marrow, increase risk of cancer, complete impairment of body functions and eventually death in livestock (Propst et al., 1999; Abioye et al., 2012; Nolin et al., 1990; El-Fadel and Khoury, 2001; Osweiler et al., 1973; Sas, 1989; ATSDR, 1997). Through food chain toxins accumulate in plants and animals and they could move up the food chain affecting the health of human beings.

Citation Info: Nazifi, H. M., Pekşen, E., Gürbüz, E., Gülen, L. 2024. Time-lapse ground penetrating radar (GPR) imaging of used engine oil contamination. Bulletin of the Mineral Research and Exploration 173, 175-188. <https://doi.org/10.19111/bulletinofmre.1282076>

\*Corresponding author: Hafız Mohammed NAZİFİ, [mohammednazifi@gmail.com](mailto:mohammednazifi@gmail.com)

UEO is classified as Light Nonaqueous Phase Liquids (LNAPLs). LNAPLs are organic liquids that are lighter than water. Other examples of LNAPLs include gasoline, diesel, and jet fuel. LNAPLs tend to accumulate above and marginally below the water table. Disparities in the chemical and physical characteristics of water and LNAPL result in the formation of a physical interface between the liquids which impedes the mixture of the two fluids.

Investigation, management and remediation of LNAPL-affected sites are challenging due to their complexity (USEPA, 1993; Charbeneau et al., 1995; USEPA, 1996; Tomlinson et al., 2017; Ebrahimi et al., 2019; Boumaiza et al., 2022). Despite these challenges, there are many reports of successes in subsurface LNAPL investigation and detection. Methods of detecting the extent of contaminations, the migration patterns, and the evolution of LNAPL contaminated sites are broadly classified under two categories. These are the discrete point sampling of fluids and soil using wells or multi-level piezometers and the indirect measurement through surface or borehole geophysical techniques. Geophysical techniques offer opportunities for non-intrusive investigation of LNAPL contaminated sites.

Direct and indirect detection of LNAPL is possible with different geophysical methods such as resistivity, Induced Polarization, Electromagnetic Induction, GPR and Magnetic Susceptibility and others. This detection depends on the type and quantity of LNAPL, the earth material (such as clay contents), aqueous phase distribution and ionic strength (Monier-Williams, 1995). In general, electrical conductivity, and to a lesser extent GPR, can directly detect the presence of organic contaminants by measuring changes in soil conductivity caused by chemical compounds. The ability of geophysical methods to detect, characterize, and map organic pollutants at contaminated sites depends on the depth of the contamination. Smaller concentrations of pollutants could be detected using geophysical methods (USEPA, 2000; Arato et al., 2014; Ameen et al., 2014).

GPR has proven to be successful in mapping LNAPL and it has been ranked second after electrical methods for its ability to detect organic contaminants

(Atekwana and Atekwana, 2010). Fresh contaminated sites produced enhanced GPR signal amplitude and clean GPR reflection while 'aged' contaminations are characterized by high conductivity or GPR reflection signal reduction below conductive zones, usually at the top of aquifers. Another reason for the decrease in reflection zone or amplitude attenuation zone is increase in vapor pressure from volatile components in LNAPLs (Olhoeft, 1992; Douglas et al., 1992; Daniels et al., 1995; Grumman and Daniels, 1995; Maxwell and Schmock, 1995; Bermejo et al., 1997; Kim et al., 2000; Atekwana et al., 2002; Werkema et al., 2003).

Among site conditions which have been reported as favourable for detecting and monitoring LNAPLs using GPR include thick pools of contaminant, clay free, granular soils, diminishing capillary fringe thicknesses in more granular materials, shallow exploration depths, and homogeneity within the near-surface region (Olhoeft, 1986; Redman et al., 1994; Barber and Morey, 1994; Grumman and Daniels, 1995). The subsurface migration trends of LNAPL contaminants are due to a few factors that include subsurface geology and geological structures. According to Mineo et al. (2022), the fracturing of the rock mass and the presence of subsurface structures, probably of tectonic origin, are responsible for the contamination plume taking a preferential path under the dynamic conditions caused by anthropic activities. This supports the need for subsurface geology and geological structural knowledge in monitoring contaminant migrations. Azimi et al. (2020), who studied the movement of LNAPL into monitoring wells, stated that monitoring LNAPL migrations exposed to fluctuations in groundwater levels is a complex phenomenon. They point out that to understand the subsurface distribution of LNAPL, factors such as aquifer grain sizes and LNAPL properties must be considered.

According to Olhoeft (1992), most hydrocarbons are LNAPLs with low relative dielectric permittivity and higher vapor pressure. These LNAPLs can be delineated by GPR, both directly as a reflection from the dielectric contrast of a thick layer or due to a change in the water table reflection (generally higher reflectivity) from flattening or sharpening of the capillary fringe. The reflections from LNAPLs

in the near surface are a function of the permittivity contrast between the LNAPLs and the host material (Daniels et al., 1995). Cassidy (2007) stated that it is common to find a range of GPR responses at any given LNAPL contamination site with shadow zones being co-incident with 'bright spot' reflections and signal reduction varying significantly over the site. The findings of Cassidy (2007) show that highest signal attenuation is associated with either mixed phase, or a smeared zone where biodegraded LNAPLs co-exist with contaminated pore and groundwater. Bertolla et al. (2014), reported a study in which an experiment in controlled condition was carried out to test the effectiveness of the use of GPR to monitor oil spill contamination. Their results show that GPR is not effective in monitoring LNAPL plume in an unsaturated (dry) sand, but effective in saturated (wet) sand. They concluded that the ability to detect the contamination plume was due to the higher contrast between the electromagnetic properties of water-saturated sand and the oil LNAPL floating on the groundwater level. They suggested the acquisition of GPR data should be carried out shortly after a period of rainfall.

Although UEO is a common contaminant, investigation of the detection, mapping, and monitoring of UEO contaminated soils and aquifers have been overlooked, neglected so far. Currently, Nazifi et al. (2022) and Lago et al. (2009) are the only available published works that used geophysical methods to map and characterize a UEO contamination. Nazifi et al. (2022) used electrical resistivity tomography (ERT) method in monitoring the evolution of UEO contamination, while Lago et al. (2009) used GPR and ERT in mapping matured UEO disposal site. Their results revealed that, the UEO beneath the disposal site has undergone microbial degradation and their radargrams were characterized by high conductivity zone or GPR reflection attenuation below conductive zones. In this paper, we report on a 26 week long investigation of UEO contamination within a specially designed experiment tank in laboratory setting using time-lapse GPR. The objectives of the study were to detect UEO contamination within a sandy environment, to monitor and map the migration of the contaminant using time-lapse GPR.

## 2. Materials and Method

### 2.1. Contaminant

UEO was used to contaminate the setup. New engine oil and UEO are classified as LNAPLs. LNAPLs are hydrocarbons that are less dense than water and immiscible in water. LNAPLs are the most common organic contaminants that are found in the subsurface that contaminate soil and groundwater (Tomlinson et al., 2017; Newell, 1995). UEO is a mixture of high and low (C15-C50) molecular weight aromatic and aliphatic hydrocarbons, lubrication additives, metals, and various organic and inorganic compounds (ATSDR, 1997). The chemical composition of UEO varies widely and depends on the additives added to the fuel. There are generally four types of the engine oil which are full synthetic oil, synthetic blend or semi-synthetic oil, mineral or conventional oil and lastly high mileage oil.

Carey (1998) reported that the dielectric constant of motor oils at room temperature ranges between 2.1 to 2.8. Kardos and Pietrikova (2016) reported that the dielectric constant of new and used motor oils ranges between 2.1 to 2.4 depending on the temperature. The dielectric constant also depends on the viscosity of the oil, the paraffinic or naphthenic content and the additive package. The viscosity of motor oil depends on temperature, and it decreases with increase in temperature (Kardos and Pietrikova, 2016).

The UEO contaminant used in this experiment is a mixture of several used engine oils. It contains some elements such as Calcium, Zinc, Phosphorus etc. The specific gravity of the oil at 15°C is 877.9 kg/m<sup>3</sup> and its kinematic viscosity at 40°C is 78.03 mm<sup>2</sup>/s. For further information on the chemical and physical properties of UEO see Table 1.

### 2.2. Experimental Setup

The experiment was carried out in a specially designed plexiglass tank. The tank has three chambers (Figure 1). The first and the third chambers have dimensions of 10 cm x 60 cm x 50 cm, and they are for water inlet and water outlet, respectively. The second (middle) chamber has the dimensions of 270 cm x 60 cm x 50 cm and it is filled with sand.

Table 1- Results of physical and chemical analysis of the UEO used in the experiment.

Parameters Measured	Method Applied	Results	Units
Metals			
Iron	IP 501	59	mg/kg
Nickel	IP 501	4.2	mg/kg
Vanadium	IP 501	<1	mg/kg
Aluminium	IP 501	14	mg/kg
Calcium	IP 501	2424	mg/kg
Zinc	IP 501	1170	mg/kg
Phosphorus	IP 501	951	mg/kg
Silica	IP 501	11	mg/kg
Sodium	IP 501	15	mg/kg
Carbon Residue Percentage Weight (Micro Method)	TS EN ISO 10370	2.27	(m/m) %
Water Content Percentage Weight	TS EN 1428	0.1	(v/v) %
Total Acidity	ASTN D 664	4.46	mgKOH/g
API, gravity (60F)	TS 1013 EN ISO 3697	29.6	API
Specific gravity at 15.0 °C		877.9	kg/m <sup>3</sup>
Kinematic Viscosity at 40.0 °C	TS EN ISO 3104	78.03	mm <sup>2</sup> /s

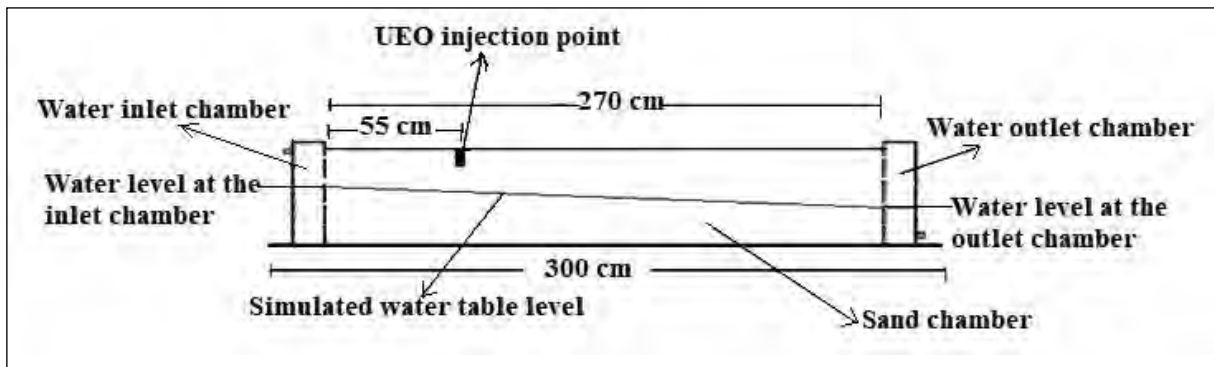


Figure 1- Sideway view (cross section) of the plexiglass tank used for the experiment.

The tank (sand chamber) was filled with a clean sand (Figure 2) obtained from the flood plain of the Sakarya river. The sand was modelled into saturated and unsaturated zone with the depth of the sand model set approximately at 45 cm from the bottom of the tank. Tap water was fed to flow through the tank. The water levels were kept at constant height of 25 cm at the inlet chamber and 15 cm at the outlet chamber, respectively.

Based on sieve analysis results, the sand consists of 1.06% of very fine sand particles, 72.05% fine and medium sand particles and 26.90% gravel. The sand was interpreted as a well sorted, clean, uniform sand with small amount of gravel.



Figure 2- Image of the plexiglass tank showing the three chambers of the tank and the profile lines (yellow lines).

The setup was first contaminated with 1.5 litres of UEO through a pit at a depth of 15 cm. But it was realized that the contaminant was not enough to migrate to the outlet end of the tank. Hence one week after the initial contamination, an additional 2.5 litres of UEO were injected through the same pit making the total volume of UEO contaminant 4.0 litres.

### 2.3. GPR Data Acquisition and Processing

GPR is a geophysical method that uses the transmission and reflection of high frequency (10 MHz to 2 GHz) EM waves within the near sub-surface. GPR signal depends on the properties of the earth such as the dielectric permittivity  $\epsilon$ , the electrical conductivity  $\sigma$ , and the magnetic permeability  $\mu$  (Knight, 2001). Further information on the fundamental principles of GPR can be found in publications by Daniels et al. (1988), Davis and Annan (1989); Knight (2001).

In our experiments GPR survey was conducted using the Zond – 12e GPR advanced (Radar System Inc.) system. Five sets of GPR data were collected and each data set consisted of eight profiles (for locations of the profiles see figure 2) making total of 40 GPR profiles. These add up to about 92 m of GPR profile data. The data were acquired in groups of eight profiles with 5 cm spacing between each profile. Figure 3 shows a photo taken during data acquisition. The data were acquired before (26.02.2020), one hour after (26.02.2020), two weeks after (04.03.2020), four weeks after (26.03.2020), and twenty-six weeks after (19.08.2020) the initial contamination.

The data were acquired with a shielded 2 GHz Zond antenna and the acquisition parameters were 1024 sample/trace and a scan rate of 40. The antenna was placed on a wooden rail during the data acquisition as seen in Figure 3. The wooden rail (Figure 3) helped in obtaining good reproducibility of the data (Bertolla et al., 2014).

Data were recorded in time window range between 0 and 1.88 m which is equivalent to 0 and 50 ns (nanoseconds), although some measurements were a bit little less than the 1.88 m. Data processing was carried out to improve signal to noise ratio and enhanced visualization. Data acquisition and post-processing were done using Prism 2 software (Radar

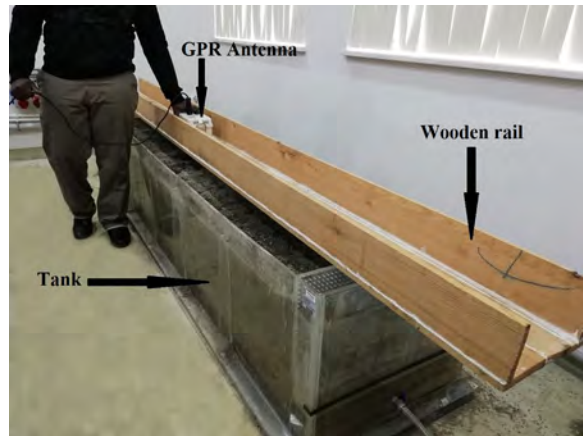


Figure 3- Image showing the plexiglass tank, the wooden rail and the GPR antenna during data acquisition.

System Inc.). The first step of the data processing was the subtraction of the data set obtained before oil contamination (this data is referred to as the background data) from all the data sets obtained after the contamination. The radar data processing included zero-time, background removal, Horizontal Low-Pass (LP) filter, move-out correction, migration [Stolt (F-K) method] and automatic gain control. Zero-time was applied to remove the effect of the wooden rail and the air between the wooden rail and the surface of the sand. Background removal was applied to efficiently suppress the background of the radargram. Horizontal LP filter was applied for the fast signal variable suppression. Move-out correction restores a profile to a pattern as if the signal radiated and recessed in a point located in the middle of the antenna. Lastly, migration is for the reconstruction of the original shape of underground interfaces and local objects by its radiolocation profile. The Stolt (F-K) method of migration provided by the Prism 2 software was used in performing migration. The hyperbola technique was used in determining the permittivity of contaminants within the experimental tank. From the hyperbola technique, the permittivity of the contaminated section of the radargram is given as 2.07. The velocity of signal through the contaminated section is given as 20.16 cm/ns. The possible surrounding medium of the hyperbola that was suggested by the software to consist of snow, ice, frozen oil and oil products. The oil product suggested by the software was due to the 2.07 permittivity is a good prediction, since the soil was contaminated with UEO. The obtained permittivity

value was used in the migration step. Automatic gain control was applied within the width of the window for each separate trace. It was used for levelling all signals in a trace. It makes the signals more visible.

Prism 2 program was used for aligning 2D profiles and converting them into 3D radargrams. Five 3D radargrams were created from the five sets of eight GPR profiles. The Easy Prism software (Radar Systems Inc.) was used for the 3D GPR visualization.

### 3. Conclusion and Discussion

2D Time-lapse vertical view of GPR radargrams from profile 5 (Figure 4 - XZ plane), 1D Time-lapse horizontal signal amplitude graphs at depth 15 cm (Figure 5), 1D Time-lapse vertical signal amplitude and attenuation graphs at a distance of 50 cm (Figure 6) and 3D cross sectional radargrams (Figure 7) were selected and presented in this paper. The radargrams as shown in Figures 4, 5, 6 and 7 were labelled a, b, c, d and e corresponding to the background, 1 hour, 2 weeks, 4 weeks, and 26 weeks after the initial contamination, respectively.

From both Figure 4 and Figure 7, one set of horizontal reflectors can be seen and they were indicated by yellow lines labelled F1 – F2 in Figure 4. The set of horizontal reflectors correspond to the simulated groundwater level are between about 24 cm to 46 cm. The reflector divides the radargrams into two parts, the upper unsaturated and the lower saturated parts. The strong reflectors are caused primarily by the sharp change in the permittivity in the transition from the unsaturated sand to the saturated sands. The UEO as LNAPLs might be displaced by water from the transition zone above the capillary fringes and therefore making a sharp interface at the top of the water saturated zone (de Castro and Branco, 2003). This might be the reason for the elevation of horizontal reflectors in Figure 4c and 4d. It was observed that the results (Figure 4b and 7b) obtained one hour after initial contamination showed a slight distortion of the groundwater level between points 0.13-1.0 m on the distance axis. The distortion of the groundwater was much pronounced after additional contamination of 2.5 litres, 2 weeks after the initial contamination (Figure 4c and 7c). The oil might have migrated both

vertically and horizontally, this is because of the anomalies revealed in both vertical and horizontal layers of Figures 7c and 7d. It can also be seen that there were afterwards, the groundwater level reflector was not much distorted compared to the background. The plume resulting from the initial contamination of the UEO could be seen on Figure 4b between 0 – 17 cm on the depth axis and between 0.13-0.88m on the distance axis. The anomalies in Figures 4c–d are much pronounced than that in Figure 4b. This is understandable, because the plume corresponding to the radargrams in Figures 4c–d is more voluminous than that in Figure 4b.

The horizontal layer shown in Figure 7 on the 3D time lapse radargrams is located at a depth of 25 cm. This was 10 cm downward of the contamination pit which was 15 cm from the surface of the tank. In reference to the background radargram (Figure 7a), we can see that there was a small anomaly in Figure 7b (1 hour after initial contamination). The anomaly is more obvious than in Figure 7c which is the results of 2 weeks after initial contamination of 1.5 litres of UEO and a week after additional contamination of 2.5 litres. The UEO migrated further downwards and horizontally and was recorded on both horizontal and vertical section of Figure 7d. The anomalies in both Figures 5e and 7e are attributed to residual UEO plume which has dielectric contrast compared to dry sand. The data of the results in Figures a-d were collected in late winter and early spring (between February and March) when the temperature relatively cold and the vadose zone is much moist. But the in Figure 7 e were collected in summer (August) when the temperature is much higher compared to winter and spring. The high temperature might have increased the evaporation of the upper vadose zone making the UEO residue to be solidified and the sand to be dry compared to the results in Figures 7a-d.

The time-lapse 3D radargrams (Figure 7) clearly show both vertical and lateral migration of UEO. The 3D radargrams are consistent with the 2D radargrams. Both the 2D and 3D results indicate that UEO initially migrated vertically (predominantly) and then horizontally. In other words, first the contaminant percolated down and then lateral migration became dominant.

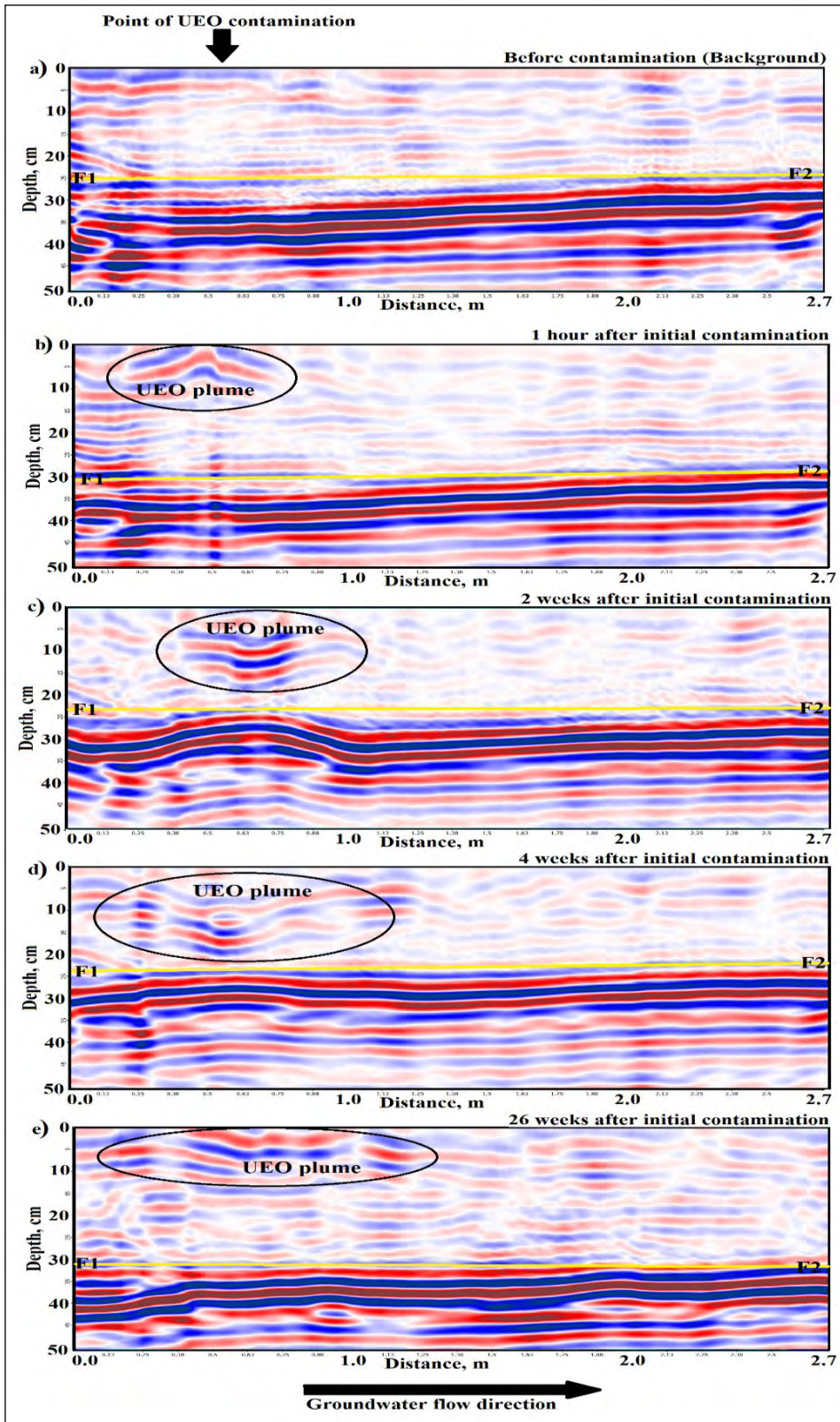


Figure 4 -2D Time-lapse vertical view of GPR radargrams from profile 5 (XZ plane). The yellow line labelled F1-F2 represents the boundaries between unsaturated and saturated sand, black circles indicate the extensions of the oil plume, a), b), c), d) and e) are the radargrams from data before contamination, one hour, 2 weeks, 4 weeks, and 26 weeks after initial contamination, respectively.

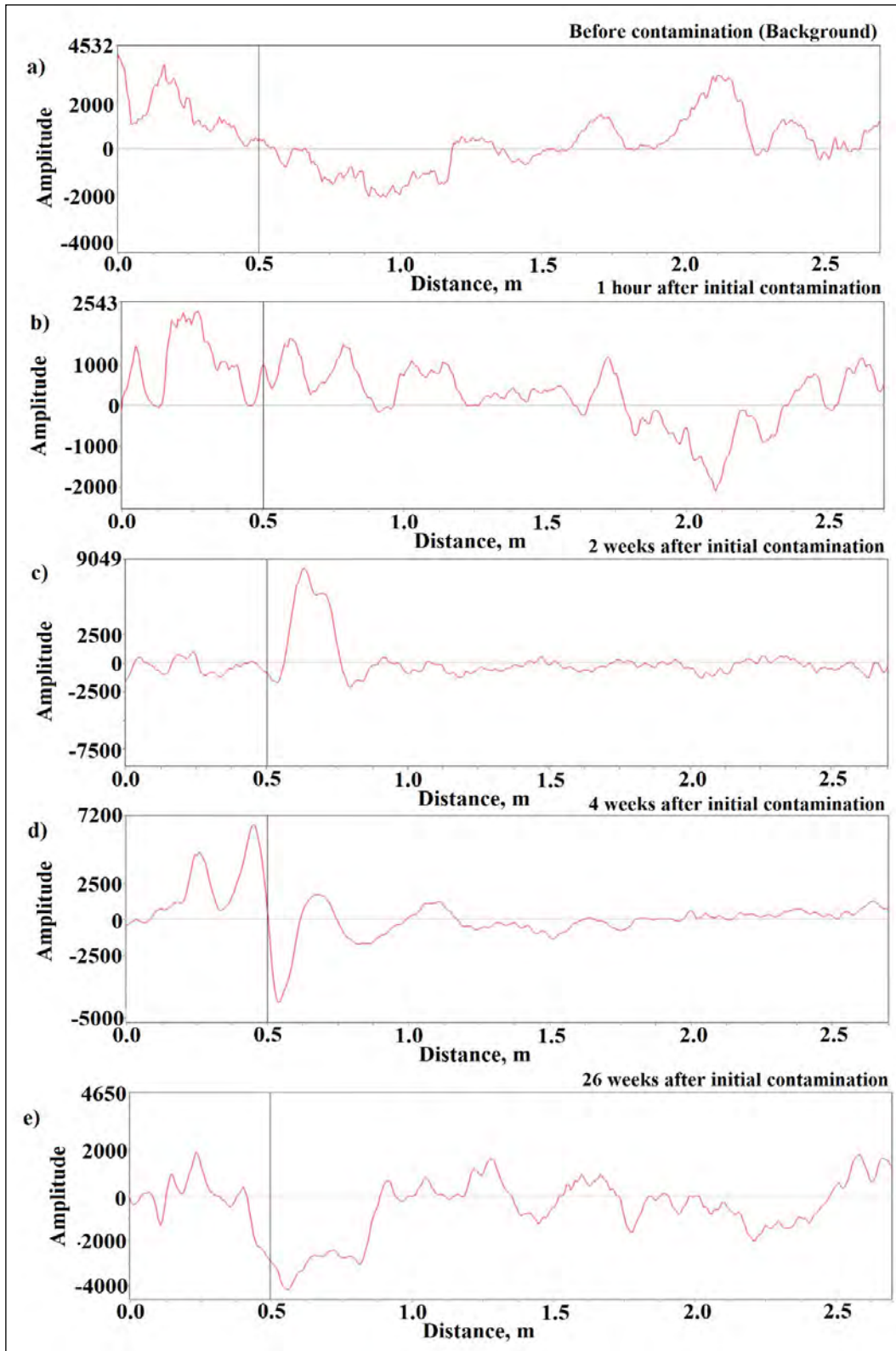


Figure 5- 1D Time-lapse horizontal signal amplitude graphs at depth 15 cm. a), b), c), d) and e) are the radargrams from data before contamination, one hour, 2 weeks, 4 weeks, and 26 weeks after initial contamination, respectively.

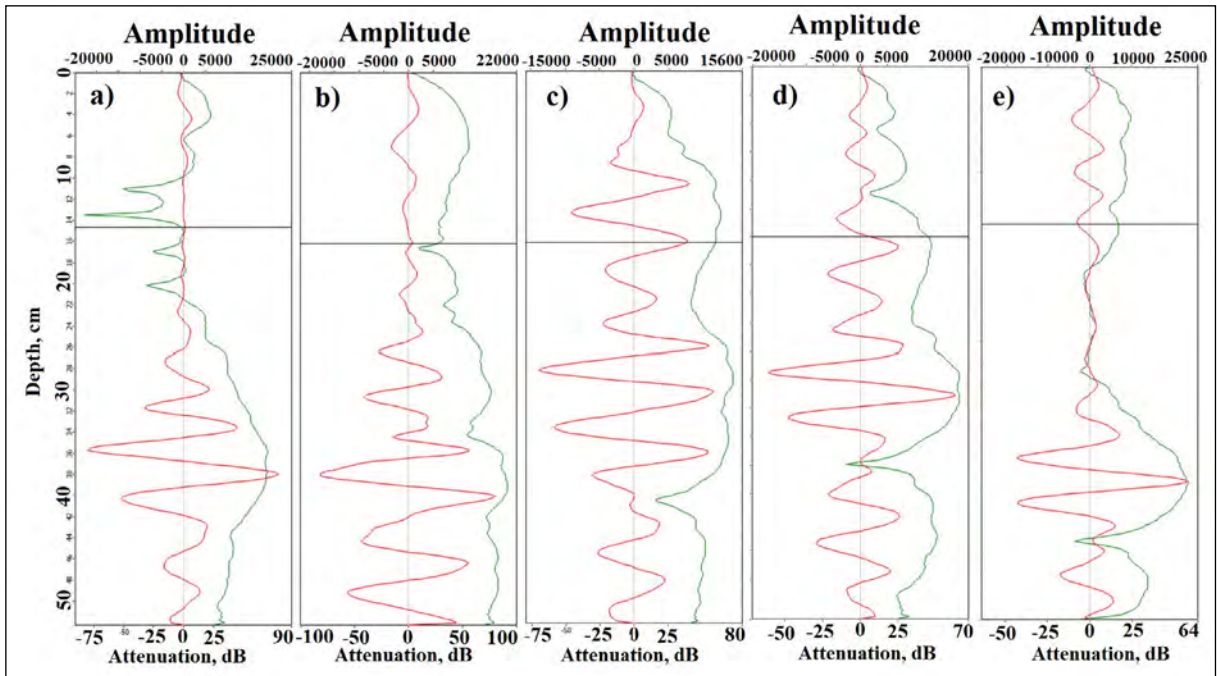


Figure 6- 1D Time-lapse vertical signal amplitude and attenuation graphs at point 50 cm. The black lines show the signal amplitudes and the red lines show the signal attenuations. a), b), c), d) and e) are the radargrams from data before contamination, one hour, 2 weeks, 4 weeks, and 26 weeks after initial contamination, respectively.

The sand was homogeneously laid down and horizontally levelled within the tank (as shown in Figure 2) to enhance uniform migration of the UEO, but as we can see from Figures 4b-e and Figures 7b-e, the migration of the UEO plume is non-uniform. Similar situation was also reported by Bano et al. (2009).

A general decrease in GPR signal amplitude in time (Figures 5 and 6) was observed below the contamination area. Similarly, a progressive decrease in signal amplitude could also be seen below the point of contamination in Figures 4c-e and Figures 7c-e. This observation was also made by several investigations such as Bertolla et al. (2014); Hagrey (2004); Bano et al. (2009); Kim et al. (2000); de Castro and Branco (2003); Bermejo et al. (1997); Sulba Rao and Chandrashekhan (2014). The unsaturated parts of the setup (Figures 4 and 7) have low reflectivity, because it is not that wet. The enhanced reflections seen directly below the point of contamination is associated with the UEO within the vadose zone. It is possible that, because of the viscous nature of the UEO, the oil migrated slowly in the vertical direction until it ended up on the water table and that during this process some

of the oil was absorbed by the sand. With the passing of time, the contaminated area within the vadose zone shows evidence of GPR signal reduction (diminished reflection) or shadow zone. Also, the distortion of the saturated part of the setup became smaller with time.

In geophysical literature, fresh contaminated sites and laboratory experiments produce enhanced GPR signal amplitude and clean GPR results, while aged contaminations are characterized by high conductivity shadow or GPR reflection reduction below the conductive zones, usually at the top of the aquifer (Atekwana and Atekwana, 2010). The findings from this experiment are an exception from the above statements in that it is relatively short term (26 weeks) but displayed characteristics of aged contamination. A study similar to the one reported here was conducted by Bertolla et al. (2014) in which they studied the migration and characterization of alkylbenzene in wet sand. They reported a slight reduction of signal amplitude within the lower vadose zone. Campbell et al. (1996) and DeRyck et al. (1993) reported that, the contamination zones that are associated with bright spots indicated floating gasoline lenses. The brightening results from an increased amplitude

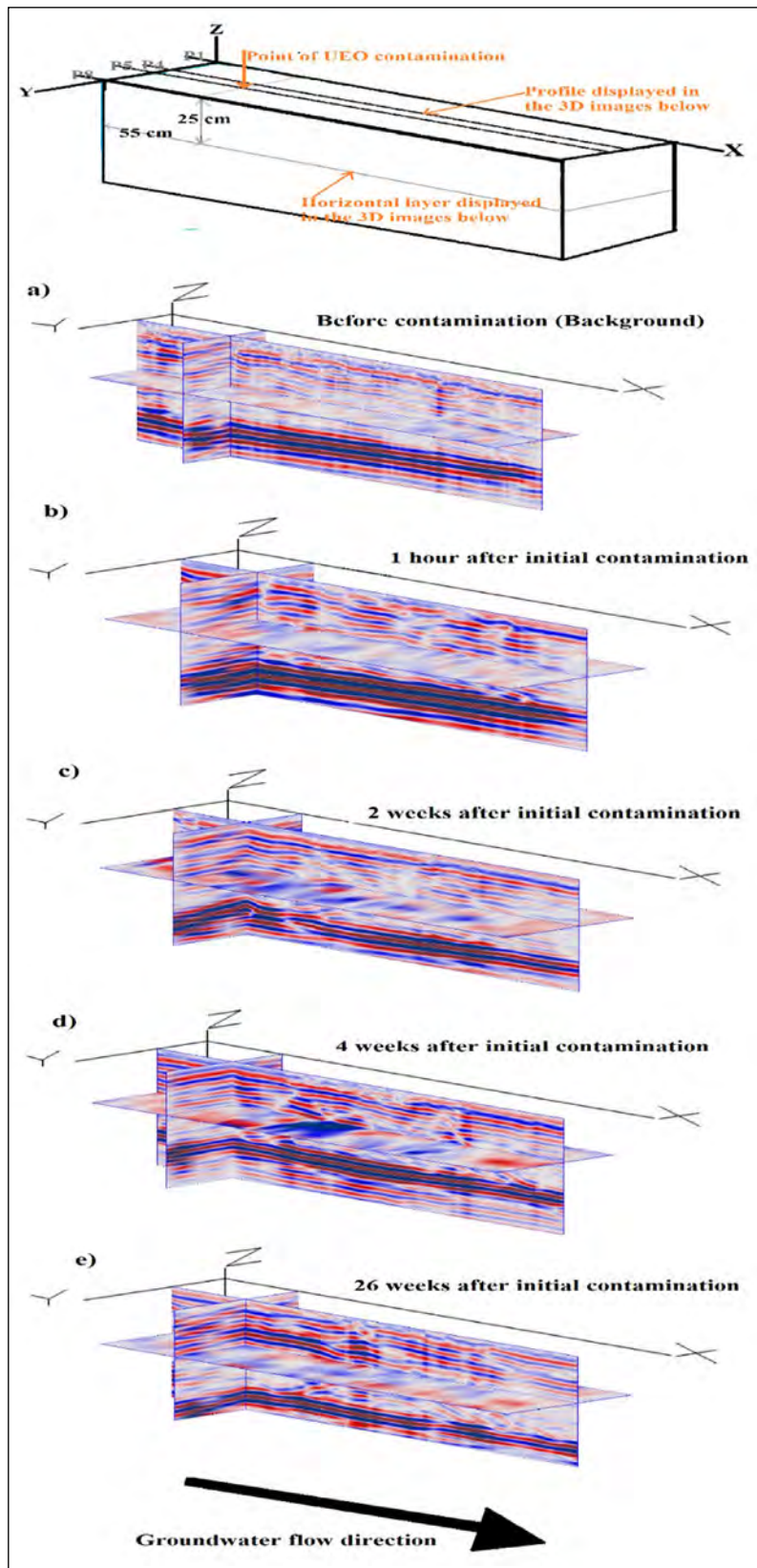


Figure 7- 3D cross sectional time-lapse of GPR radargrams showing the cross section of profile 4 and horizontal layer taken from a depth of 25cm. P1, P4, P5, P8 are the locations of profiles 1, 4, 5 and 8 respectively. a), b), c), d) and e) are the radargrams from data before contamination, one hour, 2 weeks, 4 weeks and 26 weeks after initial contamination, respectively.

(Campbell et al., 1996). Atekwana and Atekwana (2010) suggested that the replacement of water with a relatively high dielectric permittivity of  $\sim 80$  by gasoline with a relatively low dielectric permittivity of 2 resulted in a high velocity GPR layer concomitant with bright spot as revealed in the works of Campbell et al. (1996).

We interpreted the results of the reduction of the GPR signals from the contaminated section of our setup as the results of ongoing biodegradation of the UEO contaminant. We suspected that the microbial activities might have led to the obtained results, because our setup consisted of natural sand (good environment for microbial growth), constant flow of freshwater (a source of nutrients) and a carbon source (UEO). Also, during the clean-up of the experiment tank, there was a kind of rotten smell that came out of the contaminated section of the set up. The smell was not like the oily smell of the UEO before contamination.

Our experiment was open to the atmospheric environment within the laboratory. Our experiment took place between winter (26.02.2020) and summer (19.08.2020) and that temperature variations influenced the experiment. According to Zhou and Crawford (1995), increasing temperature increases the evaporation of short-chain alkanes and other low-molecular-weight hydrocarbons. In addition, increase in temperature decreases the viscosity of hydrocarbons and their solubility in soil aqueous phase. Higher temperature cause solvent-type membrane toxicity to microorganisms (Atlas, 1975). UEO is a complex mixture of low and high (C15-C50) molecular-weight aliphatic and aromatic hydrocarbon, lubrication additives, metals, and various organic and inorganic compounds (ATSDR,1997). Increase in temperature can reduce the viscosity of the UEO and may have caused the evaporation of the low-molecular-weight hydrocarbon components of the UEO. This explanation is not satisfactory to explain the reduction in the GPR signal to nearly background levels and the rotten smell of the contaminated sand during clean-up.

It has been reported by Blume et al. (2002), that microbial activities increase in high temperature (summer) as compared to low temperature (winter). Zekri and Chaalal (2005), found out that increase

in temperature increases the microbial growth which in turn increases the degradation processes of hydrocarbons. The constant freshwater flow throughout the experiment might have provided nutrient to the contaminated zone and that might have help in acceleration of the biodegradation of the UEO. Freshwater from tap contain oxygen and water as solvent might have dissolved other nutrients such as nitrogen and phosphorus from the sand and made available to the microbes to help them grow. According to Zhou and Crawford (1995), nutrients supplied either in vapor or solution enhanced the biodegradation of hydrocarbons in soil and appropriate amount of nutrients stimulate hydrocarbon biodegradation in soil.

The possible explanation of the reduction of GPR signal with time is that; microbes might have used the organic carbon available in the UEO, the nutrients from dissolved elements in the freshwater adds mineral substrate for their growth and metabolism in the sand media. Generation of metabolic by-products such as organic acids (carbonic acids) and ionic constituents might have led to changes in the physical properties of the contaminated medium and the pore fluid chemistry which in turn changes the dielectric permittivity of the medium and increases the electrolytic and interfacial conductivity of the medium. It is well known that GPR signal reduction and depth of penetration depend on electrical conductivity and the dielectric permittivity of the medium and hence change in dielectric permittivity and increase in conductivity results changes in signal reduction. These might have led to the decrease in GPR signal with time. The finding and the interpretation of the results of this study agrees with that of several authors who carried out research in this topic. Sauck et al. (1998); Bradford (2007); Cassidy (2007), Lane et al. (2006); Atekwana and Atekwana (2010), Schilling et al. (2010), support the hypothesis with data that, increase in dissolved ionic constituents during biodegradation of LNAPL result in increases in electrical conductivity that increase GPR signal reduction with time.

#### 4. Results

This study is the first step in understanding the GPR responses of UEO contaminated environment. The application of time-lapse GPR to UEO detection, monitoring and mapping in a sandy environment at

a laboratory experiment setting showed very good results. To the best of our knowledge, this is a first time GPR is being used to study UEO contamination with an experimental setup in laboratory. The presence of UEO plumes is identified as high amplitude signal with enhanced reflectivity, but with time the signal diminished to lower amplitudes which was interpreted as due to evaporation of some portion of the UEO in the vadose zone and due to the occurrence of UEO biodegradation.

The results presented in this paper showed that the GPR signal responses of UEO within a sandy environment change with time. Furthermore, our findings demonstrate the utility of GPR for characterizing UEO contaminated sites. The results of this study show that GPR geophysical technique can be used in addressing environmental problems associated with UEO contaminations.

### Acknowledgement

The authors are grateful to the Scientific and Technical Research Council of Türkiye [TÜBİTAK (Project No: 119Y193)] and the Research Fund of Sakarya University [BAPK (Project No: 2019-7-25-37)] for supporting this study. The authors are grateful to the Sakarya University Research, Development and Application Center (SARGEM) for providing laboratory space for this experiment. We thank the personnel of the TÜPRAŞ İzmit Refinery Laboratories for the determination of physical and chemical properties of the UEO that we used in this study. We thank Prof. Dr. Halim MUTLU for editorial handling and anonymous reviewers for constructive suggestions which improved the manuscript.

Contributions to the study: Hafiz MOHAMMED NAZIFI contributed to the study conception and design and he was supervised by Prof. Dr. Levent GÜLEN. Data acquisitions were performed by Hafiz MOHAMMED NAZIFI, Ertuğrul GÜRBÜZ and Ertan PEKŞEN. Data analysis and interpretation were performed by Hafiz MOHAMMED NAZIFI and supervised by Levent GÜLEN and Ertan PEKŞEN. The first draft of the manuscript was written by Hafiz MOHAMMED NAZIFI and all authors commented on previous versions of the manuscript. All authors read and approved the final manuscript.

### References

- Abioye, O. P., Agamuthu, P., Abdul Aziz, A. R. 2012. Biodegradation of used motor oil in soil using organic waste amendments. *Biotechnology Research International*, 2012, 8.
- Ameen, N. N., Klueglein, N., Appel, E., Petrovský, E., Kappler, A., Leven, C. 2014. Effect of hydrocarbon-contaminated fluctuating groundwater on magnetic properties of shallow sediments. *Studia Geophysica et Geodaetica*, 58(3), 442-460.
- Arato, A., Wehrer, M., Biró, B., Godio, A. 2014. Integration of geophysical, geochemical and microbiological data for a comprehensive small-scale characterization of an aged LNAPL-contaminated site. *Environmental Science and Pollution Research*, 21(15), 8948-8963.
- Atekwana, E. A., Atekwana, E. A. 2010. Geophysical signatures of microbial activity at hydrocarbon contaminated sites: a review. *Surveys in Geophysics*, 31(2), 247-283.
- Atekwana, E. A., Sauck, W. A., Abdel Aal, G. Z., Werkema Jr, D. D. 2002. Geophysical investigation of vadose zone conductivity anomalies at a hydrocarbon contaminated site: A implications for the assessment of intrinsic bioremediation. *Journal of Environmental & Engineering Geophysics*, 7(3), 103-110.
- Atlas, R. 1975. Effects of temperature and crude oil composition on petroleum Biodegradation. *Applied Microbiology*, 30, 396-403.
- ATSDR. 1997. Toxicological profile for used mineral-based crankcase oil.
- Azimi, R., Vaezihir, A., Lenhard, R. J., Hassanizadeh, S. M. 2020. Evaluation of LNAPL behavior in water table inter-fluctuate zone under groundwater drawdown condition. *Water*, 12(9), 2337.
- Bano, M., Loeffler, O., Girard, J. F. 2009. Ground penetrating radar imaging and time-domain modelling of the infiltration of diesel fuel in a sandbox experiment. *comptes rendus Geoscience*, 341(10-11), 846-858.
- Barber, W., Morey, R. 1994. Radar detection of thin layers of hydrocarbon contamination. In *Fifth International Conference on Ground Penetrating Radar* (pp. cp-300). European Association of Geoscientists & Engineers.
- Bermejo, J.L., Sauck, W.A., Atekwana, E.A. 1997. Geophysical discovery of a new LNAPL plume at the former Wurtsmith AFB Oscoda, MI. *Ground Water Monitoring and Remediation*, 17, 131-137.
- Bertolla, L., Porsani, J. L., Soldovieri, F., Catapano, I. 2014. GPR-4D monitoring a controlled LNAPL spill in a masonry tank at USP, Brazil. *Journal of Applied Geophysics*, 103, 237-244.

- Blume, E., Bischoff, M., Reichert, J.M., Moorman, T., Konopka, A., Turco, R.F. 2002. Surface and subsurface microbial biomass, community structure and metabolic activity as a function of soil depth and season. *Applied Soil Ecology*, 20 (3), 171–181.
- Bradford, J. H. 2007. Frequency-dependent attenuation analysis of ground-penetrating radar data. *Geophysics*, 72(3), J7-J16.
- Boumaiza, L., Chesnaux, R., Walter, J., Lenhard, R. J., Hassanizadeh, S. M., Dokou, Z., Alazaiza, M. Y. 2022. Predicting vertical LNAPL distribution in the subsurface under the fluctuating water table effect. *Groundwater Monitoring & Remediation*, 42(2), 47-58.
- Carey, A. A. 1998. The dielectric constant of lubrication oils. Computational Systems Incorporated.
- Campbell, L.D., Lucius, J.E., Maryla, D.P. 1996. Monitoring of a controlled LNAPL spill using ground penetrating radar. *The Symposium on the Application of Geophysics to Engineering and Environmental Problems*, 511–517.
- Cassidy, N. J. 2007. Evaluating LNAPL contamination using GPR signal attenuation analysis and dielectric property measurements: Practical implications for hydrological studies. *Journal of Contaminant Hydrology*, 94(1-2), 49-75.
- Charbeneau, R.J., Weaver, J.W., Lien, B.K., 1995. The Hydrocarbon spill screening model (HSSM) Volume 2: Theoretical Background and Source Codes. USEPA Publication EPA/600/R-94/039b. Washington, DC: U.S. Environmental Protection Agency.
- Daniels, D. J., Gunton, D. J., Scott, H. F. 1988. Introduction to subsurface radar, In *IEE Proceedings F, Communications, Radar and Signal Processing* 135, 4, 278-320.
- Daniels, J. J., Roberts, R., Vendl, M. 1995. Ground penetrating radar for the detection of liquid contaminants, *Journal of Applied Geophysics*, 33(1-3), 195-207.
- Davis, J.L., Annan, A.P. 1989. Ground penetrating radar for high resolution mapping of soil and rock stratigraphy. *Geophysics Prospect*, 37, 531–551.
- de Castro, D. L., Branco, R. M. G. C. 2003. 4-D ground penetrating radar monitoring of a hydrocarbon leakage site in Fortaleza (Brazil) during its remediation process: a case history. *Journal of Applied Geophysics*, 54(1-2), 127-144.
- DeRyck, S. M., Redman, J. D., Annan, A. P. 1993. Geophysical monitoring of a controlled kerosene spill, In *6th Environmental and Engineering Geophysics Society Symposium on the Application of Geophysics to Engineering and Environmental Problems*, 5-19, 209.
- Douglas, D. G., Burns, A. A., Rino, C. L., Maresca, J. W. 1992. Study to determine the feasibility of using a ground-penetrating radar for more-effective remediation of subsurface contamination, PB-92-169382/XAB).
- Ebrahimi, F., Lenhard, R. J., Nakhaei, M., Nassery, H. R. 2019. An approach to optimize the location of LNAPL recovery wells using the concept of a LNAPL specific yield, *Environmental Science and Pollution Research*, 26(28), 28714-28724.
- El-Fadel, M., Houry, R. 2001. Strategies for vehicle waste-oil management: a case study. *Resources, conservation and recycling*, 33(2), 75-91.
- Grumman Jr, D. L., Daniels, J. J. 1995. Experiments on the detection of organic contaminants in the vadose zone. *Journal of Environmental and Engineering Geophysics*, 1(A), 31-38.
- Hagrey, S. A. 2004. GPR application for mapping toluene infiltration in a heterogeneous sand model. *Journal of Environmental & Engineering Geophysics*, 9(2), 79-85.
- Kardos, S., Pietriková, A. 2016. Evaluation of motor oil characteristics and degradation factors for possibilities of continuous diagnostics, *Acta Electrotechnica et Informatica*, 16(2), 20-24.
- Kim, C., Daniels, J. J., Holt, J. J., Guy, E. D. 2000. A physical model experiment of the GPR response over gasoline, In *13th Environmental and Engineering Geophysics Society Symposium on the Application of Geophysics to Engineering and Environmental Problems*, 200, 303-310 *European Association of Geoscientists and Engineers*.
- Knight, R. 2001. Ground penetrating radar for environmental applications. *Annual Review of Earth and Planetary Sciences*, 29(1), 229-255.
- Lago, A. L., Elis, V. R., Borges, W. R., Penner, G. C. 2009. Geophysical investigation using resistivity and GPR methods: a case study of a lubricant oil waste disposal area in the city of Ribeirão Preto, São Paulo, Brazil. *Environmental Geology*, 58(2), 407-417.
- Lane, J.W., Day-Lewis, F.D., Casey, C.C. 2006. Geophysical monitoring of a field-scale biostimulation pilot project, *Ground Water*, 44(3), 430–443.
- Maceiras, R., Alfonsín, V., Morales, F. J. 2017. Recycling of waste engine oil for diesel production. *Waste management*, 60, 351-356.
- Maxwell, M., Schmock, J. 1995. Detection and mapping of an LNAPL plume using GPR: A case study, in *proceedings of the symposium on the application of geophysics to environmental and engineering problems*, *Environmental and Engineering Geophysics Society*, Englewood, Colorado, p.15-23.

- Mineo, S., Dell'Aera, F.M.L., Rizzotto, M. 2022. Evolution of LNAPL contamination plume in fractured aquifers. *Bulletin of Engineering Geology and the Environment*, 81(4), 1-14.
- Monier-Williams, M. 1995. Properties of light non aqueous phase liquids and detection using commonly applied shallow sensing geophysical techniques. *The Symposium on the Application of Geophysics to Engineering and Environmental Problems*, 1-13.
- Nazifi, H. M., Gülen, L., Gürbüz, E., Pekşen, E. 2022. Time-lapse electrical resistivity tomography (ERT) monitoring of used engine oil contamination in laboratory setting. *Journal of Applied Geophysics*, 104531.
- Newell, C. J. 1995. Light nonaqueous phase liquids. United States Environmental Protection Agency, Office of Research and Development, Office of Solid Waste and Emergency Response.
- Noln, J.J., Harris, C., Cavanaugh, P.O. 1990. *Used Oil: Disposal Options, Management Practices, and Potential Liability*, third ed. Rockville, MD: Government Institutes.
- Olhoeft, G.R. 1986. Direct detection of hydrocarbon and organic chemicals with ground penetrating radar and complex resistivity, in *Proceedings of the NWWA/API Conference on Petroleum Hydrocarbons and Organic Chemicals in Ground Water - Prevention, Detection and Restoration*, Dublin, Ohio, 284-305.
- Olhoeft, G. R. 1992. Geophysical detection of hydrocarbons and organic chemical contamination. In *5th Environmental and Engineering Geophysics Society Symposium on the Application of Geophysics to Engineering and Environmental Problems*. European Association of Geoscientists & Engineers. 587-595.
- Osweiler, G., Buck, W., Lloyd, W. 1973. Epidemiology of lead poisoning in cattle - a five-year study in Iowa. *Clinical Toxicology*, 6(3), 367-376.
- Propst, T.L., Lochmiller, R.L., Qualis, C.W., McBee, K. Jr. 1999. In situ (mesocosm) assessment of immunotoxicity risks to small mammals inhabiting petrochemical waste sites. *Chemosphere*, 38, 1049-1067.
- Redman, J.D., DeRyck, S.M., Annan, A.P. 1994. Detection of LNAPL pools with GPR: theoretical modelling and surveys of a controlled spill, in *Proceedings of the International Conference on Ground-Penetrating Radar*, Kitchener, Ontario, Canada, 1283-1294.
- Sas, B. 1989. Secondary copper deficiency in cattle caused by molybdenum contamination of fodder: A case history. *Veterinary and Human Toxicology*, 31(1), 29-33.
- Sauck, W.A., Atekwana, E.A., Nash, M.S. 1998. High conductivities associated with an LNAPL plume imaged by integrated geophysical techniques. *Journal of Environmental and Engineering Geophysics*, 2, 203-212.
- Schillig, P.C., Tsofiias, G.P., Roberts, J.A., Patterson, E.M., Devlin, J.F. 2010. Ground-penetrating radar observations of enhanced biological activity in a sandbox reactor, *Journal of Geophysical Research*, 115, G00G10.
- Sulba Rao Ch., Chandrashekhar, V. 2014. Detecting oil contamination by ground penetrating radar around an oil storage facility in Dhanbad, Jharkhand, India. *Journal of Indian Geophysical Union*, 18(4), 448-454.
- Tomlinson, D. W., Rivett, M. O., Wealthall, G. P., Sweeney, R. E. 2017. Understanding complex LNAPL sites: Illustrated handbook of LNAPL transport and fate in the subsurface. *Journal of Environmental Management*, 204, 748-756.
- US Department of Health and Human Services, Public Health Service PHS, Agency for Toxic Substances and Disease Registry
- USEPA (United States Environmental Protection Agency) 1993. *Use of Airborne, Surface, and Borehole Geophysical Techniques at Contaminated Sites*.
- USEPA (United States Environmental Protection Agency) 1996. *How to Effectively Recover Free Product at Leaking Underground Storage Tank Sites: A Guide for State Regulators*.
- USEPA (United States Environmental Protection Agency) 2000. *Innovations in Site Characterization: Geophysical Investigation at Hazardous Waste Sites*.
- Werkema Jr, D. D., Atekwana, E. A., Endres, A. L., Sauck, W. A., Cassidy, D. P. 2003. Investigating the geoelectrical response of hydrocarbon contamination undergoing biodegradation. *Geophysical Research Letters*, 30(12).
- Zekri, A. Y., Chaalal, O. 2005. Effect of temperature on biodegradation of crude oil. *Energy Sources*, 27(1-2), 233-244.
- Zhou, E., Crawford, R. L. 1995. Effects of oxygen, nitrogen, and temperature on gasoline biodegradation in soil. *Biodegradation*, 6(2), 127-140.



# Bulletin of the Mineral Research and Exploration

<http://bulletin.mta.gov.tr>



## A simple and practical tool for indirect determination of the unconfined compressive strength of most common construction materials

Kamil KAYABALI<sup>a\*</sup>, Turgay BEYAZ<sup>b</sup>, İlknur KARAASLAN ÖZDEMİR<sup>a</sup> and Deniz YILMAZ<sup>a</sup>

<sup>a</sup> University of Ankara, School of Engineering, Department of Geological Engineering, Ankara, Türkiye

<sup>b</sup> Pamukkale University, School of Engineering, Department of Geological Engineering, Denizli, Türkiye

Research Article

### Keywords:

Compressive strength, building materials, nail gun, driving energy.

### ABSTRACT

Determination of the unconfined compressive strength (UCS) of construction materials in the laboratory is tedious and time-consuming. There have been many attempts to indirectly predict UCS using simpler tools and techniques. One of them is the nail gun. The scope of this investigation is to design a nailer which can be applied all construction materials whose UCS range from 1-100 MPa. In the research, rocks, bricks, and concretes prepared in different cement/sand ratios with different strength ranges were used as materials. The unconfined compressive strength of the materials used in the experiments was first determined by conventional compression tests. The nail penetration depths were determined by conducting experiments on the same materials using a nailer with two different energy levels. An empirical relationship was developed by using nail penetration depths, driving energies, and nail diameters as the independent variables and the UCS determined by the conventional method as the dependent variable. According to the empirical relationship determined by multiple regression analysis, the UCS of building materials can be estimated with significance level of 99% by the nail penetration method. The research also revealed that the UCS of rocks might have a coefficient of variation as high as 30%.

Received Date: 05.12.2022

Accepted Date: 24.03.2023

## 1. Introduction

Building materials, especially rock, concrete, brick, briquette, and the binder of brick/briquette (mortar) are very diverse. The compressive and shear strengths of each of these materials are determined by laboratory methods. Although measurement of compressive strength (CS) in the laboratory may seem simple, given the conditions such as taking quality core samples with parallel loading planes, running the test on several “identical” samples of the same rock (or concrete) (e.g. ASTM, 2002), it requires considerable labor and is somewhat costly. Laboratory

methods are more commonly referred to as “direct test methods”. Due to both the high cost of test setups and the relatively time-consuming sample preparation and testing process, numerous studies have been carried out to date on the development of equipment and methods to determine the CS in a shorter time and at a lower cost as an alternative to the methods of direct measurement of the CS. The most prominent ones of such indirect methods are the Schmidt hardness test, needle penetration test, nail penetration test, etc.

Schmidt hardness test can be done according to ISRM (1978) and ASTM (2001) standards. The

Citation Info: Kayabali, K., Beyaz, T., Özdemir, İ., K., Yılmaz, D. 2024. A simple and practical tool for indirect determination of the unconfined compressive strength of most common construction materials. Bulletin of the Mineral Research and Exploration 173, 189-201. <https://doi.org/10.19111/bulletinofmre.1267931>

\*Corresponding author: Kamil KAYABALI, [kayabali@ankara.edu.tr](mailto:kayabali@ankara.edu.tr)

Schmidt hardness test is recommended for rocks with a CS of 20-150 MPa (ISRM, 1978); it does not give reliable results for rocks less than 10 MPa (Li et al., 2000). The main advantages of this test technique are its ease of application, low cost of the setup and zero test cost, and easy portability and repeatability. It is not considered a completely reliable test for rock/concrete strength; rather, it is a type of test that is usually done for preliminary assessment of the CS of the material tested.

The point load test (PLT; ISRM, 1985; ASTM, 1995) is recommended for rocks with CS greater than 15 MPa (Broch and Franklin, 1972). It can be applied to cylindrical, prismatic, and irregularly shaped samples. The CS is obtained by multiplying the point load strength [ $I_{s(50)}$ ] found by this test by a certain coefficient. This conversion coefficient is very speculative and may range from 6 to 105, according to Yılmaz and Sendir (2002). It may only give a rough estimate of the CS of the rocks tested.

Block Punch Index Test (BPI; Van der Schrier, 1988; Ulusay et al., 2001) is performed on specially prepared thin, disc-shaped samples. It is applied on rocks with CS ranging from 0.5-70 MPa. As in many other experiments, it was stated that the effect of sample size and anisotropy on the test results was great. This test method also requires special sample preparation. Mishra and Basu (2012) used BPI method to estimate the CS and tensile strength of some rocks and showed that the BPI method is as useful as the PLT method for measuring the CS and also concluded that estimating Brazilian tensile strength with the block punch index is more precise than point load strength.

Applied on extremely weak- to very weak rocks, the needle penetration was developed to address the shortcomings encountered in test methods such as Schmidt hardness, block punch index test, and point load test. It is also validated for use on shotcrete by considering the penetration depth (Bae et al., 2004). It can measure the CS as low as 0.3 MPa. The upper limit of measurement is 40 MPa (Maruto Corporation, 2006; Ngan-Tillard et al., 2011). When the CS is in the range of 30-40 MPa, it results in standard deviations of up to 30% compared to the values obtained from the direct measurement test. It has been reported to

contain large uncertainties in estimating the CS, and it has been proposed as an index test rather than a test that accurately determines the CS. The Equotip hardness tester was originally developed for metals. It was then applied to rocks by a limited number of researchers (e.g. Verwaal and Mulder, 1993; Aoki and Matsukura, 2008). The applicability range for CS is 0.1-100 MPa. It is not yet clear to what degree of reliability this test method gives the CS.

Liberatore et al. (2003) aimed to indirectly determine the strength of mortar in masonry structures with a special penetrometer they developed. The penetrometer assembly was driven into the mortars of different historical structures by repeated hammering operations. Penetration depths varied between 40-50 mm. It has been stated that the number of impacts required to apply 1 mm into the mortar varies between 0.54-1.23. On the other hand, Felicetti and Gattesco (1998) developed a dynamic penetrometer to measure the strength of mortar in masonry structures. It was stated that the impact energy of the penetrometer is 2.2 J. They also sought a relationship between the penetration depth of the penetrometer and the compressive strength of the mortar.

One of the recent methods to indirectly measure the CS of rocks is the nail penetration test (Kayabalı and Selçuk, 2010; Selçuk et al., 2012; Selçuk and Kayabalı, 2015). With this alternative technique, the CS can be measured in the range of 5-100 MPa. Kayabalı and Selçuk (2010) stated that the CS determined indirectly by the nail penetration test gives highly reliable results. They reported that the ability of the nail penetration test to determine CS is superior to the Schmidt hardness hammer and point loading test. Selçuk et al. (2012) also applied the nail penetration test to concrete samples. The results obtained from the nail penetration tests performed on concrete samples with different aggregates are in great agreement ( $R^2 > 0.95$ ) with the results obtained from compression tests. They stated that the nail penetration test well represents the combined effect of aggregate and cement matrix on strength. Selçuk and Kayabalı (2015), on the other hand, applied the nail penetration test with nail guns of different energy levels and different nail diameters to determine the CS. They used 5 different commercial nailers with different impact energies and

developed an empirical relationship that can predict CS as a function of nail penetration depth, nail gun energy, and nail diameter.

Palassi and Emami (2014) developed a mechanical nail driver with a mass of 4.54 kg and a drop height of 0.46 m. They carried out a series of experiments on travertines and marbles by keeping the 122J energy constant in a total of 6 driving operations. In their experiment with 3.5 mm diameter nails, they defined an exponential relationship with a coefficient of determination of 0.98 between the CS of intact rock and the nail penetration depth.

Yilmaz (2009) employed a test method called the “core strangle test” for indirectly determining the CS of rock core samples. The principle of this test is based on the “choke” type of loading of a core along a circle perpendicular to its long axis. Some researchers have correlated the results of the indentation test with the CS of rocks. Szwedzicki (1998) proposed a standard notch test as a measure of rock hardness and its use as an estimator for CS.

Another method used to measure strength by penetration is the Windsor probe, which was developed in the 1960s to measure the CS of concrete in situ. This relatively less destructive test is a kind of hardness strength test used to determine the CS of concrete in a short time. This technique is also based on the relationship between the depth of penetration and the compressive strength, measured by driving a special probe into the concrete. It has been reported

that the calibration chart provided with the apparatus does not always give reliable results (Malhotra and Carino, 1991; Pucinotti, 2005; 2009).

A simple, robust, and economical nail penetration apparatus capable of applying two different energy levels and using different nail diameters was designed and manufactured as an end product of a research project conducted by the authors. The scope of this investigation is to predict the compressive strength of different construction materials indirectly by correlating the nail penetration depths produced through this nailer and the compressive strengths obtained from test materials (mostly rocks) and to propose an empirical relationship that yields the CS as a function of the nail penetration, nail diameter, and the driving energy.

## 2. Materials and Methods

The major equipment used in the study is a nail gun that has two different energy levels and can shoot with nails of three different diameters (Figure 1). Sound (or dummy) bullets were used as an energy source. For the impact energy of this tool, nail speeds (V) were determined by shooting sound bullets firing a nail in front of a high-resolution video camera. Since the mass of a nail (m) is known, the energy of the sound bullet was calculated from  $W = 0.5 m V^2$ . The impact energy of standard sound bullets used in this investigation was found to be 150J. Considering this energy level for low-strength materials would be high, special sound bullets with a 2/3 reduction in



Figure 1- Nail gun, nails of three different diameters, and sound bullets used in the investigation.

gunpowder were manufactured upon special order. Their driving energies were determined as 50J. The point angle of the nails is 45°, the nails were subjected to heat-treatment against bending during applications.

In the study, 2 types of block brick materials, 8 cast-concrete materials prepared in different cement/sand ratios, 4 concrete materials compacted with vibrating tampers, and 34 types of intact rocks were used. Most of the rocks are of sedimentary and magmatic origin, and a few are of metamorphic origin. Concrete samples were prepared in the laboratory. Brick samples were procured from commercial suppliers.

Five core samples of 54 mm (NX) diameter were taken from the bricks (Figure 2). A press with a capacity of 1000 kN was used to determine the compressive strengths of brick and rock cores.

To perform the unconfined compression tests, the guidelines of the ASTM standard of D2938 (American Testing Society for Materials, 2002) were strictly followed. The test specimens had proper cylindrical shapes with the length to diameter ( $L/D$ ) ratio of 2.0 to 2.5. The sides of test specimens were kept smooth and free of abrupt irregularities. The ends of test specimens were cut parallel to each other and at right angles to the longitudinal axis. The ability of the spherical seat to rotate freely in its socket before each test was ensured. Two steel platens were used to transmit the axial load to the ends of the specimen. Constant load ratios of 10 kPa/s, 100 kPa/s and 500 kPa/s were applied to test specimen, depending on the expected UCS of the test material, and the loading continued until the specimen fails. For concrete samples a press of 50 kN capacity was employed to run the compression tests.



Figure 2- A view from brick cores.

Some brick specimens were shattered during the shooting of the nail gun owing to the limited size of the tested specimen. To prevent this, plaster was cast around brick specimens (Figure 3) and shots were carried out thereafter with a nail gun after the plaster had dried. While it was observed that the confining plaster was cracked ensuing the nail penetration test on some brick specimens, the confinement by the plaster and the container was sufficient to prevent shattering of brick specimens to obtain proper nail penetration.

The second type of material used in the investigation is concrete blocks prepared by mixing Portland cement and sand in different ratios (C/S). For the preparation of concrete blocks, cement/sand ratios (by volume) were selected as 1/2, 1/3, . . . , and 1/9. These ratios are only arbitrary; the purpose is to obtain a wider range for the compressive strength for concrete samples. The cement paste was poured into plastic containers (Figure 4). Cylindrical samplers with an inner diameter of 57 mm and a height of 120 mm were placed in the “wet” concrete paste in the plastic box (Figure 4). The main reason for placing samplers in the prismatic concrete block is that the concrete block to be used for nail shooting and the cores to be extracted as cylindrical samplers must have identical properties. Concrete mixtures at different Portland cement/sand ratios were left to dry in the open air for 28 days. After the drying process was completed,

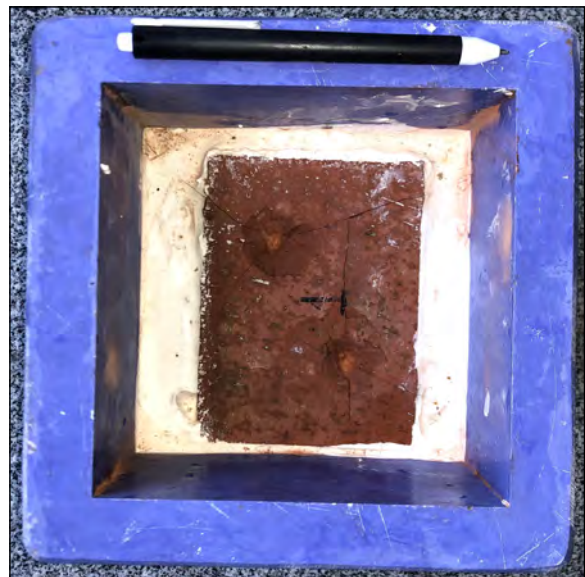


Figure 3- Encapsulated brick.



Figure 4- Casted concrete and impregnated cylindrical core samplers.

the cylindrical samplers placed in the concrete earlier were removed carefully. Five concrete core samples were prepared for each C/S ratio (Figure 5).

To increase the variety of concrete materials, prismatic samples with cement/sand (C/S) ratios of 1/2, 1/3, 1/4, and 1/5 were also prepared with a vibrating rammer. The method described in the previous paragraph was used in their preparation, except for the compaction part with a vibratory rammer.

One of the prominent advantages of the proposed tool is the variability of nail diameter. Early trials showed that a diameter of 5 mm is suitable for a wide range of UCSs. However, the application of 5 mm nails brought up two issues. One is that this nail strength was not sufficient for strong rocks ( $UCS > 60$  MPa). The application of 5 mm nails onto such rocks resulted either in breaking or bending of nails. To prevent this, 6 mm-diameter nails were preferred. Secondly, penetration depth of maximum of 60 mm on some concrete samples were exceeded even when applying the bullets of lower energy and thereby necessitated the use of 6 mm-diameter nails. The reason for also including 4 mm-diameter nails is to increase the coverage of the proposed equation with respect to the nail diameter to predict the compressive strength of tested materials. It should be noted that the distribution of nail diameters is not equal overall in the population of nail penetration test data.

Nails with a diameter of 5.0 and 6.0 mm were used in concretes with very low strength (for samples of C/S ratios of 1/9 and 1/8). The nails with a diameter



Figure 5- Core samples of concrete prepared from different cement/sand ratios.

of 4.0 mm were not used on these concretes, since the entire length of the nail (60 mm) penetrated the concrete. In concretes with a C/S ratio of 1/2 and 1/3, low-energy bullets were not sufficient to drive 6.0 mm diameter nails into the concrete. Concretes having similar C/S ratios were shot with only 4.0 mm and 5.0 mm diameter nails. In concretes with C/S ratios of 1/4, 1/5, 1/6, and 1/7 successful nail shots were performed with all three types of nail diameters (Figure 6). Bullets with an energy of 150J and nails with a diameter of 6 mm were used in concrete samples compacted with a vibratory rammer.

Five core samples were also prepared for each rock block (Figure 7). Concerning the nail penetration tests on rock blocks, the nail piercing was observable for weak- to very weak rocks. Penetration depths were measured such that the only non-penetrating part was measured via a caliper. This length was subtracted from the nail length to find the true penetration. In cases where the rock block was moderately strong to strong, it was not possible to obtain a proper penetration of nail into the rock. In such cases the nail shot onto the rock surface created a chisel-induced ditch on the surface. To determine the penetration depth, the deepest part of the ditch created by the nail on the rock was measured with a digital caliper (Figure 8). In order to make a reliable reading in cases where the surrounding of the chisel-induced ditch has an irregular rock surface, a ring of 10 mm height was placed around the ditch and the depth of the cavity

was determined (Figure 8). Since the strength of the bricks used in the study was very high, it was not possible to nail these block bricks, and the depth of the chisel-induced ditch formed by the shots made on these materials was determined similar to that in strong rocks.

### 3. Experimental Results

The penetration depths of nails driven into test materials were measured by shooting with a nail gun at the rock, concrete, and brick samples used in the research. Five nail shots were made on each test material. For rock materials, nail penetration tests were carried out on block samples, not on cores. In some rock samples where the block size is small, the number of shots (due to the fragmentation of the rock) remained around 3. Appropriate nail diameter and driving energy were selected depending on the strength level of the material. Nail penetration test results are given in Table 1. Five penetration depths for each sample were not entered in the table to save space. Instead, only the minimum, maximum, and average values are given.

The other major test employed for this investigation is the uniaxial compression test or simply the compression test. Five compression tests were performed for each of the rock, concrete and brick samples. The test results are given in Table 2 as minimum, maximum, and average compressive strengths.



Figure 6- Nails shot at the concrete surface. Back row: 6 mm-diameter nails, middle row: 5 mm-diameter nails, front row: 4 mm-diameter nails.



Figure 7- Core samples extracted from different rock types.



Figure 8- Measurement of nail penetration depth when a nail did not exhibit a piercing into rock.

Early trials towards establishing a correlation between nail penetration depths and compressive strengths were not satisfactory. To get an insight into the possible reason for this poor correlation, a statistical analysis was carried out for both the penetration depth of sound bullets and the compressive strength of the selected two rocks. Firstly, 30 shots were carried out on the same rock (lithic tuff-2) using the sound bullets of the first brand and nail penetration depths were recorded to gain an insight into the covariance of penetration depths of these sound bullets. The minimum, maximum, and mean ( $\mu$ ) penetration depths determined for these 30 shots are 6.8 mm, 18.1 mm, and 10.6 mm, respectively. The standard deviation ( $\sigma$ ) of these shots is 3.3 mm and the coefficient of variation ( $COV = \sigma / \mu * 100$ ) is 31%. Considering that this COV is unacceptably high and these sound bullets would not be suitable for this research, 30 nail shots were made on another rock (lacustrine limestone-1) using the second brand of sound bullets.

Table 1- The results of nail penetration tests ( $\Phi$ : nail diameter, h: penetration depth, E: impact energy).

No.	Name	$\phi$ (mm)	h (mm)	E (J)
1	Claystone	5	37.8/40.1/39.0	150
2	Lithic tuff-1	5	8.6/11.2/9.6	75
3	Limestone-1	5	18.5/21.0/20.2	150
4	Andesite-1	6	7.4/8.8/8.1	150
5	Limestone-2	5	8.0/8.7/8.2	150
6	Quartz arenite-1	6	6.7/7.7/7.2	150
7	Ignimbrite-1	4	16.6/20.1/17.8	75
8	Quartz arenite-2	5	12.7/14.8/13.5	150
9	Crystalline limestone	5	9.9/11.9/10.8	150
10	Trachyandesite-1	5	13.3/13.4/13.3	150
11	Marble-1	5	8.9/11.2/10.1	150
12	Granite porphyry	5	10.7/12.4/11.5	150
13	Chalk	5	20.1/21.0/20.6	150
14	Meta-limestone	5	10.4/12.1/11.1	150
15	Calcschist	5	10.8/11.4/11.2	150
16	Ignimbrite-2	4	20.1/24.7/23.2	75
17	Limestone-3	5	9.4/12.4/10.6	150
18	Trachyandesite-2	5	11.1/12.9/12.0	150
19	Granodiorite	6	6.8/7.8/7.3	150
20	Lithic tuff-2	5	20.1/26.2/23.2	150
21	Zeolithic tuff-1	5	11.7/14.0/13.0	150
22	Olivine basalt	6	6.6/9.0/8.3	150
23	Andesite-2	5	9.1/10.9/10.1	150
24	Harzburgite	6	5.4/6.7/6.1	150
25	Lacustrine limestone-1	5	18.7/24.7/21.5	150
26	Dacite	5	8.1/12.1/10.4	150
27	Andesite-3	5	11.5/13.5/12.2	150
28	Andesite-4	5	11.7/14.2/12.5	150
29	Micritic limestone	5	12.3/16.5/14	150
30	Zeolithic tuff-2	5	15.5/23.3/18.2	150
31	Crystalline tuff	5	32.9/46.6/38.6	150
31	Crystalline tuff	6	14/23.9/20.5	150
31	Crystalline tuff	5	5.8/23.6/15.3	50

No.	Name	$\phi$ (mm)	h (mm)	E (J)
31	Crystalline tuff	4	16.8/29.2/21.5	50
32	Lacustrine limestone-2	5	7.5/13.6/10.4	150
33	Marble-2	5	8.2/10.8/9.6	150
34	Lacustrine limestone-3	5	6.8/9.2/8.0	150
35	Brick-1	5	8.6/9.3/9.0	150
36	Brick-2	5	8.8/11.5/9.8	150
37	Concrete 1/9	6	21.8/30.4/27.3	50
37	Concrete 1/9	5	33.8/50.3/45.3	50
38	Concrete 1/8	6	21.2/40.8/32.6	50
38	Concrete 1/8	5	37.1/52.7/42.7	50
39	Concrete 1/7	6	20.4/27.3/23.7	50
39	Concrete 1/7	5	22.0/36.1/30.8	50
39	Concrete 1/7	4	38.9/49.4/46.5	50
40	Concrete 1/6	6	16.6/21.7/18.7	50
40	Concrete 1/6	5	18.6/33.8/25.0	50
40	Concrete 1/6	4	24.8/37.0/32.6	50
41	Concrete 1/5	6	12.3/16.7/14.9	50
41	Concrete 1/5	5	19.6/28.4/23.1	50
41	Concrete 1/5	4	21.5/30.7/27.0	50
42	Concrete 1/4	6	9.8/13.4/11.8	50
42	Concrete 1/4	5	16.0/23.9/19.6	50
42	Concrete 1/4	4	20.1/27.1/24.5	50
43	Concrete 1/3	5	14.8/23.4/17.3	50
43	Concrete 1/3	4	20.6/34.8/27.1	50
44	Concrete 1/2	5	17.2/26.2/21.6	50
44	Concrete 1/2	4	19.8/26.5/23.0	50
44	Concrete 1/2	6	33.0/38.4/34.8	150
45	Concrete 1/2*	6	19.2/19.9/19.6	150
46	Concrete 1/3*	6	20.8/23.5/21.9	150
46	Concrete 1/4*	6	23.4/24.7/24.1	150
48	Concrete 1/5*	6	25.2/27/26.3	150
48	Concrete 1/5*	4	15/19.5/17.9	50

The minimum, maximum, and average nail penetration depths recorded for these shots are 18.7 mm, 23.8 mm, and 21.5 mm, respectively. The standard deviation and the covariance are 1.5 mm and 7.0% respectively for this second trademark sound bullets which were evaluated as suitable for the research, and thereafter the nail shots were made with these sound bullets on all materials used in the investigation.

Based on the observation that the energy of the sound bullets is not constant and has a certain coefficient of variation, experimental studies have also been carried out to get an idea about the range of the coefficient of variation for a rock sample tested for compressive strength. For this, compression tests were carried out on 30 core samples (Figure 9) taken from the dacite (number 26 in Table 1). The lowest, highest, and mean compressive strengths

Table 2- The results of uniaxial unconfined compression tests.

No.	Name	$\sigma_c$ (MPa)
1	Claystone	8.9/14.3/11.0
2	Lithic tuff-1	21.6/42.5/29.7
3	Limestone-1	21.9/62.3/42.6
4	Andesite-1	77.1/94.8/84.3
5	Limestone-2	34.7/90.3/57.9
6	Quartz arenite-1	83.6/137.0/103.5
7	Ignimbrite-1	24.6/29.9/27.6
8	Quartz arenite-2	37.9/59.3/50.9
9	Crystalline limestone	34.4/45.1/39.2
10	Trachyandesite-1	30.2/63.8/51.5
11	Marble-1	41.0/46.5/43.8
12	Granite porphyry	41.7/54.5/47.7
13	Chalk	27.5/50.6/40.6
14	Meta-limestone	33.8/59.5/47.9
15	Calcschist	56.1/83.8/65.8
16	Ignimbrite-2	14.9/20.9/18.0
17	Limestone-3	47.8/73.7/54.9
18	Trachyandesite-2	50.6/75.6/65.2
19	Grandiorite	69.3/112.2/86.8
20	Lithic tuff-2	27.2/50.7/39.5
21	Zeolithic tuff-1	51.2/63.3/55.8
22	Olivine basalt	86.5/119.7/99.6
23	Andesite-2	22.4/81.2/47.0
24	Harzburgite	80.1/123.2/102.4
25	Lacustrine limestone-1	15.3/25.5/20.6

No.	Name	$\sigma_c$ (MPa)
26	Dacite	42.2/101.2/64.1
27	Andesite-3	42.7/59/50.5
28	Andesite-4	40.4/56.3/51.1
29	Micritic limestone	32.2/44.5/41.4
30	Zeolithic tuff-2	18.6/27.7/23.4
31	Crystalline tuff	10.0/12.7/11.3
32	Lacustrine limestone-2	62.6/88.8/79.4
33	Marble-2	37.2/52.2/43.8
34	Lacustrine limestone-3	46.3/99.8/70.4
35	Brick-1	67/127/96
36	Brick-2	44.8/73.7/59.9
37	Concrete 1/9	1.1/1.4/1.2
38	Concrete 1/8	1.0/1.4/1.3
39	Concrete 1/7	1.2/2.0/1.7
40	Concrete 1/6	2.7/3.1/2.9
41	Concrete 1/5	3.5/5.3/4.6
42	Concrete 1/4	4.9/7.3/5.7
43	Concrete 1/3	6.8/9.8/8.1
44	Concrete 1/2	5.5/8.7/7.3
45	Concrete 1/2*	19.2/19.9/19.6
46	Concrete 1/3*	20.8/23.5/21.9
46	Concrete 1/4*	23.4/24.7/24.1
48	Concrete 1/5*	25.2/27/26.3

(\* These concrete samples were prepared using a vibrating hammer).

found in these tests are 42.2 MPa, 101.2 MPa, and 64.1 MPa, respectively Their standard deviation and the coefficient of variation were found to be 16.1 MPa and 25%, respectively. Another attempt was also made to determine the second coefficient of variation of compressive strength using a different rock (andesite-2). The recorded minimum, maximum and mean compressive strengths for this rock are 22.4 MPa, 81.2 MPa, and 47.0 MPa, respectively. The standard deviation and the coefficient of variation of andesite-2 were determined to be 14.5 MPa and 31%, respectively. These observations indicate that the coefficient of variation of compressive strength for the tested rocks was surprisingly high. This ensues that the compressive strength of any rock (also perhaps for



Figure 9- Rock cores from dacite to be used for the coefficient of variation of compressive strength.

any concrete) is not absolute and needs to be seriously taken into consideration when attempting to determine the compressive strength using indirect test techniques. It should be noted that the only averages of UCSs for those two types of rock which were subjected to COV analyses were included in regression analyses.

The experimental data were subjected to multiple regression analyses to seek the most suitable predictive equation to indirectly determine the UCS for various type of materials. A total of 325 nail penetration depths recorded on intact rocks, concrete, and bricks along with the corresponding nail diameters and impact energies were included in the analysis. Concerning the entry for the CS, only the mean compressive strengths were employed in the regression analysis. Apparently, there are not 325 compressive strength values; it includes only 48 sets of means. That is, the compressive strength values were repetitively used in the regression analysis. For instance, two different energy levels and three different nail diameters employed for any rock or concrete sample require the use of the same compressive strength 30 times (2 energy levels x 3 nail diameters x 5 shots = 30). DATAFIT (v. 9.0; Oakdale Engineering, 2008) program was used for multiple regression analysis. In the regression analysis, nail penetration depth, nail diameter, and driving energy are independent variables, while compressive strength is the dependent variable. Different scenarios were considered as: a) All materials, b) only the rock samples, c) only the concrete samples, d) energy level of 150J alone, and e) nail diameter of 5 mm alone. The results are presented in Table 3 along with the statistical indicators such as the Root Mean Squared Errors (RMSE), the Variance Accounted For (VAF), and the Mean Absolute Percentage Error (MAPE). It appears that the inclusion of all materials along with all nail diameters and the two energy levels yields an

empirical relationship with the highest coefficient of regression ( $R^2 = 0.89$ ):

$$\sigma_c = \exp^{(0.1453\phi - 0.087h + 0.0142E + 2.14)} \tag{1}$$

for which the RMSE is reasonably small, the VAF is very close to 100%. However, the metrics of MAPE is critically high (50.3) for which the values greater than 50 are treated as no good. The significance level of equation (1) is 99% according to the chi square test. This predictive equation is very similar to the one proposed by Selçuk and Kayabalı (2015). While it consists of the same independent variables as those by Selçuk and Kayabalı (2015) the regression coefficient of the predictive Equation by those researchers is higher ( $R^2 = 0.95$ ) than that presented herein ( $R^2 = 0.89$ ). The most likely reason for this difference may be attributed to two reasons: One is that they employed gas-nailers in their research in which the COV of penetration depths should be very low owing the constant energy released by the ignition of propane while the COV of nail penetration depths herein is somewhat higher owing to possible variations in the amount of gunpowder in the sound bullets.

The exclusion of concretes and bricks from the regression analysis yield a predictive equation with a lower value of  $R^2 (=0.81)$ . The authors' preference is to use Equation (1) for all materials since the measured parameter is a common index for the three types of construction materials examined herein.

The next step included the entry of independent variables of 325 sets of nail penetration test to predict the compressive strengths indirectly. The experimentally measured compressive strengths and the computed compressive strengths using Equation (1) are plotted for 325 data sets (Figure 10). Disregarding a limited number of singular points, it is seen that the degree

Table 3- The results regression analyses ( $\phi$ : nail diameter, h: penetration depth, E: impact energy, RMSE: Root Mean Squared Error, VAF: Variance Accounted For, MAPE: Mean Absolute Percentage Error).

Case	Equation	R <sup>2</sup>	RMSE	VAF	MAPE
All materials	$\sigma_c = \exp(0.1453\phi - 0.087h + 0.0142E + 2.14)$	0.89	10.3	91.8	50.3
Rock samples	$\sigma_c = \exp(0.227\phi - 0.07h + 0.0095E + 2.25)$	0.81	11.4	93.5	15.7
Concrete samples	$\sigma_c = \exp(0.437\phi - 0.0746h + 0.0177E + 4.39)$	0.85	1.9	92.4	12.8
E=150 J only	$\sigma_c = 3.69\phi - 1.1h + 0.315E$	0.74	12.8	74.5	66.6
$\phi = 5$ mm only	$\sigma_c = 7.74\phi - 2.77h + 0.343E$	0.66	16.8	65.8	32.9

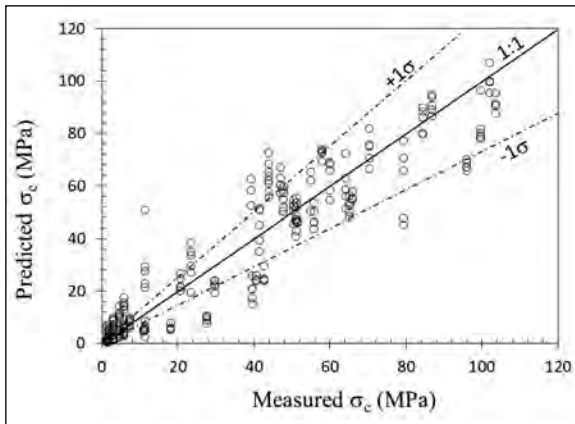


Figure 10- Graph showing the comparison between the predicted and measured compressive 348 strengths using all data.

of agreement between the computed compressive strengths and the measured compressive strengths measured is highly encouraging. The 1:1 line of the two parameters is also given in this graph. In addition,  $+1\sigma/-1\sigma$  standard deviation lines are also shown based on the 31% coefficient of variation determined for rock number 23 (andesite-2). A great majority of the predicted compressive strengths of the 48 tested materials were within the  $+1\sigma/-1\sigma$  standard deviation of the measured compressive strength.

Table 4 was constructed to offer guidelines for the professionals about using the proper nail diameters and different energy levels for different ranges of the UCS.

**4. Conclusions and Discussion**

The results obtained from this investigation are as follows:

- An empirical relationship to indirectly predict the compressive strength of building materials was established.

Table 4- Guidelines for the use of appropriate nail diameters (in millimeters) for various levels of UCS and the two levels of impact energy.

$\sigma_c$ range (MPa)	E = 50J	E = 150J
0 - 20	4, 5, 6	-
20 - 60	-	4, 5
60 - 100	-	5, 6
> 100	-	6

- The nail gun employed for this investigation to indirectly predict the compressive strengths of most common construction materials is a non-destructive test and yields a very high correlation coefficient ( $R^2 = 0.89$ ) between the predicted and measured CSs.

- Wide range of compressive strengths (1-100 MPa and higher) for building materials can be predicted with a great degree of accuracy using the nailer employed.

- The coefficient of variation of compressive strengths of two types of rock sample is surprisingly high. This finding has never been handled in earlier investigations and needs to be addressed further. A possible explanation for such a wide range of compressive strengths of the same rock could be the variations of micro-crack distribution in core samples. A comprehensive study is recommended in that the distribution of micro-cracks in each rock core is correlated to the respective CSs.

- The coefficient of variation of nail penetration depth is significantly smaller than that found for the compressive strength using the direct method.

- While the time required for obtaining a sufficient number of identical rock or concrete samples and running a series of compression tests on the cores of these materials may take up to several hours to one day per sample, obtaining the compressive strength indirectly by a nailer such as the one used in this investigation takes only as short as less than half an hour (for 5 shots).

- The nailer used for this investigation eliminates the need for using several different-energy level nailers for materials of varying levels of compressive strength.

The great variability with the compressive strength of the same rock material brings up the question of “is the compressive strength determined through conventional compression tests unique or an absolute value?”. It also holds for concrete materials. This is an important aspect of direct compression tests to be addressed in further investigations and must be validated by more evidence.

The proposed tool, along with the empirical equation, is capable of predicting compressive strengths greater than 100 MPa by measuring the depth on the rock surface created by the chiseling effect. Nail penetration depths are created this way for strong- to very-strong rocks and thus the compressive strength obtained indirectly may be questionable because the chiseling depth decreases as the compressive strength increases. Considering the pointy character of nails, the pointy part of nailers which ranges from 2-3 millimeters, more tests need to be run to demonstrate if the angle of the point or the length of the pointy part has any effect on the compressive strength.

As a further investigation about abnormally high coefficients of variation of rocks, the authors recommend comprehensive direct compression tests be done on rocks (and also on concretes) involving more variety of test materials. This way, the use of appropriate statistical methods may come up with the optimum selection of the true compressive strengths for building materials.

### Acknowledgement

The funding for this research was provided by the Scientific and Technological Research Council of Türkiye (TÜBİTAK) with grant number 120M030.

### References

- Aoki, H., Matsukura, Y. 2008. Estimating the unconfined compressive strength of intact rocks from Equotip hardness. *Bulletin of Engineering Geology and the Environment* 67, 23–29.
- ASTM. 1995. Standard test method for determination of the point load strength index of rock. ASTM Standard D5731.
- ASTM. 2001. Standard test method for determination of rock hardness by rebound hammer method. ASTM Standard D5873.
- ASTM. 2002. Standard test method for unconfined compressive strength of intact rock core specimen. ASTM D2938.
- Bae, G. J., Lee, S. W., Chang, S. H., Park, H. G., Lee, M. S., Kim, J. K. 2004. Application of pneumatic pin penetration test to estimation of compressive strength of shotcrete in Korea. *Tunneling and Underground Space Technology* 19, 432-440.
- Broch, E., Franklin, J. A. 1972. Point-load strength test. *International Journal of Rock Mechanics and Mining Sciences* 9(6), 241-246.
- Felicetti, R., Gattesco, N. 1998. A penetration test to study the mechanical response of mortar in ancient masonry buildings. *Materials and Structures* 31(5), 350-356.
- ISRM. 1978. Suggested method for determining hardness and abrasiveness of rocks. *International Journal of Rock Mechanics and Mining Sciences* 15, 89–97.
- ISRM. 1985. Suggested method for determining point-load strength. *International Journal of Rock Mechanics and Mining Sciences* 22, 53-60.
- Kayabali, K., Selçuk, L. 2010. Nail penetration test for determining the uniaxial compressive strength of rock. *International Journal of Rock Mechanics and Mining Sciences* 47, 265-271.
- Li, X., Rupert, G., Summers, D. A., Santi, P., Liu, D. 2000. Analysis of impact hammer rebound to estimate rock drillability. *Rock Mechanics and Rock Engineering* 33,1–13.
- Liberatore, D., Spera, G., Cotugno, M. 2003. A new penetration test on mortar joints. *On-site Control and Evaluation of Masonry Structures* 191-202.
- Malhotra, V. M., Carino, N. J. 1991. *Handbook on nondestructive testing of concrete*. Boca Raton, FL, CRC Press, 384.
- Maruto Corporation. 2006. *Penetrometer for soft rock: Model SH-70 instruction manual*.
- Mishra, D. A., Basu, A. 2012. Use of the block punch test to predict the compressive and tensile strengths of rocks. *International Journal of Rock Mechanics and Mining Sciences* 51, 119-127.
- Ngan-Tillard, D. J. M., Verwaal, W., Mulder, A., Engin, H. K., Ulusay, R. 2011. Application of the needle penetration test to a calcarenite, Maastricht, the Netherlands. *Engineering Geology* 123(3), 214-224.
- Oakdale Engineering 2008. *DATAFIT: Version 9.0, RC 101, 23 Tomey Road, Oakdale, PA, 15071 USA*.
- Palassi, M., Emami, V. 2014. A new nail penetration test for estimation of rock strength. *International Journal of Rock Mechanics and Mining Sciences* (66), 124-127.
- Pucinotti, R. 2005. Non destructive testing in the valuation of reinforced concrete structural degradation. *L'Industria Italiana del Cemento* 810, 446-460.
- Pucinotti, R. 2009. In situ concrete strength assessment: Influence of the aggregate hardness on the Windsor probe test results. *Journal of Building Appraisal* 5(1), 75-85.
- Selçuk, L., Kayabali, K. 2015. Evaluation of the unconfined compressive strength of rocks using nail guns. *Engineering Geology* 195(3), 164-171.

- Selçuk, L., Çoban, S., Kayabalı, K., Şimşek, O. 2012. A non-destructive testing technique: Nail penetration test. *ACI Structural Journal* 109(2), 245-252.
- Szwedzicki, T. 1998. Indentation hardness testing of rock. *International Journal of Rock Mechanics and Mining Sciences* 35, 825–829.
- Ulusay, R., Gökceoğlu, C., Sülükçü, S. 2001. Draft ISRM suggested method for determining block punch strength index (BPI). *International Journal of Rock Mechanics and Mining Sciences* 38, 1113–1119.
- Van der Schrier, J. S. 1988. The block punch index test. *Bulletin of the International Association of Engineering Geology* 38, 121-126.
- Verwaal, W., Mulder, A. 1993. Estimating rock strength with the Equotip hardness tester. *International Journal of Rock Mechanics and Mining Science Geomechanics Abstracts* 30, 659–662.
- Yılmaz, I. 2009. A new testing method for indirect determination of the unconfined compressive strength of rocks. *International Journal of Rock Mechanics and Mining Sciences* 46, 1349–1357.
- Yılmaz, I., Sendir, H. 2002. Correlation of Schmidt hardness with unconfined compressive strength and Young's modulus in gypsum from Sivas (Turkey). *Engineering Geology* 66, 211–219.





# Bulletin of the Mineral Research and Exploration

<http://bulletin.mta.gov.tr>



## Evaluation of radioactive properties and microfaunal evidence in the Bosphorus and the Dardanelles straits and Golden Horn sediments

İpek F. BARUT<sup>a\*</sup>, Engin MERİÇ<sup>b</sup>, Atike NAZİK<sup>c</sup>, Mustafa ERYILMAZ<sup>d</sup>, Feyza DİNÇER<sup>e</sup> and Erol KAM<sup>f</sup>

<sup>a</sup> Istanbul University, Institute of Marine Sciences and Management, 34134 Vefa-İstanbul, Türkiye

<sup>b</sup> Moda Hüseyin Bey Sokak No: 15/4, 34710 Kadıköy-İstanbul, Türkiye

<sup>c</sup> Cukurova University, Department of Geological Engineering, 01330 Balçalı-Adana, Türkiye

<sup>d</sup> Mersin University, Department of Geological Engineering, 33343 Yenişehir-Mersin, Türkiye

<sup>e</sup> Nevşehir University, Department of Geological Engineering, 50300 Nevşehir, Türkiye

<sup>f</sup> Istanbul Technical University, Department of Environmental Engineering 34469, Maslak-İstanbul, Türkiye

Research Article

Keywords:

Bosphorus and Dardanelles Straits (Türkiye), Sediment, Golden Horn (Istanbul), Gross alpha and beta, Microfauna (benthic foraminifera, ostracoda).

### ABSTRACT

The aim of this study is to investigate radioactive pollutants from pollution loads transported from the Black Sea to the Aegean Sea by the Turkish Straits System and their effects on microfauna (benthic foraminifera and ostracoda) assemblages. In the study, the effects of gross alpha and beta activity on the species number, species diversity, dominant species and species richness of benthic foraminiferal and ostracoda assemblages were investigated in 16 bottom sediments taken from different depths in the Golden Horn, Bosphorus and Dardanelles straits. In the studied sediment samples examined 61 genera and 64 species of benthic foraminifera, 23 genera and 26 species of ostracoda were identified. In addition two migratory foraminifera species were observed as *Spiroloculina antillarum* of Atlantic-Pacific origin and *Peneroplis pertusus* of Indo-Pacific origin. A relationship between the abundance of microfauna and high gross alpha and beta values was found in the Dardanelles samples, but not in the Bosphorus and Golden Horn samples. In this study, the highest radioactivity value was observed in the deepest bottom sediment samples. Consequently, the gross alpha and beta values were seen to be close to each other in the Dardanelles Strait and Golden Horn samples, and they had a broad-spectrum in the Bosphorus samples.

Received Date: 15.12.2022

Accepted Date: 16.06.2023

### 1. Introduction

Certain conditions can determine the rate of transport of radionuclides within and between the components of the ecosystem. These conditions are the mechanisms that cause transport, the concentration levels of radionuclides in the biotic and abiotic components of ecosystems, and the geochemical and ecological processes that affect the transport (Meriç et al., 2012; Barut et al., 2013; Zorer and Öter, 2015; Van et al., 2018).

Many research point out radionuclides fall out-derived pollutants that accumulate for a long time in living things such as invertebrate, fish, fungi and lichens and helping to evaluate the activity concentration (Kılıç et al., 2014; Biswas et al., 2015; Savino et al., 2017; Borcia et al., 2017; Duong Van et al., 2020). In a study by Kılıç et al. (2014), the activity concentrations of natural and artificial radionuclides were determined in the mussel species *Mytilus galloprovincialis* (Mollusca: Bivalvia: Mytilidae) from Mediterranean

Citation Info: Barut, İ., F., Meriç, E., Nazik, A., Eryılmaz, M., Dinçer, F., Kam, E. 2024. Evaluation of radioactive properties and microfaunal evidence in the Bosphorus and the Dardanelles straits and Golden Horn sediments. Bulletin of the Mineral Research and Exploration 173, 203-233. <https://doi.org/10.19111/bulletinofmre.1315735>

\*Corresponding author: İpek F. BARUT, [barutif@istanbul.edu.tr](mailto:barutif@istanbul.edu.tr)

mollusc species and in samples taken from the Golden Horn sediment. According to the results of the study, the concentrations of radioactivity in the particles in the <math><63\ \mu\text{m}</math> fraction of the sediment were generally higher than those found in *Mytilus galloprovincialis*. Therefore, the interaction of these radionuclides, which are the main indicators of the radiological state of the environment, and their usability in biological updates take place in various biogeochemical cycles (Mandic et al., 2010).

Again, the movements and distribution of radionuclides were influenced by differences in the sedimentation rate in the sediments of aquatic environments (lakes, estuaries, oceans and coastal seas) and atmospheric features such as floods and droughts. Therefore, it is important to evaluate the time, quality, quantity and accumulation of material together with environmental changes in past or current sediments (Carroll and Lerche, 2003; Ayçık et al., 2004; Li et al., 2006; Dai et al., 2007; Yang et al., 2009; Ruiz-Fernandez and Hillaire-Marcel, 2009).

Marine sediments have include natural records, a wealth of environmental information for organic and inorganic toxic pollutants, and high-resolution chronological transitions, that enable the examination of the anthropogenic origin of environmental changes in the past (Callaway et al., 1996; Vongunten et al., 1997; Fuller et al., 1999; Dai et al., 2007; Zhou et al., 2015; Hanfi et al., 2019, 2021). Radionuclides that are found locally in river and lake bottom sediments above certain limit values ( $^3\text{H}$ ,  $^{90}\text{Sr}$ ,  $^{137}\text{Cs}$ ,  $^{238}\text{U}$ ,  $^{234}\text{U}$ ,  $^{238}\text{Pu}$ ,  $^{239}\text{Pu}$ ,  $^{240}\text{Pu}$ ,  $^{241}\text{Am}$ , gross alpha, gross beta ve gross gama) are caused by air particles dispersed into the atmosphere as a result of surface nuclear weapons test studies and passing to other environments with radionuclide fallouts and radioactive clouds (McLin and Lyons, 2002).

Various pollution loads are transported from the Black Sea to the Marmara and Aegean Seas via the Bosphorus and Dardanelles Straits. An important part of the pollution in the Black Sea is the waste brought by the Danube River (Rank et al., 1990; Pantelic et al., 2002; Maringer et al., 2015; Borcia et al., 2017). The study of radiochemical processes has been revealed the existence of radioactive and chemical pollution

risks in the lower parts of the Danube, in the Black Sea coastal region where some complex processes occur together with the Danube spill area in the Black Sea (Bologa and Patrascu, 1997; Borcia et al., 2017). For example after the Chernobyl accident, some of the activation products that emerged in the marine environment samples as a result of radioactive fallout in the ecosystem, as well as some of the other fission products were transported to the Eastern Black Sea Region and other regions (Bologa, 1994; Bologa and Patrascu, 1997; Bologa et al., 1998; Patrascu, 2002). Besides, the Dnieper, Dniester, Kuban, Don, Çoruh, Kızılırmak, Sakarya and Yeşilırmak rivers and their tributaries around the Black Sea are also effective in transporting pollution in general and industrial pollution in particular.

Radioactivity in the water comes from three main sources: natural radioactivity, radioactive precipitation and radiological facilities. Examination of qualitative and quantitative content of the radioactivity concentration levels found in nature is important in assessing of the environmental risk and the case (Tuncer and Tuğrul, 1992; Er and Tuğrul, 1995; Şahin, 2000; Tuğrul et al., 2001). Natural radionuclide concentrations in the aquatic ecosystem are connected to the physicochemical conditions and the geological features of the region.

Another recent study (Savino et al., 2017) conducted after the Chernobyl accident, starting from September 1986, included four monitoring periods to assess the activity concentration of four isotopes ( $^{134}\text{Cs}$ ,  $^{137}\text{Cs}$ ,  $^{103}\text{Ru}$  and  $^{106}\text{Ru}$ ). Moreover, Savino et al. (2017), twenty-eight years after the accident in December 2014, carried out another sampling process. Only  $^{137}\text{Cs}$  was revealed beyond the detection limits, measuring activity concentrations ranging from 20 to 40 Bq/kg, while other radionuclides were no longer observed due to their shorter half-life (Savino et al., 2017). Beacuse of the elements and radioactive contaminants in the soil transported and distributed by water, aquatic ecosystem is effected by radioactive materials (Santschi and Honeyman, 1989). Particulate matter containing dissolved organic and inorganic substances are transported from the land to the sea via rivers.

Owing to the presence of uranium in disequilibrium with its daughter isotopes in lake and river sediments, the radioactivity is low. In contrast, the oceanic sediments contain an important value, radionuclides. At the same time, the oceans serve as a redistribution agent for radioactive elements (Friedlander et al., 2005). Some radionuclide concentrations in the Black Sea are higher than those in the Mediterranean. However, studies on the radiological results of the radionuclides measured in the oceans and the Mediterranean show that the radiation dose emitted from Black Sea anthropogenic radionuclides is low (Emiroğlu, 2014). Studies are ongoing for countries surrounding the Black Sea to develop regionally coordinated monitoring and emergency response programs for radionuclides in the marine environment and to evaluate key processes that control the fate of the pollutants in the Black Sea using radioactive tracers (Topçuoğlu, 2000).

The elements that are carried out to seas and coastal ecosystems, and have a pollutant effect are causing a change in the quality of the sea water, deterioration of the environment at the seabed, disappearance of dissolved oxygen in the bottom mud and emergence of anaerobic conditions. At the end of this process, the ecological balance deteriorates with the change of living conditions in the marine environment. Radioactive contaminations that cause abnormal formations on fauna and flora classified by the World Health Organization (WHO) are among these pollutants.

The distribution and abundance of benthic foraminifera individuals are mainly controlled by the temperature, salinity of the sea surface water (Thunell, 1979; Sen Gupta, 1999). Benthic foraminifera are very sensitive to changes in physicochemical and biological characteristics of the ecological environment (sea water temperature, salinity, pH, dissolved oxygen, availability of food, etc.). The distribution and abundance of benthic foraminifera individuals are affected by ecological conditions in the marine environment. Therefore, the properties of benthic foraminifera tests, including their morphology, abundance, stable isotopic and trace metal composition, provide valuable information on

past climatic and oceanographic changes such as sea level, monsoons density, temperature, salinity, and ocean circulation (Saraswat and Nigam, 2013).

In general, both natural and anthropogenic factors of the marine environment affect the abundance and distribution of different microfauna (benthic foraminifera, ostracoda) genera and species, abnormal morphological deformations and coloration of their foraminifera tests or ostracoda carapaces. In some recent studies (Meriç et al., 2008, 2009, 2012, 2017, 2018*a, b*, 2020; Barut et al., 2013; Yokeş et al., 2014) carried out at different locations of the Eastern Aegean Sea, highly different ecological conditions including radioactivity concentrations and geochemical properties of the sediment were found to be influenced by the presence of potential sub marine thermal springs. Likewise, while the physical, chemical and radioactive properties of seawater were effective on benthic foraminiferal assemblages in terms of genera and species abundance, distribution, abnormal individual and colored shell formation, they did not show any effect on ostracoda individuals (Barut et al., 2018; Meriç et al., 2018*a, b*; 2020).

In the study by Meriç et al. (2018*a*) carried out at Aliğa Cove (İzmir), the gross alpha and gross beta (Bq/l) values in water collected from the sea and inside the cave at the location were higher than the reference values. Besides, according to the results of their study, it is in question that among ecological conditions, both differences in temperature value limits and the radioactive properties of waters may be effective on the distribution of the genera and species of certain benthic foraminifera (Meriç et al., 2018*a*).

Our study aims to investigate the effects of radioactive pollutants transported from the Black Sea to the Aegean Sea through the Turkish Straits System on microfaunal assemblages. In this context, multidisciplinary analyses were carried out including paleontological analyses, radioactivity analyses and statistical analyses in the sediment samples. The Bosphorus, the Dardanelles and the Golden Horn were selected as the areas of study because they are significant transportation routes of bottom sediments reaching the Marmara and Aegean Seas from the Black Sea (Figure 1).

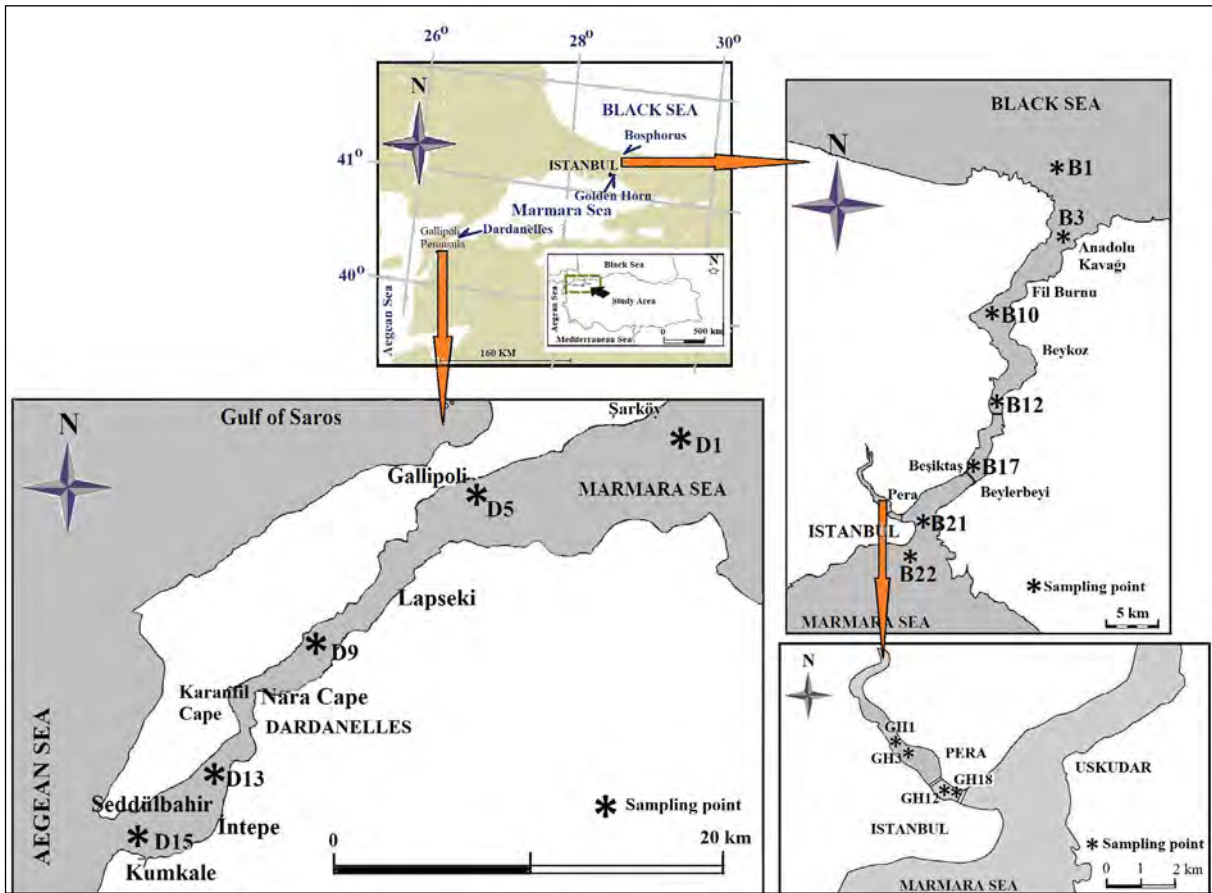


Figure 1- Location map of the study area.

The results of our studies conducted in environments with different ecological characteristics including thermal submarine freshwaters in gulfs, bays and surroundings of the Eastern Aegean coasts were evaluated together with the results obtained in this study. Therefore, this study investigates the effects of gross alpha and beta activity concentrations on the number of individual species, number of species diversity, number of dominant species and species richness of benthic foraminifera and ostracoda assemblages (Figure 1).

## 2. Oceanographic Features of the Bosphorus

The surface water temperature was measured along the profile in the Bosphorus, with average values between 8.0-9.0°C in spring and 19.0 - 24.0°C in summer. The surface water temperature is measured around 18.5-19.0°C in autumn. The temperature of the bottom water is around 14.5°C. In winter, the surface water temperature drops to around 5.5- 6.5°C.

The temperature of the bottom water does not change in general and is around 14-14.5°C in all seasons (Eryılmaz, 1995, 1997, 2002; Eryılmaz et al., 2000; Yücesoy-Eryılmaz et al., 2003a, b) (Figure 2).

The presence of two layers in the Bosphorus may be observed more easily with salinity data (Figure 2). Surface salinity is measured as 17.68‰ in spring, while it is 36.0‰ at 30 m and 36.8‰ at 60 m of depth. It is 17.89‰ on the surface in summer, 34.19‰ at 30 m, and 38.28‰ at 60 m of depth. It is 17.38‰ on the surface in autumn, 17.59‰ at 30 m, and 38.46‰ at 60 m. It is 17.15‰ in winter, 26.49‰ at 30 m, and 37.25‰ at 60 m of depth (Eryılmaz, 1995, 1997; Eryılmaz et al., 2000; Yücesoy-Eryılmaz et al., 2003a, b).

In the Bosphorus, two different waters pass in opposite directions, the surface and bottom currents are caused by the level and density differences between the Black Sea and the Aegean Sea. These currents differ based on meteorological factors and seasons. It

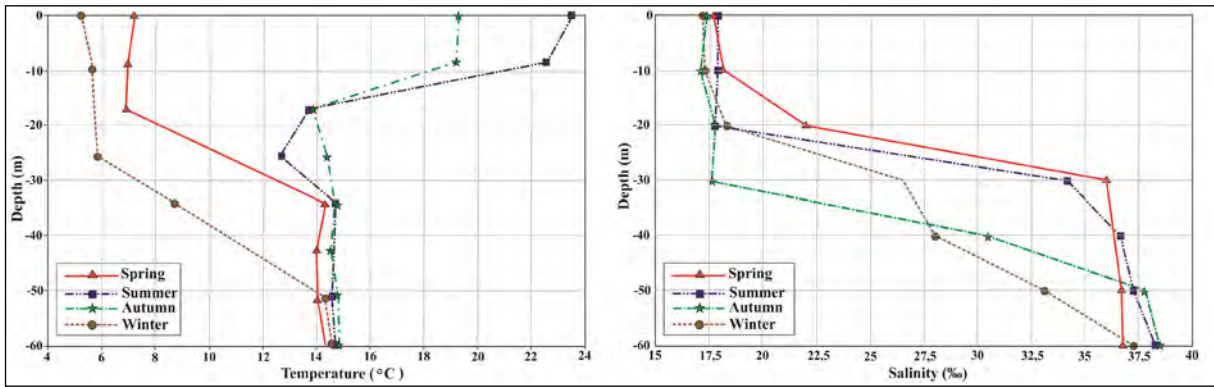


Figure 2- Seasonal change of average sea water temperature (°C), salinity (‰) by depth in the Bosphorus.

was observed that the surface current velocity at the northern entrance of the Bosphorus is 0.5-0.7 knots, ½ knots at Fil Burnu (Figure 1), 1-1.5 knots in front of Anadolu Kavağı, 2-3 knots in front of Çubuklu, 4-5 knots in front of Akıntı Burnu and Beylerbeyi, the narrowest parts of the strait, and between 3 and 4 knots in Üsküdar-Beşiktaş (Figure 1). However, this velocity increases to 7-8 knots with northern winds (Figure 2) (Eryılmaz, 1995, 1997; Eryılmaz et al., 2000; Yücesoy-Eryılmaz et al., 2003a, b).

### 3. Oceanographic Features of the Dardanelles

The reverse currents of Mediterranean and Black Seas origin waters observed in the Bosphorus Strait are also seen in the Dardanelles. However, contrary to the Bosphorus, the thickness of the Mediterranean origin water is higher and the thickness of the Black Sea origin water is lower. This factor is one of the most important elements that affect the vertical temperature distribution in the water of the Dardanelles Strait. The water temperature on the surface in the spring is

16.8-17.6°C and 14.8-15.2°C at 40 m depth. It is 19.8-22.3°C on the surface in summer and 15.4-15.7°C at 45 m. It is 16.4-17.7°C on the surface in autumn and 15.7-17.2°C at 75 m of depth. It is 13.0-13.2°C in winter, 15.5-16.6°C in 80 m of depth (Figure 3) (Eryılmaz, 1998; Eryılmaz et al., 2001; Yücesoy-Eryılmaz and Eryılmaz, 1998, 2000, 2002).

Surface salinity in spring is 22.7-23.0‰, it is 38.9-39.1‰ at 30 m of depth. In summer, it is 23.5-28.0‰ at the surface and 38.6-39.1‰ at 30 m depth. In autumn, it is 23.6-26.4‰ at the surface and 39.0‰ at 30 m depth. It is 23.5-26.4‰ in winter and 38.9-39.0‰ at 30 m depth (Figure 3) (Eryılmaz, 1998; Eryılmaz et al., 2001; Yücesoy-Eryılmaz and Eryılmaz, 1998, 2000, 2002).

The surface and bottom currents in the Dardanelles Strait are caused by the level and density differences between the Black Sea and the Aegean Sea. Here, as in the Bosphorus, two different strata of water pass in opposite directions. In the Dardanelles Strait, due

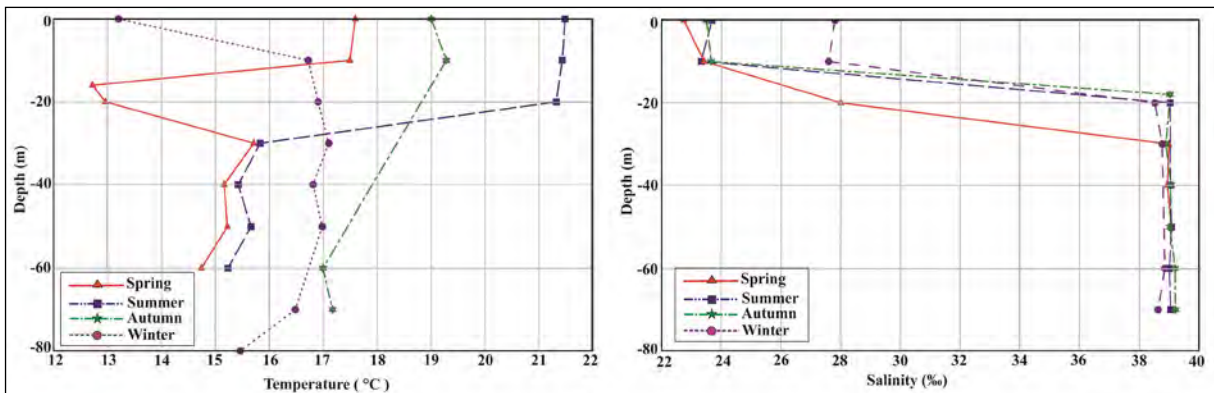


Figure 3- Seasonal change of average sea water temperature (°C), salinity (‰) by depth in the Dardanelles.

to the high density of Mediterranean origin waters coming from the Aegean Sea, they flow from the bottom to the Marmara Sea while the less dense Black Sea origin waters from the Marmara Sea pass into the Aegean Sea from the surface. Surface currents flow into the Aegean Sea in some places like a river conforming to the coastal shape. Current velocities are low at the northern entrance of the strait, but they increase towards south. The surface current velocity is 0.5 knots at the entrance to the Marmara Sea. It is 1.0-1.5 knots between Lapseki and Nara (Figure 1). Under normal conditions, the current velocity in front of Nara Cape is 1.5-2.0 knots and may reach up to 5.0 knots with winds blowing from the northeast. It is 4.0 knots between Çanakkale-Karanfil Cape, 2.0 knots between İntepe and Kumkale, and 2-3 knots between Seddülbahir and Kumkale (Figure 1). While the Dardanelles Strait surface currents increase with northeastern winds, they decrease with southwest winds. The bottom current velocity is 0.2-0.3 knots between Seddülbahir and Kumkale. Between İntepe and the Nara Cape, the undercurrent velocity is 0.2 knots, 0.5 knots in front of Nara Cape, 0.3-0.4 knots between Nara and Gelibolu, and it decreases to 0.1 knots at the Marmara exit of the strait (Figure 3) (Eryılmaz, 1998; Eryılmaz et al., 2001; Yücesoy-Eryılmaz and Eryılmaz, 1998, 2000, 2002).

#### 4. Oceanographic Features of the Dardanelles Inlet (NW Marmara Island) of the Marmara Sea

The temperature distributions measured depending on the depth at the Dardanelles Inlet of the Marmara Sea (NW Marmara Island) are 7.97°C on the surface

in spring, 14.64°C at 100 m; 23.55°C on the surface in summer, 14.64°C at 100 m; 19.31°C on the surface in autumn, 14.88°C at 100 m; 13.09°C on the surface in winter, 14.61°C at 100 m (Figure 4) (Eryılmaz, 1995; Yücesoy-Eryılmaz et al., 2003a, b).

The measured average salinity values are 24.50‰ on the surface in spring, 38.61‰ at 100 m; 22.15‰ on the surface in August, 38.86‰ at 100 m; 22.84‰ on the surface in autumn; 38.71‰ at 100 m; 26.80‰ on the surface in winter, 38.71‰ at 100 m (Figure 4) (Eryılmaz, 1995; Yücesoy-Eryılmaz et al., 2003a, b).

#### 5. The Oceanographic Characteristics of the Golden Horn

In the Golden Horn, the water temperature on the surface in spring is 9.93-10.67°C, 11.15-11.77°C at 10 m of depth, 13.29-14.08°C at 20 m depth, 13.93-14.61°C at 30 m of depth; 24.65-25.12°C on the surface in summer, 11.85-12.26°C at 10 m of depth, 11.68-12.32°C at 20 m of depth, 14.17-14.69°C at 30 m of depth; 19.05-19.60°C on the surface in autumn, 17.82-18.35°C at 10 m of depth, 13.87-14.41°C at 20 m of depth, 13.69-14.53°C at 30 m of depth; 05.44-6.08°C on the surface in winter, 05.74-06.41°C at 10 m of depth; 09.81-10.39°C at 20 m of depth; 12.83-13.51°C at 30 m of depth. Seasonal temperature variations according to depth are given in Figure 5 illustrating the development of a thermocline in spring between 9 and 20 m, in summer between 10 and 26 m, autumn between 8.5 and 19 m and in winter between 14 and 25 m (Figure 5) (Eryılmaz and Kara, 1996; Eryılmaz, 1998, 2002).

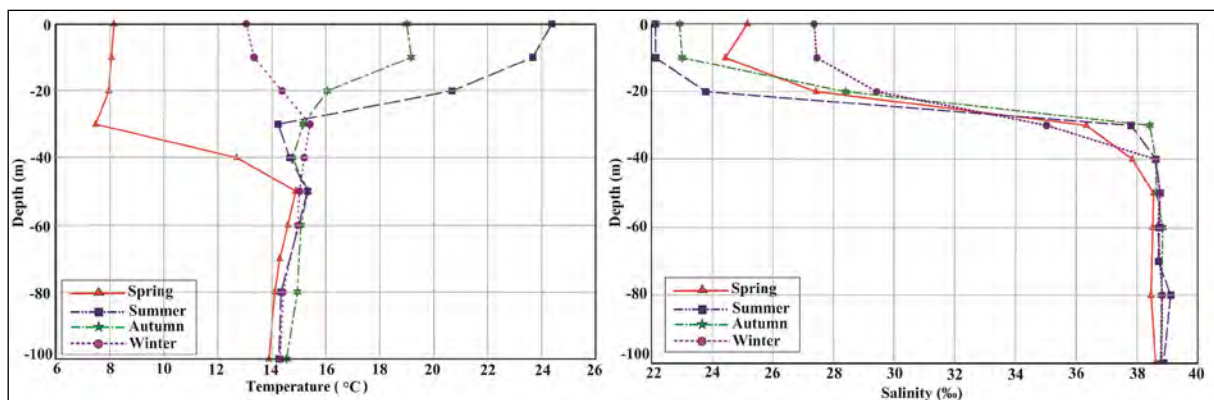


Figure 4- Seasonal change of average sea water temperature (°C), salinity (‰) by depth in the Marmara Sea, entrance of the Dardanelles (NW Marmara Island).

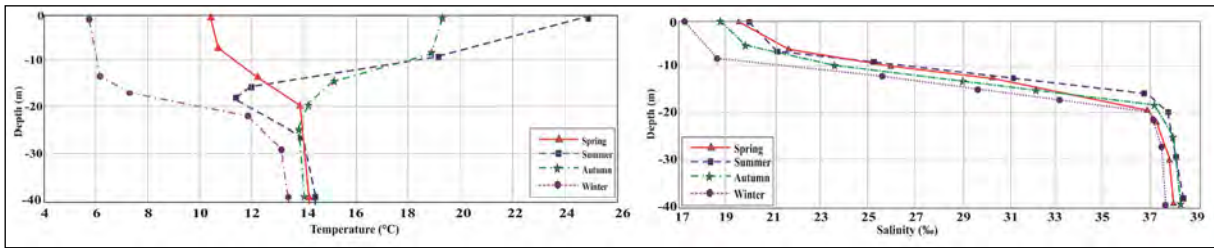


Figure 5- Seasonal change of average sea water temperature (°C), salinity (‰) by depth in the Golden Horn.

The salinity difference between the surface and the substrates is almost absent. Salinity differences in the surface layers depend on meteorological factors. Seasonal average variations of the seawater salinity in the Golden Horn are 19.29‰ on the surface in spring, 25.26‰ at 10 m, 37.01‰ at 20 m, 37.56‰ at 30 m; 19.72‰ on the surface in summer, 26.21‰ at 10 m, 37.77‰ at 20 m, 38.11‰ at 30 m; 18.58‰ on the surface in autumn, 26.22‰ at 10 m, 37.42‰ at 20 m, 38.08‰ at 30 m; 17.19‰ on the surface in winter, 18.44‰ at 10 m, 36.95‰ at 20 m, 37.58‰ at 30 m (Figure 5) (Eryılmaz and Kara, 1996; Eryılmaz, 1998).

**6. Materials and Methods**

**6.1. Study Area and Sampling**

Multidisciplinary studies were carried out in the region in the summer months of 2005 by the TCG

Çubuklu Ship affiliated to the Turkish Naval Forces Command Office Of Navigation, Hydrography and Oceanography (ONHO). Bottom sediment samples from 16 different points and depths, which constitute the basic data of this study, were collected by the Van Veen grab sampler. The depths at which the samples were taken varied between 7.00 and 80.00 m (Figure 1, Table 1).

From the Dardanelles, five sediment samples were taken, while seven were taken from the Bosphorus and four from the Golden Horn. The samples were processed as described below. For each sample, 5 g of dried sediments was weighed, 10% hydrogen peroxide (H<sub>2</sub>O<sub>2</sub>) was added, and the mix was kept on hold for 24 hours, then washed under tap water after filtering in a 0.063-mm sieve. This way, each sediment sample was oven-dried at 50°C. Following this procedure, the

Table 1- Geographical coordinates, water depths, values of gross alpha and beta activity concentrations of sediment in sampling locations.

	Sample no.	Geographical Coordinates		Water Depth (m)	Gross alpha (Bq/kg)	Gross beta (Bq/kg)
		Latitude	Longitude			
Bosphorus	B1	41° 14'408"N	29° 06'976"E	39	451 ± 53	939 ± 51
	B3	41° 12'22"N	29° 07'22"E	20	87 ± 29	203 ± 28
	B10	41° 09'20"N	29° 02'53"E	33	547 ± 57	884 ± 51
	B12	41° 05'30"N	29° 03'40"E	67	253 ± 42	792 ± 47
	B17	41° 02'636"N	29° 01'888"E	47	621 ± 61	893 ± 49
	B21	41° 00'49"N	28° 59'26"E	30	274 ± 42	579 ± 41
	B22	40° 59'952"N	28° 59'061"E	10	315 ± 45	762 ± 47
Golden Horn	GH1	41° 02'02"N	28° 57'12"E	7	532 ± 56	987 ± 52
	GH3	41° 01'54"N	28° 57'14"E	10	439 ± 52	918 ± 51
	GH12	41° 01'31"N	28° 57'52"E	36	607 ± 60	991 ± 53
	GH18	41° 01'14"N	28° 58'06"E	52	718 ± 65	1005 ± 53
Dardanelles	D1	40° 34'648"N	27° 14'088"E	80	550 ± 57	1062 ± 57
	D5	40° 27'42"N	26° 45'17"E	42	586 ± 59	1039 ± 53
	D9	40° 16'17"N	26° 31'21"E	65	535 ± 57	1002 ± 52
	D13	40° 05'12"N	26° 20'42"E	66	435 ± 51	895 ± 50
	D15	40° 01'06"N	26° 15'06"E	59	540 ± 57	988 ± 51

samples were examined under a binocular microscope by sieving them in 2.00-, 1.00-, 0.500-, 0.250- and 0.125-mm mesh sizes. The standard procedure of paleontological studies was followed based on the reports of Babin (1980), Bignot (1985) and Murray (1973).

At the laboratory stage, the benthic foraminifera and ostracoda content of each sample was determined, the species forming the assemblages were separated and named, and they were counted in a foraminifera count plate (5/7 grid). The analyses performed on the foraminifera and ostracoda assemblages in the Paleontology Laboratory were completed by sequencing the forms to be used in the final definitions in a certain order for SEM imaging studies.

## 6.2. Measurements of the Gross Alpha and Gross Beta Activities

Gross alpha and gross beta activity concentrations were determined in 16 sediment samples collected from the Bosphorus and Dardanelles Straits and the Golden Horn. The gross alpha and gross beta counts of the samples were made at Çekmece Nuclear Research and Training Center (ÇNAEM). For the gross alpha and gross beta counts, the samples were first milled to 200 mesh and then dried. The sample kept in the desiccator was weighed by 12 g, mixed with 3 g wax, placed in a mold 40 mm diameter and turned into pellets using 35 tons of pressure. A Berthol LB770-PC 10 (Low Level Counter) channel low-level Alpha/Beta planchet counter was used for the measurements made on 16 sediment samples that were pelleted under suitable conditions for measurement. The measured results were obtained in units of Bq/kg. The measurement uncertainty was in the range of:  $\pm 2\sigma$ .

In the calculation of the activity concentrations of the samples, the background correction, self-absorption correction, counting and total uncertainty that occurred during the preparation of the sample for counting were calculated. Accordingly, the total uncertainty was in the range of:  $\pm 2\sigma$  with 95% confidence interval. The low-level counting system was commonly used for measuring environmental samples with low natural background radiation. Its calibration was carried out with standard solutions that

contained known activities of  $^{241}\text{Am}$  for alpha values and  $^{90}\text{Sr}$  for beta values which were similar to the sample geometry. The minimum detectable activity (MDA) that could be achieved with the detection system was obtained as

$$MDA(\text{Bq/l}) = \frac{L_d}{VT\epsilon 60};$$

where  $V$  is the sample volume,  $T$  is the duration of the measurements (in min),  $\epsilon$  is the counting efficiency (Currie, 1968).  $L_d$  was defined as

$$L_d = 2.71 + 4.65\sqrt{C_B T};$$

with  $C_B$  being the background level in counts/min.

## 6.3. Statistical Analysis

The PAST (PAleontological STatistics): paleontological statistics software package for education and scientific data analysis (Hammer et al., 2001) was used for the statistical analysis. In quantitative paleontology PAST is a comprehensive, but simple-to-use software package for executing a range of standard numerical analyses and operations. PAST also includes many functions that are specific to paleontology and ecology, and these functions are not found in standard, more extensive, statistical packages.

## 7. Results

### 7.1. Benthic Foraminiferal Assemblages

In our study, 61 genera and 64 species benthic foraminifera individuals were determined in 16 bottom sediment samples taken from the Bosphorus, Dardanelles and Golden Horn. The taxonomic descriptions of previous studies were used (Cimerman and Langer, 1991; Hatta and Ujiie, 1992; Hottinger et al., 1993; Sgarella and Moncharmont-Zei, 1993; Loeblich and Tappan, 1994; Avşar and Meriç, 2001; Avşar, 2002; Meriç et al., 2002a, b, 2003a, b, c, 2009; Avşar et al., 2006; Avşar and Meriç, 2008). Additionally, the classification of foraminifera by Loeblich and Tappan (1988) was considered.

In this study, which was carried out in recent bottom sediments, it was understood that the benthic foraminifera assemblages in the sediment samples were under the influence of the Aegean Sea and Mediterranean fauna. While microfauna was abundant

in the sediment samples from the Dardanelles, it was not abundant in the Bosphorus and Golden Horn samples. In addition to the fact that the bottom sediments of the Dardanelles have a very rich foraminiferal fauna, it was revealed that the warm and salty Mediterranean waters also show an active nature in the Bosphorus.

Additionally, two migratory foraminifera species were observed as *Spiroloculina antillarum* d'Orbigny (in D13 and GH3 samples) of Atlantic-Pacific origin

and *Peneroplis pertusus* (Forskål) (in D9, GH3 and GH12 samples) of Indo-Pacific origin. In our study, no abnormal morphological disorder was observed in the collected microfaunal individuals. The dominant species of benthic foraminifera were determined as *Quinqueloculina seminula* (Linne), *Brizalina spathulata* (Williamson), *Cassidulina carinata* Silvestri, *Lobatula lobatula* (Walker ve Jacob), *Ammonia compacta* (Hofker), *A.tepida* (Cushman) (Table 2) (Plates I-II).

Table 2- Distribution counts of benthic foraminifera genera and species in Bosphorus and Dardanelles straits and Golden Horn.

FORAMINIFERA	Sample ID												
	B10	B12	B17	B21	B22	GH1	GH3	GH12	D1	D5	D9	D13	D15
<i>Spiroplectinella sagittula</i>					1						2		
<i>Textularia bocki</i>										1			
<i>Textularia</i> sp.											1		
<i>Adelosina cliarensis</i>											2		3
<i>Adelosina mediterraneensis</i>											2	2	
<i>Spiroloculina antillarum</i>							1					2	
<i>Spiroloculina ornata</i>					2								
<i>Spiroloculina tenuiseptata</i>					2				3		2		2
<i>Siphonaperta aspera</i>				2								3	
<i>Cycloforina contorta</i>					2							1	
<i>Cycloforina tenuicollis</i>													2
<i>Cycloforina villafranca</i>				1								1	
<i>Massilina secans</i>								1					
<i>Quinqueloculina berthelotiana</i>							2						
<i>Quinqueloculina bidentata</i>				1									
<i>Quinqueloculina disparilis</i>		2											
<i>Quinqueloculina laevigata</i>				1									
<i>Quinqueloculina lamarckiana</i>			2										
<i>Quinqueloculina seminula</i>	2	3	1		3				3	2	3		5
<i>Miliolinella semicostata</i>											1		
<i>Miliolinella subrotunda</i>										2			
<i>Pseudotriloculina oblonga</i>													2
<i>Phyrgo elongata</i>													3
<i>Sigmoilinita costata</i>											3		4
<i>Sigmoilinita edwardsi</i>									2	2			
<i>Sigmoilopsis schlumbergeri</i>										2	3		
<i>Peneroplis pertusus</i>							1	1			1		
<i>Lenticulina cultrata</i>									2				
<i>Amphicoryna scalaris</i>											3		
<i>Polymorphina</i> sp. 1									1				

Continued Table 2

FORAMINIFERA	Sample ID												
	B10	B12	B17	B21	B22	GH1	GH3	GH12	D1	D5	D9	D13	D15
<i>Fissurina</i> sp.											2		1
<i>Brizalina alata</i>					2				1				4
<i>Brizalina spathulata</i>					3				2	4	6		8
<i>Cassidulina carinata</i>					4				3	3	6	2	6
<i>Globocassidulina subglobosa</i>											2		2
<i>Rectuvigerina phlegeri</i>											4		3
<i>Bulimina elongata</i>			1							3	4		6
<i>Bulimina marginata</i>									2		3		
<i>Globobulimina affinis</i>											2		3
<i>Globobulimina pseudospinescens</i>									1				
<i>Reussella spinulosa</i>										2	2		2
<i>Valvulineria bradyana</i>					2					3	4		2
<i>Gavelinopsis praegeri</i>					2								
<i>Neoconorbina terquemi</i>	1				3						3		3
<i>Rosalina bradyi</i>													3
<i>Rosalina globularis</i>											2	2	
<i>Siphonina reticulata</i>											1		
<i>Discorbinella bertheloti</i>					3				2	3	3		
<i>Hyalinea balthica</i>									1				
<i>Cibicides advenum</i>											2		
<i>Lobatula lobatula</i>	1		1		3				1	2	3	2	
<i>Planorbulina mediterraneensis</i>											1		
<i>Asterigerinata mamilla</i>							1			1	2	2	
<i>Nonion depressulum</i>									2				
<i>Nonionella turgida</i>									1				2
<i>Melonis pompilioides</i>									3		2		3
<i>Ammonia compacta</i>	1	2	3	2	5	2	2	2		2	4	4	4
<i>Ammonia tepida</i>	8			3	8	2	4	3		4	8	5	6
<i>Criboelphidium poeyanum</i>	4							1		2			3
<i>Porosonion subgranosum</i>													2
<i>Elphidium aculeatum</i>											2		
<i>Elphidium advenum</i>									1				
<i>Elphidium complanatum</i>					1							3	
<i>Elphidium crispum</i>	2			2						1		2	

## 7.2. Ostracoda Assemblages

In this study, ostracoda individuals were found to include 23 genera and 26 species in 10 of the 16 sediment samples that were collected. The studies of Van Morkhoven (1963), Hartman and Puri (1974), Breman (1975), Bonaduce et al. (1975), Yassini (1979), Guillaume et al. (1985), Athersuch et al.

(1989), Guernet et al. (2003), Joachim and Langer (2008) were utilized for determination of ostracoda genera and species. (Table 3).

The high number of genera and species in Dardanelles is associated with the mixing of Mediterranean and Aegean Sea waters. In our study, genera and species common in the Aegean and

Table 3- Distribution counts of ostracoda genera and species in Bosphorus and Dardanelles straits and Golden Horn

OSTRACODA	Sample ID									
	B10	B17	B21	B22	GH1	D1	D5	D9	D13	D15
<i>Aurila convexa</i>		1		1				1		
<i>Basslerites berchoni</i>							3			1
<i>Bosquetina carinella</i>				1			1	1	1	
<i>Buntonia sublatissima</i>								3		2
<i>Callistocythere intricatoides</i>	1									
<i>Carinocythereis carinata</i>									7	
<i>Carinocythereis rhombica</i>									1	
<i>Costa edwardsii</i>				1		3	14		6	2
<i>Cyprideis torosa</i>									2	
<i>Cytherella alvearium</i>							7	2		3
<i>Cytherella vulgata</i>							2	3	2	
<i>Cytheridea acuminata</i>							13			1
<i>Cytheridea neapolitana</i>							5		3	3
<i>Cytheropteron latum</i>								2		
<i>Heterocypris salinus</i>			2							
<i>Hiltermannicythere turbida</i>									2	
<i>Leptocythere sp.</i>							3		1	
<i>Loxococoncha rhomboidea</i>	1		1	1			4	2	6	1
<i>Neonesidea corpulenta</i>	1			1				1		
<i>Paradoxostoma triste</i>	1									
<i>Pontocythere elongata</i>	3									
<i>Pterygocythereis jonesii</i>							4	2	1	2
<i>Semicytherura inversa</i>		1							3	
<i>Tyrrenocythere amnicola</i>	2									
<i>Urocythereis oblonga</i>								2		
<i>Xestoleberis communis</i>					1			1		1

Mediterranean were determined in the sediment samples in which the ostracoda assemblage was observed. The *Tyrrenocythere amnicola* (Sars) living in low-salt environments, which is also observed only in the B10 sediment sample, reflects the current low-salinity conditions of the Black Sea. *Cyprideis torosa* (Jones) is euryhaline and a cosmopolitan species and was observed only in the D13 sample. *Heterocypris salina* (Brady) was observed in the B21 (30m) sediment sample. It is a halophilic cosmopolitan species known to tolerate different levels of environmental variables, including high levels of salinity changes. It prefers both small and slightly salty coastal and inland waters. Additionally, it also occurs in pure freshwater habitats (Akdemir and Klkylođlu, 2021). Thus, it

indicates that the salinity levels in the water body it is in have increased. Considering that it is determined in the B21 sediment that at the Marmara entrance of the Bosphorus and at 30 m depth, it suggests that it may have been transported.

In the sediment sample D1 that was collected at the deepest location (80 m), ostracoda numbers were low (only three carapaces). Again, in this study, no ostracoda individuals were found in the B1 (39 m), B3 (20 m), B12 (67 m) and GH18 (52 m) sediment samples. Only two ostracoda individuals were observed in the sediment sample B17 (47 m). Additionally, no ostracoda individuals were found in the GH3 (10 m), GH12 (36 m) and GH18 (52 m)

sediments, and only one carapace was observed in the GH1 (7 m) sample. The samples of the Dardanelles included a very rich ostracoda assemblage. In the comparison of the ostracoda species richness levels among the sediments, it was determined that the highest number of individuals was in D5 (42 m) with 56 species.

7.3. Determination of Gross Alpha and Gross Beta Radioactivity Concentration in Sediment Samples

In this study, gross alpha and gross beta radioactivity concentrations were determined in the sampled Bosphorus and Dardanelles Straits and Golden Horn sediments (Table 1). In order to determine whether there is radioactive contamination, gross alpha and beta radioactivity values should be determined. In the Dardanelles samples, the gross alpha count was

measured in the range of  $435 \pm 51$ - $586 \pm 59$  Bq/kg, and the gross beta count was between  $895 \pm 50$  and  $1062 \pm 57$  Bq/kg. In the Golden Horn samples, the gross alpha count was found in the range of  $439 \pm 52$ - $718 \pm 65$  Bq/kg, and the gross beta count was between  $918 \pm 51$  and  $1005 \pm 53$  Bq/kg. In addition to these, in the samples of the Bosphorus Strait, the gross alpha count was found in the range of  $87 \pm 29$  and  $621 \pm 61$  Bq/kg, and the gross beta count was between  $203 \pm 28$  and  $939 \pm 51$  Bq/kg. In the sediment samples, the gross alpha concentration was the highest in B17, GH12 and GH18 and the lowest in B3 (Figure 6 a). The gross beta concentration was the highest in D1 and B5 and the lowest in B3 (Figure 6 b). The distributions of the gross alpha and gross beta concentrations according to the sediment samples were in a linear relationship with each other.

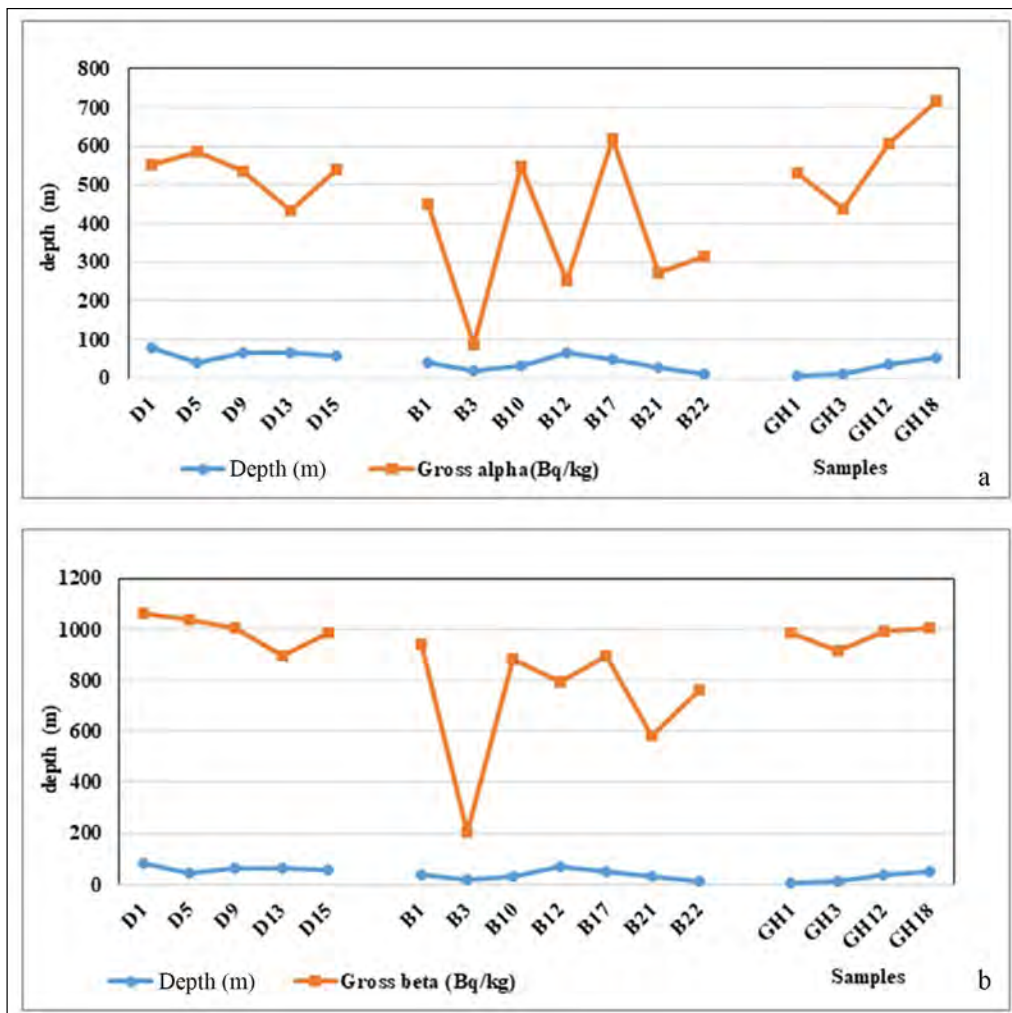


Figure 6- Distribution of, a) gross alpha and b) gross beta values with depth of sediments in investigation area.

While the gross alpha concentration distributions were close to each other in the Dardanelles and Golden Horn samples, they had a substantial variability between  $87 \pm 29$  and  $621 \pm 61$  Bq/kg in the Bosphorus samples. The gross beta concentration distributions were close to each other in the Golden Horn samples but variable in the Bosphorus and Dardanelles samples.

Considering the relationship between depth and gross alpha concentration, the highest activity value ( $586 \pm 59$  Bq/kg) was measured only at the minimum depth sediment sample of the Dardanelles Strait (D5, 42 m), thus an inverse proportion with depth was observed (Figure 6 a). While the highest gross alpha value was found ( $718 \pm 65$  Bq/kg) in the deepest sedimentary sample (GH18, 52 m) in the Golden Horn, the lowest gross alpha value ( $87 \pm 29$  Bq/kg) was found in the sediment sample collected from the minimum depth (B3; 20 m) in the Bosphorus (Figure 6b). A linear relationship was found between gross beta concentration and depth, in the Golden Horn (GH18; 52 m;  $1005 \pm 53$  Bq/kg) and Dardanelles Strait (D1; 80 m;  $1062 \pm 57$  Bq/kg), and the highest activity value was found in these sediment samples collected from the maximum depth (in GH18 and D1 samples).

In the sediment samples collected at the deepest location D1 (80 m), the numbers of benthic foraminifera and ostracoda are low, whereas the gross alpha and beta values are high. The highest gross beta value was measured at B1 (39 m), where benthic foraminifera and ostracoda are not observed, whereas the lowest gross beta was measured at B3 (20 m). In B17 (47 m), the highest gross alpha and beta values and a small number of microfauna are found. The highest abundance (46 numbers) and diversity (16 numbers) of benthic foraminiferal assemblages were determined at a minimum depth in B22 (10 m) from the Bosphorus sediments (Table 2). Also at GH18 (52 m), the gross alpha and beta values are the highest, but no microfauna was found.

#### 7.4. Statistical Analysis for Benthic Foraminifera and Ostracod Assemblages

The parameters that were used in the calculation of benthic foraminifera diversity and species richness (PAST) in this study included the number of species (Taxa\_S), species diversity (Simpson\_1-D),

dominance number of species (Dominance\_D), species diversity (Shannon\_H) and richness of species (Margalef). In the calculation of benthic foraminiferal diversity and species richness (PAST), Shannon (3.36), Simpson (0.9603) and Margalef (7.094) parameter results were recorded at the highest in D9. The dominance in the sediments was at the highest in D9 based on the Simpson Dominance Index (0.9603). The Simpson's Diversity Index shows the dominance of the environment as inversely proportional to the diversity of the environment. The Shannon Species Diversity and Simpson Population Density relationship was calculated as the highest (3.36; 0.9603) in the D9 sample and the lowest (0.6931; 0.5) in the GH1 sample. When the benthic foraminifera species richness was compared among the sediments, it was determined that D9 contained the most species, with 33 species. For the Margalef Index, the same foraminiferal assemblages are compared in the sediment samples, and this index was found to be highest in D9 and lowest in GH1 (Table 4).

According to the PAST statistical analysis of the distribution of ostracoda, the Shannon parameter was determined in D13 (2.404), the Simpson parameter was determined in D9 (0.9032) and the Margalef parameter was determined in B22 (9.783) (Table 5). The Simpson Dominance Index in the sediments was the highest in D9 (0.9032). Again, the relationship between the Shannon species diversity and the Simpson population density of ostracoda was found to be the highest at D9 (0.9032) and D13 (2.404), the lowest (0) at GH1 and D1 samples (Table 5). When the richness values of ostracoda species in the sediments were compared, it was determined that D5 contained the most species, with 56 species. The Margalef Index was compared for the assessment of the same ostracoda assemblages between different sediment samples and in B22 sample was found to be the highest (Table 5).

## 8. Discussion and Conclusion

The geology of the Bosphorus Strait consists of terrestrial clayey pebbles of the quaternary sedimentary sequence within the Thrace Formation (Şimşek, 1987). The sediments contain sandstone, siltstone, claystone and quartz pebbles of different

Table 4- The evaluation with PAST of benthic foraminifera.

ID	Count of foraminifera	Taxa_S	Dominance_D	Simpson_1-D	Shannon_H	Margalef
B10	19	7	0.2521	0.7479	1.631	2.038
B12	7	3	0.3469	0.6531	1.079	1.028
B17	8	5	0.25	0.75	1.494	1.924
B21	12	7	0.1667	0.8333	1.864	2.415
B22	46	15	0.09032	0.9097	2.558	3.722
GH1	4	2	0.5	0.5	0.6931	0.7213
GH3	11	6	0.2231	0.7769	1.642	2.085
GH12	8	6	0.2099	0.7901	1.677	2.276
D1	31	17	0.06972	0.9303	2.74	4.659
D5	39	17	0.06772	0.9323	2.757	4.367
D9	91	33	0.03973	0.9603	3.36	7.094
D13	31	13	0.09261	0.9074	2.47	3.494
D15	84	25	0.0496	0.9504	3.109	5.417

Table 5- The evaluation with PAST of ostracoda.

	Count of tracob	Taxa_S	Dominance_D	Simpson_1-D	Shannon_H	Margalef
B10	9	6	0.1827	0.8173	1.747	6.056
B17	2	2	0.5	0.5	0.6931	0
B21	3	2	0.5256	0.4744	0.6673	0
B22	5	5	0.2	0.8	1.609	9.783
GH1	1	1	1	0	0	0
D1	3	1	1	0	0	0
D5	56	10	0.1126	0.8874	2.238	4.502
D9	20	11	0.09685	0.9032	2.365	6.38
D13	35	12	0.09701	0.903	2.404	5.909
D15	16	9	0.1201	0.8799	2.157	5.946

sizes, with short intervals of repetitive pebbles, less silty, very compact sand, dark gray coarse shells, sandy pebbles and especially abundant shells. Again, these sediment distributions consist of mostly gray, poorly graded shell fragmented, very loose-loose-medium compact silty sands (Yıldırım et al., 1992).

In the Bosphorus, due to the undercurrents, the sediments are either absent or very thin in some places at the bottom of the channel. In general, they are represented by gravel, sand, shell fragments and silt in some places. The distribution of the sediments in the Bosphorus consists of three groups including block-rocky, gravel and sand as well as a small amount of silt units (Meriç et al., 2001). In the studies carried

out on the recent sediments (Meriç et al., 2001; Aşar and Meriç, 2001), a benthic foraminifera assemblage, which was rich in genera and species, representing mostly a Mediterranean-based shallow marine environment was observed. Again, at the Black Sea exit of the Bosphorus, benthic foraminifera genera and species which represented a shallow marine environment of Mediterranean origin were dominant in some places (Aşar and Meriç, 2001).

The sediments distribution in the Dardanelles is affected by the flow system, the bathymetry and the morphological structure of the strait. In regions where the flow velocity is high, fine-grained sediments does not accumulate, coarse-grained material is generally

deposited and, in these places the current sediment thickness is low. In general, sandy units, shell fragments and silt are seen in some places. In places such as small bays, gulfs and harbors on the shores of the strait, sandy and pebbly material and fine-grained silt, clay and mud-composed sediments are deposited. As the bottom current and the slope increase, it is not possible for sediment to accumulate (Yücesoy-Eryılmaz and Eryılmaz, 1998, 2002; Yücesoy-Eryılmaz et al., 2003a, b).

The Golden Horn sediments consist of silty clay deposits called “Golden Horn Clay”, whose thickness is around 35 meters and is deposited in a stagnant environment. On the sea floor of the Golden Horn, there is a very soft, recent mud layer with high black organic content and a gray sandy clayey gravel string with a thickness of between 2.0 m and 8.5 m. The Golden Horn sediments had characteristics of four environments: river, sea, brackish water and shallow brackish to freshwater conditions, and they contained grains (or particle size) in the size of gravel, sand, mud and clay (Meriç et al., 1988; Derman, 1990). Except for *Ammonia tepida* (Cushman) (Yanko, 1993), which can live in almost every environment, the Golden Horn sediments have benthic foraminifera assemblage (Şamlı, 1996) of Mediterranean and Atlantic origin generally living on the continental shelf where they are dominant (Murray, 1970, 1971; Meriç and Sakınç, 1990; Meriç et al., 1991; Sgarella and Moncharmont-Zei, 1993).

The morphological structure of the strait, the current system and other oceanographic factors have been effective in the development of the ongoing sediments in the Bosphorus and Dardanelles. The bottom sediments of the Dardanelles are composed of sand, silty sand, muddy sand, sandy silt, silt, mud and sandy mud. In a study conducted in the Dardanelles (Meriç et al., 2009), the average gravel was found as 6%, the average grain size of sand was 25%, the average silt was 46%, and the average clay was 22%, and the average mud was 68%. Additionally, the mud distribution which is 68% on average in these samples varies between 27% and 99% and shows differences (Meriç et al., 2009). In the sediments of the Dardanelles and the Marmara Sea transition zone, the most silt was detected in the Dardanelles

Strait (72.5%) and the most clay was determined in the Dardanelles Strait-Marmara Sea inlet samples (65.2%) (Yücesoy-Eryılmaz and Eryılmaz, 2002).

Dardanelles sediments have rich benthic foraminifera assemblages (Meriç et al., 2009). The benthic foraminifera assemblages of the region are similar to the genera and species that characterize the Aegean and Mediterranean Seas fauna (Avşar, 2002; Meriç et al., 2004a, b; 2009). Moreover, among the foraminifera assemblages identified, *Cushmanina striatopunctata* (Parker and Jones) (Meriç et al., 2009), a species found in the North Atlantic, and *Fissurina* sp. (Hottinger et al., 1993) were also determined in this study. According to our study when the benthic foraminiferal and ostracoda assemblages of the Bosphorus and the Dardanelles are compared; it is revealed that the number of both foraminifera and ostracoda genera and species and the number of individuals belonging to them observed are lower numbers in the Bosphorus and in the Golden Horn than the Dardanelles. In addition as in foraminifera tests, ostracoda valves/carapaces were not affected by ambient conditions and morphological abnormalities were not observed in their valves.

The effect of the sediment feature on benthic foraminifera and ostracoda assemblages is significant on their number of species (Taxa\_S), species diversity (Simpson\_1-D), dominance number of species (Dominance\_D), species diversity (Shannon\_H) and richness of species (Margalef). When the benthic foraminifera species richness was compared among the sediments, it was determined that D9 contained the most species, with 33 species. For the Margalef Index, the same foraminiferal assemblages are compared in the sediment samples, and this index was found to be highest in D9 and lowest in GH1. The relationship between the Shannon Species Diversity and the Simpson Population Density of ostracoda was found to be the highest at D9 (0.9032) and D13 (2.404), the lowest (0) at GH1 and D1 samples. When the richness values of ostracoda species in the sediments were compared, it was determined that D5 contained the most species, with 56 species. The Margalef Index was compared for the assessment of the same ostracoda assemblages between different sediment samples and in B22 sample was found to be the highest.

As a result, high gross alpha and beta concentrations in D9 sample resulted in a decrease in species dominance in benthic foraminifera and an increase in the number, diversity and richness of species. Additionally high gross beta values in GH1 sample increased species dominance and resulted in a decrease in species number, diversity and richness. The species diversity in the ostracoda assemblages have increased in D9 sample, which has high gross beta values. While high gross beta concentrations in GH1 and D1 samples indicate high species dominance in the ostracoda assemblages, the number of species, diversity and richness of the species have resulted in a decrease. Again, low gross alpha concentration in B22 sample resulted in low species numbers and high species richness in the ostracoda assemblages.

In our study, six of the sediment samples (D1, D5, D9, D13, D15 and B22) contained a rich benthic foraminifera assemblage. In light of these pieces of information, it is understood that the study area is under the influence of the Aegean Sea and Mediterranean fauna. *Quinqueloculina seminula*, *Brizalina spathulata*, *Cassidulina carinata*, *Lobatula lobatula*, *Ammonia compacta* and *A. tepida* are the dominant benthic foraminifera species. *Spiroloculina antillarum* (in D13 and GH3 samples) of Atlantic-Pacific origin and *Peneroplis pertusus* (in D9, GH3 and GH12 samples) of Indo-Pacific origin were observed as two migratory foraminifera. According to these data, it is revealed that the current bottom sediments of the Dardanelles have a very rich foraminiferal fauna, and the thermal and salty Mediterranean waters have an active feature in the Bosphorus (Sakınç et al., 2000; Meriç et al., 2004a; Barut et al., 2012). According to the results of the correlation analysis there was a negative relationship between the gross alpha and gross beta activity concentrations and depth in the sediment samples taken from the Dardanelles. While the correlation between the gross alpha and gross beta activity concentrations and depth was positive and linear in the B1, B3 and B10 samples taken from the Bosphorus, this correlation was negative in the others (in B12, B17, B21 and B22 samples). There was a positive correlation in all sediment samples except for the GH1 sample taken from the Golden Horn.

In the comparison of the benthic foraminifera and ostracoda assemblages of the Bosphorus and Dardanelles Straits, it was determined that the numbers of genera and species observed in the Bosphorus were lower than those of the Dardanelles. The main factor in the more dominant genera and species of microfauna at the Dardanelles is the effect of the thickness of the Mediterranean water mass (Eryılmaz et al., 2001) on this environment. This means that the effect of the system of sea currents on the biodiversity in the Dardanelles is very significant (Meriç et al., 2018a). Thus, microfauna assemblages that originate from the Pacific Ocean, the Indian Ocean, the Red Sea and rarely the Atlantic Ocean are transported on the Suez Canal-Mediterranean-Aegean Sea route under the significant influence of current flow systems and inside the ballast waters of ships traveling to different points of the Aegean Sea. As a result, microfaunal individuals that adapt to the environment in the living area multiply and disperse (Meriç et al., 2018a).

At the Dardanelles Strait, where two different masses of water flow in opposite directions, the surface and bottom currents occur as a result of the level and density differences between the Black Sea and the Aegean Sea. While high-density waters with Mediterranean origin flow towards the Marmara Sea from the bottom, the waters of Black Sea origin with a lower density flow towards the Aegean Sea from the surface. The surface water thickness which is 20 m on the side of the Marmara Sea decreases down to 5 m towards the Aegean Sea. This factor is one of the most significant factors affecting the vertical temperature distribution at the Dardanelles Strait (Meriç et al., 2009).

The surface water with 17-18‰ salinity at the Black Sea entrance of the Bosphorus Strait which is represented with a two-layer water system disperses into the Marmara Sea through the Bosphorus Strait, and its salinity values increase up to the range of 20-25‰. At the Aegean Sea entrance of the Dardanelles Strait, the surface water salinity reaches 29‰ due to its mixing with bottom water. The bottom water at the Aegean Sea entrance and the Marmara Sea entrance of the Dardanelles Strait with ~39‰ salinity does not show a noticeable change inside the Marmara

Sea and is limited to values in the range of 37-38%. At the Black Sea entry of the Bosphorus Strait, the salinity of the bottom water drops down to 35.5% (Beşiktepe et al., 1994). This system is shaped by the entry of the low-saline (18‰) Black Sea water through the Bosphorus Strait and the high-saline (39‰) Mediterranean water through the Dardanelles Strait into the Marmara Sea (ISKI, 2005). Between these two water masses with different densities, the Mediterranean water forms the bottom layer, the Black Sea water forms the top layer, and these develop a constant system of currents that flow opposite to each other. The depth of the intermediate layer separating these two different water masses (pycnocline) is 20-25 m from the water surface (Ünlüata et al., 1990). There need to be certain temperature and salinity values for the living conditions of ostracoda, mollusca and foraminifera genera and species. Besides this, it is known that among ecological conditions, temperature limits are different for some benthic foraminifera species and genera.

In the study of (Meriç et al., 2009), ostracoda assemblages of Mediterranean origin species are very rich in Dardanelles sediment samples. In our study, ostracoda assemblages belonging to rich Mediterranean origin species were dominant in Dardanelles sediment samples, especially in D5 and D13. The depths of sediment samples containing this rich ostracoda genera and species fauna of Mediterranean origin vary between 42 m and 66 m. The relationship between the increase and decrease in the gross alpha values of the D5 and D9 samples and the number of ostracoda genera and species was linear and positive. However, a negative relationship was observed in the other samples (in D13 and D15 samples). Only one ostracoda species with Mediterranean origin was found in the sample GH1 from the Golden Horn. Again, the number of ostracoda genera and species of Mediterranean origin varied between 2 and 9 in the Bosphorus sediments (Figure 7 a, b).

The highest gross alpha and beta values were measured in GH18 sample, and no benthic foraminifera was found. In B17 sample, where the gross alpha value was high, five species were observed, whereas six species were observed in GH17. The abundance

of benthic foraminifera assemblages was observed in D1, D5, D9 and D15 samples where the gross beta values were measured to be the highest (Figure 4). The correlation between the gross alpha and gross beta values and the numbers of species of benthic foraminifera assemblages (Figure 5 a, b) appeared to be negative in all samples of the Dardanelles except for D13 and D15.

There was a negative correlation between the gross alpha and beta values and the depths in the Dardanelles samples. Among the Bosphorus samples, in B1, B3 and B10, the relationship between these parameters was positive and linear, while it was negative in the others. In the Golden Horn samples, the correlation was positive except for GH1 (Figure 8). A relationship was found between microfauna density and high gross alpha and beta values in the Dardanelles samples, but not in the Bosphorus and Golden Horn samples.

Karahan (1997) found that the average gross alpha concentration of the Marmara Sea was 1.42 Bq/l, and its average gross beta concentration was 5.47 Bq/l. In the same study, the average alpha activity concentration of Black Sea water was found as 0.375 Bq/l, and the average beta activity concentration of it was 5.63 Bq/l. In another study (Özger, 2005), the alpha activity concentration of Mediterranean water was found to be 0.703 Bq/l, and its beta activity concentration was 6.81 Bq/l. As seen here, the beta activity concentration of Mediterranean water was higher than the beta activity concentration values in the Marmara Sea and the Black Sea. This may be explained by the fact that the salinity value of Mediterranean water is higher than water from the Black Sea and Marmara Sea. The reason for the high alpha and beta activities in sea-water was due to the excess amount of potassium in sea water.

The gross alpha values reported by Karahan (1997), were higher than those found in other studies (Karahan et al., 2000; Otansev et al., 2016) conducted in the Black Sea and Marmara Sea. The gross beta values were determined by Karahan et al. (2000) and Otansev et al. (2016) to be the same, on the other hand. As seen in the Table 6, the values of rainfall and snow water were also similar to the lake for comparison. In the study by Otansev et al. (2016), Marmara gross

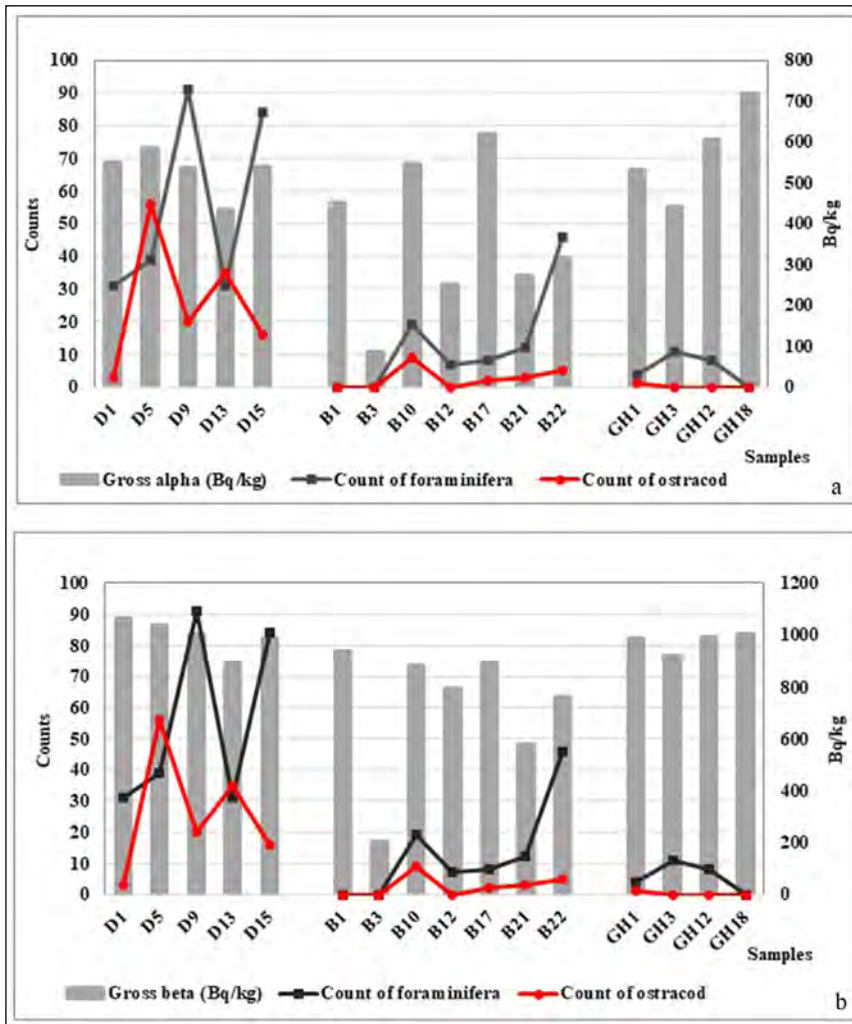


Figure 7- Distribution of benthic foraminifera and ostracoda numbers according to a) gross alpha and b) gross beta values of samples.

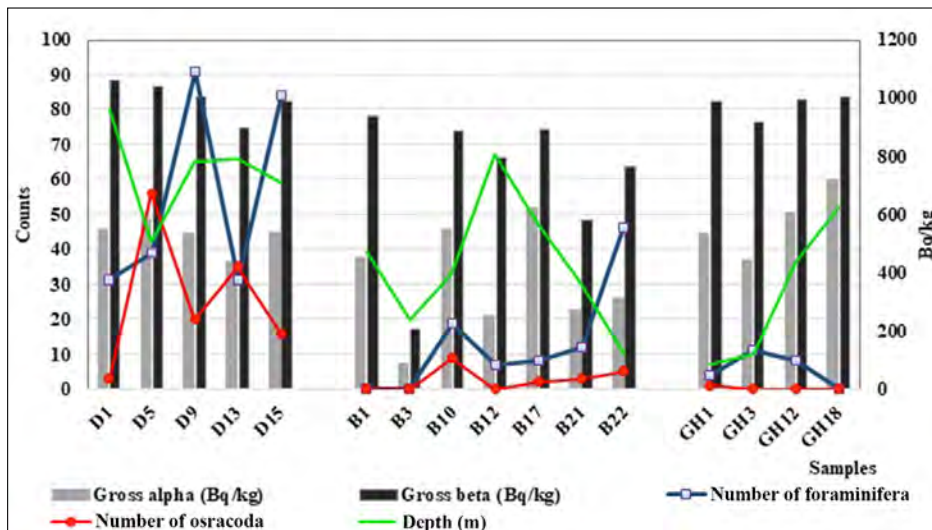


Figure 8- Distribution of benthic foraminifera and ostracoda numbers with gross alpha and gross beta values according to depth of samples.

alpha values were found to be the lowest, while gross beta values were found to be high. The sea water gross beta value of the Romanian coasts was the highest (Patrascu, 2002). In the comparison of sediments, the results were very variable in Romania sediments (30-3000 Bq/kg), but in the results of our study, they were in the same range as submerged sediments.

The natural radionuclide distribution depends on the geological and geographical conditions of each region. The obtained results showed that the geological formation and agricultural areas strongly affected the occurrence of natural radioactivity. It was also shown that the gross-alpha and gross-beta radioactivity concentrations in the soil and sediment samples were found to be relatively higher than those observed in other studies (Yuanxun et al., 2003; Stephen, 2004).

As a result of a recent study (Önce and Kam, 2019) the maximum gross alpha value was found around the investigation areas of Şarköy and Mürefte as  $301 \pm 15.9$  Bq/kg (Şarköy Port, on the southwestern coast of the Marmara Sea-Türkiye), and the lowest value was found as  $989 \pm 16.5$  Bq/kg (Şarköy Port). When

these values were compared to the results of our study, both gross alpha and gross beta concentration values were found to be high in our study. The main reason why the gross alpha and beta concentrations were generally high was that fertilizers used in agriculture contain uranium, thorium and their degradation products, as well as natural  $^{40}\text{K}$  (Eisenbud and Gessel, 1997). Keser et al. (2013) studied the radioactivity levels in sediment and rock samples of İkizdere and the Kaptanpaşa Valley. They found the gross alpha activity to be generally lower than the corresponding gross beta activity for some rock samples.

The radioactivity of lake and river sediments is generally low in Lake Van in May. The average value of gross alpha activity (Bq/g) was reported as  $1.134 \pm 0.664$ , while the average value of gross beta activity (Bq/g) was reported as  $0.482 \pm 0.181$ . In August these values were as gross alpha (Bq/g):  $1.082 \pm 0.642$  and gross beta (Bq/g):  $5.529 \pm 2.541$  (Zorer et al., 2009a). Again, in the study in question, it was observed that the gross alpha and gross beta radioactivity concentrations ranged respectively from

Table 6- Comparison of gross alpha and gross beta radioactivity levels and in various places and different studies

Sample Locations	Gross alpha	Gross beta	References
Marmara Sea (Bq/l)	1.42	5.47	Karahan 1997
Black Sea (Bq/l)	0.375	5.63	Karahan 1997
K. Çekmece Lake (Bq/l)	$0.06 \pm 0.04$	$3 \pm 1$	Karahan et al., 2000
B. Çekmece Lake (Bq/l)	$0.05 \pm 0.01$	$0.3 \pm 0.07$	Karahan et al., 2000
Terkos Lake (Bq/l)	$0.02 \pm 0.009$	$0.2 \pm 0.05$	Karahan et al., 2000
Ömerli Dam Lake (Bq/l)	$0.034 \pm 0.008$	$0.04 \pm 0.005$	Karahan et al., 2000
İstanbul coasts Sea water (Bq/l)	$0.4 \pm 0.1$	$4.9 \pm 0.9$	Karahan et al., 2000
Black Sea water (Bq/l)	$0.4 \pm 0.2$	$5.6 \pm 1.1$	Karahan et al., 2000
Marmara Sea water (Bq/ l)	$0.5 \pm 0.1$	$5.0 \pm 1.2$	Karahan et al., 2000
Black Sea and Bosphorus water (Bq/l)	$0.3 \pm 0.006$	$5.3 \pm 1.3$	Karahan et al., 2000
Rain water (Bq/l)	$0.03 \pm 0.008$	$0.13 \pm 0.03$	Karahan et al., 2000
Snow water (Bq/l)	$0.08 \pm 0.004$	$0.14 \pm 0.03$	Karahan et al., 2000
Marmara Sea water (Bq/l)	0.042	13.402	Otansev et al., 2016
Romanian coast sediment emerged (Bq/kg)		30-8000	Patrascu, 2002
Romanian coast sediment submerged (Bq/kg)		459-980	Patrascu, 2002
Romanian coast Seawater (Bq/l)		3300 -- 7500	Patrascu, 2002
Average of Bosphorus sediment Bq/kg)	364	721.71	<b>This study</b>
Average of Golden Horn (Bq/kg)	574	975.25	<b>This study</b>
Average of Dardanelles (Bq/kg)	441	831	<b>This study</b>

0.782 to 4.596 Bq/g and from 0.482 to 10.372 Bq/g in May and from 0.580 to 5.824 Bq/g and from 0.303 to 9.702 Bq/g in August (Zorer et al., 2009b).

The mechanism of the transfer of radioelements from the ocean to pelagic deposits was discussed, and points of uncertainty in the interpretation of the distribution of gross beta-activity were indicated (Arrhenius and Goldberg, 1955). The alpha activity had so far been investigated only in the grain size fraction  $> 5\mu$  of recent sediments, to a large extent due to radium and its variant elements radon and radium. All of them are stated to be practically completely bound to zeolite minerals such as phillipsite (K- and Na-) (Arrhenius and Goldberg, 1955).

### Acknowledgements

The authors sincerely thank Prof. Dr. H. İbrahim Sur (Black Sea Permanent Secretariat Executive Directorate) and ONHO (Turkish Naval Forces Office of Navigation, Hydrography and Oceanography) for their contributions during the sampling stage of the study. The authors also present their special thanks to Mr. Tuğrul Tüzüner (TPAO Research Center-Ankara) for SEM photography (Jeol JSM-5600).

### References

- Akdemir, D., Külköylüoğlu, O. 2021. Effects of Temperature Changes on the Spatial Distribution and Ecology of Ostracod (Crustacea) Species. *Journal of Limnology and Freshwater Fisheries Research* 7(1): 1-13.
- Arrhenius, G., Goldberg, E.D. 1955. The distribution of radioactivity in pelagic clays. *Tellus* 7, 226-231.
- Athersuch, J., Home, D.J., Whittaker, J.E. 1989. Marine and Brackishwater Ostracods. *Linnean Society Synopses of the British Fauna (New Series)*, No. 43. E. J. Brill, Leiden, Netherlands, 343.
- Avşar, N. 2002. Gökçeada, Bozcaada ve Çanakkale üçgeni kıta sahanlığı (KD Ege Denizi) bentik foraminifer dağılımı ve taksonomisi. *Hacettepe Üniversitesi Yerbilimleri Dergisi* 26, 53-75.
- Avsar, N., Meriç, E. 2001. Çeşme-Ilıca Koyu (İzmir) bölgesi güncel bentik foraminiferlerinin sistematik dağılımı. *Hacettepe Üniversitesi Yerbilimleri Dergisi* 24, 13-22.
- Avşar, N., Meriç, E. 2008. Taxonomy and ecology of foraminifera from the sea of Marmara (NW Turkey). *The Fifth International Conference on Environmental Micropaleontology, Microbiology and Meiobenthology, EMMM'2008, University of Madras, India.* 34-36.
- Avşar, N., Aksu, A., Dinçer, F. 2006. Erdek Körfezi (GB Marmara Denizi) bentik foraminifer toplulukları. *Hacettepe Üniversitesi Yerbilimleri Dergisi* 27(3), 125-141.
- Ayçık, G.A., Citaku, D., Erten, H.N., I., Salihoğlu, I. 2004. Dating of Black Sea sediments from Romanian coast using natural  $^{210}\text{Pb}$  and fallout  $^{137}\text{Cs}$ . *Journal of Radio Analytical and Nuclear Chemistry* 259 (1), 177-180.
- Babin, C. 1980. *Elements of Palaeontology*. Chichester: Wiley, 446.
- Barut, I. F., Meriç, E., Kam, E., Avşar, N., Nazik, A. 2012. The impact in distribution of radioactive to recent meiofauna assemblages: A case of the Bosphorous and the Dardanelles straits and Golden Horn sediments. *ECSA 50 and Estuarine, Coastal Shelf Science (Today's Science for tomorrow's management)*, (3-7 June 2012), Venice Italy, (O9.5)
- Barut, I. F., Meriç, E., Kam, E., Avşar, N., Nazik, A. 2013. Effects of oceanographic properties to the Meiofauna assemblages: The North coasts of Karaburun Peninsula (Eastern Aegean Sea). *World Academy of Science, Engineering and Technology (WASET)* 76, 887-896.
- Barut, I. F., Ergin M., Meriç, E., Avşar N., Nazik, A., Suner, F. 2018. Contribution of natural and anthropogenic effects in the İznik Lake bottom sediment: geochemical and microfauna assemblages evidence. *Quaternary International (Paleoclimatic and Paleocological Studies in Turkey's Lakes-TURQLAKES2016)* 486, 129-142.
- Beşiktepe, Ş.T., Sur, H.İ., Özsoy, E., Latif, M.A., Oğuz, T., Ünlüata, Ü. 1994. The circulation and hydrography of the Marmara Sea. *Progress in Oceanography* 34, 285-334.
- Bignot, G. 1985. *Elements of Micropaleontology*. London, Graham & Trotman, 217.
- Biswas, S., Ferdous, J., Begum, A., Ferdous, N. 2015. Study of Gross Alpha and Gross Beta Radioactivities in Environmental Samples. *Journal Of Scientific Research* 7(1-2), 35-44.
- Bologa, A.S. 1994. Marine science research priorities in Romania. *Mediul inconjurator* 5 (1), 3-13.
- Bologa A.S., Pătrascu V. 1997. Radioactivity in the Romanian Black Sea Sector – One Decade after Chernobyl. *IAEA International Conference "One Decade after Chernobyl: Summing Up the Radioecological Consequences of the Accident"*.

- Vienna, 8-12 April 1996; IAEATECDOC-964, 2, 469-475.
- Bologa, A.S., Pătrascu, V., Cuingiöglu, E. 1998. Distribution of Total Beta Radioactivity, Sr-90 and 137Cs Content in the Romanian and NW Black Sea Sector between 1994-1995. Rapport Commission International Mer Mediterranee 35, 234-235.
- Bonaduce, G., Ciampo, G., Masoli, M. 1975. Distribution of Ostracoda in the Adriatic Sea. Pubblicazioni della Stazione Zoologica di Napoli 40 (suppl.): 304.
- Borcia, C., Rădulescu, C., Ciucă, R., Blendea, V. 2017. Radioactivity of the lower sector of Danube River and the Black Sea coastal zone in relation to some hydrological characteristics. Ovidius University Annals Series: Civil Engineering 19, 15-27.
- Breman, E. 1975. The distribution of ostracodes in the bottom sediments of the Adriatic Sea. Vrije Universiteit te Amsterdam, Krips Repro, Meppel, 165.
- Callaway, J. C., Delaune, R. D., Patrick, W.H. 1996. Chernobyl Cs-137 used to determine sediment accretion rates at selected north European coastal wetlands. Limnology and Oceanography 41 (3), 444-450.
- Carroll, J., Lerche, I. 2003. Sedimentary Processes: Quantification Using Radionuclides. Elsevier, Oxford, 272.
- Cimerman, F., Langer, M. R. 1991. Mediterranean foraminifera. Slovenska Akademija Znanosti in Umetnosti. Academia Scientiarum et Artium Slovenica, 118.
- Currie, L.A. 1968. Limits for Qualitative Detection and Quantitative Determination: Application to Radiochemistry, Analytical Chemistry 40, 586-593.
- Dai, J. C., Song, J. M., Li, X.G., Yuan, H.M., Li, N., Zheng, G.X. 2007. Environmental changes reflected by sedimentary geochemistry in recent hundred years of Jiaozhou Bay, North China. Environmental Pollution 145 (3), 656-667.
- Derman, A. S. 1990. Genç çökellerin (Holosen) sedimentolojik özellikleri ve ortamsal yorumu. E. Meriç (Ed.), İstanbul Boğazı Güneyi ve Haliç'in Geç Kuvaterner Dip Tortulları 5-11.
- Duong Van, H., Le Luong, H., Nguyen Dinh, C., Nguyen Thanh, D., Hegedüs, M., Csordás, A., Kovács, T. 2020. Gross alpha and gross beta activities in selected marine species in Vietnam. Environmental Science and Pollution Research 27, 33385-33392.
- Eisenbud, M., Gesell, T. 1997. Environmental Radioactivity from Natural, Industrial and Military Sources. Academic Press, 4th Edition, New York. 656.
- Emiroğlu, A. 2014. Karadeniz'in Kirliliği ve Katılımcı Çözüm Önerileri (The Black Sea Pollution and Participative Solution Offers). Vergil, H., Sezer, Ö., Dökmen G. (Eds.), 1. Karadeniz ve Balkan Ekonomik ve Politik Araştırmalar Sempozyumu, Zonguldak (3-5 Eylül 2014). Bildiriler Kitabı, 173-187.
- Er, Z., Tuğrul, A.B. 1995. Çeşitli Madensuyu ve Sodalrın Radyoaktivite Seviyelerinin Tayini. V. Ulusal Medikal Fizik Kongresi, İstanbul, (11-15 Eylül 1995).
- Eryılmaz, M. 1995. Marmara Denizi, İstanbul ve Çanakkale Boğazları Fiber optik kablo güzergahı çalışmaları, İstanbul Teknik Üniversitesi Gemi İnşaatı ve Deniz Teknolojisi Teknik Kongresi 1995, 2, 445-456.
- Eryılmaz, M. 1997. Türkiye, İstanbul Boğazı yüzey sediment dağılım haritası (tane büyüklüğüne göre), Ölçek, 1: 100.000, Dz.K.K. Sey. Hid. ve Oşi. Dairesi Başkanlığı, (SHOD).
- Eryılmaz, M. 1998. Türkiye, Çanakkale Boğazı yüzey sediment dağılım haritası, Dz.K.K. Sey. Hid. ve Oşi. Dairesi Başkanlığı, 1: 200.000 ölçekli, Dz.K.K. Sey. Hid. ve Oşi. Dairesi Başkanlığı (SHOD).
- Eryılmaz, M. 2002. İstanbul Boğazı ve Haliç, Oşinografi Çalışmaları, Dz.K.K. Sey.Hid. ve Oşi. Dairesi Başkanlığı (SHOD), Unpublished Report, Archiv, 30s.
- Eryılmaz, M., Kara, S. 1996. Valide Sultan Köprüsü'nün Haliç Oşinografisi ve Hidrografisi Üzerine Etkileri. Dz.K.K., Sey., Hid. ve Oşi. Dairesi Başkanlığı (SHOD), Unpublished Report, Archiv, 23s.
- Eryılmaz, M., Türker, A., Aydın, Ş., Kırca, Z. 2000. İstanbul Boğazı'nda güncel çökel dağılımı. Z.Uysal, İ. Salihoğlu (Eds.), 1. Ulusal Deniz Bilimleri Konferansı ODTÜ, (30 Mayıs-2 Haziran 2000), 281-283.
- Eryılmaz M., Yücesoy-Eryılmaz F., Aydın, Ş., Türker, A., Kırca, Z. 2001. Çanakkale Boğazı'nın güncel çökel dağılımı. 54. Türkiye Jeoloji Kurultayı (7-10 Mayıs 2001) Ankara. Bildiri Özleri, CD 5-6.
- Friedlander, B., Burger, J., Gochfeld, M. 2005. Review of radionuclides in the marine environment. (In: Powers, C.W., Burger, J., Kosson, D., Gochfeld, M., Barnes, D. (Eds.), Amchitka Independent Science Assessment: Biological and Geophysical Aspects of Potential Radionuclide Exposure in the

- Amchitka Marine Environment). Consortium for Risk Evaluation with Stakeholder Participation, Piscataway, New Jersey (Appendix 2A).
- Fuller, C.C., Geen, A.V., Baskaran, M., Anima, R. 1999. Sediment chronology in San Francisco Bay, California, defined by <sup>210</sup>Pb, <sup>234</sup>Th, <sup>137</sup>Cs, and <sup>239</sup>, <sup>240</sup>Pu. *Marine Chemistry* 64, 7-27.
- Guernet, C., Lemeille, F., Sorel, D., Bourdillon, Ch., Berge-Thierry, C., Manakou, M. 2003. Les Ostracodes et le Quaternaire d'Aigion (Golfe de Corinthe, Grèce). *Revue de Micropaléontologie*, 46, 73-93.
- Guillaume, M.C., Peypouquet, J.P., Tetart, J. 1985. Quaternaire et actuel. Atlas des Ostracodes de France. *Bulletin des centres de recherches exploration-production Elf-Aquitaine* 9, 337-377.
- Hammer, Ø., Harper, D.A.T., Ryan, P.D. 2001. Past: Paleontological Statistics Software Package for Education and Data Analysis. *Palaeontologia Electronica* 4 (1), 9pp., 178kb. [http://palaeo-electronica.org/2001\\_1/past/issue1\\_01.htm](http://palaeo-electronica.org/2001_1/past/issue1_01.htm)
- Hanfi, M. Y., Yarmoshenko, I.V., Seleznev, A. A., Zhukovsky, M. V. 2019. The gross beta activity of surface sediment in different urban landscape areas. *Journal of Radioanalytical and Nuclear Chemistry* 321, 831-839.
- Hanfi, M. Y., Yarmoshenko, I., Seleznev, A.A. 2021. Gross Alpha and Gross Beta Activity Concentrations in the Dust Fractions of Urban Surface-Deposited Sediment in Russian Cities. *Atmosphere* 12, 571, 1-8.
- Hartman, G., Puri, H. 1974. Summary of Neontological and Paleontological Classification of Ostracod. *Mitteilungen aus dem Hamburgischen Zoologischen Museum und Institut* 20, 7-73.
- Hatta, A., Ujiie, H. 1992. Benthic foraminifera from Coral Seas between Ishigaki and Iriomote Islands, Southern Ryukyu Island Arc, Northwestern Pacific. *Bulletin of the College of Science University of Ryukyus* 53, 49-119; 54, 163-287.
- Hottinger, L., Halicz, E., Reiss, Z. 1993. Recent foraminifera from the Gulf of Aqaba, Red Sea. *Slovenska Akademija Znanosti in Umetnosti, Ljubljana* 179. (pl. 1-230)
- İSKİ, 2005. Su kalitesi İzleme Çalışması, Sonuç Raporu. İstanbul.
- Joachim, C., Langer, M. R. 2008. The 80 most common Ostracods from the Bay of Fetovaia Elba Island (Mediterranean Sea), *Universität Bonn*, 29.
- Karahan, G. 1997. İstanbul'un çevresel radyoaktivitesinin tayini ve doğal radyasyonların yıllık etkin doz eşdeğeri. *Doktora Tezi, İTÜ, Nükleer Enerji Enstitüsü, İstanbul*. 118s.
- Karahan, G., Öztürk, N., Bayülken, A. 2000. Natural radioactivity in various surface waters in İstanbul, Turkey. *Water Research* 34(18), 4367-4370.
- Keser, R., Korkmaz-Görür, F., Alp, İ., Okumuşoğlu, N. T. 2013. Determination of radioactivity levels and hazards of sediment and rock samples in İkizdere and Kaptanpaşa Valley, Turkey. *International Journal of Radiation Research* 11 (3), 155-165.
- Kılıç, Ö., Belivermiş, M., Gözel, F., Carvalho, F. P. 2014. Radioactivity levels in mussels and sediments of the Golden Horn by the Bosphorus Strait, Marmara Sea. *Marine Pollution Bulletin* 86 (1-2), 555-561.
- Li, F. Y., Li, X. G., Song, J. M., Wang, G. Z., Cheng, P., Gao, S., 2006. Sediment flux and source in northern Yellow Sea by <sup>210</sup>Pb technique. *Chinese Journal of Oceanology and Limnology* 24 (3), 255-263.
- Loeblich, Jr.A.R., Tappan, H. 1988. Foraminiferal genera and their classification. *Van Nostrand Reinhold Company*, 970, 842 pls.
- Loeblich, A. R., Tappan, H. 1994. Foraminifera of the Sahul Shelf and Timor Sea. *Cushman Foundation for Foraminiferal Research Special Publication*, 31.
- Mandic, L. J., Dragović, R., Dragović, S. 2010. Distribution of lithogenic radionuclides in soils of the Belgrade region (Serbia). *Journal of Geochemical Exploration* 105 (1-2), 43-49.
- Maringer, F.J., Baumgartner, A., Seidel, C., Stietka, M. 2015. Radioactivity in the Danube. I. Liska (Ed.) In: *The Handbook of Environmental Chemistry* 39. The Danube River Basin. Springer. 271-284.
- McLin, S. G., Lyons, D. W. 2002. Background Radioactivity in River and Reservoir Sediments near Los Alamos, New Mexico, report, New Mexico. University of North Texas Libraries, UNT Digital Library, crediting UNT Libraries Government Documents Department.
- Meriç, E., Sakınç, M., Eroskay, O. 1988. İstanbul Boğazı ve Haliç çökellerinin evrim modeli. *Mühendislik Jeolojisi Bülteni*, 10, 10-14.
- Meriç, E., Sakınç, M. 1990. Foraminifera. E. Meriç (Ed.), İstanbul Boğazı Güneyi ve Haliç'in Geç Kuvaterner (Holosen) Dip Tortulları. 15-41.
- Meriç, E., Oktay, F.Y., Sakınç, M., Gülen, D., Inal, A. 1991. Sedimentary geology and palaeoecology of the Quaternary sequences of Ayamama (Bakırköy-İstanbul) Çukurova Üniversitesi Yerbilimleri (Geosound) 8(1), 93-100.
- Meriç, E. Aşar, N., Eryılmaz, M., Yücesoy-Eryılmaz, F. 2001. İstanbul Boğazı'nın Güncel Bentik

- Foraminifer Topluluğu ve çökel dağılımı. Çukurova Üniversitesi Yerbilimleri (Geosound), 38, 93-108.
- Meriç, E., Avşar, N., Nazik, A. 2002 *a*. Bozcaada (Kuzey Ege Denizi) bentik foraminifer ve ostrakod faunası ile bu toplulukta gözlenen yerel değişimler. Çukurova Üniversitesi Yerbilimleri (Geosound), 40-41, 97-119.
- Meriç, E., Avşar, N., Bergin, F. 2002 *b*. Midilli Adası (Yunanistan-Kuzeydoğu Ege Denizi) bentik foraminifer faunası ve bu toplulukta gözlenen yerel değişimler. Çukurova Üniversitesi Yerbilimleri (Geosound), 40-41, 177-193.
- Meriç, E., Avşar, N., Bergin, F., Barut, İ. F. 2003 *a*. Edremit Körfezi (Kuzey Ege Denizi) güncel çökellerindeki bentik foraminifer topluluğu ile ekolojik koşulların incelenmesi. Çukurova Üniversitesi Yerbilimleri (Geosound), 43, 169-182.
- Meriç, E., Avşar, N., Bergin, F., Barut, İ.F. 2003 *b*. Dikili Körfezi'nde (Kuzeydoğu Ege Denizi) bulunan üç anormal bentik foraminifer örneği: *Peneroplis planatus* (Fichtel ve Moll), *Rosalina* sp. Ve *Elphidium crispum* (Linné) hakkında. Maden Tetkik ve Arama Dergisi 127, 67-81.
- Meriç, E., Kerey, İ. E., Avşar, N., Tuğrul, A. B., Suner, F., Sayar, A. 2003 *c*. Haliç (İstanbul) kıyı alanlarında (Unkapı- Azapkapı) gözlenen Holosen çökelleri hakkında yeni bulgular. Hacettepe Üniversitesi Yerbilimleri 28, 9-32.
- Meriç, E., Avşar, N., Nazik, A., Eryılmaz, M., Yücesoy-Eryılmaz, F. 2004 *a*. Saros Körfezi'nin (Kuzey Ege Denizi) güncel bentik ve planktik foraminifer toplulukları ile çökel dağılımı. Çukurova Üniversitesi Yerbilimleri (Geosound), 44-45, 1-44. (in Turkish with English abstract)
- Meriç, E., Avşar, N., Bergin, F. 2004 *b*. Benthic foraminifera of Eastern Aegean Sea (Turkey) Systematics and Autoecology. Turkish Marine Research Foundation and Chamber of Geological Engineers of Turkey, Publication No: 18: 306, 33 plates.
- Meriç, E., Avşar, N., Nazik, A., Tunoğlu, C., Yokeş, B., Barut, İ.F., Yücesoy-Eryılmaz, F., Tuğrul, B., Görmüş, M., Öncel, M. S., Orak, H., Kam, E., Dinçer, F. 2008. Harmantaşı Mevkii deniziçi kaynakları çevresindeki foraminifer ve ostrakod topluluğuna bu alandaki çevresel koşulların etkisi. Maden Tetkik ve Arama Dergisi 136, 63-84.
- Meriç, E., Avşar, N., Nazik, A., Yokeş, B., Ergin, M., Eryılmaz, M., Yücesoy-Eryılmaz, F., Göktaşan, E., Suner, F., Tur, H., Aydın, Ş., Dinçer, F. 2009. Çanakkale Boğazı'nın güncel bentik foraminifera, ostrakod ve mollusk topluluğunu denetleyen faktörler ile çökel dağılımının jeokimyası. Türkiye Jeoloji Bülteni, 52 (2), 155-215.
- Meriç, E., Avşar, N., Nazik, A., Yokeş, B., Barut, İ.F., Eryılmaz, M., Kam, E., Taşkın, H., Başarı, A., Dinçer, F., Bircan, C., Kaygun, A. 2012. Ilica Bay (Çeşme-İzmir) Benthic Foraminifera-Ostracoda Assemblages And Pacific Ocean – Red Sea Originated Foraminifera And Abnormal Individuals. Bulletin of the Mineral Research and Exploration 145, 62-78.
- Meriç, E., Avşar, N., Nazik, A., Yokeş, B., Barut, İ.F., Suner, F., Sarı, E., Eryılmaz, M., Yücesoy-Eryılmaz, F., Dora, Ö., Kam, E., Dinçer, F. 2017. A multi disciplinary overview of factors controlling on meiofauna assemblages around Maden and Alibey islands in Ayvalık (Balıkesir, Eastern Aegean Sea). Journal of African Earth Sciences 129, 558-578.
- Meriç, E., Barut, İ.F., Nazik, A., Avşar, N., Yokeş, M.B., Eryılmaz, M., Yücesoy-Eryılmaz, F., Kam, E., Sonuvar, B., Dinçer, F. 2018 *a*. The Effect Of Submarine Thermal Springs Of Doğanbey Cape (Seferihisar - İzmir) On Foraminifer, Ostracoda And Mollusca Assemblages. Bulletin of the Mineral Research and Exploration 156, 87-116.
- Meriç, E., Nazik, A., Yokeş, M.B., Barut, İ.F., Kumral, M., Eryılmaz, M., Yücesoy-Eryılmaz, F., Gündoğan, İ., Sonuvar, B., Dinçer, F. 2018 *b*. The effects of submarine springs on meiobenthic assemblages (benthic foraminifers, ostracods and molluscs) on the coasts of Aliağa (İzmir). Geological Bulletin of Turkey 61, 269-290.
- Meriç, E., Avşar, N., Yokeş, M.B., Barut, İ.F., Dinçer, F., Bircan, C., Kam, E. 2020. Ecology of benthic foraminifera of the eastern Aegean Sea coasts, International Journal of Environment and Geoinformatics (IJEGEO), 7(1): 06-22
- Murray, J. W. 1970. Foraminifers of the western approaches to the English Channel. Micropaleontology 16/4, 471-485.
- Murray, J. W. 1971. An atlas of British recent foraminiferids. 1-244, 1: 95, Heineman Educational Books, London.
- Murray, J. W. 1973. Distribution and Ecology of Living Benthic Foraminiferids, Heinemann Educational Books Ltd., London, 274.
- Otansev, P., Taşkın, H., Başarı, A., Varınlıoğlu, A. 2016. Distribution and environmental impacts of heavy metals and radioactivity in sediment and seawater samples of the Marmara Sea. Chemosphere 154, 266-275.
- Önce, M., Kam, N. 2019. Gross Alpha and Gross Beta Activity Levels of Holocene Sediments Between Şarköy and Mürefte (Tekirdağ). Journal of

- Engineering Technology and Applied Sciences 4 (2), 63-69.
- Özger, A.G. 2005. Ceyhan, Yumurtalık ve Pozantı Bölgelerinin Doğal Radyoaktivite Düzeylerinin Belirlenmesi. Yüksek Lisans Tezi, Çukurova Üniversitesi, Fen Bilimleri Enstitüsü.
- Pantelic, G., Eremic, M., Petrovic, I., Javorina, L., Tanaskovic, I., Vancsura, P., Varga, A.L., Kövágó, J. 2002. Radioactivity control of the Danube at Yugoslav-Hungarian border area. Environmental Recovery of Yugoslavia, Vinca Institute, Belgrade, Serbia. 193-201.
- Patrascu, V. 2002. Radioactivity level in marine ecosystem. Agata Olariu, Kristina Stenstrom, Ragnar Helborg (Eds.), In book: Proceedings of the International Conference on Application of High Precision Atomic & Nuclear Methods, (2-6 Sept 2002), Neptun, Romania. Edition 2005, Publisher: Ed. Academia Romana, 53-56.
- Rank, D., Maringer, F.J., Terlunen, J. 1990. The radioactivity of sediments in Danube reservoirs in Austria before and after the Chernobyl accident. Water Science and Technology (UK) 22, 211-218.
- Ruiz-Fernandez, A.C., Hillaire-Marcel, C. 2009. 210Pb-derived ages for the reconstruction of terrestrial contaminant history into the Mexican Pacific coast: potential and limitations. Marine Pollution Bulletin 59, 134-145.
- Sakinç, M., Yalırak, C., Oktay, F.Y. 2000. Kuzeybatı Türkiye’de (Trakya) Tetis-Paratetis ilişkisi ve Trakya Neojen Havzası’nın paleocoğrafyası ve tektonik evrimi. Cumhuriyet’in 75. Yıldönümü Yer Bilimleri ve Madencilik Kongresi Bildiriler Kitabı, 1, 107-135.
- Santschi, P.H., Honeyman, B.D. 1989. Radionuclides in aquatic environments. Radiation Physics and Chemistry 34, 213-240.
- Saraswat, R., Nigam, R. 2013. Benthic Foraminifera. Elias, S.A. (Ed.), In: The Encyclopaedia of Quaternary Science, Amsterdam, Elsevier. 2, 765-774.
- Savino, F., Pugliese, M., Quarto, M., Adamo, P., Loffredo, F., De Cicco, F., Roca, V. 2017. Thirty years after Chernobyl: Long-term determination of <sup>137</sup>Cs effective half-life in the lichen *Stereocaulon vesuvianum*. Journal of Environmental Radioactivity 172, 201-206.
- Sen Gupta, B. K. 1999. Introduction to modern foraminifera. Sen Gupta, B.K. (Ed.), Modern Foraminifera, Kluwer Academic Publisher, Netherlands, 3-6.
- Sgarella, F., Moncharmont-Zei, M. 1993. Benthic foraminifera of the Gulf of Naples (Italy), systematic and autoecology. Bulletino della Società Paleontologica Italiana, 32 (2), 145-264.
- Stephen, G.M. 2004. Background radioactivity in sediments near Los Alamos, New Mexico. Science of the Total Environment, 328, 143-159.
- Şahin, S. 2000. Radyoaktivite Seviye Tayini ile Kuvaterner İstifi İncelemesi ve Yeni Bir Değerlendirme, Doktora Tezi, İTÜ Nükleer Enerji Enstitüsü, İstanbul.
- Şamlı, A.C. 1996. Haliç (İstanbul) Holosen dip çökellerinin bentik foraminifer faunası. Türkiye Jeoloji Bülteni, 39(2), 87-102.
- Şimşek, O. 1987. İstanbul Boğazı Tüp Geçiş Güzergahının Jeolojisi. Yüksek Lisans Tezi, İstanbul Üniversitesi Jeoloji Mühendisliği Bölümü, İstanbul.
- Thunell, R.C. 1979. Pliocene-Pleistocene paleotemperature and paleosalinity history of the Mediterranean Sea: results from DSDP Sites 125 and 132. Marine Micropaleontology, 4, 173-187.
- Topçuoğlu, S. 2000. Black Sea ecology, pollution research in Türkiye of the marine environment. IAEA Bulletin, 42, 12-14.
- Tuğrul, B., Meriç, E., Avşar, N., Baytaş, F., Altınsoy, N., Ayaz, B., Doğan, N., Şahin, S., Yılmaz, I. 2001. Haliç Geç Kuvaterner (Holosen) İstifinin Radyoaktivite Seviyesi Tayini İle Değerlendirilmesi ve Diğer Değerlendirme Teknikleri İle Karşılaştırılması. Haliç 2001 Sempozyumu, (3-4 Mayıs 2001), 253-267.
- Tuncer, S., Tuğrul, B. 1992. Radioactivity Levels in Drinking Water of West Side of Turkey. First Tatarstan Symposium on Energy, Environment and Economics, (9-4 August 1992), Kazan-Tatarstan. 182.
- Ünlüata, Ü., Oğuz, T., Latif, M.A., Özsoy, E. 1990. On the physical oceanography of the Turkish straits. Pratt, L.J. (Ed.), In: The physical oceanography of sea straits. NATO/ASI series, Kluwer, Dordrecht, 25-60.
- Van, T., Bat, L., Nhan, D., Quang, N., Cam, B., Hung, L. 2018. Estimation of radionuclide concentrations and average annual committed effective dose due to ingestion for the population in the Red River Delta, Vietnam. Environmental Management 63 (4), 444-454.
- Van Morkhoven, F.P.C.M. 1963. Post Palaeozoic Ostracoda. Elsevier Amsterdam, 2, 478.
- Vongunten, H.R., Sturm, M., Moser, R.N. 1997. 200-year record of metals in lake sediments and natural background concentrations. Environmental Science and Technology 31, 2193-2197.

- Yang, W.F., Chen, M., Li, G.X., Cao, J.P., Guo, Z.G., Ma, Q., Liu, J., Yang, J.H. 2009. Relocation of the Yellow river as revealed by sedimentary isotopic and elemental signals in the East China Sea. *Marine Pollution Bulletin* 58, 923-927.
- Yanko, V. 1993. Stratigraphy and paleostratigraphy of the marine Pleistocene and Holocene deposits of the southern seas of the USSR. *Mem. Soc. Geol. Inst.*, 44, 167-187.
- Yassini, I. 1979. The littoral system ostracodes from the Bay of bou, İsmail, Algeria, Algeria: *Revista Espanola de micropaleontologica* 11 (3), 353-416.
- Yıldırım, M., Özyayın, K., Erguvanlı, A. 1992. İstanbul Boğazı Güneyi ve Haliç'in Jeolojik Yapısı ve Geoteknik Özellikleri. *Jeoloji Mühendisliği Bülteni*, 40, 4-14.
- Yokeş, M.B., Meriç, E., Avşar, N., Barut, İ., Tas, S., Eryılmaz, M., Dinçer, F., Bircan, C. 2014. Opinions and comments on the benthic foraminiferal assemblage observed around the mineral submarine spring in Kuşadası (Aydın, Turkey). *Marine Biodiversity Records*, Marine Biological Association of the United Kingdom, 7/2014; e103, 1-17.
- Yuanxun, Z., Erhkang, L., Deyi, L., Yinsong, W., Yuehchung, Y., Changwan, W., Waiguo, S., Min, Z., Guilin, Z., Yan, L. 2003. PIXE and radioactivity measurements for elemental determination in river water and sediment samples. *Journal of Radioanalytical and Nuclear Chemistry* 258 (2), 415-419.
- Yücesoy-Eryılmaz, F., Eryılmaz, M. 1998. Çanakkale Boğazı ve çevresi güncel çökellerinde metal dağılımı. Türkiye'nin Kıyı ve Deniz alanları II. Ulusal Konferansı (22-25 Eylül 1998), ODTÜ, Ankara. E. Özhan (Ed.), Türkiye Kıyıları 1998 Konferans Bildiriler kitabı, 649-658.
- Yücesoy-Eryılmaz, F., Eryılmaz, M. 2000. Kuzeydoğu Ege Denizi-Çanakkale Boğazı-Çanakkale Boğazı Marmara Denizi girişindeki ince taneli çökellerin ağır metal dağılımına etkisi. 53. Türkiye Jeoloji Kurultayı, (21-25 Şubat 2000) Ankara, Bildiri Özleri, 126-127.
- Yücesoy-Eryılmaz F., Eryılmaz, M. 2002. Kuzeydoğu Ege Denizi ve Marmara Denizi geçiş bölgesi çökellerinde ince tane boyunun ağır metal dağılımına etkisi. *Türkiye Jeoloji Bülteni*, 45 (1), 111-124.
- Yücesoy-Eryılmaz, F., Eryılmaz, M., Özdemir, Z. 2003a. Sedimentology and Geochemistry of the Bosphorus, Junction of the Marmara Sea and Black Sea with the Bosphorus surface sediments. A. Yılmaz (Ed.), *Oceanography of the Eastern Mediterranean and Black Sea, (Similarities and differences of two interconnected basins)*, 948-952, 944-947.
- Yücesoy-Eryılmaz, F., Eryılmaz, M., Özdemir, Z. 2003b. İstanbul Boğazı, Marmara ve Karadeniz çıkışı güncel çökellerinde ağır metal dağılımı. Mersin Üniversitesi Mühendislik Fakültesi Jeoloji Mühendisliği Bölümü 10.Yıl Sempozyumu (15-18 Ekim 2003), Bildiri Özleri Kitabı, 102.
- Zorer, Ö., Öter, Ç. 2015. Evaluation of gross radioactivity in foodstuffs. *Kerntechnik* 80 (2), 174-179.
- Zorer, Ö.S., Ceylan, H., Doğru, M. 2009a. Gross alpha and beta radioactivity concentration in water, soil and sediment of the Bendimahi River and Van Lake (Turkey). *Environmental Monitoring and Assessment* 148 (1-4), 39 – 46.
- Zorer, Ö. S., Ceylan, H., Doğru, M. 2009b. Determination of Heavy Metals and Comparison to Gross Radioactivity Concentration in Soil and Sediment Samples of the Bendimahi River Basin (Van, Turkey). *Water, Air, and Soil Pollution* 196, 75-87.
- Zhou, P., Li, D., Li, H., Fang, H., Huang, C., Zhang, Y., Zhang, H., Zhao, L., Zhou, J., Wang, H., Yang, J. 2015. Distribution of radionuclides in a marine sediment core off the waterspout of the nuclear power plants in Daya Bay, northeastern South China Sea. *Journal of Environmental Radioactivity* 145, 102-112.



## **PLATES**

**Plate I**

1. *Siphonaperta aspera* (d'Orbigny). Side view, Station B21, 30 m, Bosphorus,
2. *Quinqueloculina berthelotiana* d'Orbigny. Side view, Station H3, 10 m, Golden Horn,
3. *Quinqueloculina disparilis* d'Orbigny. Side view, Station B12, 67 m, Bosphorus,
4. *Quinqueloculina lamarckiana* d'Orbigny. Side view, Station B17, 67 m, Bosphorus,
5. *Quinqueloculina seminula* (Linne). a and b, side views, Station B12, 67 m, Bosphorus,
6. *Phyrgo elongata* (d'Orbigny). Side view, Station D15, 30 m, Dardanelles,
7. *Sigmoilinita costata* (Schlumberger). Side view, Station D9, 30 m, Dardanelles,
8. *Sigmoilopsis schlumbergeri* (Silvestri). Side view, Station D9, 30 m, Dardanelles,
9. *Amphicoryna scalaris* (Batsch). Side view, Station D9, 30 m, Dardanelles,
10. *Fissurina* sp. a and b, side views, Station D9, 30 m, Dardanelles,
11. *Brizalina alata* (Seguenza). Side view, Station B22, 30 m, Bosphorus,
12. *Brizalina spathulata* (Williamson). Side view, Station D5, 30 m, Dardanelles,
13. *Rectuvigerina phlegeri* le Calvez. Side view, Station D9, 30 m, Dardanelles,
14. *Bulimina elongata* d'Orbigny. Side view, Station D5, 10 m, Dardanelles,
15. *Globobulimina affinis* (d'Orbigny). Side view, Station D15, 30 m, Dardanelles,
16. *Reussella spinulosa* (Reuss). Side view, Station D5, 10 m, Dardanelles.

PLATE 1

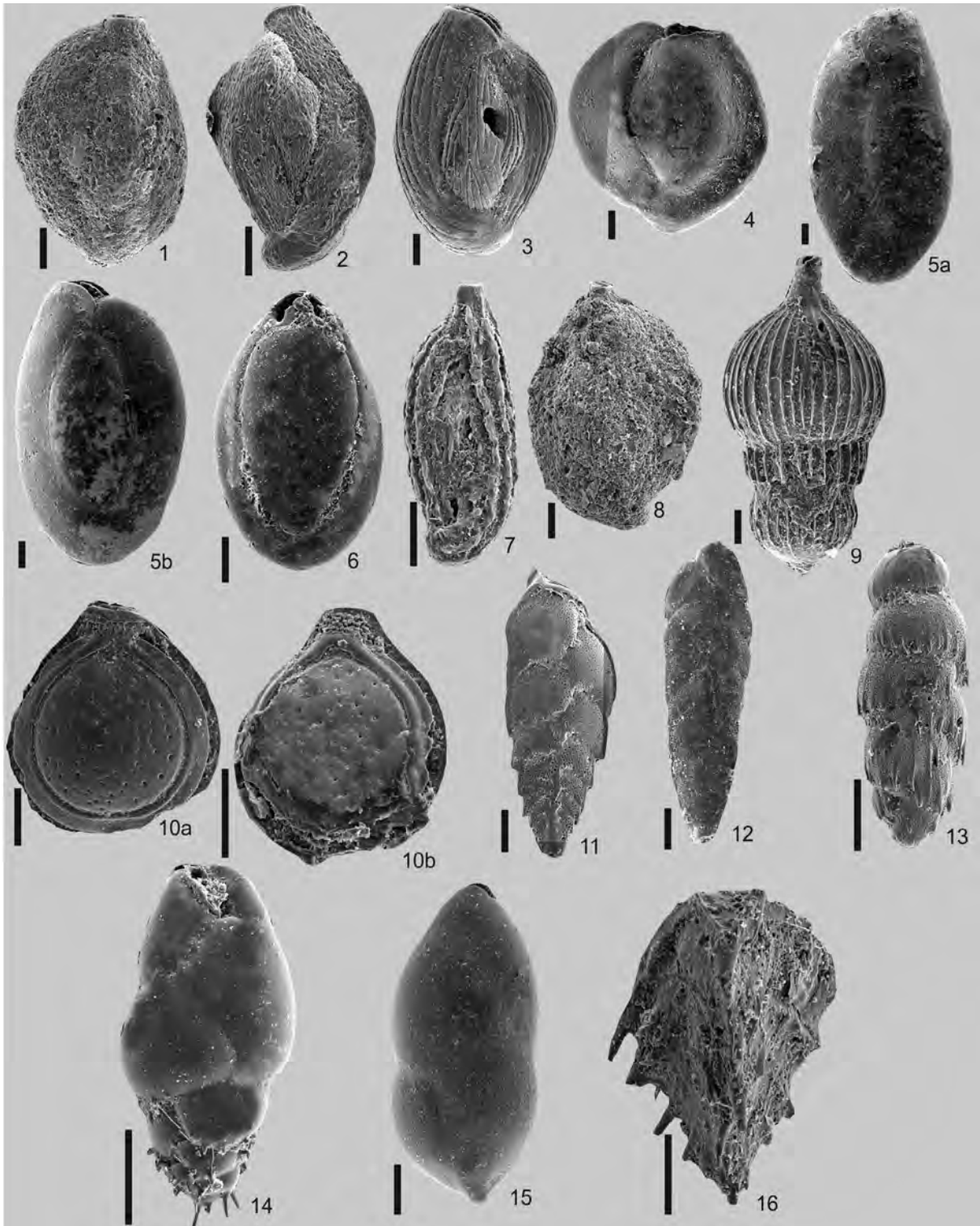
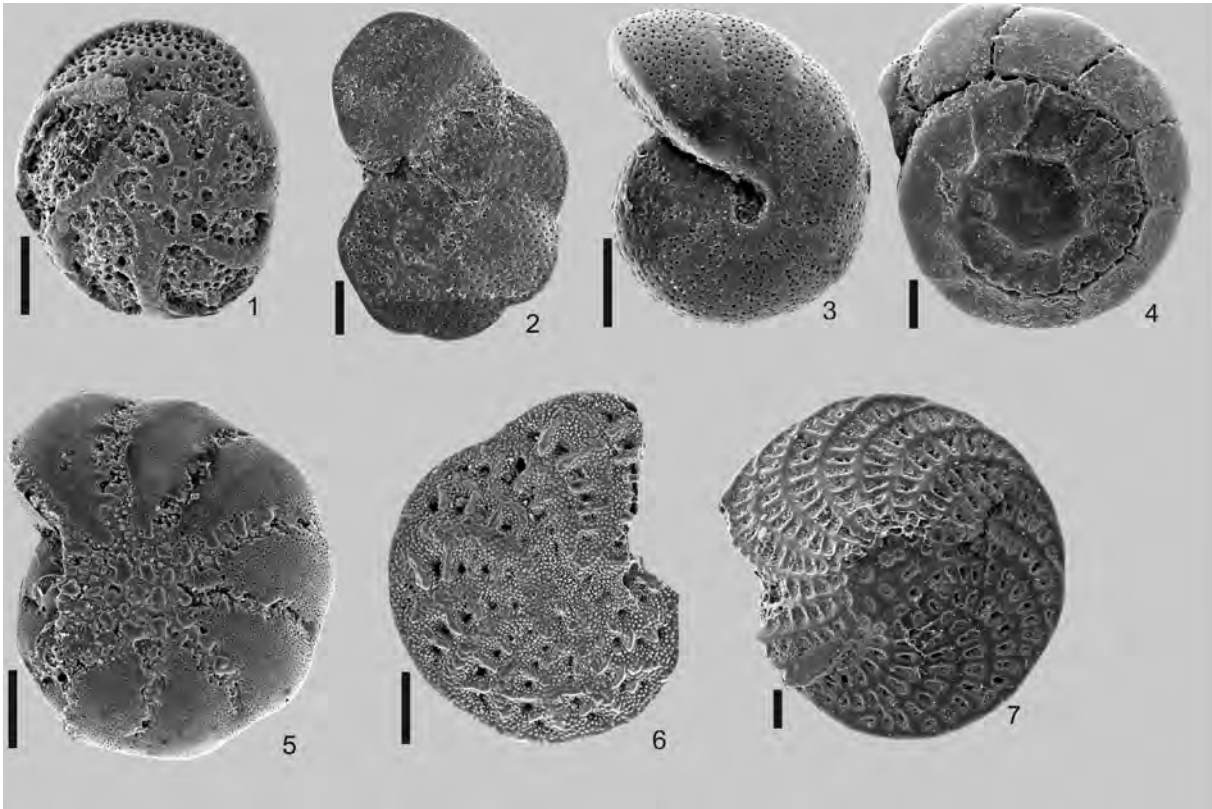


**Plate II**

1. *Rosalina bradyi* Cushman. Spiral side, Station D15, 30 m, Dardanelles,
2. *Lobatula lobatula* (Walker and Jacob). Spiral side, Station B22, 30 m, Bosphorus,
3. *Melonis pompilioides* (Fichtel and Moll). Side view, Station D1, 30 m, Dardanelles,
4. *Ammonia compacta* Hofker. Spiral side, Station D13, 30 m, Dardanelles,
5. *Cribroelphidium poeyanum* (d'Orbigny). Side view, Station B10, 30 m, Bosphorus,
6. *Elphidium complanatum* (d'Orbigny). Side view, Station D13, 30 m, Dardanelles,
7. *Elphidium crispum* (Linné). Side view, Station D13, 30 m, Dardanelles.

PLATE II







# Bulletin of the Mineral Research and Exploration

<http://bulletin.mta.gov.tr>



## Anthropogenic problems threatening major cities: Largest surface deformations observed in Hatay, Türkiye based on SBAS-InSAR

Şükrü Onur KARACA<sup>a\*</sup>, Gültekin ERTEN<sup>a</sup>, Semih ERGİNTAV<sup>b</sup> and Shuhab D. KHAN<sup>c</sup>

<sup>a</sup> General Directorate of Mineral Research and Exploration, Department of Geological Research, Remote Sensing and GIS Division, Ankara, Türkiye

<sup>b</sup> Boğaziçi University, Kandilli Observatory and Earthquake Research Institute, Department of Geodesy, İstanbul, Türkiye

<sup>c</sup> University of Houston, Department of Earth and Atmospheric Sciences, Houston, TX, USA

Research Article

### Keywords:

Multi-temporal InSAR, Radar interferometry, Surface deformation, Hatay-Güzelburç, Türkiye.

### ABSTRACT

The surface deformation caused by tectonic activities and anthropogenic factors poses a great threat to cities worldwide. The investigation and monitoring of these deformations are crucial in order to create risk analysis for the future. The problem in this case is to investigate the surface deformations and their negative effects caused by groundwater use and to identify possible landslide areas. In this study, the surface deformations in Hatay province were analyzed using SBAS-InSAR. The results from these analyses were evaluated by field observations. Sentinel-1 descending (183 datasets) and ascending (147 datasets) track geometries were selected to determine the surface deformation and its temporal evolution. Both east-west and vertical surface deformations were calculated, and the surface deformation profiles, surface 3D models and time series were created. These time series were associated with monthly precipitation data. The deformation area was interpreted with regard to available well-log data and geological setting of the study area. As a result of the study, a surface deformation resembling a bowl like structure was observed in the industrial zone located in the city center of Hatay-Güzelburç. The deformation rates are approximately 22.3 cm/year in the form of subsidence, 3.6 cm/year in the form of eastern movement and 10.1 cm/year in the form of western movement. The deformation of this bowl-like structure decelerated in the winter and accelerated in the summer due to excessive water use. The average monthly precipitation dataset supports these results. The stratigraphic data from water wells and the presence of limestone outside the eastern boundary of the deformation area show a thick clay layer in the eastern block of the bowl-shaped deformation structure. The difference between these two units, which causes a sharp anomaly at the eastern border of the deformation area, is interpreted as a probable normal fault. The second study area where surface deformations are observed is the landslide zone. The deformation was found to be 7.5 cm/year in a westward direction and 1.5 cm/year as subsidence.

Received Date: 08.02.2023

Accepted Date: 17.05.2023

## 1. Introduction

The surface deformation induced by geological processes causes widespread infrastructural damage in urban areas and is a common geological hazard worldwide. Numerous studies have been conducted by researchers to detect and understand landform

deformations using satellite systems and radar interferometry (Amelung et al., 1999; Strozzi et al., 2001; Raucoules et al., 2007; Zhang et al., 2012; Khan et al., 2014; Motagh et al., 2017; Solari et al., 2018). Interferometric Synthetic Aperture Radar (InSAR) is one of the methods widely used in recent years to investigate surface deformations. This method utilizes

Citation Info: Karaca, O., Ş., Erten G., Ergintav S. Khan D. S., 2024. Anthropogenic problems threatening major cities: Largest surface deformations observed in Hatay, Türkiye based on SBAS-InSAR. Bulletin of the Mineral Research and Exploration 173, 235-252. <https://doi.org/10.19111/bulletinofmre.1298494>

\*Corresponding author: Şükrü Onur KARACA, [onurkaraca87@hotmail.com](mailto:onurkaraca87@hotmail.com)

the phase difference between the radar image pairs to determine the deformation rates of various surface motions (Hung et al., 2011; Tomás et al., 2014; Brunori et al., 2015; Aslan et al., 2018; Khan et al., 2022).

One of the most common factors that cause subsidence in major cities is the excessive use of groundwater (Motagh et al., 2007; Anderssohn et al., 2008; Tomás and Li, 2017). For example, one of the highest subsidence rates of 3,5 cm/year is reported from Mexico City that is caused by the excess pumping of groundwater (Strozzi and Wegmuller, 1999; Cabral-Cano et al., 2008; Lopez-Quiroz et al., 2009; Osmanoglu et al., 2011; Yan et al., 2012; Cabral-Cano et al., 2015; Sowter et al., 2016; Cigna and Tapete, 2021). Another area that shows extensive land subsidence is in the vicinity of Konya, Türkiye. Konya City is located in the Central Türkiye that displays karstic terrain of highly erodible rocks typical of the Mediterranean and the Central Anatolia regions of Türkiye. Since karstic units in such regions have a structure that is easily soluble in water especially when groundwater combines with carbon dioxide, they form large cavities in underground called sinkholes (Ford and Williams, 1989; Waltham and Fookes, 2003). One of the study conducted by Orhan (2021) in the Karapınar district of Konya revealed that there was 7 cm/year of subsidence in this area using InSAR, Global Navigation Satellite System (GNSS) and groundwater level data. Another study conducted in Konya province determined the amount of subsidence in the region between the years 2004 and 2020 using Envisat, ALOS-1, and modeled this subsidence area by Sentinel-1 A/B data (Şireci et al., 2021). İmamoğlu et al. (2019) carried out a study in the Turkish province of Afyon - Bolvadin region which has similar geology and structure to Konya. İmamoğlu et al. (2019) utilized InSAR to analyze the surface deformations (Sentinel-1 dataset between 2014-2018) and compared the results with the geology of the region, groundwater data and field observations in his study. Maximum subsidence of 3.5 cm/year observed in the southern part of the study area shows that this area is characterized by the presence of soft alluvial deposits. They stated that the northeastern part of the deformed region composed of slope debris and pebbles has a relatively lower subsidence rate (İmamoğlu et al., 2019). Aslan et al.

(2019) characterized and monitored the subsidence of the Bursa Plain (the southern Marmara region of Türkiye). They measured the subsidence patterns and correlated them with the lithology by using InSAR data and suggested a strong lithological control on subsidence. They concluded that the maximum rate of ground subsidence occurs where agricultural activity relies on groundwater exploitation (Aslan et al., 2019).

According to the “Geological and Geophysical Preliminary Survey Report for Hatay - Güzelburç Municipality Settlement Area (Türkiye)” prepared by the General Directorate of Natural Disasters in 2006, a remarkable deformation of the ground in the settlements, serious cracks in houses and buildings of the area were investigated. It was reported that the deformations in the region increased especially in 2004-2005, therefore some houses were completely evacuated or demolished (Kuran et al., 2006).

This study aims to reveal the surface deformations, boundaries, and causes of surface deformations around Hatay province, including the Güzelburç neighborhood with InSAR-SBAS, and to evaluate the results with field studies, average precipitation data, and geology of the region. This study is an attempt to reveal the surface deformations and their causes in Hatay province and to analyze the risks that may occur in the future due to surface deformation. In this context, this study presents suggestions for the effects of identified deformation on populated areas, determines their boundaries, investigates the risks arising from deformation, and reveals the causes and solutions to the problems related to the deformation for industrial zone.

As a cost-effective monitoring method, InSAR-SBAS technology has been considerably practiced in landslide identification and deformation monitoring. (Yao et al., 2017, 2022; Liu et al., 2021). We also try to identify landslide zone comprehensively and determine deformation characteristics.

## 2. Tectonic and Geological Setting of the Study Area

The Hatay Triple Junction (HTJ), defined as a tectonically complex region in southeastern Türkiye and northwestern Syria that forms the plate boundary

between Arabia, Africa, and Anatolia, is located at the intersection of the left-lateral thrust East Anatolian Fault (EAF), west of the Cyprus Plunge Arc (CA) and north of the Dead Sea Fault (DSF) (Figure 1a) (Mahmoud et al., 2005, 2013). The study area covers the city center of Hatay province focusing on surface deformation in two different regions (Figure 1b). The first region is the industrial zone, which spans the area where the Asi River meanders relatively north of the study area (Figure 1c); and the second region is the landslide zone in the south of the study area (Figure 1d).

The geology of the region was well described in Sarıfakıoğlu's (2018) study, and the well-log data obtained from the General Directorate of State Hydraulic Works (DSI) was used. The bedrock of the

region consists of the Kızıldağ Ophiolite (Kko) of the Cenomanian-Turonian age. It is unconformably overlain by the Lutetian-Bartonian Okçular formation (Teo) and by discordantly overlain Aquitanian-Burdigalian Balyatağı Formation (Tmb) (consisting of conglomerates and sandstones). The Balyatağı Formation is discordantly overlain by the Sofular Formation (Tms) consisting of reefal limestones of the same age. The Tepehan Formation (Tmt) was deposited in the Langhian-Serravalian interval, and the Nurzeytin Formation (Tmn) was deposited in the Middle-Upper Miocene and consists of sandstone, clayey limestone, claystone and marl. The Samandağ Formation (Tpls) was discordantly deposited in the Pliocene and overlain by Quaternary alluvium (Qal) and Slope debris (Qym) (Figure 1e). The log

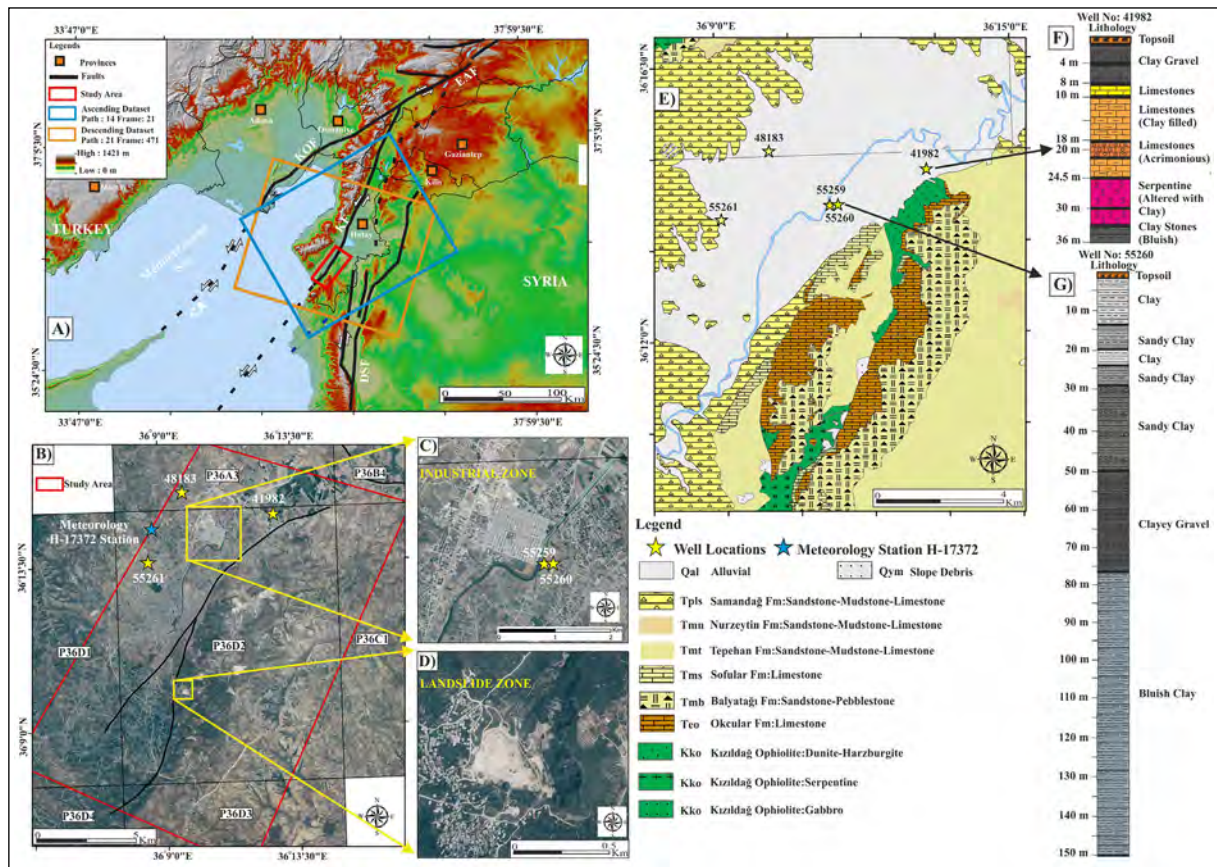


Figure 1- a) Digital elevation model (Aster-GDEM, 1 arc-sec - V2) of the study area. Red frame in the province of Hatay shows the study area. Ascending (path: 14, frame 114) and descending (path: 21, frame 471) geometry orthophoto datasets are represented with light blue and orange frames, respectively. Provinces in Türkiye are presented in orange squares. Abbreviations for faults: Dead Sea Fault, DSF; East Anatolian Fault, EAF; Karasu Fault, KF; Karataş-Osmaniye Fault, KOF; and Cyprus Arc, CA. Faults are modified after Mahmouda et al., (2013), b) The location map of the study areas. Yellow stars display the location of the wells, c) Industrial zone, d) Landslide zone (Orthophotos were obtained from the General Directorate of Mapping, 2022), e) Geological map (Sarıfakıoğlu, 2018), f) and g) well logs (Well data were obtained from the General Directorate of State Hydraulic Works (DSI), 2022).

of the well-41982 located on the eastern border of the deformation area shows limestone penetration immediately after a few meters of cover in the area (Figure 1f). Limestone unit continues to deposit until it comes in contact with a serpentinite unit at 24.5 m depth. The thickness of the relatively resistant limestone unit is approximately at 15-20 m depth (Figure 1f). This well lithology includes a thin layer of reefal limestone of the Sofular Formation followed by clayey limestone of the Tepehan Formation and finally serpentinites of the Kızıldağ Ophiolite. In contrast, the well 55260 (shown in Figure 1g) was drilled in clayey units that is succeeded by a sandy clay unit for 150 meters.

### 3. Materials and Methods

#### 3.1. InSAR Method

Synthetic Aperture Radar Interferometry (InSAR) is a remote sensing method that can reveal surface deformations with centimeter-level accuracy and has wide coverage (Zebker and Goldstein, 1986; Rucci et al., 2012; Simons et al., 2015; Aimaiti et al., 2017). This geodetic method uses two or more synthetic aperture radar images to produce maps of surface deformation or digital elevation using differences in the phase of the waves returning to the satellite (Massonnet and Feigl, 1998; Burgmann et al., 2000).

#### 3.2. SBAS (Small BAseline Subset) Method

SBAS method, which is a multi-temporal InSAR technique using multiple radar images, instead of the two radar images before and after the deformation, is currently used in many studies. Among these studies, the investigations of deformations caused by excess groundwater exploitation (Bell et al., 2008; Motagh et al., 2017; İmamoğlu et al., 2019; Orhan, 2021; Şireci et al., 2021), landslide occurrences (Zhu et al., 2014; Béjar-Pizarro et al., 2016; Liu et al., 2018, Liu et al., 2021) and active tectonic movements (Wöppelmann et al., 2013; Conesa-García et al., 2016 Karaca et al., 2021) can be considered.

SBAS, which is an InSAR algorithm, was first developed by Berardino et al. (2002) for the temporal assessment of surface deformations. Generally, in cases where the phase coherence in the preferred SAR data date ranges is low, the coherence between the most

appropriate binary images cannot be established and it is difficult to reveal or observe surface deformations on the earth's surface. Several parameters affect the analysis of image pairs like weather conditions, topography, trajectory, geometric orthogonal base lengths, and temporal differences. To eliminate or minimize such factors, the SBAS algorithm was developed using multi-temporal (multiple) images (Berardino et al., 2002). In this study, the minimum temporal baseline was chosen to be 120 days for the city center and the normal baseline was chosen to be 5% to improve the consistency of the stacked image pairs with the vertical baseline threshold (Figure 2). A 1 arc-sec Shuttle Radar Topography Mission Height (SRTM HGT) (30 m) digital elevation model was used to enhance the topographic correction. In addition, the reference ground control points (GCPs) were selected on high coherence pixels without phase jumps (coherence > 0,7) to remove the ramp and phase constant during re-smoothing and refinement, away from actively deforming areas and evenly distributed across the study area. Additionally, atmospheric components were subtracted date by date from displacement measurements. The atmospheric correction is performed by the following two filtering procedures; Atmosphere low and high pass. Finally, in the geocoding process, the reference digital elevation model was used to transit from radar geometry to ground geometry (Figure 2). As a result of data processing, the surface deformation rates and displacement time series were generated. All data were processed in Envi 5.6.1-Sarscape 5.6.0 software (Figure 2).

In this study, Sentinel-1 147 ascending and 183 descending InSAR datasets (Table 1) were processed. In addition, 1 arc-sec Shuttle Radar Topography Mission Height (SRTM HGT) (30 m) was used as a digital elevation model.

#### 3.3. Average Precipitation and Well Information Data

To investigate the correlation between the deformation areas in the region and groundwater level and the effect of monthly precipitation on deformation, the average precipitation data were obtained from the H-17372 station located in the study area from the General Directorate of Meteorology (Figure 1b).

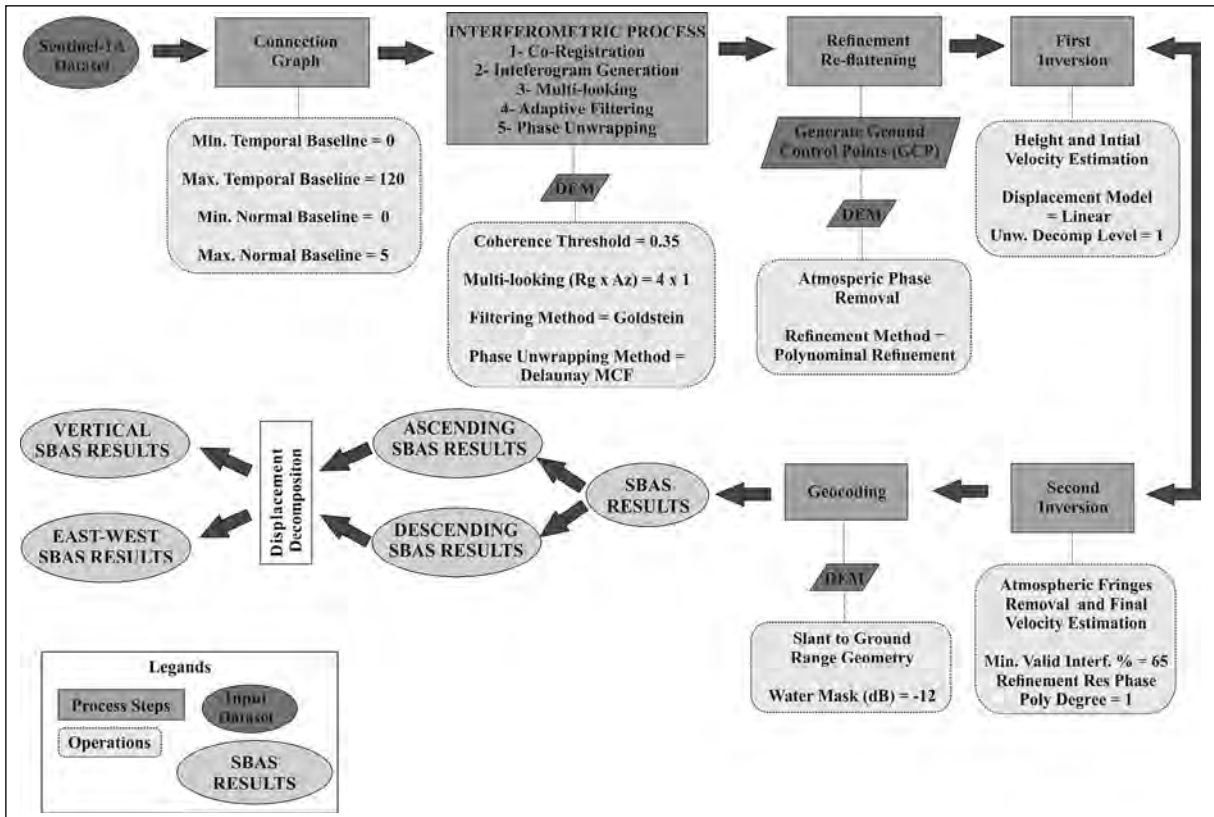


Figure 2- InSAR processing workflow using Small Baseline Subset technique.

Table 1- Information about Sentinel-1A/B datasets features. The product type is L1 single look complex (SLC) with ascending and descending geometry. Interferometric wide swath beam mode (IW). The following acronyms were used in the table: maximum perpendicular baseline (Bp) and maximum temporal baseline (Bt). Asc refers to ascending, des refers to descending. VH refers to cross-polarization which describes as vertical transmit and horizontal receive.

Product Type	Mode	Orbit Direction	Start Date	End Date	Quantity	Orbit	Path	Frame No.	Polarization	Wavelength	Max Bp (%)	Max Bt (Days)
S1-A/B	IW	Ascending	2017/05/23	2022/02/26	147	18111	14	114	VH	5.6 cm	5	120
S1-A/B	IW	Descending	2015/11/19	2022/01/22	183	16893	21	471	VH	5.6 cm	5	120

However, any data, related to the static and dynamic information about the aquifer dynamics in the region is not available. Only, the station H-17372 were used due to availability and this monthly precipitation data cover same period of the InSAR dataset from 2015/11/19 to 2022/01/22. Additionally, this rainfall dataset was plotted with time series (Figure 4d and 4h).

#### 4. Results and Discussion

##### 4.1. Spatio-Temporal Properties of the Deformations

In this study, SAR images (ascending and descending) of Sentinel-1A satellite were used to determine the displacement rate of the center of Hatay

province and its surrounding areas with the SBAS algorithm using the InSAR method. As it is known, one of the limitations of the InSAR method is that the results of the data processing give only the movement towards or away from the satellite direction. However, the ascending and descending images of the study area are applied together to estimate the east-west and upward-downward movements of the surface deformation. Accordingly, the InSAR-SBAS results for Hatay province were presented below.

The positions of the images used in data processing and image pairs for which interferograms were created are shown in Figures 3a and 3c, while Figures 3b and

3d show the base lengths between the image pairs for ascending and descending data sets, respectively. In Figure 3, the yellow diamonds represent the reference image pair (master) while the green diamonds represent the slave image pairs.

In Figure 4, descending and ascending Sentinel-1 datasets of Hatay province illustrate the results of SBAS analysis, respectively. In this figure, the negative values indicate the movement away from the satellite, while the positive values indicate the movement towards the satellite. In addition, in Figures 4D and 4H, the average monthly precipitation data and seasonal time information are shown together with the time series. To provide the vertical and horizontal velocity, the decomposition tool for descending and ascending geometries was applied. The ENVI SARscape tool decomposes the displacement and calculates local

incidence angles. The two local incidence angles calculated are described as Inclination Line of Sight (ILOS) and Azimuth Line of Sight (ALOS). Consequently, the ascending and descending InSAR-SBAS results were evaluated together to obtain both east-west and up-down SBAS results (Figure 5). In Figures 4 and 5, all minimum and maximum velocities are shown in Table 2.

For industrial zone, figures 6a and 6b show the vertical and east - west surface deformation velocities. Figures 6c and 6d show interferograms, 6e and 6f show unwrapped phase, 6g and 6h show re-flattened unwrapped phase, and 6i and 6j show re-flattened filtered interferograms for both ascending and descending datasets. In Figure 6, all images depict a relatively more precise deformation difference on the west side of the industrial zone than on the east side

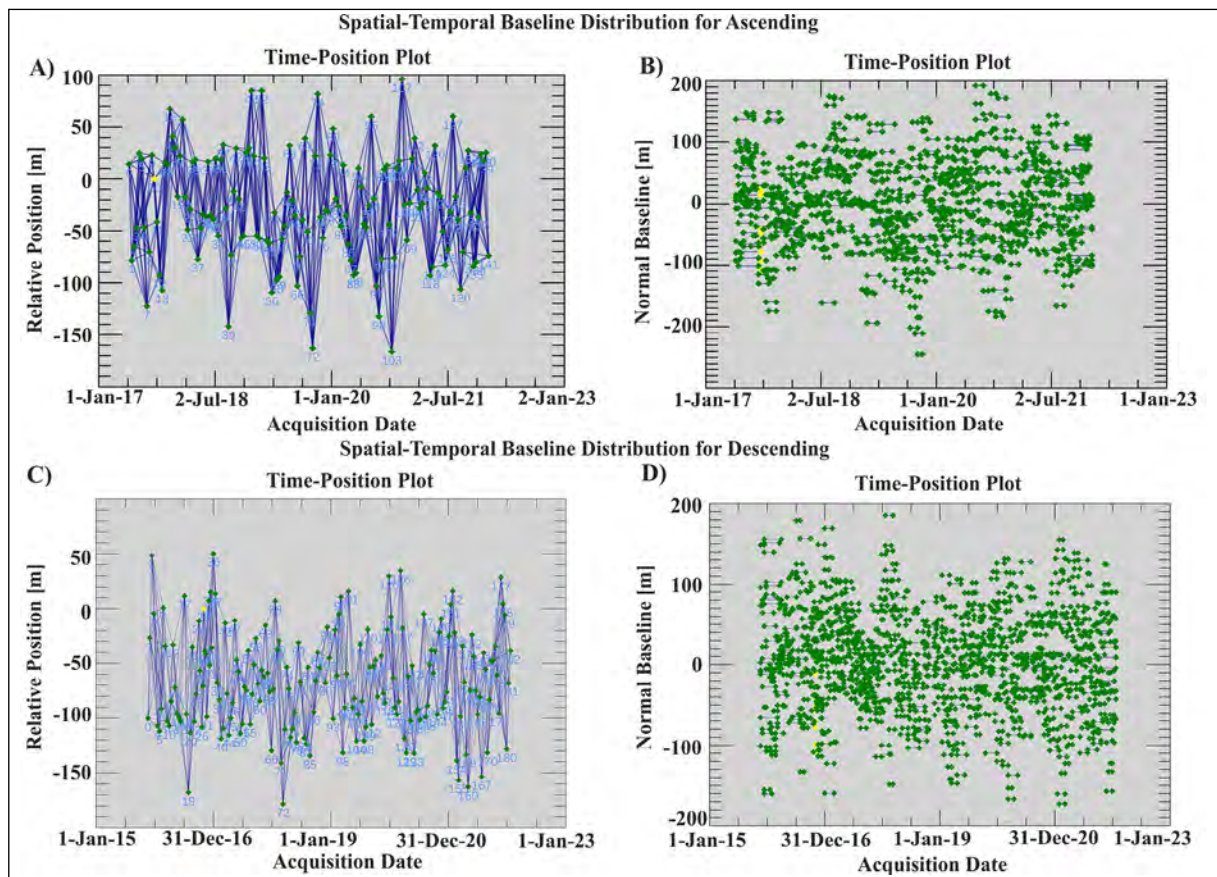


Figure 3- a) and b) Links between the pairs of SAR images showing the spatio-temporal distribution for ascending and descending, respectively. Each image is represented by a diamond with its ID number, c) and d) Represents the relative positions of all pairs of interferograms generated between Sentinel-1 datasets for ascending and descending, respectively. The yellow diamonds represent the reference image pair (master), while the green diamonds represent the slave image pairs. While, for ascending dataset, the date of master image is 2017/09/20, for descending dataset, the date of master image is 2016/12/31.

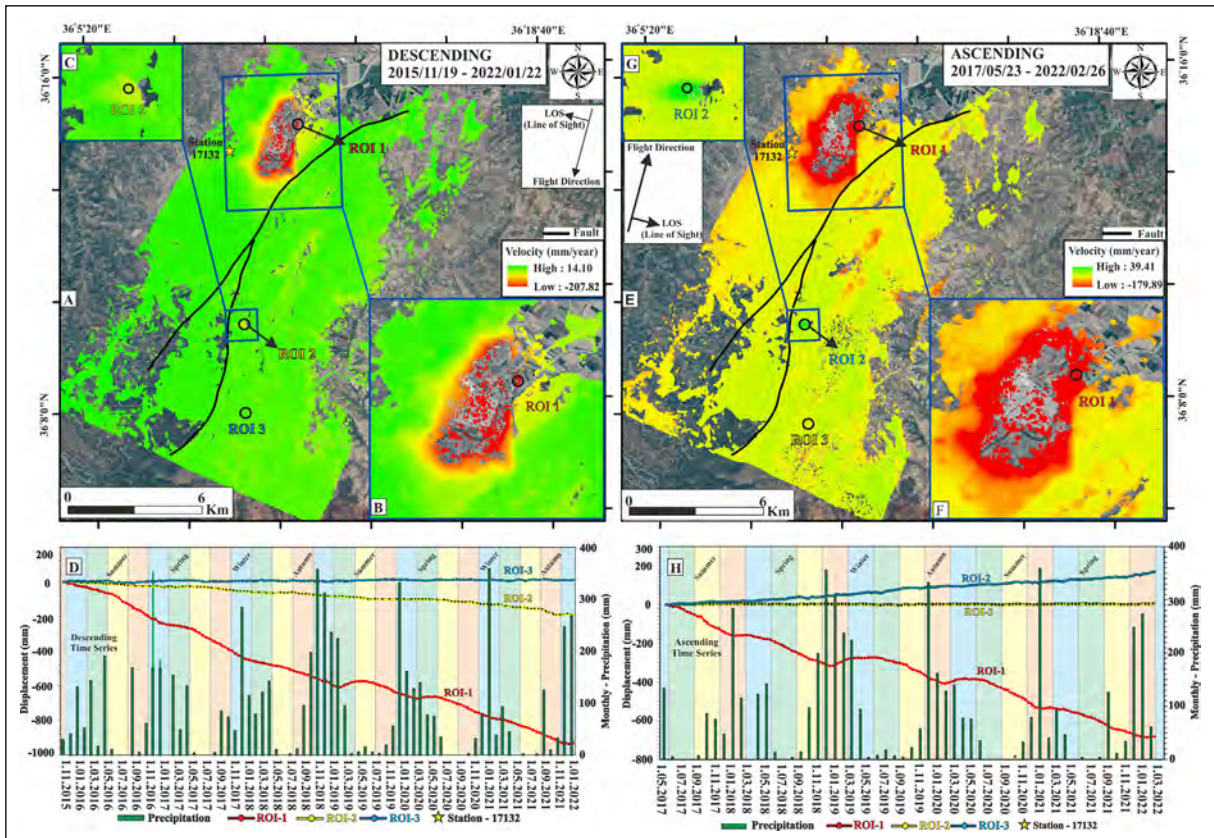


Figure 4- a) and e) Descending and ascending Sentinel-1 datasets of Hatay province illustrate the results of SBAS analysis. Positive values are interpreted as movement towards the satellite line of sight direction (LOS) and negative values as movement away from the satellite direction, b) and f) details of the industrial zone, c) and g) details of landslide zone, d) and h) shows the time series, and bars illustrate the average monthly precipitation data provided by the General Directorate of Meteorology, and colored areas represent seasons. The black lines show the active faults published by the MTA (Emre et al., 2012).

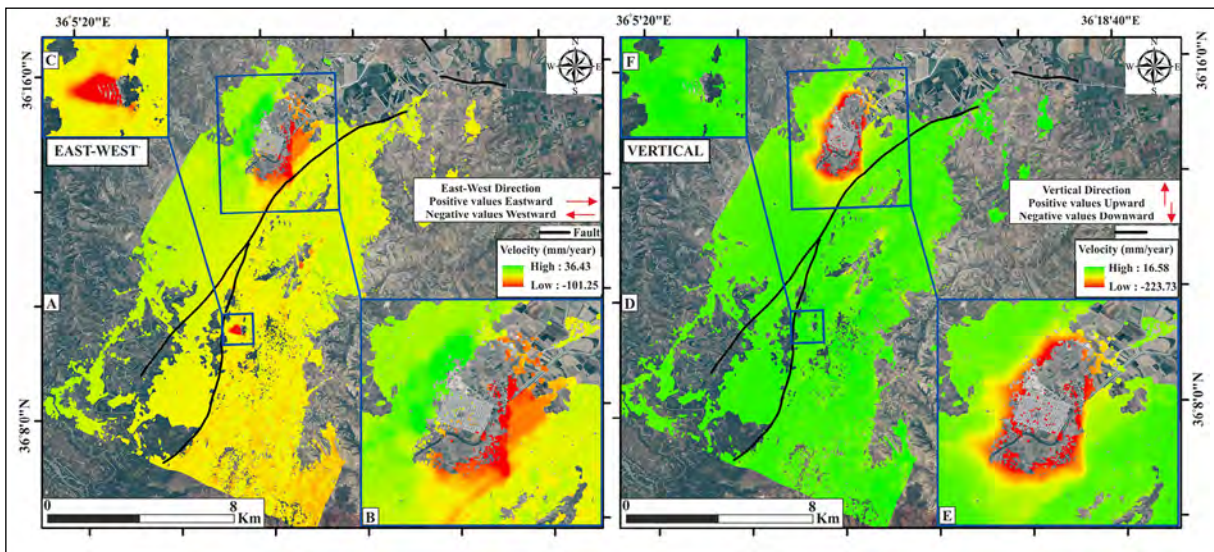


Figure 5- The result of the decomposition of Sentinel-1 descending and ascending data sets belonging to Antakya province, a) east - west component, b) details of Industrial zone, c) Landslide zone, d) vertical component, e) details of Industrial zone and f) Landslide zone. Positive values indicate uplift and negative values indicate subsidence. The black lines show the active faults published by the MTA (Emre et al., 2012).

Table 2- Max and Min velocities and displacement values from Figures 4 and 5.

	Max Velocities (cm/year)	Min Velocities (cm/year)	ROI-1 Displacement (cm)	ROI-2 Displacement (cm)	ROI-3 Displacement (cm)
Ascending 2017/05/23 - 2022/02/26	3.94 cm/year	-17.98 cm/year	~ -70 cm	~ 20 cm	~ 0 cm
Descending 2015/11/19 - 2022/01/22	1.41 cm/year	-20.78 cm/year	~ -90 cm	~ -20 cm	~ 0 cm
Vertical	1.65 cm/year	-22.37 cm/year			
East-West	3.64 cm/year	10.12 cm/year			

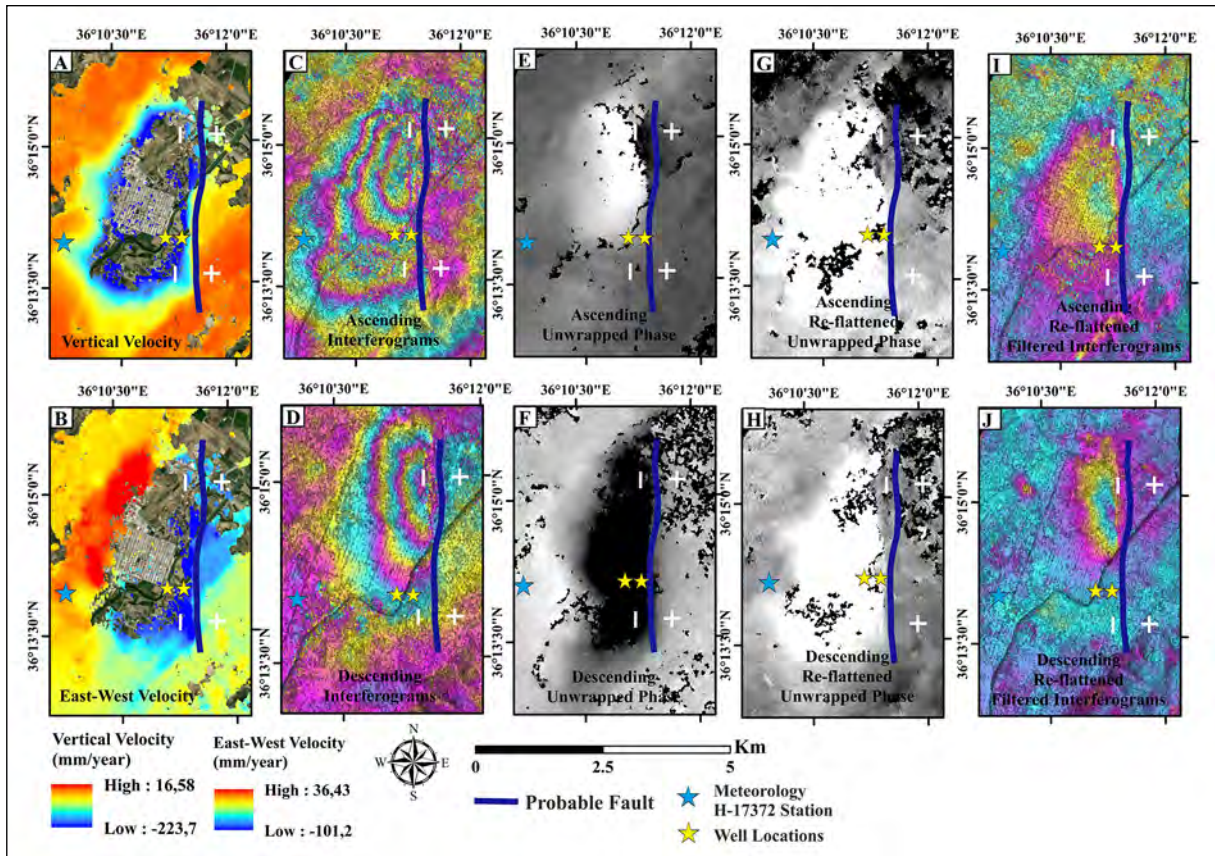


Figure 6- Deformation area of industrial zone of the Hatay province, a) Uplift - subsidence deformations. Positive values indicate an uplift; negative values indicate a subsidence, b) East-west deformations, Positive values mean east direction, and negative values mean west direction, c) and d) ascending (2018/07/29 – 2018/09/27) and descending (2019/12/28–2020/02/14) interferogram examples, e) and f) ascending and descending unwrapped phases, g) and h) ascending and descending re-flattened unwrapped phases, i) and j) ascending and descending re-flattened filtered interferograms, respectively.

which is seen in both ascending and descending data in both interferograms and unwrapped phases. Based on the well information in figures 1f and 1g and the data in Figure 6, the eastern boundary of the deformation zone indicates a probable normal fault.

In Figures 7a and 8a, the time series profiles obtained from the ascending and descending SBAS results of the Industrial zone of Hatay province and the Google Earth profiles corresponding to the relevant

profiles are shown, respectively. Both figures depict the deformation amounts in the time series in the LOS direction. In Figures 7a and 8a, a sharp deformation area was determined in the area to the northwest of the industrial zone in the area where the meandering of the Asi River begins (Figure 7a - profiles B-B', C-C' and H-H'; and Figure 8a profiles C-C' and H-H'). Surface deformations, which are relatively similar to the bowl structure, have been observed in the remaining regions

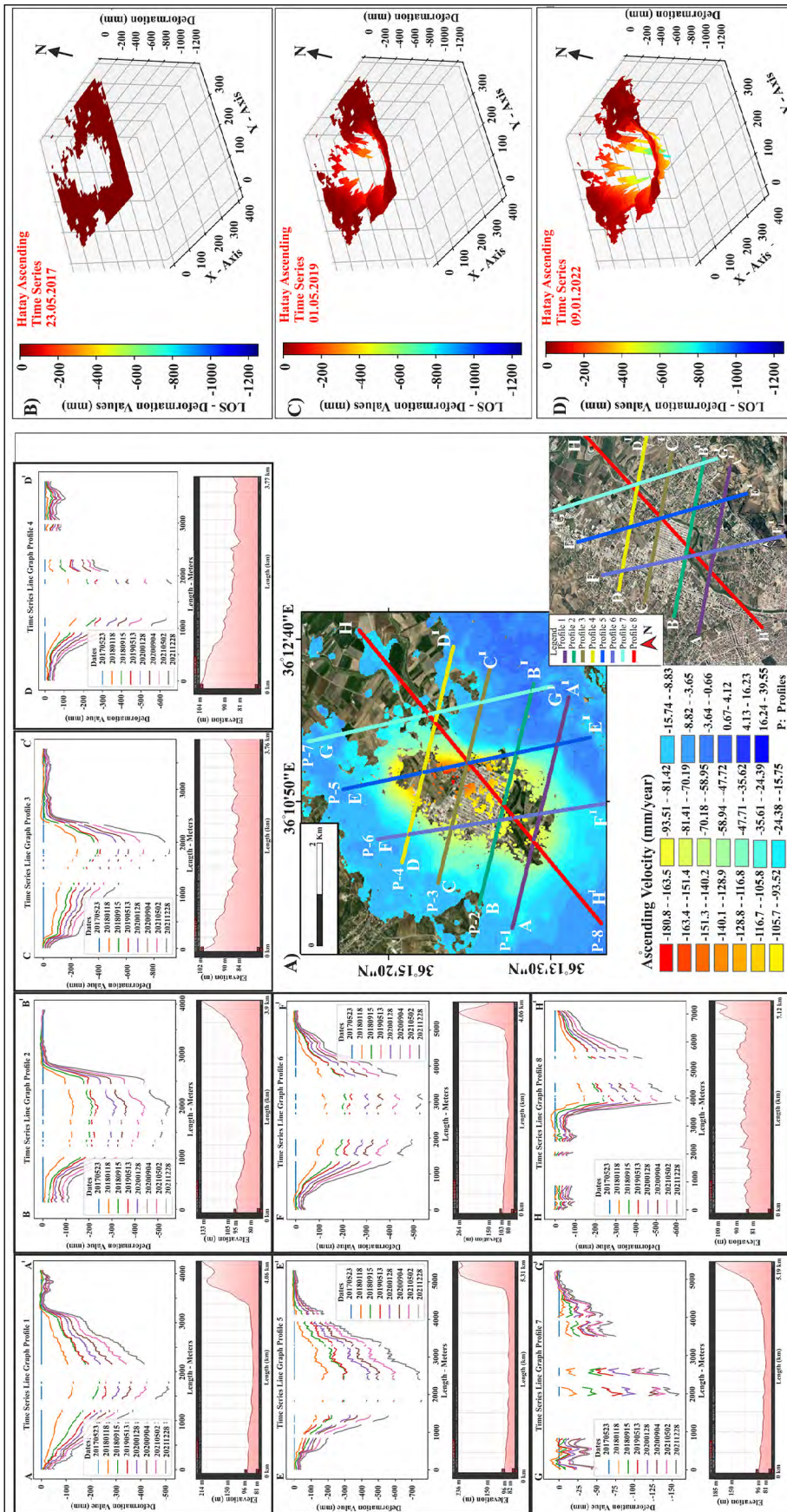


Figure 7 - a) Time series cross sections for ascending geometry and google earth terrain profiles of the Hatay industrial zone, The amount of velocity in time series interprets as the direction of LOS, b), c) and d) 3D view of the time series corresponding to the specified dates for ascending geometry.

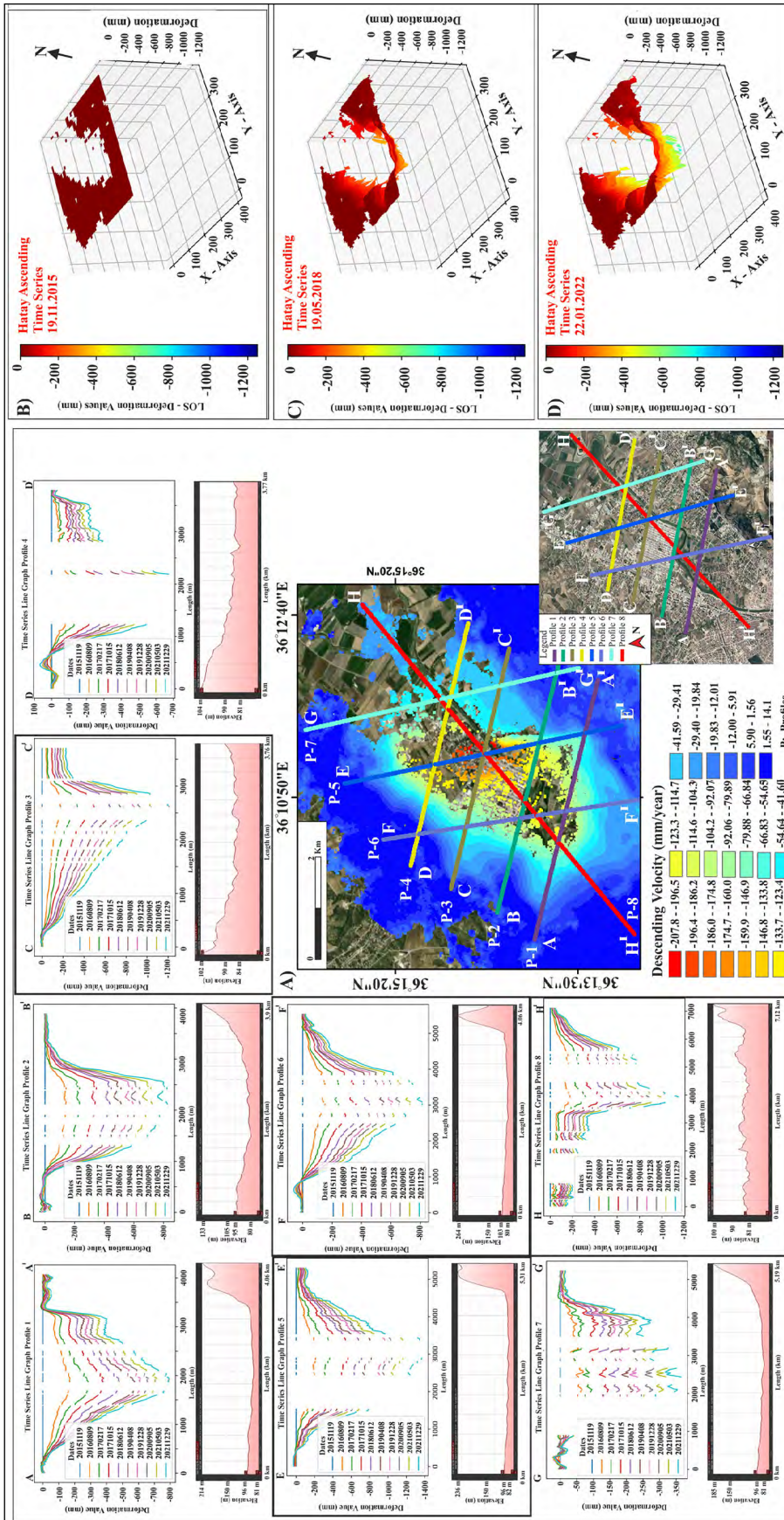


Figure 8- a) Time series cross sections for descending geometry and google earth terrain profiles of the Hatay industrial zone. The amount of velocity in time series interprets as the direction of LOS, b), c) and d) 3D view of the time series corresponding to the specified dates for descending geometry.

except for the northwest of the industrial zone (Figure 7a profiles A-A', E-E' and F-F' and; Figure 8a profiles E-E' and F-F'). Figures 7b and 8b show the 3D view of the time series corresponding to the dates for ascending and descending geometries, respectively.

The second deformation area is the landslide zone located in the central part of the study area (Figure 9). Figure 9a shows the 3D image of the landslide zone obtained from the orthophotos and Figure 9b shows the satellite orbital movements. Figure 9c shows the deformation field of the landslide zone obtained from the data with ascending geometry. Red areas show movement towards the satellite direction (LOS direction) with a velocity of 3.0 cm/year. In Figure 9d, the area of deformation with light green,

there is a movement away from the satellite direction (LOS direction) at a rate of 4.5 cm/year. Figure 9e shows movements in east-west direction. There is a westward movement of the landslide zone at a rate of approximately -8.5 cm/year (Figure 9e). Figure 9f shows the vertical movements in the landslide zone. Accordingly, the landslide zone shows a subsidence at a rate of approximately 4 cm/year (Figure 9f). Figure 9g shows the east-west oriented A-A' elevation profile taken from Google Earth.

The results obtained are divided into two parts. Accordingly, the first study area is the industrial zone and the second area is the landslide zone. In the following sections, their deformations were characterized in detail.

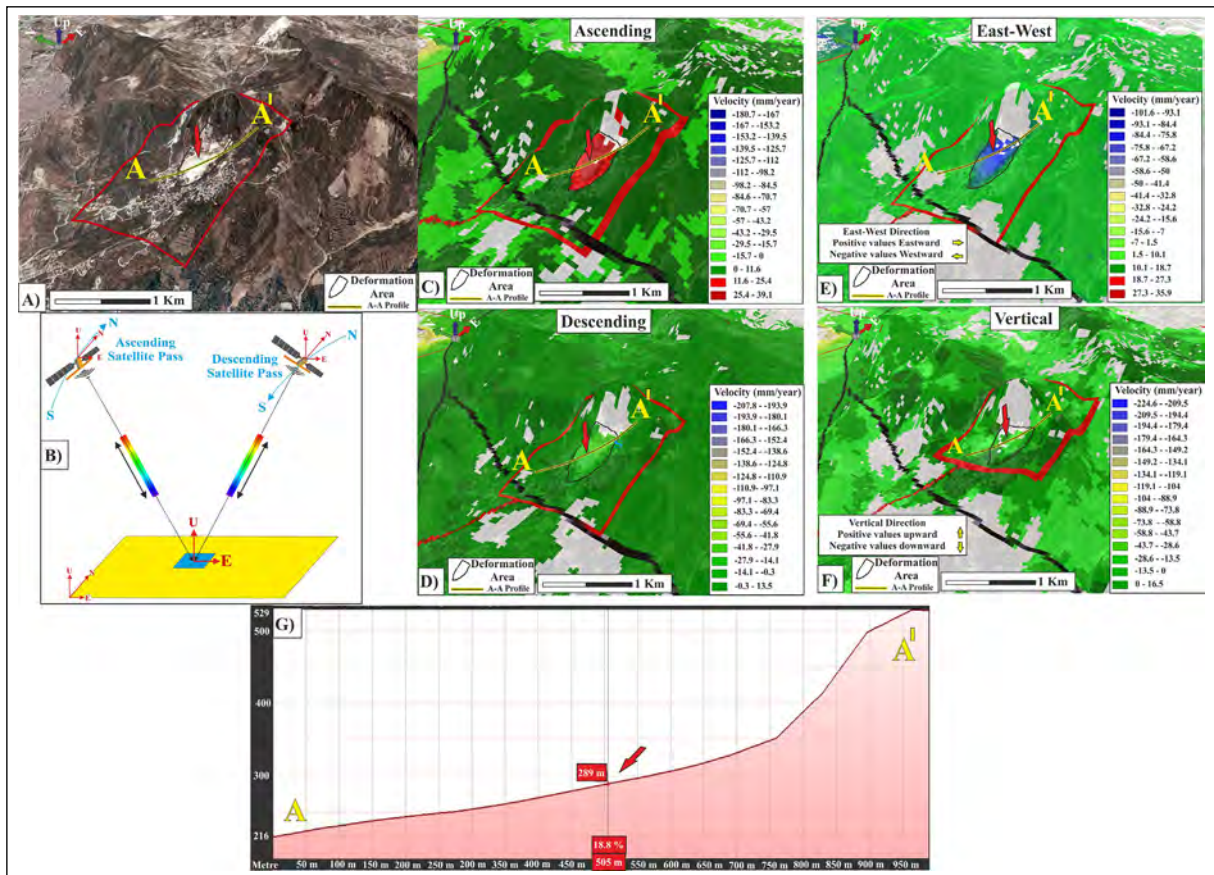


Figure 9- Deformation images of the landslide zone, a) 3D image created from orthophotos of the landslide zone, b) Satellite movement geometries, c) and d) ascending and descending velocity of deformation. While positive values are interpreted as movements towards the satellite direction, negative values are interpreted as movements away from the satellite direction, e) East - west deformations. Positive values are interpreted in the east direction and negative values are interpreted in the west direction, f) Vertical deformation. Negative values indicate subsidence and positive values indicate uplifting, g) Elevation profile from Google Earth corresponding to profile A-A' in figures 12a, 12c, 12d and 12e.

#### 4.2. Evaluation of Surface Deformations of the Industrial Zone

In the industrial zone located northwest of the study area, the surface deformation in both the east-west direction (Figure 5b) and subsidence (Figure 5e) is observed in an area of approximately 9.5 km<sup>2</sup>. According to the profiles taken from Figures 8, 9, 10, and 11 it is evident that there is a bowl structure.

It was observed that the eastern part of this bowl structure moved relatively faster than the western part (Figure 5b). In the profiles taken from the deformation areas, obtained from the ascending and descending datasets (Figures 8 and 10) and the 3D models (Figures 13 and 15), a sharp deformation difference occurs in the eastern border of the deformation area. The deformation is caused by different geological units in the eastern and western regions and the presence of a probable fault system (Figures 1f and 1g). In Figure 1g, the well log 55260, which is close to the center of the deformation zone, shows that the clay unit reaches

about 150 m in thickness. However, in Figure 1f, the well log 41982 obtained from the eastern part of the deformation zone shows that this same clay unit becomes thinner (8 m thick) and cuts sandstone and limestone. For this reason, it was determined that the deformation in the relatively less resistant clay unit reaching 150 m was higher than the more resistant sandstone and limestone in the eastern region, leading to a sharp deformation difference between these two units. For this reason, a probable fault plane between the two units was considered as shown in Figure 12A. This probable fault structure is also supported by the interferograms in Figure 6, which show that the fringe patterns become wider towards the west and are abruptly interrupted in the east (Figure 6). This probable fault zone is visible in the time series profiles (C-C' - H-H') taken from Figures 8 and 10.

From the time series of the deformation fields obtained from ascending and descending geometries (Figures 4d and 4h), it is seen that the deformations

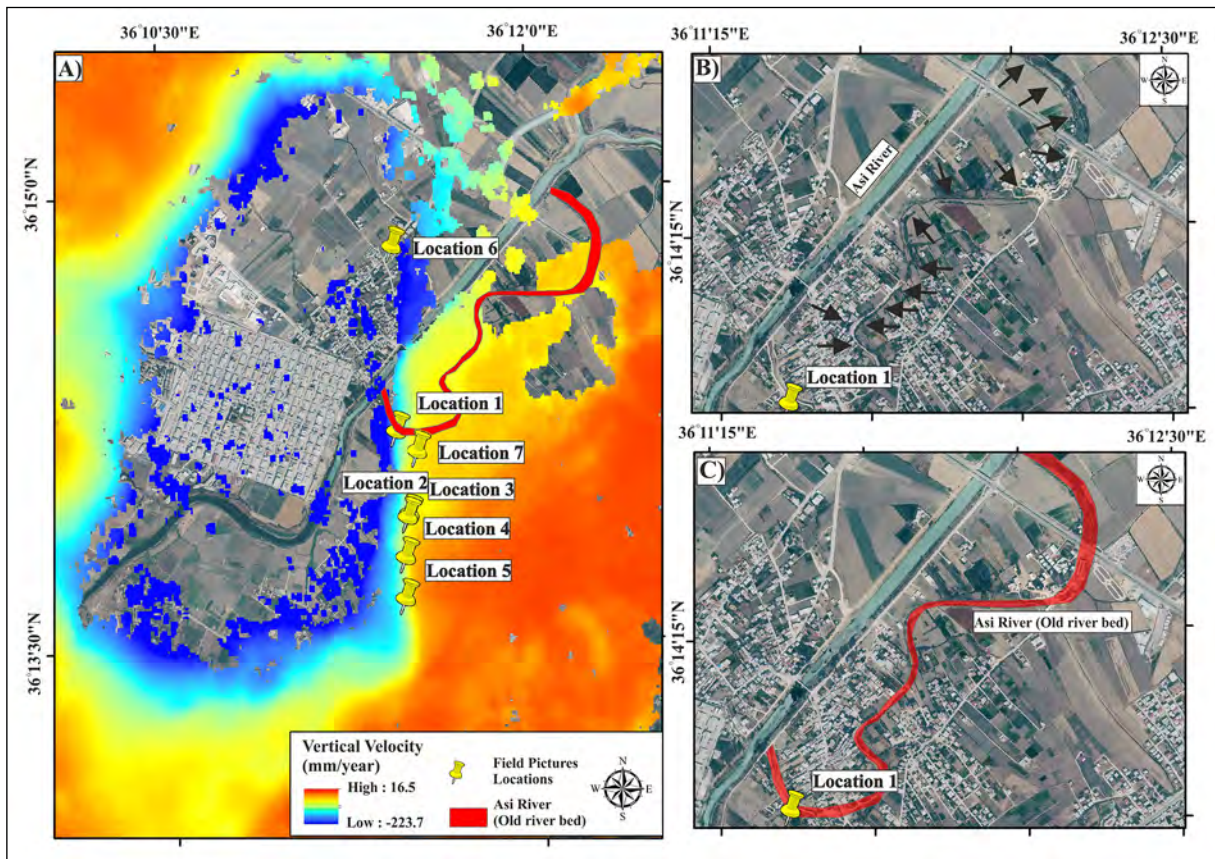


Figure 10- a) The vertical deformation for the industrial zone and the locations of the photos taken from the field (Figure 10a taken from Figure 5e). Positive values show uplift and negative values show subsidence, b) and c) old river bed detected from orthophoto images.

in winter and autumn seasons are relatively less than in spring and summer seasons. The amount of deformation accelerates in summer and spring (Figures 4d and 4h). This is thought to be due to the decrease in water use in the winter and autumn months or excessive rainfall. The graphs in Figures 4d and 4h show that the amount of water that tries to reach its previous level (recharging) is due to precipitation during the autumn and winter seasons. For all these reasons it was evaluated that there was an indirect correlation between the precipitation data obtained and the deformation rate (Figures 4d and 4h).

The surface deformation in the region is thought to have several causes. The main reason is excessive or improper groundwater usage accompanied by the industrial zone laying in the center of this deformation. It is determined that this region and its surroundings have been deformed in the east - west and vertical direction, resembling a bowl structure.

The second factor that affects this deformation is the geological structure of the units in the region. The location of the well 55260, which has a thicker clay unit that is relatively less resistant, is located further west than the well 41982 which lies closer to the center of the deformation zone (Figures 1g and 1f). Given the well log data, the eastern side of the deformation area is closer to the bedrock and the sudden deformation here is associated with the probable fault plane (Figure 12a). Figures 12c and 12d show the interferogram model with surface deformation corresponding to the probable well water withdrawal and Figures 12e and 12f show the expected interferogram models with surface deformation in case of probable faulting. The interferogram structures in Figure 6 obtained as a result of data processing coincide with the interferogram patterns in Figure 12f (Figures 12g and 12h). In addition, the time series profiles as shown in Figures 12i and 12j, the sudden downward movement of the eastern side of the bowl structure and the



Figure 11- Photos were taken during field studies (Locations are shown in Figure 10a).

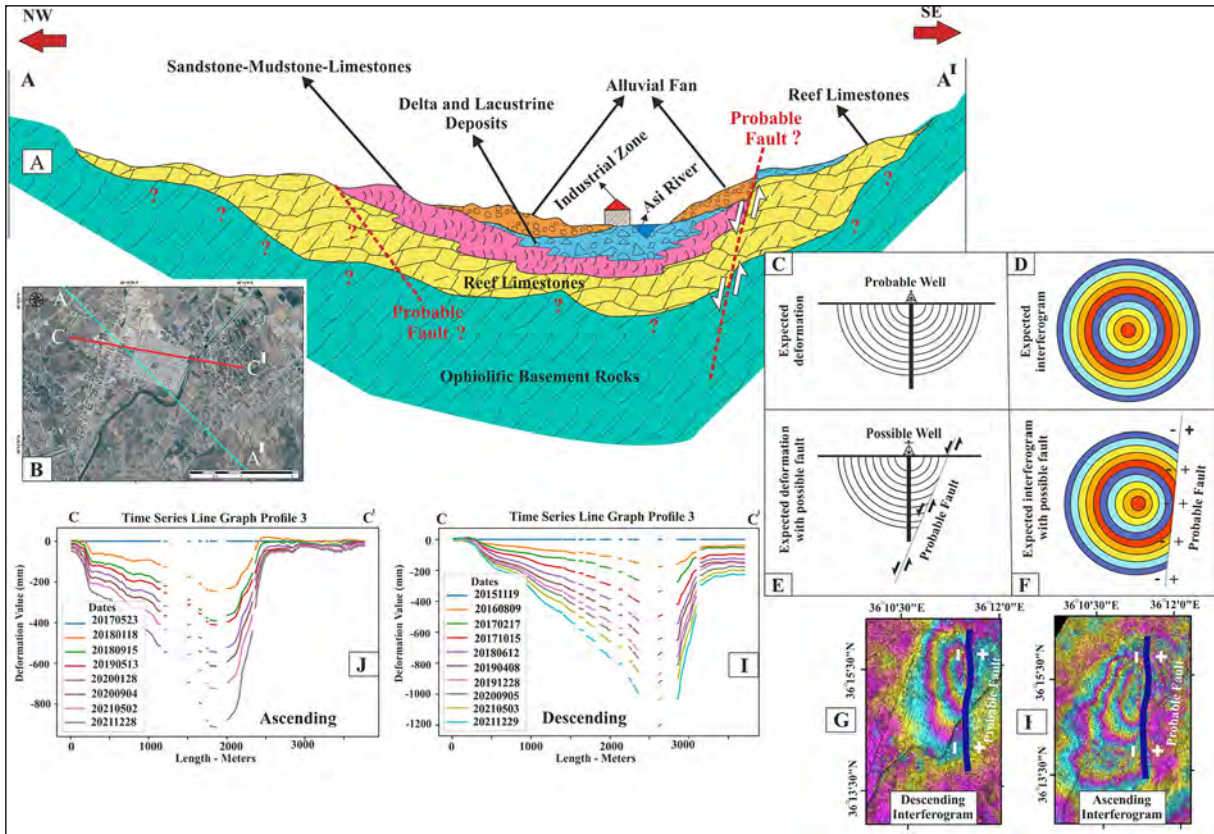


Figure 12- a) Geological cross-section and probable fault model formed on the industrial zone, b) Orthophoto image corresponding to the A-A' section, c) The expected deformation depth cross-section with possible well, d) The expected interferogram in the case of deformation due to draft in figure c, e) The expected deformation area due to the draft in the case of a probable normal fault in figure a, f) The expected interferogram in the case of deformation due to draft in Figure e, g) and h) sample interferograms were taken from Figures 6d and 6c, j) and i) time series profiles from Figures 7a and 8a.

relatively slower downward movement of the western side with certain time intervals indicate the presence of a probable fault systems on the eastern side. This occurs because the eastern block of the bowl structure is closer to the bedrock (Figure 12a).

Another factor affecting this deformation area is the meandering of the Asi River where the industrial zone is located (Figure 10a). It is considered that the velocity of the Asi River slows down in this region (due to meandering) and the amount of water accumulated here is higher than in other regions (Figure 10a). In addition, due to the reclamation of the Asi River outside the deformation area (Figures 14b and 13c), it is considered that the water velocity of the Asi River in this region has changed, its natural structure has deteriorated and this situation has affected the deformation area. The weight of the industrial zone and the use of water are foreseen as a reason also affecting the deformation in the region.

During the field surveys, it was reported that the houses and business centers in the area were affected by deformation, and even the Barış Arslan Elementary and Intermediate School (Location 5) was closed due to deformation (Figures 14h and 14i). The General Directorate of Natural Disasters Report prepared by Kuran et al. (2006), states that there was a deformation in 2004-2005 and even some houses in the region were demolished intentionally due to deformation. Viewing the results in this report in this study, it appears that the deformation in 2004 has continued until 2022.

In summary, it is thought that the main causes of deformation in the region are primarily the groundwater level and excess water use in the region due to the rainfall data, time series (Figures 4d and 4h) and the bowl-shaped structure of the deformation (Figures 8, 9, 10 and 11). Another factor is thought to be the geological structure of the region, which is located in the middle of clayey alluvial units which

is compacted due to the weight of the industrial zone (Figure 1e). The proximity of the deformation area to the bedrock in the eastern parts and the thicker levels of clay units in the western parts are thought to account for the sharp deformation difference in the eastern block (Figure 12). This deformation boundary is interpreted as a probable fault due to tectonism (Figures 6 and 12). Finally, another reason affecting the deformation is the reclamation and straightening of a section of the Asi River and the meandering structure in the deformation zone (Figure 10).

Similar to the situation in Mexico City, where the surface deformation due to excessive groundwater withdrawal reached 35 cm per year (Strozzi and Wegmuller, 1999; Cabral-Cano et al., 2008; Osmanoglu et al., 2011, Cigna and Tapete, 2021), the annual deformation in the industrial zone of the Hatay province are about 3 cm in the east direction, about 10 cm in the west direction and about 22 cm in the vertical direction.

#### 4.3. Evaluation of the Landslide Zone Surface Deformations

The second study area where significant surface deformation is observed is the area corresponding to the landslide zone. The area of the landslide zone with a surface deformation of about 0.3 km<sup>2</sup> is shown in Figure 9a. The surface deformation vectors obtained in Figures 9c and 9d are decomposed into their components, as deformation movements both in the eastern direction and subsidence. It is seen that the eastward movement is about 7 cm/year and the subsidence movement is about 2 cm/year. Comparing Figures 9e and 9f, it can be seen that the velocity of the area in this region is higher for the eastern component as well as the subsidence motion. The geographical structure of the area and the eastern slope of the mountainous area support the deformation movement in the eastern direction (Figures 9a and 9g). Therefore, the deformation here is considered as a landslide zone.

### 5. Conclusion

It is crucial to investigate surface deformations that may occur in large cities due to the natural or anthropogenic causes and take measures for the future. In this study, the surface deformations of the

Hatay province were revealed with the remote sensing method InSAR-SBAS, and the results of the study were checked by field studies, average precipitation data, well data and geological findings. Surface deformations, time series and models of the industrial and landslide zone in the study area were presented.

As a result, four main factors are thought to affect the industrial zone's deformation;

1. The most important factor affecting the deformation in the industrial zone is the groundwater level. Time series and average monthly precipitation data show that the deformation accelerates in the summer and spring, and decreases in the winter and fall. This supports the idea that the deformation in the region is related to the excess water use and precipitation rates.

2. The industrial zone is located on clayey alluvial units. Due to its weight and the geologic structure of the region, the nature of the deformation is affected. The difference in deformation rates between the eastern and western borders shows the presence of a probable fault on the eastern border. Probable fault in the study area may act as barriers to the horizontal migration of the groundwater. The fact is that the ground deformation rates are still high for most of the urban area. Improved urban planning and water management could reduce subsidence or changing water extraction from various aquifers might be the solution to prevent subsidence.

3. There is an indirect correlation between the precipitation data obtained and the deformation rate. The deformations in the winter and autumn are relatively less than in the spring and summer.

4. The meandering structure of the Asi River can affect the deformation because the changing course of the river increases the rate of deformation.

The second studied area was identified as the landslide zone which shows deformation in both eastern and vertical directions. Considering the Hatay location in the 1st degree earthquake zone, other geophysical studies are recommended for the thorough investigation of water use in the area. Further research should be conducted to determine the deformation and

how could this affect the Infrastructural integrity of the city. In addition, the province of Hatay should take similar measures to that of Mexico City by prohibiting water withdrawal and drilling of new wells. Providing that the decline in water level corresponds with the decrease in subsidence in the following years.

### Data Availability

Sentinel-1 data are available online through Copernicus (<https://scihub.copernicus.eu>) platforms. Precise orbits were downloaded from European Space Agency's Sentinel1 website (<https://qc.sentinel1.eo.esa.int/>, in March 2022). SRTM data are provided on Earthdata portal (<https://earthdata.nasa.gov>). We thank the Turkish State Hydraulic Works for providing groundwater level data and the Turkish State Meteorological Service for the precipitation data. Thanks to the European Space Agency for giving free access to the Sentinel-1 data through the Copernicus Hub.

### Acknowledgments

This study was supported by the General Directorate of Mineral Research and Exploration (MTA), Department of Geological Researches, within the scope of the "Investigation of the Activity of Active Faults on Cities" Project (Project No: 2022-30-14-02-2) conducted between 2021-2022. We express our gratitude to Dr. Bahadır Şahin, Dr. Selim Özalp, Hasan Elmacı, Cem Özerk, and Adem Özata for their valuable contributions to field observations and discussions. Additionally, we thank Prof. Dr. Derman Dondurur for his constructive comments. Our thanks are also extended to Doç. Dr. Şule Gürboğa, the editor of the Bulletin of Mineral Research and Exploration, and the three referees. Finally, we convey our deepest appreciation and heartfelt gratitude to Tiffany Faller Karaca for her support.

### References

- Aimaiti, Y., Yamazaki, F., Liu, W., Kasimu, A. 2017. Monitoring of land-surface deformation in the Karamay oilfield, Xinjiang, China, using SAR interferometry. *Applied Sciences* 7, 8.
- Amelung, F., Galloway, D. L., Bell, J. W., Zebker, H. A., Lacznik, R. J. 1999. Sensing the ups and downs of Las Vegas: InSAR reveals structural control of land subsidence and aquifer-system deformation. *Geology* 27, 6, 483–486.
- Anderssohn, J., Wetzel, H. U., Walter, T. R., Motagh, M., Djamour, Y., Kaufmann, H. 2008. Land subsidence pattern controlled by old alpine basement faults in the Kashmar Valley, northeast Iran: Results from InSAR and leveling. *Geophysical Journal International* 174, 1, 287–294.
- Aslan, G., Çakır, Z., Ergintav, S., Lasserre, C., Renard, F. 2018. Analysis of secular ground motions in istanbul from a long-term InSAR time-series (1992-2017). *Remote Sensing* 10, 3.
- Aslan, G., Çakır, Z., Lasserre, C., Renard, F. 2019. Investigating subsidence in the Bursa Plain, Turkey, using ascending and descending sentinel-1 satellite data. *Remote Sensing* 11, 1.
- Béjar-Pizarro, M., Guardiola-Albert, C., García-Cárdenas, R. P., Herrera, G., Barra, A., Molina, A. L., Tessitore, S., Staller, A., Ortega-Becerril, J. A., García-García, R. P. 2016. Interpolation of GPS and geological data using InSAR deformation maps: Method and application to land subsidence in the alto guadalestín aquifer (SE Spain). *Remote Sensing* 8, 11.
- Bell, J. W., Amelung, F., Ferretti, A., Bianchi, M., Novali, F. 2008. Permanent scatterer InSAR reveals seasonal and long-term aquifer-system response to groundwater pumping and artificial recharge. *Water Resources Research* 44, 2.
- Berardino, P., Fornaro, G., Lanari, R., Sansosti, E. 2002. A new algorithm for surface deformation monitoring based on small baseline differential SAR interferograms. *IEEE Transactions on Geoscience and Remote Sensing* 40,1, 2375–2383.
- Brunori, C. A., Bignami, C., Albano, M., Zucca, F., Samsonov, S., Groppelli, G., Norini, G., Saroli, M., Stramondo, S. 2015. Land subsidence, ground fissures and buried faults: InSAR monitoring of Ciudad Guzmán (Jalisco, Mexico). *Remote Sensing* 7, 7, 8610–8630.
- Burgmann, R., Rosen, P. A., Fielding, E. J. 2000. Synthetic aperture radar interferometry to measure earth's surface topography and its deformation. *Annual Review of Earth and Planetary Sciences* 28.
- Cabral-Cano, E., Dixon, T. H., Miralles-Wilhelm, F., Díaz-Molina, O., Sánchez-Zamora, O., Carande, R. E. 2008. Space geodetic imaging of rapid ground subsidence in Mexico City. *Bulletin of the Geological Society of America* 120, 11–12, 1556–1566.
- Cabral-Cano, E., Solano-Rojas, D., Oliver-Cabrera, T., Wdowinski, S., Chaussard, E., Salazar-Tlaczani, L., Cigna, F., DeMets, C., Pacheco-Martinez,

- J. 2015. Satellite geodesy tools for ground subsidence and associated shallow faulting hazard assessment in central Mexico. *Proceedings of the International Association of Hydrological Sciences* 372, 255–260.
- Conesa-García, C., Tomás, R., Herrera, G., López-Bermúdez, F., Cano, M., Navarro-Hervás, F., Pérez-Cutillas, P. 2016. Deformational behaviours of alluvial units detected by advanced radar interferometry in the vega media of the segura river, southeast Spain. *Geografiska Annaler, Series A: Physical Geography* 98, 1, 15–38.
- Cigna, F., Tapete, D. 2021. Present-day land subsidence rates, surface faulting hazard and risk in Mexico City with 2014–2020 Sentinel-1 IW InSAR. *Remote Sensing of Environment* 253.
- DSİ, 2022. General Directorate of General Directorate of State Hydraulic Works.
- Emre, Ö., Duman, T. Y., Olgun, Ş., 2012. 1:250,000 Scale Active Fault Map Series of Turkey, Antakya (NJ 37-13) Quadrangle. Serial Number: 39 General Directorate of Mineral Research and Exploration, Ankara, Turkey.
- Ford, D., Williams, P. W. 1989. *Karst Geomorphology and Hydrology*. Unwin Hyman, London/Boston.
- Hung, W. C., Hwang, C., Chen, Y. A., Chang, C. P., Yen, J. Y., Hooper, A., Yang, C. Y. 2011. Surface deformation from persistent scatterers SAR interferometry and fusion with leveling data: A case study over the Choushui River Alluvial Fan, Taiwan. *Remote Sensing of Environment* 115, 4, 957–967.
- İmamoğlu, M., Kahraman, F., Cakir, Z., Sanli, F. B. 2019. Ground deformation analysis of Bolvadin (W. Turkey) by means of multi-temporal InSAR techniques and sentinel-1 data. *Remote Sensing* 11, 9.
- Karaca, S. O., Abir, I. A., Khan, S. D., Özsayın, E., Qureshi, K. A. 2021. Neotectonics of The Western Suleiman Fold Belt, Pakistan: Evidence for bookshelf faulting. *Remote Sensing* 13, 18.
- Khan, S. D., Huang, Z., Karacay, A. 2014. Study of ground subsidence in northwest Harris county using GPS, LiDAR, and InSAR techniques. *Natural Hazards* 73, 3, 1143–1173.
- Khan, S. D., Gadea, O. C. A., Tello Alvarado, A., Tirmizi, O. A. 2022. Surface Deformation Analysis of the Houston Area Using Time Series Interferometry and Emerging Hot Spot Analysis. *Remote Sensing* 14, 15.
- Kuran, U., Gürbüz, M., Mirzaoğlu, M., Şahinbaz, D., Eravcı, B., Yaman, M. 2006. Antakya-Güzelburç Belediyesi Yerleşim Sahasına Ait Jeolojik ve Jeofizik Ön Etüt Raporu, Afet İşleri Genel Müdürlüğü Deprem Araştırma Dairesi.
- Liu, X., Zhao, C., Zhang, Q., Peng, J., Zhu, W., Lu, Z. 2018. Multi-temporal loss landslide inventory mapping with C-, X- and L-band SAR Datasets-A case study of Heifangtai loess landslides, China. *Remote Sensing* 10, 11.
- Liu, X., Zhao, C., Zhang, Q., Lu, Z., Li, Z., Yang, C., Zhu, W., Liu-Zeng, J., Chen, L., Liu, C. 2021. Integration of Sentinel-1 and ALOS/PALSAR-2 SAR datasets for mapping active landslides along the Jinsha River corridor, China. *Engineering Geology* 284.
- López-Quiroz, P., Doin, M. P., Tupin, F., Briole, P., Nicolas, J. M. 2009. Time series analysis of Mexico City subsidence constrained by radar interferometry. *Journal of Applied Geophysics* 69, 1, 1–15.
- Mahmoud, S., Reilinger, R., McClusky, S., Vernant, P., Tealeb, A. 2005. GPS evidence for northward motion of the Sinai Block: Implications for E. Mediterranean tectonics. *Earth and Planetary Science Letters* 238, 1–2, 217–224.
- Mahmouda, Y., Masson, F., Meghraoui, M., Cakir, Z., Alchalbi, A., Yavasoglu, H., Yönlü, O., Daoud, M., Ergintav, S., İnan, S. 2013. Kinematic study at the junction of the east anatolian fault and the dead sea fault from GPS measurements. *Journal of Geodynamics* 67, 30–39.
- Massonnet, D., Feigl, K. L. 1998. Radar interferometry and its application to changes in the earth's surface. *Reviews of Geophysics* 36, 4, 441–500.
- Motagh, M., Djamour, Y., Walter, T. R., Wetzel, H. U., Zschau, J., Arabi, S. 2007. Land subsidence in Mashhad Valley, northeast Iran: Results from InSAR, leveling and GPS. *Geophysical Journal International* 168, 2, 518–526.
- Motagh, M., Shamshiri, R., Haghshenas Haghighi, M., Wetzel, H. U., Akbari, B., Nahavandchi, H., Roessner, S., Arabi, S. 2017. Quantifying groundwater exploitation induced subsidence in the Rafsanjan plain, southeastern Iran, using InSAR time-series and in situ measurements. *Engineering Geology* 218, 134–151.
- Orhan, O. 2021. Monitoring of land subsidence due to excessive groundwater extraction using small baseline subset technique in Konya, Turkey. *Environmental Monitoring and Assessment* 193, 4.
- Osmanoğlu, B., Dixon, T. H., Wdowinski, S., Cabral-Cano, E., Jiang, Y. 2011. Mexico City subsidence observed with persistent scatterer InSAR. *International Journal of Applied Earth Observation and Geoinformation* 13, 1, 1–12.

- Raucoules, D., Colesanti, C., Carnec, C. 2007. Use of SAR interferometry for detecting and assessing ground subsidence. *Comptes Rendus - Geoscience* 339, 5, 289–302.
- Rucci, A., Ferretti, A., Monti Guarnieri, A., Rocca, F. 2012. Sentinel 1 SAR interferometry applications: The outlook for sub millimeter measurements. *Remote Sensing of Environment* 120, 156–163.
- Sarıfakıoğlu, E. 2018. Türkiye Jeoloji Haritaları Serisi 1/100.000 Ölçekli Antakya P36-P37 ve Hama R36 Paftaları, Maden Tetkik ve Arama Genel Müdürlüğü, Ankara.
- Simons, M., Rosen, P. A. 2015. Interferometric Synthetic Aperture Radar Geodesy. In *Treatise on Geophysics: Second Edition* 3, 339-385.
- Solari, L., del Soldato, M., Bianchini, S., Ciampalini, A., Ezquerro, P., Montalti, R., Raspini, F., Moretti, S. 2018. From ERS 1/2 to Sentinel-1: Subsidence Monitoring in Italy in the Last Two Decades. In *Frontiers in Earth Science* 6.
- Sowter, A., bin Che Amat, M., Cigna, F., Marsh, S., Athab, A., Alshammari, L. 2016. Mexico City land subsidence in 2014–2015 with Sentinel-1 IW TOPS: Results using the Intermittent SBAS (ISBAS) technique. *International Journal of Applied Earth Observation and Geoinformation* 52, 230–242.
- Strozzi, T., Wegmuller, U. 1999. Land Subsidence in Mexico City Mapped by ERS Differential SAR Interferometry.
- Strozzi, T., Wegmiiller, U., Tosl, L., Bitelli, G., Spreckels, V. 2001. Land Subsidence Monitoring with Differential SAR Interferometry.
- Şireci, N., Aslan, G., Çakır, Z. 2021. Long-term spatiotemporal evolution of land subsidence in Konya metropolitan area (Turkey) based on multisensor sar data. *Turkish Journal of Earth Sciences* 30, 5, 681–697.
- Tomás, R., Romero, R., Mulas, J., Marturià, J. J., Mallorquí, J. J., Lopez-Sanchez, J. M., Herrera, G., Gutiérrez, F., González, P. J., Fernández, J., Duque, S., Concha-Dimas, A., Cocksley, G., Castañeda, C., Carrasco, D., Blanco, P. 2014. Radar interferometry techniques for the study of ground subsidence phenomena: A review of practical issues through cases in Spain. *Environmental Earth Sciences* 71, 1, 163–181.
- Tomás, R., Li, Z. 2017. Earth observations for geohazards: Present and future challenges. In *Remote Sensing* 9, 3.
- Waltham, A. C., Fookes, P. G. 2003. Engineering classification of karst ground conditions.
- Wöppelmann, G., le Cozannet, G., de Michele, M., Raucoules, D., Cazenave, A., Garcin, M., Hanson, S., Marcos, M., Santamaría-Gómez, A. 2013. Is land subsidence increasing the exposure to sea level rise in Alexandria, Egypt *Geophysical Research Letters* 40, 12, 2953–2957.
- Yan, Y., Doin, M. P., López-Quiroz, P., Tupin, F., Fruneau, B., Pinel, V., Trouvé, E. 2012. Mexico City subsidence measured by InSAR time series: Joint analysis using PS and SBAS approaches. *IEEE Journal of Selected Topics in Applied Earth Observations and Remote Sensing* 5, 4, 1312–1326.
- Yao, J., Yao, X., Liu, X. 2022. Landslide Detection and Mapping Based on SBAS-InSAR and PS-InSAR: A Case Study in Gongjue County, Tibet, China. *Remote Sensing* 14, 19.
- Yao, X., Li, L., Zhang, Y., Zhou, Z., Liu, X. 2017. Types and characteristics of slow-moving slope geo-hazards recognized by TS-InSAR along Xianshuihe active fault in the eastern Tibet Plateau. *Natural Hazards* 88, 3, 1727–1740.
- Zebker, H.A., Goldstein, R. M. 1986. Topographic Mapping from Interferometric Synthetic Aperture Radar Observations. *Journal of Geophysical Research* 91, 4993-4999.
- Zhang, L., Lu, Z., Ding, X., Jung, H. S., Feng, G., Lee, C. W. 2012. Mapping ground surface deformation using temporarily coherent point SAR interferometry: Application to Los Angeles Basin. *Remote Sensing of Environment* 117, 429–439.
- Zhu, W., Zhang, Q., Ding, X., Zhao, C., Yang, C., Qu, F., Qu, W. 2014. Landslide monitoring by combining of CR-InSAR and GPS techniques. *Advances in Space Research* 53, 3, 430–439.

## Publication Rules for the “Bulletin of the Mineral Research and Exploration”

### 1. Purposes

- To contribute to the establishment of scientific communication issues in earth sciences both in Türkiye and internationally.
- To contribute to economic (mining, oil and gas, geothermal etc.), environmental and social (geoheritage etc.) studies in Türkiye and in the World.
- To make the earth science scientific research and applications made by the MTA on publicly known,
- To use the bulletin as an effective tool in the international publication exchange by keeping it at a high level in terms of quality, scope and format,

### 2. Scope-Attribute

In order for manuscripts to be published in the Bulletin of the Mineral Research and Exploration, they must have at least one of the following qualifications:

#### 2.1. Research Articles and Reviews

##### 2.1.1. Original Scientific Researches

- Such articles cover original scientific research and its results that contribute to the fundamental issues of earth sciences, research and evaluation of underground resources, and examine the environmental problems in terms of earth sciences,
- It covers research that apply new approaches and methods in solving problems related to earth sciences.

##### 2.1.2. Review Articles

- They cover studies that compile previous research on subjects of earth sciences with a critical approach and put forward a new opinion on that subject.

#### 2.2. Criticism and Response Articles

- Articles that criticize all or part of an article of the bulletin in the latest issue are published in the following first issue, if submitted within six months at the latest from the date of publication digitally.
- Before the publication, review articles are sent to the responsible author of the criticized article to make a response.
- If the criticism is not responded within foreseen time, the criticism letter is published alone, subsequent replies are not published. Replies are not allowed to be re-criticized.

- In criticizing and replying, scientific discussion and ethical rules should be followed. Criticism and response manuscripts should not exceed four pages, including figures, if available.

### 2.3. Brief Notes

- In “Brief Notes” section of the Bulletin of the Mineral Research and Exploration, the brief, objective and concise articles reflecting the data obtained from scientific researches and applications carried out in the area of earth sciences or new findings related to previously unknown geosciences in Türkiye are given place.
- The articles arranged in the “Brief Notes” section are published without waiting in the first or in the second issue the latest, after the date they are sent to the Chair of the Editorial Board in order to ensure rapid communication.
- Articles requested to be published in the “Brief Notes” section should not exceed four pages, including all figures and tables.

### 3. Submission and Acceptance for Manuscripts

- The manuscripts submitted to be published in the Bulletin of the Mineral Research and Exploration should be prepared in ENGLISH in accordance with the Publishing Rules of the Bulletin of the Mineral Research and Exploration, and submitted via electronic application at <http://dergi.mta.gov.tr/index.php>.
- The manuscript must not have been previously published partially or completely elsewhere (except in abstract form).
- Manuscripts submitted with the request for publication in the Bulletin of the Mineral Research and Exploration should not exceed 30 pages, including all illustrations. The articles exceeding 30 pages can be published if deemed appropriate by referees and editors.
- In the submitted manuscript, the number of figures and tables should be given in proportion to the main text in a ratio of 1/3.
- Corresponding author is asked to suggest at least three referees for the evaluation of the manuscript. (The proposed referees and the authors should not have any joint work within the last two years).

- Manuscripts that do not comply with the Publishing Rules for the Bulletin of the Mineral Research and Exploration in terms of quality and form are directly returned without being examined in terms of content.
- Manuscripts deemed appropriate in terms of format are sent to at least two expert referees for review by the Editorial Board of the Bulletin of the Mineral Research and Exploration.
- Authors should make the referee corrections and suggestions sent to them within 20 days and upload to the system.
- Comments from referees are evaluated by the Editors and associated editors. Manuscripts deemed necessary to be corrected are sent back to the authors with a request for correction. Whether the suggested corrections have been made or not is checked by the Editorial Board.
- In the revision proposals given by the editors and referees, if there are suggestions that are not accepted by the author and have not been corrected, a report explaining the reason for rejecting these suggestions by the author should be sent to the Editorial Board together with the corrected copies.
- After the last control at the printing stage, the pre-print of the manuscript is sent to the authors in pdf format and the printing control is requested.
- Articles, not accepted for publication are not returned to the authors, for the unpublished articles, a letter is written to the responsible author indicating the reason for rejection.

#### **4. Language and Period of Publication**

- The Bulletin of the Mineral Research and Exploration is published three times a year, each issue as being in English (printed and online) and in Turkish (online) languages.
- The spelling rules of the Turkish Language Association are valid for the spelling rules for the Turkish issue. However, in spelling of the words related to earth sciences, the spelling forms of technical terms are used in accordance with the decision of the Editorial Board (For example; underground, ground, earth's crust, etc.).

#### **5. Spelling Draft**

- The text of the manuscripts to be sent for the first review with the request to be published in the

Bulletin of the Mineral Research and Exploration should be written in A4 (29.7 x 21 cm) size, word format, Times New Roman 10 pt., normal with 2.0 line spacing.

- At the bottom, top, left and right of the page 2.5 cm indent must be left. Formulas that require the use of special letters and symbols should be presented in computer media.
- In all subtitles, the initials of all words must be capital. First degree headings to be used in the article should be written in Times New Roman, 10 pt., bold and left aligned by giving numbers. Secondary headings should be written in Times New Roman, 10 pt., normal font and left aligned by giving numbers. Third-degree headings should be written in Times New Roman, 10 pt., italic font and left-aligned by giving numbers. Fourth-order headings should be written in Times New Roman, 10 pt., italic, aligned to the left, without giving numbers, and the text should continue after the title without a colon and a paragraph (see example article: [www.dergi.mta.gov.tr](http://www.dergi.mta.gov.tr)).
- One blank line should be left after paragraphs in the text.
- Paragraph headings should be written 0.5 mm indentation.
- One article should respectively contain;
  - Title
  - Author's Name and Surname and \* sign
  - Abstract
  - Keywords
  - Introduction
  - Main Text
  - Discussion
  - Results
  - Acknowledgements
  - Reference sections.
- Line and page numbers must be added to the article text.

#### **5.1. Title of the Article**

- The title should reflect the subject of the article as briefly, clearly and adequately as possible. Subjects that are not sufficiently covered in the article should not be included in the title. The first letter of the title

should be capitalized and the other words should be in lowercase letters (except for proper names) in Times New Roman, 10 pt. and bolded.

### **5.2. Author Name, Address and E-Mail Address**

- The first name of the authors should be in lowercase (except the first letter), and the surname should be in capital letter and without any title.
- Only the name of the organization should be specified in the occupational address after the name and surname of the authors (position should not be specified).
- ORCID number should be taken from [www.orcid.org](http://www.orcid.org) and placed under the address.
- In articles written by more than one author, numbers should be placed on surnames of the authors, the address information should be included in the bottom line with a single line spacing. In this section, the corresponding author of the article should be indicated by using an asterisk (\*) and the corresponding author's e-mail, telephone and other contact information must be provided.
- Abbreviations should not be used in writing the author's name and address. Addresses should be given in Turkish in Turkish publication (online) and in English in English publication (printed).

### **5.3. Abstract**

- Abstract should be written at a level that can be understood without referring to the other parts of the article.
- The abstract should be organized as a brief presentation of the sections in the article, reflect the purpose of the article, be informative, and should be written in a way to emphasize new data and results on the subject.
- Short and simple sentences should be used in writing the abstract.
- In the abstract, there should not be any reference to other parts and illustrations of the article or to other articles.
- Information not mentioned in the main text should not be included in the abstract.
- The abstract should not exceed approximately 200 words and should be written as a single paragraph.
- Abstract should be written in Times New Roman, 10 pt., normal text with single line spacing.

- “ABSTRACT” should not be placed for the articles to be included in “Brief Notes” section.
- The English abstract should be given under the heading “ABSTRACT”.

### **5.4. Keywords**

In order to facilitate searches, five keywords that will indicate the general content of the article should be selected and specified in this section. Words used in the title should not be repeated.

### **5.5. Introduction**

- In this section, the necessary information for preparatory and facilitative to understand the article such as the purpose of the study, its location, methods of study and previous reviews on the subject should be given.
- If an unusual way is followed in naming, classification and abbreviations within the text of the manuscript, its reason should be stated in this section.
- Each of the topics to be included in this section can create a separate paragraph or a subtitle can be given for each of them when necessary (e.g. method, material, terminology and etc.).
- This section can again be used when reminder information is needed to facilitate the understanding of the article (e.g. statistical information, formulas, experimental or application methods and etc.).

### **5.6. Main Body of Article**

- Constitutes the main body of the article.
- In this section, the data, findings and opinions that are intended to be transferred to the reader on the subject are mentioned.
- The data used in other parts of the article such as “Abstract”, “Discussions”, “Results” originate from this part.
- Care should be taken not to deviate from the purpose stressed in the “Introduction” section of the article when dealing the topics. Information that does not contribute to the achievement of the purpose of the article or that is not used to reach the conclusion should not be included.
- All data used in this section and all opinions put forward should be proven by the findings obtained from the studies or based on a source by reference.

- The way and method to be followed in handling the topics vary according to the characteristics of the topics covered.
- Subject headings in necessary numbers with different stages should be used in this section.

### 5.7. Discussions

- The data and findings objectively conveyed in the “Main Text” section of the article should be discussed by the author in this section. Discussions should be separate from the “Results” section.

### 5.8. Results

- New data and findings obtained from the review that constitutes the subject of the article should be stated concisely and concretely in this section.
- Subjects that are not adequately addressed and / or covered in the main text should not be included in this section.
- The results can be given as items in order to emphasize the research results and make the expression understandable.

### 5.9. Acknowledgements

- In this section, important contributions in the realization of the study, which is the subject of the article, are indicated. An attitude that will distract this section from its main purpose should not be taken in the Acknowledgements.

Contribution should be stated as short and concise as possible to the persons and/or organizations that provided assistance (reading, writing, language assistance, etc.) during the research, and should not take an attitude that would distract this section from its main purpose.

### 5.10. References

- In this section, only the documents mentioned in the article should be included in complete.
- Abbreviations should be avoided in naming the publications and journals.
- The mentioned documents should be written in Times New Roman and 9 pt.
- The first line of the references should be written as justified to the left margin of the page, and the other lines should be written by giving a hanging indent value of 1.25.

- The references should be listed in alphabetical order, taking into account the surnames of the authors.
- If one author has more than one work in the same year, lowercase alphabet letters should be used right after the year of publication and the letters should be italic (e.g. Saklar, 2011*a, b*).
- If more than one document of the same author is cited, first his / her single-name publications in chronological order, then double-names according to the chronological order, and then multi-names according to chronological order should be given.

#### *For example:*

- Corradini, C. 2007. The conodont genus *Pseudooneotodus* Drygant from the Silurian and Lower Devonian of Sardinia and the Carnic Alps (Italy). *Bollettino-Societa Paleontologica Italiana* 46 (2/3), 139-148.
- Corradini, C., Serpagli E. 1999. A Silurian conodont biozonation from late Llandovery to end Pridoli in Sardinia (Italy), In Serpagli (Ed.), *Studies on conodonts: Proceedings of the 7th European Conodont Symposium*. *Bollettino della Società Paleontologica Italiana* 37 (2-3) (1998), 255-273.
- Corradini, C., Corriga, M. G. 2010. Silurian and lowermost Devonian conodonts from the Passo Volaja area (Carnic Alps, Italy). *Bollettino della Società Paleontologica Italiana* 49 (3), 237-253.
- Corradini, C., Corriga, M. G. A. 2012. Pridoli – Lochkovian conodont zonation in Sardinia and the Carnic Alps: implications for a global zonation scheme. *Bulletin of Geosciences* 87 (4), 635-650.
- Corradini, C., Leone, F., Loi, A., Serpagli, E. 2001. Conodont Stratigraphy of A Highly Tectonised Silurian-Devonian Section in The San Basilio Area (Se Sardinia, Italy). *Bollettino Della Societa Paleontologica Italiana* 40 (3), 315-323, 1 Pl.
- Corradini, C., Pondrelli, M., Serventi, P., Simonetto, L. 2003. The Silurian cephalopod limestone in the Monte Cocco area (Carnic Alps, Italy): conodont biostratigraphy. *Revista Española de Micropaleontologia* 35 (3), 285-294.

Corradini, C., Corrigan, M. G., Männik, P., Schönlaub, H. P. 2015. Revised conodont stratigraphy of the Cellon section (Silurian, Carnic Alps). *Lethaia* 48 (1), 56-71.

- If documents of different authors with the same surname are mentioned, they should be written in alphabetical order, considering their first names.
- If documents of different author(s) with the same surname are mentioned in the same year, they should be cited as given below. Same publication rule should be applied for the single author.

***For example:***

“Usta, M., Yetiş, C., Nazik, A. 2018. Anamur (Mersin) dolayının stratigrafisi ve Kambriyen yaşlı kuvarsitler ile dolomitlerin endüstriyel hammadde potansiyeli. Çukurova Üniversitesi Fen ve Mühendislik Bilimleri Dergisi 35, 6, 11-22, Adana”

should be cited as (Usta, M. et. al., 2018)

“Usta, D., Ateş, Ş., Çoban, M., Deveci, Ö, Sağlam, F.M. 2014. Adıyaman-Sincik-Hilvan arasındaki bölgenin stratigrafisi ve kaya türü özellikleri. 67. Türkiye Jeoloji Kurultayı Bildiri Özleri, Ankara, 98-99”

should be cited as (Usta, D. et. al., 2018)

“Usta, M. 2018. Anamur (Mersin) dolayının stratigrafisi ve Kambriyen yaşlı kuvarsitler ile dolomitlerin endüstriyel hammadde potansiyeli. Çukurova Üniversitesi Fen ve Mühendislik Bilimleri Dergisi 35, 6, 11-22, Adana”

should be cited as (Usta, M., 2018)

“Usta, D. 2014. Adıyaman-Sincik-Hilvan arasındaki bölgenin stratigrafisi ve kaya türü özellikleri. 67. Türkiye Jeoloji Kurultayı Bildiri Özleri, Ankara, 98-99”

should be cited as (Usta, D., 2018)

- If the document is in a periodical publication (if it is an article), information about the document is given in the following order: Authors ‘ surname, first letters of the authors’ first names. Year of publication. The name of the article. The name of the publication in which the article was published, volume number and / or issue number with the first letters in capital, the numbers of the first and last page of the document.

Punctuation marks like comma and etc. after journal names should not be used.

- In the examples below, the information about the mentioned documents is organized according to different document types, taking into account the punctuation marks.

***For example:***

Gürsoy, M. 2017. Munzur Dağları Alt Miyosen çökelleri mollusk topluluğu ve paleoekolojisi (Doğu Anadolu, Türkiye). *Maden Tetkik ve Arama Dergisi* 155, 75-99.

Pamir, H. N. 1953. Türkiye’de kurulacak bir Hidrojeoloji Enstitüsü hakkında rapor. *Türkiye Jeoloji Bülteni* 4 (1), 63-68.

Robertson, A. H. F. 2002. Overview of the genesis and emplacement of Mesozoic ophiolites in the Eastern Mediterranean Tethyan region. *Lithos* 65, 1-67.

- If the document is a book: authors’ surnames, authors’ first names. Year of publication. Title of the book with capital letters. The name of the publishing organization or the name of the publication in which the document was published, the volume and / or issue number, and the total number of pages of the book should be specified, respectively.

***For example:***

Einsele, G. 1992. *Sedimentary Basins*. Springer Verlag, 628.

Ketin, İ., Canitez, N. 1956. *Yapısal Jeoloji*. İTÜ, 308.

Meriç, E. 1983. *Foraminiferler*. Maden Tetkik ve Arama Genel Müdürlüğü Eğitim Serisi, 26, 280.

- If the document is published in a book containing the articles of various authors, the usual order for the document included in a periodical publication is followed until the end of the document title. Then the editors’ surnames and initials and the abbreviation of the editor word “Ed.” is written in parentheses. Then, the title of the book in which the document is located is written with the first letters in capital letters. Name of publishing organization. The place of publication, the volume number of the publication in which the document was published, and the numbers of the first and last pages of the document should be written.

**For example:**

Anderson, L. 1967. Latest information from seismic observations. Gaskell, T. F. (Ed.). The Earth's Mantle. Academic Press. London, 335-420.

Göncüoğlu, M. C., Turhan, N., Şentürk, K., Özcan, A., Uysal, S., Yalınız, K. 2000. A geotransverse across northwestern Türkiye. Bozkurt, E., Winchester, J. A., Piper, J. D. A. (Ed.). Tectonics and Magmatism in Türkiye and the Surrounding Area. Geological Society of London. Special Publication, 173, 139-162.

- If it is desired to specify the name of a book in which the writings of various authors are collected as a document; following the surnames and names of the book's editors, in parentheses the "Ed." statement is written. Year of publication. Title of the book with capital letters. The name of the publishing organization or the name of the publication in which the document was published, the volume and / or issue number and the total number of pages of the book should be specified.

**For example:**

Gaskel, T. F. (Ed.). 1967. The Earth's Mantle. Academic Press, 520.

- If the document is "published abstract", information about the document is given in the following order: Authors' surnames, authors' first names. Year of publication. Name of the document (paper). The name, date and place of the meeting where the paper is published, and the first and last page numbers in the book containing the abstract should be written.

**For example:**

Öztunalı, Ö., Yenyol, M. 1980. Yunak (Konya) yöresi kayaçlarının petrojenezi. Türkiye Jeoloji Kurumu 34. Bilim Teknik Kurultayı, Ankara, 36.

Yılmaz, Y. 2001. Some striking features of the Anatolian geology. 4. International Turkish Geology Symposium, 24-28 Eylül 2001, Adana, 13-14.

- If the mentioned document has not been published like report, lecture notes and etc., the word "unpublished" should be written at the end of the information about the document in parentheses after the information about the document is given

in the usual order for the document in a periodical publication.

**For example:**

Akyol, E. 1978. Palinoloji ders notları. EÜ Fen Fakültesi Yerbilimleri Bölümü, 45, İzmir (unpublished).

Özdemir, C., Biçen, C. 1971. Erzincan ili, İliç ilçesi ve civarı demir etütleri raporu. Maden Tetkik Arama Genel Müdürlüğü, Rapor No: 4461, 21, Ankara (unpublished).

- For unpublished courses, seminars and similar notes, the course organizer after document name. The place of the meeting. Title of the book and relevant page numbers should be given.

**For example:**

Walker, G.R., Mutti, E. 1973. Turbidity facies and facies associations. Society for Sedimentary Geology Pacific Section Short Course. Anaheim. Turbitides and Deep Water Sedimentation, 119-157.

- If the document is a thesis; author's surname, initial of the author's first name. Year of publication. Name of the thesis. The type of the thesis, the university where it was given, the total number of pages, its province and the word "unpublished" are written in parentheses.

**For example:**

Akıllı, H. 2019. Polatlı-Haymana (Ankara) civarı sıcak sularının izotop jeokimyası ( $\delta^{18}O$ ,  $\delta D$ ,  $3H$ ,  $\delta^{13}C$ ,  $\delta^{34}S$ ,  $87Sr/86Sr$ ) ve ana iz element bileşimleri ile incelenmesi. PhD Thesis, Ankara University, 255, Ankara (unpublished).

Argun Aktan, Ö. 2019. Marmara Denizi Batı Kıta Sahaneliği Yüzeysel Çökellerinde Jeojenik ve Antropojenik Ağır Metal Zenginleşmesine Yönelik Araştırmalar (Şarköy Kanyonu, KB Türkiye). MSc Thesis, Ankara University, 179, Ankara.

- Anonymous works should be arranged according to the publishing institution.

**For example:**

MTA. 1964. 1/500.000 ölçekli Türkiye Jeoloji Haritası, İstanbul Paftası. Maden Tetkik ve Arama Genel Müdürlüğü, Ankara.

- For the documents that are in print, no date is put after the name of the author, the name of the article and the source to be published should be specified and the word “in print” and / or “in review” should be written at the end (in parentheses).

***For example:***

Ishihara, S. The granitoid and mineralization. Economic Geology 75<sup>th</sup> Anniversary (in press).

- Information downloaded from the Internet should be given in the form of the name of the institution, its web address, and the date on which the web address was accessed. Turkish references should be given directly in Turkish and should be written in Turkish characters.

***For example:***

ERD (Earthquake Research Department of Türkiye). <http://www.afad.gov.tr>. 3 March 2013.

- While citing the source, the original language should be adhered to, and the title of the article should not be translated.

## **6. Illustrations**

- All of the drawings, photographs, plates and tables used in the article are referred to as “illustrating”.
- Illustrations should be used when their use is unavoidable or when they make the subject easier to understand.
- In the selection and arrangement of the format and size of the illustrations, an attitude should be made to prevent loss of space as much as possible considering the page length and layout of the bulletin.
- The number of illustrations used should be proportional to the size of the text.
- All illustrations should be submitted in separate files regardless of the text.
- Abbreviations should not be used in illustration explanations in the text and should be numbered in the order of mention within the text.
- Photographs and plates must be submitted as a computer file in which all details can be seen for the examination of the article, with EPS, TIFF or JPEG extension and at least 300 dpi resolution.

## **6.1. Figures**

- Drawings and photographs other than the plate to be included in the article are evaluated together as “Figure” and numbered in the order of mention in the text.
- The figures should be prepared in computer considering the dimensions of a single column width as 7.4 cm or double column width as 15.8 cm. The figure area with its caption should not exceed 15.8x21 cm.
- While preparing the figures, unnecessary details should not be included and care should be taken not to use more space than necessary for the transfer of information.
- In figure descriptions, a space should be left after the word “Figure” is written, and the number is given in the usual sequence number, followed by a hyphen (-) and a space again, and a description of the relevant figure should be written. If the figure legend exceeds the bottom lines, the following lines should to be written after the “Figure 1-” statement alignment. Figure descriptions should be created as follows, without exceeding the edges of the figure and justified on both sides.

***For example:***

Figure 1- The district of Sandıklı (Afyon); a) geological map of the southwest, b) the general vertical section of the study area (Seymen, 1981), c) Türkiye’s most important neotectonic structures (modified from Koçyiğit, 1994).

- Drawings should be drawn in computer properly, clean and with care.
- The use of thin lines that may disappear when minimized in figures should be avoided.
- Symbols or letters used in all drawings should not be less than 2 mm (7 pt.) in Times New Roman.
- All standardized symbols used in the drawings should preferably be explained in the drawing, if they are too long then they should be explained in the figure below.
- Bar scale should be used in all drawings and the north direction should be indicated on all maps.
- The name of the author, description of the figure, figure number should not be included in the drawing.

- Photographs should reflect the aims of the subject and should be in adequate numbers.
- Figures should be framed.

## 6.2. Plates

- Plates should be used in cases where multiple photographs are required to be printed together on a special paper.
- Plate dimensions must be equal to the size of the bulletin's usable area of the page.
- Figure numbers should be written under each of the figures on the plate and bar scale should be used.
- Original plates must be attached to the final copy to be submitted in the case of acceptance of the manuscript.
- Figures and plates should be numbered among themselves and independently. Figures should be numbered with Latin numerals and plates with Roman numerals (eg Figure 1, Plate I).
- There should be no explanation text on the figures inside the plate.

## 6.3. Tables

- All tables should be arranged in word format and should be prepared in Times New Roman.
- Tables should not exceed the size of 15x8 cm together with the table caption.
- Table explanations should be created without exceeding the edges of the figure and justified as in the example below.

### *For example:*

Table 1- Hydrogeochemical analysis results of geothermal waters in the study area.

## 7. Nomenclature and Abbreviation

- Abbreviations must be in the accepted international or national form. Unusual nomenclature and abbreviations that are not standardized in the article should be avoided. In cases where it is deemed necessary to use such nomenclature and abbreviations, the way and method followed should be explained.
- There should not be a dot between the words initials used in standard abbreviations (such as MTA, DSİ).
- Abbreviations of geography aspects should be made in English (N, S, E, W, NE and etc.).

The word group to be abbreviated should be written clearly where it is mentioned first time and the abbreviation should be given in parentheses, then only the abbreviated form should be written throughout the article.

- Systems with international validity (m, inch, etc.) should be used as the unit of measure. Decimals should be separated with commas in Turkish articles and with a period in English articles.
- The names of figures, plates and tables in the article should not be abbreviated. For example, "As seen in the generalized stratigraphic section of the region (Figure 1) ....."

## 7.1. Chronostatigraphic and Geochronologic Nomenclature

- "International Chronostratigraphic Chart" (<https://stratigraphy.org/chart>), which is updated annually by the International Stratigraphic Committee, should be taken into consideration in chronostratigraphic and geochronological nomenclature.
- Position within a chronostratigraphic unit can be expressed in adjectives indicating the position, for example: lower, middle, upper and etc. When using these adjectives, it should be decided whether the lower, middle and upper distinction is formal / informal in the International Chronostratigraphic Chart.

### *For example:*

lower Miocene, Upper Holocene and etc.

- When stating the time where a geochronological unit is, temporal adjectives such as; early, middle, late and etc. are used. When using these adjectives, the International Chronostratigraphic Chart should be taken into consideration to decide whether the adjectives begin with capital or lowercase letters.

### *For example:*

early Miocene, Late Holocene etc.

## 7.2. Paleontological Nomenclature and Spelling of Fossil Names

- Original names of fossils should be used.

### *For example:*

*Nummulites* with limestone

- Fossil genus and species names are written in italics, cf., aff. and gr. etc. expressions are written as normal (perpendicular). When writing fossil names for the first time, the surnames of the people who identify them and the year in which they were first defined should be written. In later uses, the surnames and the year in which they are defined may not be written. The surnames and dates of identifiers coming at the end of the fossil names are not references, they should not be included in the mentioned documents.

**For example:**

*Alveolina aragonensis* Hottinger, 1960 not a reference.

*Alveolina* cf. *aragonensis* Hottinger, 1960 not a reference.

*Alveolina* aff. *aragonensis* Hottinger, 1960 not a reference.

*Alveolina* gr. *aragonensis* Hottinger, 1960 not a reference.

- After the first use of the same genus in the text is written clearly, it can be abbreviated as in the example so that it will not be confused with another genus in later use.

**For example:**

*Alveolina aragonensis*, *A. polathensis*, *A. ellipsoidalis* etc.

- If the date is in parentheses after the person describing it after the name of the fossil in the text, this is a reference and should be included in the mentioned documents.

**For example:**

*Alveolina aragonensis* Hottinger (1960) is a reference.

- The following rules should be taken into account when writing the systematic paleontologic section.
  - a. First of all, genus, species and subspecies to be identified should be written in hierarchical order like the order, upper family, family type species and so on. Later, the species to be described should be written together with the surnames and date of the people who defined the subspecies name. If there is a photograph of the described fossil, the plate or figure with the photograph should be added under the fossil name. The names of the authors listed here are not references, so they are not included in the reference.

**For example:**

Order: Foraminiferida Eichwald, 1830

Superfamily: Alveolinacea Ehrenberg, 1839

Family: Alveolinidae Ehrenberg, 1839

Type Genus: *Borelis* de Montfort, 1808

Type Species: *Borelis melenoides* de Montfort, 1808  
= *Nautilus melo* Fichtel and Moll, 1798

*Borelis vonderschmitti* (Schweighauser, 1951)

(Plate II, Figure 3-5 or Figure 3A-H).

- b. Similar or synonyms (synonym) list should be left-aligned in chronological order. The page and figure number of the synonymous fossil in the relevant study should be included in the synonymous list. Authors in the synonymous list are references and must be included in the references.

**For example:**

**1951** *Neoalveolina vonderschmitti* **Schweighauser**, page 468, Figures 1-4.

**1974** *Borelis vonderschmitti* (Schweighauser), **Hottinger**, page 67, plate 98, Figures 1-7.

- c. After the synonymous list is given, the definition, explanations (similarities and differences), dimensions, material, stratigraphic distribution (according to the characteristics of the fossil) should be written.
- d. If the fossil is defined for the first time (new species) in the systematic paleontology section, the origin of the name, holotype, type locality, material, description, explanation (similarity and differences), age and geographical distribution, dimensions (according to the features that define the fossil) should be written. Photographs of the fossil identified for the first time by the authors must necessarily be placed in plates or figures.
- e. Bar scale indicating the size of fossils must be used definitely in plates / figures.

**8. References**

- In the references to be made in the Main Text, only the surnames of the authors and the publication year of the mentioned article should be specified. Referencing should be arranged according to one of the following examples:
- Referring to a publication with a single author (in chronological order):

-Altınlı (1972, 1976) defined the Bilecik sandstone in detail.

It is known that the fold axes of the Devonian and Carboniferous units around İstanbul are N-S trending (Ketin, 1953, 1956; Altınlı, 1999).

- Referring to a publication with two authors:
  - The upper parts of the unit include Ilerdian fossils (Sirel and Gündüz, 1976; Keskin and Turhan, 1987, 1989).
- Referring to a publication with more than two authors:
  - According to Caner et al. (1975), the Alıcı formation reflects the conditions of fluvial environment.
  - Unit disappears by wedging towards E (Tokay et al., 1984).
- Referring to a reference in another publication:

It is known that Lebling mentioned about the existence of Liassic around Çakraz (Lebling, 1932; Charles, 1933).

- When referring to the works of the authors with the same surname in the same year, referring the authors' first names by writing their initials:
  - Many studies have been done in the field of structural geology in the study area (Gutnic et al., 1979; Yılmaz A., 1983; Yılmaz, İ., 1983; Poisson et al., 1984 etc.).

## 9. Prints Sent to Authors

Two copies of the relevant issue published in the Bulletin of the Mineral Research and Exploration are sent to the authors.

## 10. Terms of Publication and Copyrights

- Some or all of the articles to be published in the Bulletin of the Mineral Research and Exploration should not have been published before.
- Authors who submit a publication to the Bulletin of the Mineral Research and Exploration are deemed to have accepted the bulletin's publication rules in advance.
- The copyright of the manuscripts accepted for publication and converted into publications belongs to the General Directorate of Mineral Research and Exploration (MTA).

The authors of the study sign the relevant forms within the scope of the provisions specified in the Regulation of the Editorial Board regarding the transfer of copyright and submit them to the Editorial Board. After the publication of the article, MTA may pay royalty fees to the authors of the article for their declarations within the scope of the "Regulation on the Editorial and Processing Fees to be paid by the Public Organizations and Institutions".

NOTE: Information and forms about Bulletin of the Mineral Research and Exploration can be accessed from the website: <http://dergi.mta.gov.tr/index.php>.